

**OFFICE OF CIVILIAN RADIOACTIVE WASTE MANAGEMENT
ANALYSIS/MODEL COVER SHEET**
Complete Only Applicable Items

1. QA: QA

Page: 1 of 313

<p>2. <input type="checkbox"/> Analysis Check all that apply</p> <table border="1" style="width:100%; border-collapse: collapse;"> <tr> <td style="width:20%;">Type of Analysis</td> <td> <input type="checkbox"/> Engineering <input type="checkbox"/> Performance Assessment <input type="checkbox"/> Scientific </td> </tr> <tr> <td>Intended Use of Analysis</td> <td> <input type="checkbox"/> Input to Calculation <input type="checkbox"/> Input to another Analysis or Model <input type="checkbox"/> Input to Technical Document <input type="checkbox"/> Input to other Technical Products </td> </tr> <tr> <td colspan="2">Describe use:</td> </tr> </table>	Type of Analysis	<input type="checkbox"/> Engineering <input type="checkbox"/> Performance Assessment <input type="checkbox"/> Scientific	Intended Use of Analysis	<input type="checkbox"/> Input to Calculation <input type="checkbox"/> Input to another Analysis or Model <input type="checkbox"/> Input to Technical Document <input type="checkbox"/> Input to other Technical Products	Describe use:		<p>3. <input checked="" type="checkbox"/> Model Check all that apply</p> <table border="1" style="width:100%; border-collapse: collapse;"> <tr> <td style="width:20%;">Type of Model</td> <td> <input checked="" type="checkbox"/> Conceptual Model <input type="checkbox"/> Abstraction Model <input checked="" type="checkbox"/> Mathematical Model <input type="checkbox"/> System Model <input checked="" type="checkbox"/> Process Model </td> </tr> <tr> <td>Intended Use of Model</td> <td> <input type="checkbox"/> Input to Calculation <input checked="" type="checkbox"/> Input to another Model or Analysis <input checked="" type="checkbox"/> Input to Technical Document <input type="checkbox"/> Input to other Technical Products </td> </tr> <tr> <td colspan="2">Describe use: This model is used to provide TH information and data for use in other technical products.</td> </tr> </table>	Type of Model	<input checked="" type="checkbox"/> Conceptual Model <input type="checkbox"/> Abstraction Model <input checked="" type="checkbox"/> Mathematical Model <input type="checkbox"/> System Model <input checked="" type="checkbox"/> Process Model	Intended Use of Model	<input type="checkbox"/> Input to Calculation <input checked="" type="checkbox"/> Input to another Model or Analysis <input checked="" type="checkbox"/> Input to Technical Document <input type="checkbox"/> Input to other Technical Products	Describe use: This model is used to provide TH information and data for use in other technical products.	
Type of Analysis	<input type="checkbox"/> Engineering <input type="checkbox"/> Performance Assessment <input type="checkbox"/> Scientific												
Intended Use of Analysis	<input type="checkbox"/> Input to Calculation <input type="checkbox"/> Input to another Analysis or Model <input type="checkbox"/> Input to Technical Document <input type="checkbox"/> Input to other Technical Products												
Describe use:													
Type of Model	<input checked="" type="checkbox"/> Conceptual Model <input type="checkbox"/> Abstraction Model <input checked="" type="checkbox"/> Mathematical Model <input type="checkbox"/> System Model <input checked="" type="checkbox"/> Process Model												
Intended Use of Model	<input type="checkbox"/> Input to Calculation <input checked="" type="checkbox"/> Input to another Model or Analysis <input checked="" type="checkbox"/> Input to Technical Document <input type="checkbox"/> Input to other Technical Products												
Describe use: This model is used to provide TH information and data for use in other technical products.													

4. Title:

Multiscale Thermohydrologic Model

5. Document Identifier (including Rev. No. and Change No., if applicable):

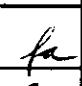


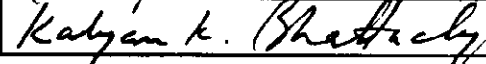
ANL-EBS-MD-000049 REV 00

6. Total Attachments:

0

7. Attachment Numbers - No. of Pages in Each:

See block 12 for attachment numbers

	Printed Name	Signature	Date
8. Originator	Thomas Buscheck	<i>for</i> 	Date 4/17/00
9. Checker	Hang Yang, Ming Lin	<i>for</i> 	04/17/2000
10. Lead/Supervisor	Thomas Buscheck	<i>for</i> 	4/17/00
11. Responsible Manager	Dwayne Chesnut	<i>for</i> 	4/17/00

12. Remarks:

I-2, II-6, III-2, IV-2, V-3, VI-3, VII-2, VIII-2, IX-4, X-2, XI-3, XII-2, XIII-2, XIV-3, XV-3, XVI-3, XVII-4, XVIII-1, XIX-7, XX-2

**OFFICE OF CIVILIAN RADIOACTIVE WASTE MANAGEMENT
ANALYSIS/MODEL REVISION RECORD**

Complete Only Applicable Items

1. Page: 2 of:

2. Analysis or Model Title:

Multiscale Thermohydrologic Model

3. Document Identifier (including Rev. No. and Change No., if applicable):

ANL-EBS-MD-000049 REV 00

4. Revision/Change No.

5. Description of Revision/Change

00

Initial Issue

CONTENTS

	Page
1. PURPOSE.....	16
1.1 OBJECTIVES	16
1.2 WORK SCOPE	16
1.3 PRIMARY TASKS	18
2. QUALITY ASSURANCE.....	22
3. COMPUTER SOFTWARE AND MODEL USAGE.....	23
3.1 DESCRIPTION OF SOFTWARE	24
3.1.1 NUFT v3.0s	24
3.1.2 RADPRO v3.22	24
3.1.3 XTOOL v10.1.....	24
3.1.4 MSTHAC v6.2.....	24
3.2 DESCRIPTION OF ROUTINES AND MACROS.....	25
3.2.1 MakeColumns v1.0.....	25
3.2.2 Rme6 v1.1.....	25
3.2.3 Define_EBS_fineGrid v1.3.....	25
3.2.4 ReadsUnits v1.0.....	25
3.2.5 AddLayers v1.0.....	26
3.2.6 Heat_DDT v1.0.....	26
3.2.7 Heat_SMT v1.0.....	26
3.2.8 Cover v1.1.....	26
3.2.9 ColumnInfiltration v1.1	26
3.2.10 Chim_surf_TP v1.0.....	26
3.2.11 Chim_wt_TP v1.0.....	27
3.2.12 Xairtab v1.8	27
3.2.13 Infiltrab v1.0.....	27
3.2.14 Rock_sun v1.0	27
3.2.15 SMT_surf_bc v1.1	27
3.2.16 SMT_bot_bc v1.1	28
3.2.17 Bound v1.0.....	28
3.2.18 Addlay v1.0.....	28
3.2.19 INPUT ASSEMBLY	28
3.2.20 HeatgenAge v1.2	28
3.2.21 SplitEXT v1.0.....	29
3.2.22 YMESH v1.53	29
3.2.23 CONVERTCOORDS v1.1	29
3.3 DATA FLOW.....	29
4. INPUTS	54
4.1 DATA AND PARAMETERS.....	54

4.1.1	Geometric Description of the EBS and Material Properties.....	54
4.1.1.1	Repository Footprint.....	54
4.1.1.2	Drift Spacing and Waste-Package Sequencing	54
4.1.1.3	Waste Package Spacing.....	54
4.1.1.4	Drift Diameter	54
4.1.1.5	Angle of Repose of Backfill.....	55
4.1.1.6	Minimum Depth of Backfill Cover	55
4.1.1.7	Location of Backfill Peak.....	55
4.1.1.8	Intersection Between Backfill and Drift Wall	55
4.1.1.9	Drip Shield Thickness	55
4.1.1.10	Drip Shield Radius	55
4.1.1.11	Location of Waste Package	55
4.1.1.12	Waste Package Diameter.....	56
4.1.1.13	Gap Between Waste Package and Drip Shield.....	56
4.1.1.14	Gap Between Waste Package and Invert.....	56
4.1.1.15	Invert Height.....	56
4.1.1.16	Properties of Air at Model Boundaries.....	56
4.1.1.17	Properties of EBS Materials.....	56
4.1.1.18	Hydrologic and Thermal Properties of Stratigraphic Units.....	57
4.1.1.19	Thermal Properties of Air Inside the Drifts.....	57
4.1.1.20	Thermal Properties of Stratigraphic Units for SMT Submodels...	58
4.1.1.21	Effective Thermal Conductivity of Cavities Inside Drifts	58
4.1.2	Stratigraphy.....	62
4.1.3	Infiltration Flux.....	62
4.1.4	Heat-Generation Rate	62
4.1.5	Boundary Conditions	62
4.1.6	Enthalpy	63
4.2	CRITERIA.....	64
4.3	CODES AND STANDARDS	65
5.	ASSUMPTIONS.....	68
5.1	BOUNDARY CONDITIONS	68
5.1.1	AREAL BLOCK MODEL.....	68
5.1.2	Gaussian Interpolation	68
5.1.3	Inverse Distance Interpolation	68
5.1.4	Relative Humidity at Ground Surface.....	69
5.1.5	LDTH Boundary Conditions.....	69
5.1.6	SMT, DDT, and SDT Boundary Conditions	69
5.2	MATERIAL PROPERTIES	69
5.2.1	Permeability of Drip Shield and Waste Package	69
5.2.2	Tortuosity of Backfill and Invert Materials	70
5.2.3	Satiated Saturation of Invert and Backfill Materials.....	70
5.2.4	Thermal Conductivity Used in Conduction-Only Submodels	70
5.2.5	Saturated-Zone Thermal Conductivity	70
5.2.6	Thermal Conductivity and Density for the Active Fracture Model	71

5.3	HEAT TRANSFER.....	71
5.3.1	Horizontal Thermal Conduction.....	71
5.3.2	Constant Heat Flux	71
6.	ANALYSIS / MODEL	74
6.1	MSTHM CONCEPTUAL MODEL.....	75
6.2	SMT SUBMODELS	76
6.2.1	SMT Repository Footprint.....	76
6.2.2	SMT-Submodel Mesh.....	77
6.2.3	SMT Submodel Boundary Conditions.....	77
6.2.4	SMT Submodel Heat Generation Rates.....	77
6.2.5	SMT Submodel Material Properties	77
6.2.6	Submodel Simulations	78
6.3	LDTH SUBMODELS	78
6.3.1	LDTH Submodel Locations.....	79
6.3.1.1	Stratigraphic Columns.....	79
6.3.1.2	Vertical Location of Repository Horizon.....	83
6.3.2	LDTH Submodel Mesh.....	84
6.3.2.1	Pre-closure LDTH Submodel Mesh.....	84
6.3.2.2	Post-closure LDTH Submodel Mesh	85
6.3.3	LDTH Submodel Boundary Conditions	85
6.3.4	LDTH Submodel Heat Generation Rates	86
6.3.5	LDTH Submodel Material Properties.....	87
6.3.6	Infiltration Flux.....	87
6.3.7	LDTH Submodel Simulations	87
6.4	SDT SUBMODELS	88
6.4.1	SDT Submodel Locations.....	88
6.4.2	SDT Submodel Mesh.....	88
6.4.3	SDT Submodel Boundary Conditions	88
6.4.4	SDT Submodel Heat Generation Rates	89
6.4.5	SDT Submodel Material Properties.....	89
6.4.6	SDT Submodel Simulations	89
6.5	DDT SUBMODELS.....	90
6.5.1	DDT Submodel Location.....	90
6.5.2	DDT Submodel Mesh.....	90
6.5.2.1	Pre-closure DDT Submodel	91
6.5.2.2	Pre-closure (Restart) DDT Submodel	91
6.5.2.3	Post-closure DDT Submodel.....	91
6.5.3	DDT Submodel Boundary Conditions.....	91
6.5.4	DDT Submodel Heat Generation Rates.....	92
6.5.5	DDT Submodel Material Properties	92
6.5.6	DDT Submodel Simulations.....	93
6.6	MSTHAC METHODOLOGY	93
6.6.1	Accounting for the Influence of Drift Ventilation	93
6.6.2	Accounting for the Emplacement of Backfill	94

6.6.3	Computing Drift-Wall Temperatures.....	94
6.6.4	Computing Host-Rock Temperatures	96
6.6.5	Computing Backfill, Drip Shield, and Invert Temperatures.....	96
6.6.6	Computing Waste Package Temperatures	96
6.6.7	Computing Drift-Wall Relative Humidity	97
6.6.8	Computing Host-Rock Relative Humidity	97
6.6.9	Computing Relative Humidity on the Drip Shield	97
6.6.10	Computing Relative Humidity in the Backfill	98
6.6.11	Computing Relative Humidity in the Invert	98
6.6.12	Computing Waste-Package Relative Humidity	98
6.6.13	Computing Liquid-Phase Flux in the Host Rock.....	99
6.6.14	Computing Liquid-Phase Flux on the Drip Shield	99
6.6.15	Computing Liquid-Phase Flux in the Backfill	99
6.6.16	Computing Liquid-Phase Flux in the Invert	99
6.6.17	Computing Liquid Saturation at the Drift Wall.....	100
6.6.18	Computing Liquid Saturation on the Drip Shield.....	100
6.6.19	Computing Liquid Saturation in the Invert.....	100
6.6.20	Computing Gas-Phase Air-Mass Fraction Adjacent to Drip Shield	100
6.6.21	Computing Gas-Phase Pressure Adjacent to Drip Shield.....	100
6.6.22	Computing Gas-Phase Flux of Air	100
6.6.23	Computing Gas-Phase Flux of Water Vapor	100
6.6.24	Computing Capillary Pressure on the Drip Shield.....	101
6.6.25	Computing Capillary Pressure on the Drift Wall.....	101
6.6.26	Computing Capillary Pressure in the Invert.....	101
6.6.27	Computing Evaporation Rate on the Drip Shield	101
6.6.28	Computing Evaporation Rate at the Top of the Backfill	101
6.6.29	Computing Evaporation Rate in the Invert	101
6.6.30	Binning TH Results	102
6.7	OVERVIEW OF DATA FLOW	102
6.8	SUBMODEL PREPARATION	102
6.8.1	Mesh Generation.....	103
6.8.1.1	YMESS Input	103
6.8.1.2	Drift-Scale-Submodel Meshes	104
6.8.1.3	Mountain-Scale Submodel Mesh	105
6.8.2	Material Properties.....	106
6.8.3	Heat-Generation Rate	106
6.8.4	Infiltration Flux.....	106
6.8.5	Boundary Conditions	107
6.9	SUBMODEL EXECUTION	108
6.9.1	LDTH Simulations.....	108
6.9.2	SDT Simulations.....	109
6.9.3	DDT Simulations	109
6.9.4	SMT Simulations	110
6.10	MSTHAC EXECUTION	110
6.11	MSTHM RESULTS.....	111

6.11.1	Temperature Distributions	114
6.11.1.1	Temperature Distributions for Mean Infiltration Case.....	114
6.11.1.2	Temperature Distributions for High Infiltration Case.....	114
6.11.1.3	Temperature Distributions for Low Infiltration Case.....	115
6.11.1.4	Temperature Analysis.....	115
6.11.2	Relative Humidity Distributions.....	117
6.11.2.1	Relative Humidity Distributions for Mean Infiltration Case.....	117
6.11.2.2	Relative Humidity Distributions for High Infiltration Case.....	117
6.11.2.3	Relative Humidity Distributions for Low Infiltration Case	117
6.11.2.4	Relative Humidity Analysis	118
6.11.3	Gas-Phase Air-Mass Fraction Distributions	119
6.11.3.1	Gas-Phase Air-Mass Fraction Distributions for Mean Infiltration Case	119
6.11.3.2	Gas-Phase Air-Mass Fraction Distributions for High Infiltration Case	119
6.11.3.3	Gas-Phase Air-Mass Fraction Distributions for Low Infiltration Case	119
6.11.3.4	Gas-Phase Air-Mass Fraction Analysis.....	120
6.11.4	Liquid-Phase Flux Distributions.....	120
6.11.4.1	Liquid-Phase Flux Distributions for Mean Infiltration Case.....	120
6.11.4.2	Liquid-Phase Flux Distributions for High Infiltration Case.....	123
6.11.4.3	Liquid-Phase Flux Distributions for Low Infiltration Case	125
6.11.4.4	Liquid-Phase Flux Analysis	128
6.11.5	Evaporation Rate Distributions.....	128
6.11.5.1	Evaporation Rate Distributions for Mean Infiltration Case	129
6.11.5.2	Evaporation Rate Distributions for High Infiltration Case	129
6.11.5.3	Evaporation Rate Distributions for Low Infiltration Case	130
6.11.5.4	Evaporation Rate Analysis	130
6.11.6	Influence of Variability of Heat Generation from Waste Packages.....	130
6.11.6.1	Temperature and Relative Humidity on Different Waste-Package Types	131
6.11.7	Influence of Overburden Thickness.....	131
6.12	MODEL VALIDATION	131
6.12.1	Comparison of NUFT TH Model against the Large Block Test.....	132
6.12.2	Comparison of NUFT TH Model against the Drift Scale Test.....	133
6.12.3	Comparison of MSTHM against an Alternative Conceptual Model	134
7.	CONCLUSIONS	302
7.1	UNCERTAINTIES OF THE AMBIENT AND THERMALLY PERTURBED SYSTEM.....	306
8.	INPUTS AND REFERENCES.....	308
8.1	DOCUMENTS CITED	308
8.2	PROCEDURES CITED	310
8.3	SOURCE DATA.....	310

9. ATTACHMENTS.....	313
---------------------	-----

FIGURES

Figure 1-1. Schematic of conceptual models used by the MSTHM, including (a) SDT submodel, (b) LDTH submodel, (c) DDT submodel, and (d) SMT submodel.....	19
Figure 1-2. Overall data flow diagram for the MSTHM.	20
Figure 1-3. Data flow diagram for the MSTHM that shows the relationship between the input data and submodels for the three infiltration flux scenarios addressed in Rev 00.	21
Figure 3-1. Legend for data flow diagrams.	43
Figure 3-2. Generation of numerical meshes for all submodels.....	44
Figure 3-3. Preparation of heat generation curves for all submodels.....	45
Figure 3-4. Preparation of infiltration data for LDTH submodels.	46
Figure 3-5. Preparation of boundary conditions for submodels.	47
Figure 3-6. Creation of scripts to generate families of LDTH submodels.	48
Figure 3-7. Material properties of the natural system.	49
Figure 3-8. Material properties of the EBS.	49
Figure 3-9. Execution of LDTH submodels.	50
Figure 3-10. Execution of SDT submodels.	51
Figure 3-11. Execution of DDT submodels.	52
Figure 3-12. Execution of SMT submodels.	53
Figure 4-1. Diagram showing drift spacing, WP lengths, and WP spacing that is used in Rev 00 of this AMR (DTN: SN9908T0872799.004).	66
Figure 4-2. The cross-sectional geometry of the emplacement drift after backfill is emplaced that is used in Rev 00 of this AMR (DTN: SN9908T0872799.004).....	67
Figure 5-1. Comparison of the actual repository footprint and the approximation of the repository footprint that is assumed in the MSTHM.....	72
Figure 5-2. The 31 drift-scale submodel locations used in the MSTHM.....	73
Figure 6-1. Repository-scale numerical mesh of the repository area used in the MSTHM.	137

Figure 6-2. Cross-sectional view of the numerical mesh used in the pre-closure LDTH submodels.....	138
Figure 6-3. Cross-sectional view of the numerical mesh used in the post-closure LDTH submodels.....	139
Figure 6-4. Cross-sectional view of the numerical mesh used in the pre-closure DDT submodel.	140
Figure 6-5. Cross-sectional view of the numerical mesh used in the pre-closure DDT submodel that is used to generate the restart file to start the post-closure DDT submodel.....	141
Figure 6-6. Cross-sectional view of the numerical mesh used in the post-closure DDT submodel.	142
Figure 6-7. Temperature on the surface of a 21-PWR WP for the mean infiltration-flux case for the indicated times.....	143
Figure 6-8. Temperature on the crown of the drift (or upper drift wall) immediately above a 21-PWR WP for the mean infiltration-flux case for the indicated times.	149
Figure 6-9. Temperature on the lower drift wall immediately below a 21-PWR WP for the mean infiltration-flux case for the indicated times.	152
Figure 6-10. Temperature on the surface of a 21-PWR WP for the high infiltration-flux case for the indicated times.....	155
Figure 6-11. Temperature on the surface of a 21-PWR WP for the low infiltration-flux case for the indicated times.....	161
Figure 6-12. The complementary cumulative distribution function (CCDF) for the maximum lateral extent of the boiling point ($T = 96^{\circ}\text{C}$) isotherm is plotted for the mean, high, and low infiltration-flux cases.....	167
Figure 6-13. Temperature history on the surface of a 21-PWR WP for the mean infiltration-flux case at (a) the geographical center of the repository and (b) a location 27.5 m from the eastern edge of the repository.	168
Figure 6-14. Peak WP temperature for the mean, high, and low infiltration-flux cases.	169
Figure 6-15. Peak temperature on the lower drift wall (below the invert) for the mean, high, and low infiltration-flux cases.....	170
Figure 6-16. Relative humidity on the surface of a 21-PWR WP for the mean infiltration-flux case for the indicated times.	171

Figure 6-17. Relative humidity on the surface of a 21-PWR WP for the high infiltration-flux case for the indicated times.	179
Figure 6-18. Relative humidity on the surface of a 21-PWR WP for the low infiltration-flux case for the indicated times.	187
Figure 6-19. The complementary cumulative distribution function (CCDF) for the time required to attain a relative humidity <i>RH</i> of 85% is plotted for the mean, high, and low infiltration-flux cases.	196
Figure 6-20. Relative humidity history on the surface of a 21-PWR WP for the mean infiltration-flux case at (a) the geographical center of the repository and (b) a location 27.5 m from the eastern edge of the repository.	197
Figure 6-21. Relative humidity history on the surface of a 21-PWR WP for the high infiltration-flux case at (a) the geographical center of the repository and (b) a location 27.5 m from the eastern edge of the repository.	198
Figure 6-22. Relative humidity history on the surface of a 21-PWR WP for the low infiltration-flux case at (a) the geographical center of the repository and (b) a location 27.5 m from the eastern edge of the repository.	199
Figure 6-23. Gas-phase air-mass fraction averaged over the perimeter of the drip shield at the location of a 21-PWR WP for the mean infiltration-flux case for the indicated times.	200
Figure 6-24. Gas-phase air-mass fraction averaged over the perimeter of the drip shield at the location of a 21-PWR WP for the high infiltration-flux case for the indicated times.	204
Figure 6-25. Gas-phase air-mass fraction averaged over the perimeter of the drip shield at the location of a 21-PWR WP for the low infiltration-flux case for the indicated times.	208
Figure 6-26. Liquid-phase flux 5 m above the crown of the drift for the mean infiltration-flux case for the indicated times.	212
Figure 6-27. Liquid-phase flux 0.2 m above the crown of the drift for the mean infiltration-flux case for the indicated times.	217
Figure 6-28. Liquid-phase flux averaged over the upper surface of the drip shield for the mean infiltration-flux case for the indicated times.	221
Figure 6-29. Liquid-phase flux adjacent to the lower side of the drip shield (i.e., adjacent to the base of the drip shield) for the mean infiltration-flux case for the indicated times.	225
Figure 6-30. Liquid-phase flux averaged over the invert for the mean infiltration-flux case for the indicated times.	228

Figure 6-31. Liquid-phase flux 5 m above the crown of the drift for the high infiltration-flux case for the indicated times.	232
Figure 6-32. Liquid-phase flux 0.2 m above the crown of the drift for the high infiltration-flux case for the indicated times.	237
Figure 6-33. Liquid-phase flux averaged over the upper surface of the drip shield for the high infiltration-flux case for the indicated times.	241
Figure 6-34. Liquid-phase flux adjacent to the lower side of the drip shield (i.e., adjacent to the base of the drip shield) for the high infiltration-flux case for the indicated times.	245
Figure 6-35. Liquid-phase flux averaged over the invert for the high infiltration-flux case for the indicated times.....	248
Figure 6-36. Liquid-phase flux 5 m above the crown of the drift for the low infiltration-flux case for the indicated times.	252
Figure 6-37. Liquid-phase flux 0.2 m above the crown of the drift for the low infiltration-flux case for the indicated times.	259
Figure 6-38. Liquid-phase flux averaged over the upper surface of the drip shield for the low infiltration-flux case for the indicated times.	263
Figure 6-39. Liquid-phase flux adjacent to the lower side of the drip shield (i.e., adjacent to the base of the drip shield) for the low infiltration-flux case for the indicated times.	268
Figure 6-40. Liquid-phase flux averaged over the invert for the low infiltration-flux case for the indicated times.....	272
Figure 6-41. Liquid-phase flux history at indicated drift-scale locations for the mean infiltration-flux case at (a) the geographical center of the repository and (b) a location 27.5 m from the eastern edge of the repository.....	276
Figure 6-42. Evaporation rate summed over the upper surface of the drip shield for the mean infiltration-flux case for the indicated times.	277
Figure 6-43. Evaporation rate summed over the upper surface of the drip shield for the high infiltration-flux case for the indicated times.	283
Figure 6-44. Evaporation rate summed over the upper surface of the drip shield for the low infiltration-flux case for the indicated times.	288
Figure 6-45. Evaporation rate summed over the upper surface of the dripshield for the mean infiltration-flux case at (a) the geographical center of the repository and (b) a location 27.5 m from the eastern edge of the repository	293

Figure 6-46. Temperature and relative humidity on the WP surface for the mean infiltration-flux case is plotted at the geographical center of the repository for the 4 different WP types and 8 different WP locations (along the drift) considered in the MSTHM (see Figure 4-1 for WP locations).	294
Figure 6-47. The infiltration-flux distribution for the mean infiltration-flux case is plotted, including the present-day, monsoonal, and glacial climate periods.	295
Figure 6-48. The infiltration-flux distribution for the high infiltration-flux case is plotted, including the present-day, monsoonal, and glacial climate periods.	296
Figure 6-49. The infiltration-flux distribution for the low infiltration-flux case is plotted, including the present-day, monsoonal, and glacial climate periods.	297
Figure 6-50. Comparison of the NUFT-simulated and measured temperatures along Borehole TT1 is given at six times from 30 to 400 days.	298
Figure 6-51. Comparison of the NUFT-simulated and measured liquid-phase saturation along Borehole TN3 is given at three times from 100 to 500 days.	299
Figure 6-52. Comparison of the NUFT-simulated and measured temperatures along Borehole ESF-HD-137 is given at 365 and 547 days.	300
Figure 6-53. Comparison of predicted temperatures at (a) center of the repository (14c3 location in Table 2-2 of Buscheck et al., 1998) and (b) 100m from the edge of the repository (14c1 location) for the 12/97 TSPA-VA base-case I x 1 $\alpha_{f,mean}$ parameter set, where the symbol I stands for the nominal infiltration-flux q_{inf} map (average $q_{inf} = 7.8\text{mm/yr}$) for the present-day climate and the variable α_f is the van Genuchten “alpha” parameter for fractures.	301

TABLES

Table 1-1. List of NFE and EBS TH variables calculated with the MSTHM at each repository subdomain.	17
Table 3-1a. Software Validation	23
Table 3-1b. Software Execution.....	23
Table 3-2. N-Table	31
Table 3-3. E-Table.....	32
Table 3-4. File Groups	33
Table 3-5. Software Routine Input and Output Files	35
Table 3-6. LDTH Nuft Input and Output Files.....	39
Table 3-7. SDT Nuft Input and Output Files.....	40
Table 3-8. DDT Nuft Input and Output Files.....	41
Table 3-9. SMT Nuft Input and Output Files.....	42
Table 4-1. Backfill and Invert Material Properties.....	57
Table 4-2. Matrix Properties of Stratigraphic Units.....	59
Table 4-3. Fracture Properties of Stratigraphic Units	60
Table 4-4. Thermal Properties of Stratigraphic Units	61
Table 6-1. Stratigraphic columns used in the 31 drift-scale-submodel locations.	79
Table 6-2. Summary of the vertical location of the repository horizon at the 31 drift-scale-submodel locations.....	84
Table 6-3. Boundary conditions used in the drift-scale submodels (LDTH, SDT, and DDT)....	86
Table 6-4. List of plots of TH conditions that are included in this report.....	113
Table 6-5. RMSD and MD for temperature profile along TT1 using driftscale data set.	133

ACRONYMS

AFC	Active-Fracture Concept
AML	Areal Mass Loading
CCDF	Complementary Cumulative Distribution Function
CRWMS M&O	Civilian Radioactive Waste Management System Management and Operating Contractor
CSNF	Commercial Spent Nuclear Fuel
DDT	Discrete-heat-source, Drift-scale, Thermal-conduction Submodel
DHLW	Defense High-Level Waste
DKM	Dual-Permeability Method
DMTH	Discrete-heat-source, Mountain-scale, Thermohydrologic Submodel
DSNF	Defense Spent Nuclear Fuel
EBS	Engineered Barrier System
HLW	High-Level Waste
IRSR	Issue Resolution Status Report
KTI	Key Technical Issue
LDTH	Line-averaged-heat-source, Drift-scale, Thermohydrologic Submodel
LMTH	Line-averaged-heat-source, Mountain-scale, Thermohydrologic Submodel
MSTHAC	Multiscale Abstraction Code
MSTHM	Multiscale Thermohydrologic Model
NF	Near Field
NFE	Near-field Environment
NRC	Nuclear Regulatory Commission
NUFT	Nonisothermal Unsaturated-Saturated Flow and Transport
RH	Relative Humidity
SDT	Smeared-heat-source, Drift-scale, Thermal-conduction Submodel
SMT	Smeared-heat-source, Mountain-scale, Thermal-conduction Submodel
SZ	Saturated Zone
TBV	To Be Verified
TH	Thermohydrologic
UZ	Unsaturated Zone
WP	Waste Package

1. PURPOSE

The purpose of the Multiscale Thermohydrologic Model (MSTHM) model is to describe the thermohydrologic evolution of the near-field environment (NFE) and EBS throughout the high-level nuclear waste repository at Yucca Mountain for a particular engineering design (CRWMS M&O 2000c). The process-level model will provide TH information and data (such as in-drift temperature, relative humidity, liquid saturation, etc.) for use in other technical products. This data is provided throughout the entire repository area as a function of time (see Table 1-1).

The MSTHM (Figure 1-1) couples the Smeared-heat-source Drift-scale Thermal-conduction (SDT), Line-average-heat-source Drift-scale Thermohydrologic (LDTH), Discrete-heat-source Drift-scale Thermal-conduction (DDT), and Smeared-heat-source Mountain-scale Thermal-conduction (SMT) submodels such that the flow of water and water vapor through partially-saturated fractured rock is considered. The MSTHM accounts for 3-D drift-scale and mountain-scale heat flow, repository-scale variability of stratigraphy and infiltration flux, and WP-to-WP variability in heat output from WPs. All submodels use the NUFT simulation code. The MSTHM is implemented in several data-processing steps (Figure 1-2 and Figure 1-3). The four major steps are (1) submodel input-file preparation, (2) execution of the four submodel families with the use of the NUFT code, (3) execution of the multiscale abstraction code (MSTHAC), and (4) binning and post-processing (i.e., graphics preparation) of the output from MSTHAC. The MSTHM is described in detail in Section 6.

This model is important in assessing post-closure performance.

1.1 OBJECTIVES

The objectives of this Analyses and Model Report (AMR) are to investigate near field (NF) and EBS thermohydrologic environments throughout the repository area at various evolution periods, and to provide TH data that may be used in other process model reports.

1.2 WORK SCOPE

The calculations described in this report do not include the coupling of geochemical or geomechanical processes to predicted TH behavior. The calculations in this report are conducted using the MSTHM and will be based on the following information:

- a. Repository footprint for EDA II will be modeled for a total of 70,000 MTU of waste, including 63,000 MTU of CSNF and 7000 MTU of DHLW. (Extended waste inventories will be addressed in subsequent revisions)
- b. The TSPA-SR base-case hydrologic properties set for the case of no perching, including three infiltration-flux scenarios: (1) low flux, (2) mean flux, and (3) high flux. Future climate change will be addressed with a time-varying infiltration flux.
- c. Emplacement drifts are ventilated for the entire pre-closure period. The pre-closure period is assumed to be 50 years. (Extended ventilation periods will be addressed in subsequent revisions.)
- d. Emplacement drifts are backfilled at the end of the pre-closure period. Drip shields are emplaced at the same time as backfill.

- e. The distribution of hydrostratigraphic units used in the site-scale UZ flow model (based on GFM version 3.1) will be used in the numerical grids that are built (using YMESH), for all of the submodels used in the MSTHM.
- f. The drift-scale models will use grid discretization that is comparable to or better than that used in the Multiscale NF/EBS TH Model calculations for Phase II of LADS.

Table 1-1. List of NFE and EBS TH variables calculated with the MSTHM at each repository subdomain.

TH Variable	Drift-Scale Location
Temperature	NFE host rock (5 m above crown of drift)
	NFE host rock (mid-pillar at repository horizon)
	Maximum lateral extent of boiling
	Upper drift wall (crown of the drift of drift)
	Lower drift wall (below invert)
	Drift wall (perimeter average)
	Backfill (crown)
	Drip shield (perimeter average)
	Drip shield (upper surface)
	WP (surface average)
	Invert (average)
Relative humidity	Drift-wall (perimeter average)
	Backfill (crown)
	Drip shield (perimeter average)
	Waste package
	Invert (average)
Liquid-phase saturation (matrix)	Drift wall (perimeter average)
	Drip shield (perimeter average)
	Invert (average)
Liquid-phase flux	NFE host rock (5 m above crown of drift)
	NFE host rock (3 m above crown of drift)
	NFE host rock (0.2 m above crown of drift)
	Drip shield (crown)
	Drip shield (upper surface average)
	Drip shield (lower side at the base)
	Invert (average)
Gas-phase air-mass fraction	Drip shield (perimeter average)
Gas-phase pressure	Drip shield (perimeter average)
Capillary pressure	Drip shield (perimeter average)
	Invert (average)
	Drift wall (crown, in matrix)
	Drift wall (crown, in fractures)
Gas-phase (water vapor) flux	Drift wall (perimeter average)
Gas-phase (air) flux	Drift wall (perimeter average)
Evaporation rate	Backfill (crown)
	Drip shield (crown)
	Drip shield (perimeter total)
	Invert (total)

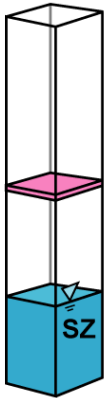
The specific criteria for the calculations conducted in this AMR are given in Section 4.2.

1.3 PRIMARY TASKS

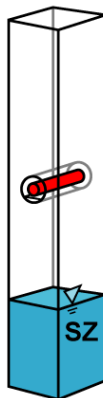
The primary tasks completed in the preparation of this document are:

1. Calculate TH conditions (i.e., performance measures) in the NF host rock and in the EBS throughout the repository area, using the MSTHM. The TH performance measures include temperature, liquid-phase saturation, relative humidity, gas-phase air-mass fraction, evaporation rate, and liquid-phase flux. These performance measures will be given in histogram bins for each of the repository subregions. The distribution of these performance measures will also be described for the entire repository area, using complementary cumulative distribution functions.
2. Describe all submodels that are implemented in the MSTHM as well as the Multiscale TH Abstraction Code (MSTHAC).

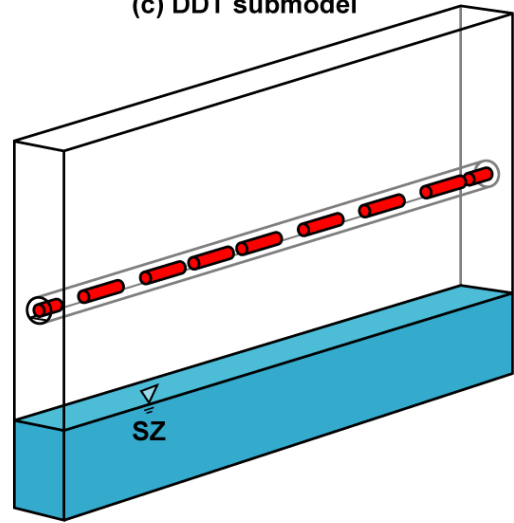
(a) SDT submodel



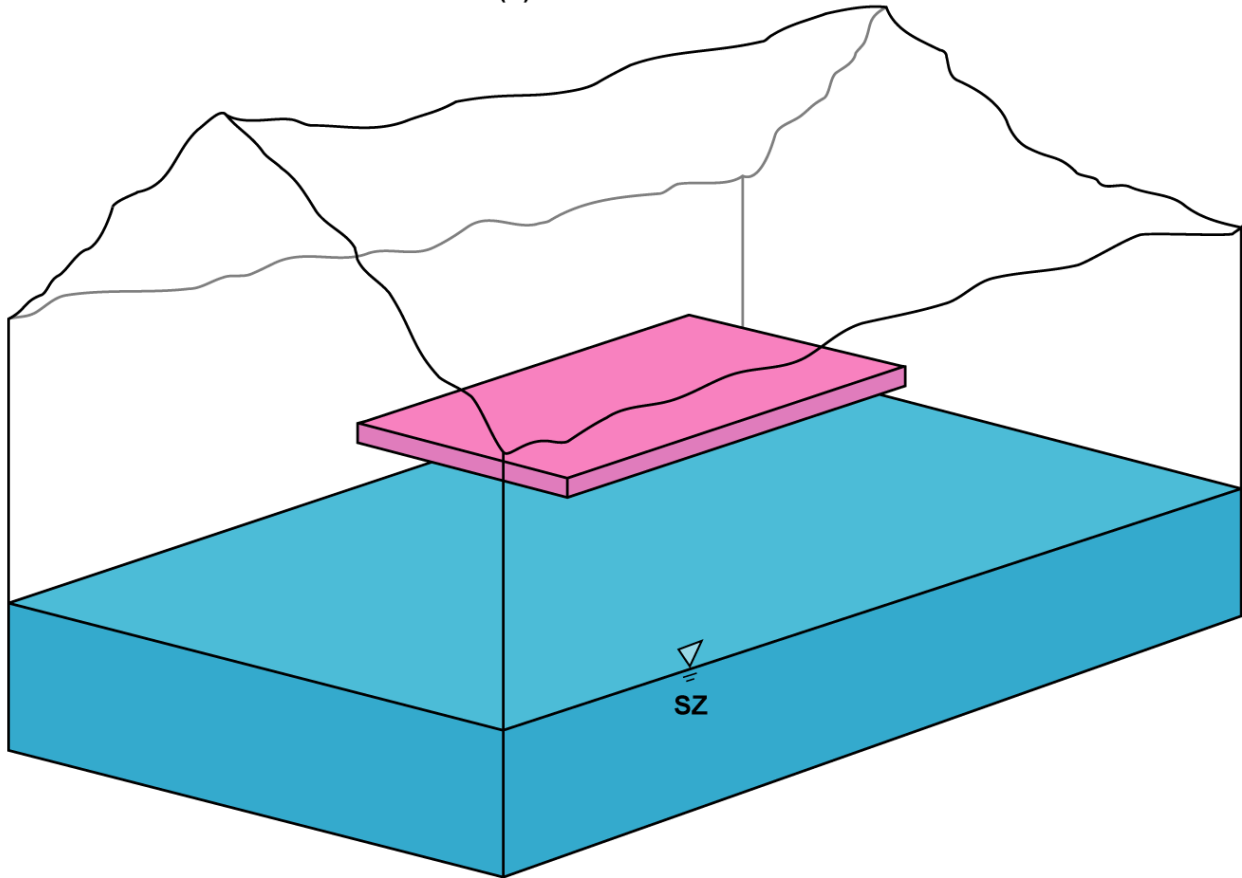
(b) LDTH submodel



(c) DDT submodel

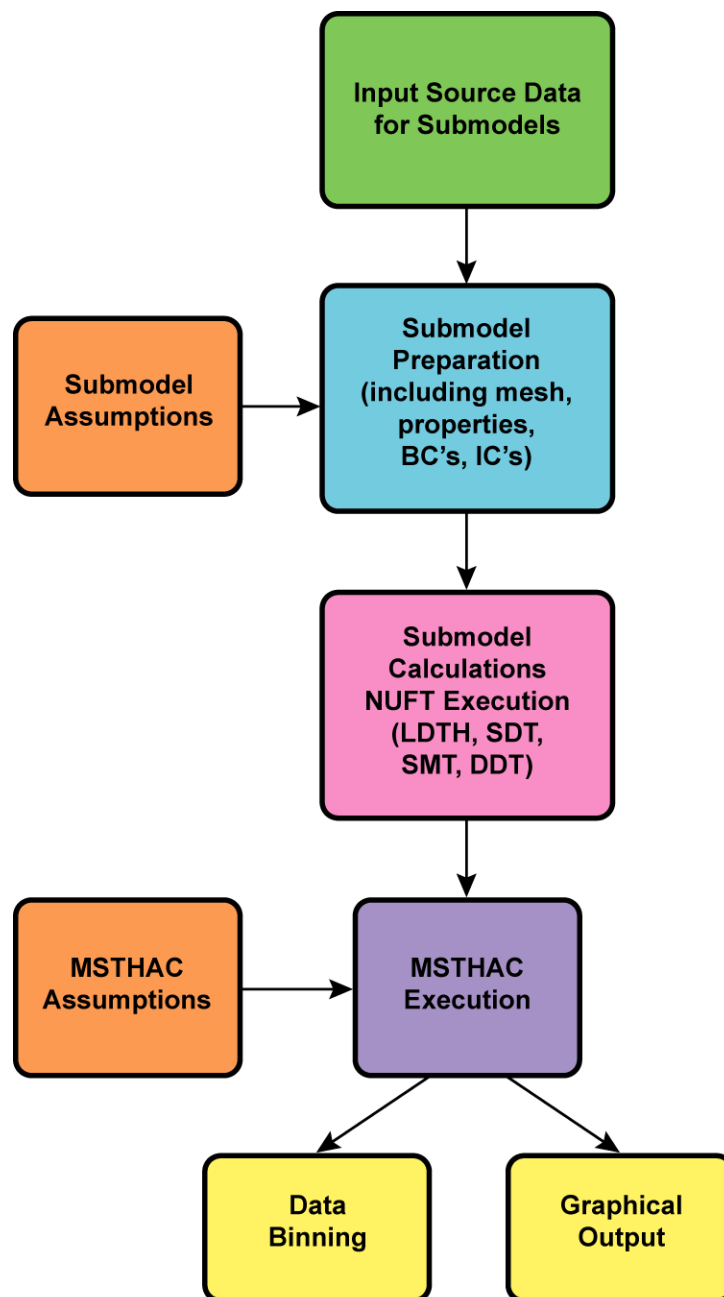


(d) SMT submodel



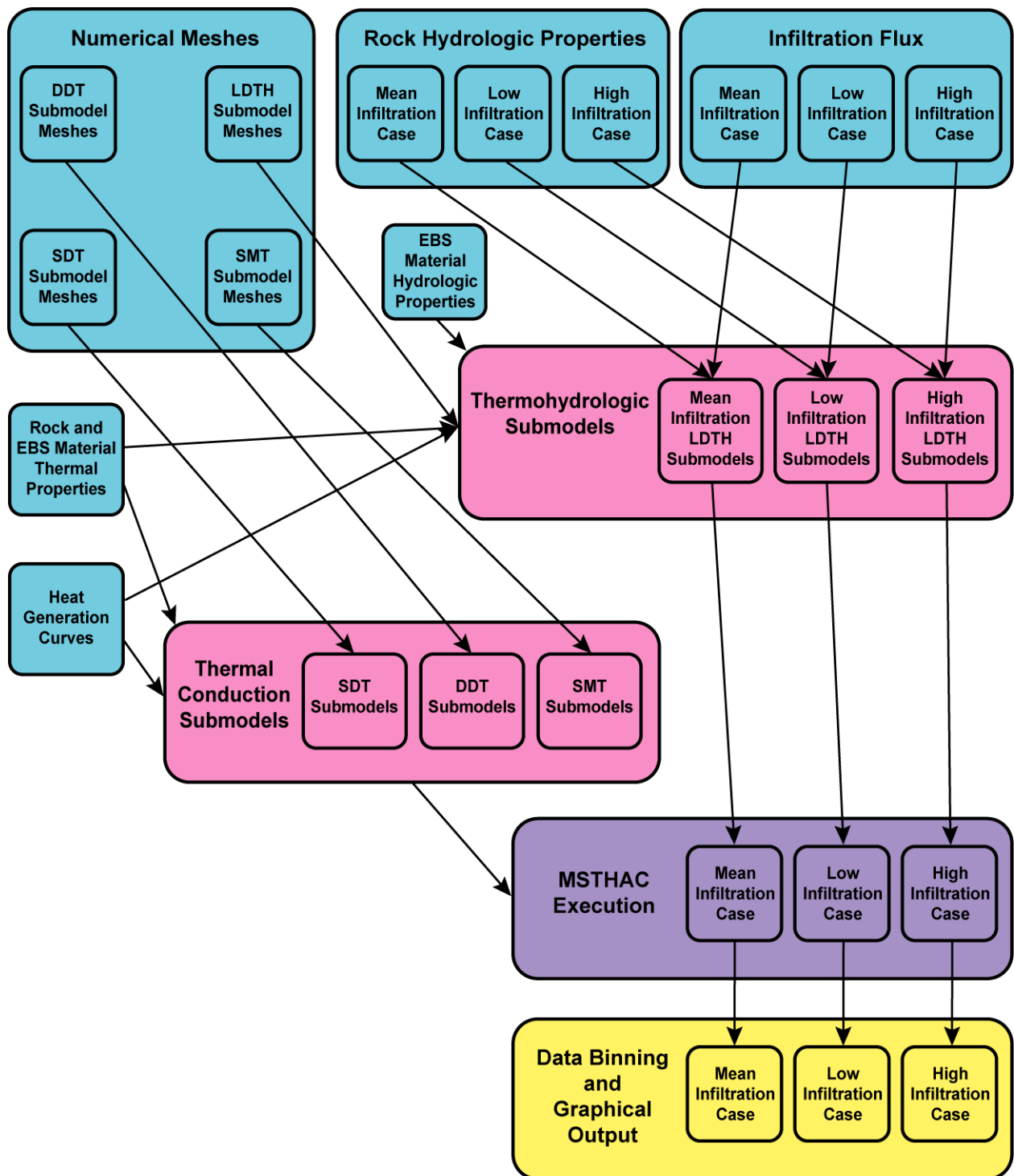
TB_AMR_fig1-1submod-schem

Figure 1-1. Schematic of conceptual models used by the MSTHM, including (a) SDT submodel, (b) LDTH submodel, (c) DDT submodel, and (d) SMT submodel.



TB_AMR_fig1-2_MSTHM_flow

Figure 1-2. Overall data flow diagram for the MSTHM.



TB_AMR_fig1-3_MSTHM_flow2

Figure 1-3. Data flow diagram for the MSTHM that shows the relationship between the input data and submodels for the three infiltration flux scenarios addressed in Rev 00.

2. QUALITY ASSURANCE

This document was prepared in accordance with AP-3.10Q, *Analyses and Models*, and the development plan (CRWMS M&O 2000c), which was prepared in accordance with AP-2.13Q, *Technical Product Development Plan*, and is subject to quality assurance controls. A Technical Change Request (T2000-0140) was approved in accordance with AP-3.4Q, *Level 3 Change Control*.

The activity related to preparing this document has been evaluated (CRWMS M&O 1999b) in accordance with QAP-2-0, *Conduct of Activities*, and has been determined to be subject to the requirements of the *Quality Assurance Requirements and Description* (DOE 2000). The QAP-2-3, *Classification of Permanent Items*, evaluation, *Classification of the MGR Ex-Container System*, (CRWMS M&O 1999c, p. 8) has identified the ex-container system as QL-1, important to radiological safety. Water drainage is not specifically addressed in the *Q-List* (YMP 1998, p. II-9), but is a characteristic of the ex-container system. For this document, the classification of water drainage features are considered QL-1, important to radiological safety. The engineered barrier system is identified on the *Q-List* (YMP 1998, p. II-9) and is identified as QL-1, important to radiological safety; and QL-2, important to waste isolation.

Qualified and accepted input data and references have been identified. Unqualified data used in this report are tracked in accordance with AP-3.15Q, *Managing Technical Product Inputs*. AP-3.10Q, *Analyses and Models*, requires that output resulting from unqualified software be designated as unqualified to-be-verified (TBV) in accordance with AP-3.15Q, *Managing Technical Product Inputs*. Computer software and model usage is discussed in Section 3.

Model validation is discussed in Section 6.12. Software and routines used in this report are subject to AP-SI.1Q, *Software Management*, as discussed in Section 3 of this document.

Per Section 5.9 of AP-3.10Q, *Analyses and Models*, if the data developed in this document are determined to be needed by organizations outside of the Engineered Barrier Systems Operations the results of this model will be submitted to the Technical Data Management System in accordance with AP-SIII.3Q, *Submittal and Incorporation of Data to the Technical Data Management System*. The resulting data tracking numbers (DTN's) are: LL000113904242.089, LL000114004242.090, and LL000114104242.091.

3. COMPUTER SOFTWARE AND MODEL USAGE

Software and routines were used in the preparation of this AMR. Table 3-1a gives a complete list of software and routines used. Table 3-1b contains a list of the CPU's where these programs were executed. These programs were all executed at Lawrence Livermore National Laboratory.

Table 3-1a. Software Validation

Code	Attachment where qualified (or STN)	Software Type
NUFT v3.0s	10088-3.0s-00	Software
RADPRO v3.22	10204-3.22-00	Software
XTOOL v10.1	10208-10.1-00	Software
MSTHAC v6.2	10290-6.2-00	Software
CONVERTCOORDS v1.1	10209-1.1-00	Routine
YMESS v1.53	10172-1.53-00	Routine
makeColumns v1.0	I	Routine
define_EBS_fineGrid v1.3	II	Routine
readsUnits v1.0	III	Routine
addLayers v1.0 & addlay v1.0	IV	Routine
heat_DDT v1.0 & heat_SMT v1.0	V	Routine
xairstab v1.8	VI	Routine
infiltab v1.0	VII	Routine
rock_sun v1.0	VIII	Routine
SMT_surf_bc v1.1 & SMT_bot_bc v1.1	IX	Routine
bound v1.0	X	Routine
assembly scripts LDTH*corey, SDT-01* v1.0	XI	Routine
heatgenAge v1.0	XII	Routine
chim_surf_TP v1.0 & chim_wt_TP v1.0	XIII	Routine
columnInfiltration v1.1	XIV	Routine
cover v1.1	XV	Routine
rme6 v1.1	XVI	Routine
splitEXT v1.0	XIX	Routine

Table 3-1b. Software Execution

Workstation Name	Physical Location
s139	T1487 Rm 150A
s89	T1487 Rm 150
s116	T1401 Rm 1119
s117	T1487 Rm 112
s187	T1487 Rm 153
s70	T1487 Rm 149
s11	T1487 Rm 146
s08	T1487 Rm 145
s28	T1487 Rm 154
s13	T1487 Rm 124
s188	T1487 Rm 138
s175	T1487 Rm 114

3.1 DESCRIPTION OF SOFTWARE

All unqualified software codes used in the preparation of this document are under software configuration management in accordance with AP-SI.1Q, *Software Management* and have associated software tracking numbers. The names and software tracking numbers for the unqualified codes used in this document are NUFT v3.0s (NUFT, STN: 10088-3.0s-00), RADPRO v3.22 (RADPRO, STN: 10204-3.22-00), XTOOL v10.1 (XTOOL, STN: 10208-10.1-00), and MSTHAC v6.2 (MSTHAC, STN: 10290-6.2-00). The software described in this section is used in the following data-flow diagrams (Figure 3-1 through Figure 3-12). A more detailed description of these diagrams is given in following sections of this AMR. The computer software used was run on computers located in Lawrence Livermore National Laboratories. The specific office locations are as given in Table 3-1a.

3.1.1 NUFT v3.0s

NUFT v3.02 classified as an unqualified software program (per AP-SI.1Q, *Software Management*), and was obtained from configuration management. NUFT was run on a Sun Ultra 10 workstation with a SunOS 5.6 operating system. NUFT is used to predict the conditions in the EBS and NBS. NUFT is appropriate for this task.

3.1.2 RADPRO v3.22

RADPRO v3.22 is classified as an unqualified software program (per AP-SI.1Q, *Software Management*), and was obtained from configuration management. RADPRO was run on a Sun Ultra 10 workstation with a SunOS 5.6 operating system. RADPRO is used to predict the radiative heat transfer in the drift. RADPRO is appropriate software for this task.

3.1.3 XTOOL v10.1

XTOOL v10.1 is classified as an unqualified software program (per AP-SI.1Q, *Software Management*), and was obtained from configuration management. The output from XTOOL is graphical (no actual data is produced with XTOOL). XTOOL is tracked in accordance with AP-SI.1Q because it is not commercial software. XTOOL is used to develop graphical representations of the results in the NUFT output files (XVIII-files: *.out). XTOOL is appropriate software for this task. Software programs used to produce figures that are not used for model validation are exempt from AP-SI.1Q requirements. XTOOL was run on a Sun Ultra 10 workstation with a SunOS 5.6 operating system.

3.1.4 MSTHAC v6.2

MSTHAC v6.2 is classified as an unqualified software program (per AP-SI.1Q, *Software Management*), and was obtained from configuration management. MSTHAC was run on a Sun Ultra 10 workstation with a SunOS 5.6 operating system. MSTHAC is used to predict the final conditions based on the various NUFT runs. MSTHAC is appropriate software for this task.

3.2 DESCRIPTION OF ROUTINES AND MACROS

All routines and macros used in the preparation of this document are qualified in this document (see Table 3-1) or have associated software tracking numbers. The routines qualified in this document are given in Table 3-1 and Sections 3.2.1 – 3.2.21. The qualified routines used in this document are CONVERTCOORDS v1.1 (CONVERTCOORDS, STN: 10209-1.1-00), and YMESH v1.53 (YMESH, STN: 10172-1.53-00).

3.2.1 MakeColumns v1.0

MakeColumns v1.0 is classified as a routine per AP-SI.1Q. It creates a family of YMESH input files to generate a family of chimney meshes at a set of specified locations. The input files to makeColumns are column_template and column.data (CRWMS M&O 2000a). This routine is qualified in Attachment I and is appropriate for its purpose. MakeColumns was run on a Sun Ultra 2 workstation with a SunOS 5.5.1 operating system. MakeColumns was developed using a C++ compiler.

3.2.2 Rme6 v1.1

Rme6 v1.1 is classified as a routine per AP-SI.1Q. It converts world view data files to a format readable by YMESH. The input files to rme6 are tspa99_primary_mesh and UZ99_3.grd (CRWMS M&O 2000a). The output file is LBL99-YMESH (CRWMS M&O 2000a). Rme6 is qualified in Attachment XVI and is appropriate for its purpose. Rme6 was run on a Sun Ultra 2 workstation with a SunOS 5.5.1 operating system. Rme6 was developed using a C++ compiler.

3.2.3 Define_EBS_fineGrid v1.3

Define_EBS_fineGrid v1.3 is classified as a routine per AP-SI.1Q. Its purpose is to convert NUFT genmsh files, created with YMESH, to separate sets of “matrix” and “fracture” mesh definition instructions, and to add a mapping of materials for the EBS to the mesh. Input files for the routine are *.nft (CRWMS M&O 2000a). Output files are *.nft.msh.dkm.m, *.nft.msh.dkm.f, *.nft.msh.dkm0, *.nft.msh.dkm0.m, and *.nft.msh.dkm0.f (CRWMS M&O 2000a). Define_EBS_fineGrid is qualified in Attachment II, and is appropriate for its purpose). Define_EBS_fineGrid was run on a Sun Ultra 2 workstation with a SunOS 5.5.1 operating system. Define_EBS_fineGrid was developed using C++ compiler.

3.2.4 ReadsUnits v1.0

ReadsUnits v1.0 is classified as a routine per AP-SI.1Q. It converts YMESH column type output to NUFT comments indicating for each rock layer how thick the layer is for a given column. It adds together the widths of adjoining zones of the same material, if any. The input to readsUnits is a file “results” and the output is called “results.units” (CRWMS M&O 2000a). ReadsUnits is qualified in Attachment III and is appropriate for its purpose. ReadsUnits was run on a Sun Ultra 2 workstation with a SunOS 5.5.1 operating system. ReadsUnits was developed using C++ compiler.

3.2.5 AddLayers v1.0

AddLayers v1.0 is classified as a routine per AP-SI.1Q. AddLayers modifies NUFT mesh input data by adding an atmosphere or “atm” layer to the top and a water table or “wt” layer to the bottom of the zones for a chimney. The atm layer has depth zero, and the wt layer falls below the lowest rock layer. The routine is qualified in attachment IV and is appropriate for its purpose. AddLayers was run on a Sun Ultra 2 workstation with a SunOS 5.5.1 operating system. AddLayers was developed using C++ compiler.

3.2.6 Heat_DDT v1.0

Heat_DDT v1.0 is classified as a macro per AP-SI.1Q. It extracts heat generation data for chimneys from file DWpermeter (CRWMS M&O 2000a) and rewrites it in NUFT heat generation input data format. Heat_DDT is qualified in Attachment V and is appropriate for its purpose. Heat_DDT was run on a Sun Ultra 2 workstation with a SunOS 5.5.1 operating system. Heat_DDT was developed using Matlab.

3.2.7 Heat_SMT v1.0

Heat_SMT v1.0 is classified as a macro per AP-SI.1Q. It extracts heat generation data for the mountain scale model from file heatTSPA00.dat and rewrites it in NUFT heat generation input data format. Heat_SMT is qualified in Attachment V and is appropriate for its purpose. Heat_SMT was run on a Sun Ultra 2 workstation with a SunOS 5.5.1 operating system. Heat_SMT was developed using Matlab.

3.2.8 Cover v1.1

Cover v1.1 is classified as a macro per AP-SI.1Q. The purpose of cover.m v1.1 is to make a block model of the plan view of the repository that approximates the area and location of the emplacement. This macro is qualified in Attachment XV and is appropriate for its purpose. Cover was run on a Sun Ultra 2 workstation with a SunOS 5.5.1 operating system. Cover was developed using Matlab.

3.2.9 ColumnInfiltration v1.1

ColumnInfiltration v1.1 is classified as a routine per AP-SI.1Q. The purpose of this routine is to interpolate the infiltration at a given (x,y) location using a Gaussian weighting function (4.1.2). This routine is qualified in Attachment XIV and is appropriate for its purpose. This routine was run on a Sun Ultra 2 workstation with a SunOS 5.5.1 operating system. ColumnInfiltration was developed using C++ compiler.

3.2.10 Chim_surf_TP v1.0

Chim_surf_TP v1.0 is classified as a routine per AP-SI.1Q. The purpose of chim_surf_TP is to interpolate the temperature and pressure at the ground surface for a given location using the inverse distance cubed method. This routine is qualified in Attachment XIII and is appropriate

for its purpose. Chim_surf_TP was run on a Sun Ultra 2 workstation with a SunOS 5.5.1 operating system. Chim_surf_TP was developed using a Fortran compiler.

3.2.11 Chim_wt_TP v1.0

Chim_wt_TP v1.0 is classified as a routine per AP-SI.1Q. The purpose of chim_wt_TP is to interpolate the temperature and pressure at the water table for a given location using the inverse distance cubed method. This routine is qualified in Attachment XIII and is appropriate for its purpose. Chim_wt_TP was run on a Sun Ultra 2 workstation with a SunOS 5.5.1 operating system. Chim_wt_TP was developed using a Fortran compiler

3.2.12 Xairtab v1.8

Xairtab v1.8 is classified as a routine per AP-SI.1Q. Xairtab reads the boundary condition file chimney_surface_TP (CRWMS M&O 2000a) and computes air mass fraction and liquid enthalpy at the surface for each chimney. Xairtab is qualified in Attachment VI and is appropriate for its purpose. Xairtab was run on a Sun Ultra 2 workstation with a SunOS 5.5.1 operating system. Xairtab was developed using a C++ compiler

3.2.13 Infiltrab v1.0

Infiltrab v1.0 is classified as a macro per AP-SI.1Q. It extracts infiltration flux data from the input file infiltration.tex (CRWMS M&O 2000a) and writes the following 9 output files (CRWMS M&O 2000a) in matrix format: Median_g.dat, Median_m.dat, Median_p.dat, low_g.dat, low_m.dat, low_p.dat, upper_g.dat, upper_m.dat, and upper_p.dat. Infiltrab.m is qualified in Attachment VII and is appropriate for its purpose. Infiltrab was run on a Sun Ultra 2 workstation with a SunOS 5.5.1 operating system. Infiltrab was developed using Matlab.

3.2.14 Rock_sun v1.0

Rock_sun v1.0 is classified as a macro per AP-SI.1Q. Its purpose is to extract material property data from the 1d_driftscale*.prn files (CRWMS M&O 2000a) and rewrite it formatted as input for NUFT. Rock_sun is qualified in Attachment VIII and is appropriate for its purpose. Rock_sun was run on a Sun Ultra 2 workstation with a SunOS 5.5.1 operating system. Rock_sun was developed using Matlab.

3.2.15 SMT_surf_bc v1.1

SMT_surf_bc v1.1 is classified as a routine per AP-SI.1Q. The purpose of SMT_surf_bc is to interpolate the temperature at the ground surface for a given location using the inverse distance squared method. It was demonstrated to perform in the expected manner (see Attachment IX). SMT_surf_bc was run on a Sun Ultra 2 workstation with a SunOS 5.5.1 operating system. SMT_surf_bc was developed using a Fortran compiler.

3.2.16 SMT_bot_bc v1.1

SMT_bot_bc v1.1 is classified as a routine per AP-SI.1Q. The purpose of SMT_bot_bc is to interpolate the temperature at the ground botace for a given (x,y) location using the inverse distance squared method. It was demonstrated to perform in the expected manner (see Attachment IX). SMT_bot_bc was run on a Sun Ultra 2 workstation with a SunOS 5.5.1 operating system. SMT_bot_bc was developed using a Fortran compiler.

3.2.17 Bound v1.0

Bound v1.0 is classified as a macro per AP-SI.1Q. Bound computes temperatures at 1000 meters below the water table. Bound takes as input a thermal conductivity file, tcond_wet.dat, the *.units file generated by readsUnits from YMESH column output (containing material thicknesses), the temperature_S surface temperature from LDTH boundary conditions, and the temperature_W water table temperature also from LDTH boundary conditions. It writes the file T_bottom.dat. Bound was demonstrated to behave according to expectations (see Attachment X). Bound was run on a Sun Ultra 2 workstation with a SunOS 5.5.1 operating system. Bound was developed using Matlab.

3.2.18 Addlay v1.0

Addlay v1.0 is classified as a routine per AP-SI.1Q. Addlay v1.0, like addLayers, reads a NUFT genmsh file generated by YMESH and inserts an atmospheric and a water table layer at the top and bottom of the mesh. In addition, it removes the five lines of NUFT instructions preceding the vertical zone thickness definitions and the final closing parenthesis. Addlay demonstrated correct behavior relative to its objective (see Attachment IV). Addlay was run on a Sun Ultra 2 workstation with SunOS 5.5.1 operating system. Addlay was developed using a C++ compiler.

3.2.19 INPUT ASSEMBLY

The following twelve input assembly scripts, all v1.0, are classified as routines per AP-SI.1Q: LDTH-i-li-corey, LDTH-i-mi-corey, LDTH-i-ui-corey, LDTH-01-li-corey, LDTH-01-mi-corey, LDTH-01-ui-corey, LDTH-01v-li-corey, LDTH-01v-mi-corey, LDTH-01v-ui-corey, SDT-01i, SDT-01, SDT-01v. These scripts build NUFT input files from component subfiles of various types. The scripts were shown to perform in the expected manner (see Attachment XI). The scripts were run on a Sun Ultra 2 workstation with a SunOS 5.5.1 operating system. Input assembly scripts were developed using the c-shell V5.1.1.

3.2.20 HeatgenAge v1.2

HeatgenAge v1.2 is classified as a routine per AP-SI.1Q. HeatgenAge reads a heat generation file and performs two transformations on it: 1) aging the fuel by a number of years, skipping ahead a number of years in the data set and subtracting that number of years from the times of the remaining entries and 2) ventilating the system for a number of years, removing a specified fraction of the heat during the aging period. HeatgenAge performed as expected (see Attachment

XII). HeatgenAge was run on a Sun Ultra 2 workstation with a SunOS 5.5.1 operating system. HeatgenAge was developed using a C++ compiler.

3.2.21 SplitEXT v1.0

SplitEXT v1.0 is classified as a routine per AP-SI.1Q. SplitEXT splits the .ext output file from MSTHAC into separate .ext files containing the output for each variable. If the input file is <name>.ext, then the output files will be <name>.<var>.ext for all variables. SplitEXT is qualified in Attachment XIX. It was run on a Sun Ultra 2 workstation with a SunOS 5.5.1 operating system. SplitEXT was developed using a C++ compiler.

3.2.22 YMESH v1.53

YMESH v1.53 is classified as routine per AP-SI.1Q, has the following associated STN: 10172-1.53-00, and was obtained from configuration management. YMESH is used in this model to interpolate the thickness of the stratigraphic units at given locations. The input file for YMESH is LBL99-YMESH (CRWMS M&O 2000a). The output from this software is column.dat (CRWMS M&O 2000a). YMESH is appropriate software for this task. YMESH was run on a Sun Ultra 2 workstation with a SunOS 5.5.1 operating system.

3.2.23 CONVERTCOORDS v1.1

CONVERTCOORDS v1.1 is classified as routine per AP-SI.1Q, has the following associated STN: 10209-1.1-00, and was obtained from configuration management. CONVERTCOORDS is used to convert from Universal Transverse Mercator coordinates to Nevada State Plane coordinates, as well as to reformat the data (CRWMS M&O 2000a, files: *.inf). The desired format is columns of data, with the input files in a matrix format. CONVERTCOORDS is appropriate software for this task. CONVERTCOORDS was run on a Sun Ultra 2 workstation with a SunOS 5.5.1 operating system.

3.3 DATA FLOW

Tables 3-2 – 3-9 allow for more efficient use of Figures 3-1 – 3-12. There are three kinds of alpha-numeric codes used in the data flowchart figures.

1. Those starting with an N represent an operation explained in a footnote that results in the creation of one or more files. These operations have output files, but no input files. An explanation of the operations involved is given in Table 3-2.
2. Alpha-numeric codes starting with an E represent editing type operations. These operations have input and output files. An explanation of the operations involved is given in Table 3-3.
3. All other codes represent groups of files that flow from one page to the next. A listing of these files, as well as the Figure of origin and figure(s) of destination is given in Table 3-4.

Table 3-5 gives the name of the input and output file for software routines used in this document, as well as the figure(s) where the routine is used and the input source(s). Tables 3-6 – 3-9 gives similar information for NUFT. Attachment XVIII provides the names of the input and output files for RADPRO, XTOOL, MSTHAC, YMESH, and CONVERTCOORDS.

Table 3-2. N-Table

α # *	Fig.	Output File Names	Notes
N:M1	3-2	SDT:\column_template	Mesh column_template for LDTH and SDT
N:M2	3-2	LDTH:\column_template	The grid files for the SMT model are specified by applying several criteria: - The east boundary is to be parallel to the actual repository boundary. - The repository edge has a finer grid to allow the MSTHM algorithm to treat edge effects appropriately. - The grid blocks are each to correspond to an integral number of drifts in order to simplify the final parameter mapping.
N:L1	3-9	run_control_param_LDTH-v00 run_control_param_LDTH-v01	Run control parameters provide setup of the numerical control of the simulation code itself to achieve reasonable efficiency in the computation
N:L2	3-9	<aml>infil <aml>pre-closure <aml>post-closure	LDTH Templates
N:L3	3-9	output.times-00v output.times-<aml>-00	Run control parameters provide setup of the numerical control of the simulation code itself to achieve reasonable efficiency in the computation
N:S1	3-10	SDT-00tplt	SDT Templates
N:S2	3-10	output.times-00v output.times-<aml>-00	The output times files contain the list of times for which parameter values are to be written to the output stream. The criterion for the choice of times is to achieve suitable time resolution, especially when the relative humidity in the drift is varying rapidly. An appropriate choice of times was discovered
N:D1	3-11	run_control_param_DDT-v01 run_control_param_DDT-v02	Run control parameters provide setup of the numerical control of the simulation code itself to achieve reasonable efficiency in the computation
N:D2	3-11	output.times-DDT30-00	The output times files contain the list of times for which parameter values are to be written to the output stream. The criterion for the choice of times is to achieve suitable time resolution, especially when the relative humidity in the drift is varying rapidly. An appropriate choice of times was discovered empirically
N:D3	3-11	DDT60-03.radin DDT60-03v.radin DDT60-03pbf.radin	The radin files are used to specify which surfaces may be coupled via radiation, and to provide emissivity assignments to the surfaces.
N:T1	3-12	run_control_param_SMT-v01	Run control parameters provide setup of the numerical control of the simulation code itself to achieve reasonable efficiency in the computation.
N:T2	3-12	output.times-SMT60-00	The output times files contain the list of times for which parameter values are to be written to the output stream. The criterion for the choice of times is to achieve suitable time resolution, especially when the relative humidity in the drift is varying rapidly. An appropriate choice of times was discovered empirically
N:T3	3-12	SMT-1Dds-mi-sz	Set properties of natural system materials in the saturated zone. The material is assumed to be identical to that found at the bottom of the unsaturated zone.

* This column gives the alpha numeric designator used in the figure referenced in the "Fig." column.

N:xx allows a free-form textual note to be attached to a given operation. In this case, there is not typically an input file to the step, but the information originates in some sort of analyst input from domain expertise, and is at this point encapsulated. The analyst input involved is briefly described in the table notes, and a larger explanation may be found in the text.

Table 3-3. E-Table

α # *	Fig.	Input File Name(s)**	Output File Names**	Notes
E:M1	3-2	l4c3.dat	l4c3.03v.dat	Refine the input LDTH grid to sufficiently describe thermal radiation processes.
E:M2	3-2	DTN file, l4c3.03v.dat	l4c3.dat	Refine grid within drift to properly describe post-closure engineered system material distribution, especially drip shield emplacement.
E:M3	3-2	shape.dat	column.data	Chimney locations are chosen in a regular array parallel to the major axis (East side) of the MSTHM repository footprint.
E:M4	3-2	PAtem1Att10817	dft1.dat	Removed the column headers.
E:H1	3-3	heatTSPA-SR-99184.dat	heatTSPA00.dat	Removed the column headers and reorganized the parameter values into a matrix format for Matlab to read.
E:H2	3-3	2-DWperimeter.dat	Dwperimeter.txt	
E:H3	3-3	2-DWperimeter.dat	line-load-heat	Place the data columns of Time and Averaged Heat Transfer into NUFT format (in a compflux block).
E:B1	3-5	chimney_surface_TP	temperature_s	The files chimney_wt_TP and chimney_surface_TP are transformed into temperature_W and temperature_S, respectively, by laying out the temperature data found in the source file into an array format of 7x5 rather than a list. All other (non-temperature) source data is discarded.
E:B1	3-5	chimney_wt_TP	temperature_w	
E:C1	3-6	B-1, B-2, I-L0	LDTH-i-li-corey	LDTH initial script
E:C1	3-6	B-1, B-2, I-M0	LDTH-i-mi-corey	
E:C1	3-6	B-1, B-2, I-U0	LDTH-i-ui-corey	
E:C2	3-6	B-1, B-2, I-L0, I-L1	LDTH-01v-li-corey	LDTH ventilation script
E:C2	3-6	B-1, B-2, I-M0, I-M1	LDTH-01v-mi-corey	
E:C2	3-6	B-1, B-2, I-U0, I-U1	LDTH-01v-ui-corey	
E:C3	3-6	B-1, B-2, I-L0, I-L1	LDTH-01-li-corey	LDTH main script
E:C3	3-6	B-1, B-2, I-M0, I-M1	LDTH-01-mi-corey	
E:C3	3-6	B-1, B-2, I-U0, I-U1	LDTH-01-ui-corey	
E:R1	3-7	dkm-afc-1Dds-mc-mi-00	SDT-1Dds-mi	Removed all hydrologic properties and set thermal properties to the appropriate wet material properties.
E:P1	3-8	DTN unknown file name	R-1,R-1v,R-2,R-3,R-D	Tabulated In-drift and Thermal Properties Used in Drift-scale Models for TSPA-SR (Rev 01) to create EBS material properties files
E:S1	3-10	B-1	SDT-01i	SDT initial script
E:S2	3-10	B-1	SDT-01v	SDT ventilation script
E:S3	3-10	B-1	SDT-01	SDT main script
E:D1	3-11	M-D1	l4c3-DDT60-03v.in	DDT initial script
E:D2	3-11	M-D2	l4c3-DDT60-03pbf.in	DDT ventilation script
E:D3	3-11	M-D2	l4c3-DDT60-03bff.in	DDT main script
E:T1	3-12	thermal_UZ.xls	SMT-1Dds-mi-flt	Manually format rock property information for materials in fault areas into NUFT input file format.

* This column gives the alpha numeric designator used in the figure referenced in the "Fig." column.

** File sets denoted with alpha numeric designators are listed in Table 3-4.

E:xx refers to an editing operation. This indicates that the transformation from input to output file incorporates some analyst input not previously encapsulated in the input file to the step, or that unnecessary information was removed.

The analyst input involved is briefly described in the table notes, and a larger explanation may be found in the text.

Table 3-4. File Groups

α #	Figure		File names
M-1	3-2	3-5	column.data
M-M0	3-2	3-5	tspa00-mesh00
M-M1	3-2	3-12	tspa00-mesh01
M-M2	3-2	3-12	tspa00-mesh02
M-D1	3-2	3-11	l4c3.03v.nft.msh.ddt
M-D2	3-2	3-11	l4c3.nft.msh.ddt
M-L0<column>	3-2	3-9	LDTH:\<column>.col.units <column>.nft.msh.dkm0.f <column>.nft.msh.dkm0.m
M-L1<column>	3-2	3-9	<column>.col.units <column>.nft.msh.dkm.f <column>.nft.msh.dkm.m
M-S<column>	3-2	3-5, 3-10	<column>.nft.msh.dkm0 SDT:\<column>.col.units
H-D0	3-3	3-11	SMT-0.3Qheat-1e6y_vent-00v
H-D1	3-3	3-11	SMT-0.3Qheat-50y_vent-00
H-L0	3-3	3-9, 3-10	LDTH-SDT-0.3Qheat-1e6y_vent-00v
H-L1	3-3	3-9, 3-10	LDTH-SDT-0.3Qheat-50y_vent-00
H-M0	3-3	3-12	SMT-0.3Qheat-1e6y_vent-02v
H-M1	3-3	3-12	SMT-0.3Qheat-50y_vent-02
I-L0	3-4	3-6	low p.dat
I-L1	3-4	3-6	low_g.dat low m.dat
I-M0	3-4	3-6	Median p.dat
I-M1	3-4	3-6	Median_g.dat Median m.dat
I-U0	3-4	3-6	upper p.dat
I-U1	3-4	3-6	upper_g.dat upper m.dat
B-1	3-5	3-6, 3-10	chimney_wt_TP chimney surface TP
B-2	3-5	3-6	Enthalpy.dat X.air
B-3	3-5	3-12	SMT_surfbcb
B-4	3-5	3-12	SMT_bsmtbcb
XL-0<infil>	3-6	3-9	LDTH-i-li-corey LDTH-i-mi-corey LDTH-i-ui-corey
XL-1<infil>	3-6	3-9	LDTH-01v-li-corey LDTH-01v-mi-corey LDTH-01v-ui-corey
XL-2<infil>	3-6	3-9	LDTH-01-li-corey LDTH-01-mi-corey LDTH-01-ui-corey

* This column gives the alpha numeric designator used in the respective figure.

Table 3-4. (continued).

α #	Figure		File names
	Origin	Dest.	
R-S	3-7	3-10, 3-11, 3-12	SDT-1Dds-mi
R-L<um>	3-7	3-9	dkm-afc-1Dds-mc-li-00 dkm-afc-1Dds-mc-mi-00 dkm-afc-1Dds-mc-ui-00
R-1	3-8	3-9, 3-11	modprop_dr-up-00
R-1v	3-8	3-9, 3-11	modprop_dr-up-00v
R-2	3-8	3-9	dkm-afc-pbf-EBS_Rev10
R-3	3-8	3-9	dkm-afc-EBS_Rev10
R-D	3-8	3-9, 3-11	DDT-EBS_Rev00
LDTH-0<AIC>	3-9	LDTH out	<column>-LDTH<aml>-1Dds_mc-<infil>-01v.ext
LDTH-1<AIC>	3-9	LDTH out	<column>-LDTH<aml>-1Dds_mc-<infil>-01.ext
SDT-0<AC>	3-10	SDT out	<column>-SDT-<aml>-01v.ext
SDT-1<AC>	3-10	SDT out	<column>-SDT-<aml>-01.ext
S-Z	3-10	3-11	I4c3-SDT-01-i.ztab
DDT-0	3-11	DDT out	I4c3-DDT60-03v.EBS.ext
DDT-1	3-11	DDT out	I4c3-DDT60-03bff.EBS.ext
SMT-0	3-12	SMT out	SMT60-02v.rep.ext
SMT-1	3-12	SMT out	SMT60-02.rep.ext

* This column gives the alpha numeric designator used in the respective figure.

Table 3-5. Software Routine Input and Output Files

Name/Number	Description	Number or location of validation	Data Flowchart Figure	Input source	Input File name	# of files	Output File Name	# of files
addLayers v1.0	Routine	Attach. IV	3-2	YMESH output	l4c3.nft	1	l4c3.nft.msh.ddt	1
			3-2	YMESH output	l4c3.03v.nft	1	l4c3.03v.nft.msh.ddt	1
addlay v1.0	Routine	Attach. IV	3-2	YMESH output	SDT:\<column>.nft	31	SDT:\<column>.nft.msh.dkm0	31
bound v1.0	Routine	Attach. X	3-5	E:B1 output E:B1 output addlay output readUnits output LB99EBS1233129.001	temperature_W temperature_S <column>.nft.msh.dkm0 SDT:\<column>.col.units tcond_wet.dat	1 1 31 31 1	T_bottom.dat	1
Chim_Surf_TP v1.0	Routine	Attach. XIII	3-5	LB99EBS1233129.001	tspa99_primary_mesh	1	outpt	1
				LB99EBS1233129.003	bcs_99.dat	1	surf_TP.out	1
Chim_wt_TP v1.0	Routine	Attach. XIII	3-5	LB99EBS1233129.001	tspa99_primary_mesh	1	oupt_wt	1
				LB99EBS1233129.003	bcs_99.dat	1		
ColumnInfiltration v1.1	Routine	Attach. XIV	3-4	convertCoords output	*.NV	9	infiltration.tex	1
				E:M3	column.data	1		
Cover v1.1	Routine	Attach. XV	3-2	MO9911MWDEBSWD .000	dft1.dat	1	shape1.dat figure1.dat	1
define_EBS_fine Grid v1.3	Routine	Attach. II	3-2	YMESH output	LDTH:\<column>.nft	31	<column>.nft.msh.dkm.f <column>.nft.msh.dkm.m <column>.nft.msh.dkm0.f <column>.nft.msh.dkm0.m	31 31 31 31

Table 3-5. Software Routine Input and Output Files (continued)

Name/Number	Description	Number or location of validation	Data Flowchart Figure	Input source	Input File name	# of files	Output File Name	# of files
heat_DDT v1.0	Routine	Attach. V	3-3	E:H2	DWperimeter.txt	1	DDT-heat-01	1
heat_SMT v1.0	Routine	Attach. V	3-3	E:H1	heatTSPA00.dat	1	SMT-heat-00	1
heatgenAge v1.2	Routine	Attach. XII	3-3	E:H3	DDT-heat-01	1	DDT-0.3Qheat-1e6y_vent-00v	1
				heat_DDT ouput	line-load-heat	1	DDT-0.3Qheat-50y_vent-00	1
							LDTH-SDT-0.3Qheat-1e6y_vent-00v	1
							LDTH-SDT-0.3Qheat-50y_vent-00	1
heat_SMT output	SMT-heat-00	1	SMT-0.3Qheat-1e6y_vent-00v	1				
			SMT-0.3Qheat-50y_vent-00	1				
infiltrab v1.0	Routine	Attach. VII	3-4	columnInfiltration output	infiltration.tex	1	low_g.dat	1
							low_m.dat	1
							low_p.dat	1
							Median_g.dat	1
							Median_m.dat	1
							Median_p.dat	1
							upper_g.dat	1
							upper_m.dat	1
							upper_p.dat	1
LDTH assembly scripts: LDTH*corey v1.0	Routine	Attach. XI	3-9	XL-0<infil> N:L2	LDTH-i-<infil>-corey	3	<aml><infil><column>	
				XL-1<infil> N:L2	<aml>infil	1		
				XL-2<infil> N:L2	LDTH-01v-<infil>-corey	3		
				XL-2	<aml>pre-closure	1		
				LDTH-01-<infil>-corey	3			
<aml>post-closure	1	<aml><infil><column>						

Table 3-5. Software Routine Input and Output Files (continued)

Name/Number	Description	Number or location of validation	Data Flowchart Figure	Input source	Input File name	# of files	Output File Name	# of files
makeColumns v1.0	Routine	Attach. I	3-2	N:M1 E:M3	LDTH:\column_template column.data	1 1	LDTH:\<column>.dat	31
				N:M1 E:M3	SDT:\column_template column.data	1 1	SDT:\<column>.dat	31
readsUnits v1.0	Routine	Attach. III	3-2	YMESS output	LDTH:\<column>.col	31	LDTH:\<column>.col.units	31
				YMESS output	SDT:\<column>.col	31	SDT:\<column>.col.units	31
rme6 v1.1	Routine	Attach. XVI	3-2	LB99EBS1233129.001 LB99EBS1233129.001 ? If so, from <column>.dat	tspa99_primary_mesh UZ99_3.grd l4c3.dat	1 1 1	LBL99-YMESS	1
rock_sun v1.0	Routine	Attach. VIII	3-7	LB990861233129.001	1d-driftscale_ basecase2_flow.prn	1	dkm-afc-1Dds-mc-mi-00	1
				LB990861233129.001	1d-driftscale_ basecase2_th.prn	1		
				LB990861233129.003 LB990861233129.003	1d-driftscale_lowinf_flow.prn 1d-driftscale_lowinf_th.prn	1 1	dkm-afc-1Dds-mc-li-00	1
				LB990861233129.002 LB990861233129.002	1d-driftscale_ upperinf_flow.prn 1d-driftscale_upperinf_th.prn	1 1	dkm-afc-1Dds-mc-ui-00	1
SDT assembly scripts: SDT-01* v1.0	Routine	Attach. XI	3-10	E:S1 N:S1	SDT-01i SDT-00-i-tplt	1 1	SDT initial.<column><aml>	1
				E:S2 N:S1	SDT-01v SDT-00-tplt	1 1	<column>-SDT<aml>-01.in	1
				E:S3 N:S1	SDT-01 SDT-00-tplt	1 1	<column>-SDT<aml>-01v.in	1
SMT_surf_bc v1.1	Routine	Attach. IX	3-5	chim_surf_TP output	surf_TP.out	1	SMT_surf_bc.out	1
				YMESS output	tspa00-mesh00	1		

Table 3-5. Software Routine Input and Output Files (continued)

Name/Number	Description	Number or location of validation	Data Flowchart Figure	Input source	Input File name	# of files	Output File Name	# of files
SMT_bot_bc v1.1	Routine	Attach. IX	3-5	bound output	T_bottom.dat	1	SMT_bsmtbc.out	1
				YMESH output	tspa00-mesh00	1		
				E:M3	column.data	1		
splitEXT v1.0	Routine	Attach. XIX	NA	MSTHAC output	TSPA_SR_<infil>.ext	3	TSPA_SR_<infil>_ <variable>.ext	111
					TSPA_SR_<infil>_T_pillar_Xdist.ext	3		
xairtab v1.8	Routine	Attach. VI	3-5	renamed from outpt	chimney_surface_TP	1	Enthalpy.dat	1
							X.air	1

Table 3-6. LDTH Nuft Input and Output Files

Description	Data Flowchart Figure	Input source	File α#	Input File name	# of files	Output File Name	# of files
LDTH Initialization	3-9	define_EBS_fineGrid output	M-L0 <column>	<column>.nft.msh.dkm0.f	31	Include files	
		define_EBS_fineGrid output		<column>.nft.msh.dkm0.m	31		
		readUnits output		LDTH:\<column>.col.units	31		
		rock_sun output	R-L0 <infil>	dkm-afc-1Dds-mc-mi-00	1		
		rock_sun output		dkm-afc-1Dds-mc-li-00	1		
		rock_sun output		dkm-afc-1Dds-mc-ui-00	1		
		N:L1		run_control_param_LDTH-v00	1		
		corey output		<column>-LDTH<aml>-1Dds_mc-<infil>-i.in	465	<column>-LDTH<aml>-1Dds_mc-<infil>-i.ext	465
LDTH restart include files	3-9	define_EBS_fineGrid output	M-L1 <column>	<column>.nft.msh.dkm.f	31	Include files	
		define_EBS_fineGrid output		<column>.nft.msh.dkm.m	31		
		readUnits output		LDTH:\<column>.col.units	31		
		rock_sun output	R-L <infil>	dkm-afc-1Dds-mc-mi-00	1		
		rock_sun output		dkm-afc-1Dds-mc-li-00	1		
		rock_sun output		dkm-afc-1Dds-mc-ui-00	1		
		E:P1	R-1v	modprop_dr-up-00v	1		
		E:P1	R-2	dkm-afc-pbf-EBS_Rev10	1		
		heatgenAge output	H-L0	LDTH-SDT-0.3Qheat-1e6y_vent-00v	1		
		NUFT output	Init.	LDTH:\<aml><infil><column>			
		N:L1		run_control_param_LDTH-v01	1		
		N:L3		output.times-00v	1		
Pre-closure		corey output		<column>-LDTH<aml>-1Dds_mc-<infil>-01v.in	465	<column>-LDTH<aml>-1Dds_mc-<infil>-01v.ext	465
LDTH restart include files	3-9	define_EBS_fineGrid output	M-L1 <column>	listed in LDTH restart above		Include files	
		readUnits & roack_sun output	R-L <infil>	listed in LDTH restart above			
		E:P1	R-1	modprop_dr-up-00	1		
		E:P1	R-3	dkm-afc-EBS_Rev10	1		
		heatgenAge output	H-L1	LDTH-SDT-0.3Qheat-50y_vent-00	1		
		NUFT output	pre-clos	LDTH:\<aml><infil><column>			
		N:L1		run_control_param_LDTH-v01	1		
		N:L3		output.times-<aml>-00			
Post-closure		corey output		<column>-LDTH<aml>-1Dds_mc-<infil>-01.in	465	<column>-LDTH<aml>-1Dds_mc-<infil>-01.ext	465

Table 3-7. SDT Nuft Input and Output Files

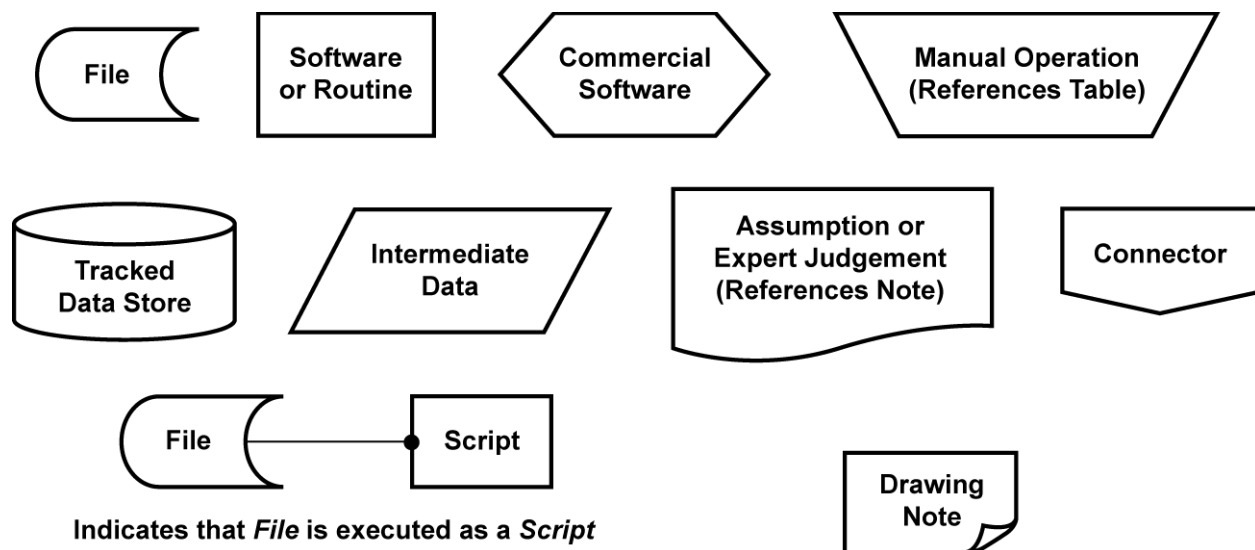
Description	Data Flowchart Figure	Input source	File α #	Input File name	# of files	Output File Name	# of files
SDT Initialization	3-10	define_EBS_fineGrid output	M-S	<column>.nft.msh.dkm0	31	Include files	
		readUnits output	<column>	SDT:\<column>.col.units	31		
		rock_sun output	R-S	SDT-1Dds-mi	1		
		SDT-01i output		<column>-SDT-01-i.in	31	<column>-SDT<aml>-i.ext	31
SDT restart include files	3-10	define_EBS_fineGrid output	M-S	<column>.nft.msh.dkm0	31	Include files	
		readUnits output	<column>	SDT:\<column>.col.units	31		
		rock_sun output	R-S	SDT-1Dds-mi	1		
		heatgenAge output	H-L0	LDTH-SDT-0.3Qheat-1e6y_vent-00v	1		
		N:S2		output.times-00v	1		
		NUFT output	pre-clos	SDT:\<aml><column>. Ztab files			
Pre-closure		SDT-01v output		<column>-SDT<aml>-01v.in	155	<column>-SDT<aml>-01v.ext	155
SDT restart include files	3-10	define_EBS_fineGrid output	M-S	<column>.nft.msh.dkm0	31	Include files	
		readUnits output	<column>	SDT:\<column>.col.units	31		
		rock_sun output	R-S	SDT-1Dds-mi	1		
		heatgenAge output	H-L1	LDTH-SDT-0.3Qheat-50y_vent-00	1		
		N:S2		output.times-<aml>-00	1		
		NUFT output	pre-clos	SDT:\<aml><column>. Ztab files			
Post-closure		SDT-01 output		<column>-SDT<aml>-01.in	155	<column>-SDT<aml>-01.ext	155

Table 3-8. DDT Nuft Input and Output Files

Description	Data Flowchart Figure	Input source	File α #	Input File name	# of files	Output File Name	# of files
DDT Initialization	3-11	define_EBS_fineGrid output	R-1	modprop_dr-up-00	1	Include files	
		readUnits output	R-S	SDT-1Dds-mi	1		
		E:P1	R-D	DDT-EBS_Rev00	1		
		NUFT output	S-Z	I4c3-SDT-01-I.ztab	1		
		heatgenAge output	H-D0	DDT-0.3Qheat-1e6y_vent-00v	1		
		N:D1		run_control_param_DDT-v01	1		
		N:D2		output.times-DDT60-00	1		
		Radpro output		DDT60-03v.radout	1		
		E:D1	M-D1	I4c3-DDT60-03v.in	1	I4c3-DDT60-03v.EBS.ext	1
DDT Preclosure	3-11	E:P1	R-1v	modprop_dr-up-00v	1	Include files	
		readUnits output	R-S	SDT-1Dds-mi	1		
		E:P1	R-D	DDT-EBS_Rev00	1		
		NUFT output	S-Z	I4c3-SDT-01-I.ztab	1		
		heatgenAge output	H-D1	DDT-0.3Qheat-50y_vent-00	1		
		N:D1		run_control_param_DDT-v01	1		
		N:D2		output.times-DDT60-00	1		
		Radpro output		DDT60-03pbf.radout	1		
		E:D1	M-D1	I4c3-DDT60-03pbf.in	1	I4c3-DDT60-03pbf.res	1
DDT Postclosure	3-11	define_EBS_fineGrid output	R-1	modprop_dr-up-00	1	Include files	
		readUnits output	R-S	SDT-1Dds-mi	1		
		E:P1	R-D	DDT-EBS_Rev00	1		
		NUFT output		I4c3-DDT60-03pbf.res	1		
		heatgenAge output	H-D1	DDT-0.3Qheat-50y_vent-00	1		
		N:D1		run_control_param_DDT-v02	1		
		N:D2		output.times-DDT60-00	1		
		Radpro output		DDT60-03pbf.radout	1		
		E:D1	M-D1	I4c3-DDT60-03bff.in	1	I4c3-DDT60-03bff.EBS.ext	1

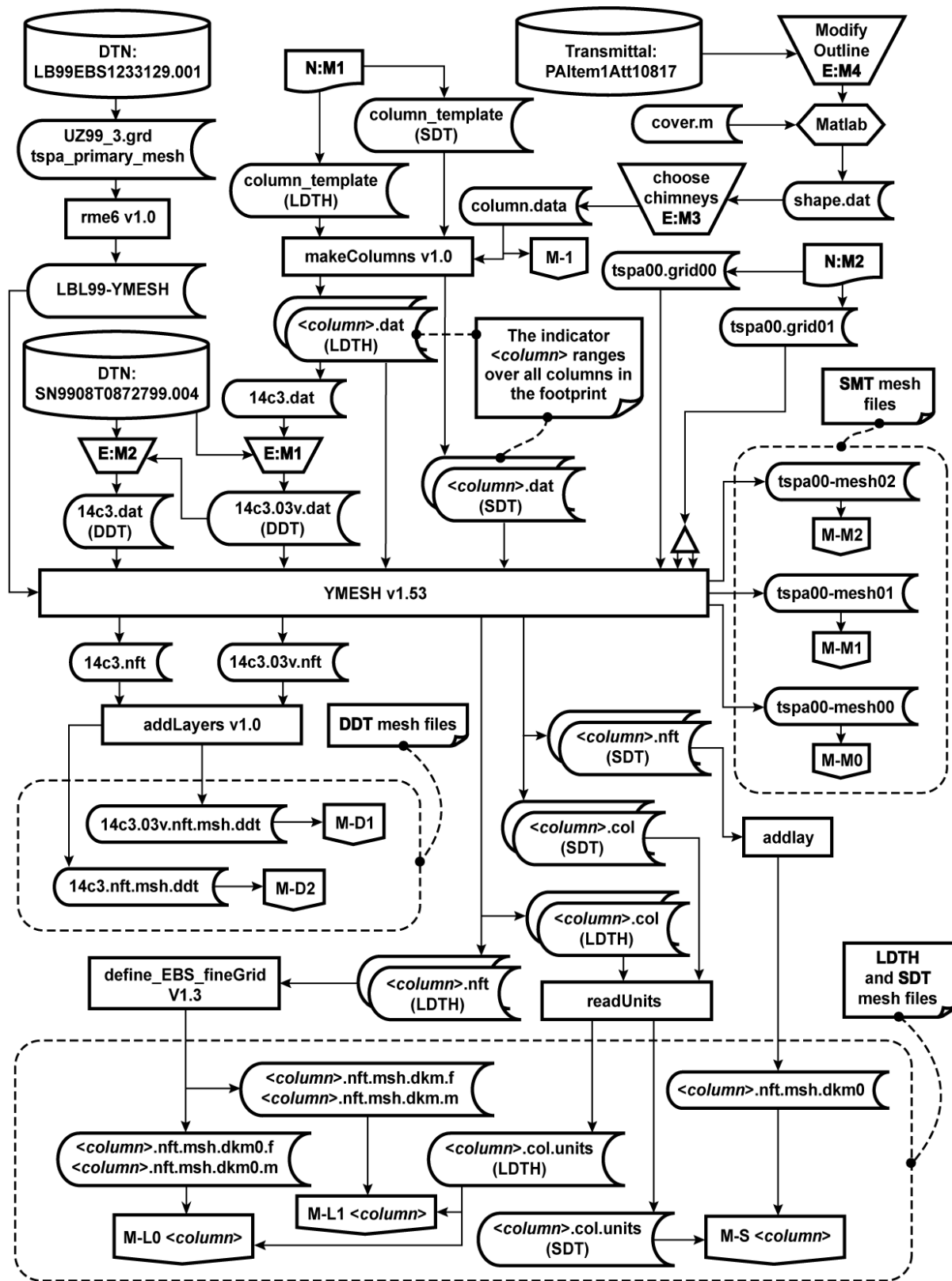
Table 3-9. SMT Nuft Input and Output Files

Description	Data Flowchart Figure	Input source	File α #	Input File name	# of files	Output File Name	# of files
SMT Initialization	3-12	readUnits output	R-S	SDT-1Dds-mi	1	Include files	
		heatgenAge output	B-3	SMT_surfbc	1		
		YMESS output	M-M1	tspa00-mesh01	1		
		N:T1		run_control_param_SMT-v01	1		
			B-4	SMT_bsmtbc	1		
		N:T3		SMT-1Dds-mi-sz	1		
		E:T1		SMT-1Dds-mi-flt	1		
		user developed		SM60-01-i-in	1	SM60-01-i-rst	1
SMT Preclosure	3-12	readUnits output	R-S	SDT-1Dds-mi	1	Include files	
		heatgenAge output	H-M0	SMT-0.3Qheat-1e6y_vent-02v	1		
		YMESS output	M-M2	tspa00-mesh02	1		
		N:T1		run_control_param_SMT-v01	1		
		N:T2		output.times-SMT60-00	1		
		N:T3		SMT-1Dds-mi-sz	1		
		E:T1		SMT-1Dds-mi-flt	1		
		NUFT output		SMT60-01-i-rst	1		
		user developed		SM60-02v.in	1	SM60-02v.rep.ext	1
SMT Postclosure	3-12	readUnits output	R-S	SDT-1Dds-mi	1	Include files	
		heatgenAge output	H-M1	SMT-0.3Qheat-50y_vent-02v	1		
		YMESS output	M-M1	tspa00-mesh01	1		
		N:T1		run_control_param_SMT-v01	1		
		N:T2		output.times-SMT60-00	1		
		N:T3		SMT-1Dds-mi-sz	1		
		E:T1		SMT-1Dds-mi-flt	1		
		NUFT output		SMT60-01-i-rst	1		
		user developed		SM60-02.in	1	SM60-02.rep.ext	1



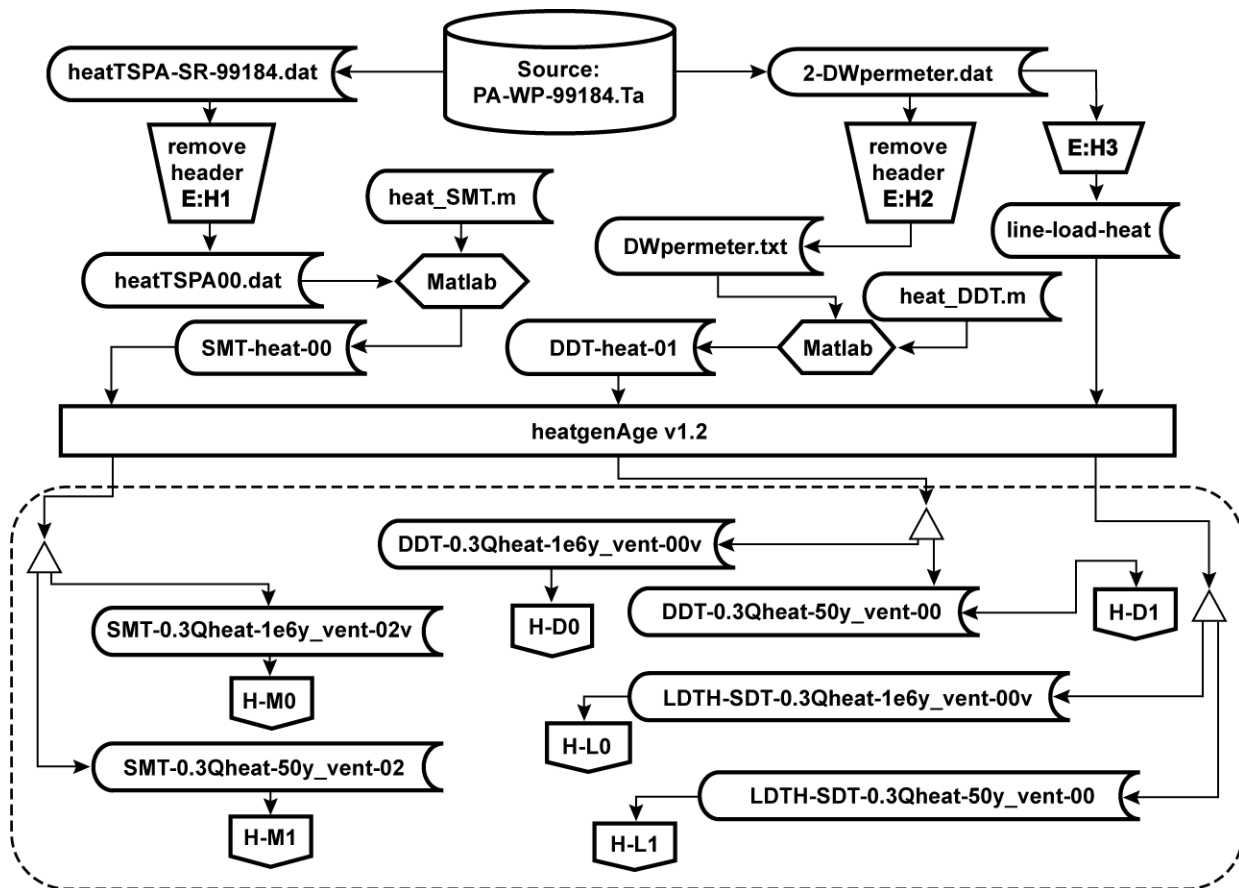
TB_AMR_fig3-1_wr_legend

Figure 3-1. Legend for data flow diagrams.



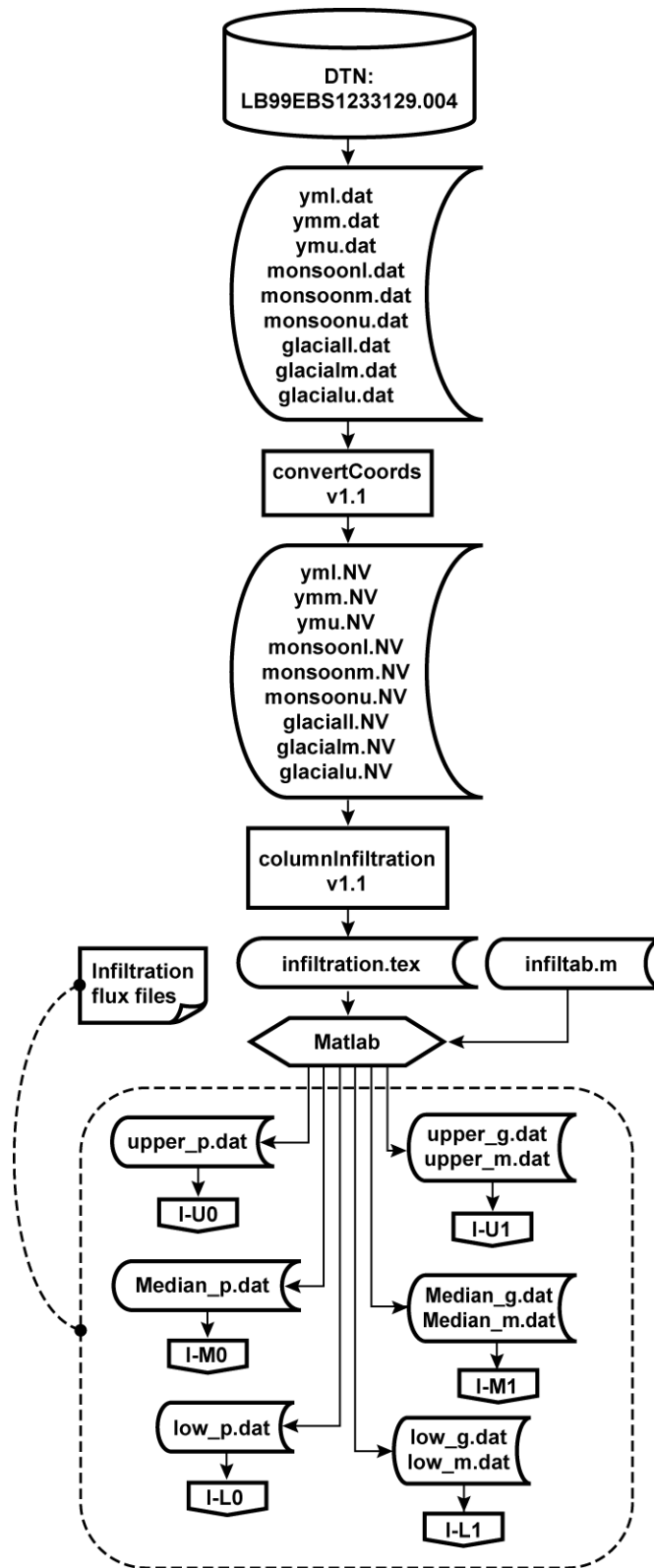
TB_AMR_fig3-2_wr_mesh

Figure 3-2. Generation of numerical meshes for all submodels.



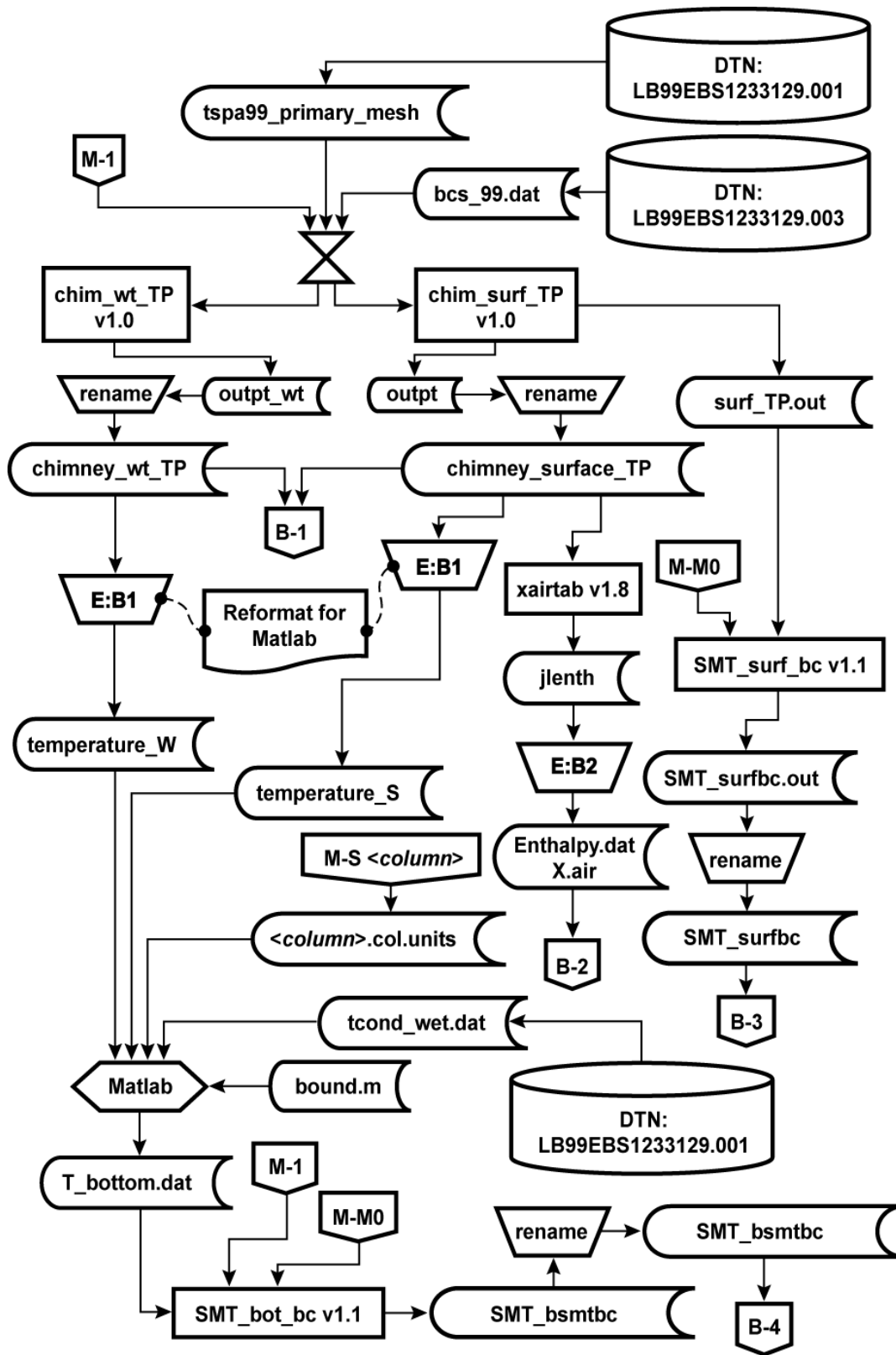
TB_AMR_fig3-3_wr_heat

Figure 3-3. Preparation of heat generation curves for all submodels.



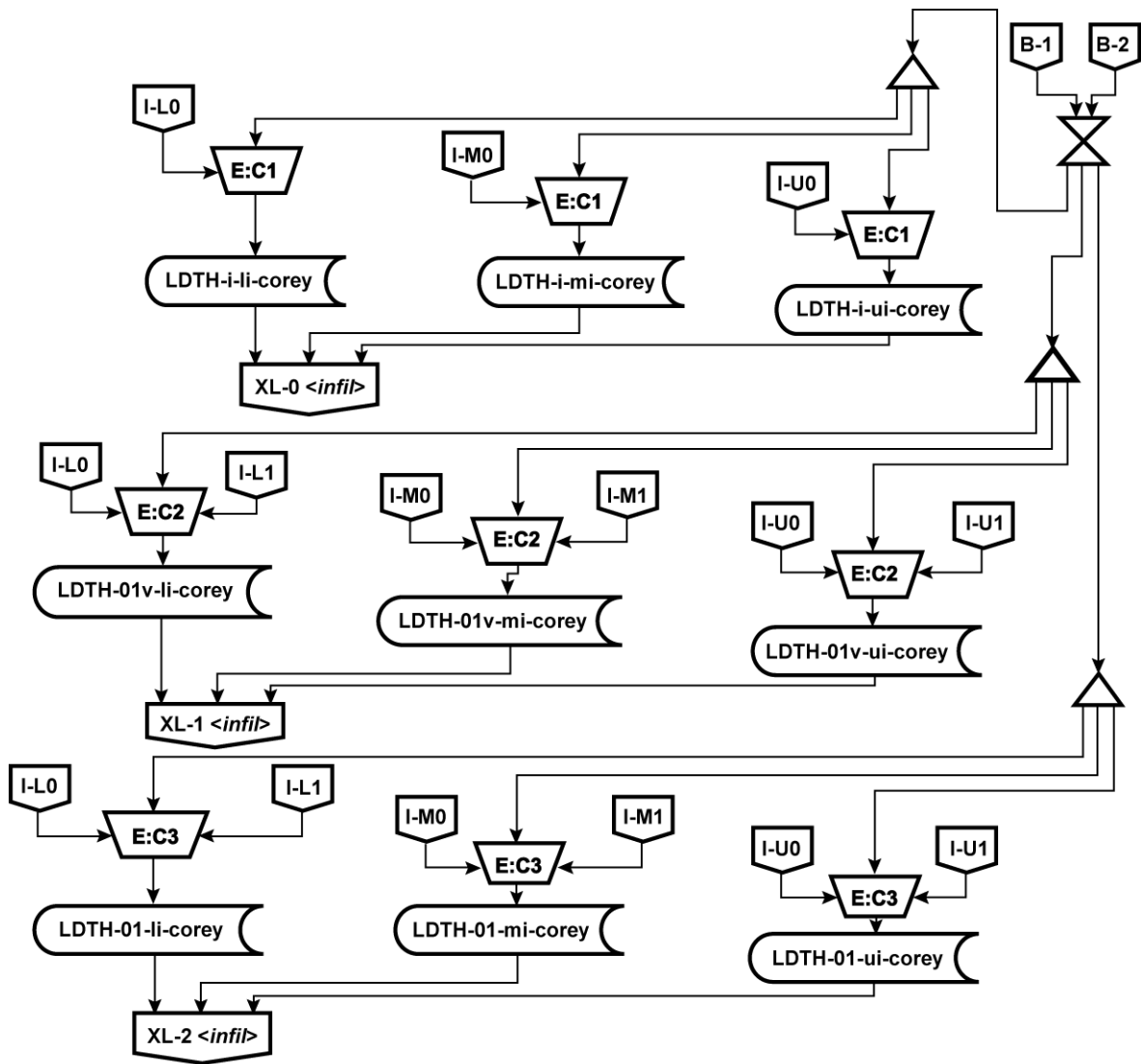
TB_AMR_fig3-4_wr_infil

Figure 3-4. Preparation of infiltration data for LDTH submodels.



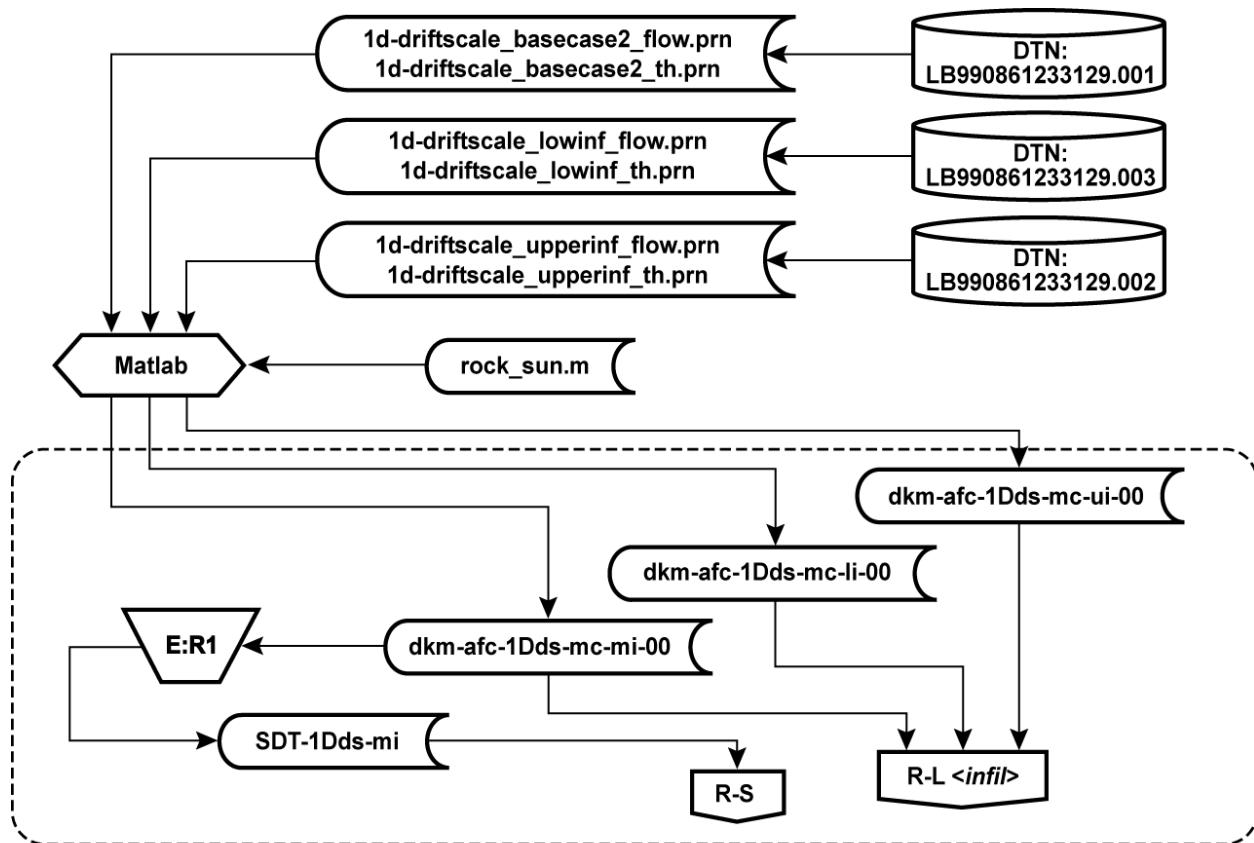
TB_AMR_fig3-5_wr_bc

Figure 3-5. Preparation of boundary conditions for submodels.



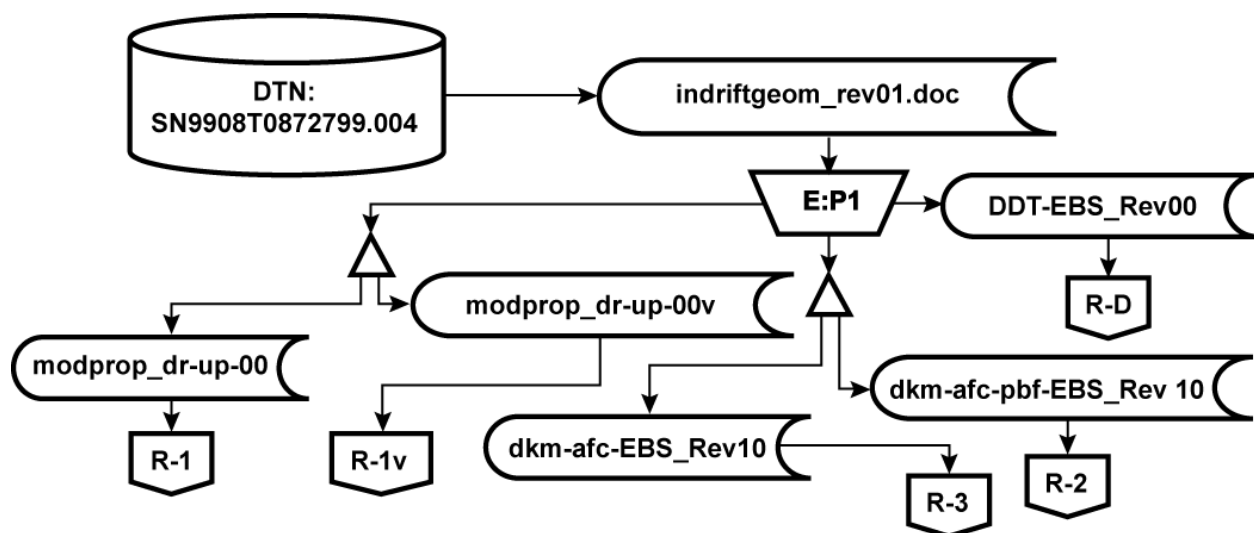
TB_AMR_fig3-6_wr_corey

Figure 3-6. Creation of scripts to generate families of LDTH submodels.



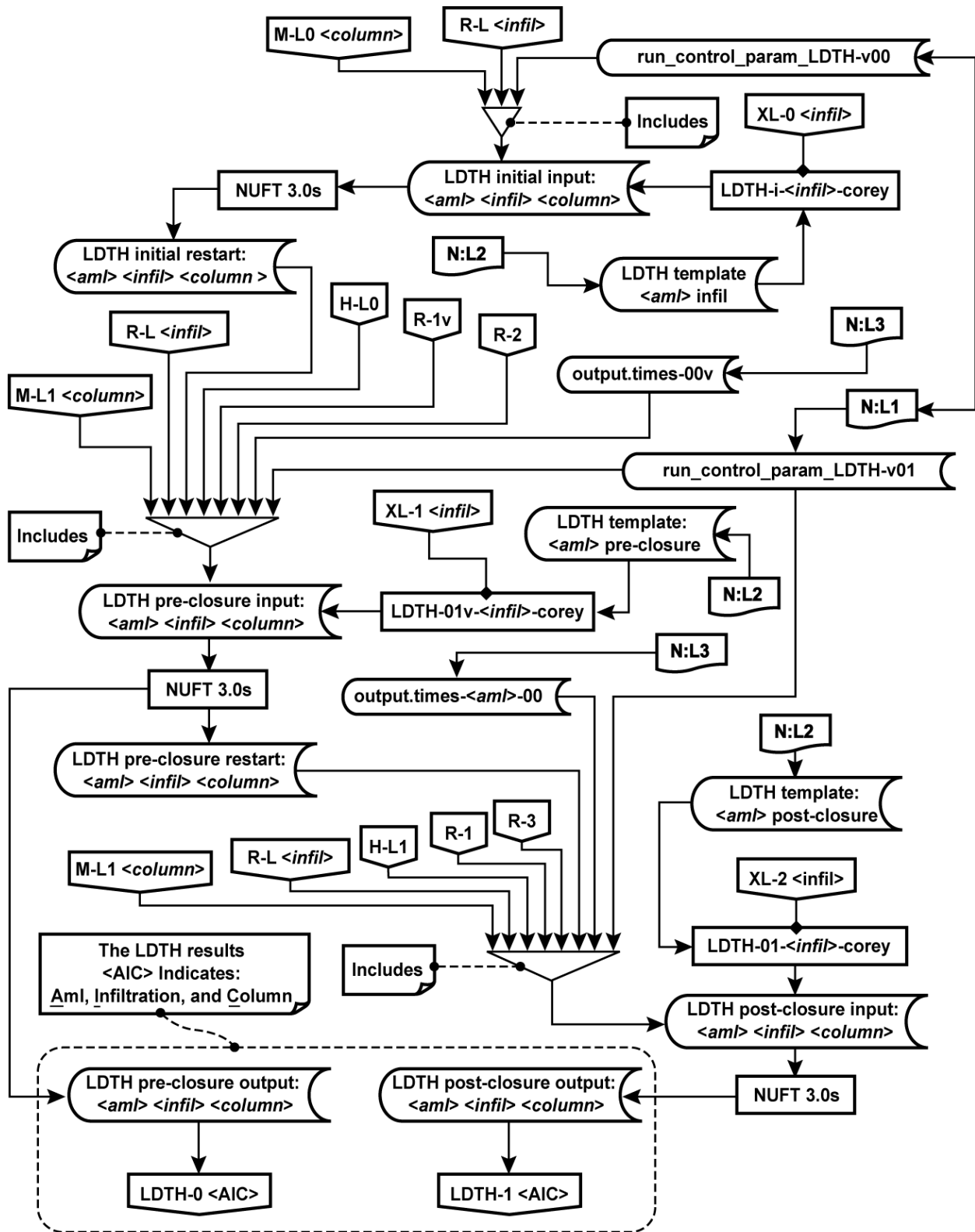
TB_AMR_fig3-7_wr_rock

Figure 3-7. Material properties of the natural system.



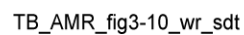
TB_AMR_fig3-8_wr_ebs

Figure 3-8. Material properties of the EBS.

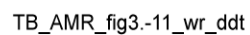


TB_AMR_fig3-9_wr_ldth

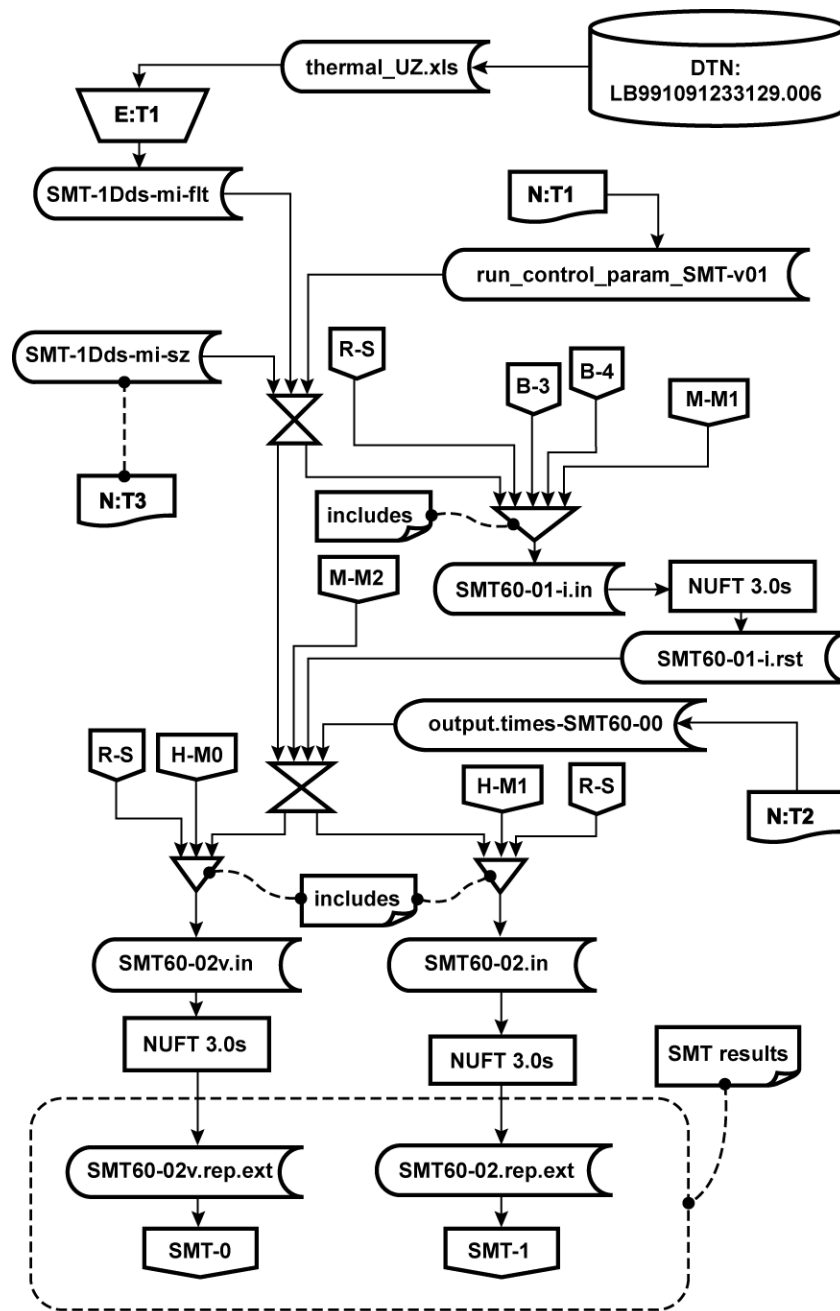
Figure 3-9. Execution of LDTH submodels.



ANL-EBS-MD-000049 REV 00



ANL-EBS-MD-000049 REV 00



TB_AMR_fig3-12_wr_smt

Figure 3-12. Execution of SMT submodels.

4. INPUTS

The inputs to the Multiscale Thermohydrologic Model (MSTHM) are presented in the following sections: Section 4.1 Data and Parameters, Section 4.2 Criteria, and Section 4.3 Codes and Standards.

4.1 DATA AND PARAMETERS

Inputs are outlined in the following sections.

4.1.1 Geometric Description of the EBS and Material Properties

The geometric description of the EBS consists of both longitudinal dimensions (along the longitudinal axis of the emplacement drifts) and the vertical and lateral dimensions in a vertical cross-sectional plane that is orthogonal to the longitudinal axis of the drifts.

4.1.1.1 Repository Footprint

The coordinates of the drift endpoints are given in the file dft1.dat (DTN: MO9911MWDEBSWD.000). These coordinates were used to develop the repository footprint representation used in the SMT submodel (Section 6.2.1), and to generate the 31 LDTH submodel locations in Section 6.3.1. Figure 5-2 illustrates the actual and modeled repository footprint. (TBV). This input is appropriately used.

4.1.1.2 Drift Spacing and Waste-Package Sequencing

Emplacement drifts have an 81-m centerline to centerline spacing (DTN: SN9908T0872799.004, File: indriftgeom_rev01.doc). This information is used in the Discrete-heat-source, Drift-scale, Thermal-conduction (DDT) submodels (Section 6.5). Figure 4-1 shows the drift spacing, WP lengths, and WP sequencing (including WP-to-WP spacing) that is used in this AMR. (TBV). This input is appropriately used.

4.1.1.3 Waste Package Spacing

There is a 0.1-m gap between WPs (DTN: SN9908T0872799.004, File: indriftgeom_rev01.doc). (TBV). This information is used in the DDT submodels (Section 6.5). This input is appropriately used.

4.1.1.4 Drift Diameter

The diameter of the emplacement drifts is 5.5m (DTN: SN9908T0872799.004, File: indriftgeom_rev01.doc). (TBV). Figure 4-2 shows all of the details of the cross-sectional geometry of the emplacement drift after the drip shield and backfill are emplaced. These geometric details are used in this AMR. This information is used in the LDTH submodels (Section 6.3) and in the DDT submodels (Section 6.5). This input is appropriately used.

4.1.1.5 Angle of Repose of Backfill

The angle of repose of the backfill is 26° (DTN: SN9908T0872799.004, File: indriftgeom_rev01.doc). (TBV). This information is used in the LDTH submodels. This input is appropriately used.

4.1.1.6 Minimum Depth of Backfill Cover

The minimum depth of the backfill cover (occurs at an angle equivalent to the angle of repose measured off the vertical drawn from the WP centerline) is 1.495 m (DTN: SN9908T0872799.004, File: indriftgeom_rev01.doc). (TBV). This information is used in the LDTH submodels (Section 6.3). This input is appropriately used.

4.1.1.7 Location of Backfill Peak

The backfill peak crosses the drift centerline 2.25 m above the drift springline (DTN: SN9908T0872799.004, File: indriftgeom_rev01.doc). (TBV). This information is used in the LDTH submodels (Section 6.3). This input is appropriately used.

4.1.1.8 Intersection Between Backfill and Drift Wall

The backfill profile intersects the drift wall 1.0m above the drift springline (DTN: SN9908T0872799.004, File: indriftgeom_rev01.doc). (TBV). This information is used in the LDTH submodels (Section 6.3). This input is appropriately used.

4.1.1.9 Drip Shield Thickness

The drip shield is 0.02m thick (DTN: SN9908T0872799.004, File: indriftgeom_rev01.doc). (TBV). This information is used in the DDT submodels (Section 6.5). This input is appropriately used.

4.1.1.10 Drip Shield Radius

The portion of the drip shield above the centerline of the WP has an inside radius of 1.231 m (DTN: SN9908T0872799.004, File: indriftgeom_rev01.doc). (TBV). This information is used in the LDTH submodels (Section 6.3) and in the DDT submodels (Section 6.5). This input is appropriately used.

4.1.1.11 Location of Waste Package

The WP centerline is 1.945m above the bottom of the drift and 0.805 m below the springline (DTN: SN9908T0872799.004, File: indriftgeom_rev01.doc). (TBV). This information is used in the LDTH (Section 6.3) and DDT submodels (Section 6.5). This input is appropriately used.

4.1.1.12 Waste Package Diameter

The WP outer diameter is 1.67 m (DTN: SN9908T0872799.004, File: indriftgeom_rev01.doc). (TBV). This information is used in the DDT submodels (Section 6.5). This input is appropriately used.

4.1.1.13 Gap Between Waste Package and Drip Shield

The gap between the top half of the WP and the drip shield is 0.396 m (DTN: SN9908T0872799.004, File: indriftgeom_rev01.doc). (TBV). This information is used in the DDT submodels (Section 6.5). This input is appropriately used.

4.1.1.14 Gap Between Waste Package and Invert

The gap between the bottom of the WP and the invert is 0.504 m (DTN: SN9908T0872799.004, File: indriftgeom_rev01.doc). (TBV). This information is used in the DDT submodels (Section 6.5). This input is appropriately used.

4.1.1.15 Invert Height

The top of the invert is 0.606 m above the bottom of the drift (DTN: SN9908T0872799.004, File: indriftgeom_rev01.doc). (TBV). This information is used in the LDTH (Section 6.3) and DDT submodels (Section 6.5). This input is appropriately used.

4.1.1.16 Properties of Air at Model Boundaries

The thermal conductivity of air at 16°C (ground surface) is 0.0254 W/m-K (Bolz and Tuve 1973, p. 11, interpolated). The solid density of air at 24.8°C (intake to emplacement drifts) is 1.185 kg/m³ (Bolz and Tuve 1973, p. 11, interpolated). The specific heat of air at 25°C (intake to emplacement drifts) is 1006 joules/kg (Bolz and Tuve 1973, p. 11). This information is used in the SMT, DDT, and SDT models through incorporation in the file SDT-1Dds-mi. (Accepted data/established fact, handbook value). This input is appropriately used.

4.1.1.17 Properties of EBS Materials

Material properties for the EBS originated in source SN9908T0872799.004 (from the Tabulated In-drift and Thermal Properties Used in Drift-scale Submodels for TSPA-SR). (TBV). The emissivity of the waste package is 0.80 (Lide 1995, pg. 10-298)(accepted data/established fact, handbook value). The value from carbon steel is used as an approximation. This input is appropriately used.

Backfill and invert material properties are given in Table 4-1. This information is used in the LDTH and DDT submodels.

Table 4-1. Backfill and Invert Material Properties

Property	Units	Overton Sand Backfill	Crushed Tuff Invert	Waste Package	Drip Shield
Permeability	m ²	1.43×10^{-11}	6.15×10^{-10}	NA	NA
Porosity	Fraction	0.41	0.545	NA	NA
Van Genuchten a	1/Pa	2.7523×10^{-4}	1.2232×10^{-3}	NA	NA
Van Genuchten b	dimensionless	2	2.7	NA	NA
Residual Saturation	Fraction	0.024	0.092	NA	NA
Grain Density	Kg/m ³	2700	2530	8189.2	4501.72
Grain Specific Heat	J/Kg K	795.492	948	488.86	551.32
Conductivity	W/m-K	0.33	0.66	14.42	20.55
Emissivity	dimensionless	0.93	0.93	0.80*	0.63

Source: (DTN: SN9908T0872799.004, File: indriftgeom_rev01.doc).

* (Lide 1995, pg. 10-298) The value from carbon steel is used as an approximation.

4.1.1.18 Hydrologic and Thermal Properties of Stratigraphic Units

Each stratigraphic unit has two sets of properties, one for its matrix and the other for its fractures. The matrix properties are: permeability, porosity, Van Genuchten α parameter, Van Genuchten β parameter, residual saturation, and saturated saturation. The fracture parameters include the six categories used for the matrix of the rock (although the values for the fractures are different) and 3 additional parameters: active fracture parameter, fracture frequency, and fracture to matrix area. The thermal properties include grain density, grain specific heat, wet thermal conductivity, dry thermal conductivity, and tortuosity. There are three infiltration cases (each corresponding to an expected climate) over which the repository is being modeled. There is a set of hydrologic properties for each of these infiltration cases.

The matrix properties, fracture properties, and thermal properties corresponding to the basecase infiltration flux are given in the file 1d-driftscale_basecase.xls (LB990861233129.001). Properties corresponding to the upper infiltration flux are given in the file 1d-driftscale_upperinf.xls (LB990861233129.002). Properties corresponding to the lower bound infiltration flux are given in the file 1d-driftscale_lowinf.xls (LB990861233129.003).

The basecase matrix properties are reproduced in Table 4-2. The basecase fracture properties are reproduced in Table 4-3. Thermal properties are reproduced in Table 4-4. The tortuosity factor is 0.7.

The hydrologic property sets are used in Section 6.3.5. (TBV). This input is appropriately used.

4.1.1.19 Thermal Properties of Air Inside the Drifts

The thermal conductivity of in-drift air in the DDT submodels is from *Fundamentals of heat and mass transfer* (Incropera and DeWitt 1996, pg. 839: lines 4-12 of the table). The input data is given as a function of temperature in Fahrenheit that is converted to Celsius and used in the file DDT-EBS-Rev00. (TBV). This input is appropriately used.

4.1.1.20 Thermal Properties of Stratigraphic Units for SMT Submodels

The uncalibrated thermal properties of the stratigraphic units are given in Table 4-4. The source of this data is thermal_UZ.xls (LB991091233129.006). This data is edited to create the file SMT-1Dds-mi-flt as described in the editing function E:T1 in Table 3-3 (also see Figure 3-12). This information is used in Section 6.5. This input is appropriately used.

4.1.1.21 Effective Thermal Conductivity of Cavities Inside Drifts

Thermal radiative heat transfer inside cavities within the emplacement drifts can be represented with the use of an effective thermal conductivity, which is given as a function of time. Effective thermal conductivity versus time relationships have been developed in SN9907T0872799.002 (nuftmodprop.txt). (TBV). Portions of this file was copied directly into the file nuftmodprop_dr-up-00 (LDTH and DDT models, post closure runs, thermal k above backfill. The file was also developed from information. For the extended preclosure ventilation cases, the source data is from SN9912T0872799.005 (nuftinpwprec.txt). This file is copied directly into the file nuftmodprop_dr-up-00v with two changes (commented out the last line and moved to the rocktab file, and dr1 was renamed to dr on line 24. The resulting file (nuftmodprop_dr-up-00v) was used in all preclosure LDTH and DDT submodels. This input is appropriately used.

Table 4-2. Matrix Properties of Stratigraphic Units

Unit	Permeability (m ²)	Porosity (Fraction)	Van Genuchten α (Pa ⁻¹)	Van Genuchten β	Residual Saturation (Fraction)	Satiated Saturation (Fraction)
tcw11	3.86E-15	0.253	4.00E-05	0.47	0.07	1
tcw12	2.74E-19	0.082	1.81E-05	0.241	0.19	1
tcw13	9.23E-17	0.203	3.44E-06	0.398	0.31	1
ptn21	9.90E-13	0.387	1.01E-05	0.176	0.23	1
ptn22	2.65E-12	0.439	1.60E-04	0.326	0.16	1
ptn23	1.23E-13	0.254	5.58E-06	0.397	0.08	1
ptn24	7.86E-14	0.411	1.53E-04	0.225	0.14	1
ptn25	7.00E-14	0.499	5.27E-05	0.323	0.06	1
ptn26	2.21E-13	0.492	2.49E-04	0.285	0.05	1
tsw31	6.32E-17	0.053	3.61E-05	0.303	0.22	1
tsw32	5.83E-16	0.157	3.61E-05	0.333	0.07	1
tsw33	3.08E-17	0.154	2.13E-05	0.298	0.12	1
tsw34	4.07E-18	0.11	3.86E-06	0.291	0.19	1
tsw35	3.04E-17	0.131	6.44E-06	0.236	0.12	1
tsw36	5.71E-18	0.112	3.55E-06	0.38	0.18	1
tsw37	4.49E-18	0.094	5.33E-06	0.425	0.25	1
tsw38	4.53E-18	0.037	6.94E-06	0.324	0.44	1
tsw39	5.46E-17	0.173	2.29E-05	0.38	0.29	1
ch1z	1.96E-19	0.288	2.68E-07	0.316	0.33	1
ch1v	9.90E-13	0.273	1.43E-05	0.35	0.03	1
ch2v	9.27E-14	0.345	5.13E-05	0.299	0.07	1
ch3v	9.27E-14	0.345	5.13E-05	0.299	0.07	1
ch4v	9.27E-14	0.345	5.13E-05	0.299	0.07	1
ch5v	9.27E-14	0.345	5.13E-05	0.299	0.07	1
ch2z	6.07E-18	0.331	3.47E-06	0.244	0.28	1
ch3z	6.07E-18	0.331	3.47E-06	0.244	0.28	1
ch4z	6.07E-18	0.331	3.47E-06	0.244	0.28	1
ch5z	6.07E-18	0.331	3.47E-06	0.244	0.28	1
ch6	4.23E-19	0.266	3.38E-07	0.51	0.37	1
pp4	4.28E-18	0.325	1.51E-07	0.676	0.28	1
pp3	2.56E-14	0.303	2.60E-05	0.363	0.1	1
pp2	1.57E-16	0.263	2.67E-06	0.369	0.18	1
pp1	6.40E-17	0.28	1.14E-06	0.409	0.3	1
bf3	2.34E-14	0.115	4.48E-06	0.481	0.11	1
bf2	2.51E-17	0.259	1.54E-07	0.569	0.18	1

DTN: LB990861233129.001

Table 4-3. Fracture Properties of Stratigraphic Units

Unit	Permeability (m ²)	Porosity	Van Genuchten α (Pa ⁻¹)	Van Genuchten β	Residual Saturation (Fraction)	Saturated Saturation (Fraction)	Active Fracture Parameter	Frequency (1/m)	Fracture to matrix area (m ² /m ³)
tcw11	2.41E-12	0.028	3.15E-03	0.627	0.01	1	0.30	0.92	1.56
tcw12	1.00E-10	0.02	2.13E-03	0.613	0.01	1	0.30	1.91	13.39
tcw13	5.42E-12	0.015	1.26E-03	0.607	0.01	1	0.30	2.79	3.77
ptn21	1.86E-12	0.011	1.68E-03	0.58	0.01	1	0.09	0.67	1.00
ptn22	2.00E-11	0.012	7.68E-04	0.58	0.01	1	0.09	0.46	1.41
ptn23	2.60E-13	0.0025	9.23E-04	0.61	0.01	1	0.09	0.57	1.75
ptn24	4.67E-13	0.012	3.37E-03	0.623	0.01	1	0.09	0.46	0.34
ptn25	7.03E-13	0.0062	6.33E-04	0.644	0.01	1	0.09	0.52	1.09
ptn26	4.44E-13	0.0036	2.79E-04	0.552	0.01	1	0.09	0.97	3.56
tsw31	3.21E-11	0.0055	2.49E-04	0.566	0.01	1	0.06	2.17	3.86
tsw32	1.26E-12	0.0095	1.27E-03	0.608	0.01	1	0.41	1.12	3.21
tsw33	5.50E-13	0.0066	1.46E-03	0.608	0.01	1	0.41	0.81	4.44
tsw34	2.76E-13	0.01	5.16E-04	0.608	0.01	1	0.41	4.32	13.54
tsw35	1.29E-12	0.011	7.39E-04	0.611	0.01	1	0.41	3.16	9.68
tsw36	9.91E-13	0.015	7.84E-04	0.61	0.01	1	0.41	4.02	12.31
tsw37	9.91E-13	0.015	7.84E-04	0.61	0.01	1	0.41	4.02	12.31
tsw38	5.92E-13	0.012	4.87E-04	0.612	0.01	1	0.41	4.36	13.34
tsw39	4.57E-13	0.0046	9.63E-04	0.634	0.01	1	0.41	0.96	2.95
ch1z	3.40E-13	0.0002	1.43E-03	0.631	0.01	1	0.10	0.04	0.11
ch1v	1.84E-12	0.0007	1.09E-03	0.624	0.01	1	0.13	0.10	0.30
ch2v	2.89E-13	0.0009	5.18E-04	0.628	0.01	1	0.13	0.14	0.43
ch3v	2.89E-13	0.0009	5.18E-04	0.628	0.01	1	0.13	0.14	0.43
ch4v	2.89E-13	0.0009	5.18E-04	0.628	0.01	1	0.13	0.14	0.43
ch5v	2.89E-13	0.0009	5.18E-04	0.628	0.01	1	0.13	0.14	0.43
ch2z	3.12E-14	0.0004	4.88E-04	0.598	0.01	1	0.10	0.14	0.43
ch3z	3.12E-14	0.0004	4.88E-04	0.598	0.01	1	0.10	0.14	0.43
ch4z	3.12E-14	0.0004	4.88E-04	0.598	0.01	1	0.10	0.14	0.43
ch5z	3.12E-14	0.0004	4.88E-04	0.598	0.01	1	0.10	0.14	0.43
ch6	1.67E-14	0.0002	7.49E-04	0.604	0.01	1	0.10	0.04	0.11
pp4	3.84E-14	0.0004	5.72E-04	0.627	0.01	1	0.10	0.14	0.43
pp3	7.60E-12	0.0011	8.73E-04	0.655	0.01	1	0.46	0.20	0.61
pp2	1.38E-13	0.0011	1.21E-03	0.606	0.01	1	0.46	0.20	0.61
pp1	1.12E-13	0.0004	5.33E-04	0.622	0.01	1	0.10	0.14	0.43
bf3	4.08E-13	0.0011	9.95E-04	0.624	0.01	1	0.46	0.20	0.61
bf2	1.30E-14	0.0004	5.42E-04	0.608	0.01	1	0.10	0.14	0.43

DTN: LB990861233129.001

Table 4-4. Thermal Properties of Stratigraphic Units

Model Layer	Rock Grain Density	Rock Grain Specific	Dry Conductivity	Wet Conductivity
	Kg/m ³	Heat (J/Kg K)	W/m K	W/m K
tcw11	2550	823	1.6	2
tcw12	2510	851	1.24	1.81
tcw13	2470	857	0.54	0.98
ptn21	2380	1040	0.5	1.07
ptn22	2340	1080	0.35	0.5
ptn23	2400	849	0.44	0.97
ptn24	2370	1020	0.46	1.02
ptn25	2260	1330	0.35	0.82
ptn26	2370	1220	0.23	0.67
tsw31	2510	834	0.37	1
tsw32	2550	866	1.06	1.62
tsw33	2510	882	0.79	1.68
tsw34	2530	948	1.56	2.33
tsw35	2540	900	1.2	2.02
tsw36	2560	865	1.42	1.84
tsw37	2560	865	1.42	1.84
tsw38	2360	984	1.69	2.08
tsw39	2360	984	1.69	2.08
ch1z	2310	1060	0.7	1.31
ch1v	2310	1060	0.7	1.31
ch2v	2240	1200	0.58	1.17
ch3v	2240	1200	0.58	1.17
ch4v	2240	1200	0.58	1.17
ch5v	2240	1200	0.58	1.17
ch2z	2350	1150	0.61	1.2
ch3z	2350	1150	0.61	1.2
ch4z	2350	1150	0.61	1.2
ch5z	2350	1150	0.61	1.2
ch6	2440	1170	0.73	1.35
pp4	2410	577	0.62	1.21
pp3	2580	841	0.66	1.26
pp2	2580	841	0.66	1.26
pp1	2470	635	0.72	1.33
bf3	2570	763	1.41	1.83
bf2	2410	633	0.74	1.36

DTN: LB991091233129.006

4.1.2 Stratigraphy

The primary input for stratigraphy to map rock materials onto the computational mesh is from two files. The first is `tspa99_primary_mesh` [renamed, original filename is `UZ99_3_3D.mesh` (LB99EBS1233129.001)], which is the numerical mesh for the site-scale UZ flow model. The second is `UZ99_3.grd` (LB99EBS1233129.001), which is the vertices file for that mesh. These two files, which define the numerical mesh for the 3-D site-scale UZ-flow model, are used to generate the numerical meshes for each submodel (Sections 6.2.2, 6.3.2, 6.4.2 and 6.5.2). This input is appropriately used.

4.1.3 Infiltration Flux

Infiltration flux is given for three climate periods: [present climate ($0 < t < 600$ yr:), monsoonal climate ($600 < t < 2000$ yr), and glacial climate ($2000 < t < 1000000$ yr)] in the nine files `monsoon*.dat`, `glacial*.dat`, and `ymp*.dat` (*represents l, m and u) (source of these nine files: LB99EBS1233129.004). This information is used in Section 6.3.6. This input is appropriately used.

4.1.4 Heat-Generation Rate

Heat-generation decay curves for each of the MSTHM submodel types are based on information in the files `2-Dwperimeter.xls` and `heatTSPA-SR-99184.txt`. The file `2-Dwperimeter.xls` contains:

- decay curves for CSNF (CRWMS M&O 1999d, Item 2: Table 2, pp 3-6) (TBV),
- decay curves for DHLW (SNT05071897001.004, file: `nrctor4pck.txt`) (TBV),
- decay curves for DSNF (SNT05071897001.004, file: `avgdhlw.txt`) (TBV), and
- a seven waste package model of the waste stream (CRWMS M&O 1999d, Item 2: Worksheet 2, p 16) (TBV).

The CSNF decay curves in `2-Dwperimeter.xls` are duplicated in `heatTSPA-SR-99184.txt`.

This information is used by all submodels (Section 6.2, Section 6.3, Section 6.3, and Section 6.5) through inclusion in the above mentioned files. This input is appropriately used.

4.1.5 Boundary Conditions

Temperature and pressure for the 3-D site-scale UZ-flow model are in the file `bcs99.dat` (LB99EBS1233129.003). This information is used to generate boundary conditions for all submodels (Section 6.2, Section 6.3, Section 6.3, and Section 6.5). This input is appropriately used.

4.1.6 Enthalpy

Liquid enthalpy at 16 and 17 degrees Celsius is 67.19 J/gram and 71.38 J/gram, respectively (Keenan et al 1969, p. 2). Accepted Data (established fact, handbook value) used in Attachment VI. This input is appropriately used.

4.2 CRITERIA

Specific Criteria for this AMR has not been developed at this time.

The calculations for this AMR are based on the following criteria:

1. Repository footprint for EDA II is modeled for a total of 70,000 MTU of waste, including 63,000 MTU of civilian spent nuclear fuel (CSNF) and 7000 MTU of defense high-level water (DHLW), which includes both high-level waste (HLW) WPs and defense spent nuclear fuel (DSNF) WPs.. Extended waste inventories may be addressed in subsequent revisions (Stroupe 2000, Attachment I, p.1).
2. Emplacement drifts are ventilated for the entire preclosure period. The preclosure period is assumed to be 50 yr and drift ventilation is assumed to remove 70% of the heat output from WPs throughout the repository area (Stroupe 2000, Attachment I, p.1).
3. Emplacement drifts are backfilled at the end of the preclosure period. Drip shields are emplaced at the same time as backfill (Stroupe 2000, Attachment I, p.1).

4.3 CODES AND STANDARDS

No codes and standards were used in the preparation of this document.

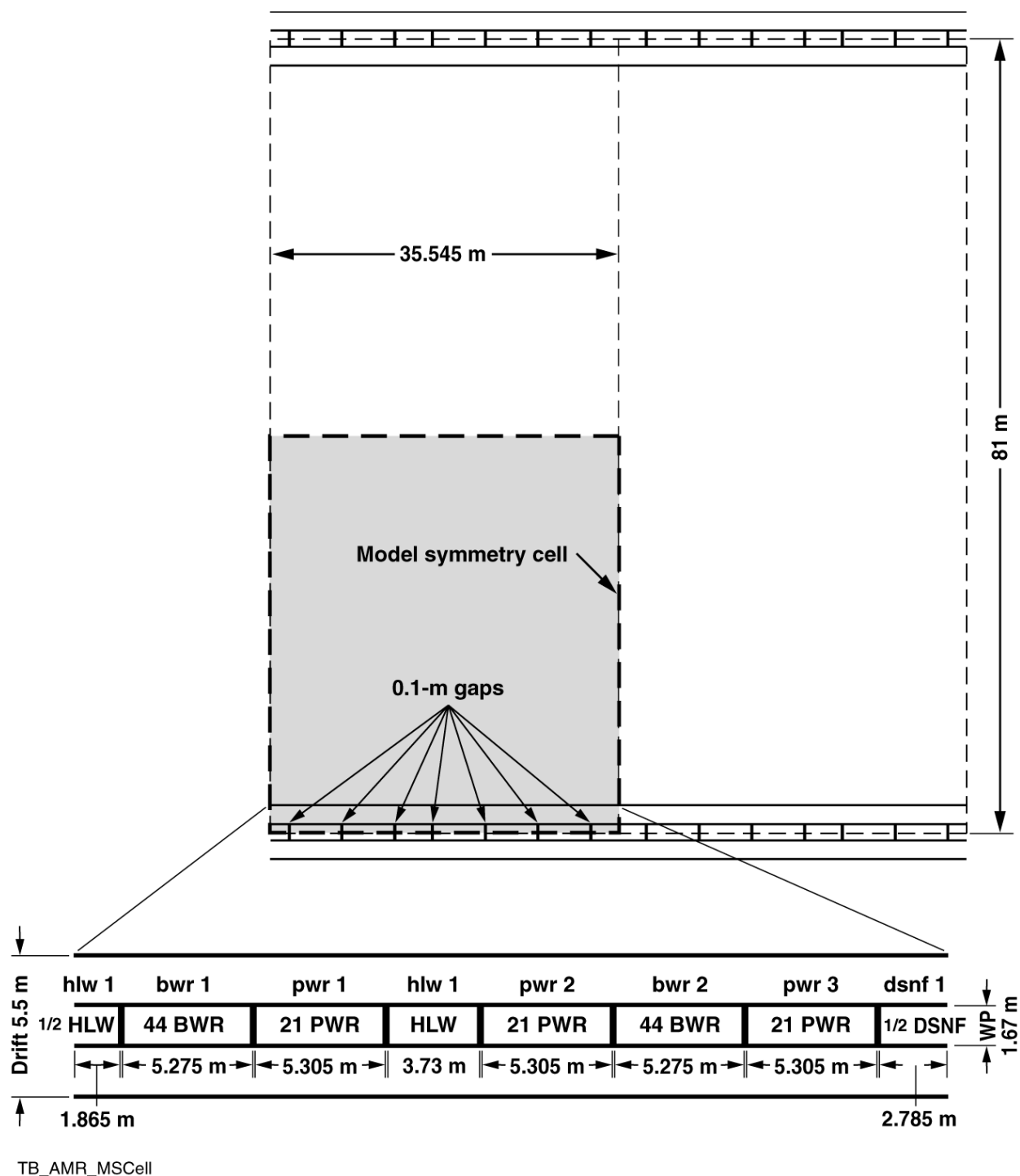
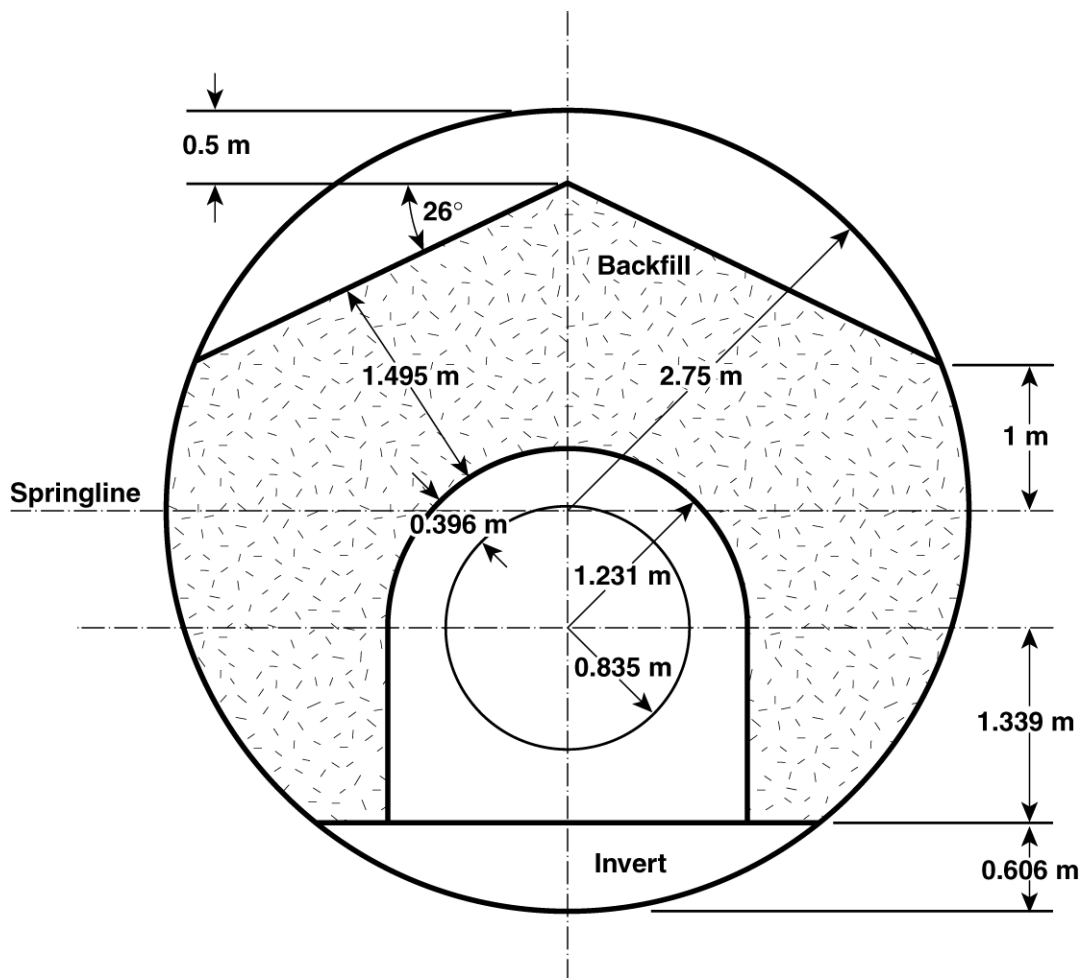


Figure 4-1. Diagram showing drift spacing, WP lengths, and WP spacing that is used in Rev 00 of this AMR (DTN: SN9908T0872799.004). The names of the respective WPs (hlw 1, bwr 1, etc.) used in the DDT submodel (Section 6.5) are given above each WP.



TB_AMR_In-drift_data

Figure 4-2. The cross-sectional geometry of the emplacement drift after backfill is emplaced that is used in Rev 00 of this AMR (DTN: SN9908T0872799.004).

5. ASSUMPTIONS

5.1 BOUNDARY CONDITIONS

5.1.1 AREAL BLOCK MODEL

The repository footprint is adequately represented with the repository model outline shown in Figure 5-1. The variability of stratigraphy, temperature, pressure, and infiltration across the top boundary of the repository is adequately represented by determining these values at the 31 locations in column.data (CRWMS M&O 2000a) and illustrated in Figure 5-2. This assumption is implicit in the file column.data (CRWMS M&O 2000a). Used in Sections 6.3.1 and 6.4.1.

Rationale: The actual repository footprint has an area of 4,310,041 ft² (Table XV-2) and the block model has a cross sectional area of 4,216,139 ft² (Table XV-1). This is a difference of less than three percent. As can be seen in Figure 5-1, the area enclosed by the actual and modeled repository is similar. The 31 locations are evenly spaced within the repository model. The MSTHM grid resolution is precise enough that the results would not be affected by increasing the grid resolution. This assumption does not require confirmation.

5.1.2 Gaussian Interpolation

The normalized results from Gaussian interpolation [(Isaaks and Srivastava 1989, p. 208) and (Kitanidis 1997, p. 54); see Eq. XIV-2] adequately represent infiltration rates.

This assumption is used in all LDTH submodels (Section 6.3) through incorporation in the NUFT input files (CRWMS M&O 2000a, files: *.in). The interpolated data is in the files output from ColumnInfiltration (CRWMS M&O 2000a, 9 files: *.out; see Figure 3-4). The normalization is done in Table XVII-1.

Rationale: The Gaussian method strongly weights the closest points. For a given point, the infiltration rates at relatively close points are the best indicators. It was authors choice to use this method for its application in this document. This assumption does not require confirmation.

5.1.3 Inverse Distance Interpolation

The inverse distance equation (Isaaks and Srivastava 1989, p. 258. See Table XIII-1 for this equation) is appropriate for interpolating temperature and pressures at model boundaries. Chim_surf_TP and chim_wt_TP (validated in Attachment XIII) interpolate the temperature and pressure at the ground surface and water table using the inverse distance cubed equation. SMT_surf_TP and SMT_bot_TP use the inverse distance squared equation to interpolate temperatures at the boundaries of the SMT submodels (Section 6.2.3 and Attachment IX).

Rationale: The inverse distance method strongly weights the closest points. The actual power chosen is subjective and has a negligible effect on the numerical results. For a given point, the temperature and pressure at relatively close points are the best indicators. It was authors choice to use this method for its application in this document. This assumption does not require confirmation.

5.1.4 Relative Humidity at Ground Surface

The relative humidity at the ground surface is assumed to be 100%. This assumption is used in Section 6.3.3, and impacts all LDTH submodel input files.

Rationale: This bounds humidity effects by minimizing evaporation. This assumption does not require confirmation.

5.1.5 LDTH Boundary Conditions

The density of the upper boundary is assumed to have a value of $1 \times 10^8 \text{ Kg/m}^3$. The heat capacity of the upper boundary is assumed to have a value of $1 \times 10^8 \text{ J/Kg-K}$. The thermal conductivity of the upper boundary is assumed to have a value of 0.17 W/m-K .

Rational: The values used for this boundary condition are required in the NUFT input files, but the specific values chosen have no numerical impact. The thickness of this boundary is $1 \times 10^{-30} \text{ m}$ and the conditions are held constant by NUFT. These values are used in 6.3.3 through incorporation in the files: dkm-afc-1Dds-mc-li-00, dkm-afc-1Dds-mc-mi-00, and dkm-afc-1Dds-mc-ui-00. This assumption does not require confirmation.

5.1.6 SMT, DDT, and SDT Boundary Conditions

The density of the upper boundary is assumed to have a value of 1.185 Kg/m^3 . The heat capacity of the upper boundary is assumed to have a value of $1 \times 10^3 \text{ J/Kg-K}$. The thermal conductivity of the upper boundary is assumed to have a value of 0.0254 W/m-K . These values are used in 6.2.3, 6.4.3, and 6.5.3 through incorporation in the file SDT-1Dds_mi (CRWMS M&O 2000a).

Rational: The values used for this boundary condition are required in the NUFT input files, but the specific values chosen have no numerical impact. The thickness of this boundary is $1 \times 10^{-30} \text{ m}$ and the conditions are held constant by NUFT. This assumption does not require confirmation.

5.2 MATERIAL PROPERTIES

5.2.1 Permeability of Drip Shield and Waste Package

The drip shield and WP are assumed to be impermeable for the entire duration of the MSTHM simulation. This assumption is implicit by the absence of permeable or semi-permeable barriers in the EBS (used throughout).

Rationale: These EBS components will take a long time to fail, and it is beyond the scope of this document to model their failure. Even after these components have been perforated, the capillarity of the overlying Overton sand backfill will prevent (or greatly limit) the flux of water that can enter the perforations. This assumption does not require confirmation.

5.2.2 Tortuosity of Backfill and Invert Materials

The assumed value for tortuosity of the backfill and invert materials is 0.7. This assumption is used in all NUFT input files (used throughout). (TBV).

Rationale: This value is consistent with the tortuosity values in Section 4.1.1.18. This assumption does not require confirmation.

5.2.3 Saturated Saturation of Invert and Backfill Materials

The assumed value for saturated saturation of the invert and backfill materials is 1.0. This assumption is used in all NUFT input files (used throughout).

Rationale: This is an upper bound for this parameter, and is therefore conservative. This assumption does not require confirmation.

5.2.4 Thermal Conductivity Used in Conduction-Only Submodels

The thermal conductivity data is provided for both dry and wet conditions. The conduction-only submodels (SDT, DDT, and SMT submodels) cannot explicitly represent the influence of liquid saturation on thermal conductivity. Because the rock is predominately closer to being fully saturated (i.e., wet), it was decided to assume the wet value of thermal conductivity (See Table 4-4) for all of the conduction-only submodels. This assumption is used in Sections 6.2.5 and 6.4.5, and has no effect on the results of the MSTHM.

Rationale: This assumption has no effect on the MSTHM results because the influence of liquid saturation is explicitly represented by the LDTH submodels. The scanning curves that relate LDTH temperature to SDT temperature (see Section 6.6 for MSTHAC methodology) automatically correct for the influence of TH processes (including liquid saturation) on temperature. As long as the SDT and SMT submodels utilize consistent assumptions (and data) concerning the thermal conductivity of the stratigraphic units, then the influence of liquid saturation on temperature is rigorously accounted for. As for the validity of this assumption in the DDT submodel, it is important to note that the DDT submodel is only used for two purposes: (1) calculating the temperature difference between the WP and drip shield and (2) calculating the longitudinal temperature variations along the drift axis. Neither of these quantities are influenced by whether wet or dry thermal conductivity is applied in the host rock. This assumption does not require confirmation.

5.2.5 Saturated-Zone Thermal Conductivity

The SMT submodel (Section 6.2) is the only submodel that explicitly represents the saturated zone (SZ). A description of the distribution of the stratigraphic units below the water table is not available; therefore, there was no available data source for determining the distribution of the stratigraphic units in the SZ portion of the SMT submodel. An assumption is made that the SZ is comprised of the pp1 unit (Table 4-1) because it is the predominant stratigraphic unit at the water

table for the 31 drift-scale-submodel locations. At 14 out of 31 drift-scale-submodel locations, the pp1 unit is at the water table. Used in Section 6.2.

Rationale: The pp1 unit is the predominant unit at the water table of the 31 drift-scale-submodel locations (with 14 out of 31 locations having the pp1 unit at the water table). Furthermore, for the 5 stratigraphic units (pp4, pp3, pp2, pp1, bf3, and bf2) that reside at the water table in the 31 drift-scale-submodel locations, the average wet thermal conductivity is 1.375 W/m-K [$1.375 = (1.21 + 1.26 + 1.26 + 1.33 + 1.83 + 1.36)/6$], which is very close to the value of wet thermal conductivity in the pp1 unit (Table 4-4, 1.33 W/m-K). The output of this report is not sensitive to this assumption, and therefore this assumption does not need confirmation.

5.2.6 Thermal Conductivity and Density for the Active Fracture Model

The thermal conductivity and density values of the fracture and matrix are apportioned by the following

fracture conductivity = total conductivity x (fracture porosity)

matrix conductivity = total conductivity x (1 - fracture porosity)

fracture density = total density x (fracture porosity)

matrix density = total density x (1 - fracture porosity)

There is no commonly accepted approach to apportioning fracture and matrix conductivity and density. However, it is important to note that we conserve the total value of conductivity and the total value of density. Therefore, the total conductive heat flow is the same as a single continuum with the same total value of thermal conductivity. Similarly, during the transient (heatup) period, we honor the correct mass density of the rock mass. This assumption has no impact on this model. This method is used in all submodels (used throughout). This assumption does not require confirmation.

5.3 HEAT TRANSFER

5.3.1 Horizontal Thermal Conduction

Heat transfer in the horizontal direction is negligible. This assumption is conservative from a temperature standpoint because if energy was lost in the horizontal direction the result would be lower temperatures. Used in Attachment X and Section 6.2.3. This assumption does not require confirmation.

5.3.2 Constant Heat Flux

The present day heat flux from the ground surface to the water table is constant. This assumption allows a simplification in the heat transfer equations used in Attachment X. This assumption has no impact on this model, and does not require confirmation. Used in Attachment X and Section 6.2.3.

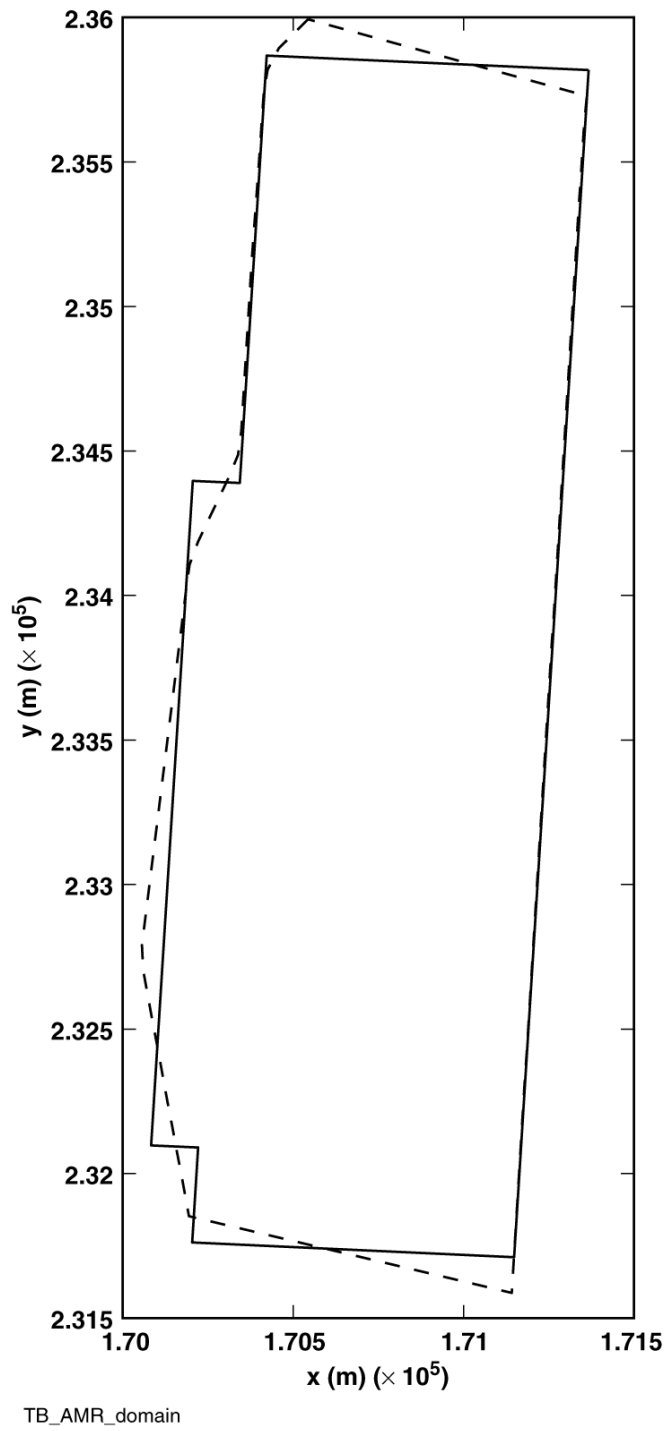
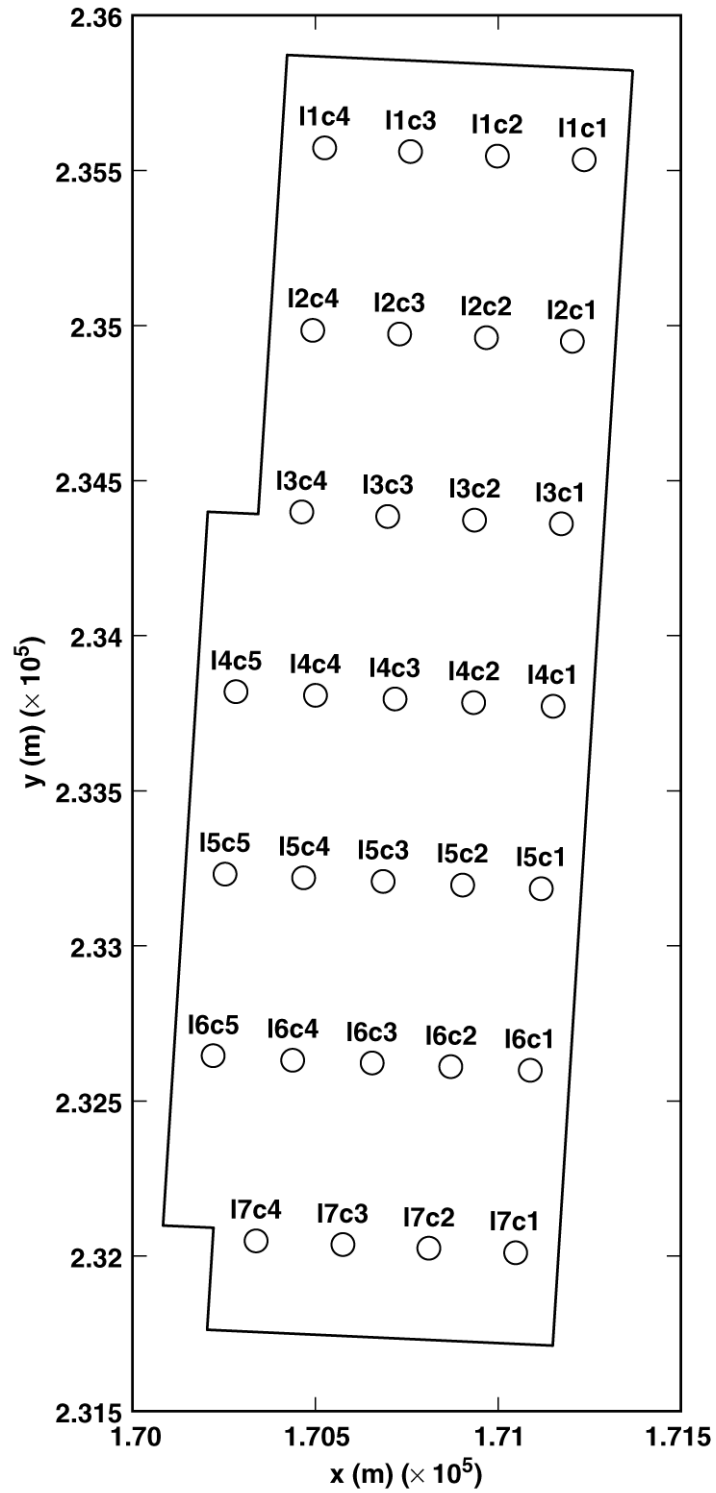


Figure 5-1. Comparison of the actual repository footprint and the approximation of the repository footprint that is assumed in the MSTHM.



TB_AMR_footprint

Figure 5-2. The 31 drift-scale submodel locations used in the MSTHM.

6. ANALYSIS / MODEL

The MSTHM is a computationally efficient means of determining TH conditions in the NFE and EBS as a function of location in the repository and WP type; such determination would otherwise require millions of grid blocks if a brute-force monolithic numerical model were used. The MSTHM captures the key factors affecting NFE and EBS TH conditions:

- Repository-scale variability of percolation flux.
- Temporal variability of percolation flux (as influenced by climate change).
- Uncertainty in percolation flux (as addressed by the mean, high, and low flux scenarios).
- Repository-scale variability in hydrologic properties (e.g., those governing matrix imbibition diffusivity and capillary wicking in fractures).
- Edge-cooling effect (which increases with proximity to the edge of the repository).
- Dimensions and properties of the EBS components, such as the drip shield, engineered backfill and the invert.
- WP-to-WP variability in heat-generation rate.
- Repository-scale variability in overburden thickness.
- Repository-scale variability in thermal conductivity (with an emphasis on the host-rock units).

The influence of these factors on NFE and EBS TH conditions is analyzed in Section 6.11.

The MSTHM calculates 38 NFE and EBS TH variables (Table 1-1). These TH variables are calculated for 623 repository subdomains distributed throughout the repository area (Figure 6-1). Four different WP types (in the specific sequence shown Figure 4-1) are modeled. Because there are 8 different WP locations, this results in 8 different WPs that are considered at each of the 623 repository subdomains. Thus, at each of the 623 repository subdomains, 38 TH variables are calculated for 8 different WPs, resulting in $623 \times 38 \times 8 = 189,392$ TH variables at each calculational timestep. Because there are 352 timesteps, this results in $189,392 \times 352 = 66,855,376$ TH data points per infiltration-flux case. Because there are three infiltration-flux cases (mean, high, and low flux) considered in this AMR, there are a total of $66,855,376 \times 3 = 200,566,128$ TH data points calculated by the MSTHM in this AMR.

6.1 MSTHM CONCEPTUAL MODEL

The need for a multiscale modeling approach stems from the fact that the performance measures depend on TH behavior within a few meters of the emplacement drifts and also on thermal and TH behavior on a repository (or mountain) scale. A single numerical model (e.g., embedding a 3-D drift-scale model with a relatively fine mesh into a 3-D mountain-scale model with a coarse mesh) would require an unfeasible number (millions) of grid blocks. The MSTHM has been developed for estimating the results that would be obtained if such a single model were possible. In addition to coupling the drift scale and mountain scale, the MSTHM also allows for consideration of the effect of different waste packages types (e.g., different CSNF waste packages, co-disposal of defense HLW on the various performance measures.

The MSTHM consists of 4 major submodels (Figure 1-1) and includes multiple scales (mountain and drift), multiple dimensions (1-D, 2-D and 3-D) and varying assumptions regarding the coupling of heat transfer to fluid flow (conduction-only and fully coupled thermohydrologic). These 4 submodels are:

- LDTH (Line-averaged-heat-source, Drift-scale, Thermohydrologic) Submodel
- SMT (Smeared-heat-source, Mountain-scale, Thermal-conduction) Submodel
- SDT (Smeared-heat-source, Drift-scale Thermal-conduction) Submodel
- DDT (Discrete-heat-source, Drift-scale Thermal-conduction) Submodel

It is useful to think of the LDTH submodel as the "core" submodel. These 2-D drift-scale TH submodels are run for 31 locations (Figure 5-2) spaced evenly throughout the repository area for several Areal Mass Loading (AML) values (nominal value and lower) to represent the influence of edge-cooling effects. The LDTH submodel includes the hydrologic processes and parameters (e.g., surface infiltration rates, hydrologic properties) used to describe a location, given specific coordinates within the repository.

The remaining three submodels, which are conduction only, are required to account for the influence of 3-D mountain-scale heat flow and 3-D drift-scale heat flow on drift-scale TH behavior. The coupling of 3-D mountain-scale heat flow to 2-D drift-scale TH behavior is accomplished with the SMT and the SDT submodels. The SMT is 3-D and includes the influence of thermal-property variation in the mountain, lateral heat loss at the repository edges, and overburden-thickness variation with location, assuming a uniform, planar (i.e., smeared) heat source throughout the repository area. The SDT submodel is a 1-D (vertical) submodel, run at the same 31 locations and for the same AMLs as the LDTH submodels. To obtain the "line-averaged" drift-wall temperature (which is roughly equivalent to an average WP location), the relationship between the drift-wall temperature in the LDTH submodel and the "smeared" repository-plane temperature in the SDT submodel is used to modify the temperatures in the SMT submodel, thereby resulting in an MSTHM drift-wall temperature that approximates the effects of the most important TH processes at the drift-scale and the geometry effects of the

mountain scale. At this stage of the MSTHM abstraction methodology, the influence of 3-D drift-scale heat flow has not yet been added.

Because the SMT and SDT submodels both share the same smeared-heat-source approximation and thermal-conduction representation of heat flow, the relationship between the SDT submodel temperature and the LDTH submodel drift-wall temperature allows for the SMT submodel temperature to be "corrected" for both the influence of TH processes on temperature and for the influence of 2-D drift-scale dimensionality (orthogonal to the axis of the drift). The SMT, SDT, and LDTH submodels all share a blended heat-generation history, which blends the heat-generation histories of the entire WP repository; hence, the heat-generation history is effectively that of an "average" WP. The DDT submodel is a 3-D drift-scale submodel which includes individual WPs (with distinctive heat-generation histories) and accounts for thermal radiation in addition to thermal conduction between the WPs and drift surfaces. The drift-wall temperatures for an average WP, calculated with the combined use of the LDTH, SMT and SDT submodels, are then further modified to account for waste-package-specific deviations using the DDT submodel. This is accomplished by relationships between local temperatures at various "point" locations along the drift (such as on the drift wall, drip shield surface, and WP surface) and the corresponding "line-averaged" temperature in the DDT submodel.

The results of the MSTHM submodels are integrated with the use of the MSTHAC. Details of MSTHAC and the 4 submodels (LDTH, SMT, SDT and DDT) are discussed in Section 6.11.

6.2 SMT SUBMODELS

The 3-D SMT submodel is used to determine the repository-scale variations in host-rock temperature T resulting from the heat output from the entire inventory of 70,000 MTU of waste, including 63,000 MTU of civilian spent nuclear fuel (CSNF) and 7000 MTU of DHLW, which includes both HLW WPs and DSNF WPs (Section 4.1.4). The SMT submodel includes the influence of mountain-scale thermal-property distribution, the edge-cooling effect, which results from lateral heat loss at the repository edges, and the overburden-thickness distribution. (Overburden thickness is defined to be the depth of the repository horizon below the ground surface.) The SMT submodel domain extends from the ground surface to 1000 m below the present-day water table and the lateral (adiabatic) boundaries are far enough away from the repository so that they do not affect repository temperatures. The temperature 1000m below the water table is found by extrapolation using the routine bound. The extrapolation equation used is developed in Attachment XX, and the use of results from bound requires assumptions

6.2.1 SMT Repository Footprint

The actual and modeled repository footprint (Figure 5-1) both cover similar areas of approximately 4 km² (pg. XV-2). The repository footprint corresponds to the area that is heated by the smeared-heat-source representation of heat generation from WPs. The areal distribution of gridblocks in the repository area of the SMT submodel is the same as that shown in Figure 6-1, except that the northernmost and southernmost rows of repository subdomains are further subdivided in the SMT submodel to better represent the influence of edge cooling along the northern and southern edges of the repository. (MO9911MWDEDSWD)

6.2.2 SMT-Submodel Mesh

The SMT-submodel mesh is constructed so that boundary effects have a negligible effect on the predicted temperatures near the repository. This is accomplished by extending the lateral boundaries beyond the repository edges and extending the lower boundary 1000m below the water table.

The SMT mesh files are output from YMESH (CRWMS M&O 2000a; tspa00-mesh00, tspa00-mesh01, and tspa00-mesh02). The process of generating the numerical mesh for the SMT submodel is illustrated in Figure 3-2.

6.2.3 SMT Submodel Boundary Conditions

The SMT submodel domain extends from the ground surface to 1000 m below the present-day water table. The lateral boundaries, which are adiabatic boundaries, are situated far enough away from the repository so that they do not affect thermal behavior in the repository. The temperature at the lower boundary of the model domain is extrapolated vertically from the temperature gradient at the water table, based on the calculated temperature field from the UZ Site-Scale Model (Section 4.1.3) and the equation developed in Attachment XX based on Assumptions 5.3.1, 5.3.2 and Equation 5. Thermal conditions at the water table vary with location, so the extrapolated temperature varies on the model boundary. The temperature at the ground surface are calculated from the UZ Site-Scale Model, using an inverse distance cubed method discussed in Section 5.1.3. The data-flow chart for the preparation of boundary conditions is given in Figure 3-5; this process is described in Section 6.8.5.

The density of the upper boundary is 1.185 kg/m^3 (5.1.6). The heat capacity of the upper boundary is $1 \times 10^3 \text{ J/Kg-K}$ (5.1.6). The thermal conductivity of the upper boundary is 0.0254 W/m-K (5.1.6). This data is incorporated into the SMT submodel through inclusion in the file: SDT-Dds_mi (CRWMS M&O 2000a).

6.2.4 SMT Submodel Heat Generation Rates

The heat generation rate for the SMT submodel is in the form of a heat versus time table located in NUFT include files. During preclosure the file used is output from heatgenAge (CRWMS M&O 2000a, SMT-0.3Qheat-50y_vent-02). The heat output represented in this file accounts for removal of 70% of the total heat due to ventilation. The postclosure heat generation table is also output from heatgenAge (CRWMS M&O 2000a, SMT-0.3Qheat-1e6y_vent-02v).

6.2.5 SMT Submodel Material Properties

The SMT submodel uses thermal-conduction properties (for the stratigraphic units) consistent with the SDT submodel (Section 6.4.5). These properties are based on Sections 4.1.1.20 and Section 5.2.4 through incorporation in the include file SDT-1Dds-mi (CRWMS M&O 2000a) as illustrated in Figures 3-7 and 3-12. This file incorporates assumption 5.2.4 by using the wet thermal conductivity. Where SZ thermal properties are required the wet thermal conductivity of pp1 are used (Section 5.2.5).

6.2.6 Submodel Simulations

Two SMT-submodel simulations were conducted for this AMR. The first, which is required to calculate pre-closure TH conditions in the MSTHM, was run with the heat-generation rate reduced by 70%. However, only the first 50 years of this simulation is used as the ventilation period ends at that point (Section 4.2). The second, which is required to calculate post-closure TH conditions in the MSTHM, was run for a simulation period of 1,000,000 yr using a step-function heat-generation rate, with the rate reduced by 70% for the first 50 yr and the full nominal rate from 50 yr to 1,000,000 yr. The two SMT simulations are used in all three infiltration-flux (mean, high, and low flux) cases.

6.3 LDTH SUBMODELS

The 2-D LDTH submodels use the dual-permeability method (DKM), modified with the active-fracture concept (AFC), to represent two-phase heat and fluid flow in the fractured porous rock. The LDTH submodels are run at the 31 drift-scale-submodel locations (Figure 5-2) and for 5 different values of Areal Mass Loading (AML = 15, 25, 36, 50, and 60 MTU/acre). Representing the influence of edge-cooling effects requires that most of the LDTH submodel runs use an AML that is less than the nominal value.

These submodels are required to obtain functional relationships (also called “scanning curves”) between “line-averaged” temperatures predicted by the LDTH submodel and the “smeared” host-rock temperatures predicted by the SDT submodel.

The USNT module of NUFT, is used to model flow through a fractured porous media in the LDTH submodels. The key NUFT options used for LDTH simulations include the DKM and the AFC. These modeling methods are NUFT options selected in the NUFT input files.

The DKM conceptualizes the fractured rock as having two interacting materials, one representing the matrix and one representing the fractures. The interaction between the fractures and the matrix is explicitly calculated from the local temperature and pressure differences, thus allowing transient behavior to be predicted. The DKM underestimates the fracture-matrix interaction for steep temperature and pressure gradients (Hardin et al 1998, p. 2). Simulations in this model are at isothermal, so there are no steep temperature or pressure gradients. Therefore, the DKM is appropriate for the model developed in this document.

The active fracture concept accounts for the contact area between the fracture and the matrix (Table 4-3), as well as the frequency of fractures (Table 4-3). The AFC is that fracture flow only occurs through some of the fractures. This is more conservative than assuming the influx flows evenly through all fractures. The flux through a fracture is greater when it has higher saturation and, therefore, focusing flow through a portion of the fractures (i.e., to active fractures) maximizes flux and results in fast pathways for flux through the mountain.

The rock properties in Section 4.1.1.18 were calibrated using an inverse modeling technique that assumes the properties will only be used in DKM employing AFC. Therefore, the DKM and AFC are appropriate NUFT options.

The rock properties in Section 4.1.1.18 were calibrated using an inverse modeling technique that assumes the properties will only be used in DKM employing AFC. Therefore, the DKM and AFC are appropriate NUFT options.

6.3.1 LDTH Submodel Locations

The LDTH submodel locations are in the file column.data. The repository footprint is output from Cover in the file shape.dat (CRWMS M&O 2000a). The manual operation E:M3 in Figure 3-2 is used to grid the repository into 31 representative locations, which are located in the file column.data.

The LDTH submodel locations are shown in Figure 5-2, and represent repository-scale variability of thermal properties, hydrologic properties, infiltration flux, and overburden thickness.

6.3.1.1 Stratigraphic Columns

The stratigraphic columns corresponding to the LDTH submodel locations are output from YMESH in the file <column>.nft (CRWMS M&O 2000a). The software used in manipulating the source data into a YMESH input file (excluding the location file, column.data) are rme6 and makeColumns. The thickness of the stratigraphic units at each location is output from readUnits (CRWMS M&O 2000a, 31 files: <column.col.units>), and is tabulated in Table 6-1.

Table 6-1. Stratigraphic columns used in the 31 drift-scale-submodel locations.

Stratigraphic unit	Drift-scale submodel location								
	I1c1	I1c2	I1c3	I1c4	I2c1	I2c2	I2c3	I2c4	I3c1
tcw11	0.000	1.904	34.922	0.000	0.000	0.000	0.000	0.000	15.908
tcw12	36.856	0.000	36.504	0.000	33.692	0.000	0.000	48.955	90.996
tcw13	7.910	7.617	6.885	3.838	3.867	0.000	1.816	4.746	4.805
ptn21	6.855	7.354	8.115	8.701	6.797	7.500	7.764	8.496	5.918
ptn22	8.760	8.496	8.555	9.111	6.445	5.654	5.156	5.420	6.211
ptn23	6.621	6.387	6.387	6.885	5.010	4.307	3.779	4.043	5.068
ptn24	24.844	22.910	20.449	19.336	15.762	14.707	12.305	10.986	10.254
ptn25	48.164	48.955	50.479	50.947	31.728	33.252	38.408	39.756	22.939
ptn26	11.309	11.514	12.100	12.393	10.137	10.430	11.309	12.773	12.041
tsw31	1.992	1.992	1.992	2.021	1.992	1.992	1.992	1.992	1.992
tsw32	47.139	45.176	41.132	37.442	49.570	48.633	45.732	41.836	52.354
tsw33	76.465	79.160	81.211	81.064	84.160	83.780	85.478	86.982	85.616
tsw34	35.820	36.552	37.051	36.826	32.270	31.352	33.320	34.092	35.700
tsw35	107.316	103.389	98.263	97.218	116.003	113.171	101.807	98.603	115.600
tsw36	7.422	10.625	12.432	11.500	16.406	18.750	28.271	22.422	31.729
tsw37	3.691	5.273	6.240	8.852	8.203	9.375	14.121	11.172	15.850
tsw38	16.348	16.729	16.914	17.559	17.168	16.875	17.461	18.867	18.281
tsw39	6.680	7.207	7.344	7.471	5.713	6.006	6.973	6.943	3.281
ch1v	0.000	0.000	0.000	0.000	0.000	0.000	0.000	0.000	0.000
ch2v	0.000	0.000	0.000	0.000	0.000	0.000	0.000	0.000	0.000
ch3v	0.000	0.000	0.000	0.000	0.000	0.000	0.000	0.000	0.000
ch4v	0.000	0.000	0.000	0.000	0.000	0.000	0.000	0.000	0.000

	Drift-scale submodel location								
ch5v	0.000	0.000	0.000	0.000	0.000	0.000	0.000	0.000	0.000
ch1z	13.623	13.594	11.162	8.828	18.721	19.365	14.648	9.785	15.527
ch2z	33.105	28.682	28.330	26.387	24.082	23.818	21.592	19.219	21.299
ch3z	33.135	28.682	28.330	26.367	24.082	23.789	21.562	19.248	21.328
ch4z	33.105	28.652	28.330	26.367	24.082	23.818	21.592	19.248	21.328
ch5z	33.105	28.682	28.301	26.367	24.082	23.818	21.562	19.219	21.299
ch6	20.596	19.248	19.219	18.779	18.896	18.867	17.783	16.963	17.666
pp4	14.766	16.875	16.758	16.816	18.369	19.365	19.863	19.541	13.652
pp3	7.617	7.676	6.064	6.211	16.084	15.762	13.066	13.359	0.000
Pp2	27.041	30.850	35.977	37.178	6.738	16.729	15.293	15.557	0.000
Pp1	0.000	22.881	48.955	76.465	0.000	0.000	25.869	73.330	0.000
Bf3	0.000	0.000	0.000	0.000	0.000	0.000	0.000	0.000	0.000
Bf2	0.000	0.000	0.000	0.000	0.000	0.000	0.000	0.000	0.000

Table 6-1. (continued)

Stratigraphic unit	Drift-scale submodel location								
	I3c2	I3c3	I3c4	I4c1	I4c2	I4c3	I4c4	I4c5	I5c1
tcw11	0.000	0.000	30.762	0.000	9.199	0.000	32.900	0	0.000
tcw12	38.702	77.930	79.307	73.652	81.416	83.086	89.004	20.801	41.426
tcw13	5.010	4.629	4.541	5.537	5.625	5.391	4.951	4.717	4.717
ptn21	6.152	7.207	8.232	3.838	4.014	4.893	5.947	6.768	2.842
ptn22	5.303	4.600	4.512	3.809	3.750	3.193	2.490	2.812	1.641
ptn23	4.365	3.838	3.838	2.578	2.812	2.754	2.373	2.49	0.000
ptn24	9.727	9.316	8.379	7.236	7.324	7.061	6.533	6.475	6.738
ptn25	22.412	24.785	25.723	16.611	16.025	15.410	14.443	14.561	7.939
ptn26	11.953	11.777	13.096	13.096	13.682	14.619	15.498	15.41	12.393
tsw31	1.992	2.021	1.992	1.992	1.992	2.021	1.992	2.021	2.021
tsw32	49.951	46.260	41.250	50.918	49.482	46.318	42.070	38.466	42.626
tsw33	87.178	88.438	90.176	86.664	84.258	87.412	88.711	89.062	82.676
tsw34	33.750	31.524	31.836	29.700	34.200	31.586	30.254	31.084	32.824
tsw35	117.687	118.965	113.262	105.082	104.424	108.981	111.895	112.638	101.912
tsw36	28.857	24.756	22.725	37.295	35.625	31.348	27.119	23.184	39.375
tsw37	14.414	12.393	11.367	18.633	17.812	15.674	13.594	12.305	19.688
tsw38	19.922	20.654	22.412	15.850	17.842	21.035	23.408	24.688	11.104
tsw39	3.369	4.219	4.717	1.875	2.051	2.871	3.779	4.16	3.545
ch1v	0.000	0.000	8.145	0.000	0.000	0.000	10.166	8.027	20.596
ch2v	0.000	0.000	0.000	0.000	0.000	0.000	0.000	0	16.758
ch3v	0.000	0.000	0.000	0.000	0.000	0.000	0.000	0	16.729
ch4v	0.000	0.000	0.000	0.000	0.000	0.000	0.000	0	0.000
ch5v	0.000	0.000	0.000	0.000	0.000	0.000	0.000	0	0.000
ch1z	15.234	12.451	0.000	17.109	17.080	14.004	0.000	0	0.000
ch2z	19.688	18.281	15.938	20.537	18.926	16.523	14.414	13.096	0.000
ch3z	19.688	18.281	15.908	20.537	18.896	16.523	14.414	13.066	0.000
ch4z	19.688	18.252	15.938	20.566	18.926	16.523	14.414	13.096	16.758
ch5z	19.688	18.281	15.938	20.537	18.926	16.523	14.414	13.096	16.758
ch6	18.135	18.252	17.900	17.666	17.988	18.896	19.629	19.277	16.670
pp4	15.938	16.553	15.498	11.865	11.338	9.932	8.086	8.027	9.258
pp3	22.939	23.115	24.170	17.168	27.246	30.732	33.691	33.34	31.582
pp2	5.273	16.582	16.025	0.000	9.961	16.846	14.707	14.561	18.105
pp1	0.000	25.488	78.457	0.000	0.000	29.619	61.055	55.752	7.295
bf3	0.000	0.000	0.000	0.000	0.000	0.000	17.402	51.533	0.000
bf2	0.000	0.000	0.000	0.000	0.000	0.000	0.000	14.766	0.000

Table 6-1. (continued)

Stratigraphic unit	Drift-scale submodel location								
	I5c2	I5c3	I5c4	I5c5	I6c1	I6c2	I6c3	I6c4	I6c5
tcw11	0.000	0.000	17.080	0.000	0.000	0.000	0.000	28.418	25.723
tcw12	47.607	76.465	92.724	79.805	82.910	63.721	82.324	96.006	97.266
tcw13	5.039	5.068	6.445	6.709	4.834	4.980	4.863	4.658	4.482
ptn21	2.900	2.607	2.314	2.783	2.285	2.461	2.725	2.461	3.164
ptn22	1.992	1.875	2.197	2.637	0.000	0.000	1.904	2.930	3.076
ptn23	0.000	0.000	1.523	1.699	0.000	1.699	0.000	1.963	2.109
ptn24	7.412	7.178	6.240	6.562	4.863	4.482	6.885	7.061	7.002
ptn25	9.023	7.793	7.412	8.145	4.922	4.834	4.189	4.043	3.398
ptn26	13.477	13.242	13.916	14.912	10.400	10.957	11.455	12.451	11.953
tsw31	2.021	1.992	2.021	1.992	1.992	1.992	1.992	1.992	1.992
tsw32	42.568	40.694	38.614	36.446	35.450	34.952	33.632	32.900	31.612
tsw33	83.926	82.520	81.826	82.998	74.297	75.225	73.184	72.480	69.814
tsw34	32.656	31.406	33.555	33.486	36.200	37.422	38.632	39.288	41.338
tsw35	103.194	104.054	103.331	108.507	90.354	92.149	94.933	95.812	97.737
tsw36	36.211	36.211	32.920	25.625	43.740	40.693	35.908	33.740	29.706
tsw37	18.105	18.105	16.436	14.141	21.885	20.361	17.959	16.054	15.664
tsw38	14.912	14.385	16.992	21.055	7.852	9.785	12.305	14.805	14.648
tsw39	3.281	3.691	3.984	4.102	7.090	5.947	5.332	4.805	4.883
ch1v	18.105	18.164	15.264	11.221	23.613	22.354	18.398	14.092	13.184
ch2v	15.264	14.209	12.480	11.279	15.000	13.008	10.576	9.258	8.496
ch3v	15.234	14.209	12.451	0.000	15.000	13.037	10.576	0.000	0.000
ch4v	0.000	0.000	0.000	0.000	15.000	0.000	0.000	0.000	0.000
ch5v	0.000	14.209	0.000	0.000	15.029	13.008	10.576	0.000	0.000
ch1z	0.000	0.000	0.000	0.000	0.000	0.000	0.000	0.000	0.000
ch2z	0.000	0.000	0.000	0.000	0.000	0.000	0.000	0.000	0.000
ch3z	0.000	0.000	0.000	11.309	0.000	0.000	0.000	9.258	8.496
ch4z	15.264	14.209	12.451	11.279	0.000	13.037	10.576	9.229	8.496
ch5z	15.264	0.000	12.480	11.309	0.000	0.000	0.000	9.258	8.496
ch6	17.549	17.168	17.578	18.252	14.092	14.561	15.264	15.938	15.732
pp4	8.350	8.057	7.207	6.826	10.430	8.613	7.324	7.383	7.500
pp3	33.838	34.980	36.943	36.797	32.666	35.215	38.115	39.053	39.668
pp2	15.820	14.883	12.773	12.217	20.977	17.227	13.154	10.840	10.635
pp1	38.760	53.438	63.545	55.137	17.314	58.066	70.312	64.365	64.629
bf3	0.000	0.000	28.389	79.336	0.000	0.000	39.580	88.916	107.051
bf2	0.000	0.000	0.000	0.000	0.000	0.000	0.000	0.000	0.000

Table 6-1. (continued)

Stratigraphic unit	Drift-scale submodel location			
	I7c1	I7c2	I7c3	I7c4
tcw11	0.000	0.000	0.000	5.391
tcw12	68.730	91.142	104.122	105.908
tcw13	6.035	6.006	5.186	6.240
ptn21	3.018	3.164	3.633	3.545
ptn22	0.000	0.000	1.641	1.611
ptn23	0.000	0.000	0.000	0.000
ptn24	5.068	5.244	5.508	5.127
ptn25	0.000	2.139	2.432	2.256
ptn26	11.602	9.990	10.107	10.020
tsw31	2.021	1.992	1.992	1.992
tsw32	27.188	27.129	28.477	27.393
tsw33	67.168	66.826	66.416	65.391
tsw34	39.492	40.772	41.914	41.894
tsw35	87.227	85.997	87.028	90.234
tsw36	36.855	35.146	35.297	29.738
tsw37	18.428	17.578	16.641	16.094
tsw38	12.334	13.184	12.656	13.164
tsw39	10.049	9.229	7.939	8.906
ch1v	23.906	23.906	18.809	18.047
ch2v	12.861	10.723	0.000	0.000
ch3v	12.861	10.723	0.000	0.000
ch4v	12.861	10.723	0.000	0.000
ch5v	12.861	10.723	0.000	0.000
ch1z	0.000	0.000	0.000	0.000
ch2z	0.000	0.000	8.965	8.525
ch3z	0.000	0.000	8.965	8.555
ch4z	0.000	0.000	8.965	8.525
ch5z	0.000	0.000	8.965	8.525
ch6	16.963	15.264	14.678	14.531
pp4	3.516	4.834	6.328	6.270
pp3	35.654	37.441	39.229	39.756
pp2	23.555	21.211	16.934	18.604
pp1	64.277	77.490	70.312	69.668
bf3	0.000	27.158	75.586	89.238
bf2	0.000	0.000	0.000	0.000

6.3.1.2 Vertical Location of Repository Horizon

The EBS is added to the stratigraphic columns (CRWMS M&O 2000a, <column>.nft) by the routine define_EBS_fineGrid. This routine changes the grid blocks at the location of the EBS to the appropriate material. The routine also changes the size of the mesh near the EBS.

The vertical location of the repository horizon at the LDTH submodel locations column.data, in the stratigraphic columns <column>.nft, are tabulated by readUnits (CRWMS M&O 2000a, <column>.col.units) and shown in Table 6-2.

Table 6-2. Summary of the vertical location of the repository horizon at the 31 drift-scale-submodel locations

Submodel location	Host-rock unit	Repository elevation (m)	Overburden thickness (m)	Repository height above water table (m)
I1c1	tsw35	1047.788	352.483	317.799
I1c2	tsw35	1048.672	328.371	318.688
I1c3	tsw35	1049.553	418.821	319.576
I1c4	tsw35	1050.438	360.480	320.446
I2c1	tsw35	1055.706	294.329	325.729
I2c2	tsw35	1056.589	264.504	326.608
I2c3	tsw35	1057.473	281.038	327.486
I2c4	tsw35	1058.356	355.187	328.366
I3c1	tsw34	1063.624	333.000	333.639
I3c2	tsw35	1064.506	282.492	334.518
I3c3	tsw35	1065.390	343.449	335.396
I3c4	tsw35	1066.274	405.744	336.295
I4c1	tsw34	1071.505	278.830	341.520
I4c2	tsw34	1072.314	308.479	342.340
I4c3	tsw35	1073.124	326.642	343.131
I4c4	tsw35	1073.934	395.403	343.951
I4c5	tsw35	1074.744	324.505	344.772
L5c1	tsw34	1079.423	234.543	349.429
L5c2	tsw35	1080.232	267.521	350.250
L5c3	tsw35	1081.042	299.739	351.070
L5c4	tsw35	1081.851	359.211	351.881
L5c5	tsw35	1082.662	363.880	352.682
L6c1	tsw34	1087.340	250.852	357.340
L6c2	tsw35	1088.149	261.623	358.160
L6c3	tsw35	1088.960	313.693	358.980
L6c4	tsw35	1089.770	389.661	359.790
L6c5	tsw35	1090.580	397.366	360.582
L7c1	tsw35	1095.294	249.221	365.308
L7c2	tsw35	1096.178	299.543	366.188
L7c3	tsw35	1097.062	341.653	367.067
L7c4	tsw35	1097.944	357.200	367.944

6.3.2 LDTH Submodel Mesh

The cross-sectional dimensions of the drift for the post-closure period is shown in Figure 4-2; these dimensions were used to build the numerical meshes of the LDTH submodels.

6.3.2.1 Pre-closure LDTH Submodel Mesh

The numerical mesh for the pre-closure LDTH submodel (Figure 6-2) assumes the same representation for the WP and drip shield as is used in the numerical mesh for the post-closure LDTH submodel (Figure 6-3). This lumped approximation of the drip shield and WP is corrected by the manner in which the pre-closure DDT submodel (Figure 6-4), which rigorously

accounts for the actual dimensions of the WP (without the presence of the drip shield), is applied in the MSTHAC methodology (Section 6.6).

6.3.2.2 Post-closure LDTH Submodel Mesh

The numerical mesh for the post-closure submodel (Figure 6-3) assumes that the drip shield and WP are lumped. This lumped approximation of the drip shield and WP is corrected by the manner in which the post-closure DDT submodel (Figure 6-5), which rigorously accounts for the actual WP and drip shield dimensions (including the correct dimensions of the gap between the WP and drip shield), is applied in the MSTHAC methodology (Section 6.6).

6.3.3 LDTH Submodel Boundary Conditions

Because the LDTH submodels are for a symmetry cell between the vertical plane down the center of the drift and the vertical midplane between drifts, the lateral boundaries are adiabatic and no-mass-flow boundaries. The LDTH submodels require temperature, pressure, and gas-phase air-mass fraction at the upper boundary, which represents the ground surface and the lower boundary, which represents the water table (Table 6.3). Both boundaries have constant conditions with time. The density of the upper boundary is $1 \times 10^8 \text{ Kg/m}^3$ (5.1.5). The heat capacity of the upper boundary is $1 \times 10^8 \text{ Kg/m}^3$ (5.1.5). The thermal conductivity of the upper boundary is 0.17 (5.1.5). These values are incorporated in the files dkm-afc-1Dds-mc-li-00, dkm-afc-1Dds-mc-mi-00, and dkm-afc-1Dds-mc-ui-00 (CRWMS M&O 2000a).

The temperature and pressure are based on the grid in Section 4.1.2, the temperatures and pressures in Section 4.1.5, and the locations in column.data (CRWMS M&O 2000a). An interpolation routine is used to relate the temperatures and pressures at various points to the LDTH submodel locations. The routines used for this interpolation are chim_surf_TP and chim_wt_TP. The air mass fraction and liquid enthalpy is found given the resulting temperature and pressure, along with a bounding assumption of 100% humidity (Section 5.1.4). The routine used for this calculation is X.air.

Table 6-3. Boundary conditions used in the drift-scale submodels (LDTH, SDT, and DDT).

Submodel location	Ground-surface			Water Table
	Temperature (°C)	Gas-phase pressure (Pa ⁻¹)	Gas-phase air-mass fraction	Temperature (°C)
l1c1	16.779	8.5320688e+04	0.9860	28.658
l1c2	16.633	8.5178711e+04	0.9861	28.651
l1c3	15.903	8.4462820e+04	0.9866	28.765
l1c4	16.436	8.4987852e+04	0.9862	28.871
l2c1	17.032	8.5583062e+04	0.9858	29.083
l2c2	17.175	8.5722703e+04	0.9857	29.049
l2c3	16.944	8.5497703e+04	0.9859	29.203
l2c4	16.355	8.4923633e+04	0.9863	29.508
l3c1	16.654	8.5236117e+04	0.9861	30.719
l3c2	16.817	8.5393297e+04	0.9860	30.683
l3c3	16.415	8.4996156e+04	0.9862	30.781
l3c4	16.036	8.4626445e+04	0.9865	30.895
l4c1	16.994	8.5587211e+04	0.9858	32.356
l4c2	16.826	8.5418938e+04	0.9860	32.350
l4c3	16.544	8.5134164e+04	0.9862	32.390
l4c4	15.910	8.4510758e+04	0.9866	32.544
l4c5	16.193	8.4794422e+04	0.9864	32.460
l5c1	17.390	8.5986297e+04	0.9855	32.505
l5c2	16.915	8.5510719e+04	0.9859	32.517
l5c3	16.522	8.5125812e+04	0.9862	32.472
l5c4	16.186	8.4795891e+04	0.9864	32.549
l5c5	16.119	8.4729391e+04	0.9865	32.596
l6c1	17.085	8.5700695e+04	0.9858	31.199
l6c2	16.941	8.5551477e+04	0.9859	31.455
l6c3	16.519	8.5129719e+04	0.9862	31.815
l6c4	15.949	8.4569531e+04	0.9866	31.915
l6c5	16.295	8.4910359e+04	0.9863	31.920
l7c1	17.063	8.5692555e+04	0.9858	30.259
l7c2	16.734	8.5359688e+04	0.9860	30.682
l7c3	16.422	8.5048141e+04	0.9862	31.007
l7c4	16.139	8.4765539e+04	0.9864	31.258

6.3.4 LDTH Submodel Heat Generation Rates

The heat generation rates for the LDTH submodels are in the form of heat versus time tables located in NUFT include files. During preclosure the file used is output from heatgenAge (CRWMS M&O 2000a, LDTH-SDT-0.3Qheat-50y_vent-00). The heat output represented in this file accounts for removal of 70% of the total heat due to ventilation. The postclosure heat generation table is also output from heatgenAge (CRWMS M&O 2000a, LDTH-SDT-0.3Qheat-1e6y_vent-00v).

Because any given LDTH submodel cover the same model domain (including the same area in plan view) as the corresponding SDT submodel, the LDTH and corresponding SDT submodel use the same heat-generation rate versus time tables (files).

6.3.5 LDTH Submodel Material Properties

Material properties are output from rock_sun into three files (CRWMS M&O 2000a, dkm-afc-1Dds-mc-mi-00, dkm-afc-1Dds-mc-li-00, dkm-afc-1Dds-mc-ui-00), each one corresponding to an infiltration rate.

1d-driftscale_basecase.xls (LB990861233129.001). Properties corresponding to the upper infiltration flux are given in the file 1d-driftscale_upperinf.xls (LB990861233129.002). Properties corresponding to the lower bound infiltration flux are given in the file 1d-driftscale_lowinf.xls (LB990861233129.003).

The fracture and matrix properties are in the files 1d-driftscale_basecase.xls, 1d-driftscale_upperinf.xls, 1d-driftscale_lowinf.xls (4.1.1.18). These files are renamed and read into the routine rock_sun.). These files are renamed and read into the routine rock_sun (see Figure 3-8). There are three sets of matrix and fracture properties that correspond to the three infiltration cases.

The LDTH EBS properties are based on inputs in Sections 4.1.2.2-4.1.2.5.

6.3.6 Infiltration Flux

Infiltration data is in the nine files from Section 4.1.3, representing three cases (low, mean, and upper, each having three climates (present day, monsoon, and glacial). Infiltration rates at each submodel location in column.data (CRWMS M&O 2000a) are found using a routine that interpolates, and then normalizing the results from the 31 locations.

ConvertCoords prepares the input data for the interpolation routine, columnInfiltration (see Figure 3-4). The output from columnInfiltration is one large file (CRWMS M&O 2000a, infiltration.tex). This file is split into the nine constituent infiltration rates with the routine infiltab. The average of the 31 infiltration rates was found to differ from the average of all the infiltration rates in the source data that were within the repository footprint. To account for this the infiltration rates are normalized with respect to the average of the source data over the repository footprint. The normalization is completed in Attachment XVII.

6.3.7 LDTH Submodel Simulations

Because of the manner in which the MSTHM temperatures are abstracted, it is necessary to account for drift ventilation scenarios by conducting two complete (parallel) MSTHM abstractions (with one that pertains to the pre-closure period and one that pertains to the post-closure period) and then splicing the results of these two MSTHM abstractions at the end of the pre-closure period (i.e., when ventilation ceases). Therefore, it is necessary to run two complete sets of MSTHM submodels to account for ventilation for a given infiltration-flux case.

The LDTH submodel is the only submodel type that has to be run for each of the three infiltration-flux cases (mean, high, and low flux). The simulations for the other three submodel types are applied to all three flux cases.

For a given infiltration-flux case, two sets of LDTH-submodel simulations are required. The first set, which is required to calculate pre-closure TH conditions in the MSTHM, was run with the heat-generation rate reduced by 70%. The second set, which is required to calculate post-closure TH conditions in the MSTHM, was run for a simulation period of 1,000,000 yr using a step-function heat-generation rate, with the rate reduced by 70% for the first 50 yr, and with the full nominal rate applied from 50 yr to 1,000,000 yr.

Each LDTH-submodel set consists of 155 simulations, which comes from 31 drift-scale-submodel locations (Section 6.3.1) and 5 AML values run at each location ($31 \times 5 = 155$). Thus, because there are two sets, a total of 310 LDTH simulations are conducted for a given infiltration-flux case. Because there are three infiltration-flux cases, there are a total of 930 LDTH simulations conducted for this AMR.

6.4 SDT SUBMODELS

The 1-D smeared-heat-source drift-scale thermal-conduction (SDT) submodels are run in parallel with the LDTH submodels at the same 31 locations and for the same AMLs (15, 25, 36, 50, and 60 MTU/acre). These submodels are required to obtain functional relationships (also called “scanning curves”) between “line-averaged” temperatures predicted by the LDTH submodel and the “smeared” host-rock temperatures predicted by the SDT submodel.

6.4.1 SDT Submodel Locations

The SDT submodels are run at the same 31 drift-scale-submodel locations as the LDTH submodel (Section 6.3.1).

6.4.2 SDT Submodel Mesh

The SDT submodels use the same vertical discretization of grid blocks as is used in the SMT submodels (Section 6.2.2). The manner in which the LDTH-SDT temperature scanning curves are developed and used to modify SMT-predicted host-rock temperatures (Section 6.6.3) demands consistency between how heat flow is modeled in the respective SDT and SMT submodels, including consistency in the vertical grid-block discretization in the respective submodels.

6.4.3 SDT Submodel Boundary Conditions

The SDT boundary conditions are the same as the corresponding LDTH submodel (Section 6.3.3). Consistent upper and lower boundary temperatures assures self-consistency with respect to how the LDTH and SDT submodels are used to generate LDTH-temperature versus SDT-temperature scanning curves and how these scanning curves are used in the MSTHAC methodology to correct SMT-predicted temperatures to LMTH conditions (Section 6.3.3). The

data-flow chart for the preparation of boundary conditions is given in Figure 3-5; this process is described in Section 6.8.5.

Because the SDT submodels are for a symmetry cell between the vertical plane down the center of the drift and the vertical midplane between drifts, the lateral boundaries are adiabatic and no-mass-flow boundaries. The SDT submodels require temperature, pressure, and gas-phase air-mass fraction at the upper boundary, which represents the ground surface and the lower boundary, which represents the water table (Table 6.3). Both boundaries have constant conditions with time.

The density of the upper boundary is $1 \times 10^8 \text{ Kg/m}^3$ (5.1.6). The heat capacity of the upper boundary is $1 \times 10^8 \text{ J/Kg-K}$ (5.1.6). The thermal conductivity of the upper boundary is 0.17 (5.1.6). This data is incorporated into the SDT submodel through inclusion in the file: SDT-Dds_mi (CRWMS M&O 2000a).

The temperature and pressure are based on the grid in Section 4.1.2, the temperatures and pressures in Section 4.1.5, and the locations in column.data (CRWMS M&O 2000a). An interpolation routine is used to relate the temperatures and pressures at various points to the SDT submodel locations. The routines used for this interpolation are chim_surf_TP and chim_wt_TP. The air mass fraction and liquid enthalpy is found given the resulting temperature and pressure, along with a bounding assumption of 100% humidity (Section 5.1.4). The routine used for this calculation is X.air.

6.4.4 SDT Submodel Heat Generation Rates

Because any given SDT submodel covers the same model domain (including the same area in plan view) as the corresponding LDTH submodel, the SDT and corresponding LDTH submodel use the same heat-generation rate versus time tables. These are nuft include files output from heatgenAge (CRWMS M&O 2000a, LDTH-SDT-0.3Qheat-50y_vent-00 and LDTH-SDT-0.3Qheat-1e6y_vent-00v), as discussed in Section 6.3.4.

6.4.5 SDT Submodel Material Properties

The SDT submodel uses the same thermal-conduction properties (for the stratigraphic units) that are used in the SMT submodel (Section 6.2.5). These properties are based on Sections 4.1.1.20 and Section 5.2.4 through incorporation in the include file SDT-1Dds-mi (CRWMS M&O 2000a) as illustrated in Figures 3-7 and 3-10.

6.4.6 SDT Submodel Simulations

Two sets of SDT-submodel simulations were conducted for this AMR. The first set, which is required to calculate pre-closure TH conditions in the MSTHM, was run with the heat-generation rate reduced by 70%. The second set, which is required to calculate post-closure TH conditions in the MSTHM, was run for a simulation period of 1,000,000 yr using a step-function heat-generation rate, with the rate reduced by 70% for the first 50 yr, and with the full nominal rate applied from 50 yr to 1,000,000 yr.

Each SDT-submodel set consists of 155 simulations, which comes from 31 drift-scale-submodel locations (Figure 5-2) and 5 AML values run at each location ($31 \times 5 = 155$). Thus, a total of 310 SDT simulations are conducted for this AMR. These two sets of SDT simulations are used in all three infiltration-flux (mean, high, and low flux) cases.

6.5 DDT SUBMODELS

The 3-D DDT submodel is used to account for WP-specific heat output and for thermal radiation between all WP and drift surfaces to determine WP-specific deviations (relative to line-averaged-heat-source conditions) in temperatures in the NFE and EBS (e.g., drift wall, drip shield, and WP). For the pre-closure period (prior to the emplacement of the drip shield and backfill), thermal radiation between the WP and drift surfaces controls the longitudinal temperature deviations along the drift. For the post-closure period (when backfill is present), heat conduction in the backfill controls temperature deviations along the drift. In either case, the values of thermal conductivity in the host rock play a minor role on the magnitude of longitudinal temperature deviations along the drift (Hardin et. al 1998, Section 3.7.5.4).

The DDT submodel is only run at one drift-scale-submodel location (l4c3 in Figure 5-2). The DDT submodel is only used for two purposes: (1) calculating the temperature difference between the WP and drip shield and (2) calculating the longitudinal temperature variations along the drift axis. Neither of these quantities are significantly influenced by the thermal conductivity in the host rock (or in any of the other stratigraphic units). Therefore, it is not necessary to run the DDT submodels at multiple locations because the only potential benefit of running at multiple locations would be to capture the influence of the local thermal conductivity values, which is relatively unimportant with regards to the two quantities that the DDT submodel is required to predict. Advective heat transfer driven by TH behavior in the host rock has little effect on axial temperature variation in the drift. In other words, TH processes in the host rock do not contribute significantly to equalization of axial temperature variations in the drift. Therefore, the conduction-only DDT model adequately represents longitudinal deviations in NFE and EBS temperatures (relative to line-average-heat-source conditions) along the drift.

6.5.1 DDT Submodel Location

The l4c3 drift-scale-submodel location (CRWMS M&O 2000a, column.data) is used for all DDT submodels.

6.5.2 DDT Submodel Mesh

The cross-sectional dimensions of the drift for the post-closure period is shown in Figure 4-2; these dimensions were used to build the numerical meshes of the DDT submodels. For pre-closure conditions, the backfill and drip shield in Figure 4-2 are not present; otherwise all other dimensions are the same as in the post-closure case. All of the DDT-submodel meshes assume a square cross section for the WP, drift wall, and drip shield (were it is present). As was demonstrated previously (Wilder 1996, Table 1.10.4.1), a circular WP in a circular drift can be accurately represented by a square WP in a square drift, provided that the respective circular and square cross-sectional areas are equal.

The longitudinal dimensions of the drift are shown in Figure 4-1. The DDT submodel utilizes symmetry in all four directions: (1) about the vertical midplane down the center of the drift, (2) the vertical midplane down the center of the rock pillar between drifts, (3) the vertical plane that is orthogonal to and intersects the “hlw1” WP, and (4) the vertical plane that is orthogonal to and intersects the “dsnf1” WP (Figure 4-1).

Two DDT-submodel meshes are used; both meshes share the same grid-block spacing in the longitudinal direction. Two of DDT submodels share the same mesh (Section 6.5.2.2 and Section 6.5.2.3), which uses fine grid-block spacing in the lateral and vertical direction in the drift to account for the drip-shield cross section, the gap between the WP and drip shield, and (3) thermal conduction in the backfill and invert. The only difference between these two submodels (Section 6.5.2.2 and Section 6.5.2.3) is the material distributions inside the drift. The other mesh, which is used in the pre-closure DDT submodel, is able to utilize coarser grid-block spacing without diminishing its ability to accurately account for thermal radiation within the drift.

6.5.2.1 Pre-closure DDT Submodel

The pre-closure DDT-submodel mesh (Figure 6-4) is designed to address thermal radiation inside the emplacement; therefore, it does not require to have as fine gridding inside the drift as is required by the post-closure DDT submodel. The grid-block spacing used in this submodel is fine enough to accurately represent thermal radiation inside the drift.

6.5.2.2 Pre-closure (Restart) DDT Submodel

Because the pre-closure DDT submodel and the post-closure DDT submodel have different grid-block spacing inside the drift, it is necessary to have a second pre-closure DDT submodel to produce the restart file required by the post-closure DDT submodel at 50 yr (when the post-closure submodel is started). The “restart” DDT submodel (Figure 6-5) is the same as the post-closure DDT submodel except that all of the gridblocks between the WP and drift wall have air as the specified material; the air in this submodel uses the effective thermal conductivity versus time relationship that was developed to represent thermal radiation inside the drift (Section 4.1.2.6).

6.5.2.3 Post-closure DDT Submodel

The post-closure DDT-submodel mesh (Figure 6-6) is designed to address the details of (1) thermal radiation between the WP and drip shield, (2) thermal conduction in the relatively thin drip shield, and (3) thermal conduction in the backfill and invert. The grid-block spacing used in this submodel (Figure 6-6) is fine address to accurately model these processes.

6.5.3 DDT Submodel Boundary Conditions

The boundary conditions for the DDT submodels are the same as those for the SDT submodel (Figure 6-4) at the l4c3 drift-scale-submodel location (Figure 5-2).

The DDT boundary conditions are the same as the corresponding LDTH submodel (Section 6.3.3).

Because the DDT submodels are for a symmetry cell between the vertical plane down the center of the drift and the vertical midplane between drifts, the lateral boundaries are adiabatic and no-mass-flow boundaries. The DDT submodels require temperature, pressure, and gas-phase air-mass fraction at the upper boundary, which represents the ground surface and the lower boundary, which represents the water table (Table 6.3). Both boundaries have constant conditions with time.

The density of the upper boundary is $1 \times 10^8 \text{ Kg/m}^3$ (5.1.6). The heat capacity of the upper boundary is $1 \times 10^8 \text{ J/Kg-K}$ (5.1.6). The thermal conductivity of the upper boundary is 0.17 (5.1.6). This data is incorporated into the DDT submodel through inclusion in the file: SDT-Dds_mi (CRWMS M&O 2000a).

The temperature and pressure are based on the grid in Section 4.1.2, the temperatures and pressures in Section 4.1.5, and the locations in column.data (CRWMS M&O 2000a). An interpolation routine is used to relate the temperatures and pressures at various points to the DDT submodel locations. The routines used for this interpolation are chim_surf_TP and chim_wt_TP. The air mass fraction and liquid enthalpy is found given the resulting temperature and pressure, along with a bounding assumption of 100% humidity (Section 5.1.4). The routine used for this calculation is X.air.

6.5.4 DDT Submodel Heat Generation Rates

Heat-generation-rate versus time tables, taken from the source data described in Section 4.1.4, are required for the 8 different WPs represented in the DDT submodels (Figure 4-1). The heat generation rate for the DDT submodel is in the form of a heat versus time table located in NUFT include files. During preclosure the file used is output from heatgenAge (CRWMS M&O 2000a, DDT-0.3Qheat-50y_vent-00). The heat output represented in this file accounts for removal of 70% of the total heat due to ventilation. The postclosure heat generation table is also output from heatgenAge (CRWMS M&O 2000a, SMT-0.3Qheat-1e6y_vent-00v).

6.5.5 DDT Submodel Material Properties

The DDT submodel uses the same thermal-conduction properties (for the stratigraphic units) that are used in the SMT and SDT submodels (Section 6.2.5 and Section 6.4.5). These properties are based on Sections 4.1.1.20 and Section 5.2.4 through incorporation in the include file SDT-1Dds-mi (CRWMS M&O 2000a) as illustrated in Figures 3-7 and 3-12. This file incorporates assumption 5.2.4 by using the wet thermal conductivity. In addition to the properties for the stratigraphic units, the DDT submodels require the thermal-conduction properties for the EBS materials (Table 4-1). For the Overton-sand backfill, drip shield, and crushed-tuff invert, the DDT submodels use the same thermal-property values as those used in the LDTH submodels.

For the pre-closure DDT submodel (Figure 6-4), the thermal properties of the gap between the WP and dripshield are those of air (Section 4.1.1.19).

For the pre-closure DDT submodel (Figure 6-5), which is used to start the post-closure DDT submodel (Figure 6-6), the same effective thermal conductivity versus time table (Section 4.1.1.21) is used for the air gap between the WP and drift wall as is used in the pre-

closure LDTH submodels (Figure 6-2). For the post-closure DDT submodel (Figure 6-6), the same effective thermal conductivity versus time table (Section 4.1.1.19) is used for the air gap between the upper backfill surface and the crown of the drift as is used in the post-closure LDTH submodels (Figure 6-3). The solid density and specific heat of the air gap in the drift are standard handbook values (Section 4.1.1.19).

6.5.6 DDT Submodel Simulations

Three DDT-submodel simulations were conducted for this AMR. The three DDT simulations are used in all three infiltration-flux (mean, high, and low flux) cases.

The first, which is required to calculate pre-closure TH conditions in the MSTHM, was run with the heat-generation rate reduced by 70%. The first DDT submodel has no backfill or drip shield in the drift (Figure 6-4).

The second DDT submodel has the same heat-generation rate used in the first DDT submodel and uses the same grid spacing used in the third DDT submodel; however, it has no backfill or drip shield in the drift (Figure 6-5). The second submodel is run for a simulation time of 50 yr to generate the restart file (i.e., initial conditions) for the third DDT submodel.

The third DDT submodel, which is required to calculate post-closure TH conditions in the MSTHM, was run for a simulation period of 50 to 1,000,000 yr using the full nominal heat-generation rate. The third submodel has backfill in the drift (Figure 6-6).

6.6 MSTHAC METHODOLOGY

The conceptual model for the MSTHAC is discussed in Section 6.1. The MSTHAC methodology involves a sequence of calculational steps that is described in the following sections.

6.6.1 Accounting for the Influence of Drift Ventilation

For an MSTHM scenario that does not involve drift ventilation, the calculation sequence described in the following sections is executed once. For an MSTHM scenario that involves drift ventilation during the pre-closure period (which is the case for this AMR), the following MSTHM calculational sequence is executed twice.

As discussed in Section 6.2, Section 6.3, Section 6.4 and Section 6.5, the influence of drift ventilation is approximated by reducing the heat-generation rate during the ventilation period. Then, as ventilation ceases, the heat-generation rate abruptly jumps from its reduced value up to its nominal value. For this AMR, the heat-generation rate is reduced by 70% during the ventilation period. Because of the manner in which the MSTHM temperatures are abstracted it is necessary to account for drift ventilation scenarios by conducting two complete (parallel) MSTHM abstractions. One abstraction pertains to the pre-closure period and one pertains to the post-closure period). The results of these two MSTHM abstractions are then spliced at the end of the pre-closure period (i.e., when ventilation ceases). Therefore, it is necessary to run two

complete sets of MSTHM submodels to account for ventilation for a given MSTHM scenario (e.g., for a particular infiltration-flux scenario).

For the MSTHM abstraction that pertains to the ventilated pre-closure period, the submodels are run with a reduced heat-generation rate for the entire simulation period. For this AMR, the pre-closure submodels were run for 600 yr with the heat-generation rate reduced in all submodels by 70%, which assures that the scanning curves adequately incorporated the influence of the initial portion of the cooldown period. For the MSTHM abstraction for the post-closure period, all submodels are run with a step-function heat-generation-rate history that is reduced by 70% during the pre-closure period and then followed by an abrupt increase to the nominal heat-generation rate at the time of closure (which occurs at 50 yr for this AMR). The second set of submodels calculations are run for 1,000,000 yr.

6.6.2 Accounting for the Emplacement of Backfill

If an MSTHM abstraction involves the emplacement of backfill at the time of closure (as is the case in this AMR), it is necessary to break up the LDTH and DDT submodel calculations into two parts. For the pre-closure period, the LDTH and DDT submodels are conducted with a drift without backfill. A restart file is generated with this submodel run to start the corresponding post-closure submodel run that includes backfill in the drift; the post-closure submodel is started at the time of closure (50 yr).

6.6.3 Computing Drift-Wall Temperatures

To obtain the MSTHM drift-wall temperature for an average WP location at each of the 623 repository subdomains (see Figure 6-1) and for each of the MSTHM timesteps, the relationship between the "line-averaged" drift-wall temperature in the LDTH submodel and the "smeared" temperature in the repository plane of the SDT submodel is used to modify the "smeared" temperatures calculated with the SMT submodel. The result of this stage of the abstraction are the "line-averaged" drift-wall temperatures at each of the 623 repository subdomains and each of the MSTHM timesteps.

The "model" that results from this intermediate step in the MSTHAC calculational sequence could be called the LMTH model, which stands for line-averaged-heat-source mountain-scale thermohydrologic model. The LMTH drift-wall temperatures are further modified to account for waste-package-specific deviations using the DDT submodel. After the DDT submodel has been used to modify the drift-wall temperatures, the result are drift-wall temperatures calculated by a discrete-heat-source mountain-scale TH model (or DMTH model). Thus, the MSTHM is a DMTH model. Details of this procedure are described below.

An overview of the calculational sequence for determining drift-wall temperatures in the MSTHM is as follows:

- SMT-submodel-predicted host-rock temperatures, which is a "smeared" representation of host-rock temperatures in the plane of the repository.

- LMTH-abstracted-model-predicted drift-wall temperatures, which is a “line-averaged” representation of drift-wall temperatures along each emplacement drift in the repository.
- DMTH-abstracted-model-predicted drift-wall temperatures, which is a “discrete” representation of drift-wall temperatures at various points (i.e., specific WP locations with specific heat-generation-rate histories) along each emplacement drift in the repository.

The calculational sequence for determining drift-wall temperatures can be broken down into six steps:

Step 1: Conduct the appropriate submodel simulations. For the case of a pre-closure MSTHM abstraction, this consists of 155 LDTH submodels, 155 SDT submodels, one SMT submodel and one DDT submodel. The number 155 comes from submodel simulations being conducted at 31 drift-scale-submodel locations (Figure 5-2) and for five AML values ($31 \times 5 = 155$). In this case, the nominal repository AML is 60 MTU/acre so the five AML values chosen are: 60 MTU/acre, 50 MTU/acre, 36 MTU/acre, 25 MTU/acre and 15 MTU/acre. The SMT and DDT submodels are both run with an AML of 60 MTU/acre. For the case of a post-closure MSTHM abstraction, the number of LDTH and DDT submodels is doubled; thus, there are 310 LDTH submodels, 155 SDT submodels, 1 SMT submodel and 2 DDT submodels.

Step 2: Tabulate the SMT-submodel-predicted host-rock temperature histories. This step is conducted at each of the 623 repository subdomains (Figure 6-1) and for each of the 352 calculational timesteps used in the MSTHM in this AMR. The result of this step is the SMT-submodel-predicted host-rock temperature, which is the average (thermal-conduction) host-rock temperature at each of the 623 repository subdomains.

Step 3: Build 155 scanning curves at the 31 drift-scale-submodel locations. These curves are plots of the “line-averaged” temperature at the drift wall in the LDTH submodels versus the “smeared” host-rock temperature in the SDT submodels; five curves (for five AMLs) are constructed at each of the 31 locations.

Step 4: Build 3050 scanning curves at the 623 repository subdomains. This step is the construction of five scanning curves (for five AMLs) at each of the 623 repository subdomains (Figure 6-1), which results in 3050 scanning curves ($623 \times 5 = 3115$). This step involves an interpolation process that utilizes the scanning curves at all of the 31 drift-scale-submodel locations. For a given repository-subdomain location and a given AML scanning curve (e.g., the curve for 60 MTU/acre), a new scanning curve is developed, based on an exponentially weighted average of the scanning curves at the 31 drift-scale-submodel locations. Because the influence of any drift-scale-submodel location drops off exponentially with distance, the scanning curve at a repository location is most heavily influenced by its closest (three or four) drift-scale-submodel neighbors. The result of this step is equivalent to having had run 3115 LDTH submodels and 3115 SDT submodels and developing the scanning curve from each LDTH-SDT-submodel pair.

Step 5: Calculate LMTH drift-wall temperature at the 623 repository subdomains. This step determines a line-averaged drift-wall temperature at each of the 623 repository subdomains. This is done by interpolating a new scanning curve on the basis of the five AML scanning curves

(at a given repository subdomain) and the peak SMT-submodel temperature in that subdomain. The peak SMT-submodel temperature is compared to the peak SDT-submodel temperatures in each of the five scanning curves. The new scanning curve lies between the scanning curves that have peak SDT-submodel temperatures that bracket the peak SMT-submodel temperature. The relative distance between the new scanning curve and the two bracketing scanning curves is proportional to the relative distance between the peak SMT-submodel temperature and the two peak SDT-submodel temperatures that bracket it. The relationship between the SDT-submodel temperature and the LDTH-submodel temperature in this scanning curve is then used to adjust the SMT-submodel temperature time-history plot from step #2. This step provides 623 values of drift-wall temperature for line-averaged-heat-source conditions.

Step 6: Calculate 4880 DMTH drift-wall temperatures at the 623 repository subdomains.

This step adjusts the 623 line-averaged drift-wall temperatures from step #5 to provide WP-specific point values. The DDT submodel is used to calculate local temperature “deviations” along the drift. A local temperature deviation is the difference between the local temperature at a “point” on the drift wall and the line-averaged drift-wall temperature along the entire drift in the DDT submodel (Figure 4-1). The temperature histories from step #5 are adjusted for each of the WP locations represented in the DDT submodel (see Figure 4-1). Because there are eight different WPs treated in the DDT submodel, this results in 4880 values ($623 \times 8 = 4984$) of drift-wall temperature.

This procedure is repeated at different locations along the drift wall, including the upper drift wall (i.e., crown of the drift), the lower drift wall (below the invert), and perimeter-averaged temperature on the drift wall.

6.6.4 Computing Host-Rock Temperatures

The calculational procedure in 6.6.3 is repeated for other locations, including those in the near-field host rock, producing WP-specific host-rock temperatures.

6.6.5 Computing Backfill, Drip Shield, and Invert Temperatures

The calculational procedure in 6.6.3 is repeated for other locations, including those in the backfill, on the drip shield, and in the invert, producing WP-specific (backfill, drip-shield, or invert) temperatures.

6.6.6 Computing Waste Package Temperatures

For the pre-closure period, the procedure for calculating WP temperatures is analogous to the procedure described in section 6.6.4 for drift-wall temperatures, with the following minor distinction. The LDTH-SDT scanning curves are constructed with the average of temperatures in the grid blocks that form the outer perimeter of the modeled WP (Figure 6-2) rather than the host-rock grid blocks on the perimeter of the drift wall.

For the post-closure period, which is the time after ventilation has ceased and backfill and the drip shield have been emplaced, an additional calculational step is added to account for the fact that the WP and drip shield are modeled as one lumped material in the LDTH submodel. To do

this, the DDT submodel is used to compute the difference between the WP temperature and the perimeter-averaged drip shield temperature. This temperature difference is added to the WP temperature (which is the temperature of the lumped drip shield and WP) computed by the LDTH submodel. The result of this step are WP-specific WP temperatures. Because there are 8 different WPs treated in the DDT submodel (Figure 4-1) and 623 repository subdomains (Figure 6-1), this results in 4880 values ($623 \times 8 = 4984$) of WP temperature.

6.6.7 Computing Drift-Wall Relative Humidity

The procedure for calculating RH on the drift wall is similar to the procedure for calculating drift-wall temperature, described in Section 6.6.3. The primary distinction is that scanning curves are completely derived from the LDTH submodels (rather than from LDTH-SDT pairs) and that the scanning curves relate the drift-wall RH to the drift-wall temperature. After drift-wall temperature has been calculated for the 623 repository subdomains (Figure 6-1) and eight different WP locations (Figure 4-1) from Step 6 in Section 6.6.3, RH is determined from the drift-wall RH versus drift-wall T scanning curve.

6.6.8 Computing Host-Rock Relative Humidity

The procedure for calculating RH at various locations in the host rock is analogous to that used to calculate drift-wall RH . After local host-rock temperatures (e.g., five m above the crown of the drift) have been calculated for the 623 repository subdomains (Figure 6-1) and eight WP locations (Figure 4-1) from Section 6.6.4, RH is determined from the host-rock RH versus host-rock T scanning curve.

6.6.9 Computing Relative Humidity on the Drip Shield

The procedure for calculating drip shield relative humidity RH_{ds} is different from that used to calculate relative humidity on the drift-wall RH_{dw} , in that time is explicitly incorporated into the interpolation process. The necessity of explicitly including time in the calculation of RH in the drift arises from the following:

1. RH in the drift is very dependent on the magnitude of seepage flux into the drift.
2. The magnitude of seepage flux into the drift is very dependent on the magnitude of percolation flux in the host rock.
3. The magnitude of percolation flux in the host-rock is very dependent on the magnitude of infiltration flux at the ground surface.
4. Infiltration flux at the ground surface is a function of time (with three distinctive values pertaining to each of the three climate periods).

This procedure requires that RH_{dw} (Section 6.6.7) and the drip shield temperature T_{ds} (Section 6.6.5) have already been determined. Instead of using temperature as the independent variable, two value versus time curves are plotted for the five AMLs: RH_{ds}/RH_{dw} versus time and T_{ds} versus time. For each timestep, the local value of T_{ds} , (Section 6.6.5) is compared against the five values of T_{ds} in the five T_{ds} history curves. The relative position of the local T_{ds} among the

five T_{ds} history curves determines the relative position of the interpolated RH_{ds}/RH_{dw} among the five RH_{ds}/RH_{dw} history curves. For example, if the local T_{ds} is halfway between the values of T_{ds} in the 50 and 60 MTU/acre T_{ds} history curves, then the value of RH_{ds}/RH_{dw} will be halfway between the values of RH_{ds}/RH_{dw} in the 50 and 60 MTU/acre RH_{ds}/RH_{dw} history curves. Finally, for each timestep, the local value of RH_{ds} is determined by multiplying RH_{dw} (Section 6.6.7) by RH_{ds}/RH_{dw} .

6.6.10 Computing Relative Humidity in the Backfill

The procedure for calculating RH at various locations in the backfill is analogous to that used to calculate RH on the drip shield. This step requires that the local relative humidity at the drift wall (Section 6.6.7) and the local temperature in the backfill (Section 6.6.5) have already been determined.

6.6.11 Computing Relative Humidity in the Invert

The procedure for calculating RH in the invert is analogous to that used to calculate RH on the drip shield. This step requires that the local relative humidity at the drift wall (Section 6.6.7) and the local temperature in the invert (Section 6.6.5) have already been determined.

6.6.12 Computing Waste-Package Relative Humidity

For the pre-closure period, the procedure for calculating relative humidity on the WP RH_{wp} requires that the following have already been determined: RH_{dw} (Section 6.6.7), T_{dw} (Section 6.6.3), and WP temperature T_{wp} (Section 6.6.6); RH_{wp} is given by

$$RH_{wp} = RH_{dw} \frac{P_{sat}(T_{dw})}{P_{sat}(T_{wp})}, \quad (7)$$

where P_{sat} is the saturated vapor pressure. Summarizing, RH on the WP is determined by RH on the drift wall and the temperature difference between the drift wall and WP. This equation is arrived at by realizing that the vapor density is constant. This precludes a gradient of absolute humidity across an open space. Relative humidity is the ratio of actual vapor pressure to saturated vapor pressure. Therefore, the product of relative humidity and saturated vapor pressure is absolute humidity. Rearranging these terms yields equation 7.

For the post-closure, which is the time after ventilation has ceased and backfill and the drip shield have been emplaced, the procedure for calculating RH on the WP requires that the following have already been determined: drip shield relative humidity RH_{ds} (Section 6.6.7), drift-wall temperature T_{ds} (Section 6.6.3), and WP temperature T_{wp} (Section 6.6.6). Relative humidity on the WP (RH_{wp}) is given by

$$RH_{wp} = RH_{ds} \frac{P_{sat}(T_{ds})}{P_{sat}(T_{wp})}, \quad (8)$$

Summarizing, RH on the WP is primarily dependent on RH on the drip shield and the temperature difference between the drip shield and WP. Therefore, the temperature difference between the WP and drip shield plays a role in reducing RH on the WP.

6.6.13 Computing Liquid-Phase Flux in the Host Rock

Just as with RH in the emplacement drifts, the liquid-phase flux has a time dependence. This dependence is associated with the change of infiltration rate reflecting a change in climate. The process of calculating liquid-phase flux in the host rock $q_{liq,hr}$ is similar to that for calculating RH in the drift (Section 6.6.9, Section 6.6.10, and Section 6.6.11).

This procedure requires that the local host-rock temperature T_{hr} has already been determined (Section 6.6.4). Two value versus time curves are plotted for the five AMLs: $q_{liq,hr}$ versus time and T_{hr} versus time. For each timestep, the local value of T_{hr} , (Section 6.6.4) is compared against the five values of T_{hr} in the five T_{hr} history curves. The relative position of the local T_{hr} among the five T_{hr} history curves determines the relative position of the interpolated $q_{liq,hr}$ among the five $q_{liq,hr}$ history curves. For example, if the local T_{hr} is halfway between the values of T_{hr} in the 50 and 60 MTU/acre T_{hr} history curves, then the local value of $q_{liq,hr}$ will be halfway between the values of $q_{liq,hr}$ in the 50 and 60 MTU/acre $q_{liq,hr}$ history curves.

This procedure is repeated for different locations in the host rock.

6.6.14 Computing Liquid-Phase Flux on the Drip Shield

The procedure for calculating liquid-phase flux $q_{liq,ds}$ on the drip shield is analogous to that used to calculate liquid-phase flux $q_{liq,hr}$ in the host rock (Section 6.6.13). This step requires that the local temperature on the drip shield T_{ds} (Section 6.6.5) has already been determined.

This procedure is repeated for different locations on the drip shield.

6.6.15 Computing Liquid-Phase Flux in the Backfill

The procedure for calculating liquid-phase flux $q_{liq,bf}$ at various locations in the backfill is analogous to that used to calculate liquid-phase flux $q_{liq,hr}$ in the host rock (Section 6.6.13). This step requires that the local temperature in the backfill T_{bf} (Section 6.6.5) has already been determined.

This procedure is repeated for different locations in the backfill.

6.6.16 Computing Liquid-Phase Flux in the Invert

The procedure for calculating liquid-phase flux $q_{liq,inv}$ in the invert is analogous to that used to calculate liquid-phase flux $q_{liq,hr}$ in the host rock (Section 6.6.13). This step requires that the local temperature on the drip shield T_{inv} (Section 6.6.5) has already been determined.

This procedure is repeated for different locations in the invert.

6.6.17 Computing Liquid Saturation at the Drift Wall

The procedure for calculating liquid saturation $S_{liq,dw}$ at the drift wall is analogous to that used to calculate drift-wall RH . After local drift-wall temperatures (Step 6 in Section 6.6.3) have been calculated for the 623 repository subdomains (Figure 6-1) and eight WP locations (Figure 4-1), $S_{liq,dw}$ is determined from the drift-wall $S_{liq,dw}$ versus drift-wall T scanning curve.

6.6.18 Computing Liquid Saturation on the Drip Shield

The procedure for calculating liquid saturation $S_{liq,ds}$ on the drip shield is analogous to that used to calculate drift-wall RH . After local drip-shield temperatures (Section 6.6.5) have been calculated for the 623 repository subdomains (Figure 6-1) and eight WP locations (Figure 4-1), $S_{liq,ds}$ is determined from the drift-wall $S_{liq,ds}$ versus drip-shield T scanning curve.

6.6.19 Computing Liquid Saturation in the Invert

The procedure for calculating liquid saturation $S_{liq,inv}$ at the drift wall is analogous to that used to calculate drift-wall RH . After local invert temperatures (Section 6.6.5) have been calculated for the 623 repository subdomains (Figure 6-1) and eight WP locations (Figure 4-1), $S_{liq,inv}$ is determined from the drift-wall $S_{liq,inv}$ versus invert T scanning curve.

6.6.20 Computing Gas-Phase Air-Mass Fraction Adjacent to Drip Shield

The procedure for calculating gas-phase air-mass fraction $X_{air,gas,ds}$ adjacent to the drip shield is analogous to that used to calculate drift-wall RH . After local drip-shield temperatures (Section 6.6.5) have been calculated for the 623 repository subdomains (Figure 6-1) and eight WP locations (Figure 4-1), $X_{air,gas,ds}$ is determined from the $X_{air,gas,ds}$ versus drip-shield T scanning curve.

6.6.21 Computing Gas-Phase Pressure Adjacent to Drip Shield

The procedure for calculating gas-phase pressure $P_{gas,ds}$ adjacent to the drip shield is analogous to that used to calculate drift-wall RH . After local drip-shield temperatures (Section 6.6.5) have been calculated for the 623 repository subdomains (Figure 6-1) and eight WP locations (Figure 4-1), $P_{gas,ds}$ is determined from the $P_{gas,ds}$ versus drip-shield T scanning curve.

6.6.22 Computing Gas-Phase Flux of Air

The procedure for calculating gas-phase (air) flux $Q_{gas,air,dr}$ around the perimeter of the drift is analogous to that used to calculate drift-wall RH . After local drift-wall temperatures (Step 6 in Section 6.6.3) have been calculated for the 623 repository subdomains (Figure 6-1) and eight WP locations (Figure 4-1), $Q_{gas,air,dr}$ is determined from the $Q_{gas,air,dr}$ versus drift-wall T scanning curve.

6.6.23 Computing Gas-Phase Flux of Water Vapor

The procedure for calculating gas-phase (water vapor) flux $Q_{gas,wat,dr}$ around the perimeter of the drift is analogous to that used to calculate drift-wall RH . After local drift-wall temperatures (Step 6 in Section 6.6.3) have been calculated for the 623 repository subdomains (Figure 6-1)

and eight WP locations (Figure 4-1), $Q_{\text{gas,wat,dr}}$ is determined from the $Q_{\text{gas,wat,dr}}$ versus drift-wall T scanning curve.

6.6.24 Computing Capillary Pressure on the Drip Shield

The procedure for calculating capillary pressure $P_{\text{c,ds}}$ on the drip shield is analogous to that used to calculate drift-wall RH . After local drip-shield temperatures (Section 6.6.5) have been calculated for the 623 repository subdomains (Figure 6-1) and eight WP locations (Figure 4-1), $P_{\text{c,ds}}$ is determined from the $P_{\text{c,ds}}$ versus drip-shield T scanning curve.

6.6.25 Computing Capillary Pressure on the Drift Wall

The procedure for calculating capillary pressure $P_{\text{c,dw}}$ on the drift wall is analogous to that used to calculate drift-wall RH . After local drift-wall temperatures (Step 6 in Section 6.6.3) have been calculated for the 623 repository subdomains (Figure 6-1) and eight WP locations (Figure 4-1), $P_{\text{c,dw}}$ is determined from the $P_{\text{c,dw}}$ versus drift-wall T scanning curve.

This procedure is repeated for both the fracture and matrix continuum.

6.6.26 Computing Capillary Pressure in the Invert

The procedure for calculating capillary pressure $P_{\text{c,inv}}$ in the invert is analogous to that used to calculate drift-wall RH . After local invert temperatures (Section 6.6.5) have been calculated for the 623 repository subdomains (Figure 6-1) and eight WP locations (Figure 4-1), $P_{\text{c,inv}}$ is determined from the $P_{\text{c,inv}}$ versus invert T scanning curve.

6.6.27 Computing Evaporation Rate on the Drip Shield

The procedure for calculating evaporation rate E_{ds} on the drip shield is analogous to that used to calculate drift-wall RH . After local drip-shield temperatures (Section 6.6.5) have been calculated for the 623 repository subdomains (Figure 6-1) and eight WP locations (Figure 4-1), E_{ds} is determined from the E_{ds} versus drip-shield T scanning curve.

This procedure is conducted for top of the drip shield and for a sum over the entire perimeter of the drip shield.

6.6.28 Computing Evaporation Rate at the Top of the Backfill

The procedure for calculating evaporation rate E_{tbf} at the top of the backfill is analogous to that used to calculate drift-wall RH . After local backfill temperatures (Section 6.6.5) have been calculated for the 623 repository subdomains (Figure 6-1) and eight WP locations (Figure 4-1), E_{tbf} is determined from the E_{tbf} versus backfill T scanning curve.

6.6.29 Computing Evaporation Rate in the Invert

The procedure for calculating evaporation rate E_{inv} in the invert is analogous to that used to calculate drift-wall RH . After local invert temperatures (Section 6.6.5) have been calculated for the 623 repository subdomains (Figure 6-1) and eight WP locations (Figure 4-1), E_{inv} is determined from the E_{inv} versus invert T scanning curve.

6.6.30 Binning TH Results

For each of the repository subdomains, a typical WP is selected for each of the two major WP groups: CSNF and HLW. The CSNF group includes bwr1, bwr2, pwr1, pwr2, and pwr3 WPs (Figure 4-1). The HLW group includes only hlw1 and hlw2. The DSNF WPs are excluded from the binning process because they constitute such a small fraction of the inventory in the repository.

For a given repository subdomain and WP group, an average WP temperature history and an average WP relative humidity history are calculated on the basis of a simple average. For each WP in the group, the sum of the normalized differences is summed over time as follows:

$$\sum_{t=0}^{t=1,000,000} \frac{(T_{WP} - T_{WP,avg})^2}{(T_{WP,avg})^2} + \frac{(RH_{WP} - RH_{WP,avg})^2}{(T_{WP,avg})^2} \quad (8)$$

where T_{WP} is the WP temperature, RH_{WP} is the WP relative humidity, $T_{WP,avg}$ is the average WP temperature (based on a simple average) and $RH_{WP,avg}$ is the average WP relative humidity (based on a simple average) in that repository subdomain and WP group. The WP with the minimum sum is selected as being represented of that repository subdomain and WP group (Figure 6-1).

6.7 OVERVIEW OF DATA FLOW

The overall data flow in the MSTHM is shown in Figure 1-2. A more detailed description is shown in Figure 1-3. The first components (in blue) involve submodel preparation, which are covered in Section 6.8. The next set of components (in violet) are involve submodel execution, which are covered in Section 6.9. The next component (shown in purple) is the execution of MSTHAC, which is covered in Section 6.10. The last component (shown in yellow) is data binning and graphical-output preparation.

6.8 SUBMODEL PREPARATION

Generation of the full MSTHM abstraction is dependent upon the four major submodel types (LDTH, SDT, DDT, and SMT) as described in Sections 6.2 through Section 6.5. The quality of the final output is dependent on both the quality of the input data and the self-consistency of the multitude of NUFT simulation runs needed for a single MSTHM abstraction. These demands are met through the combination of automated tools for generating NUFT input files, along with a modular input file format making extensive use of the include function of NUFT.

The map of input data described in the previous section through the various stages of model generation is shown in the Data Flow Diagrams depicted in Figure 3-1 through Figure 3-12. The data manipulation required to prepare the raw input data (Section 4) for use by the NUFT-based submodels includes reformatting, change of units, averaging, and interpolation (various schemes). These operations are applied to the data in a well-defined sequence of steps to assure data consistency between all simulation runs.

Figure 3-1 provides the symbol legend applicable to all the diagrams in the following subsections. These Data Flow Diagrams comprehensively describe the processing steps applied in the modeling tasks.

6.8.1 Mesh Generation

There are two major categories of numerical meshes, corresponding to the mountain- and drift-scale submodels. For the mountain-scale (SMT) submodels, the numerical mesh is generated entirely by YMESH, prior to NUFT run time; using YMESH, the user builds the mountain-scale mesh such that the approximated shape of the heated repository footprint can be accurately represented, with sufficiently fine grid-block definition close to the edges of the repository. For the drift-scale (SDT, LDTH, and DDT) submodels, YMESH is used to generate the information that assigns the vertical distribution of the stratigraphic units as well as the grid-block resolution in the vertical direction. A combination of software scripts and hand editing is required to generate the grid-block spacing and material-type specification for the grid blocks (e.g., Figure 6-3) that represents the geometry of the EBS inside the emplacement drifts (Figure 4-2). For the drift-scale submodels, the genmsh feature of NUFT is utilized, whereby the numerical mesh is built at run time.

Mesh generation covers two main categories: the creation of a numerical grid for the computational algorithm, and the assignment of the proper material type, from natural stratigraphy or engineering design, to each grid block. The majority of the actual mapping operations are performed by YMESH, but additional steps are necessary both prior and subsequent to the use of YMESH. For all practical purposes, these pre- and post-fix operations serve as interface modules to the data pipeline.

The processing steps for generating all the numerical meshes required for the MSTHM are depicted in Figure 3-2 and described in the following sections.

6.8.1.1 YMESH Input

YMESH can be executed either in a 3-D sense or in a 1-D sense. For the mountain-scale (SMT) submodel, YMESH produces the 3-D numerical mesh file that is utilized directly by NUFT. For the 1-D and 2-D drift-scale submodels, YMESH produces information describing the 1-D vertical distribution of the grid blocks and material types of each of those grid-block layers; this information is placed in the genmsh block of the NUFT input file. For the 2-D and 3-D drift-scale submodels, the grid-block definition in the second and third dimension is assigned by scripts that the modeler develops the template for.

YMESH requires two inputs in order to generate a NUFT-compatible mesh:

- **User input.** This file includes specification of (1) the model domain (i.e., model boundaries), (2) the orientation and depth of the repository horizon, (3) the vertical dimensions (and/or the maximum allowable vertical dimensions) of the grid blocks as a function of distance from the repository horizon. For generating an SMT submodel, the areal location of the repository footprint (Figure 5-1) is accomplished by specifying a prefix to the

name of the grid blocks in the repository footprint; different prefixes can be used to specify subareas of the repository.

- **World grid.** This is the stratigraphy primary input for YMESH to map rock materials onto the computational mesh (called the “user’s mesh”). The world grid is a combination of items `tspa99_primary_mesh`, which is the numerical mesh for the site-scale UZ flow model, and `UZ99_3.grd`, which is the vertices file for that mesh (4.1.2). The files `UZ99_3.grd` and `tspa99_primary_mesh` are processed by `rme6` (Attachment XVI) to create the file `LBL99-YMESH`, which is subsequently used in all YMESH operations for both the mountain- and drift-scale submodels.

The file `PAItem1Att10817` (CRWMS M&O 2000a) is used to guide the modeler in approximating the repository footprint (Figure 5-1) for use in the mountain-scale (SMT) submodel (`tspa00.grid00` and `tspa00.grid01`). Having chosen a reasonable representation of the repository footprint, the next step is choosing the 31 locations for use in the drift scale submodels (`column.data`). In this model-building process, the modeler's judgment in producing the input files to YMESH is as important as the quality of the input data in its affect on the quality of the final model result.

Several different output types are available from YMESH. For the purposes of the work at hand, the main YMESH output type is NUFT input, and the secondary output type is rock column description, which is placed into NUFT input files as comment lines. This secondary output is also used in generating Table 6-1.

6.8.1.2 Drift-Scale-Submodel Meshes

The generation of the drift-scale meshes begins with the creation of the *column_template* files along with the *column.data* file (Figure 3-2). The *column.data* information records the locations of the individual 31 locations for the LDTH and SDT submodels, and is represented graphically in Figure 5-2. There are two *column_template* files, one for LDTH submodels, and one for SDT submodels. In each of these cases they serve the same purpose—to describe the vertical mesh resolution for the submodel type.

The routine *makeColumns* (Attachment I) reads in the *column.data* file along with a *column_template* file to produce one individual YMESH input files for each of the 31 drift-scale submodel locations (*<column>.dat*). Each of these files is run through YMESH to generate a NUFT genmsh file (*<column>.nft*) and a rock column file (*<column>.col*) for its respective submodel type and location. These drift scale mesh files then contain information of both mesh geometry, as well as one-dimensional mapping of the materials in the natural system. (The approach of mapping material in one single dimension for the drift scale model is deemed appropriate due to the comparatively small horizontal extent of these submodels.)

In both SDT and LDTH models, the rock column files are used for informational purposes. The interesting information is extracted by *readUnits* (Attachment III) and output as NUFT comment lines (*<column>.col.units*). These files will be included in the same NUFT input files which contain the contents of the corresponding *<column>.nft* information. As a final step in the

production of SDT meshes, the routine *addlay* (Attachment IV) is run on each of the *<column>.nft* files to add atmosphere and water table material layers at the top and bottom of the mesh, respectively.

The LDTH *<column>.nft* files require a more complex set of modifications, because of two additional requirements on these submodels—that they include both the engineered system and hydrologic behavior. The hydrologic modeling of the LDTH submodels utilizes the implicit dual-permeability (implicit DKM) capability of NUFT. The implicit DKM requires mapping of materials for both fracture and matrix continua. To include the engineered system, some of the material mappings of the natural system stratigraphy must be overwritten with mapping to the engineered system materials. Both these tasks are achieved with *define_EBS_fineGrid* (Attachment II). The files *<column>.nft.msh.dkm0.f* and *<column>.nft.msh.dkm0.m* contain implicit-DKM format, but no engineered system, and are for use in the initialization runs of the LDTH submodel. The files *<column>.nft.msh.dkm0.f* and *<column>.nft.msh.dkm0.m* are for use in the remaining LDTH modeling stages.

The mesh for the DDT submodel is derived from an early stage in the development of the LDTH meshes. The YMESH input file at a single submodel location (l4c3) is the starting point for development of the DDT meshes. To develop the pre-closure period file l4c3.03v.dat for the DDT model, the grid divisions in the z dimension are redefined to accommodate the eventual addition of radiation connections. For the post-closure DDT file (l4c3.dat) the mesh is further refined in order to describe the dripshield and backfill. The resulting NUFT input files are then run through *addLayers* (Attachment IV), which, similar to *addlay*, adds atmosphere and water table material layers.

6.8.1.3 Mountain-Scale Submodel Mesh

The mountain-scale mesh is the entire set of mesh information delivered, with the extrapolation of edges constrained to the needs of the abstraction modeling technique. The various modifications of the *tspa00-meshNN* files were for the purpose of marking regions of interest in grid block names. These tags had no impact on the data values transferred to the next stage in the pipeline.

The mountain-scale numerical mesh is based on the file *tspa00.grid01*, which derives itself from the motivating concerns outlined in Sections 6.2.1 and 6.2.2 (The mesh processing steps for the SMT mesh are shown in Figure 3-2.). This file is processed by YMESH to create both *tspa00-mesh01* and *tspa00-mesh02*. The differences in these two outputs are only in the names given to some of the grid blocks. In the latter file, the blocks at the repository horizon were given special names to aid in the later steps of the abstraction algorithm.

The YMESH input file *tspa00.grid00* differs from *tspa00.grid01* in that it contains a much finer mesh in the vertical direction. The file generated from this one (*tspa00-mesh00*) is only used in generation of boundary conditions (Figure 3-5), and in that role, only the horizontal dimensions of the mesh information are used, incomplete agreement with the other SMT mesh files.

6.8.2 Material Properties

The primary function of the processing performed on the material property data inputs is to reformat them in a form compatible for NUFT (see Figure 3-7 and Figure 3-8). This task involved both modifying the syntax and format of the file, and providing proper units, as well as proper assignments within the separate matrix and fracture continua simulated by NUFT in implicit DKM simulations (using the LDTH submodels). The material properties of the stratigraphic units and those of the EBS are kept in separate input files to maintain modularity.

The input files for the material properties of the stratigraphic units were processed by the routine *rock_sun.m* (Attachment VIII), to prepare them for the LDTH submodels. Each set of rock properties (from LB990861233129.001, LB990861233129.002, and LB990861233129.003), corresponding to three infiltration-flux cases (mean, high, and low flux) is processed in this manner. The rock property set used in the thermal conduction submodels is constructed from the mean infiltration file produced for the LDTH submodels by keeping only the wet thermal conduction data (Section 5.6.4).

The materials incorporated in the EBS are required only in the LDTH and DDT models. The files *dkm-afc-pbf-EBS_Rev10* and *dkm-afc-EBS_Rev10* contain the EBS material properties for the pre-closure and post-closure LDTH submodels, respectively. The EBS material properties in the DDT submodels are found in the file *DDT-EBS_Rev00*. The effective thermal conductivity of air, which is used to represent thermal radiation (Section 4.1.2.6), is found in the files *modprop_dr-up-00* and *modprop_dr-up-00v*.

6.8.3 Heat-Generation Rate

Heat-generation-rate versus time information was extracted into individual heat-generation files in NUFT syntax, as shown in Figure 3-3. For the SMT submodel, the Matlab script *heat_SMT.m* (Attachment V) extracts the data from the appropriate data source files. For the DDT submodel, the Matlab script *heat_DDT.m* (Attachment V) extracts the data from the appropriate data source files. In both of these cases, the header lines are removed in order to simplify the script code, then the script is executed to produce the intermediate file. In the case of SDT and LDTH models, the file *line-load-heat* contains the heat-generation data, which was manually transcribed into the file. Incorporating the effects of ventilation and aging of WPs into the heat-generation-rate versus time tables is accomplished via the routine *heatgenAge* (Attachment XII).

6.8.4 Infiltration Flux

To prepare the infiltration flux source data for use in the NUFT input file requires several steps. First, the routine *convertCoords* is executed on all source data to transform the coordinate representations from UTM NAD 27 coordinates to Nevada State Plane coordinates. Next, the local infiltration flux is interpolated at each of the drift-scale-submodel locations using a Gaussian weighting function implemented in the routine *columnInfiltration* (Attachment XIV). This interpolation is done for each of the three climate states (present-day, monsoonal, and glacial), and for each of the three infiltration-flux cases (mean, high, and low); for each drift-scale submodel location (Figure 5-2), this results in nine values of infiltration flux. The resulting file, *infiltration.tex*, then contains each of the nine infiltration-flux values for each of the drift-

scale submodel locations. These values are then extracted from this file by the routine *infiltrab.m* (Attachment VII) and written into individual files. The contents of these files are included in the LDTH input file creation scripts (Attachment XVI). These steps are depicted in Figure 3-4 and Figure 3-6.

At the time of LDTH input file creation (*i.e.* execution of the LDTH input file creation scripts), the three different tables of infiltration flux are used to create a time dependent infiltration flux definition. This results in an infiltration flux versus time table with a constant present-day-flux value from 0 to 600 yr, an abrupt transition at 600 yr to a constant monsoonal-flux value that lasts from 600 to 2000 yr, and an abrupt transition at 2000 yr to a constant glacial-flux value that lasts from 2000 to 1,000,000 yr.

6.8.5 Boundary Conditions

With respect to the process of building boundary conditions, the four submodel types share certain aspects, as well as having certain distinctions (Figure 3-5). All submodels have lateral boundaries that are no-heat-flow (or adiabatic) boundaries; the thermohydrologic (LDTH) submodel also has no-mass-flow lateral boundaries. Thus, the only boundary conditions that are specified in the four submodel types are at the upper and lower boundaries.

The conduction-only submodels, which include the SMT submodel (Section 6.2), SDT submodel (Section 6.4), and the DDT submodel (Section 6.5), only require that temperatures be specified at the boundaries. The thermohydrologic (LDTH) submodel (Section 6.3) requires temperature, pressure, and gas-phase air-mass fraction be specified at the boundaries. All four submodel types have the ground surface as the upper boundary; thus, at a given coordinate location, all four submodels share the same upper-boundary temperature. The three drift-scale submodels (SDT, LDTH, and DDT) have the water table as the lower boundary; thus the three drift-scale submodels share the same lower-boundary temperature. The SMT submodel has a lower boundary that is 1000 m below the water table.

The drift-scale submodels boundary conditions for temperature and pressure are interpolated using inverse distance cubed weighting (Section 4.1.6.3), implemented in the routines *chim_surf_TP* and *chim_wt_TP*. The input files are *tspa99_primary_mesh* and *bcs_99.dat*, and the output files are *outpt* and *outpt_wt* (CRWMS M&O 2000a). The additional parameters needed for the LDTH model (air-mass fraction and liquid enthalpy) are computed with *xairtab* (Attachment VI).

For the mountain-scale submodel, the routine *bound* (Attachment X) computes the expected temperatures at 1000 m below the water table. This procedure is based upon assuring the same heat flux (driven by the geothermal gradient) above and below the water table. The vertical temperature profiles for ambient conditions, as predicted by the SDT submodels at each of the 31 drift-scale model locations, are used to extrapolate the temperature to a depth of 1000 m below the water table. These calculated temperatures are interpolated on the mountain-scale grid using inverse distance squared weighting implemented in routines *SMT_surf_bc* and *SMT_bot_bc* (Attachment IX) resulting in the lower boundary conditions for the SMT submodel.

6.9 SUBMODEL EXECUTION

Several types of NUFT simulation runs are required to produce a single abstracted output dataset. The NUFT submodel-execution procedure is depicted in Figure 3-9 through Figure 3-12. Each submodel type fills a particular set of requirements, as described in Sections 6.1 through 6.5. These varying needs determine the volume of NUFT models to be run for each type of simulation. The most demanding submodels in terms of number of simulation runs required are the LDTH and SDT submodels. For this reason, these two submodel types have received the greatest attention in automation tools. In general, these submodel types are first created at a single drift-scale-submodel location (Figure 5-2), the submodel is run and refined until the analyst has deemed it ready for production, then the automation components are refined as necessary and the submodel set is generated.

6.9.1 LDTH Simulations

The LDTH submodels are run at each of the 31 drift-scale-submodel locations for five AMLs (Section 6.3). In order to be assured of consistency between the data used in these simulations, a set of scripts were developed to generate the required NUFT input files (Attachment XII). When one of these scripts is run, it generates a family of 155 NUFT input files, one for each of the five AMLs at each one of 31 locations. A total of nine such scripts were necessary for the LDTH submodels—each of the three infiltration-flux cases requires one script for each of the three stages of LDTH submodel execution: (1) initialization run (to obtain initial ambient conditions), (2) the pre-closure simulation, and (3) the post-closure simulation.

The data developed for boundary conditions and infiltration are embedded directly in the generating scripts as parameter arrays. These arrays contain one value for each drift-scale submodel location, which are transcribed into these scripts from their respective source files (Figure 3-6). The concept of operation of these scripts is that for each output file (*i.e.* generated NUFT input file), various placeholders in a template file (Figure 3-9) are replaced with data relevant to the given scenario. A single value from the data arrays described above, along with filenames containing the other important parameters for the submodel, constitute the information provided to the template by the script.

The LDTH-submodel template files serve the purpose of providing a skeleton NUFT input file for each of the three stages (initialization, pre- and post-closure) of LDTH submodel execution and for each of the five AMLs, resulting in a total of 15 LDTH template files. These files contain the description of the components of the numerical mesh in the x and y dimensions. Since the LDTH model is 2-D, the y-dimensions is only a single layer. On the other hand, the x-dimension is the item in the submodel that determines the drift spacing and thereby determines the effective AML being represented in the submodel.

The NUFT input files generated in this procedure reference mesh files (Section 6.8.1), heat generation files (Section 6.8.3), material property files (Section 6.8.2), run control parameter files, and output time files via the NUFT *include* directive. The run control parameters are chosen to meet efficiency needs in the execution of the NUFT simulations, and the output times are chosen to give the required temporal resolution.

Execution of a single LDTH submodel takes place in three stages, each of them feeding into the next one. These stages are initialization, pre-closure, and post-closure. The initialization stage is a numerical simulation of the unperturbed natural system, which is run out until the numerical simulation of the natural system achieves equilibrium. This provides the starting point for the pre-closure simulation, which simulates a ventilated system. This stage outputs a NUFT restart file at 50 years (for starting the post-closure simulation), as well as providing data output for MSTHAC (Section 6.6). The post-closure simulation, which starts with the conditions at 50 yr from the pre-closure simulation, is conducted from 50 to 1,000,000 yr.

The NUFT output data files from the pre- and post-closure LDTH simulations are later used as input to MSTHAC (Section 6.6).

6.9.2 SDT Simulations

The MSTHAC methodology (Section 6.1 and Section 6.6) requires that the SDT-submodel simulations are conducted at all locations and AMLs as the LDTH submodels. The production of the NUFT input files for the SDT submodels is automated in a similar method as for the LDTH submodels (Section 6.9.1), but the task is simpler, largely due to the lack of hydrologic data in the SDT models. Three SDT generating scripts are required, one for each stage (initialization, pre-closure, and post-closure) of the submodel execution; and only two template files are required, one for the initialization runs, and one covering both the pre- and post-closure simulations. The script files contain the data concerning boundary conditions, as well as the mesh data for the x dimension (which determines the AML).

The initialization run is used to provide the starting vertical temperature profile, not only for the pre-closure and post-closure simulation periods in the SDT submodel, but also for the DDT submodels (Section 6.9.3). The pre- and post-closure simulations are almost identical, except that the heat-generation curves for the pre-closure period is reduced by 70% to simulate ventilation (Figure 3-10).

6.9.3 DDT Simulations

The DDT submodel need only be run at a single drift-scale submodel location, as discussed in Section 6.5. The 14c3 location (Figure 5-2) was chosen because it is at the geographic center of the repository area and because the host-rock unit at this location is the tsw35, which is the predominant host-rock unit in the repository; 25 of the 31 drift-scale-submodel locations have tsw35 as the host-rock unit (Table 5-2). As discussed in Section 6.5, it would have been acceptable to have chosen any of the other 31 drift-scale-submodel locations. The MSTHM methodology also only requires DDT-submodel results for a single (*i.e.* the nominal) AML of the repository. To meet the needs for DDT-submodel results, only two sets of NUFT outputs are necessary: one for the pre-closure period, and one for the post-closure period. This greatly simplifies the task of preparing the input files, so that it is feasible to create them without automation tools (Figure 3-11).

The DDT submodel represents a much greater level of detail within the drift than the other submodels. This is the only component of the MSTHM strategy that simulates heat transfer by thermal radiation explicitly. The thermal radiative components are prepared for NUFT with the

use of RADPRO, which requires both a numerical mesh and a some additional setup information (provided in the files *DDT60-03v.radin*, *DDT60-03pbf.radin*, and *DDT60-03.radin*). The mesh is read directly from the respective NUFT input file. The additional file contains information of which combination of surfaces may radiate (to each other), and the emissivity values of the respective surfaces.

The pre-closure DDT submodel (*l4c3-DDT60-03v.in*) has a courser mesh than that for post-closure DDT submodel (*l4c3-DDT60-03bff.in*). The post-closure DDT submodel (Figure 6-6) is more refined than the pre-closure DDT submodel (Figure 6-4) inside the drift to represent the details of the in-drift geometry of drip-shield and backfill (Figure 4-2). This difference in mesh makes the pre-closure submodel incompatible for producing a restart file for the post-closure DDT submodel, as had been done in the LDTH submodel. Instead, an additional pre-closure submodel (for the purpose of producing a restart file for the post-closure DDT submodel) is required; it is built from the post-closure mesh, but with in-drift materials and heat-generation curves appropriate to the pre-closure period.

6.9.4 SMT Simulations

The overall mountain scale effects of heat flow are simulated with the SMT submodel. This submodel is prepared without the assistance of automation tools, since only two simulations are required (one pre- and one post-closure simulation), which in turn requires only three NUFT input files: initialization, pre-closure, and post-closure (Figure 3-12). The initialization file is used for the generation of initial conditions for use in each of the other simulations, and the pre- and post-closure simulations are run independently of each other, with the only difference being the heat-generation curves, as in the case of the SDT submodels.

The SMT submodel uses the same material properties as the other thermal conduction submodels, except that some additional materials appear in this submodel (in files *SMT-1Dds-mi-flt* and *SMT-1Dds-mi-sz*), which are not required for the SDT or DDT submodels. The file *SMT-1Dds-mi-flt* contains the thermal properties for the fault zones. The fault-zone materials are additional material type appearing in the site-scale UZ flow model mesh (Section 4.1.3), with property assignments derived from Section 4.1.1.20. None of the drift-scale-submodel locations intersected any of the fault zone; therefore the thermal properties for the fault zones were not required in the SDT and DDT submodels. The file *SMT-1Dds-mi-sz* contains the thermal properties for the saturated zone (SZ). Because the SDT and DDT submodels have a lower boundary at the water table, they do not include the SZ in their respective model domains; therefore, these submodels do not require the SZ thermal properties. The thermal properties of the pp1 unit (Table 4-4) are assumed for the entire SZ in the SMT (Section 5.6.5).

6.10 MSTHAC EXECUTION

For each of the three infiltration-flux cases (mean, high, and low flux), MSTHAC is executed in a series of steps.

Step 1: Extract TH data from the all pre-closure submodels. On the basis of the requested TH data (Table 1-1) and the MSTHAC methodology (Section 6.9), specific variables are extracted from specific locations in each of the pre-closure submodels.

Step 2: Abstract TH data from the all pre-closure submodels. Using the TH data that was extracted from the pre-closure submodels (step 1), the MSTHAC methodology (Section 6.9) is applied to abstract the requested TH data (Table 1-1) for the pre-closure period. This results in 600 yr of MSTHM results that corresponds to a scenario with 600 yr of drift ventilation, where the nominal heat-generation rate is reduced by 70%.

Step 3: Extract TH data from the all post-closure submodels. On the basis of the requested TH data (Table 1-1) and the MSTHAC methodology (Section 6.9), specific variables are extracted from specific locations in each of the post-closure submodels.

Step 4: Abstract TH data from the all post-closure submodels. Using the TH data that was extracted from the post-closure submodels (step 3), the MSTHAC methodology (Section 6.9) is applied to abstract the requested TH data (Table 1-1) for the post-closure period. This results in MSTHM results from 50 to 1,000,000 yr that corresponds to a scenario with 50 yr of drift ventilation, where the nominal heat-generation rate is reduced by 70%, followed by a 50 to 1,000,000 yr period where the full nominal heat-generation rate is used.

Step 5: Combine the pre-closure and post-closure abstracted TH data. The abstracted TH results for the pre-closure period (step 3) and the post-closure period (step 4) are spliced together, resulting in the 38 TH variables (Table 1-1) at each of the 623 repository subdomains (Figure 6-1) for each of the 8 WP locations (Figure 4-1) for 352 timesteps, resulting in 66,665,984 data points for a given infiltration-flux case.

Step 6: Bin the abstracted TH data. At each of the 623 repository subdomains, a binning procedure is used (Section 6.6.30) to obtain the average CSNF WP and the average HLW WP. This step results in the 38 TH variables (Table 1-1) at each of the 623 repository subdomains (Figure 6-1) for 2 WP groups (CSNF and HLW), resulting in 16,666,496 data points for a given infiltration-flux case.

6.11 MSTHM RESULTS

The MSTHM calculates 38 TH variables for 623 repository subdomains (Figure 6-1) and eight different WP locations (Figure 4-1) as a function of time for more than 352 calculational timesteps. For each timestep there are $38 \times 623 \times 8$ different data values, resulting in 189,392 data values. Multiplying by 352 calculational timesteps results in 66 million TH data values for a complete time evolution of a given infiltration flux case. The following subsections provide a comprehensive description of the variables that are of key interest to the evolution of the TH environment in the NF and EBS. This description is provided for the three infiltration-flux cases that were modeled in this AMR: mean, high, and low infiltration flux.

Contour plots are provided on a sufficiently frequent time basis to capture the major trends, as well as the peaks and major transitions, of the spatial and temporal distributions of the major TH

variables. This information is provided for a 21-PWR WP (which is the fifth WP from the left in Figure 4-1). This WP location resulted in the highest temperatures with respect to WP-to-WP variability. It should be noted that the repository design analyzed in this report employs several design measures (such as fuel blending and line-load WP spacing) that minimize WP-to-WP variability in temperature. Therefore, the following results should be considered to be fairly typical of temperature distributions in the repository. Section 6.11.6 addresses the influence of WP-to-WP variability that arises from differences in heat-generation rate among WPs. Table 6-4 lists all of the plots of TH conditions that are given in Section 6.11.

Table 6-4. List of plots of TH conditions that are included in this report

Figure Number	TH Variable	Source DTN	Source File Name
Figure 6-7	WP temperature	LL000114004242.090	TSPA_SR_mean.ext
Figure 6-8	Upper drift-wall temperature	LL000114004242.090	TSPA_SR_mean.ext
Figure 6-9	Lower drift-wall temperature	LL000114004242.090	TSPA_SR_mean.ext
Figure 6-10	WP temperature	LL000114104242.091	TSPA_SR_upper.ext
Figure 6-11	WP temperature	LL000113904242.089	TSPA_SR_lower.ext
Figure 6-12	Maximum lateral extent of boiling isotherm	LL000114004242.090	TSPA_SR_mean.ext
		LL000114104242.091	TSPA_SR_upper.ext
		LL000113904242.089	TSPA_SR_lower.ext
Figure 6-13	Temperatures in EBS	LL000114004242.090	TSPA_SR_mean.ext
Figure 6-14	Peak WP temperature	LL000114004242.090	TSPA_SR_mean.ext
		LL000114104242.091	TSPA_SR_upper.ext
		LL000113904242.089	TSPA_SR_lower.ext
Figure 6-15	Peak lower drift-wall temperature	LL000114004242.090	TSPA_SR_mean.ext
		LL000114104242.091	TSPA_SR_upper.ext
		LL000113904242.089	TSPA_SR_lower.ext
Figure 6-16	WP relative humidity	LL000114004242.090	TSPA_SR_mean.ext
Figure 6-17	WP relative humidity	LL000114104242.091	TSPA_SR_upper.ext
Figure 6-18	WP relative humidity	LL000113904242.089	TSPA_SR_lower.ext
Figure 6-19	WP relative humidity and temperature	LL000114004242.090	TSPA_SR_mean.ext
		LL000114104242.091	TSPA_SR_upper.ext
		LL000113904242.089	TSPA_SR_lower.ext
Figure 6-20	Relative humidity in EBS	LL000114004242.090	TSPA_SR_mean.ext
Figure 6-21	Relative humidity in EBS	LL000114104242.091	TSPA_SR_upper.ext
Figure 6-22	Relative humidity in EBS	LL000113904242.089	TSPA_SR_lower.ext
Figure 6-23	Gas-phase air-mass on drip shield	LL000114004242.090	TSPA_SR_mean.ext
Figure 6-24	Gas-phase air-mass on drip shield	LL000114104242.091	TSPA_SR_upper.ext
Figure 6-25	Gas-phase air-mass on drip shield	LL000113904242.089	TSPA_SR_lower.ext
Figure 6-26	Liquid-phase flux 5 m above drift	LL000114004242.090	TSPA_SR_mean.ext
Figure 6-27	Liquid-phase flux 0.2 m above drift	LL000114004242.090	TSPA_SR_mean.ext
Figure 6-28	Liquid-phase flux above drip shield	LL000114004242.090	TSPA_SR_mean.ext
Figure 6-29	Liquid-phase flux next to lower drip shield	LL000114004242.090	TSPA_SR_mean.ext
Figure 6-30	Liquid-phase flux in invert	LL000114004242.090	TSPA_SR_mean.ext
Figure 6-31	Liquid-phase flux 5 m above drift	LL000114104242.091	TSPA_SR_upper.ext
Figure 6-32	Liquid-phase flux 0.2 m above drift	LL000114104242.091	TSPA_SR_upper.ext
Figure 6-33	Liquid-phase flux above drip shield	LL000114104242.091	TSPA_SR_upper.ext
Figure 6-34	Liquid-phase flux next to lower drip shield	LL000114104242.091	TSPA_SR_upper.ext
Figure 6-35	Liquid-phase flux in invert	LL000114104242.091	TSPA_SR_upper.ext
Figure 6-36	Liquid-phase flux 5 m above drift	LL000113904242.089	TSPA_SR_lower.ext
Figure 6-37	Liquid-phase flux 0.2 m above drift	LL000113904242.089	TSPA_SR_lower.ext
Figure 6-38	Liquid-phase flux above drip shield	LL000113904242.089	TSPA_SR_lower.ext
Figure 6-39	Liquid-phase flux next to lower drip shield	LL000113904242.089	TSPA_SR_lower.ext
Figure 6-40	Liquid-phase flux in invert	LL000113904242.089	TSPA_SR_lower.ext
Figure 6-41	Liquid-phase flux in NFE& EBS	LL000114004242.090	TSPA_SR_mean.ext

Figure 6-42	Evaporation rate on upper drip shield	LL000114004242.090	TSPA_SR_mean.ext
Figure 6-43	Evaporation rate on upper drip shield	LL000114104242.091	TSPA_SR_upper.ext
Figure 6-44	Evaporation rate on upper drip shield	LL000113904242.089	TSPA_SR_lower.ext
Figure 6-45	Evaporation rate & gas-phase air-mass fraction on drip shield	LL000114004242.090	TSPA_SR_mean.ext
Figure 6-46	WP temperature and relative humidity	LL000114004242.090	TSPA_SR_mean.ext

In addition to the contour plots of TH conditions, history plots of TH conditions are also provided for several repository locations, including a location at the geographical center of the repository and a location that is relatively close to the eastern edge of the repository.

6.11.1 Temperature Distributions

Contour plots of temperature are provided for (1) the WP surface, (2) the upper drift wall (or crown of the drift), and (3) the lower drift wall (below the bottom of the invert). Contour plots of peak WP temperature and peak temperature of the lower drift wall are also provided.

6.11.1.1 Temperature Distributions for Mean Infiltration Case

The temperature evolution on WPs and on the upper and lower drift wall is summarized for the entire 1,000,000-yr simulation period in Figure 6-7, Figure 6-8, and Figure 6-9 for the mean infiltration-flux case. For the pre-closure period, peak temperatures on WPs occur around 15 yr (Figure 6-7b). For the post-closure period, peak WP temperatures occur around 60 yr, with nearly half of the 21-PWR WPs exceeding 300°C. Edge-cooling effects have a minor affect on temperatures during the pre-closure; therefore, the temperature distribution is fairly uniform throughout the repository. During the post-closure period, edge-cooling effects are seen to significantly affect the repository-scale temperature distribution. For example, at 100 yr there is a 120°C difference in WP temperature between the center and edge of the repository (Figure 6-7e).

There is a large temperature difference between the upper and lower drift wall, particularly at early time (compare Figure 6-8d with Figure 6-9d). Boiling persists considerably longer on the lower drift wall than on the upper drift wall (compare Figure 6-8h and Figure 6-8i with Figure 6-9h and Figure 6-9i).

6.11.1.2 Temperature Distributions for High Infiltration Case

The temperature evolution on WPs is summarized for the entire 1,000,000-yr simulation period in Figure 6-10 for the high infiltration-flux case. The magnitude of infiltration flux has a small effect on WP temperatures during the pre-closure period (compare Figure 6-10a, Figure 6-10b, and Figure 6-10c with Figure 6-7a, Figure 6-7b, and Figure 6-7c). During the early post-closure period, the enhanced cooling effect of the higher infiltration flux is small (compare Figure 6-10d with Figure 6-7d). At the end of the boiling period, the enhanced cooling effect of the higher infiltration flux is also small (compare Figure 6-10k with Figure 6-7k).

6.11.1.3 Temperature Distributions for Low Infiltration Case

The temperature evolution on WPs is summarized for the entire 1,000,000 yr simulation period in Figure 6-11 for the low infiltration-flux case. During the pre-closure period, the low infiltration-flux case is noticeably hotter than the mean infiltration-flux case (compare Figure 6-11 with Figure 6-7b). During the early post-closure period, the low infiltration-flux case is slightly hotter (with the region of hotter WPs also being more extensive) than in the mean flux case (compare Figure 6-11d and Figure 6-11e with Figure 6-7e and Figure 6-7f). The duration of boiling for the low infiltration-flux case is longer than for the mean flux case (compare Figure 6-11l with 6-7l).

6.11.1.4 Temperature Analysis

The maximum lateral extent of boiling (away from the drift wall) is a good indication of spatial extent of rock dryout around the emplacement drifts. The spatial extent of dryout decreases with increasing infiltration (or percolation) flux. The lateral extent of boiling is considerably greater for the low infiltration-flux case than for the mean or high infiltration-flux cases (Figure 6-12). For the median WP location, the maximum lateral extent of boiling is 8.4 m, 9.1 m, and 10.5 m for the high, mean, and low infiltration-flux cases, respectively. For the 90th percentile WP location, the maximum lateral extent of boiling is 9.1 m, 9.6 m, and 14.6 m for the high, mean, and low infiltration-flux cases, respectively. The hottest (and driest) WP location in the low infiltration-flux case has a maximum lateral extent of boiling of 18 m; therefore, because the drifts are 81 m apart (Figure 4-1), a maximum of 44.4% of the repository horizon is driven to the boiling point. The hottest (and driest) WP location in the mean infiltration-flux case has a maximum lateral extent of boiling of 9.7 m; therefore, a maximum of 24% of the repository horizon is driven to the boiling point. The hottest (and driest) WP location in the high infiltration-flux case has a maximum lateral extent of boiling of 9.7 m (which is the same as that for the mean flux case). For the range of infiltration flux considered in this AMR, the maximum percentage of the repository horizon that can be driven to the boiling point lies between 24% and 44.4%.

Summarizing, there is much less difference in lateral boiling extent between the mean and high infiltration-flux cases than between the mean and low flux cases; this observation is particularly true for the hottest (and driest) WP location. Therefore, if one considers defining a percolation-flux threshold wherein rock dryout becomes significantly limited by percolation, then this percolation-flux threshold would appear to be close to that arising from the mean infiltration-flux case. Increasing percolation fluxes above those of the mean infiltration-flux case has a diminishing effect on decreasing the extent of boiling (and rock dryout).

The time-varying influence of edge cooling is illustrated by Figure 6-13, which gives the temperature history at various locations in the EBS at the center and edge of the repository. The edge-cooling effect has a small influence on peak temperatures. However, by 100 yr, the influence of edge cooling is considerable. The large differences in WP temperature at 100 yr, with temperatures decreasing strongly with proximity to the edge (Figure 6-7d, Figure 6-10e, and Figure 6-11e), indicates a promising heat-management option for a repository with an extended ventilation period (e.g., 100 yr). Because the influence of edge-cooling has penetrated

significantly (100 to 200 m) in from the edge by 100 yr, it would be possible to emplace the hottest WPs in this edge region without incurring very high peak temperatures. The cooler WPs would be emplaced in the central repository region that does not experience edge-cooling effects.

The large temperature difference between the upper and lower drift wall is very apparent in Figure 6-13. This large temperature difference arises from the drip-shield and backfill configuration in the emplacement drift (Figure 6-13). Because Overton sand backfill (Table 4-1) has a very low thermal conductivity (0.33 W/m-K), it is a very effective thermal insulator. Because much more of this insulation lies above the WP than below the WP, this focuses much of the decay heat generation from the WPs into the floor of the drift. To reduce the large difference between the upper and lower drift-wall temperatures, it would be necessary to balance the insulation above and below the WP. This balancing requires reducing the amount of backfill above the WP and increasing the thickness of the invert below the WP. Placing insulation between the WP and invert would serve to further balance the distribution of insulation in the drift.

The influence of the low thermal conductivity (0.33 W/m-K) of the Overton sand backfill (Table 4-1) is seen as a persistent temperature difference between the drip shield and drift wall (Figure 6-13). This temperature difference is independent of proximity to the edge of the repository. The temperature difference between the drip shield and WP is small because it is governed by thermal radiation, which is a very efficient means of heat transfer.

The influence of infiltration (or percolation) flux on peak WP and drift-wall temperatures is shown in Figure 6-14 and Figure 6-15, respectively. There is a relatively small difference (about 5°C) in peak WP between the mean and high infiltration-flux cases. There is a similar small difference in peak drift-wall temperature between these two cases. There is a slightly larger difference (of about 10°C) in peak WP temperature between the mean and low infiltration-flux cases. There is a similar difference in peak drift-wall temperature between these two cases.

The sensitivity of the WP and drift-wall temperatures on the thermal conductivity of the host rock is readily apparent in Figure 6-14 and Figure 6-15. The wet and dry thermal conductivity K_{th} values (Table 4-4) of the tsw34 unit (2.33 and 1.56 W/m-K, respectively) are considerably greater than in the tsw35 unit (2.02 and 1.2 W/m-K, respectively). With the exception of the central-eastern portion of the repository, the repository host rock is comprised of the tsw35 unit. The central-eastern portion is comprised of the tsw34 unit (Figure 5-2; Table 5-2). Using the 31 drift-scale-submodel locations (Figure 5-2; Table 5-2) as an indicator of the local host-rock unit, 26 of these locations have tsw35 as the host-rock unit and 5 of these locations have tsw34 as the host-rock unit: 11c3, 11c4, 11c5, 11c6, and 12c4. The five drift-scale-submodel locations wherein tsw34 is the host-rock unit correspond to the region of the repository with the lowest peak WP temperatures (Figure 6-15) and the lower peak drift-wall temperatures (Figure 6-15). This trend is the same for all three infiltration-flux cases. Thus, WP and drift-wall temperatures decrease with increasing K_{th} of the local host-rock unit.

6.11.2 Relative Humidity Distributions

Contour plots of relative humidity on the WP surface, RH_{wp} , are given for the mean, high, and low infiltration-flux cases. For the mean and high infiltration-flux cases it is only necessary to show the contour plots for the first 10,000 yr to show the complete evolution of RH_{wp} , while for the low infiltration-flux case it is necessary to show 100,000 yr. The difference in time required for the low infiltration-flux case to attain humid ambient conditions arises from the delayed onset of seepage into the drifts (relative to the mean and high flux cases). The onset of seepage into the drifts (discussed in Section 6.11.4) is a critically important process governing how long it takes the backfill to attain humid ambient conditions.

6.11.2.1 Relative Humidity Distributions for Mean Infiltration Case

The evolution of relative humidity on WPs, RH_{wp} , is summarized for 10,000 yr in Figure 6-16 for the mean infiltration-flux case. Within 10,000 yr, RH_{wp} has attained ambient humid conditions for the mean infiltration-flux case. At the end of the pre-closure period RH_{wp} has climbed up to 70 to 80% (Figure 6-16a). Immediately after backfill is emplaced the WP temperature abruptly climbs, which drastically reduces RH_{wp} . This effect occurs uniformly throughout the repository area (Figure 6-16b). The influence of edge-cooling on reducing rock dryout and RH reduction starts to become noticeable after 100 yr (Figure 6-16d, Figure 6-16e, and Figure 6-16f). The influence of the monsoonal climate and regions of higher infiltration flux (Figure 6-47) is seen after 600 yr, as the higher percolation flux begins to seep into the drift, causing more humid conditions (Figure 6-16h) inside the drifts. Regions of lower infiltration flux are seen as regions where RH_{wp} reduction is more persistent (Figure 6-16m through Figure 6-16x).

6.11.2.2 Relative Humidity Distributions for High Infiltration Case

The evolution of relative humidity on WPs, RH_{wp} , is summarized for 10,000 yr in Figure 6-17 for the mean infiltration-flux case. During the pre-closure period, the difference between the high and the mean infiltration-flux case on RH_{wp} is small (compare Figure 6-17a with Figure 6-16a). During the early post-closure period RH_{wp} for the high infiltration-flux case is similar to that of the mean flux case (compare Figure 6-17c and Figure 6-17d with Figure 6-16c and Figure 6-16d). At later time periods (particularly after 600 yr when the monsoonal climate begins), RH_{wp} in the high infiltration-flux case is slightly more humid than in the mean flux case (compare Figure 6-17h with Figure 6-16h). The more humid conditions arise due to the greater seepage flux into the drift for the high infiltration-flux case.

6.11.2.3 Relative Humidity Distributions for Low Infiltration Case

The evolution of relative humidity on WPs, RH_{wp} , is summarized for 100,000 yr in Figure 6-18 for the low infiltration-flux case. With a lower infiltration flux, rock dryout is more persistent and the onset of seepage into the drifts is delayed (relative to the higher flux cases), which delays rewetting the backfill to humid ambient conditions. For the preclosure period, RH_{wp} for the low infiltration-flux case is considerably drier than for the mean and high flux cases (compare Figure 6-18a with Figure 6-16a and Figure 6-17a). For the postclosure period, RH_{wp} for the low infiltration flux is considerably drier (particularly after 600 yr when the monsoonal climate begins) than for the mean and high flux cases (compare Figure 6-18i with Figure 6-16i and

Figure 6-17i). After the glacial climate begins (at 2000 yr), RH_{wp} for the low infiltration-flux case continues to be considerably drier than it is for the mean and high flux cases (compare Figure 6-18o with Figure 6-16o and Figure 6-17o).

6.11.2.4 Relative Humidity Analysis

Two important performance measures for the EBS are summarized in Figure 6-19. The first important performance measure is how long it takes WP to attain humid conditions. The distribution RH -reduction performance on WPs throughout the repository area is succinctly described with the complementary cumulative distribution function (CCDF) of the time required for WPs to attain an RH of 85% (Figure 6-19a). The second important performance measure is how hot the WP is once humid conditions are attained. Figure 6-19b is the CCDF of the WP temperature at which $RH_{wp} = 85\%$ is attained. The CCDF curves in Figure 6-19a show that the mean and high infiltration-flux cases result in similar RH -reduction performance on WPs. This similarity is also indicated by the comparison of the RH_{wp} contours, which was discussed in Section 6.11.2.2. The CCDF curves in Figure 6-19a also clearly show that the low infiltration-flux case results in a much more persistent reduction in RH on WPs than the mean and high flux cases. The mean and high infiltration-flux cases also result in similar WP temperatures once an RH of 85% is attained on the WPs (Figure 6-19b), whereas the low flux case results in much lower WP temperatures at the time at which $RH_{wp} = 85\%$ is attained.

Relative humidity histories on the drift wall, drip shield, and WP are given for locations at the center and edge of the repository for the mean, high, and low infiltration-flux cases in Figure 6-20, Figure 6-21, and Figure 6-22, respectively. Several important observations can be made, including:

- **RH reduction at the drift wall** (and in the host rock) decreases strongly with proximity to the edge of the repository. Significant reduction in RH_{dw} persists for about 100 to 1000 yr (depending on proximity to the repository edge) for the mean and high infiltration-flux cases and for about 200 to 2000 yr for the low infiltration-flux case.
- **RH reduction on the drip shield** is relatively insensitive to proximity to the edge of the repository. Eventually, RH on the drip shield becomes nearly 100%. For the mean and high infiltration-flux cases this takes about 1000 to 2000 yr and for the low infiltration-flux case about 3000 to 6000 yr to occur. The end of the period of RH reduction on the drip shield corresponds to the time that the seepage into the backfill has reached a steady-state condition, essentially reaching a terminal state with respect to moisture content in the backfill.
- **RH reduction on the WP** persists long after RH reduction on the drip shield has ceased. The persistence of RH reduction between the drip shield and WP arises because of the temperature difference between the WP and drip shield. Because the interval between the WP and drip shield is an open cavity, thermal radiation controls this temperature difference. The use of an insulator (such as granular backfill) in the gap between the WP and drip shield would result in a much larger temperature difference, which would result in a much larger reduction in RH between the drip shield and WP.

6.11.3 Gas-Phase Air-Mass Fraction Distributions

Contour plots of gas-phase air-mass fraction on the drip-shield surface, $X_{\text{air,gas,ds}}$, are given for the mean, high, and low infiltration-flux cases for 20,000 yr; contours are given for this duration because it takes about 20,000 yr for $X_{\text{air,gas,ds}}$ to return to ambient values.

6.11.3.1 Gas-Phase Air-Mass Fraction Distributions for Mean Infiltration Case

The evolution of gas-phase air-mass fraction on the drip-shield surface, $X_{\text{air,gas,ds}}$, is summarized for 20,000 yr in Figure 6-23 for the mean infiltration-flux case. The value of $X_{\text{air,gas,ds}}$ declines during the period of temperature increase as water vapor displaces air from the drifts and the rock adjacent to the drifts. Boiling conditions are required to drive a significant reduction in $X_{\text{air,gas,ds}}$. During the pre-closure period, the drift wall stays below the boiling point. As a consequence, $X_{\text{air,gas,ds}}$ is not significantly reduced. During the post-closure period, after ventilation has ceased and the backfill emplaced, temperatures in the drift abruptly rise to well above the boiling point, thereby driving air away from the drifts. Consequently, during the early post-closure period, values of $X_{\text{air,gas,ds}}$ become very small (Figure 6-23a). As water vapor displaces air from the drifts (by advection), binary diffusion of air and water vapor causes air to return to the drifts. The value of $X_{\text{air,gas,ds}}$ reaches its minimum value about the same time that the peak WP and drip-shield temperatures are attained. As the drip-shield temperature then declines, the value of $X_{\text{air,gas,ds}}$ gradually increases. Because temperatures decline more quickly at the edge of the repository (as a result of the edge-cooling effect), $X_{\text{air,gas,ds}}$ increases more quickly at the repository edge (Figure 6-23b and Figure 6-23c) and the rate of increase of $X_{\text{air,gas,ds}}$ increases with proximity to the edge of the repository. In general, the shape of the X contours are similar to the contours of WP temperature (for example, compare Figure 6-23g with Figure 6-7j).

6.11.3.2 Gas-Phase Air-Mass Fraction Distributions for High Infiltration Case

The evolution of gas-phase air-mass fraction on the drip-shield surface, $X_{\text{air,gas,ds}}$, is summarized for 20,000 yr in Figure 6-24 for the high infiltration-flux case. Spatial and temporal evolution of $X_{\text{air,gas,ds}}$ for the high and mean infiltration-flux cases are similar; however, the lower temperatures in the high infiltration-flux case result in slightly higher values of $X_{\text{air,gas,ds}}$ than in the mean flux case (for example, compare Figure 6-24f with Figure 6-23f).

6.11.3.3 Gas-Phase Air-Mass Fraction Distributions for Low Infiltration Case

The evolution of gas-phase air-mass fraction on the drip-shield surface $X_{\text{air,gas,ds}}$ is summarized for 20,000 yr in Figure 6-25 for the low infiltration-flux case. The overall spatial and temporal evolution of $X_{\text{air,gas,ds}}$ for the low infiltration-flux case is similar to that of the mean and high flux case; however, values of $X_{\text{air,gas,ds}}$ for the low infiltration-flux case are not as low as in the mean and high flux cases (for example, compare Figure 6-25d with Figure 6-23d and Figure 6-24d). A secondary factor influencing $X_{\text{air,gas,ds}}$ is the local percolation flux with $X_{\text{air,gas,ds}}$ increasing slightly with decreasing percolation flux. Areas of lower percolation flux have less water returning to the boiling front; consequently the rate of water vapor generation in the immediate vicinity of the drifts is less than it is in areas where the local percolation flux is higher. In the mean and high infiltration-flux cases, the large return flux of water back to the boiling front causes the refluxing

zone to remain closer to the drifts than in the low flux case, which results in a larger vapor generation flux (close to the drifts) to drive air away from the drifts.

As the end of the boiling period is approached, the distribution of $X_{\text{air,gas,ds}}$ for the low, mean, and high infiltration-flux cases become very similar (compare Figure 6-25g, Figure 6-23g, and Figure 6-24g). After boiling has ceased, $X_{\text{air,gas,ds}}$ for the low infiltration-case is less than in the mean or high flux cases (for example, compare Figure 6-25i with Figure 6-23i and Figure 6-24i).

6.11.3.4 Gas-Phase Air-Mass Fraction Analysis

The analysis of the factors affecting gas-phase air-mass fraction are discussed in Sections 6.11.3.1 through 6.11.3.3

6.11.4 Liquid-Phase Flux Distributions

The spatial and temporal evolution of liquid-phase flux in the NFE and EBS is strongly affected by decay heat from WPs. To illustrate this influence, liquid-phase flux contours are provided for five locations in the NFE and EBS: (1) 5 m above the crown of the drift, (2) 0.2 m above the crown of the drift, (3) in the sand backfill, averaged along the top of the drip shield, (4) in the sand backfill, adjacent to the lower side of the drip shield, and (5) in the crushed-tuff invert, averaged over the invert. In the host rock, this liquid-phase flux pertains to flux in the fractures; flux in the matrix (which is smaller) is not included. In the sand backfill and crushed-tuff invert, the liquid-phase flux in the following plots pertains to the total flux.

6.11.4.1 Liquid-Phase Flux Distributions for Mean Infiltration Case

The evolution of liquid-phase flux (in fractures) 5 m above the crown of the drift, $q_{\text{liq},5\text{m}}$, is summarized in Figure 6-26 for the mean infiltration-flux case. During the pre-closure period, because the host rock remains below the boiling point, $q_{\text{liq},5\text{m}}$ is largely unaffected by decay heat. A comparison of Figure 6-26a and Figure 6-47a (which is the mean infiltration-flux contour map for present-day-climate conditions) shows the similarity between $q_{\text{liq},5\text{m}}$ and the ambient infiltration flux.; note that the differences between these two plots arise from Figure 6-47 pertaining to the total (fracture + matrix) flux, while Figure 6-26 pertains only to flux in the fractures. Five years into the post-closure period (Figure 6-26b) decay heat has already noticeably increased $q_{\text{liq},5\text{m}}$. The increase in $q_{\text{liq},5\text{m}}$ arises from heat-driven condensate flow; which occurs in the refluxing zone (also called the heat-pipe zone), just beyond where dryout is occurring. Thirty years into the post-closure period (Figure 6-26d) the heart of the heat-pipe zone has reached at least 5 m above the drift. At earlier times (Figure 6-26b and Figure 6-26c), the heart of the heat-pipe zone is less than 5 m above the drift. At later times (Figure 6-26e and Figure 6-26f), $q_{\text{liq},5\text{m}}$ is decreasing because it is proportional to the heat flux (from WPs), which is decaying with time. The decrease in $q_{\text{liq},5\text{m}}$ continues through the present-day-climate period (which lasts 600 yr). At 500 yr, $q_{\text{liq},5\text{m}}$ is comparable to the infiltration flux (compare Figure 6-26i to Figure 6-47a). Therefore, by 500 yr the influence of decay heat on $q_{\text{liq},5\text{m}}$ has become small.

After the start of the monsoonal climate period $q_{\text{liq},5\text{m}}$ increases to where it is comparable to the monsoonal-climate infiltration flux (compare Figure 6-26j with Figure 6-47b). Thus, the transition to steady-state percolation-flux conditions, controlled by the monsoonal-climate

infiltration flux, occurs relatively quickly (compare Figure 6-26j, Figure 6-26k, and Figure 6-26l). Similarly, the transition to steady-state percolation-flux conditions, controlled by the glacial-climate infiltration flux, also progresses relatively quickly (compare Figure 6-26l, Figure 6-26m, Figure 6-26n, and Figure 6-26o).

The evolution of liquid-phase flux (in fractures) 0.2 m above the crown of the drift, $q_{liq,cr}$ (where “cr” stands for crown), is summarized in Figure 6-27 for the mean infiltration-flux case. During the pre-closure period when the host rock remains below the boiling point $q_{liq,cr}$ is largely unaffected by decay heat. After ventilation ceases, temperatures in the host rock abruptly rise above the boiling point, generating a heat-pipe zone immediately above the drift, which is manifested by very high values of $q_{liq,cr}$ (Figure 6-27a and Figure 6-27b). Five years into the post-closure period (Figure 6-27d) the heart of the heat-pipe zone no longer resides 0.2 m above the crown. Rather, it has moved at least 5 m above the drift (as indicated in Figure 6-26b). For most of the repository area, the value of $q_{liq,cr}$ is zero for the period from 55 to 200 yr. The exception being areas where the local ambient percolation flux is high enough to overwhelm the local heat flux from WPs (Figure 6-27e and Figure 6-27f). As the end of the present-day-climate period is approached, about half of the repository area has a nonzero value of $q_{liq,cr}$ (Figure 6-27g).

After the start of the monsoonal climate period, $q_{liq,cr}$ increases to where it is comparable to the monsoonal-climate infiltration flux (compare Figure 6-27h with Figure 6-47b). Thus, the transition to steady-state monsoonal-climate percolation-flux conditions (i.e., controlled by the monsoonal-climate infiltration flux) occurs relatively quickly (compare Figure 6-27h and Figure 6-27i). Similarly, the transition to steady-state glacial-climate percolation-flux conditions (i.e., controlled by the glacial-climate infiltration flux) also progresses quickly (compare Figure 6-27i, Figure 6-27j, Figure 6-27k, and Figure 6-27l).

The evolution of liquid-phase flux averaged over the upper surface of the drip shield, $q_{liq,uds}$, (“uds” stands for upper drip shield), is summarized in Figure 6-28 for the mean infiltration-flux case. During the first 150 yr of the post-closure period, $q_{liq,uds}$ is zero everywhere in the repository. At 215 yr (Figure 6-28a) the first nonzero occurrence of $q_{liq,uds}$ is seen in a region of high ambient infiltration (and percolation) flux. The region of nonzero $q_{liq,uds}$ spreads (Figure 6-28b through Figure 6-28g), starting in the regions of highest infiltration flux, until it occupies all but the regions of low infiltration flux.

During the early part of the pre-closure period the backfill is dry. As the temperature at the drift wall declines below the boiling point, water is able to wick (by capillary flow) from the fractures into the Overton sand backfill. This wicking is facilitated by the van Genuchten α value for Overton sand (Table 4-1: $\alpha = 2.75 \times 10^{-4} \text{ Pa}^{-1}$) being smaller than that of the fractures in the host-rock units (Table 4-3: tsw34: $\alpha = 5.16 \times 10^{-4} \text{ Pa}^{-1}$; tsw35: $\alpha = 7.39 \times 10^{-4} \text{ Pa}^{-1}$; tsw36 and tsw37: $\alpha = 7.84 \times 10^{-4} \text{ Pa}^{-1}$). Had a coarser, well-sorted sand been used as backfill, with a value of α larger than that of the fractures in the host-rock units, then this wicking would not have taken place. The wicking flux that enters the drift is actually greater than the percolation flux in the overlying host rock because capillary suction (driven by the high capillarity of the Overton sand) augments the influence of gravity-driven fracture flow; this augmented flow “captures”

flow in fractures that would have otherwise drained around the drift. Wicking into the drift occurs at the point that backfill contacts the drift wall, which occurs 1 m above the springline (Figure 4-2) down to the interface with the invert.

The magnitude of $q_{\text{liq,uds}}$ is much larger than the ambient percolation flux because it arises from heat-driven condensate flow in the heat-pipe zone in the backfill above the drip shield. Just as the magnitude of liquid-phase flux in the heat-pipe zone in the host-rock above the drift can greatly exceed the background percolation flux, the magnitude of liquid-phase flux in the heat-pipe zone in the backfill can greatly exceed the seepage flux entering the drift. The large temperature gradient in the backfill facilitates a large vapor flux away from the drip shield, while the high capillarity of the Overton sand facilitates a large liquid-phase flux of water returning to the drip shield; when these gas-phase liquid-phase fluxes are equal, a heat pipe is established. As discussed in Section 6.11.5, this capillary-driven heat-pipe system in the Overton-sand backfill results in a very large evaporative flux on the surface of the drip shield.

Because it arises largely from heat-driven condensate flow, the value of $q_{\text{liq,uds}}$ declines along with the decaying heat-generation rate from WPs. Thus, the value of $q_{\text{liq,uds}}$ declines by more than a factor of two during the 1500-to-3000 yr time interval (Figure 6-28i and Figure 6-28j). This decrease occurred in spite of the fact that the transition from the monsoonal to glacial climate occurred over this time interval. Had the value of $q_{\text{liq,uds}}$ been controlled by percolation flux, rather than by heat-pipe conditions, then the value of $q_{\text{liq,uds}}$ should have increased significantly (rather than have decreased) during the 1500-to-3000 yr time interval. By 10,000 yr the value of $q_{\text{liq,uds}}$ is much smaller than the background percolation flux (compare Figure 6-28k with Figure 6-26n and Figure 6-27k). As discussed below, the value of $q_{\text{liq,uds}}$ is also much smaller than the liquid-phase flux at other locations in the drift. At 1,000,000 yr, the contrast between the value of $q_{\text{liq,uds}}$ and liquid-phase flux at other locations in the host rock and drift is even greater (compare Figure 6-28l with Figure 6-26o and Figure 6-27l).

The evolution of liquid-phase flux adjacent to the lower side of the drip shield, $q_{\text{liq,lds}}$, (“lds” stands for lower drip shield), is summarized in Figure 6-29 for the mean infiltration-flux case. During the first 425 yr of the post-closure period, $q_{\text{liq,lds}}$ is zero everywhere in the repository. At 500 yr (Figure 6-29a) the first nonzero occurrence of $q_{\text{liq,lds}}$ is seen in a region of high ambient infiltration (and percolation) flux. The region of nonzero $q_{\text{liq,lds}}$ spreads (Figure 6-29b through Figure 6-29i), starting in the regions of highest infiltration flux, until it occupies all but the regions of low infiltration flux. The transition to a steady-state monsoonal-climate seepage-flux condition occurs relatively quickly (compare Figure 6-29c and Figure 6-29d). The transition to a steady-state glacial-climate seepage-flux condition also occurs relatively quickly (compare Figure 6-29f through Figure 6-29i). Whereas the liquid-phase flux above the drip shield $q_{\text{liq,uds}}$ declines to a very small value, the liquid-phase flux adjacent to the lower side of the drip shield $q_{\text{liq,lds}}$ remains large.

The contour plot of $q_{\text{liq,lds}}$ during the monsoonal climate (Figure 6-29f) is qualitatively the same as that of the monsoonal-climate infiltration flux (Figure 6-47b), with differences arising from how the geometry of the EBS results in flow focussing in the drift. The contour plot of $q_{\text{liq,lds}}$ during the glacial climate (Figure 6-29h and Figure 6-29i) is also qualitatively similar to that of

the glacial-climate infiltration flux (Figure 6-47c) and the contour map of $q_{\text{liq},5\text{m}}$ (Figure 6-26n and Figure 6-26o). However, the values of $q_{\text{liq},\text{lds}}$ are about four to five times larger than $q_{\text{liq},5\text{m}}$ in the host rock. Figure 4-2 and Figure 6-3 illustrate that the width of the backfill adjacent to the lower side of the drip shield becomes very narrow just above the interface with the invert. In the LDTH submodel, the backfill adjacent to the lower side of the drip shield is only 0.6907 m wide (Figure 6-3). If all of the water trying to shed around the drift were wicked into the drift, then this capillary-driven seepage flux into the drift would be contributed by the percolation flux in a region that is at least 2.75 m wide (which corresponds to the half-width of the drift). Because the value of the van Genuchten α in the Overton sand backfill is smaller than in the fractures of the host rock, water draining down the side of the drip shield does not want to leave the backfill and enter the fractures in the host rock. Instead, all the water drains into the invert. If all of the percolation flux over a 2.75 m wide zone were focussed into the 0.6907 m wide zone next to the drip shield, this would result in a “focussing” factor of four, which is comparable to the ratio (of four to five) which is observed between $q_{\text{liq},\text{lds}}$ and $q_{\text{liq},5\text{m}}$ in the host rock. As observed earlier, because capillary suction augments gravity drainage into the drift, the source of seepage into the drift is actually contributed by percolation flux occurring over a region that is somewhat wider than 2.75 m.

The evolution of liquid-phase flux averaged across the invert, $q_{\text{liq},\text{inv}}$, (“inv” stands for invert), is summarized in Figure 6-30 for the mean infiltration-flux case. During the first 200 yr of the post-closure period, $q_{\text{liq},\text{inv}}$ is zero everywhere in the repository. At 254 yr (Figure 6-30a) the first nonzero occurrence of $q_{\text{liq},\text{lds}}$ is seen in a region of high ambient infiltration (and percolation) flux. Initially, the values of $q_{\text{liq},\text{inv}}$ are negative, indicating that water is being wicked (by capillarity) vertically upward from below the drift. The region of nonzero $q_{\text{liq},\text{inv}}$ spreads (Figure 6-30b through Figure 6-30l), starting in the regions of highest infiltration (and percolation) flux, until it occupies all but the regions of low infiltration (and percolation) flux. As nonzero values of liquid-phase flux at the lower side of the drip shield $q_{\text{liq},\text{lds}}$ begin to occur, which causes water to drain from the Overton sand backfill into the invert, the direction of flow in the invert is forced to reverse, so that it is now flowing vertically downward, driven by gravity rather than by capillarity (Figure 6-30d through Figure 6-30f).

During the present-day and monsoonal climates, regions of negative $q_{\text{liq},\text{inv}}$ persist (Figure 6-30a through Figure 6-30f). Shortly after the glacial climate begins, all regions of negative $q_{\text{liq},\text{inv}}$ are eliminated and a steady-state drainage-flux condition is eventually established in the invert (Figure 6-30f through Figure 6-30l). Qualitatively, the contour plot of $q_{\text{liq},\text{inv}}$ (Figure 6-30h through Figure 6-30l) is similar to that of the glacial-climate infiltration flux (Figure 6-47c). Because the area over which drainage occurs out the bottom of the invert is smaller than the overall footprint of the drift, a focussing effect occurs whereby the liquid-phase flux in the invert is larger than the percolation flux in the host rock.

6.11.4.2 Liquid-Phase Flux Distributions for High Infiltration Case

The evolution of liquid-phase flux (in fractures) 5 m above the crown of the drift, $q_{\text{liq},5\text{m}}$, is summarized in Figure 6-31 for the high infiltration-flux case. The observations made for the mean infiltration-flux case generally apply to the high flux case. During the pre-closure period, decay heat has almost no effect on liquid-phase flux in either the host rock or in the drift. During

the early portion of the post-closure period, decay-heat-enhanced liquid-phase fluxes are seen above the drift (Figure 6-31c). However, because the higher infiltration (and percolation) flux slows down the upward advance of the boiling and dryout fronts above the drift (relative to the mean flux case), it takes longer for the peak values of $q_{liq,5m}$ to occur (compare Figure 6-31e with Figure 6-31d with Figure 6-26d); accordingly, the upward advance of the heat-pipe zone is also slower for the high infiltration-flux case than in the mean flux case. During the present-day climate, the contribution of heat on $q_{liq,5m}$ declines until $q_{liq,5m}$ approaches a steady-state condition, controlled by the present-day climate infiltration flux (compare Figure 6-31h and Figure 6-31i with Figure 6-48a). After the monsoonal climate begins, $q_{liq,5m}$ attains a steady-state condition controlled by the monsoonal-climate infiltration flux (compare Figure 6-31j and Figure 6-31k with Figure 6-48b). After the glacial climate begins, $q_{liq,5m}$ attains a steady-state condition controlled by the glacial-climate infiltration flux (compare Figure 6-31m, Figure 6-31n, and Figure 6-31o with Figure 6-48c).

The evolution of liquid-phase flux (in fractures) 0.2 m above the crown of the drift, $q_{liq,cr}$ (“cr” stands for crown), is summarized in Figure 6-32 for the high infiltration-flux case. The observations made for the mean infiltration-flux case also apply to the high flux case. During the pre-closure period when the host rock remains below the boiling point, $q_{liq,cr}$ is largely unaffected by decay heat. During the early portion of the post-closure period, decay-heat-enhanced liquid-phase fluxes are seen above the drift (Figure 6-32a and Figure 6-32b). However, because the high percolation flux suppresses the advance of the dryout front above the drift (relative to the mean flux case), dryout never completely obliterates the presence of the heat-pipe zone 5 m above the drift (Figure 6-32d). Relatively soon after the monsoonal climate begins, $q_{liq,cr}$ attains a steady-state condition controlled by the monsoonal-climate infiltration flux (compare Figure 6-32h and Figure 6-32i with Figure 6-48b). Similarly, relatively soon after the glacial climate begins, $q_{liq,cr}$ attains a steady-state condition controlled by the glacial-climate infiltration flux (compare Figure 6-32j, Figure 6-32k, and Figure 6-32l with Figure 6-48c).

The evolution of liquid-phase flux averaged over the upper surface of the drip shield, $q_{liq,uds}$ (“uds” stands for upper drip shield), is summarized in Figure 6-33 for the high infiltration-flux case. During the first 100 yr of the post-closure period, $q_{liq,uds}$ is zero everywhere in the repository area. At 162 yr (Figure 6-33a) the first nonzero occurrence of $q_{liq,uds}$ is seen in a region of high ambient infiltration (and percolation) flux. The region of nonzero $q_{liq,uds}$ spreads (Figure 6-33b through Figure 6-33g), starting in the regions of highest infiltration (and percolation) flux, until it occupies nearly the entire repository area. The influence of the heat-pipe effect is apparent as the value of $q_{liq,uds}$ declines along with the decaying heat-generation-rate of WPs (compare Figure 6-33g, Figure 6-33h, and Figure 6-33i). Unlike the mean infiltration-flux case, after the glacial climate begins, there is a small increase in $q_{liq,uds}$; however, the magnitude of $q_{liq,uds}$ is still much smaller than the magnitude of liquid-phase flux elsewhere in the drift or in the host rock (compare Figure 6-33j with Figure 6-34g and Figure 6-31m).

The evolution of liquid-phase flux adjacent to the lower side of the drip shield, $q_{liq,lds}$ (“lds” stands for lower drip shield), is summarized in Figure 6-34 for the high infiltration-flux case. During the first 130 yr of the post-closure period, $q_{liq,lds}$ is zero everywhere in the repository. At 184 yr (Figure 6-34a) the first nonzero occurrence of $q_{liq,lds}$ is seen in a region of high ambient

infiltration (and percolation) flux. The region of nonzero $q_{liq,lds}$ spreads (Figure 6-34b through Figure 6-34i), starting in the regions of highest infiltration flux, until it occupies most of the repository area. The transition to a steady-state monsoonal-climate seepage-flux condition occurs relatively quickly (compare Figure 6-34d and Figure 6-34e). The transition to a steady-state glacial-climate seepage-flux condition also occurs relatively quickly (compare Figure 6-34e and Figure 6-34f).

The contour plot of $q_{liq,lds}$ during the monsoonal climate (Figure 6-34d and Figure 6-34e) is qualitatively the same as that of the monsoonal-climate infiltration flux (Figure 6-48b), with differences arising from how the geometry of the EBS results in flow focussing in the drift. The contour plot of $q_{liq,lds}$ during the glacial climate (Figure 6-34f through Figure 6-34i) is also qualitatively similar to that of the glacial-climate infiltration flux (Figure 6-48c) and is also qualitatively similar to the contour map of $q_{liq,5m}$ (Figure 6-31m through Figure 6-31o); however, the values of $q_{liq,lds}$ are about four times larger than $q_{liq,5m}$ in the host rock. This factor of four corresponds to the ratio of the half-drift width divided by the width of the thickness of the backfill adjacent to the lower side of the drip shield (Figure 6-3). If all of the percolation flux over a 2.75 m wide zone were focussed into the 0.6907 m wide zone next to the drip shield, this would result in a “focussing” factor of four, which is comparable to the ratio (of four) which is observed between $q_{liq,lds}$ and $q_{liq,5m}$ in the host rock.

The evolution of liquid-phase flux averaged across the invert, $q_{liq,inv}$ (“inv” stands for invert), is summarized in Figure 6-35 for the high infiltration-flux case. During the first 150 yr of the post-closure period, $q_{liq,inv}$ is zero everywhere in the repository. At 200 yr (Figure 6-35a) the first nonzero occurrence of $q_{liq,lds}$ is seen in a region of high ambient infiltration (and percolation) flux. Initially, the values of $q_{liq,inv}$ are negative, indicating that water is being wicked (by capillarity) vertically upward from below the drift. The region of nonzero $q_{liq,inv}$ spreads (Figure 6-35b through Figure 6-35f), starting in the regions of highest infiltration (and percolation) flux, until it occupies all but the regions of low infiltration (and percolation) flux. As nonzero values of liquid-phase flux at the lower side of the drip shield $q_{liq,lds}$ begin to occur, which causes water to drain from the Overton sand backfill into the invert, the direction of flow in the invert is forced to reverse, so that it is now flowing vertically downward, driven by gravity rather than by capillarity (Figure 6-35d through Figure 6-35f).

During the present-day and monsoonal climates, regions of negative $q_{liq,inv}$ persist (Figure 6-35a through Figure 6-35f). Shortly after the glacial climate begins, most of the regions of negative $q_{liq,inv}$ are eliminated and a steady-state drainage-flux condition is eventually established in the invert (Figure 6-35g through Figure 6-35l). Qualitatively, the contour plot of $q_{liq,inv}$ (Figure 6-35h through Figure 6-35l) is similar to the that of the glacial-climate infiltration flux (Figure 6-48c). Because the area over which drainage occurs out the bottom of the invert is smaller than the overall footprint of the drift, a focussing effect occurs, whereby the liquid-phase flux in the invert is larger than the percolation flux in the host rock.

6.11.4.3 Liquid-Phase Flux Distributions for Low Infiltration Case

The evolution of liquid-phase flux (in fractures) 5 m above the crown of the drift, $q_{liq,5m}$, is summarized in Figure 6-36 for the low infiltration-flux case. Because of the low percolation flux

in the host rock, boiling conditions occurred at the drift wall during the pre-closure period (Figure 6-13). Because the drift-wall attained a temperature of 100°C, boiling conditions occurred a short distance out into the host rock during the pre-closure period. However, the upper vertical extent of the heat-pipe zone has not reached 5 m above the drift at the end of the pre-closure period (compare Figure 6-36a with Figure 6-49a). Within 10 yr after the start of the post-closure period, decay-heat-enhanced values of $q_{liq,5m}$ are evident (compare Figure 6-36b through Figure 6-36d). The peak of $q_{liq,5m}$ occurs earlier in the low infiltration-flux case than in the mean and high flux cases (compare Figure 6-36f with Figure 6-26d and Figure 6-31e). The earlier peak occurs in the low infiltration-flux case because rock dryout advances far enough vertically upward (above the drift) to displace the heat-pipe zone more than 5 m above the drift.

After the monsoonal climate begins, $q_{liq,5m}$ gradually transitions to a steady-state condition, controlled by the monsoonal-climate infiltration flux (compare Figure 6-36p, Figure 6-36q, Figure 6-36r, and Figure 6-49b). After the glacial climate begins, $q_{liq,5m}$ gradually transitions to a steady-state condition, controlled by the glacial-climate infiltration flux (compare Figure 6-36s, Figure 6-36t, Figure 6-36u, and Figure 6-49c).

The evolution of liquid-phase flux (in fractures) 0.2 m above the crown of the drift, $q_{liq,cr}$ (“cr” stands for crown), is summarized in Figure 6-37 for the low infiltration-flux case. During the early post-closure period, heat-enhanced values of $q_{liq,cr}$ are less in the low infiltration-flux case than in the mean flux case (compare Figure 6-37a with Figure 6-27a). The values of $q_{liq,cr}$ are lower for the low flux case (than for the mean flux case) because the lower percolation flux allows for a more rapid advance of the dryout front above the drift, which more quickly obliterates heat-pipe conditions 0.2 m above the drift. Liquid flux $q_{liq,cr}$ is zero throughout the repository area for the low infiltration-flux case during the 55 to 198 yr time interval, and for the mean flux case $q_{liq,cr}$ is zero for the 60 to 135 yr time interval (Figure 6-37d and Figure 6-27e). This illustrates that the lower infiltration case becomes dry earlier and stays dry longer than for higher infiltration fluxes.

After the monsoonal climate begins, $q_{liq,5m}$ gradually transitions to a steady-state condition, controlled by the monsoonal-climate infiltration flux (compare Figure 6-37e through Figure 6-37h, and Figure 6-49b). After the glacial climate begins, $q_{liq,5m}$ gradually transitions to a steady-state condition, controlled by the glacial-climate infiltration flux (compare Figure 6-37i through Figure 6-37l and Figure 6-49c).

The evolution of liquid-phase flux averaged over the upper surface of the drip shield, $q_{liq,uds}$, (“uds” stands for upper drip shield), is summarized in Figure 6-38 for the low infiltration-flux case. During the first 260 yr of the post-closure period, $q_{liq,uds}$ is zero everywhere in the repository area. At 320 yr (Figure 6-38a) the first nonzero occurrence of $q_{liq,uds}$ is seen in a region of relatively high ambient infiltration (and percolation) flux. The region of nonzero $q_{liq,uds}$ spreads (Figure 6-33b through Figure 6-33d) in the regions of highest infiltration (and percolation) flux. The majority of the repository area continues to have a zero value of $q_{liq,uds}$ throughout the present-day-climate period (Figure 6-38d). The influence of the heat-pipe effect is apparent as the nonzero values of $q_{liq,uds}$ are much greater than the ambient infiltration (and percolation) flux (compare Figure 6-38a with Figure 6-49a).

During the monsoonal-climate period, the region of nonzero $q_{\text{liq,uds}}$ spreads, starting in the regions of highest infiltration flux, and progressing into the regions of lower flux (Figure 6-38e through Figure 6-38h). The influence of the heat-pipe effect is apparent as the nonzero values of $q_{\text{liq,uds}}$ are much greater than the ambient infiltration (and percolation) flux (compare Figure 6-38h with Figure 6-49b and Figure 6-36r). The influence of the heat-pipe effect is also exhibited by the decline in $q_{\text{liq,uds}}$, which corresponds to the decay in heat-generation rate from WPs (Figure 6-38h through Figure 6-38l). The value of $q_{\text{liq,uds}}$ becomes much less than the infiltration and percolation flux (compare Figure 6-38l with Figure 6-49c and Figure 6-36u).

The evolution of liquid-phase flux adjacent to the lower side of the drip shield, $q_{\text{liq,lds}}$ (“lds” stands for lower drip shield), is summarized in Figure 6-39 for the low infiltration-flux case. During the first 365 yr of the post-closure period, $q_{\text{liq,lds}}$ is zero everywhere in the repository. At 420 yr (Figure 6-39a) the first nonzero occurrence of $q_{\text{liq,lds}}$ is seen in a region of high ambient infiltration (and percolation) flux. The region of nonzero $q_{\text{liq,lds}}$ spreads (Figure 6-39b through Figure 6-39c), starting in the regions of relative high infiltration (and percolation) flux; about half of the repository area continues to have a zero value of $q_{\text{liq,lds}}$ throughout the present-day-climate period (Figure 6-39d). During the present-day-climate period, most of the nonzero values of $q_{\text{liq,lds}}$ are negative, indicating that $q_{\text{liq,lds}}$ is vertically upward, resulting from capillary-driven wicking up through the invert and into the backfill. During the present-day-climate and monsoonal-climate periods, a steady-state condition is never established in the backfill; thus decay heat continues to dominate liquid-phase flux conditions.

During the glacial-climate period, $q_{\text{liq,lds}}$ eventually develops a steady-state condition that is controlled by the glacial-climate infiltration (and percolation) flux (compare Figure 6-39h through Figure 6-39l with Figure 6-49c and Figure 6-37l). The contour plot of $q_{\text{liq,lds}}$ during the glacial climate (Figure 6-39j through Figure 6-39l) becomes qualitatively similar to that of the glacial-climate infiltration flux (Figure 6-49c) and is also qualitatively similar to the contour map of $q_{\text{liq,5m}}$ (Figure 6-36s through Figure 6-36u); however, the values of $q_{\text{liq,lds}}$ are about 4 times larger than $q_{\text{liq,5m}}$ in the host rock. This factor of 4 corresponds to the ratio of the half-drift width divided by the width of the thickness of the backfill adjacent to the lower side of the drip shield (Figure 6-3). If all of the percolation flux over a 2.75 m wide zone were focussed into the 0.6907 m wide zone next to the drip shield, this would result in a “focussing” factor of four, which is comparable to the ratio (of four) which is observed between $q_{\text{liq,lds}}$ and $q_{\text{liq,5m}}$ in the host rock.

The evolution of liquid-phase flux averaged across the invert (called $q_{\text{liq,inv}}$, where “inv” stands for invert) is summarized in Figure 6-40 for the low infiltration-flux case. During the first 345 yr of the post-closure period, $q_{\text{liq,inv}}$ is zero everywhere in the repository. At 400 yr (Figure 6-40a) the first nonzero occurrence of $q_{\text{liq,inv}}$ is seen in a region of high ambient infiltration (and percolation) flux. During the present-day-climate and monsoonal-climate periods, the values of $q_{\text{liq,inv}}$ are negative, indicating that water is being wicked (by capillarity) vertically upward from below the drift. The region of nonzero $q_{\text{liq,inv}}$ spreads (Figure 6-40b through Figure 6-40f), from the regions of highest infiltration (and percolation) flux. Most of the repository area continues to have a zero value of $q_{\text{liq,inv}}$ throughout the present-day-climate period (Figure 6-40a and Figure 6-40b). During the monsoonal-climate period, the region of nonzero $q_{\text{liq,inv}}$ spreads throughout most of the repository area (Figure 6-40c through Figure 6-40f).

During the glacial-climate period, a gradual transition occurs from nonzero values of $q_{\text{liq,inv}}$ being primarily negative to all nonzero values of $q_{\text{liq,inv}}$ being positive (Figure 6-40f through Figure 6-40l). This slow transition indicates the influence of decay heat from WPs on $q_{\text{liq,inv}}$ persisting for nearly 50,000 yr for the low-infiltration flux case. The slow transition results because decay heat delays the onset of significant seepage into the Overton sand backfill. Eventually, seepage into the drift overwhelms the influence of decay heat and the resulting drainage of water into the invert dominates the direction of liquid-phase flow in the invert. When gravity flow finally dominates liquid flow in the drift (including the invert), the distribution of $q_{\text{liq,inv}}$ (Figure 6-40l) becomes qualitatively similar to the distribution of $q_{\text{liq,5m}}$ (Figure 6-36u) and that glacial-climate infiltration flux (Figure 6-49c).

6.11.4.4 Liquid-Phase Flux Analysis

Most of the liquid-phase flux analysis is addressed in the previous three subsections (Section 6.11.4.1, Section 6.11.4.2, and Section 6.11.4.3). Not presented in the previous three subsections is a history plot of liquid-phase flux. Figure 6-41 plots the liquid phase flux at the five drift-scale locations in the NFE and EBS: (1) 5 m above the crown of the drift, (2) 0.2 m above the crown of the drift, (3) in the sand backfill, averaged along the top of the drip shield, (4) in the sand backfill, adjacent to the lower side of the drip shield, and (5) in the crushed-tuff invert, averaged over the invert. This information is given at two repository-scale locations, including the geographic center of the repository and a location 27.5 m from the eastern edge, which is approximately midway between the northern and southern boundaries of the repository.

Many of the observations made in the previous three subsections are illustrated in Figure 6-41. The early spike in the liquid-phase flux 0.2 m above the crown of the drift is seen just after 50 yr, while 5 m above the drift the heat-enhanced increase in liquid-phase flux occurs slightly later. At the edge of the repository, the heat-enhanced increase in liquid-phase flux 5 m above the drift is much less pronounced because edge-cooling prevents the neighboring drifts from reinforcing the temperature buildup enough to cause significant thermal effects on flow 5 m above the drift. At both the center and edge locations, the effect of the three climate states on liquid-phase flux above the drift is clearly evident. However, climate change has no effect on the liquid-phase flux above the drip shield. The dependence on liquid-phase flux above the drip shield on heat-generation rate is exhibited by an abrupt rise in flux at 50 yr, followed by a gradual decline to a value that is much less than the liquid-phase flux in the host rock.

Adjacent to the lower side of the drip shield and within the invert, the initial nonzero values of liquid-phase flux are negative, indicating that flow is being wicked from below the drift. Eventually, the direction of flow at these two directions is reversed and the liquid-phase flux at these locations in the drift is equal to a multiple of the percolation flux in the host rock. The factor by which the flux in the drift is greater than that in the host rock is attributed to how the EBS geometry causes flow focussing past the lower drip shield and into the invert.

6.11.5 Evaporation Rate Distributions

Evaporation can occur at a given location in the drift once the liquid-phase flux at that location is nonzero. Evaporation rate is considered to be an important performance measure because it is an

indication of the rate at which mineral precipitates are being left behind. Negative values of evaporation rate indicate areas where condensation is occurring; in such regions, mineral dissolution may be occurring. A particularly important location within the EBS with respect to the effects of evaporation and condensation is the surface of the drip shield. The following three subsections provide the complete evolution of the total evaporation rate (summed over the outer perimeter of the drip shield) during the 1,000,000 yr simulation period. The reported values of evaporation rate (in kg/yr/m) pertain to the entire outer (perimeter) surface of a 1 m long interval of the drip shield (along the longitudinal axis of the drift). In the model, the evaporation (and condensation) actually occurs in the backfill gridblocks that are immediately adjacent to the drip shield. Note that the drip shield is emplaced after the pre-closure period (50 yr); therefore, the following results begin at 50 yr.

6.11.5.1 Evaporation Rate Distributions for Mean Infiltration Case

The evolution of evaporation rate per unit length summed over the entire outer (perimeter) surface of the drip shield, $Q_{\text{evap,ds}}$ ("ds" stands for drip shield), for the mean infiltration-flux case is summarized in Figure 6-42. The evaporation rate is given per unit length of drip shield (along the longitudinal axis of the drift). During the first 20 yr of the post-closure period, all values of $Q_{\text{evap,ds}}$ are zero throughout the repository area. At 80 yr, the first nonzero values of $Q_{\text{evap,ds}}$ are seen at the very outer edge of the repository (Figure 6-42a). The region of nonzero $Q_{\text{evap,ds}}$ grows from the outer repository edges in towards the center of the repository (Figure 6-42a through Figure 6-42d). Within 1500 yr, the region of nonzero $Q_{\text{evap,ds}}$ has reached most of the central region of the repository (Figure 6-42e), however, in regions of the lowest infiltration (and percolation) flux, $Q_{\text{evap,ds}}$ is still zero at 1500 yr. Eventually, water has seeped into nearly every drift location, and nonzero $Q_{\text{evap,ds}}$ prevails over most of the entire repository area (Figure 6-42g). Because $Q_{\text{evap,ds}}$ decays along with heat-generation rate, the magnitude of $Q_{\text{evap,ds}}$ declines with time (Figure 6-42e through Figure 6-42r). Even at 1,000,000 yr, there are nonzero values of $Q_{\text{evap,ds}}$ throughout the repository area (Figure 6-42r).

6.11.5.2 Evaporation Rate Distributions for High Infiltration Case

The evolution of evaporation rate per unit length summed over the entire outer (perimeter) surface of the drip shield, $Q_{\text{evap,ds}}$ ("ds" stands for drip shield), for the high infiltration-flux case is summarized in Figure 6-43. The evaporation rate is given per unit length of drip shield (along the longitudinal axis of the drift). The evolution of $Q_{\text{evap,ds}}$ for the high infiltration-flux case is similar to that of the mean flux case. During the first 40 yr of the post-closure period, all values of $Q_{\text{evap,ds}}$ are zero throughout the repository area. At 100 yr, the first nonzero values of $Q_{\text{evap,ds}}$ are seen at the very outer edge of the repository (Figure 6-43a). The region of nonzero $Q_{\text{evap,ds}}$ grows from the outer repository edges in towards the center of the repository (Figure 6-43a through Figure 6-43c). Within 1000 yr, the region of nonzero $Q_{\text{evap,ds}}$ has reached most of the central region of the repository (Figure 6-43d), however, in regions of the lowest infiltration (and percolation) flux, $Q_{\text{evap,ds}}$ is still zero at 1000 yr. Eventually, water has seeped into nearly every drift location, and nonzero $Q_{\text{evap,ds}}$ prevails over most of the entire repository area (Figure 6-43e). Because $Q_{\text{evap,ds}}$ decays along with heat-generation rate, the magnitude of $Q_{\text{evap,ds}}$ declines with time (Figure 6-43d through Figure 6-43o). Even at 1,000,000 yr, there are nonzero values of $Q_{\text{evap,ds}}$ throughout the repository area (Figure 6-43o).

6.11.5.3 Evaporation Rate Distributions for Low Infiltration Case

The evolution of evaporation rate per unit length summed over the entire outer (perimeter) surface of the drip shield, $Q_{\text{evap,ds}}$ (“ds” stands for drip shield), for the low infiltration-flux case is summarized in Figure 6-44. The evaporation rate is given per unit length of drip shield (along the longitudinal axis of the drift). The evolution of $Q_{\text{evap,ds}}$ for the low infiltration-flux case is similar to that of the mean flux case; however, the lower percolation flux results in the delayed onset of seepage into drifts, the onset of nonzero values of $Q_{\text{evap,ds}}$ is delayed. During the first 60 yr of the post-closure period, all values of $Q_{\text{evap,ds}}$ are zero throughout the repository area. At 120 yr, the first nonzero values of $Q_{\text{evap,ds}}$ are seen at the very outer edge of the repository (Figure 6-43a). The region of nonzero $Q_{\text{evap,ds}}$ grows from the outer repository edges in towards the center of the repository (Figure 6-44a through Figure 6-44d). Within 3000 yr, the region of nonzero $Q_{\text{evap,ds}}$ has reached more than half of the repository area (Figure 6-44); however, in regions of the lowest infiltration (and percolation) flux, $Q_{\text{evap,ds}}$ is still zero at 3000 yr. Eventually, water has seeped into most of the drift locations, and nonzero $Q_{\text{evap,ds}}$ prevails over much of the entire repository area (Figure 6-44g). Because $Q_{\text{evap,ds}}$ decays along with heat-generation rate, the magnitude of $Q_{\text{evap,ds}}$ declines with time (Figure 6-44e through Figure 6-44o). Even at 1,000,000 yr, there are nonzero values of $Q_{\text{evap,ds}}$ throughout the repository area (Figure 6-44o).

6.11.5.4 Evaporation Rate Analysis

Most of the analysis of evaporation rate is addressed in the previous three subsections (Section 6.11.5.1, Section 6.11.5.2, and Section 6.11.5.3). Not given in the previous three subsections is a history plot of evaporation rate. Figure 6-45a gives the evaporation rate on drip shields $Q_{\text{evap,ds}}$ (summed over the outer perimeter on a unit length of drip shield). This information is given at two repository-scale locations, including the geographic center of the repository and a location 27.5 m from the eastern edge, which is approximately midway between the northern and southern boundaries of the repository. Figure 6-45b gives the gas-phase air-mass fraction in the drift, which is covered in Section 6.11.3.

Nonzero values of $Q_{\text{evap,ds}}$ occur for about 950 yr at the geographic center of the repository and for about 80 yr at a location 27.5 m from the edge of the repository (Figure 6-45a). The magnitude of the peak value of $Q_{\text{evap,ds}}$ is about the same for these two locations: (1) 615 kg/yr/m at the geographic center of the repository and (2) 510 kg/yr/m at the repository edge location. The decline in $Q_{\text{evap,ds}}$ is slower at the edge than at the geographic center of the repository. Eventually (after 30,000 yr), the magnitude of $Q_{\text{evap,ds}}$ is nearly the same at these locations.

6.11.6 Influence of Variability of Heat Generation from Waste Packages

All of the results presented in Sections 6.11.1 through 6.11.5 are for the hottest WP location, which corresponds to the second 21-PWR WP shown in Figure 4-1. In this section, the sensitivity of WP temperature and WP relative humidity to the variability of WP heat-generation rate is examined for the mean infiltration-flux case.

6.11.6.1 Temperature and Relative Humidity on Different Waste-Package Types

Temperature and relative humidity on the WP surface for the mean infiltration-flux case is plotted (Figure 6-46) at the geographical center of the repository for the 4 different WP types and 8 different WP locations (along the drift) considered in the MSTHM; the 4 WP types and 8 WP locations are shown in Figure 4-1. The WP temperature T_{wp} histories for these 8 WPs is relatively similar (Figure 6-46a). The difference in peak T_{wp} between the hottest and coldest WP is 42°C (Figure 6-46a). Note that the hottest WP is the 21-PWR WP that was considered throughout the rest of Section 6.11 and the coldest WP is a DSNF WP (see Figure 4-1). The duration of the boiling period (defined to be the period during which $T_{wp} > 96^{\circ}\text{C}$) is 1540 yr and 1230 yr for the hottest and coldest WP, respectively. Therefore, the range in temperature for the different WP types (and locations) considered in this AMR is relatively small. The range in WP relative humidity RH_{wp} histories for the same group of WPs is also relatively small (Figure 6-46b). The minimum RH_{wp} is 1.7% for the hottest WP and is 3.9% for the coldest WP. The range in the time required for the WPs to attain $RH_{wp} = 85\%$ varies from 1170 yr to 1460 yr.

6.11.7 Influence of Overburden Thickness

Overburden thickness (which is equal to the depth of the repository below the ground surface) affects temperatures in the repository because it determines the thickness of the (rock) insulation lying between the repository and the ground surface. Because the ground surface is a constant-temperature boundary, acts like a heat sink. The influence of overburden thickness is negligible during the first 300 to 500 yr (Hardin et. al 1998, Section 3.7.7.1). This influence is also relatively unimportant close to the repository edges and are increasingly important toward the center of the repository (Hardin et. al 1998, Section 3.7.7.1). The greatest long-term temperature rise occurs where the overburden thickness is greatest in the central region of the repository (Hardin et. al 1998, Section 3.7.7.1).

Because the largest values of overburden thickness occur close to the center of the repository, it is difficult to discern the influence of the edge-cooling effect from the influence of overburden thickness (Figure 6-7h through Figure 6-7m); both influences cause higher long-term temperatures at the center and lower long-term temperatures at the edges of the repository.

6.12 MODEL VALIDATION

The MSTHM is performed using industry standard finite-difference method that includes mass balance and energy balance. The results from finite-difference codes are only as good as the inputs. All inputs into this model are TBV, and therefore the results are TBV. The model validation includes various validation techniques described below:

- **Comparison of NUFT TH model results against the Large Block Test.** The Thermal Tests Thermal-Hydrological Analysis/Model Report (CRWMS M&O 2000b, Section 6.2.4.) documents the comparison of NUFT TH model calculations against measurements made in the Large Block Test. A brief summary of this comparison is given in Section 6.12.1 of this report.

- **Comparison of NUFT TH model results against the Drift Scale Test.** The Thermal Tests Thermal-Hydrological Analysis/Model Report (CRWMS M&O 2000b, Section 6.2.3) documents the comparison of NUFT TH model calculations against measurements made in the Drift Scale Test. A brief summary of this comparison is given in Section 6.12.2 of this AMR.
- **Comparison of MSTHM results against alternative numerical models.** Milestone Report SP4CK5M4 (Buscheck et al., 1998) documents a comparison between the results of the MSTHM against a 3-D east-west cross-sectional mountain-scale TH model developed at Lawrence Berkeley National Laboratory (Haukwa et al., 1998). A brief summary of this comparison is given in Section 6.12.3 of this AMR.
- **Inspection of model inputs and outputs.** A detailed and comprehensive analysis was conducted (Section 6.11) that carefully compared the relationship between the model inputs and the model outputs. This comparison involved more than 150 pages of contour plots and time history plots of a wide range of input and output variables. This comparison uncovered no unexpected or difficult to explain model results; the relationships between the model outputs and the model inputs (for the range of inputs considered in this AMR) are consistent with the physical processes that are accounted for in the MSTHM.
- **Validation of software routines and macros.** The submodel input files were largely built using software routines and macros; very little hand editing was used in building the input files. Each one of these routines and macros are validated (Attachments I through XIX). By minimizing hand editing, the potential for human error is greatly reduced. Because the input files are built with validated software, this assures the accuracy with which the source-input data is faithfully represented in the submodels.
- **Inspection of model input files.** A detailed visual inspection of the submodel input files was conducted to verify that the submodels faithfully represented the intended conceptual model and accurately included all source-input data. Visual inspection was conducted for all templates (used in macros and scripts) and for the very few submodels that employed any hand editing in the building of the input files (e.g., the DDT submodel, described in Section 6.5). For the input files that are generated automatically (without hand editing), this inspection process is greatly facilitated by the validation of software routines and macros used to build these file (described in the preceding bullet).

On the basis of this multi-stage model validation effort, it is determined that the MSTHM is valid for its intended use.

6.12.1 Comparison of NUFT TH Model against the Large Block Test

The NUFT model used to model the Large Block Test is described in the Thermal Tests Thermal-Hydrological Analysis/Model Report (CRWMS M&O 2000b, Section 5.4). Figure 6-50 shows the simulated versus measured temperature profile along Borehole TT1 at six times from 30 to 400 days. The DTN for all field temperatures is LL970803004244.036. The NUFT TH model of the LBT, which used the same hydrologic property set as used in this AMR, shows

some over-prediction of temperature at earlier times, but the difference between simulated and measured temperatures decreases at later times. At 300 and 400 days (25 days after power shutdown), the agreement is excellent.

Two statistical measures of goodness-of-fit, the root mean squared difference (RMSD) and mean difference (MD) between measured and simulated temperatures along Borehole TT1, were computed at various times from 30 days to 500 days. The results are tabulated in Table 6.5. As shown in the temperature profiles, the RMSD plot indicates a good fit between simulated and field temperatures. The match is good at 30 days, worsens at 100 days, and then consistently improves thereafter. The MD is always positive, which indicates that the NUFT TH model, in general, slightly overpredicts the temperatures. Again, the accuracy of the prediction consistently increases with time after 30 days, reducing to a mean error of less than 1°C at 500 days, 125 days into the cool-down phase.

Table 6-5. RMSD and MD for temperature profile along TT1 using driftscale data set.

Time (days)	RMSD (°C)	MD (°C)
30	7.25	6.90
100	14.05	10.55
200	10.56	4.34
300	9.16	1.53
400	5.82	3.53
500	0.63	0.08

Figure 6-51 shows the simulated and measured liquid-phase saturation profile along TN3, which is a vertical borehole used for neutron probe measurements of water content. NUFT model results are compared to liquid-phase saturations measured by neutron probe (DTN LL971204304244.047, LL980919304244.075). The field measurement times, 103, 361, and 501 days are compared at model times of 100, 365, and 500 days. The small differences between model and field times should have a negligible effect on the comparisons since saturation changes develop relatively slowly. The simulated dryout zone develops more slowly than the measured dryout zone. The difference between the simulated and measure dryout zones decreases with increasing time. At 365 and 500 days, the comparison between the simulated and measured dryout zones is excellent.

The good agreement between the NUFT simulation and the measurements made in the LBT indicate that the NUFT LDTH submodels, together with the use of the drift-scale hydrologic property set, are validated for their intended use.

6.12.2 Comparison of NUFT TH Model against the Drift Scale Test

The NUFT model used to model the Drift Scale Test (DST) is described in the Thermal Tests Thermal-Hydrological Analysis/Model Report (CRWMS M&O 2000b, Section 5.1 and Section 5.3.2). Figure 6-52 compares the NUFT-simulated and measured temperatures along Borehole ESF-HD-137 at 365 and 547 days. The agreement between NUFT and the measured

temperatures is good, with NUFT slightly overpredicting temperatures in the superheated zone and slightly underpredicting temperatures in the sub-boiling zone.

The RMSD, MD, and normalized averaged mean difference (NAMD) between simulated and measured temperatures were selected to serve as measures of the goodness-of-fit of the simulated values to the measured values. In general, the comparison between the simulated and measured temperatures is poor for all sensors very close to the heated drift at all times less than 100 days. This poor comparison results from the NUFT model of the DST representing the heated drift as an equivalent square rather than as the cylindrical cross section. On the other hand the LDTH submodels accurately represent the cylindrical cross-sectional geometry emplacement drift. It is judged that had the NUFT DST model accurately accounted for the cylindrical cross-sectional geometry of the heated drift, the agreement close to the heated drift would have been much better for all times and that the overall agreement between simulated and measured temperatures would have also been better.

At times in excess of 1 yr, the agreement between simulated and measured temperatures improves. The regions for which there is good agreement between simulated and measured temperatures fall into two categories: (1) the sub-boiling zone and (2) the boiling and above-boiling zone along the heated drift.

The good agreement in the sub-boiling zone indicates that heat flow there is dominated by conduction and that the assumed value of wet thermal conductivity is reasonable. Because of the relatively high liquid-phase saturation in the sub-boiling zone, the wet value of thermal conductivity applies. Because the bulk permeability k_b of the DST area is much less than the threshold k_b value at which buoyant gas-phase convection begins to significantly influence heat flow (Buscheck and Nitao, 1994), heat flow in the sub-boiling region is dominated by heat conduction.

The good agreement between the simulated and measured temperatures in the region close to the heated drift indicates the following three points. First, the representation of thermal radiation inside the heated drift is adequately represented in the NUFT DST model. Secondly, heat flow in the boiling and above-boiling zones is dominated by conduction. Thirdly, the value of dry thermal conductivity used in the NUFT DST model is reasonable.

The good agreement between the NUFT simulation and the measurements made in the DST indicate that the NUFT LDTH submodels, together with the use of the drift-scale hydrologic property set, are validated for their intended use. The good agreement also indicates that the DDT submodel (which represents how thermal radiation affects 3-D heat flow in the EBS and near field) is validated for its intended use.

6.12.3 Comparison of MSTHM against an Alternative Conceptual Model

Figure 6-53 compares the drift-wall temperature predicted by the MSTHM (Buscheck et al., 1998) with those predicted by an east-west cross-sectional mountain-scale TH model (Haukwa et al., 1998). Because the east-west TH model does not predict in-drift TH conditions and because relative humidity RH and liquid-phase saturation was not provided from that model, the

comparison is restricted to predictions of drift-wall temperatures by the respective modeling approaches.

Before discussing the differences in the temperatures predicted by the two approaches (Figure 6-53) it is important to discuss the differences in the models. The temperature predicted by the MSTHM is the perimeter-averaged drift-wall temperature adjacent to an “average” 21-PWR medium-heat CSNF WP. MSTHM discretely represents the decay-heat source from individual WPs—thus, some of the drift-wall locations are hotter than that shown in Figure 6-53, while some are considerably cooler. The drift-wall grid blocks over which the temperature is averaged extend 0.5 m into the host rock surrounding the drift. The temperature prediction in the east-west cross-sectional mountain-scale TH model is for a grid block that occupies the entire cross section of the drift—thus, it is a lumped representation of the drift temperature. Moreover, because the east-west cross-sectional mountain-scale model uses a line-averaged heat source, it axially smears out the differences between hot-WP locations and cold-WP locations along the drift.

Another difference between the modeling approaches concerns the mountain-scale dimensionality. The MSTHM represents 3-D mountain-scale heat flow for entire extent of the heated repository footprint, while the east-west cross-sectional mountain-scale TH model has a reflected boundary at the east-west midpoint of the repository. Thus, the east-west model assumes that the overburden thickness of the entire repository area can be approximated with the overburden thickness between the western repository boundary and the midpoint of the repository. Because the eastern half of the repository has much less overburden thickness than the western half, this east-west symmetry approximation effectively overrepresents the effective overburden thickness for the eastern half of the repository. The cross-sectional geometry of the east-west mountain-scale model implicitly assumes that mountain-scale heat loss in the north-south dimension is negligible, which is a reasonable assumption given the large north-south dimension of the repository.

Another difference between the two modeling approaches concerns the areal power density APD assumed in the models. The initial APD in the MSTHM is 92.3 kW/acre, while it is 99.4 kW/acre in the east-west cross-sectional mountain-scale model. Thus, the east-west model has a 7.7% larger APD than does the MSTHM.

At the center of the repository (the 14c3 location in Table 2-2 of Buscheck et al., 1998) the respective modeling approaches predict almost an identical duration of boiling (Figure 6-53a). At the edge repository location, which is 100 m from the western edge of the repository in the MSTHM (the 14c1 location in Table 2-2), the east-west cross-sectional mountain-scale model predicts a longer duration of boiling than does the MSTHM (Fig. 6-53b). One reason for this difference is that the east-west model representation of the heated repository footprint extends slightly further to the west than it does in the MSTHM.

During the post-boiling period, the temperatures predicted by the respective modeling approaches are in good agreement. During the early-time heat-up period, the coarse (lateral and axial) grid-block spacing in the east-west cross-sectional mountain-scale model does not capture the rapid drift-wall temperature rise that the more finely gridded MSTHM predicts. Because of

the coarse lateral grid-block spacing in the east-west model, it smears out the lateral temperature gradient between the drift and the mid-pillar location—thus, it tends to overpredict the temperature at the mid-pillar location and thereby prevent condensate from shedding between drifts. The fine lateral grid-block spacing in the MSTHM captures the influence that the lateral temperature gradient has on allowing condensate to shed between drifts. The tendency for the east-west cross-sectional mountain-scale model to underrepresent condensate shedding results in a more substantial condensate buildup above the repository horizon. Also, the line-averaged heat-source approximation smears out differences in temperature between otherwise hot- and cold-WP locations and thereby preventing condensate from breaking through cold-WP locations along the drift. Altogether, the underprediction of condensate shedding between drifts and condensate breakthrough at cold-WP locations causes the east-west cross-sectional mountain-scale model to build up more condensate above the repository horizon that leads to unstable heat-pipe behavior. This unstable behavior is exhibited by the rapid decline from superheated conditions to heat-pipe conditions (Figure 6-53a) and the rapid rise once again to superheated conditions at about 400 yr. Notice that during the second superheated period predicted by the east-west model, the temperature climbs to be almost exactly that predicted by the MSTHM.

Given the differences between the MSTHM and the east-west cross-sectional mountain-scale model, the agreement between the two models is quite good. On the basis of this comparison, it is determined that the MSTHM is validated for its intended use.

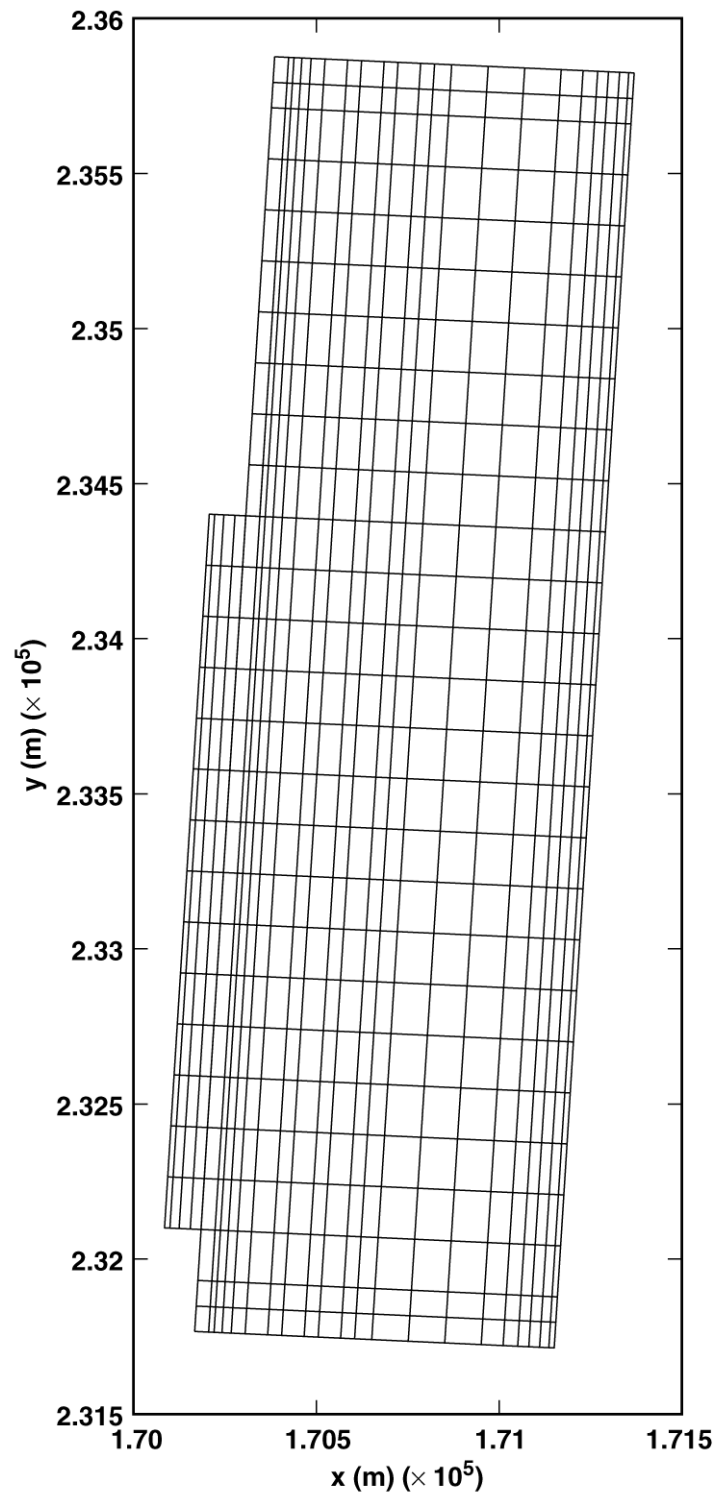
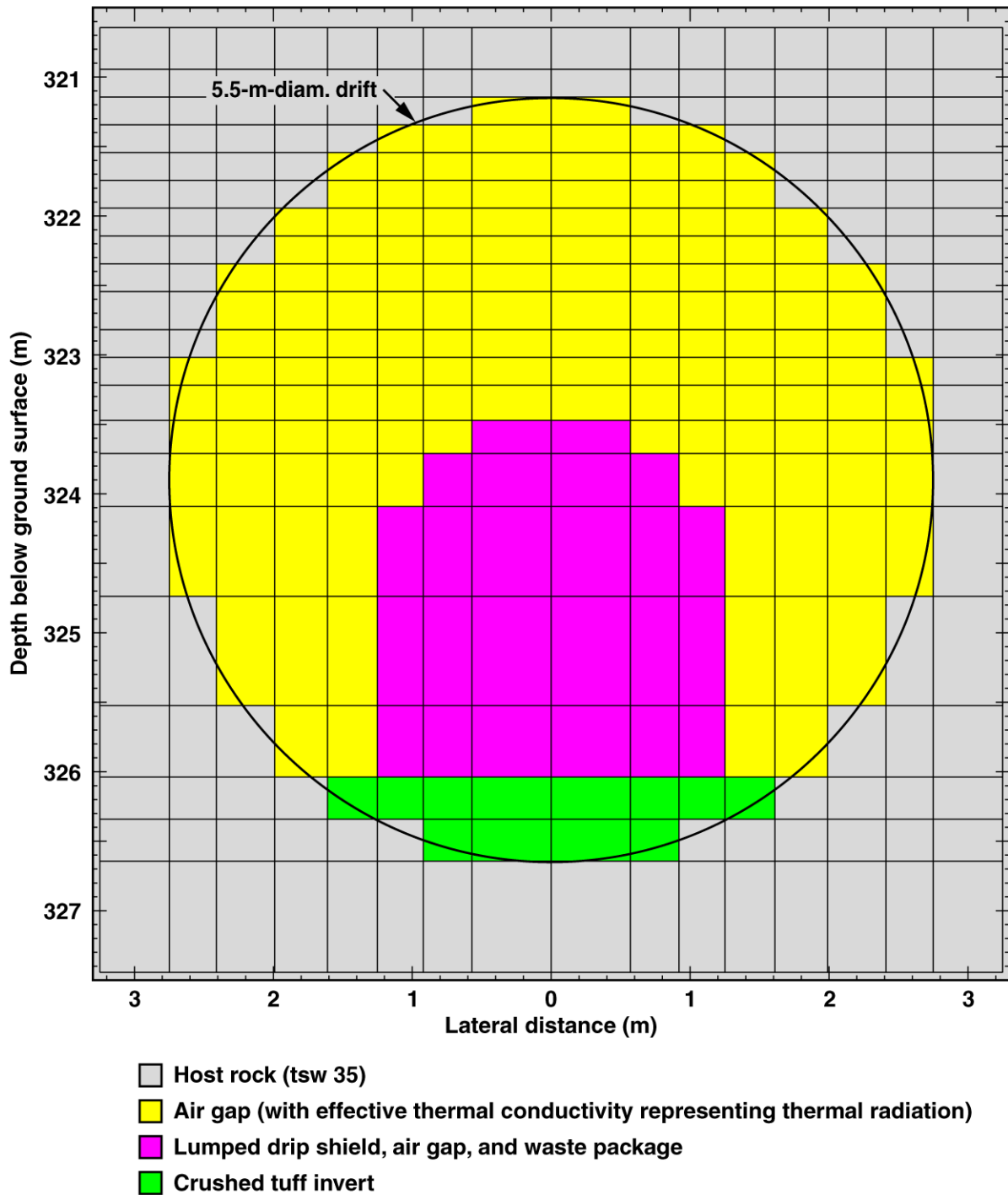


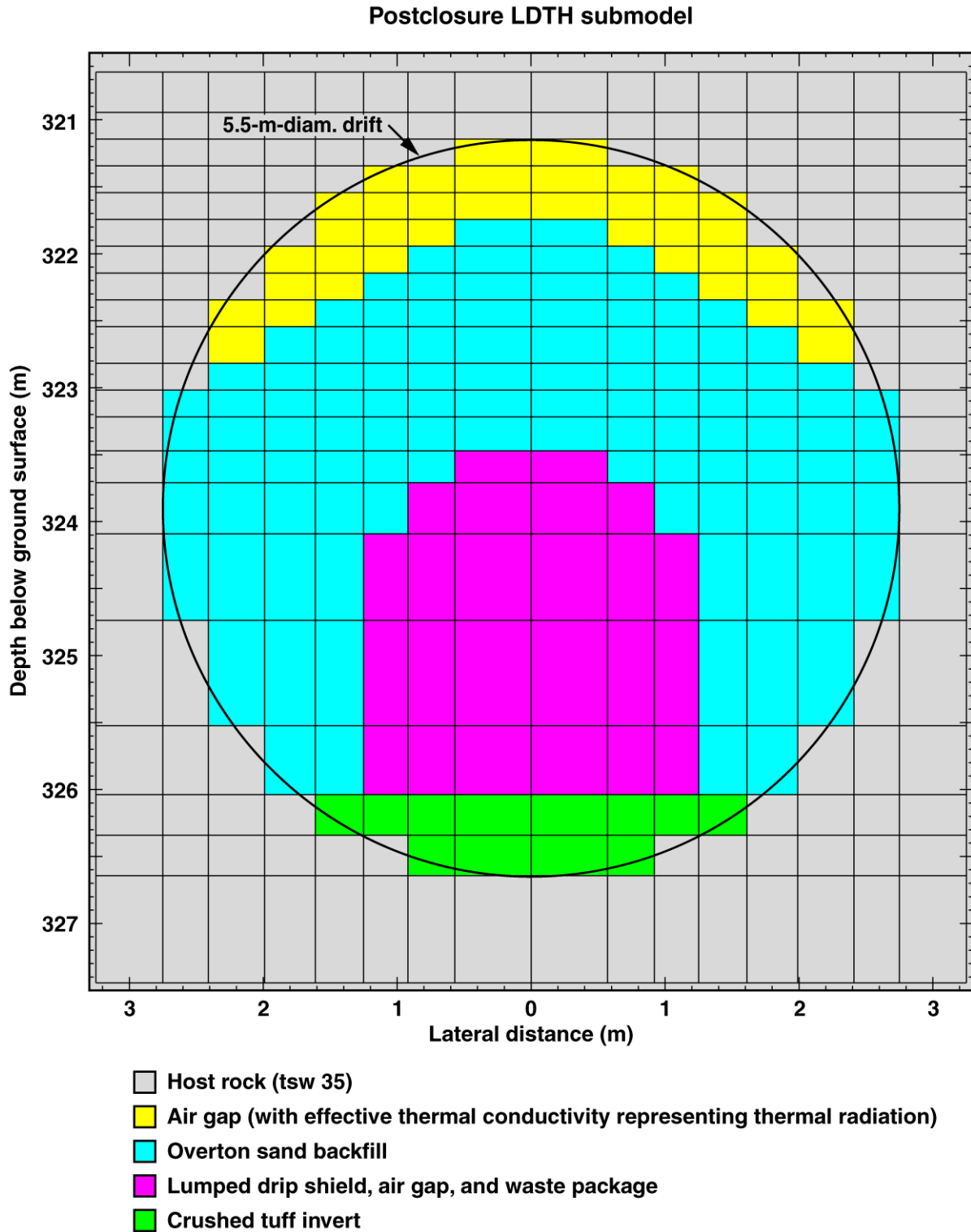
Figure 6-1. Repository-scale numerical mesh of the repository area used in the MSTHM. The NFE and EBS TH variables are calculated at each of the 623 repository subdomains in the repository plane.

Preclosure LDTH submodel



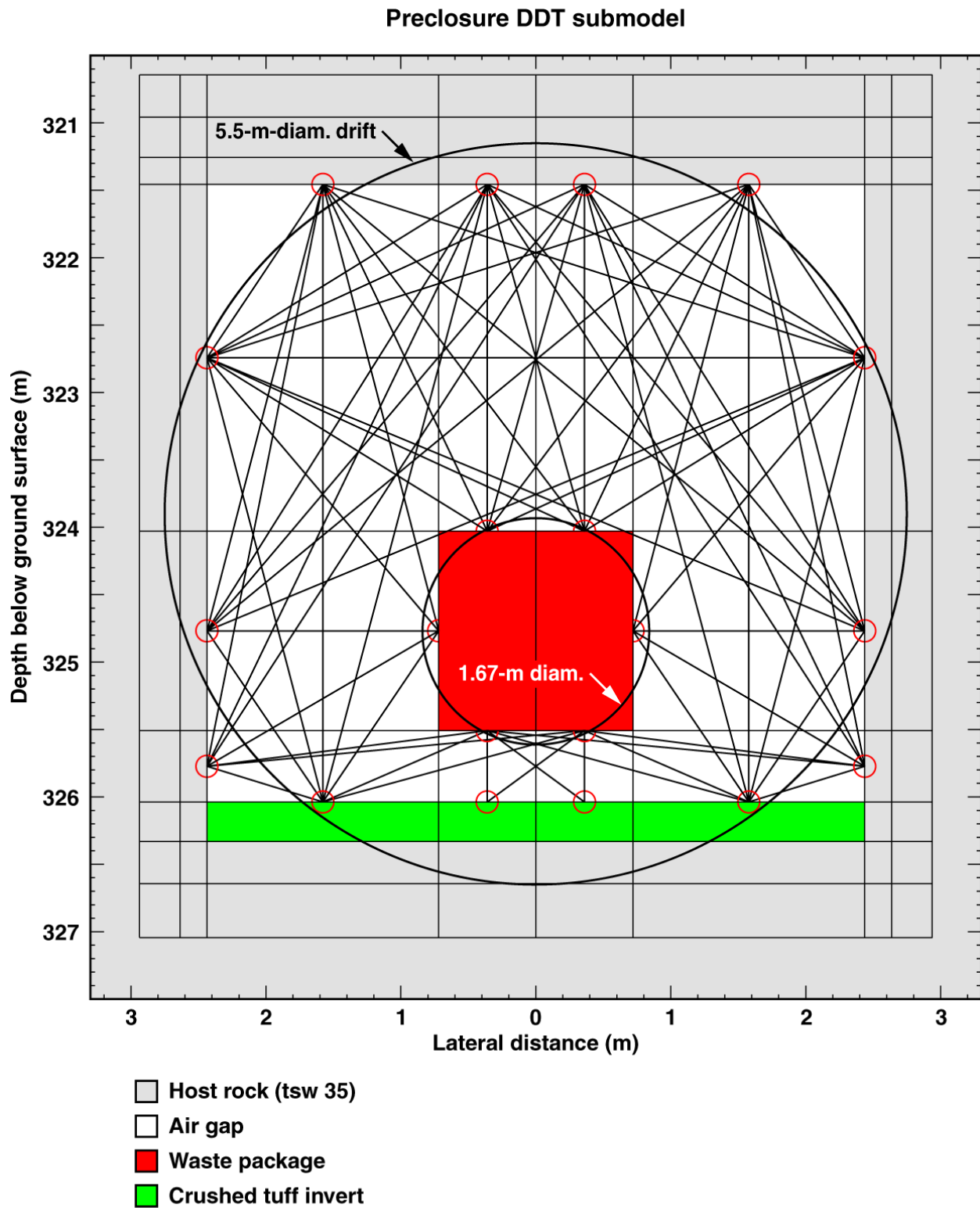
TB-LDTH-l4c3-pbf-grid

Figure 6-2. Cross-sectional view of the numerical mesh used in the pre-closure LDTH submodels.



TB-LDTH-l4c3-bf-grid

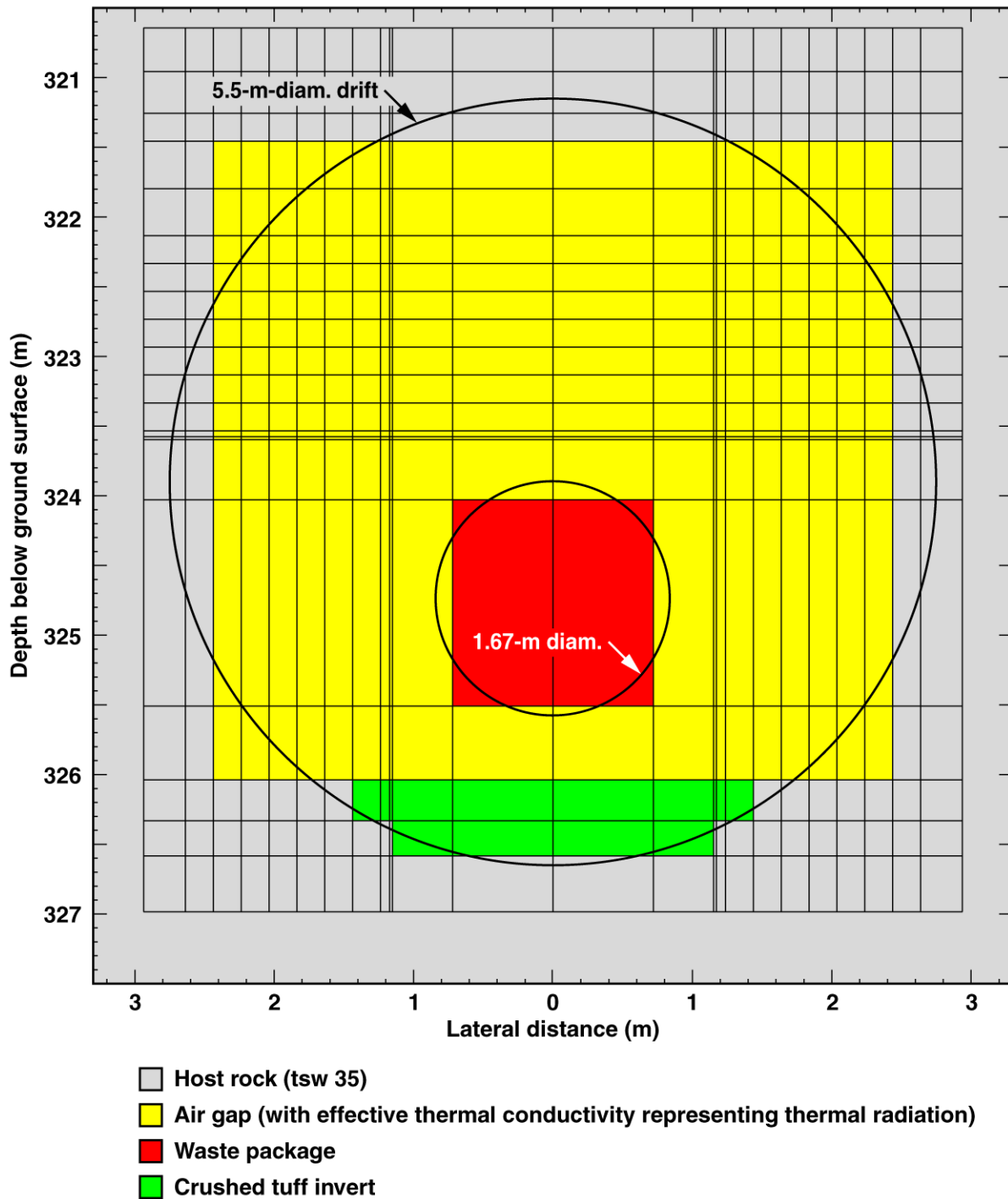
Figure 6-3. Cross-sectional view of the numerical mesh used in the post-closure LDTH submodels.



TB-DDT-I4c3-vent-grid

Figure 6-4. Cross-sectional view of the numerical mesh used in the pre-closure DDT submodel.

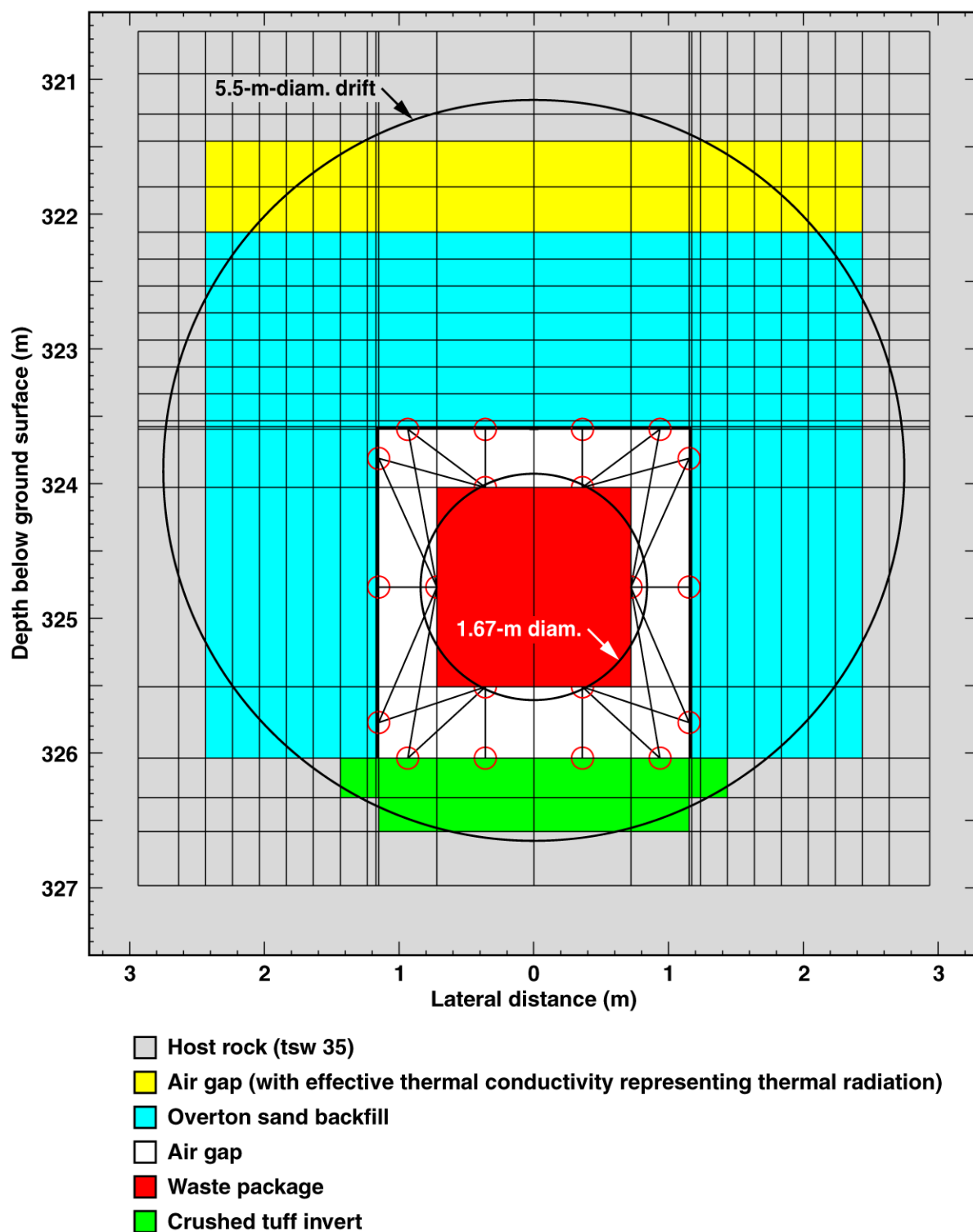
**Preclosure LDTH submodel
(for restarting postclosure DDT submodel)**



TB-LDTH/DDT-I4c3-pbf-grid

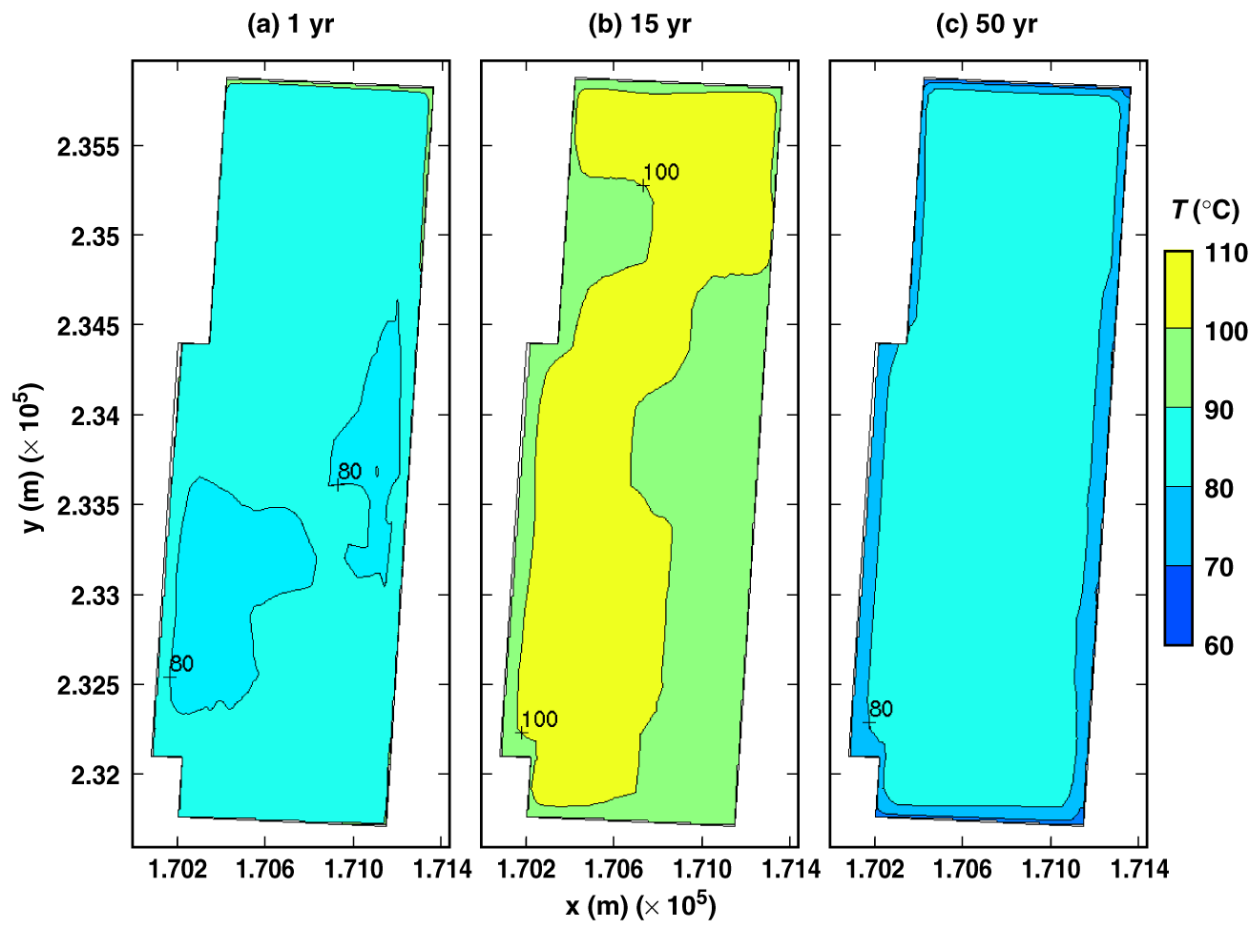
Figure 6-5. Cross-sectional view of the numerical mesh used in the pre-closure DDT submodel that is used to generate the restart file to start the post-closure DDT submodel.

Postclosure DDT submodel



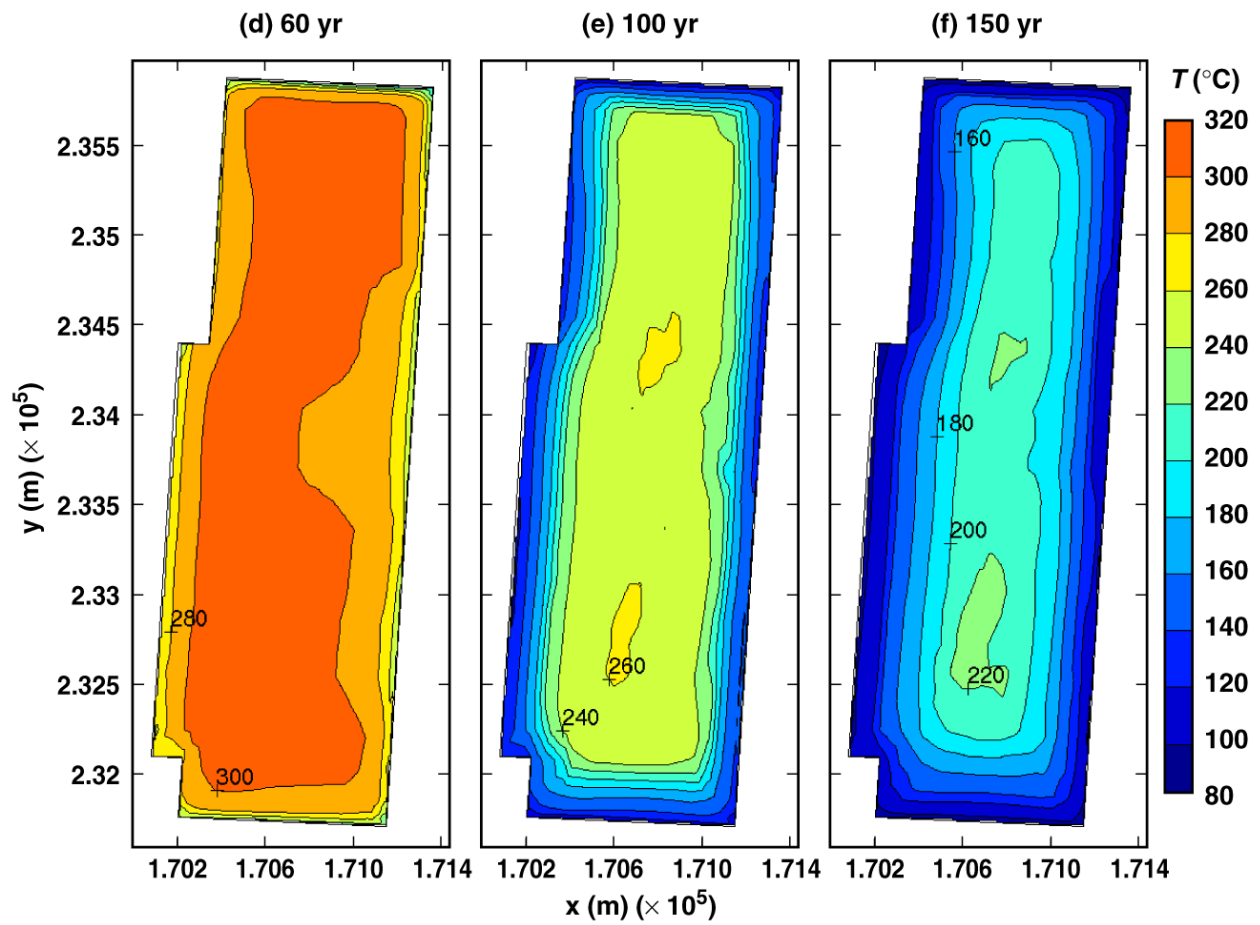
TB-DDT-l4c3-bf-grid

Figure 6-6. Cross-sectional view of the numerical mesh used in the post-closure DDT submodel.



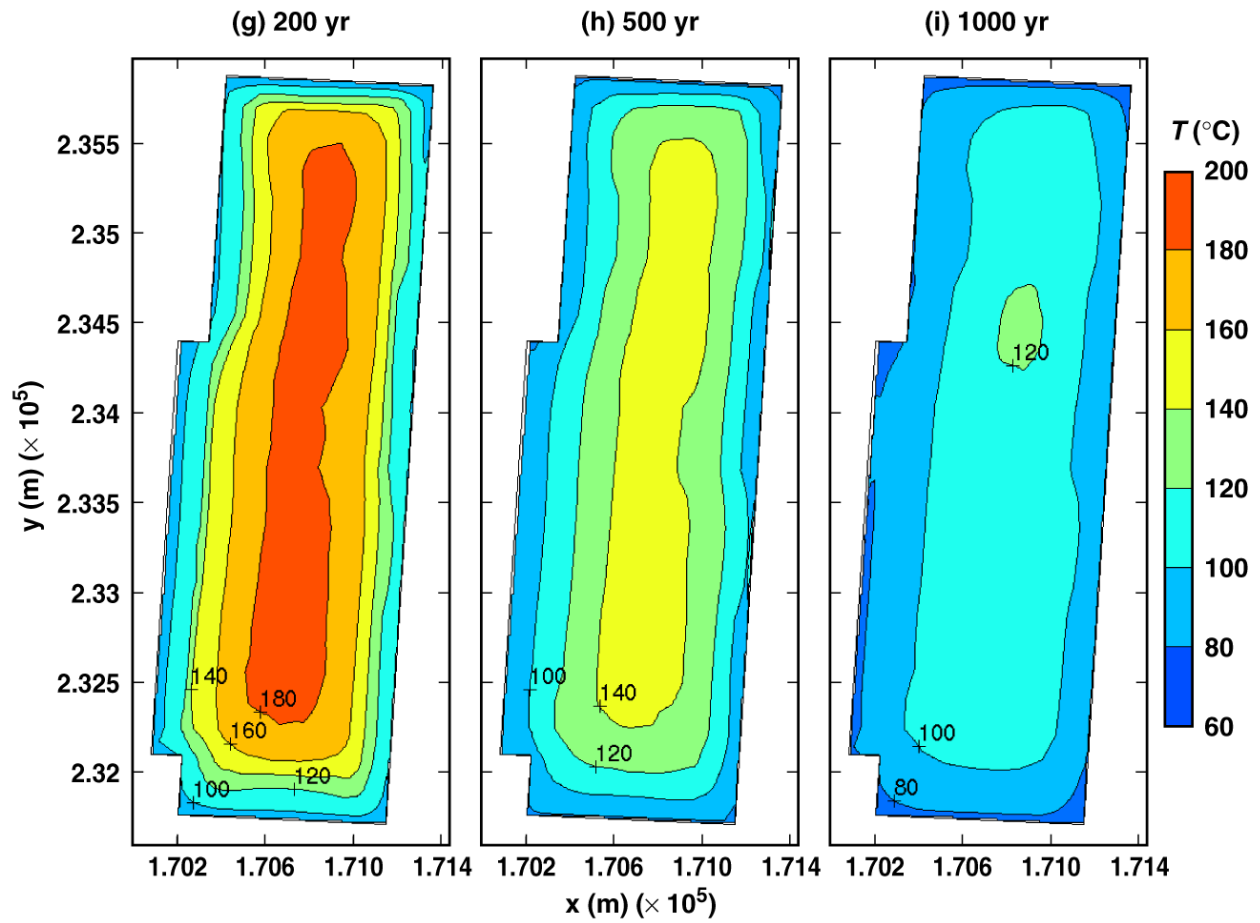
TB_AMR_mean_T_wp_pwr2_2-11

Figure 6-7. Temperature on the surface of a 21-PWR WP for the mean infiltration-flux case for the indicated times.



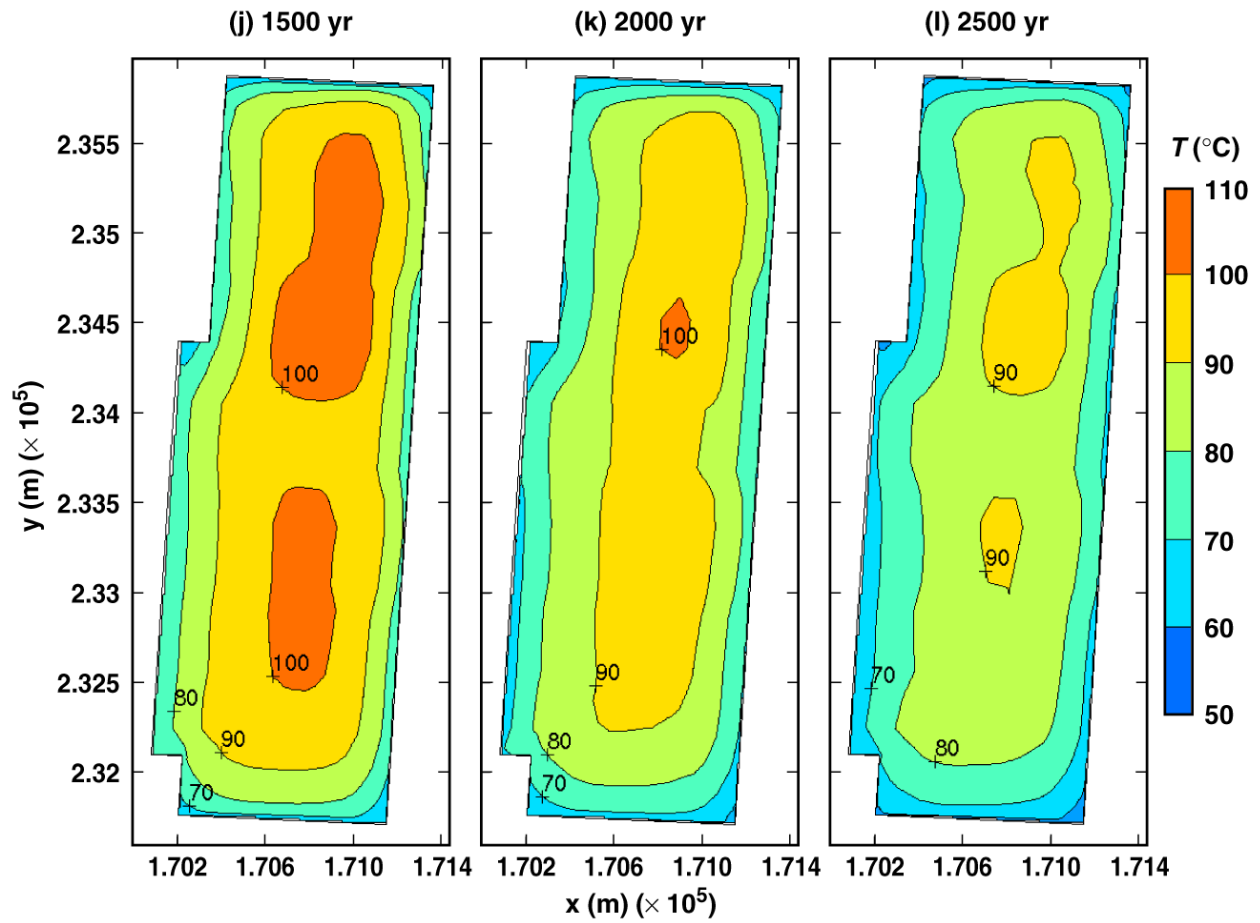
TB_AMR_mean_T_wp_pwr2_17-26

Figure 6-7. Temperature on the surface of a 21-PWR WP for the mean infiltration-flux case for the indicated times.



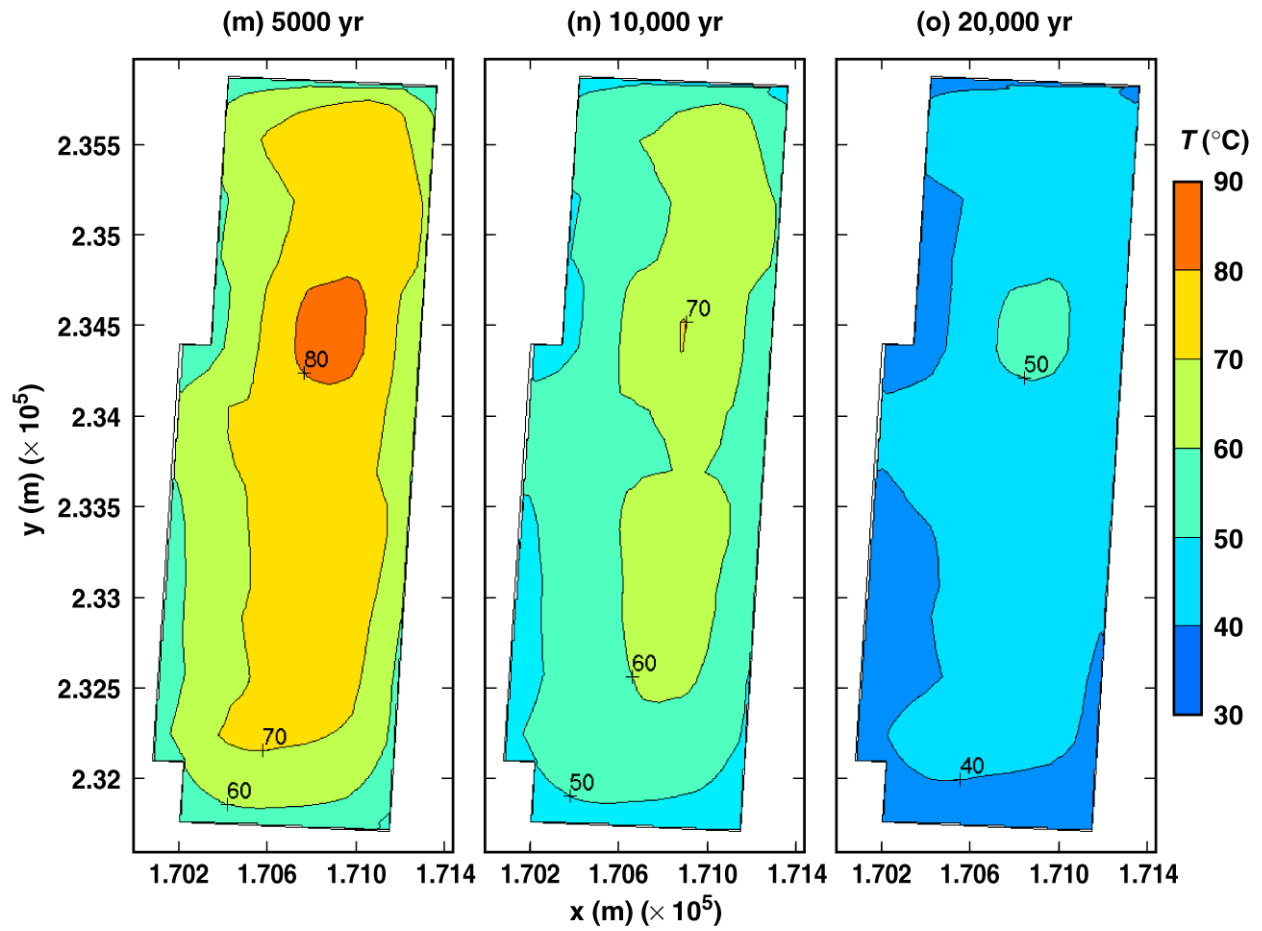
TB_AMR_mean_T_wp_pwr2_31-174

Figure 6-7. Temperature on the surface of a 21-PWR WP for the mean infiltration-flux case for the indicated times.



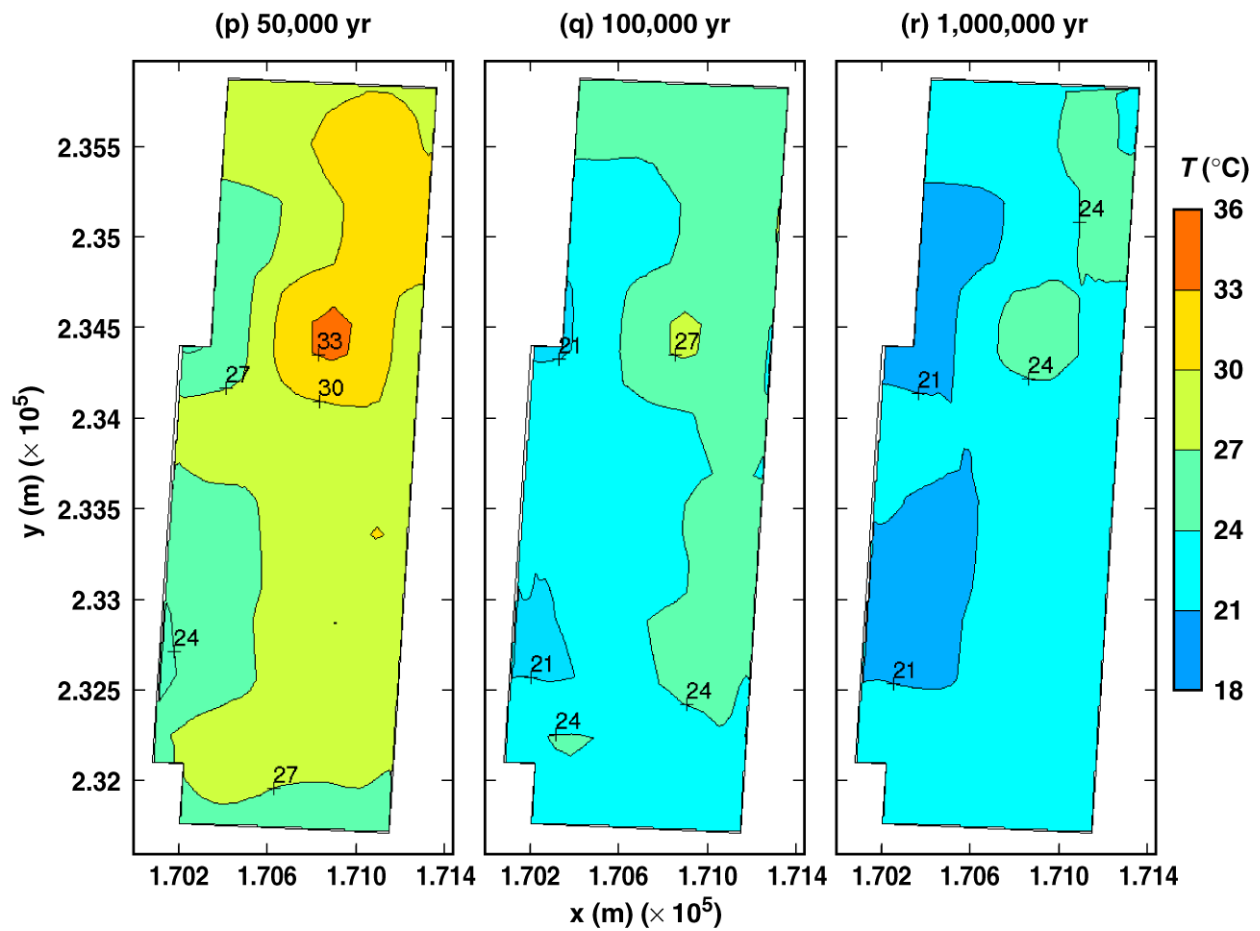
TB_AMR_mean_T_wp_pwr2_225-273

Figure 6-7. Temperature on the surface of a 21-PWR WP for the mean infiltration-flux case for the indicated times.



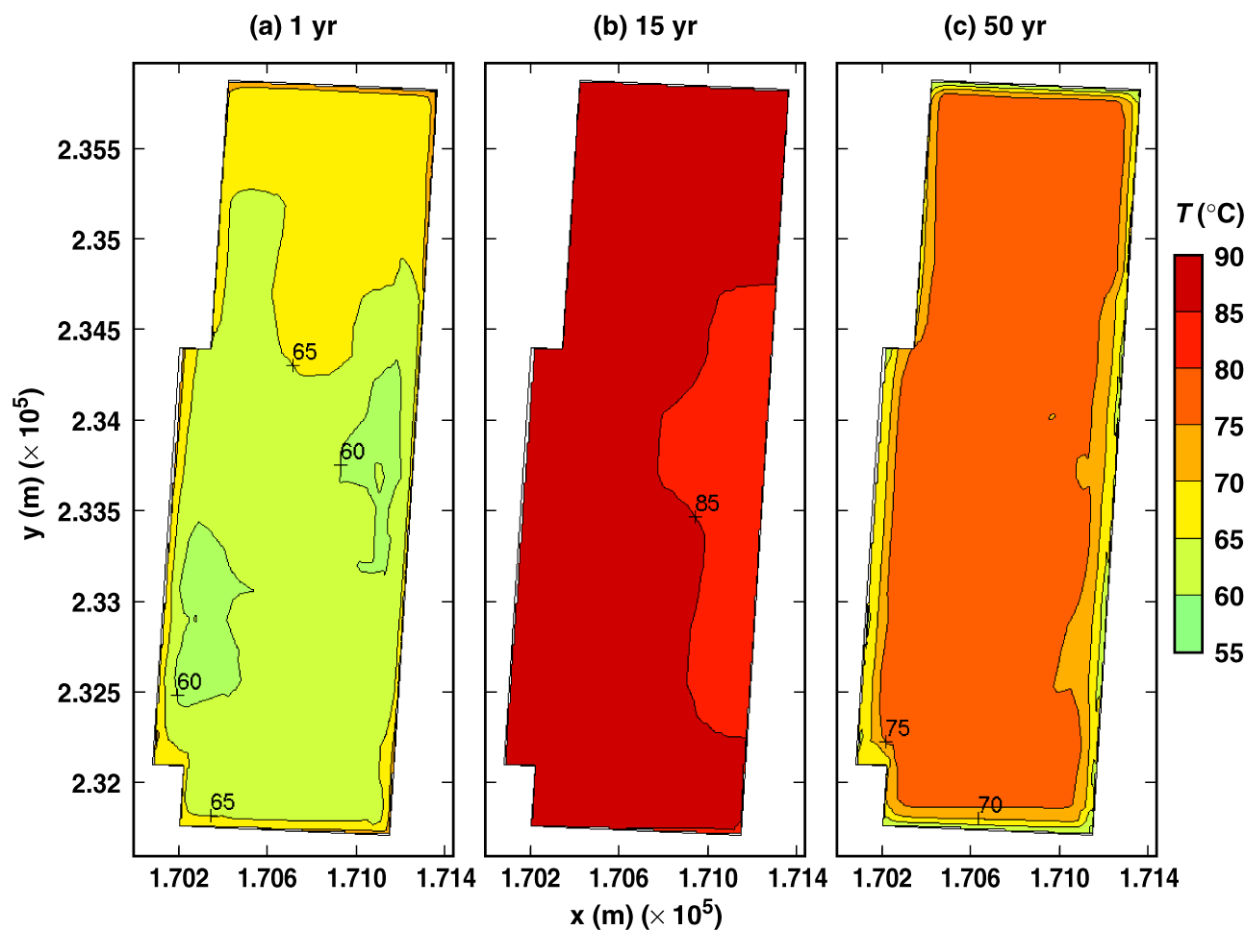
TB_AMR_mean_T_wp_pwr2_307-330

Figure 6-7. Temperature on the surface of a 21-PWR WP for the mean infiltration-flux case for the indicated times.



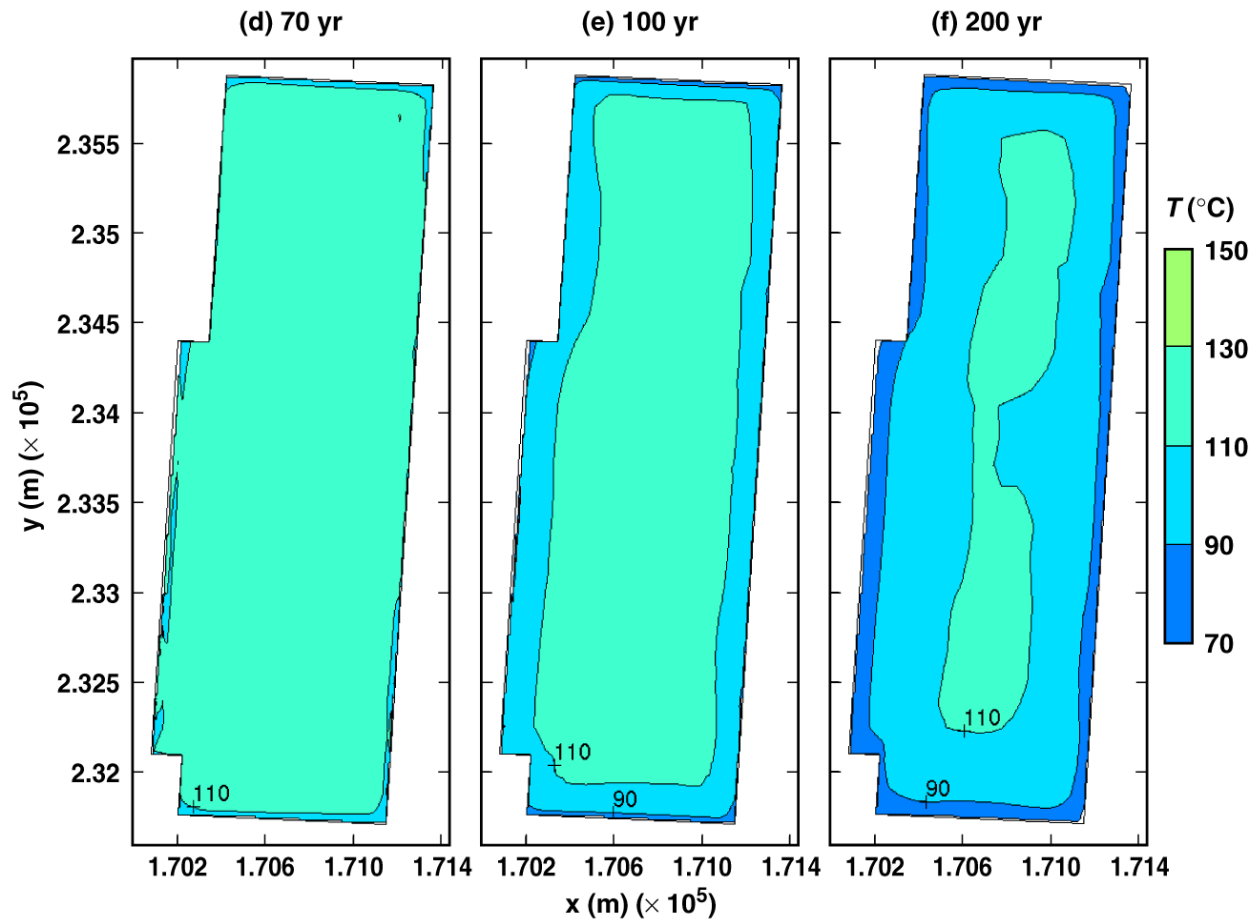
TB_AMR_mean_T_wp_pwr2_341-352

Figure 6-7. Temperature on the surface of a 21-PWR WP for the mean infiltration-flux case for the indicated times.



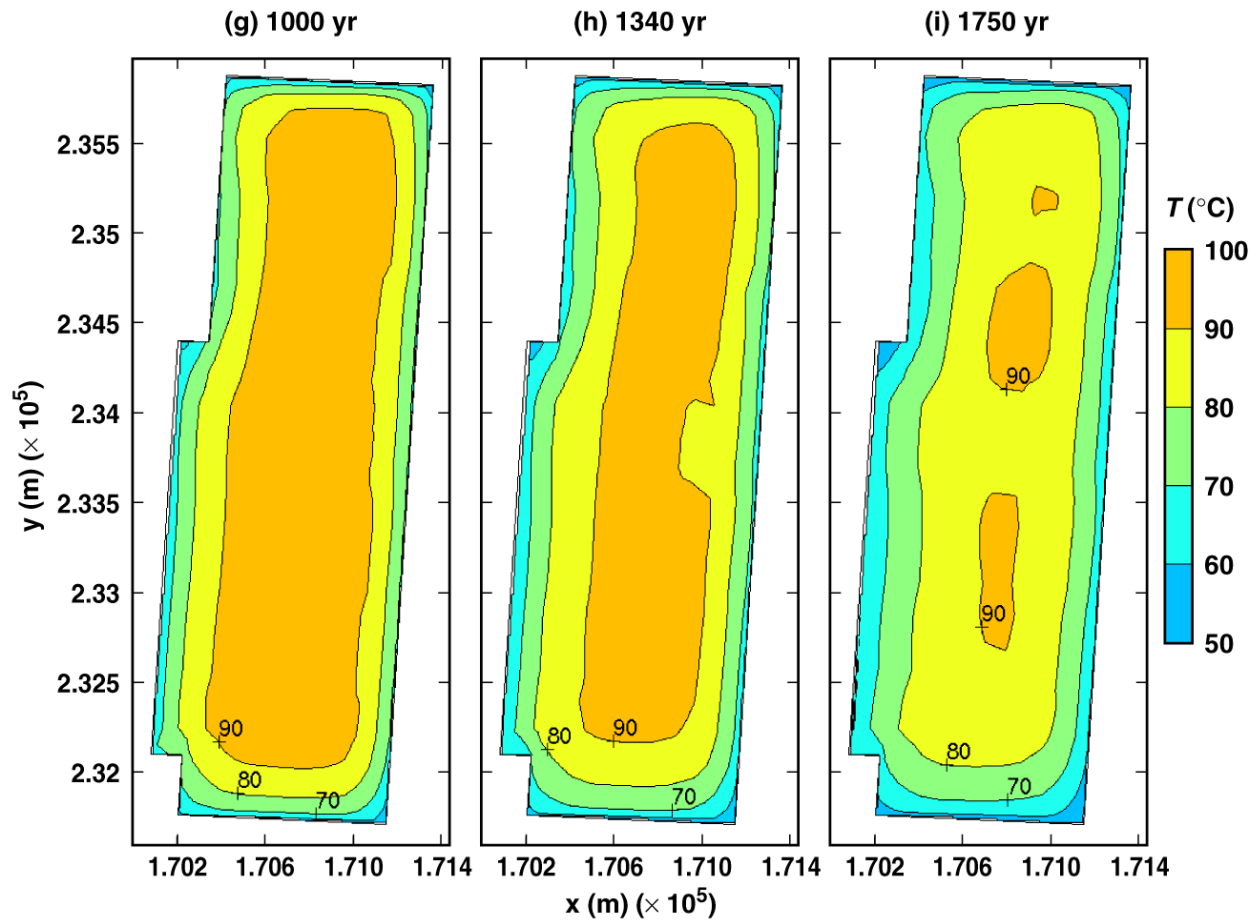
TB_AMR_mean_T_dw_upper_pwr2_2-11

Figure 6-8. Temperature on the crown of the drift (or upper drift wall) immediately above a 21-PWR WP for the mean infiltration-flux case for the indicated times.



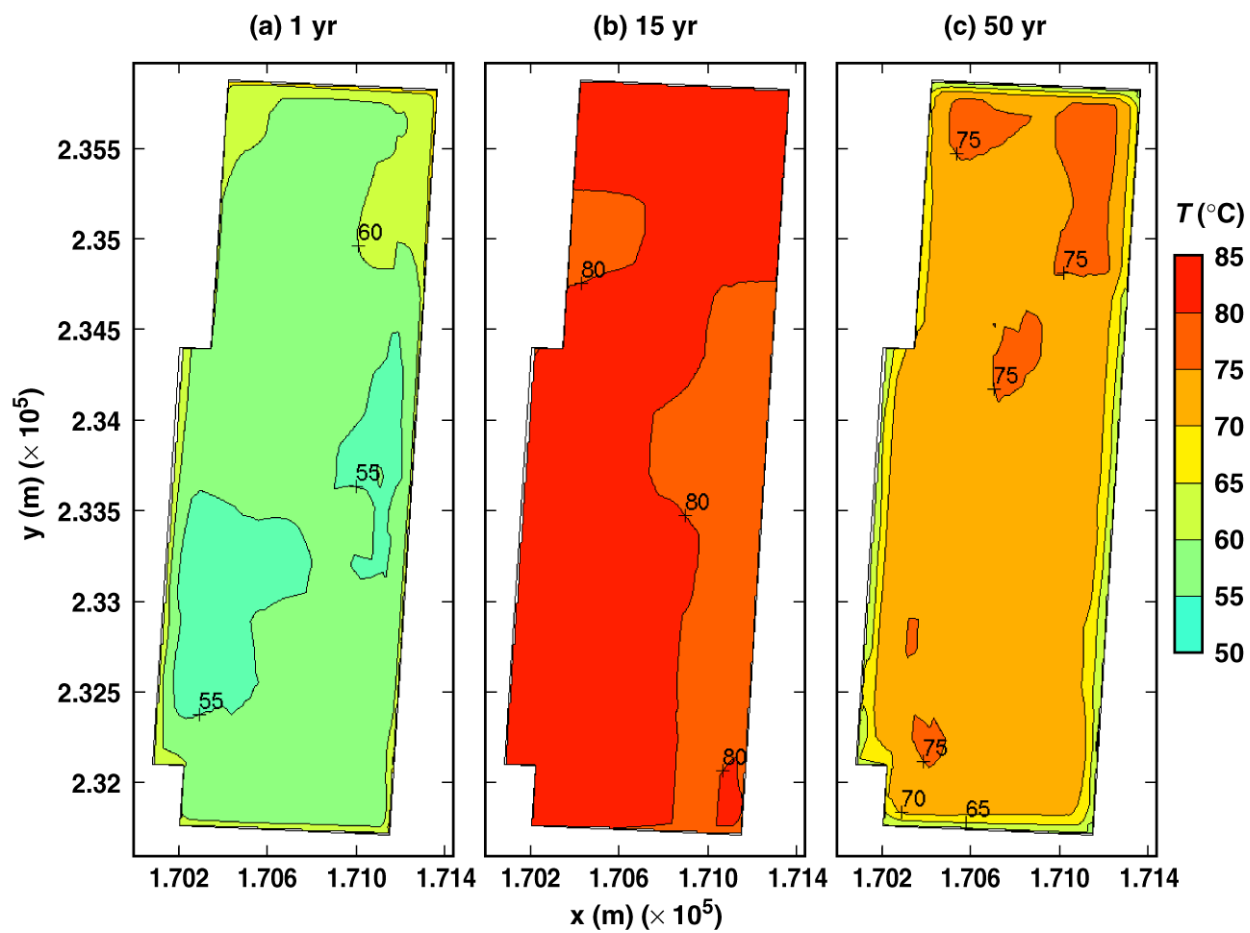
TB_AMR_mean_T_dw_upper_pwr2_19-31

Figure 6-8. Temperature on the crown of the drift (or upper drift wall) immediately above a 21-PWR WP for the mean infiltration-flux case for the indicated times.



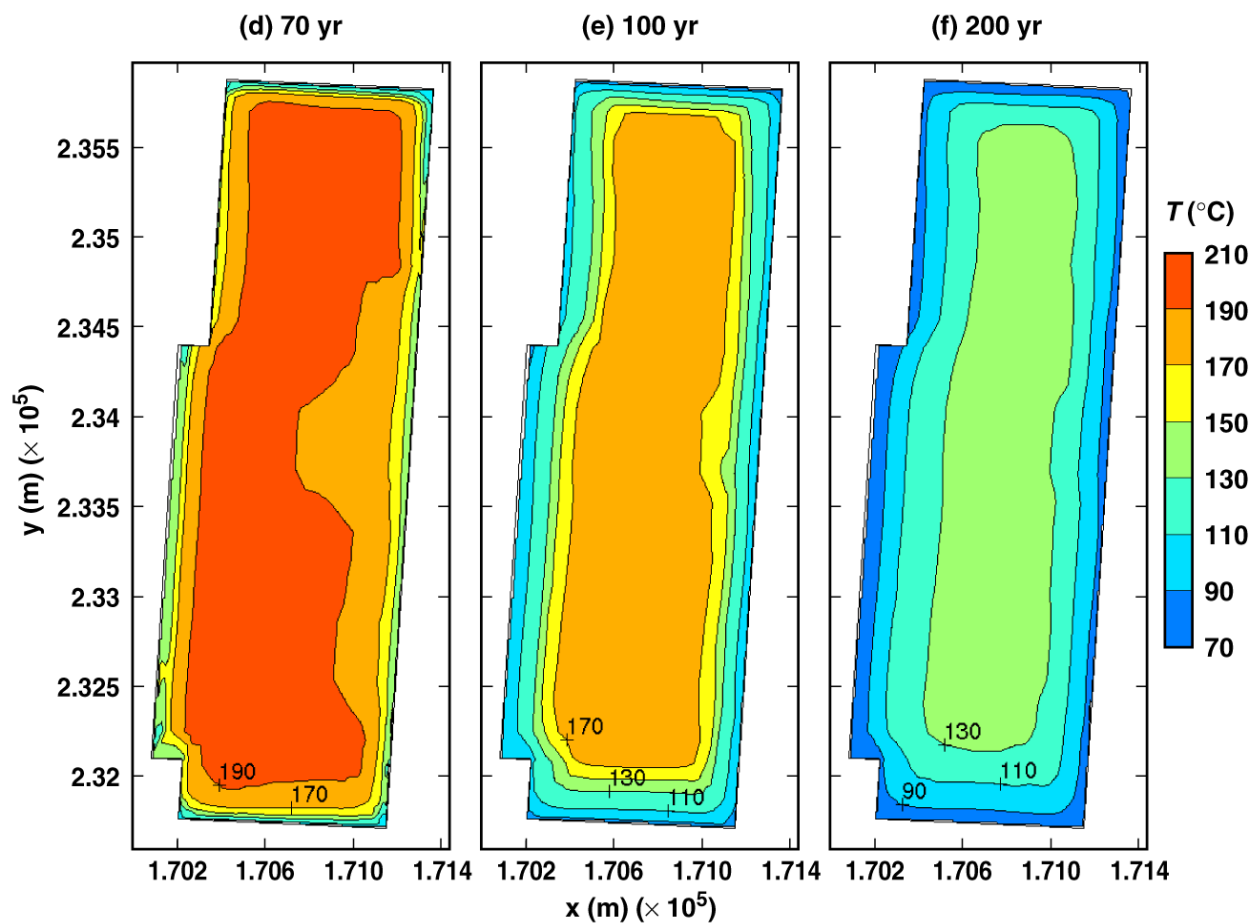
TB_AMR_mean_T_dw_upper_pwr2_174-240

Figure 6-8. Temperature on the crown of the drift (or upper drift wall) immediately above a 21-PWR WP for the mean infiltration-flux case for the indicated times.



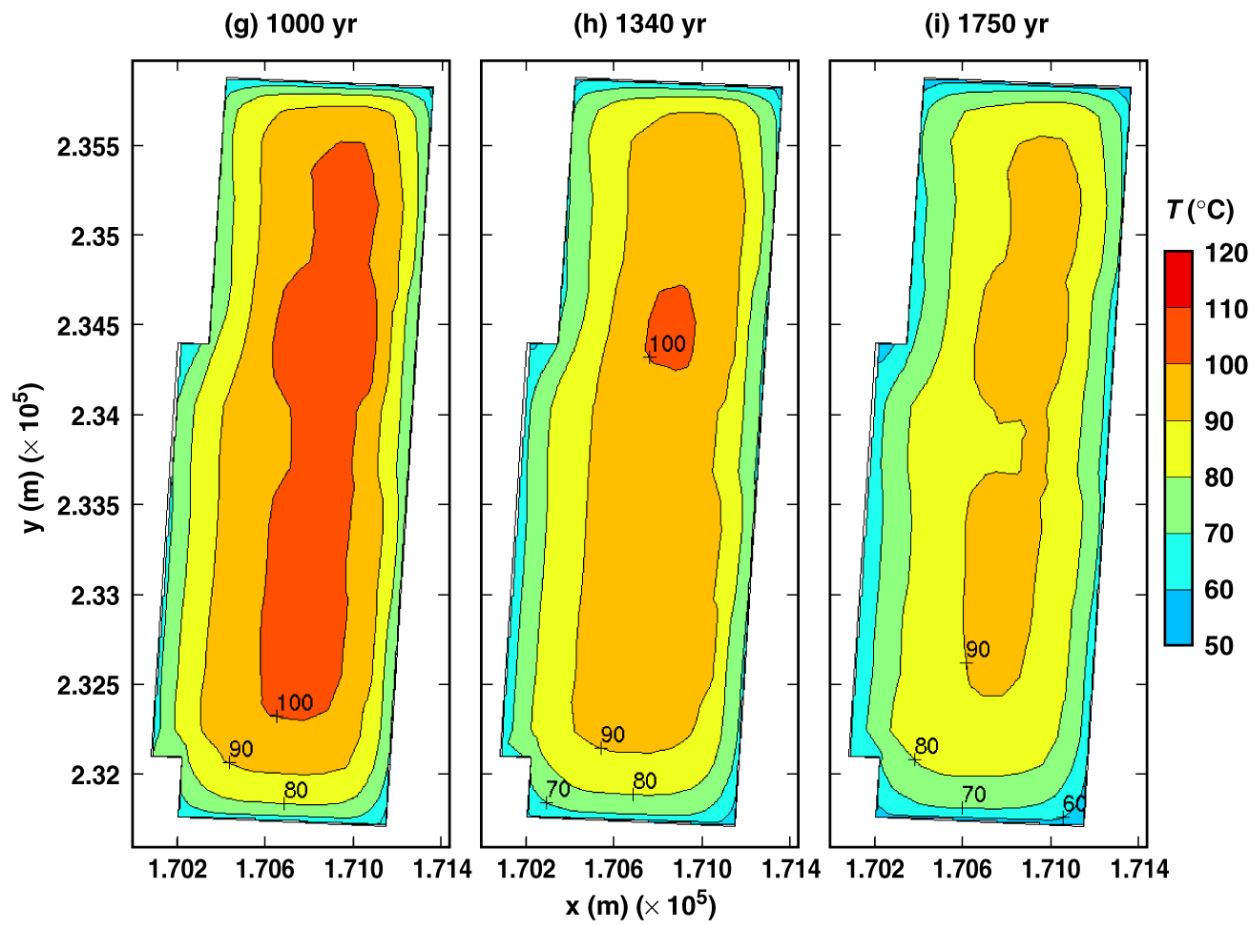
TB_AMR_mean_T_dw_lower_pwr2_2-11

Figure 6-9. Temperature on the lower drift wall immediately below a 21-PWR WP for the mean infiltration-flux case for the indicated times.



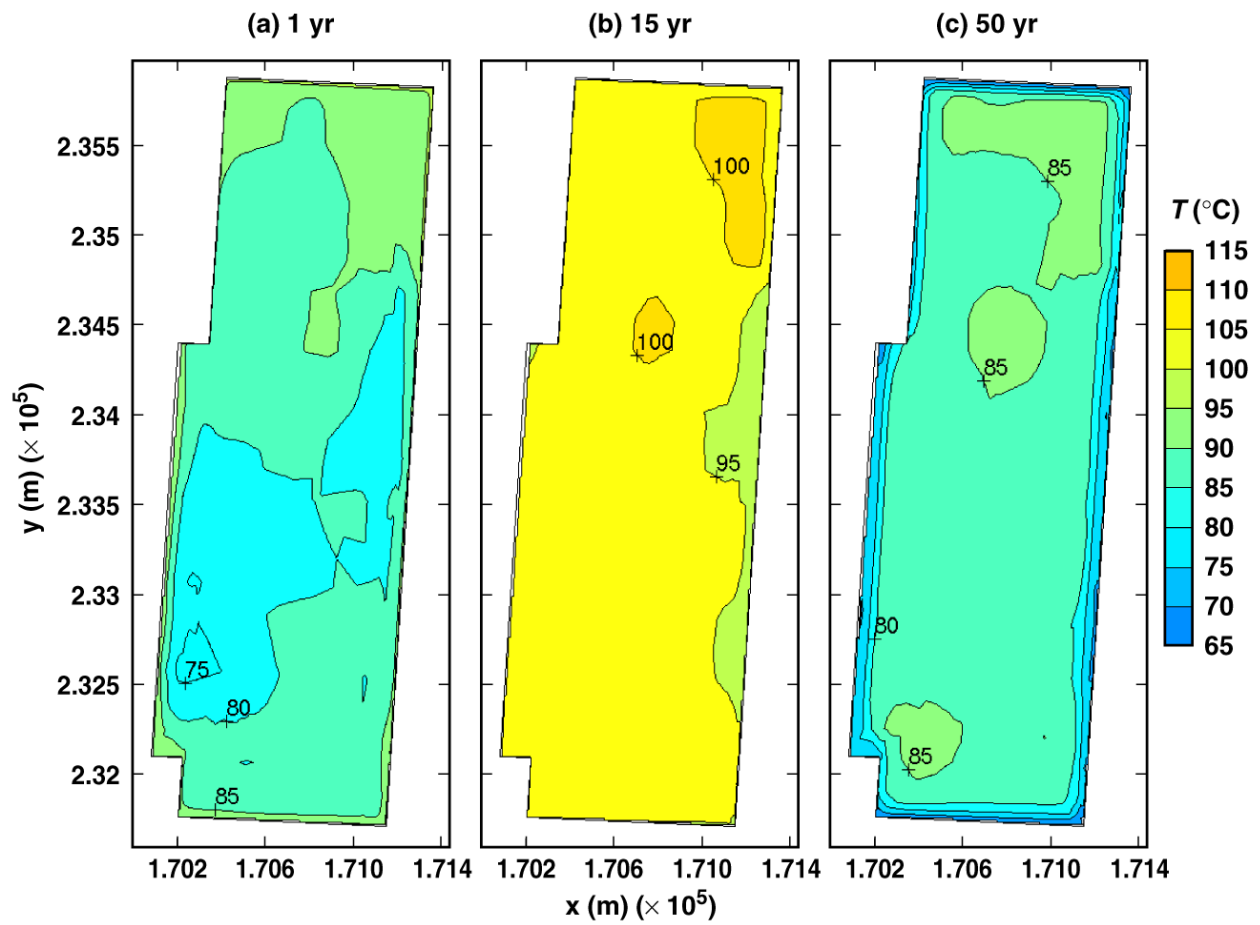
TB_AMR_mean_T_dw_lower_pwr2_19-31

Figure 6-9. Temperature on the lower drift wall immediately below a 21-PWR WP for the mean infiltration-flux case for the indicated times.



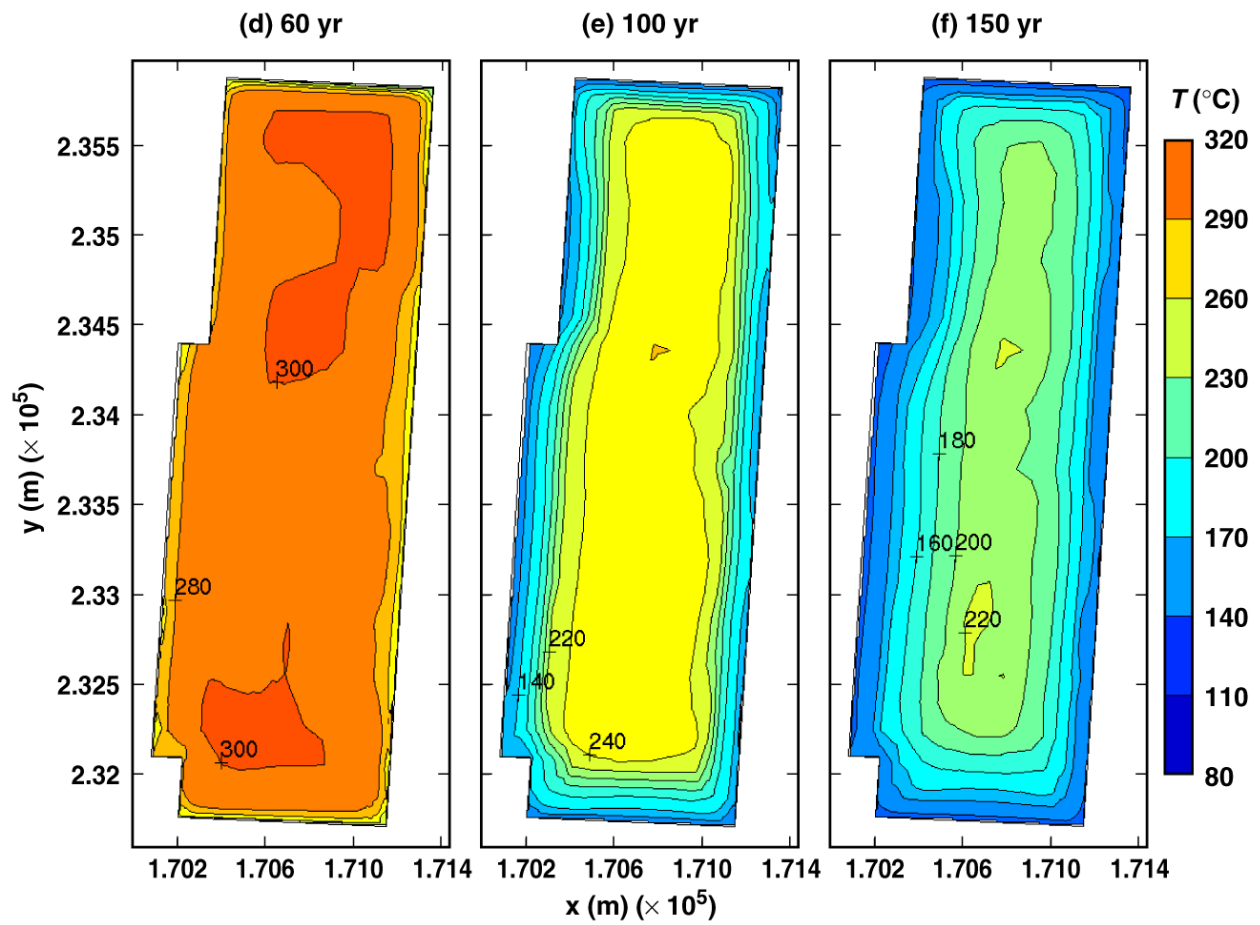
TB_AMR_mean_T_dw_lower_pwr2_174-240

Figure 6-9. Temperature on the lower drift wall immediately below a 21-PWR WP for the mean infiltration-flux case for the indicated times.



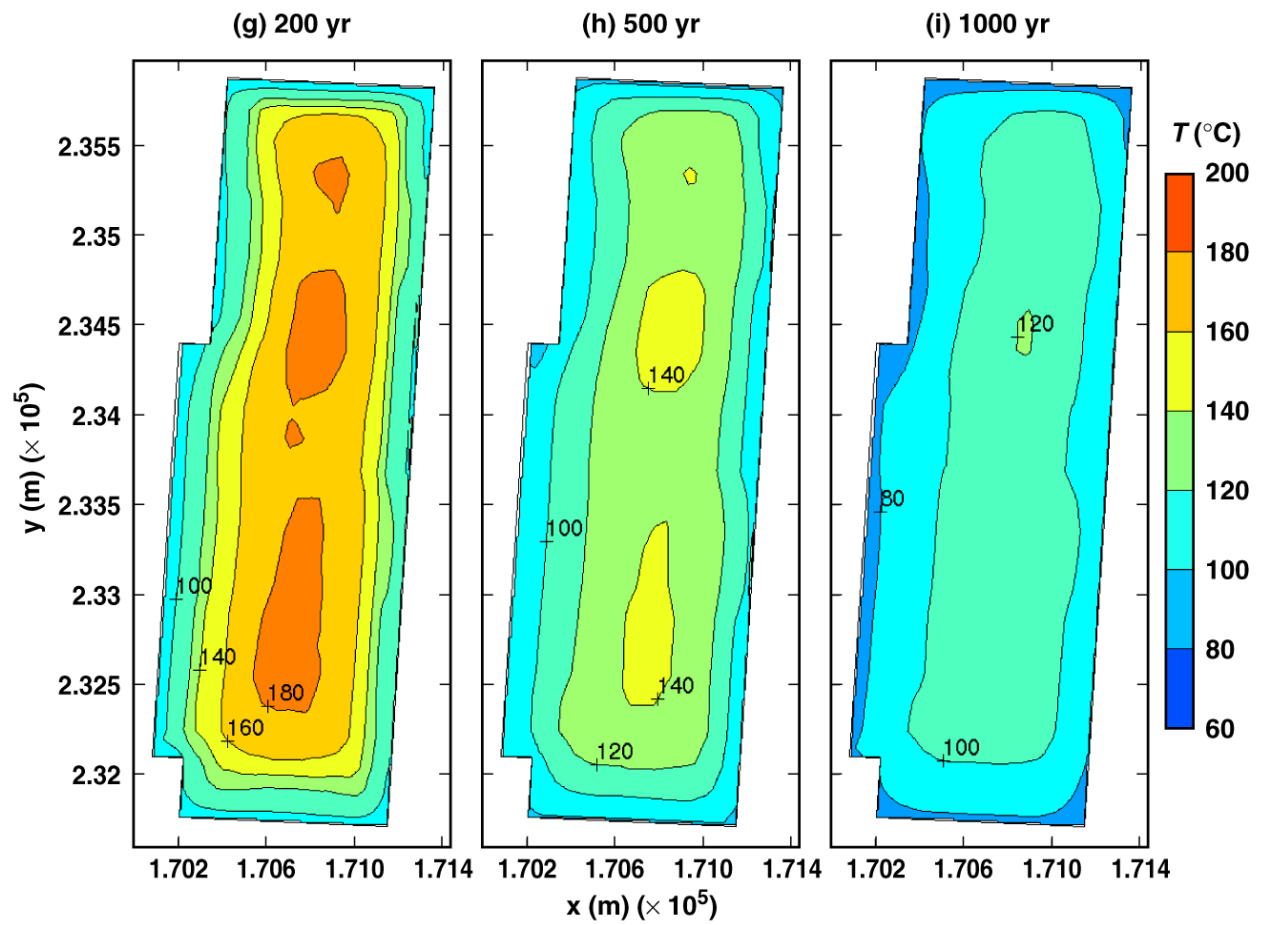
TB_AMR_upper_T_wp_pwr2_2-11

Figure 6-10. Temperature on the surface of a 21-PWR WP for the high infiltration-flux case for the indicated times.



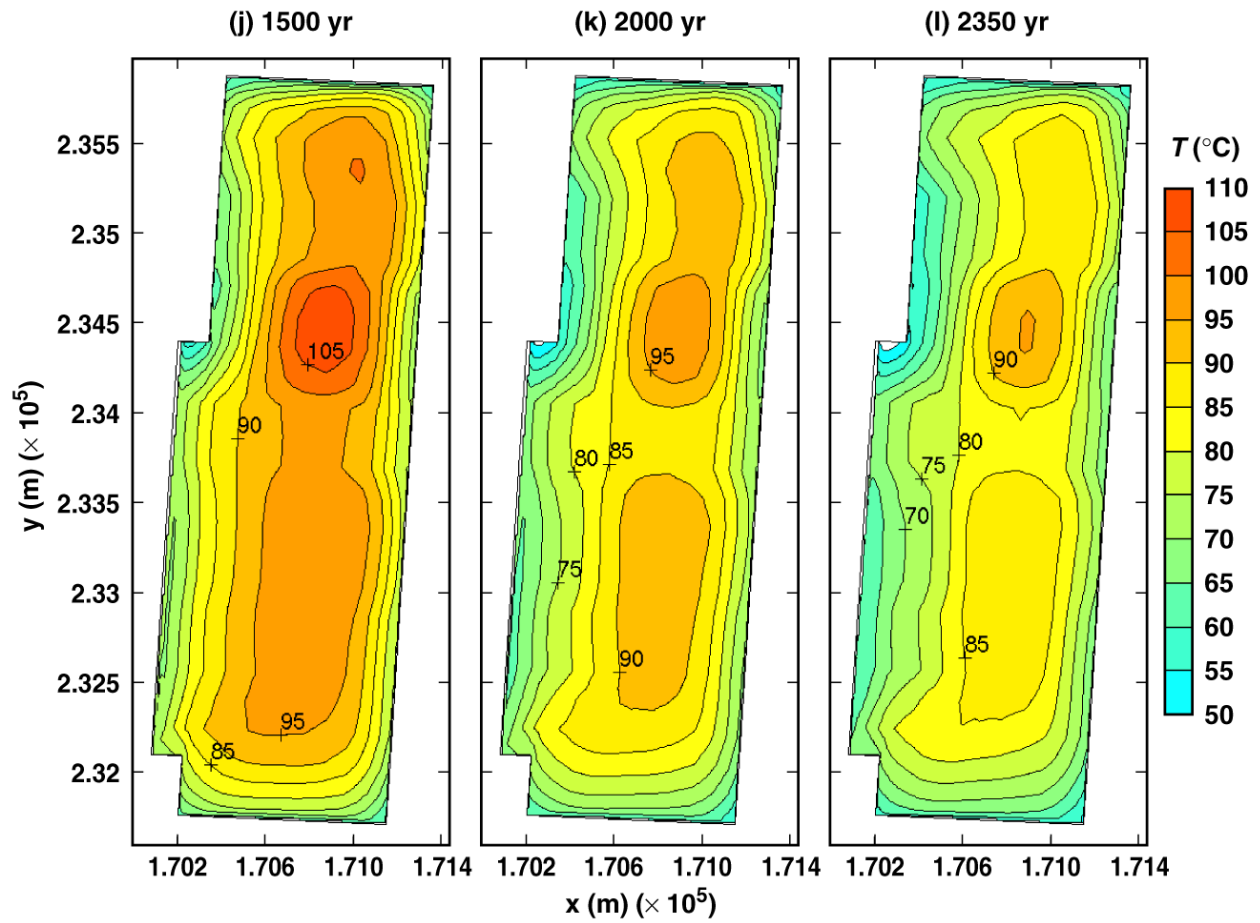
TB_AMR_upper_T_wp_pwr2_17-22

Figure 6-10. Temperature on the surface of a 21-PWR WP for the high infiltration-flux case for the indicated times.



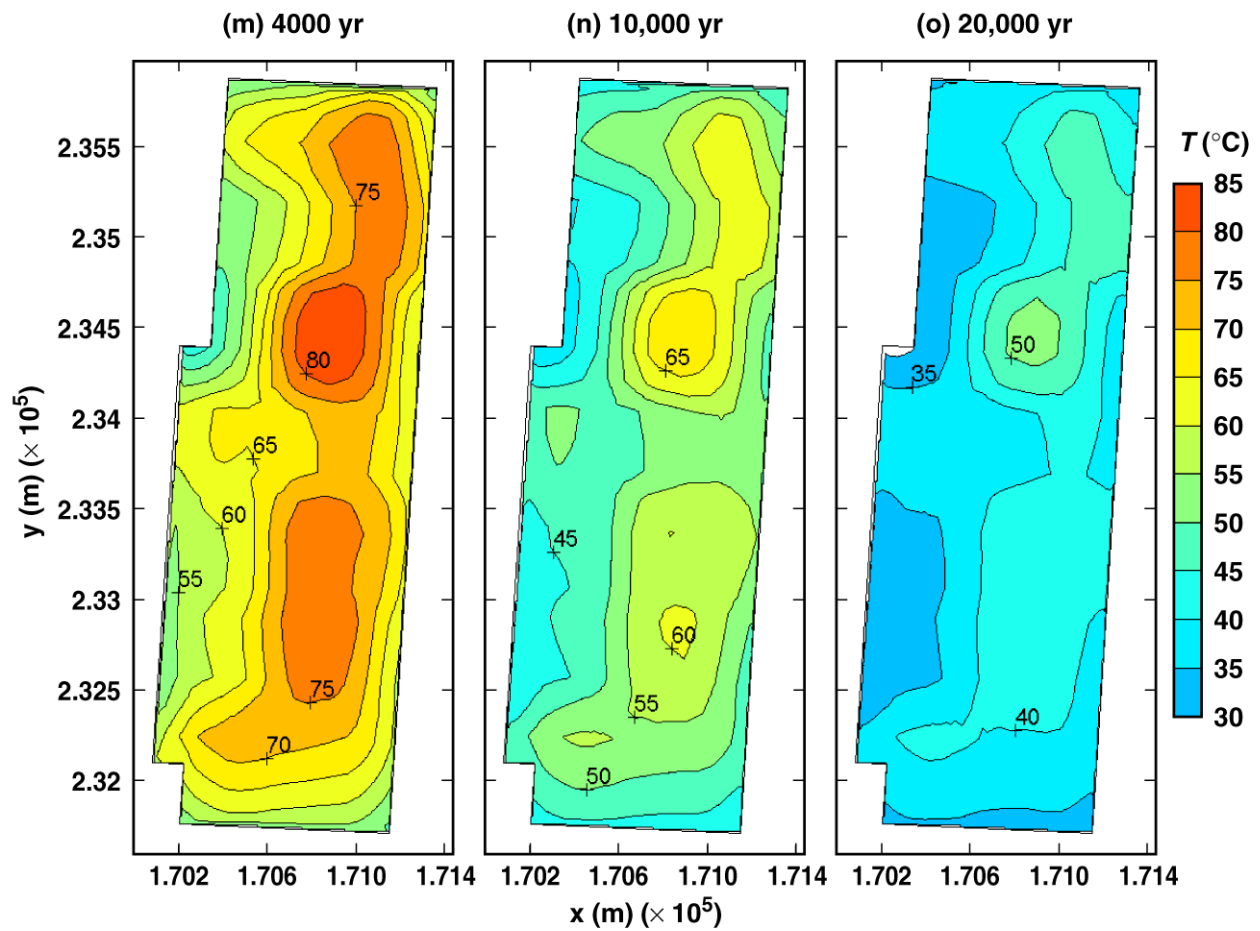
TB_AMR_upper_T_wp_pwr2_56-269

Figure 6-10. Temperature on the surface of a 21-PWR WP for the high infiltration-flux case for the indicated times.



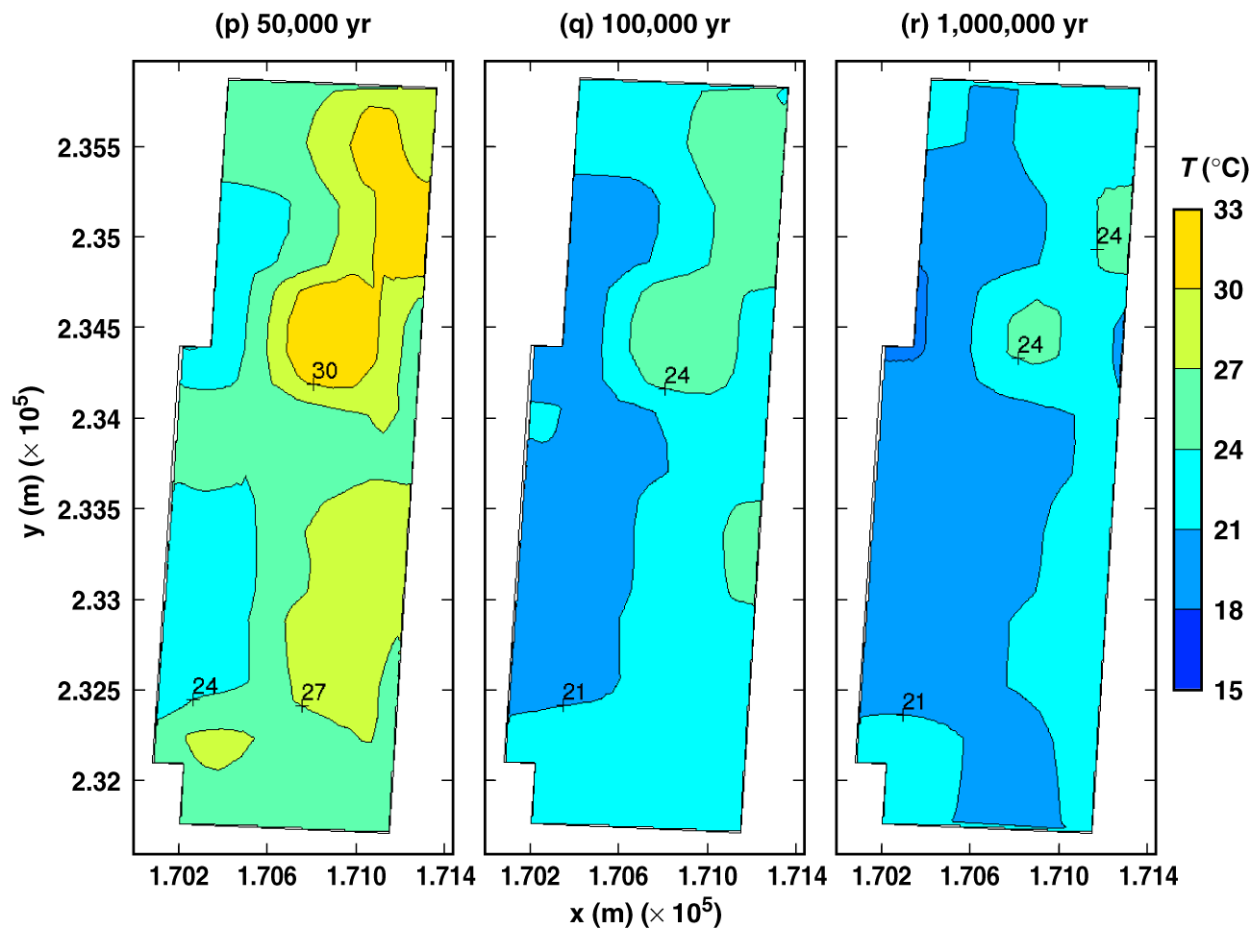
TB_AMR_upper_T_wp_pwr2_319-376

Figure 6-10. Temperature on the surface of a 21-PWR WP for the high infiltration-flux case for the indicated times.



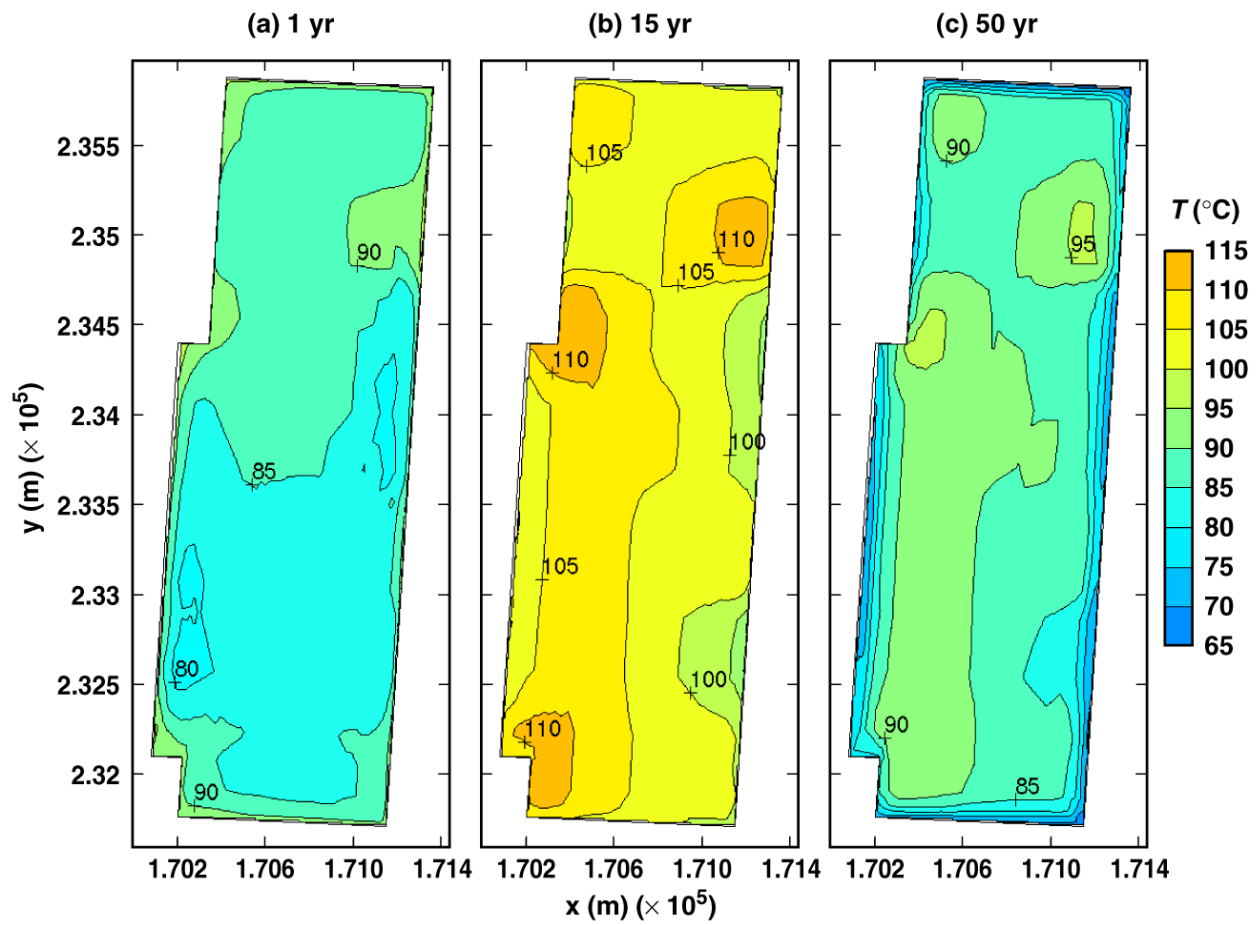
TB_AMR_upper_T_wp_pwr2_403-434

Figure 6-10. Temperature on the surface of a 21-PWR WP for the high infiltration-flux case for the indicated times.



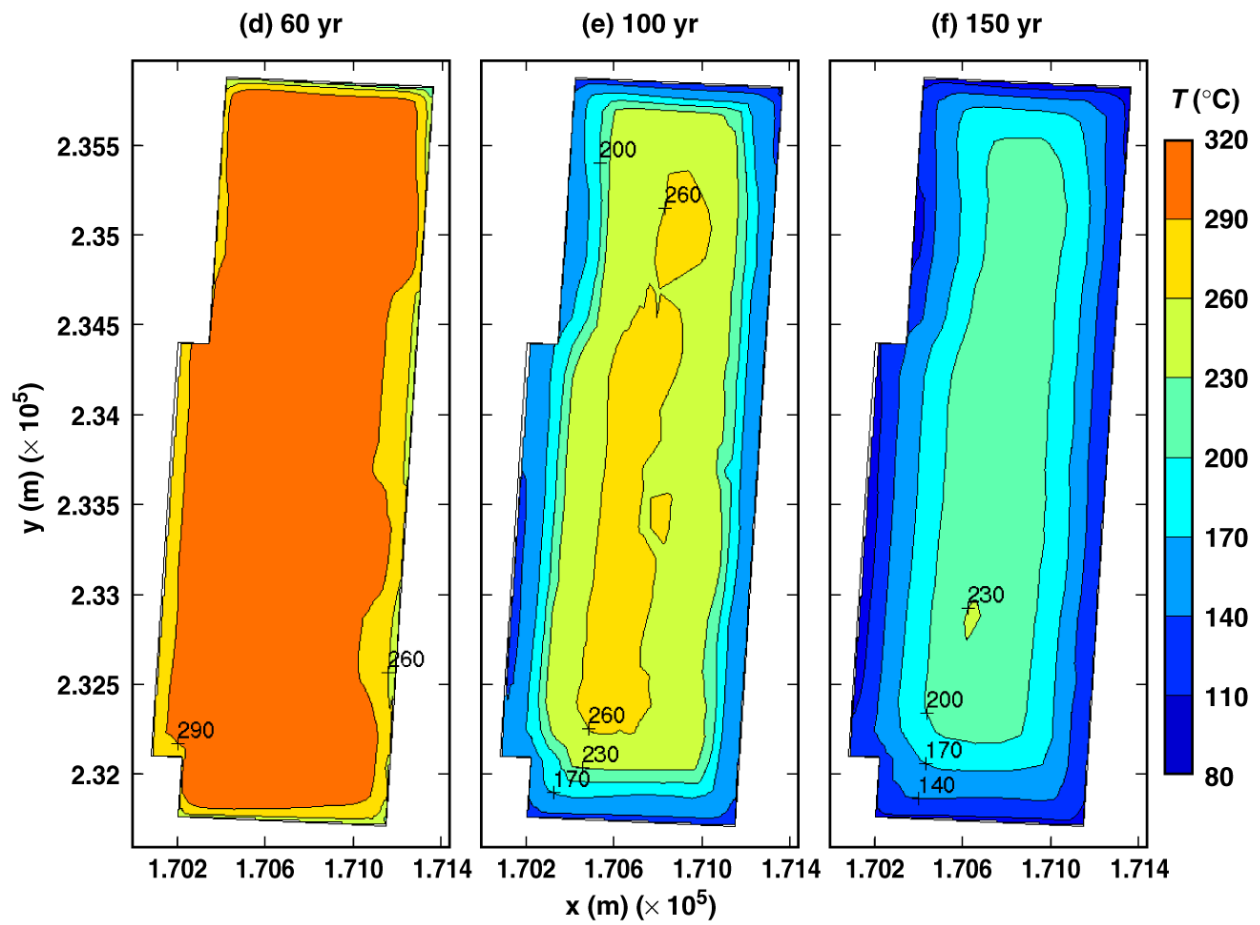
TB_AMR_upper_T_wp_pwr2_446-457

Figure 6-10. Temperature on the surface of a 21-PWR WP for the high infiltration-flux case for the indicated times.



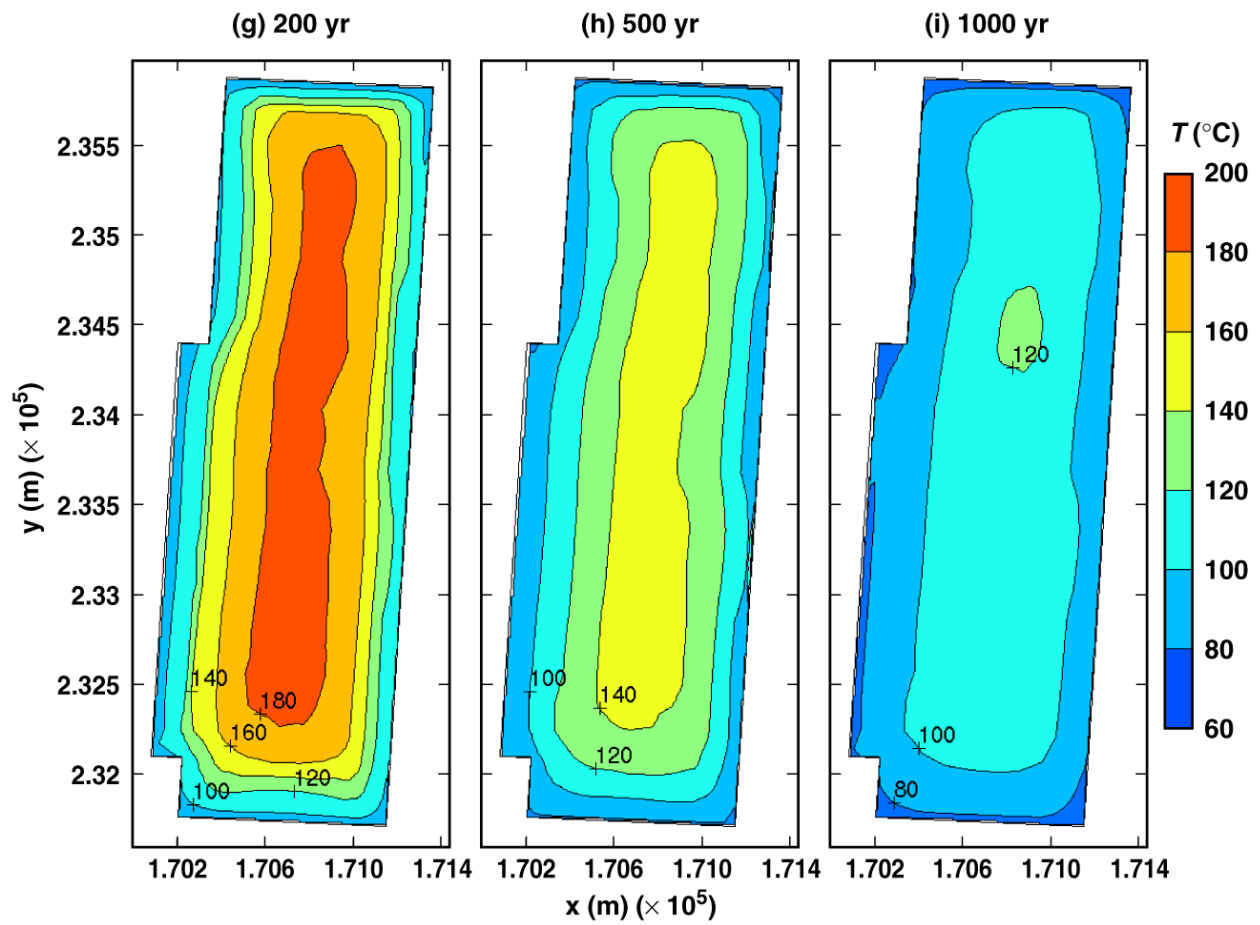
TB_AMR_lower_T_wp_pwr2_2-11

Figure 6-11. Temperature on the surface of a 21-PWR WP for the low infiltration-flux case for the indicated times.



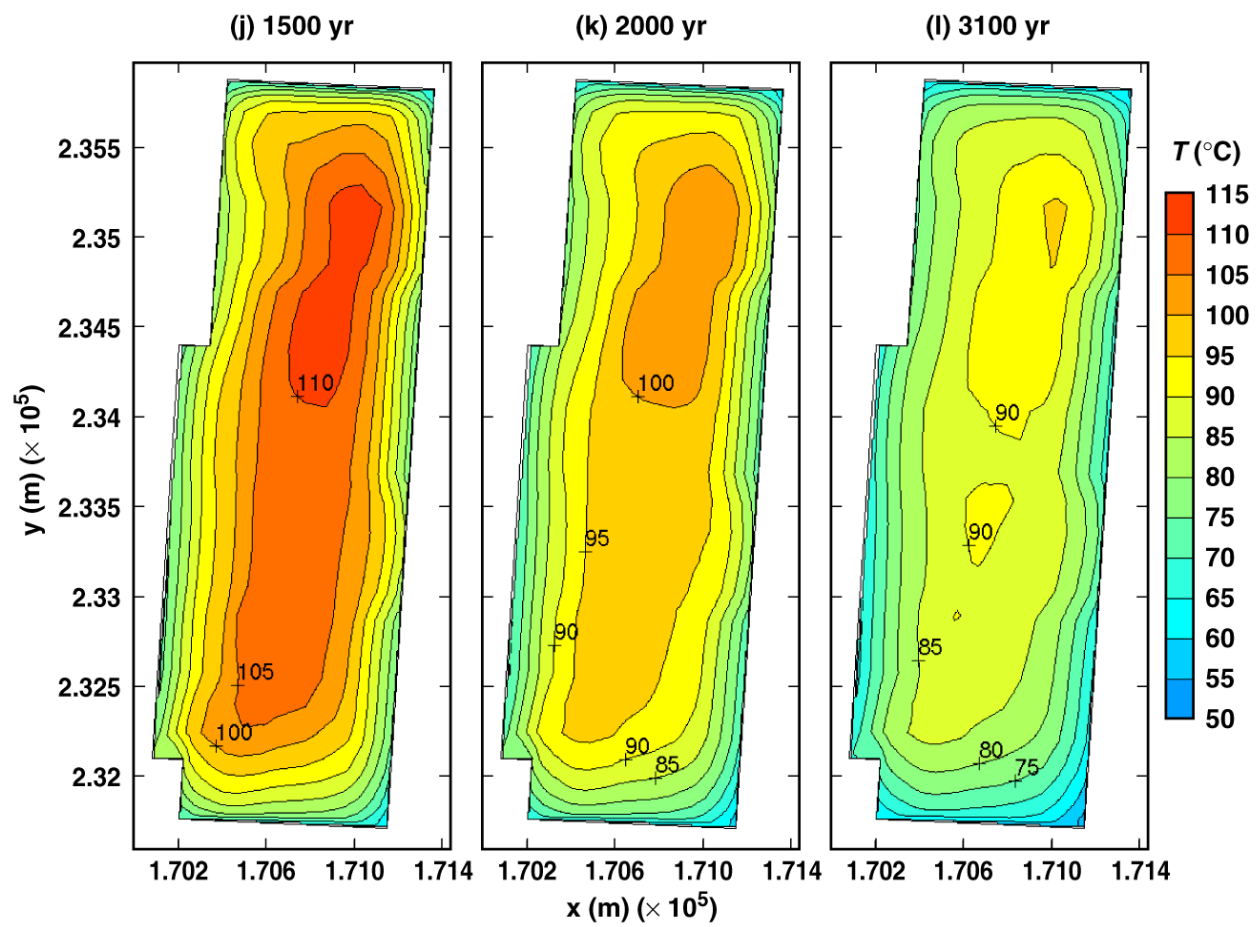
TB_AMR_lower_T_wp_pwr2_17-25

Figure 6-11. Temperature on the surface of a 21-PWR WP for the low infiltration-flux case for the indicated times.



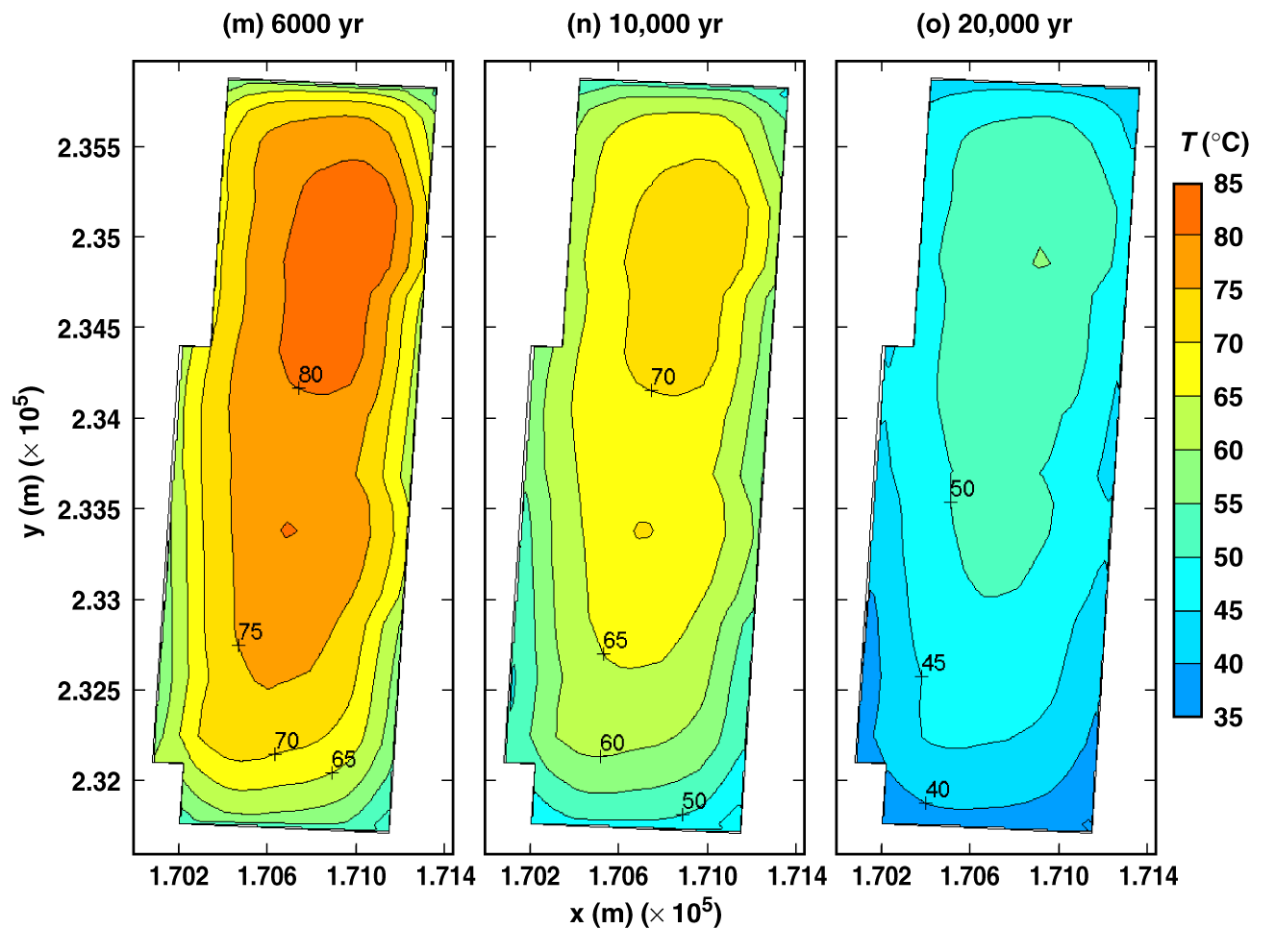
TB_AMR_lower_T_wp_pwr2_28-219

Figure 6-11. Temperature on the surface of a 21-PWR WP for the low infiltration-flux case for the indicated times.



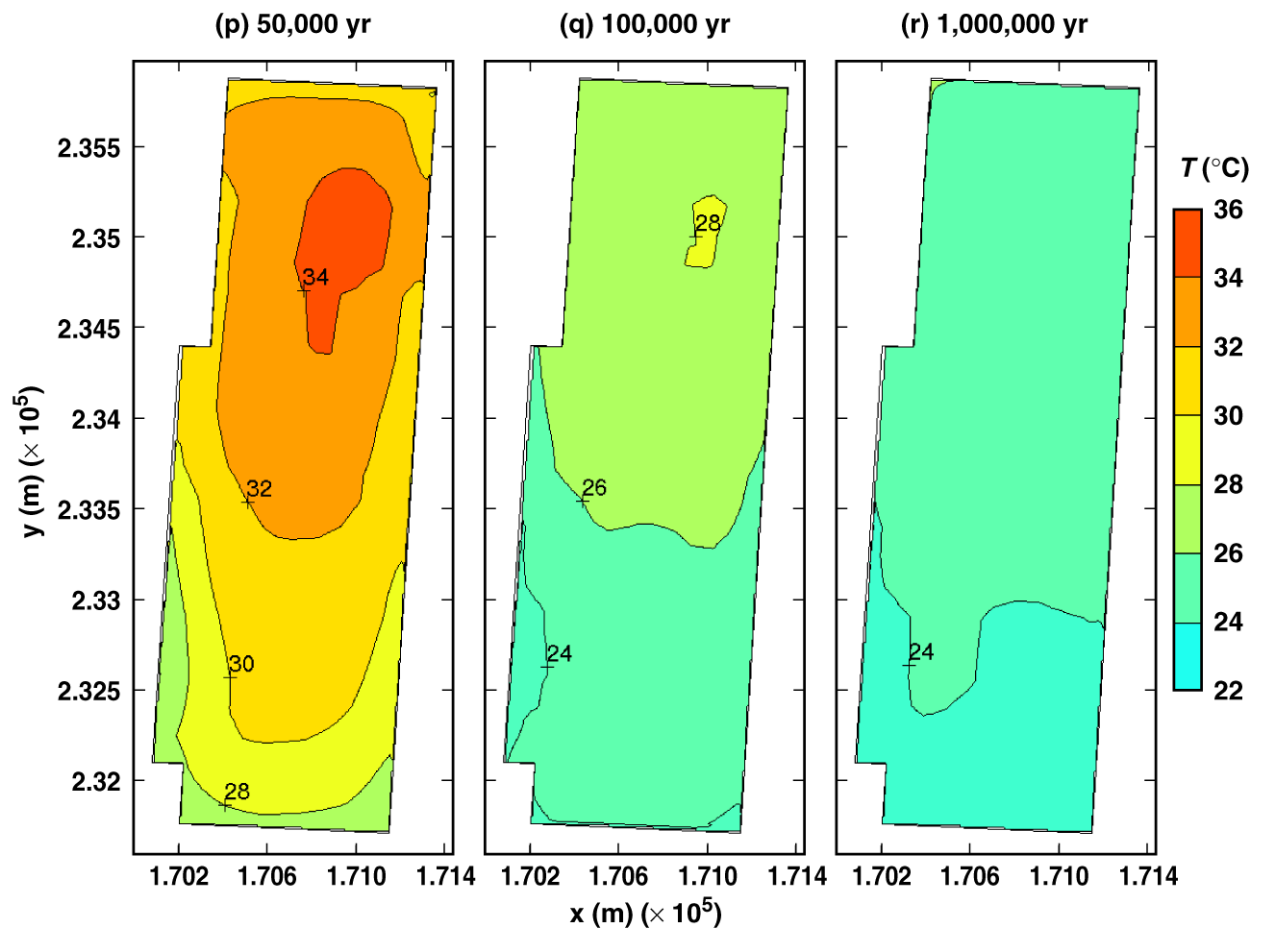
TB_AMR_lower_T_wp_pwr2_276-357

Figure 6-11. Temperature on the surface of a 21-PWR WP for the low infiltration-flux case for the indicated times.



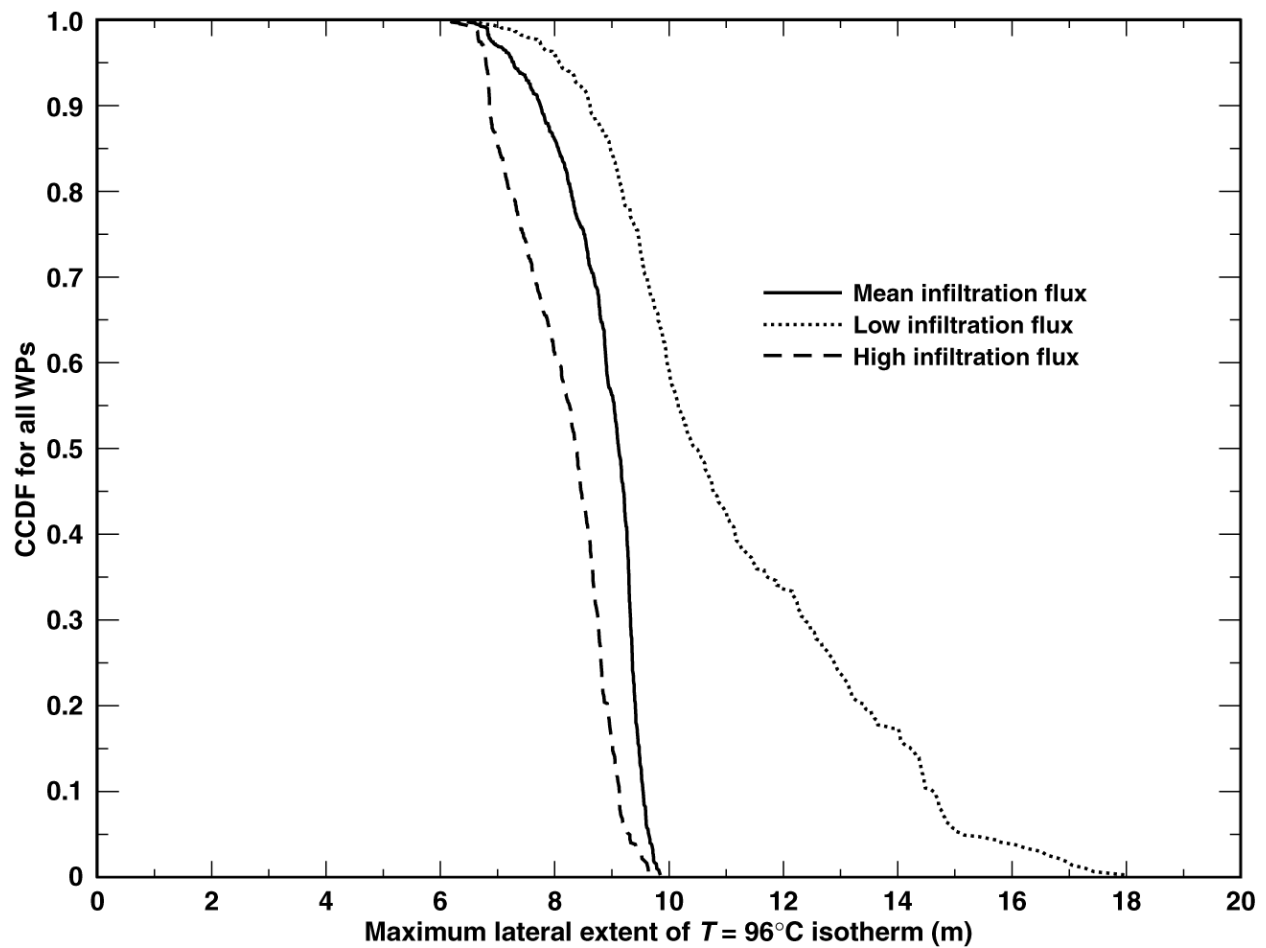
TB_AMR_lower_T_wp_pwr2_394-411

Figure 6-11. Temperature on the surface of a 21-PWR WP for the low infiltration-flux case for the indicated times.



TB_AMR_lower_T_wp_pwr2_427-442

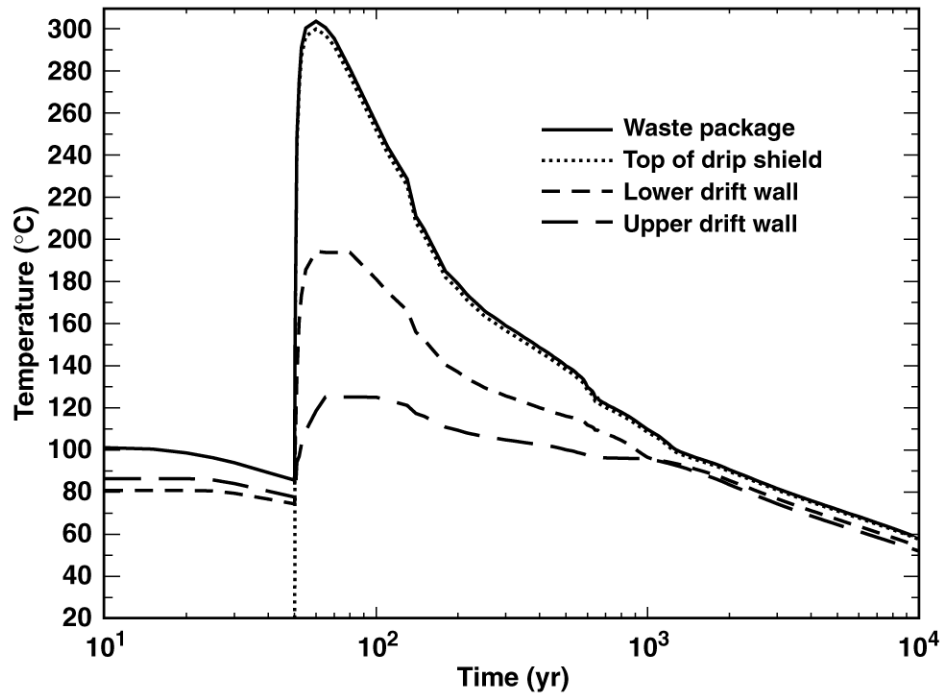
Figure 6-11. Temperature on the surface of a 21-PWR WP for the low infiltration-flux case for the indicated times.



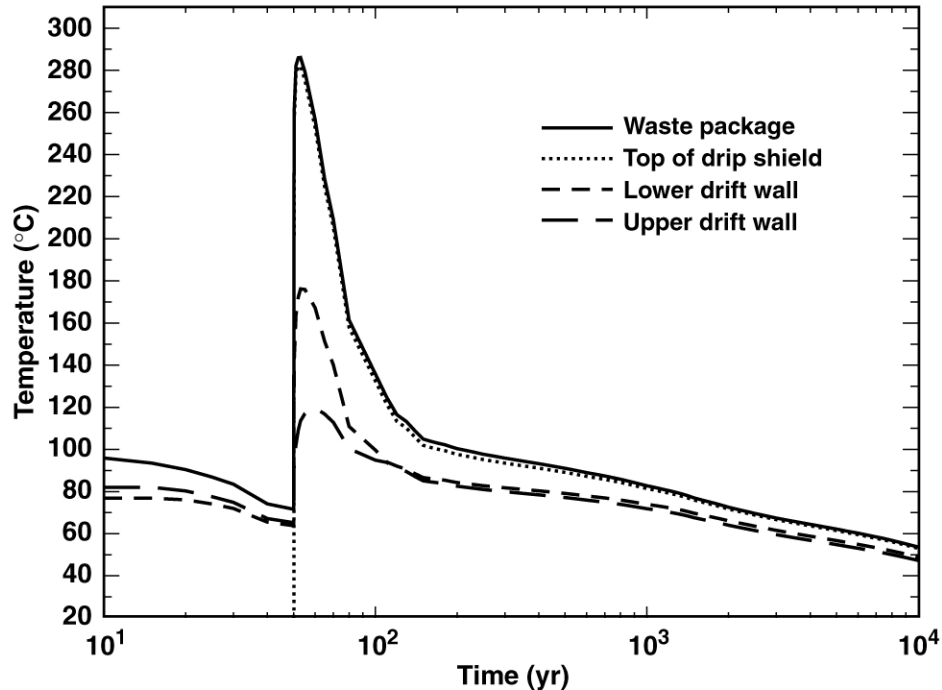
TB_AMR_CCDF_xT=96C_mlu

Figure 6-12. The complementary cumulative distribution function (CCDF) for the maximum lateral extent of the boiling point ($T = 96^{\circ}\text{C}$) isotherm is plotted for the mean, high, and low infiltration-flux cases.

(a) Center of Repository
Nevada State Coordinates: Easting = 170535.03 m, Northing = 233640.08 m

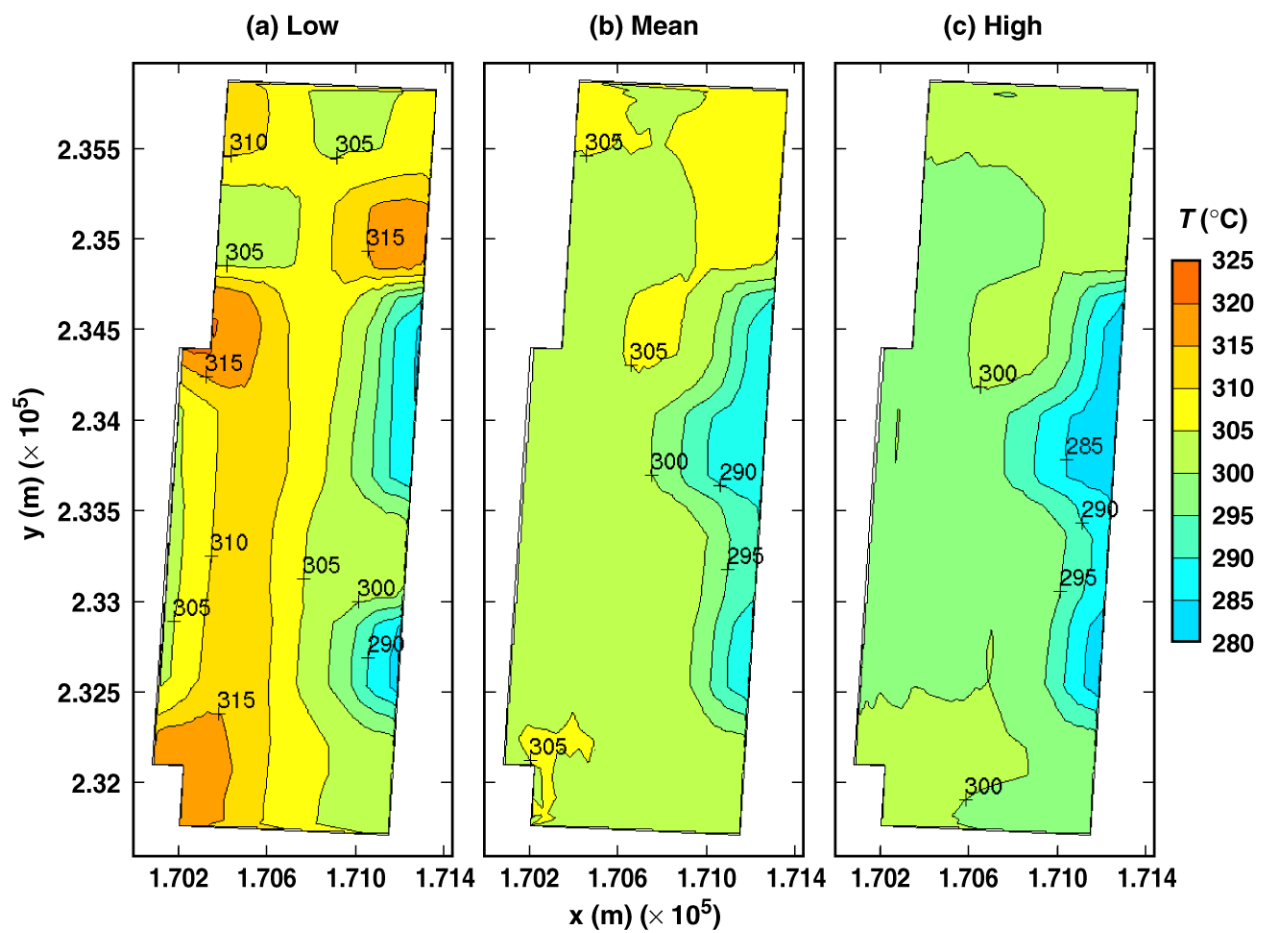


(b) Eastern Edge of Repository
Nevada State Coordinates: Easting = 171195.16 m, Northing = 233605.06 m



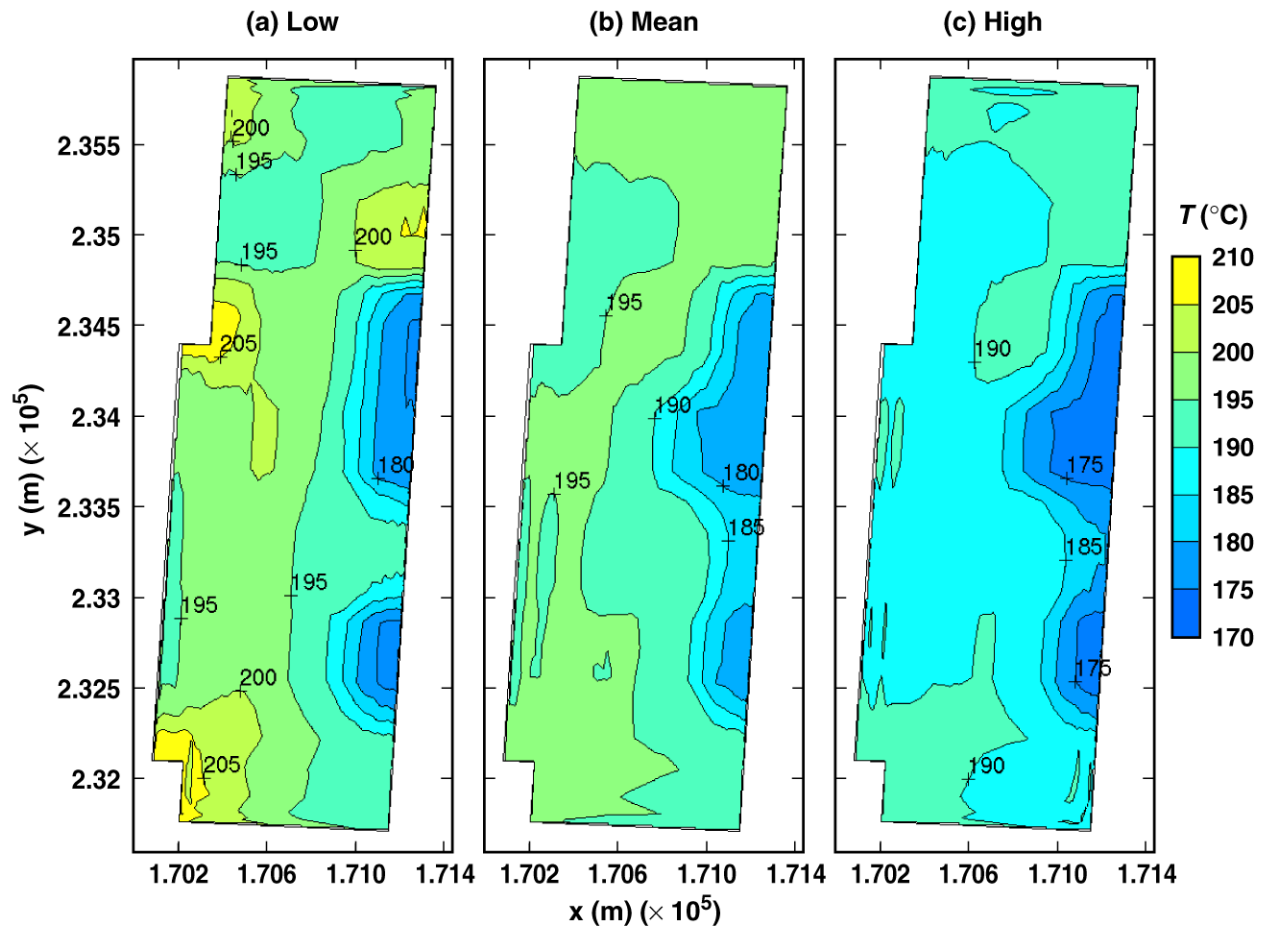
TB_AMR_T_hist_pwr2_13&24_17_mean

Figure 6-13. Temperature history on the surface of a 21-PWR WP for the mean infiltration-flux case at (a) the geographical center of the repository and (b) a location 27.5 m from the eastern edge of the repository. Note that the Nevada State coordinates are given.



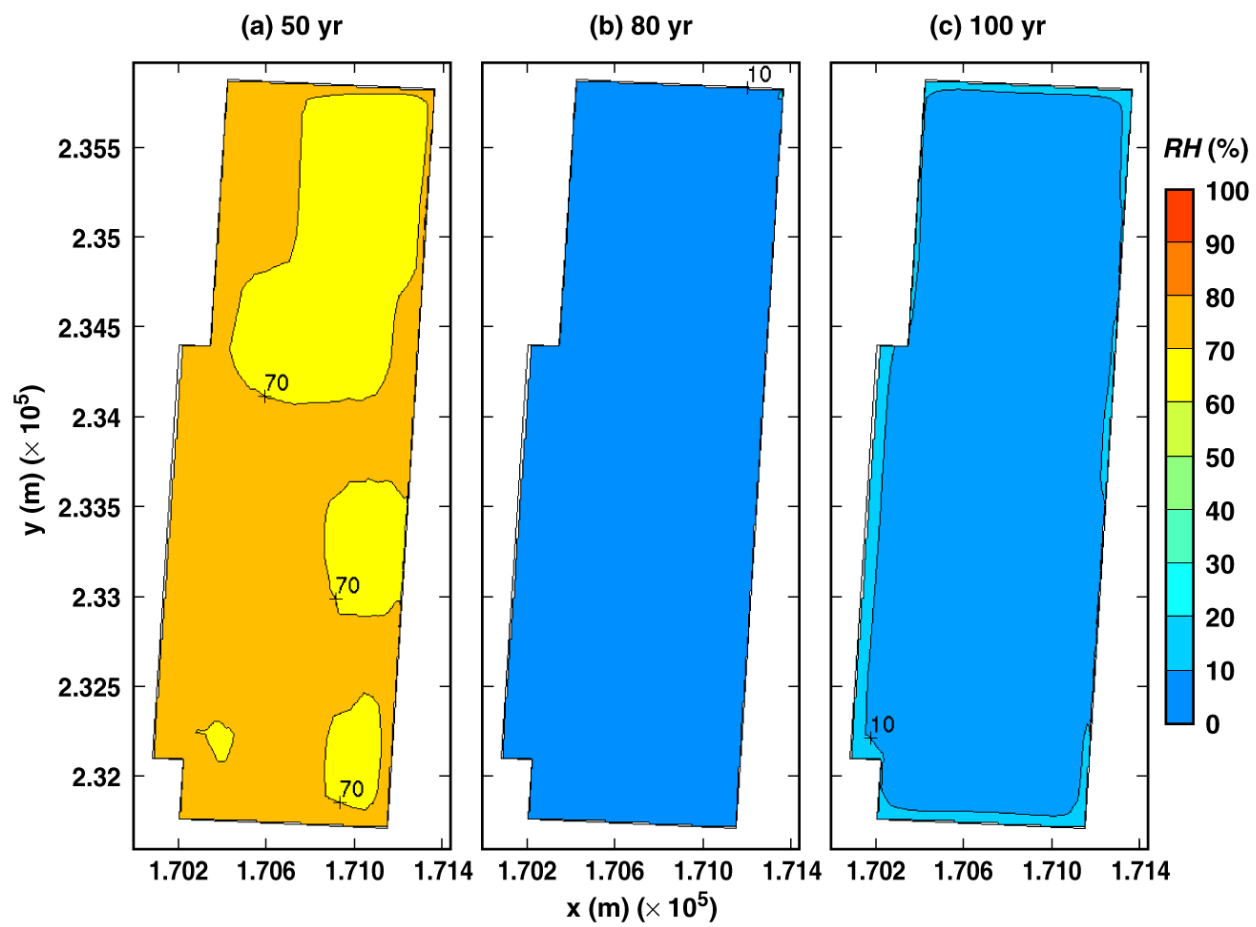
TB_AMR_lmu_T_wp_max_pwr2

Figure 6-14. Peak WP temperature for the low, mean, and high infiltration-flux cases.



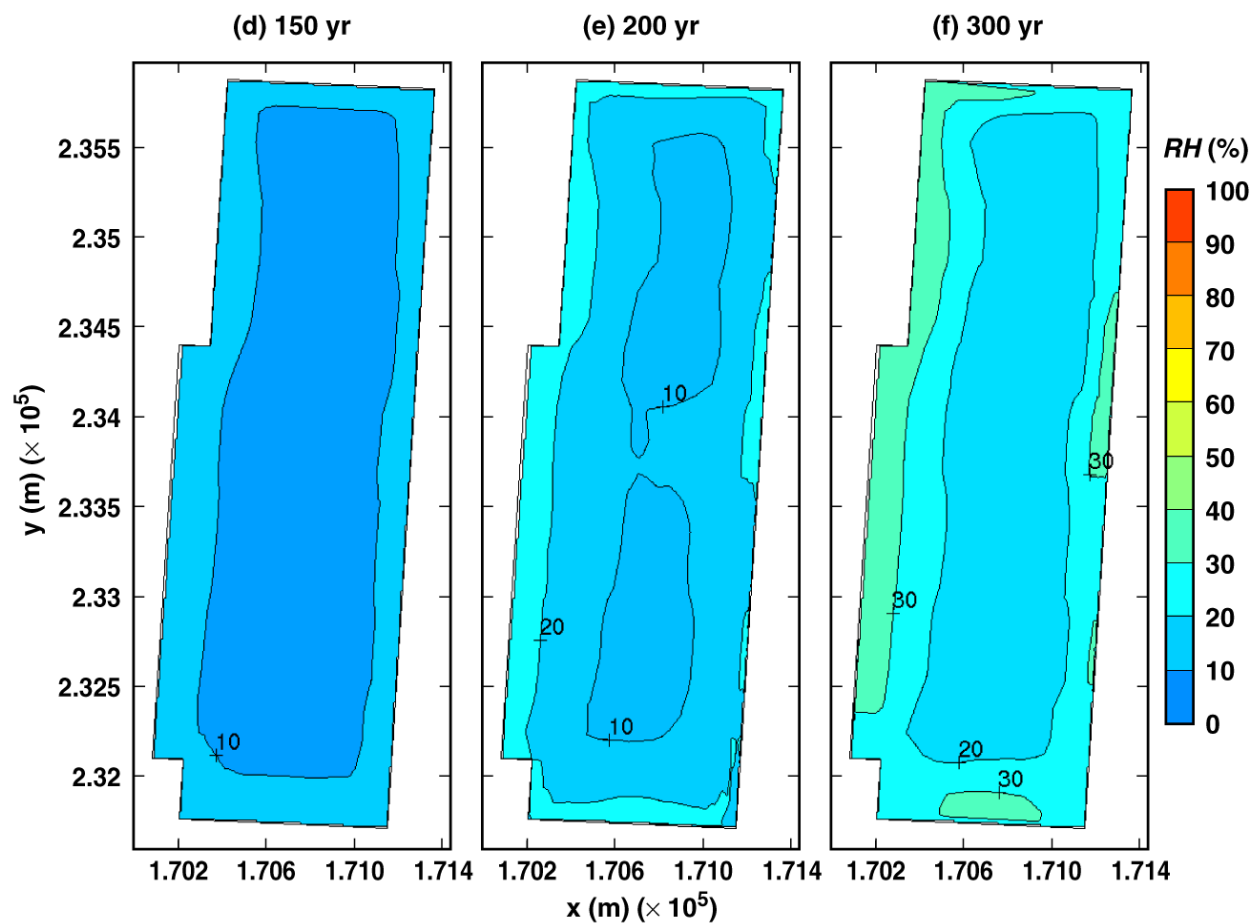
TB_AMR_lmu_T_dw_lower_max

Figure 6-15. Peak temperature on the lower drift wall (below the invert) for the low, mean, and high infiltration-flux cases.



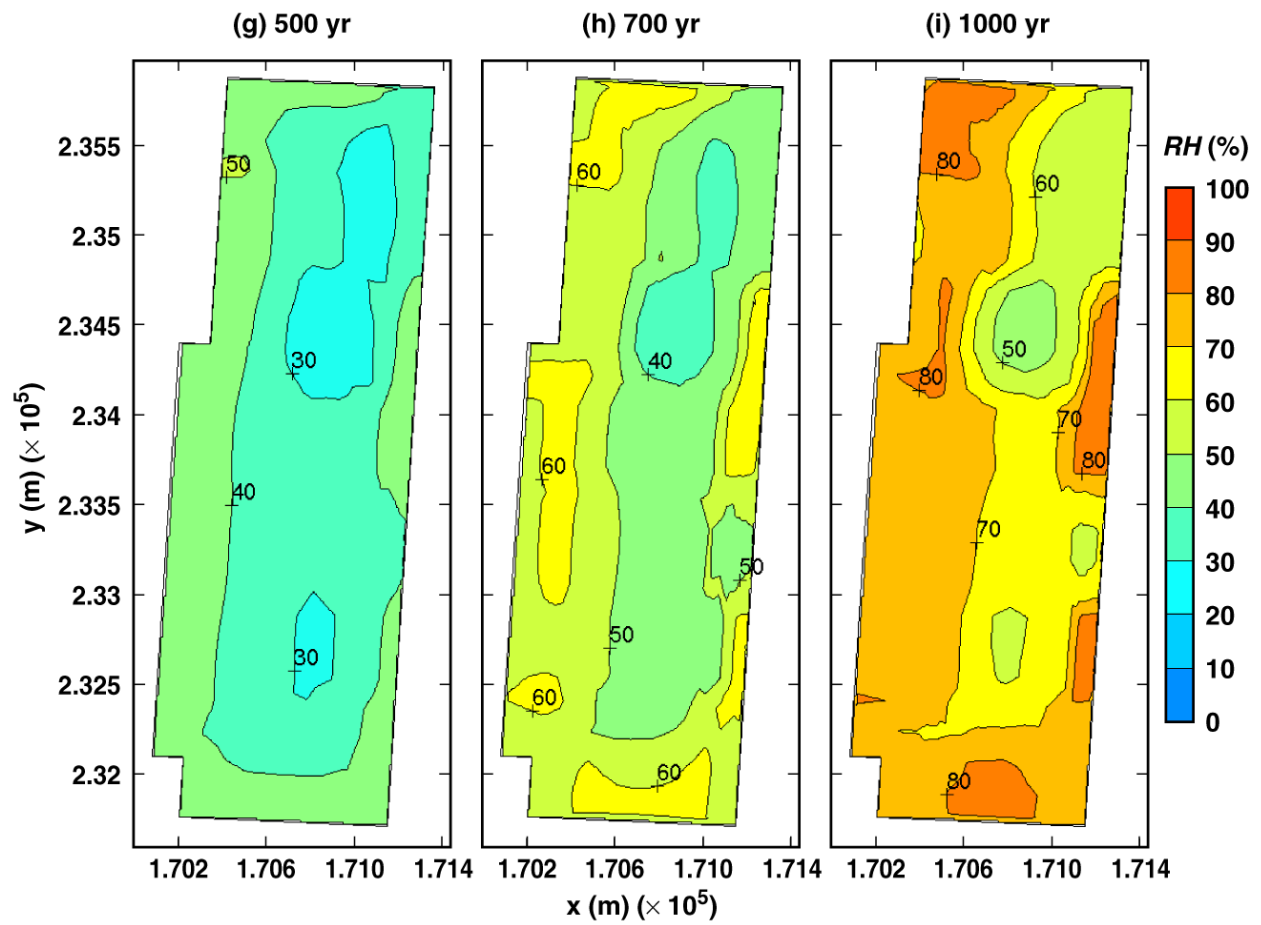
TB_AMR_mean_RH_wp_pwr2_11-21

Figure 6-16. Relative humidity on the surface of a 21-PWR WP for the mean infiltration-flux case for the indicated times.



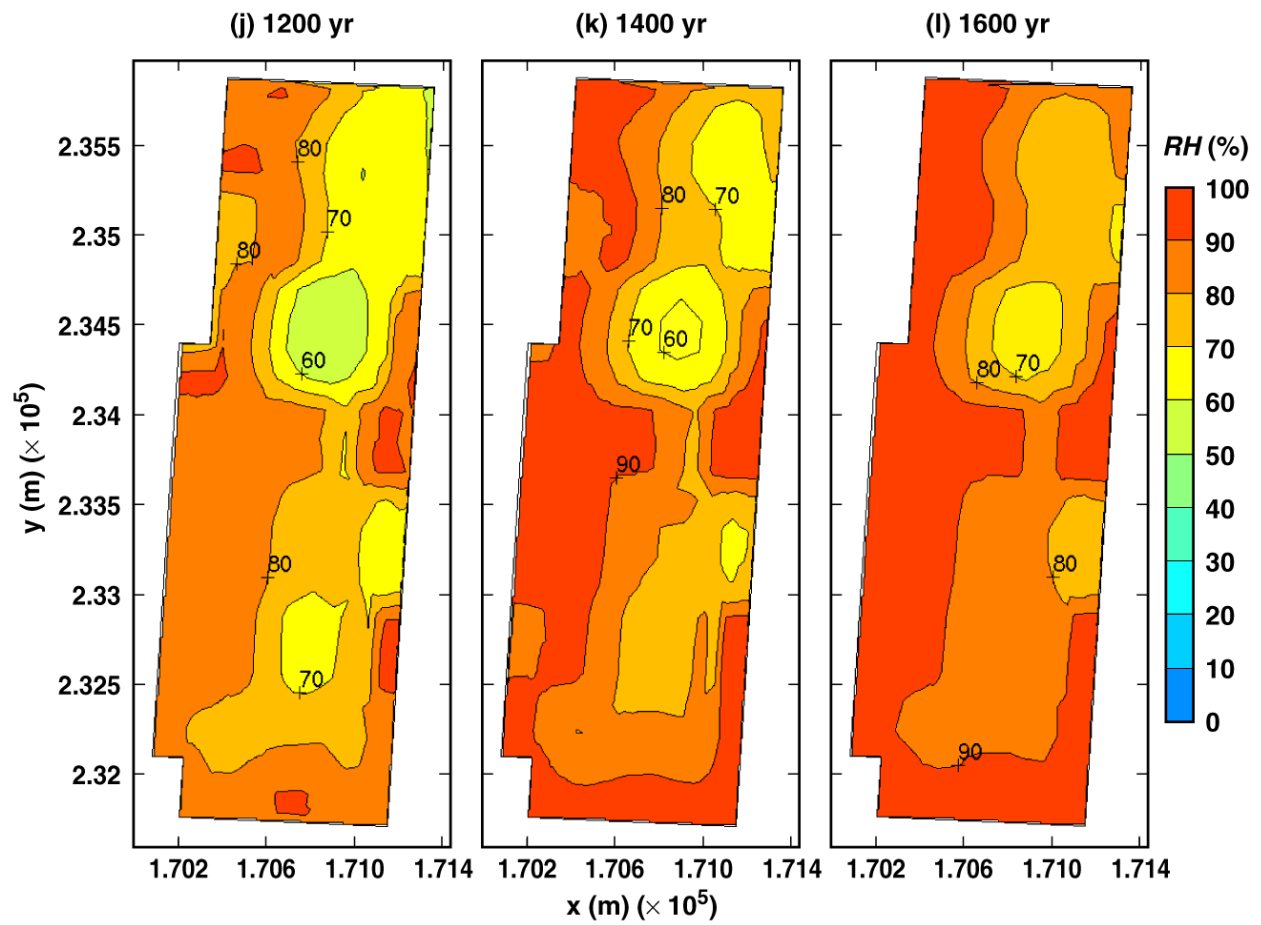
TB_AMR_mean_RH_wp_pwr2_26-64

Figure 6-16. Relative humidity on the surface of a 21-PWR WP for the mean infiltration-flux case for the indicated times.



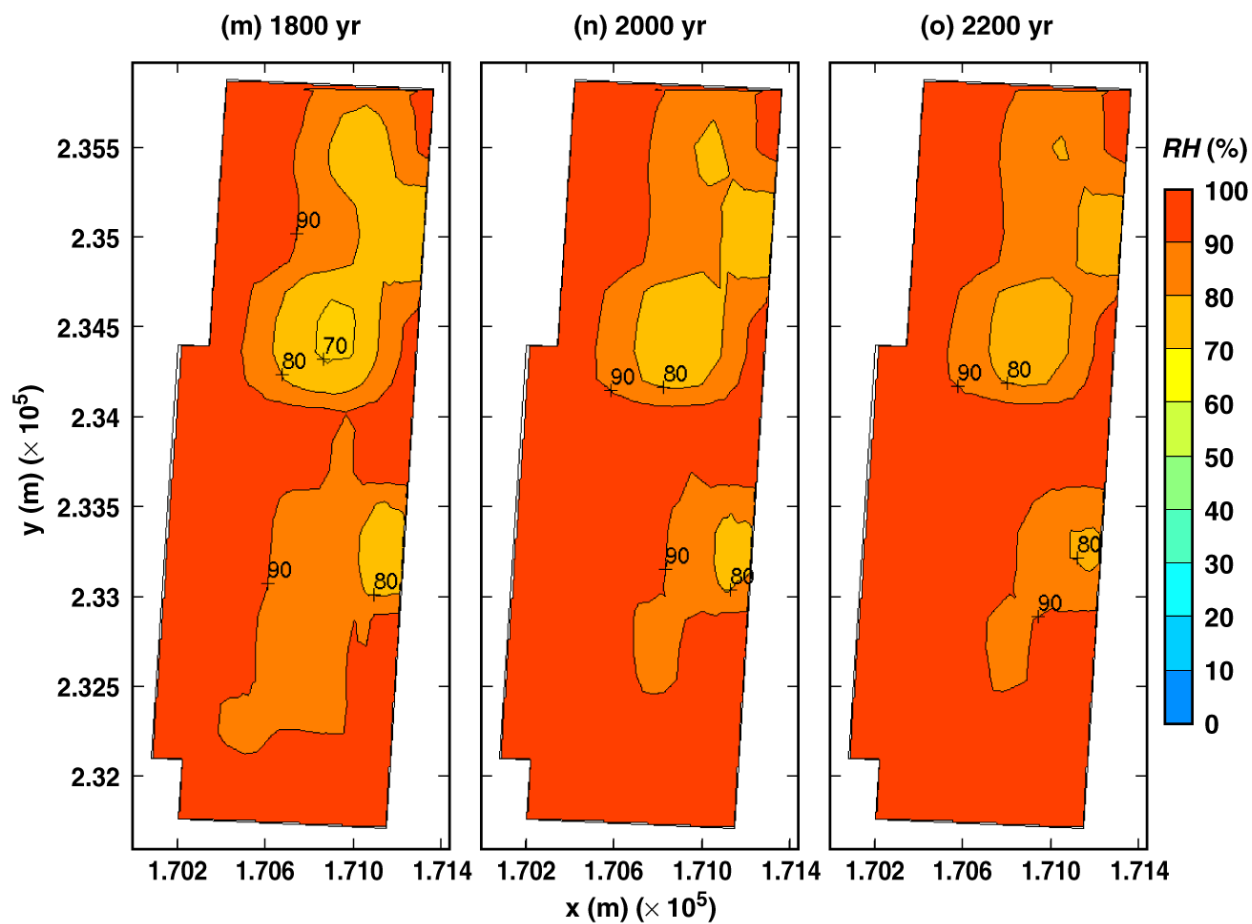
TB_AMR_mean_RH_wp_pwr2_104-174

Figure 6-16. Relative humidity on the surface of a 21-PWR WP for the mean infiltration-flux case for the indicated times.



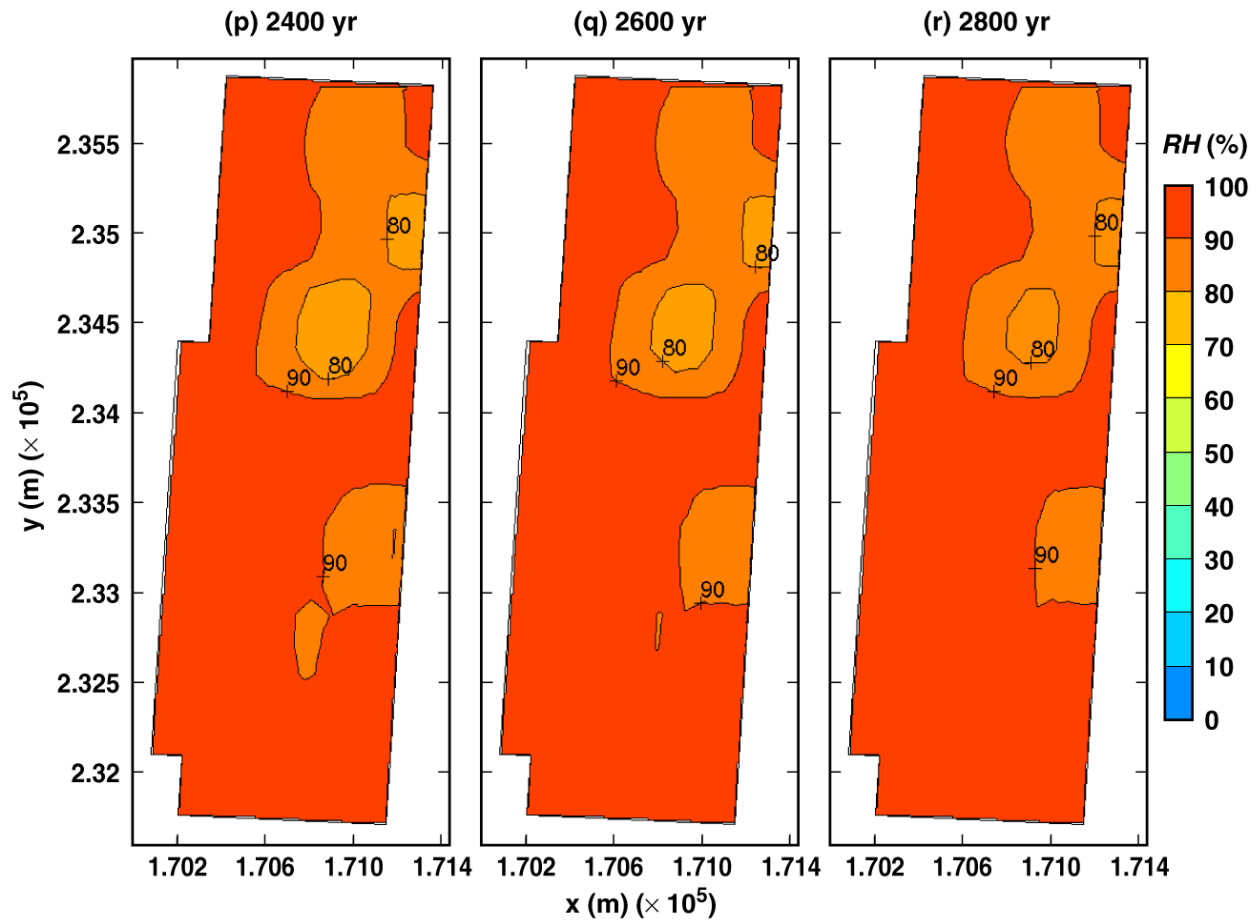
TB_AMR_mean_RH_wp_pwr2_204-231

Figure 6-16. Relative humidity on the surface of a 21-PWR WP for the mean infiltration-flux case for the indicated times.



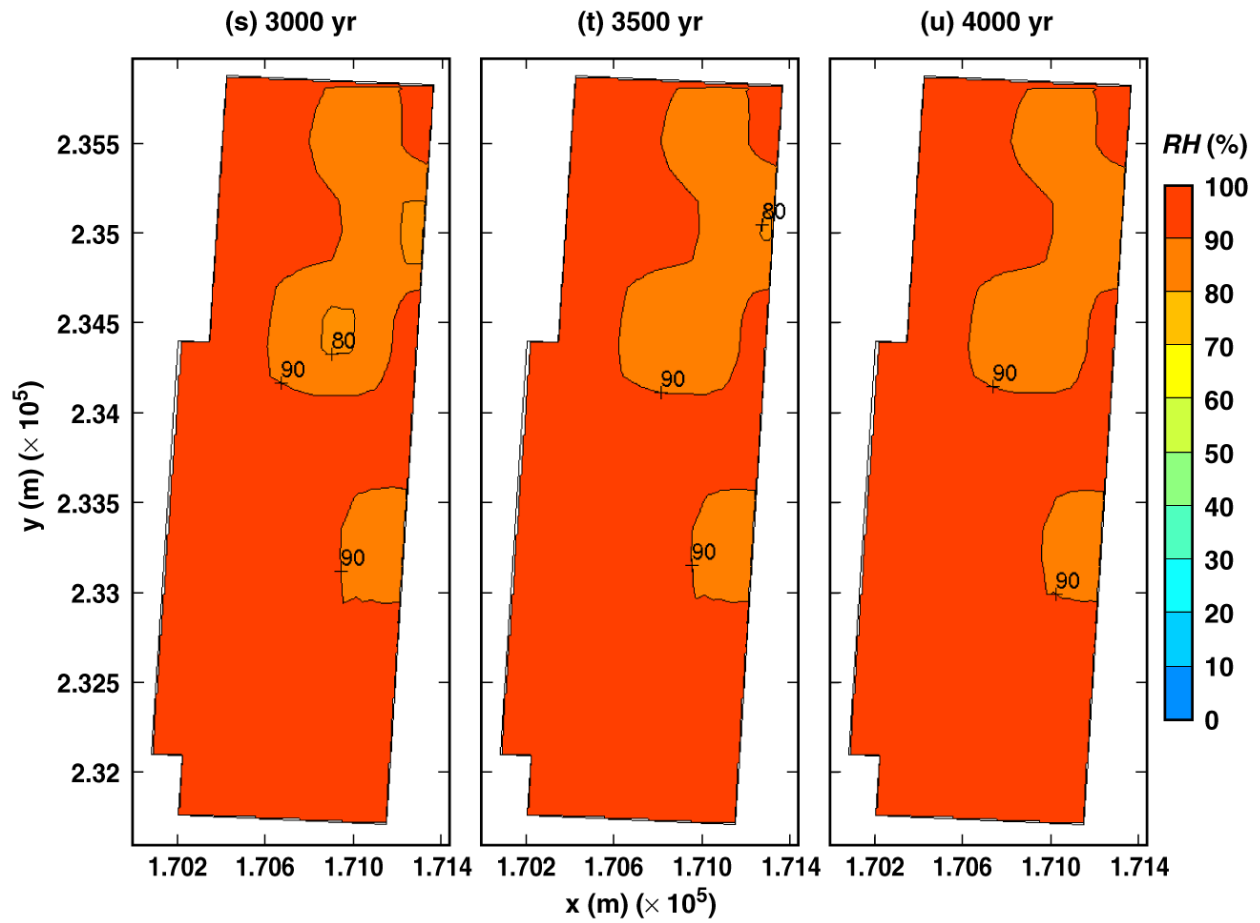
TB_AMR_mean_RH_wp_pwr2_243-266

Figure 6-16. Relative humidity on the surface of a 21-PWR WP for the mean infiltration-flux case for the indicated times.



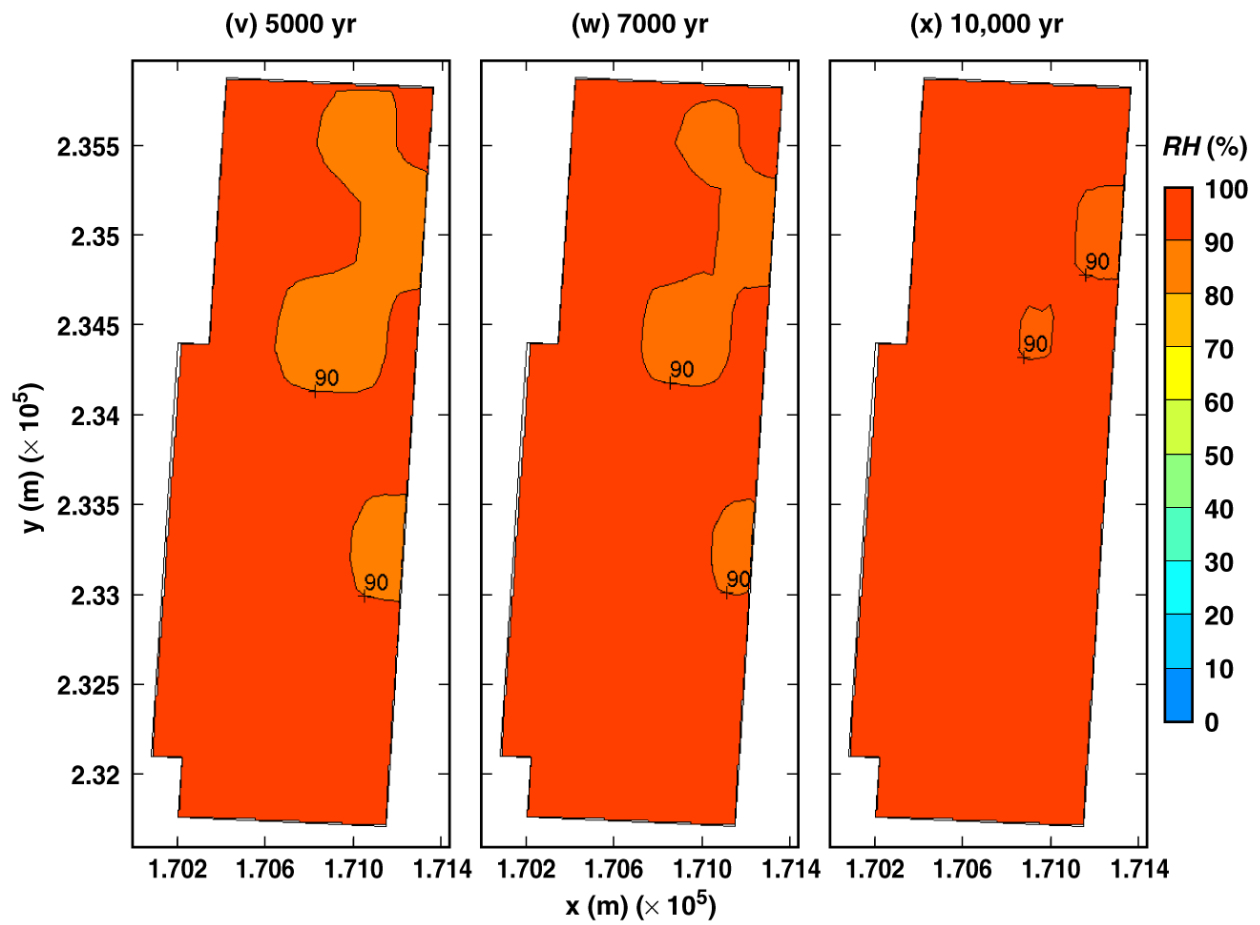
TB_AMR_mean_RH_wp_pwr2_271-279

Figure 6-16. Relative humidity on the surface of a 21-PWR WP for the mean infiltration-flux case for the indicated times.



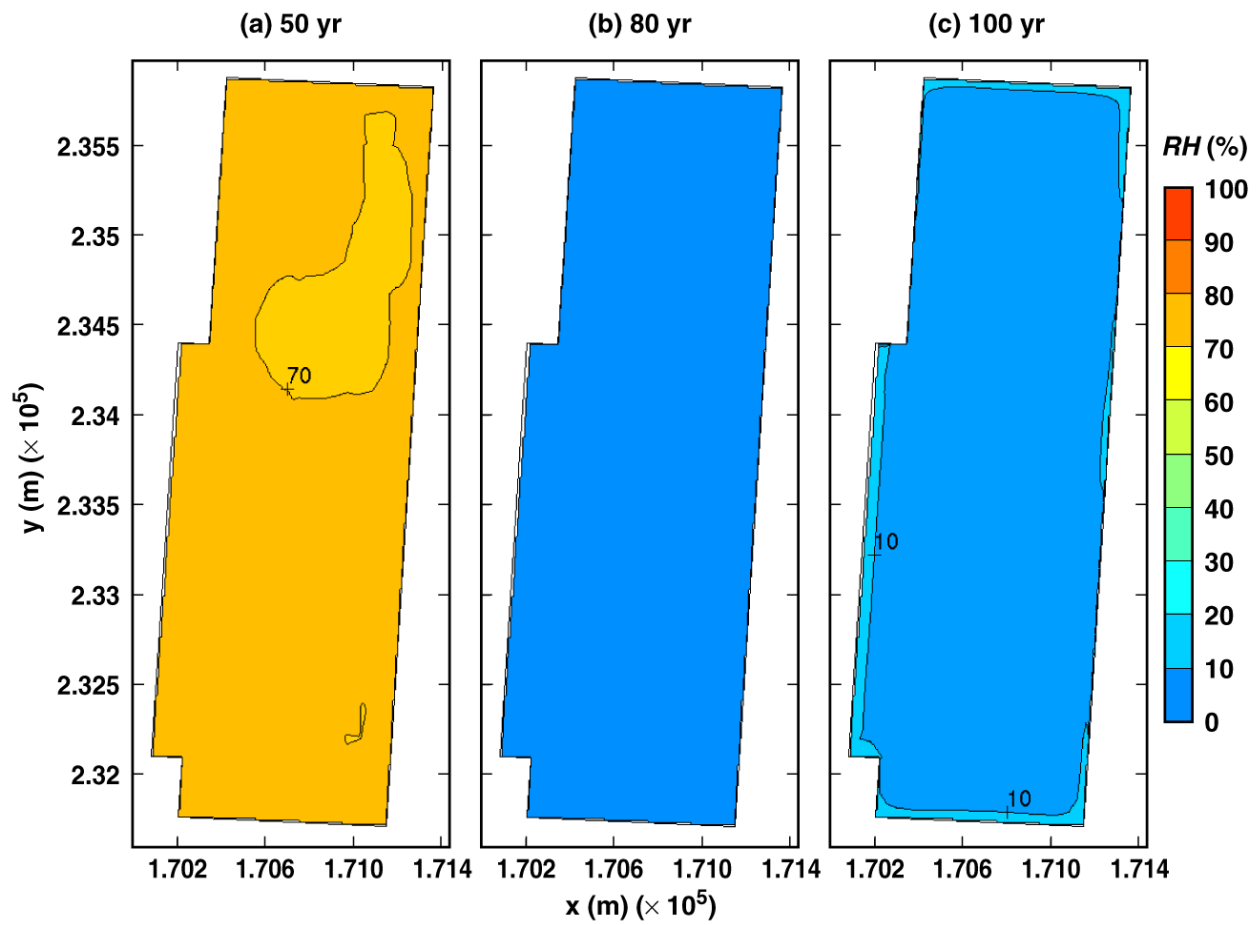
TB_AMR_mean_RH_wp_pwr2_283-297

Figure 6-16. Relative humidity on the surface of a 21-PWR WP for the mean infiltration-flux case for the indicated times.



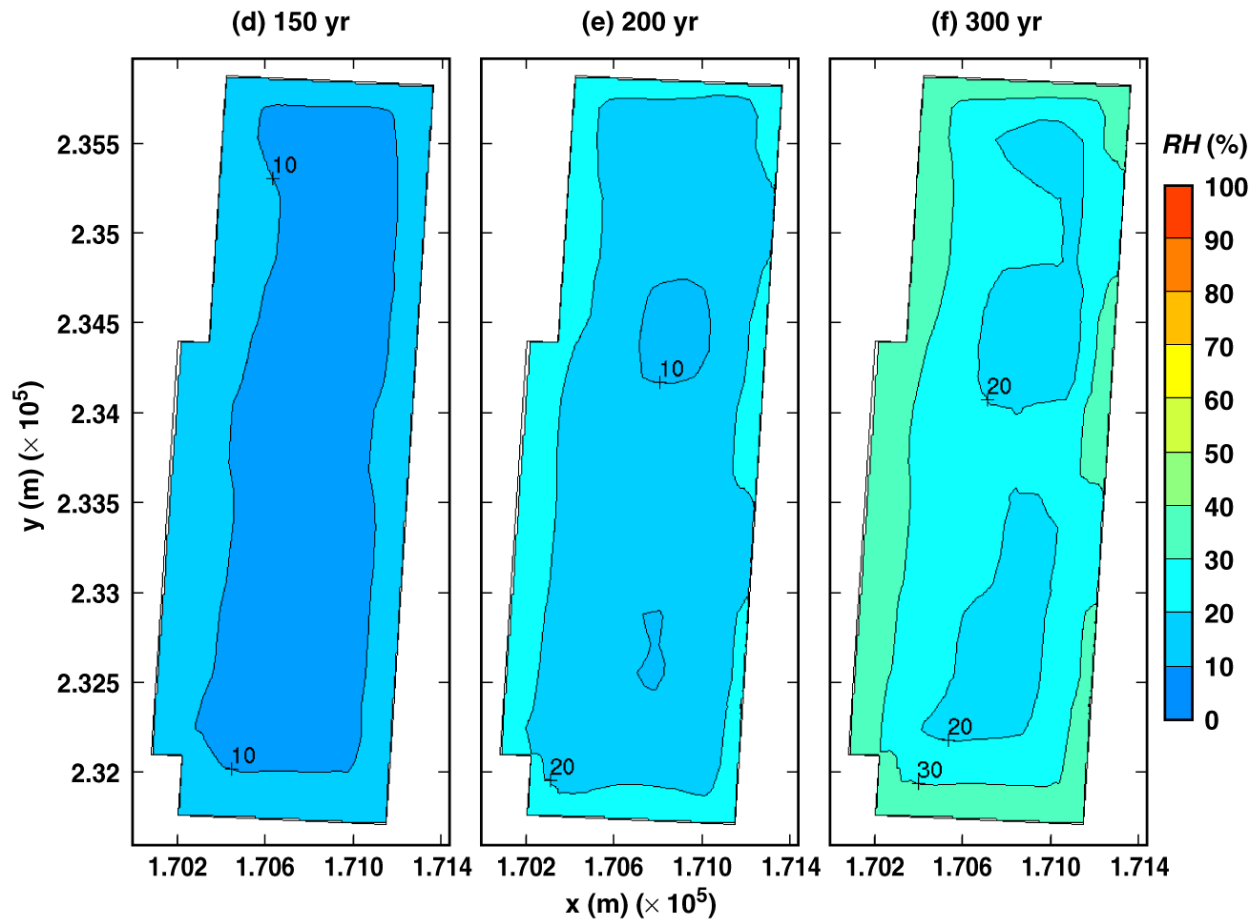
TB_AMR_mean_RH_wp_pwr2_307-319

Figure 6-16. Relative humidity on the surface of a 21-PWR WP for the mean infiltration-flux case for the indicated times.



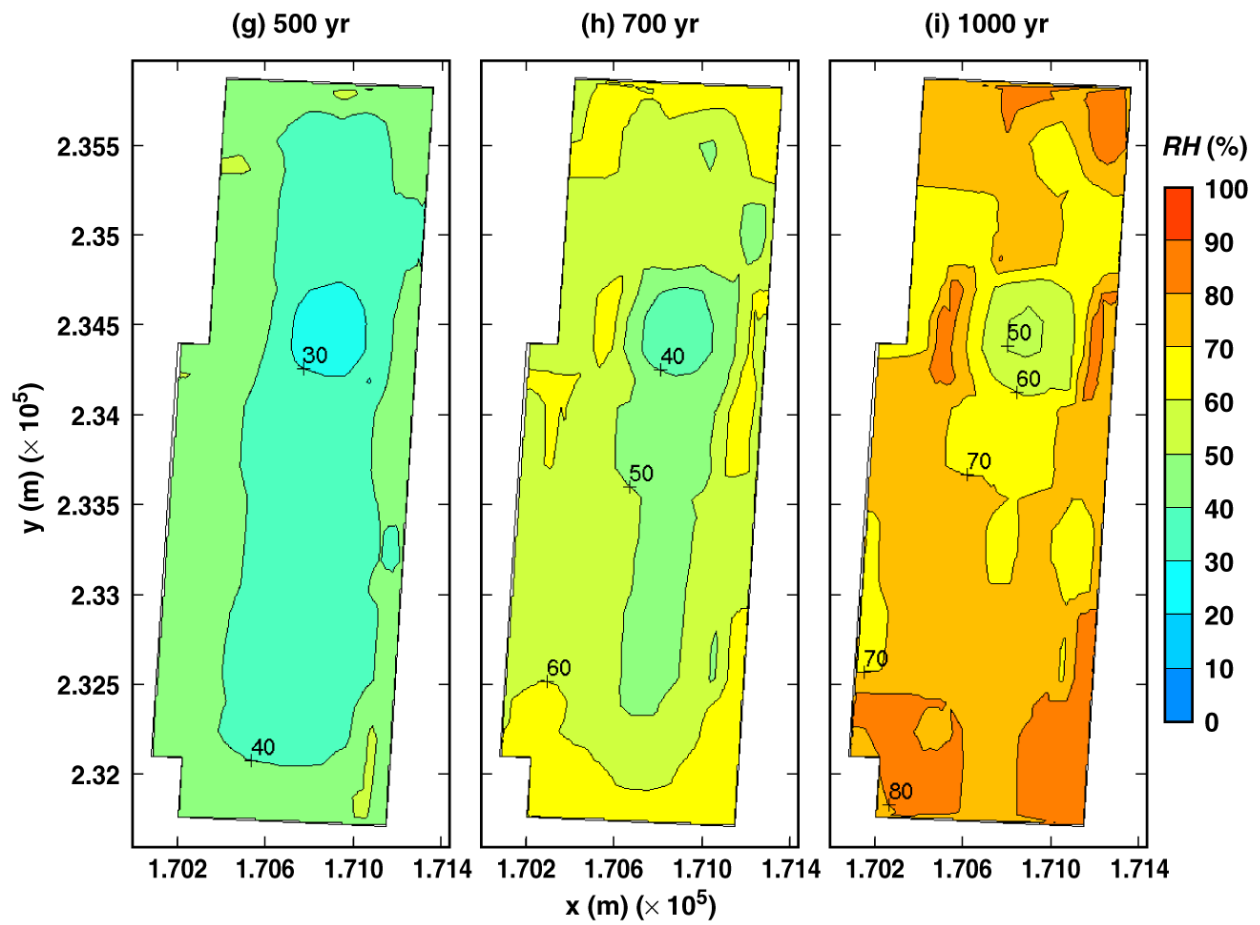
TB_AMR_upper_RH_wp_pwr2_11-22

Figure 6-17. Relative humidity on the surface of a 21-PWR WP for the high infiltration-flux case for the indicated times.



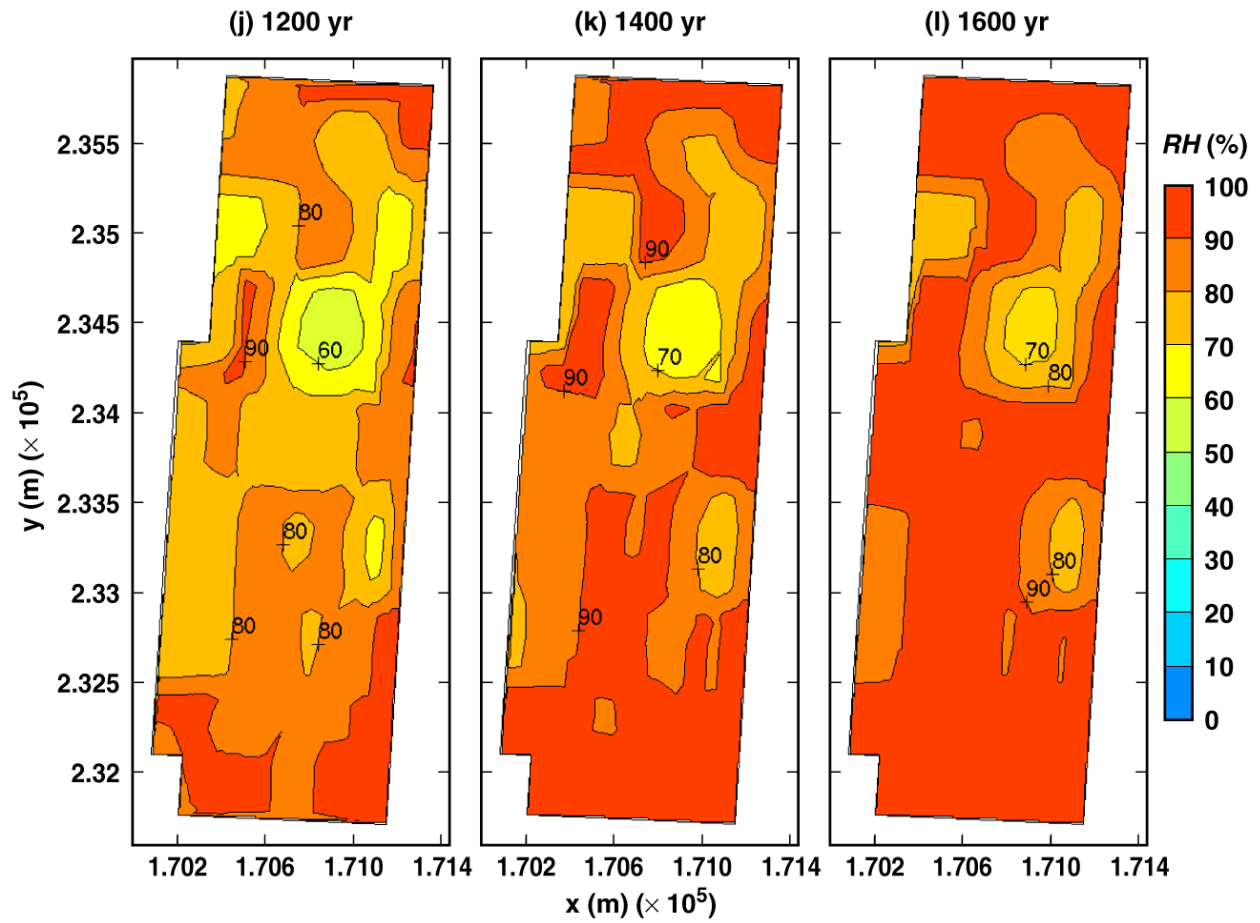
TB_AMR_upper_RH_wp_pwr2_31-107

Figure 6-17. Relative humidity on the surface of a 21-PWR WP for the high infiltration-flux case for the indicated times.



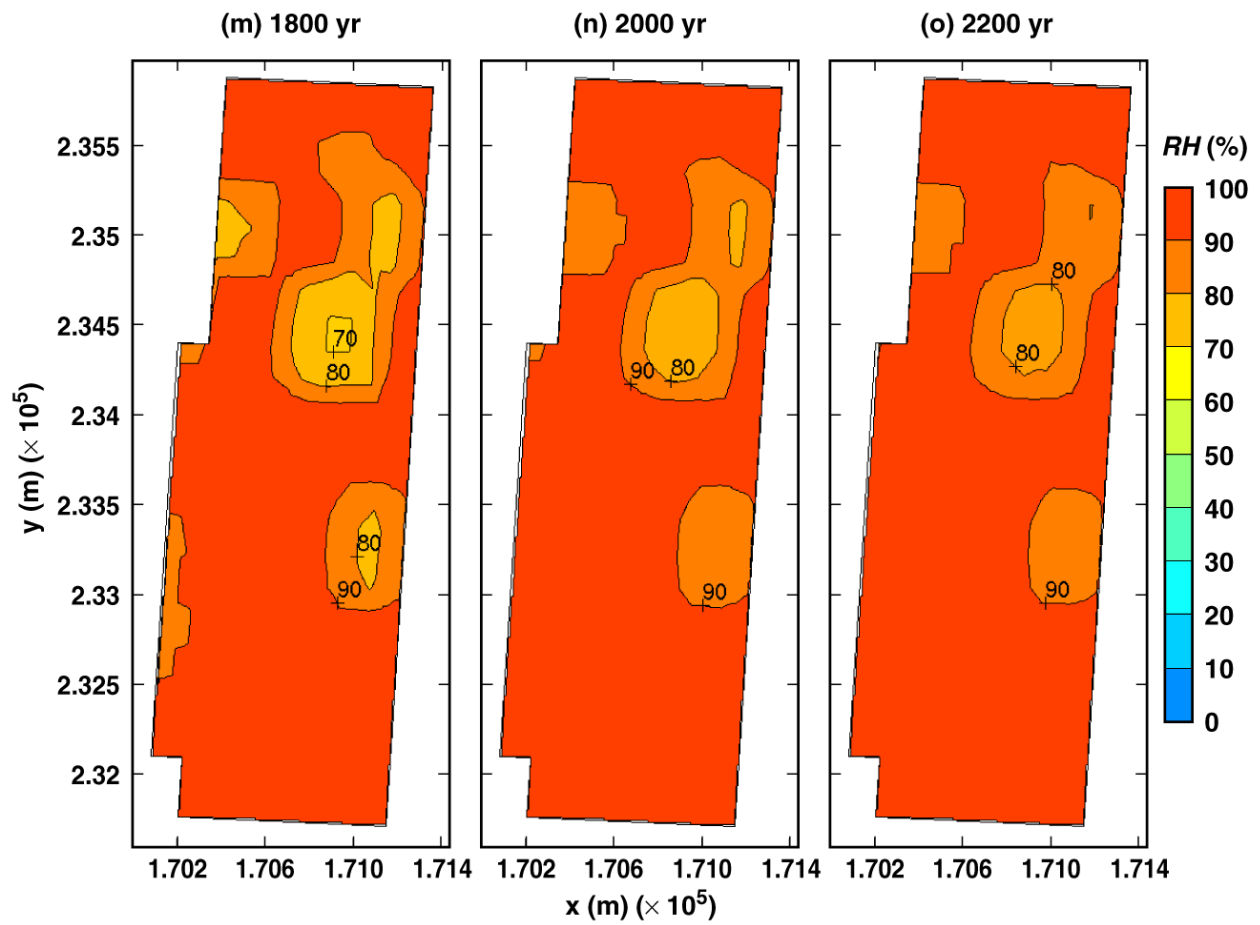
TB_AMR_upper_RH_wp_pwr2_177-269

Figure 6-17. Relative humidity on the surface of a 21-PWR WP for the high infiltration-flux case for the indicated times.



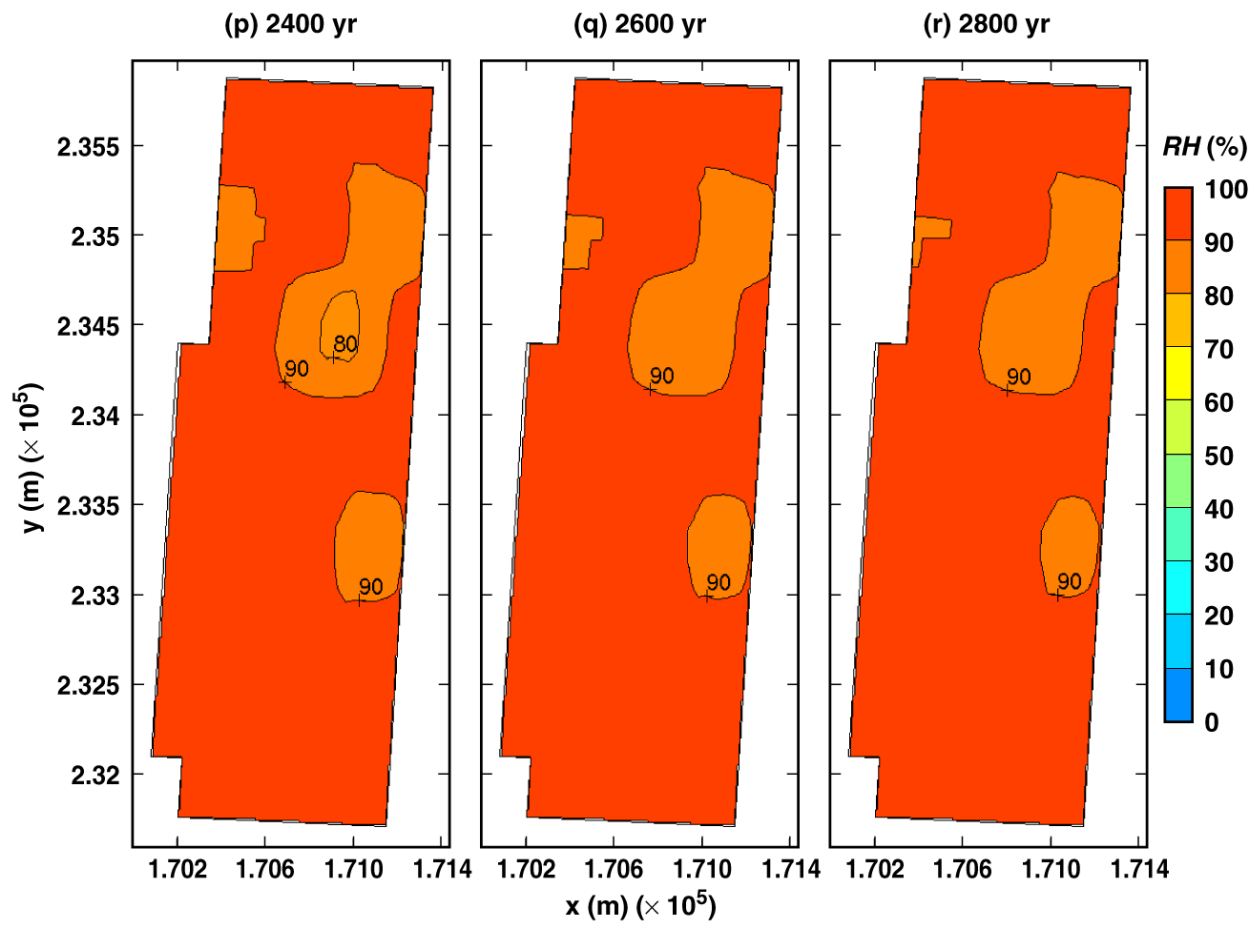
TB_AMR_upper_RH_wp_pwr2_289-329

Figure 6-17. Relative humidity on the surface of a 21-PWR WP for the high infiltration-flux case for the indicated times.



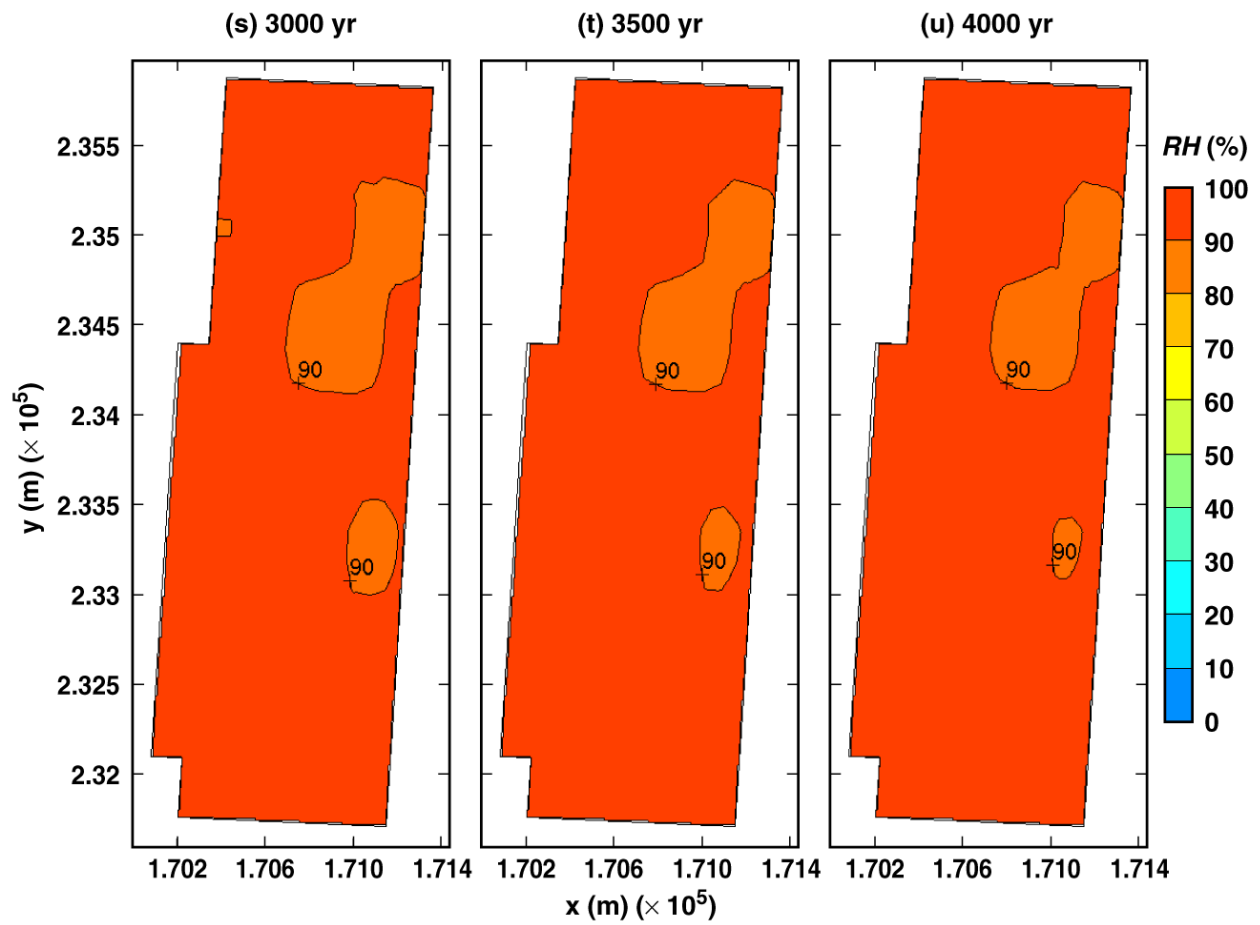
TB_AMR_upper_RH_wp_pwr2_347-372

Figure 6-17. Relative humidity on the surface of a 21-PWR WP for the high infiltration-flux case for the indicated times.



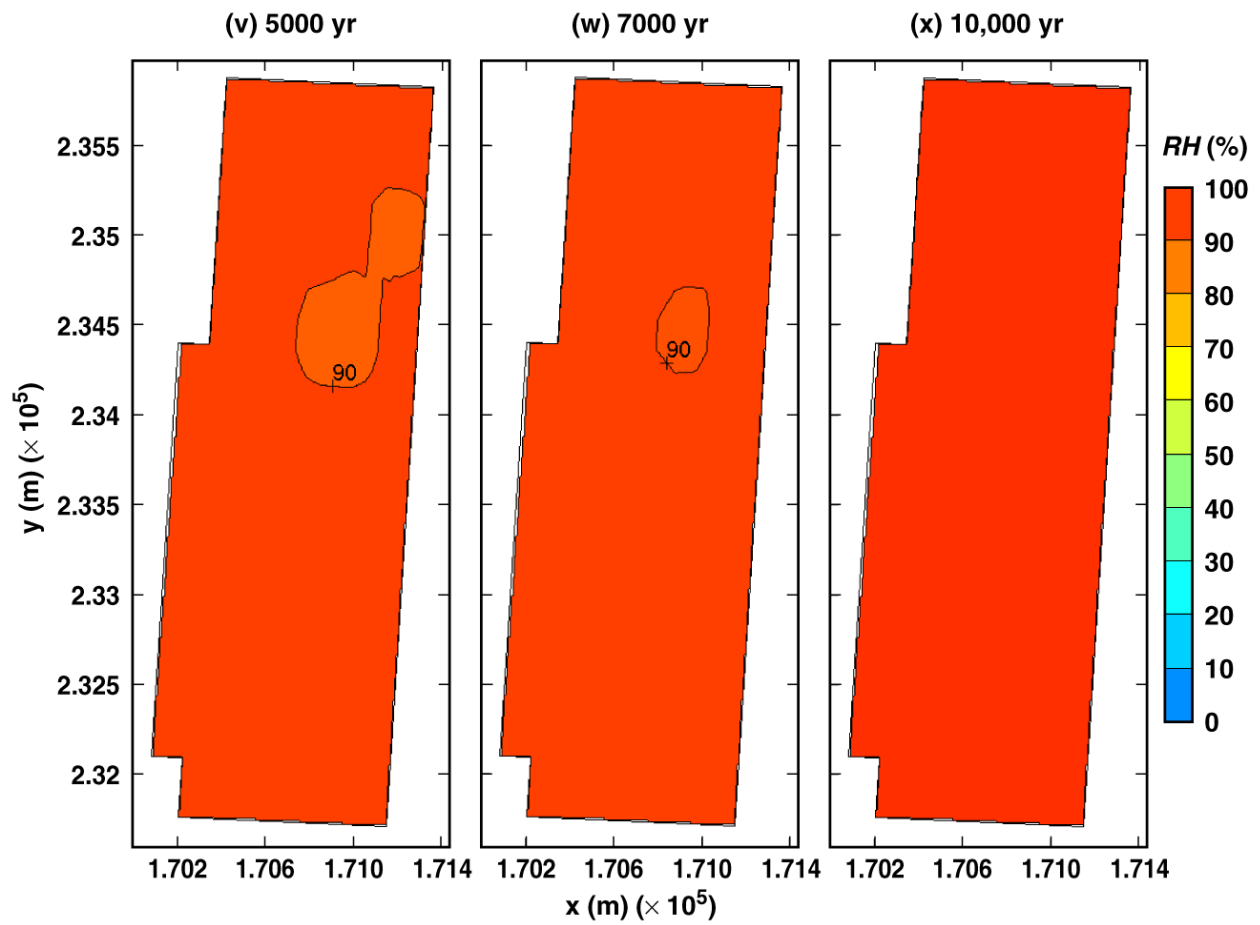
TB_AMR_upper_RH_wp_pwr2_377-385

Figure 6-17. Relative humidity on the surface of a 21-PWR WP for the high infiltration-flux case for the indicated times.



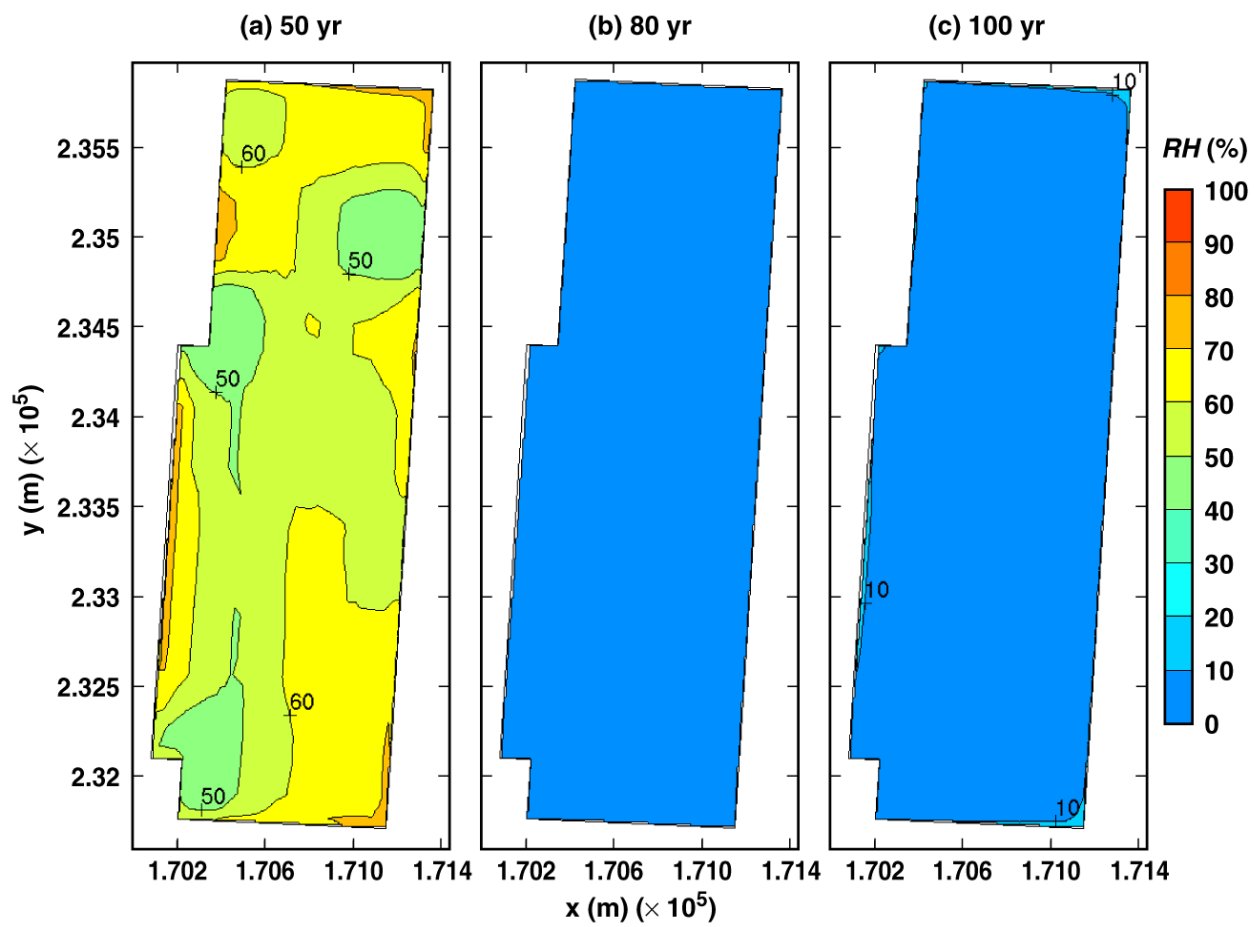
TB_AMR_upper_RH_wp_pwr2_389-403

Figure 6-17. Relative humidity on the surface of a 21-PWR WP for the high infiltration-flux case for the indicated times.



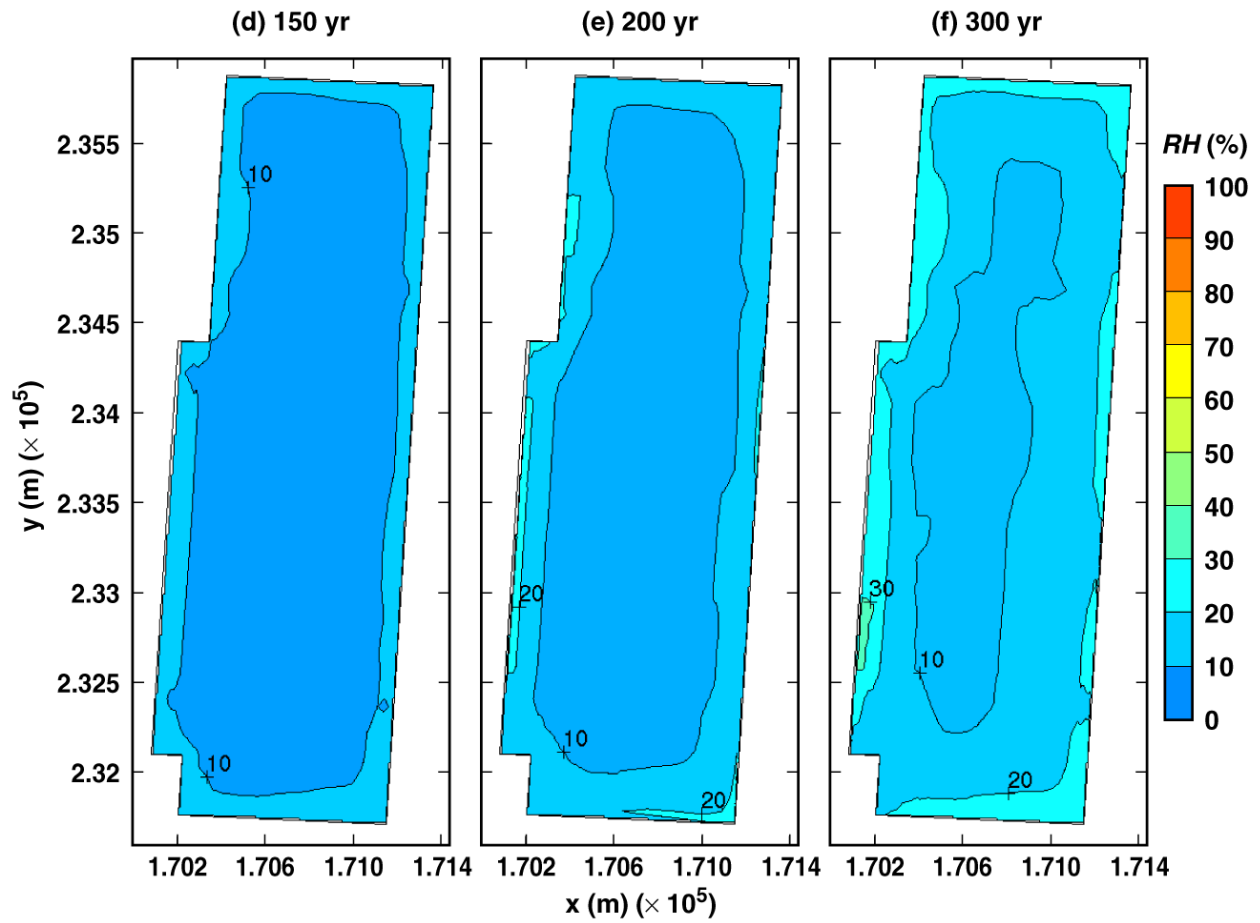
TB_AMR_upper_RH_wp_pwr2_413-425

Figure 6-17. Relative humidity on the surface of a 21-PWR WP for the high infiltration-flux case for the indicated times.



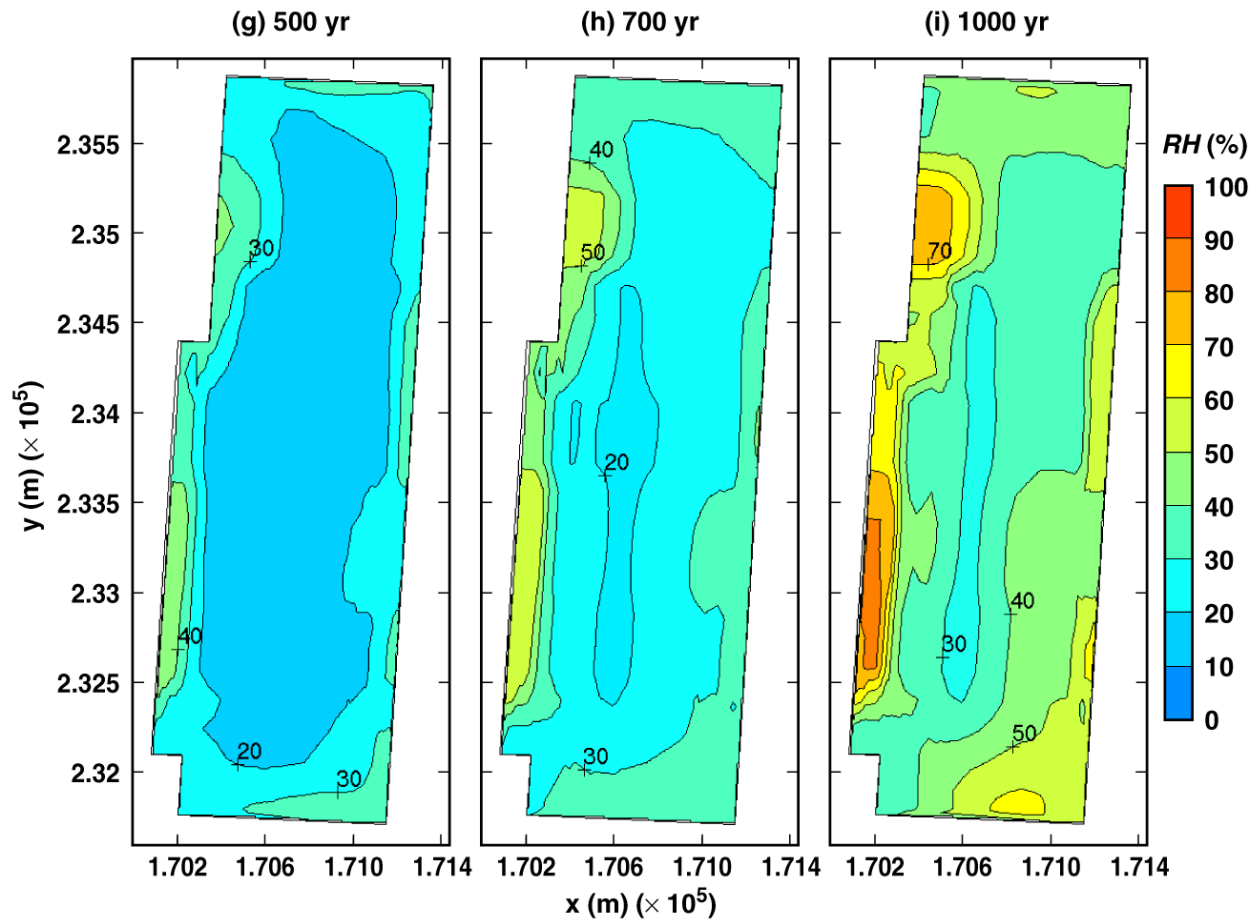
TB_AMR_lower_RH_wp_pwr2_11-22

Figure 6-18. Relative humidity on the surface of a 21-PWR WP for the low infiltration-flux case for the indicated times.



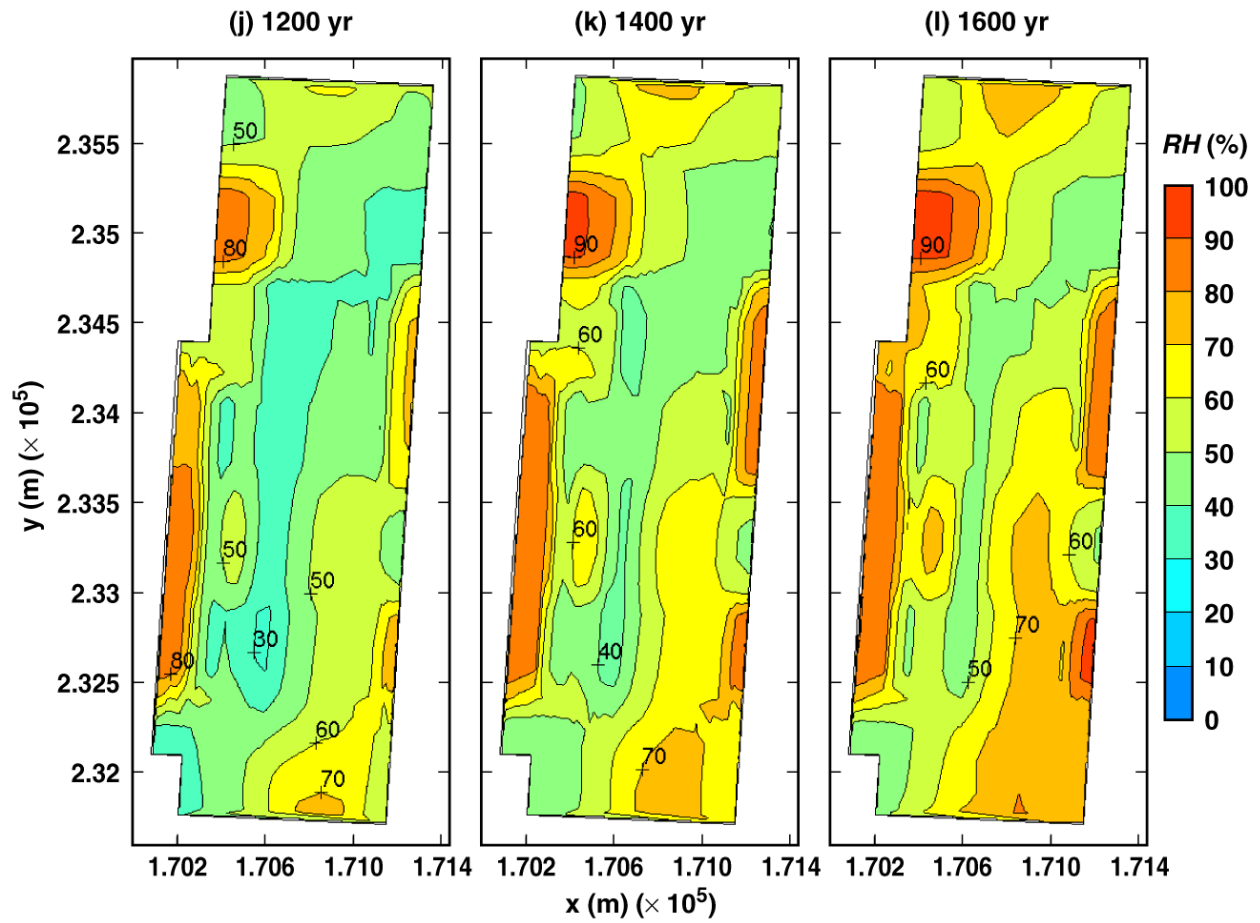
TB_AMR_lower_RH_wp_pwr2_25-36

Figure 6-18. Relative humidity on the surface of a 21-PWR WP for the low infiltration-flux case for the indicated times.



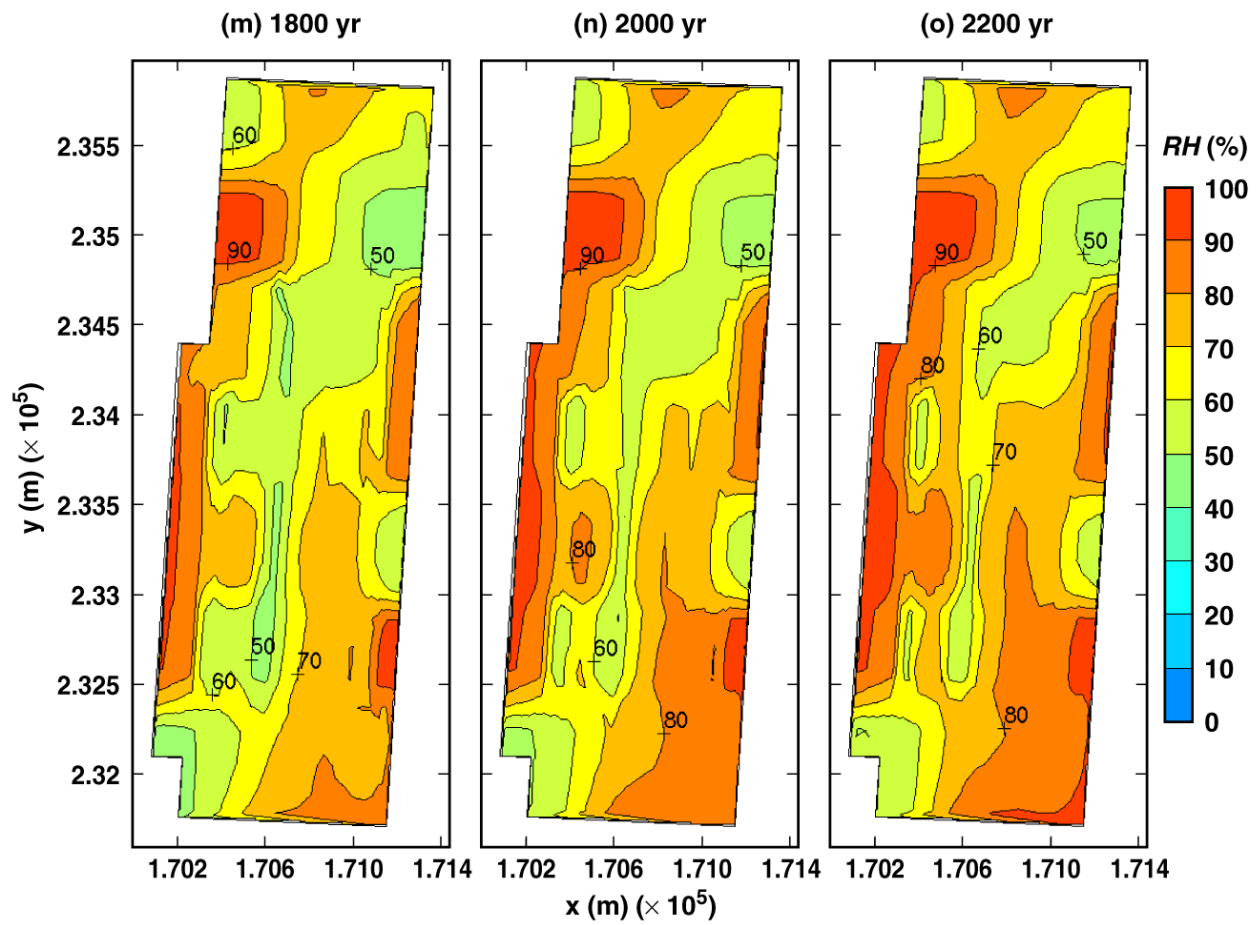
TB_AMR_lower_RH_wp_pwr2_77-219

Figure 6-18. Relative humidity on the surface of a 21-PWR WP for the low infiltration-flux case for the indicated times.



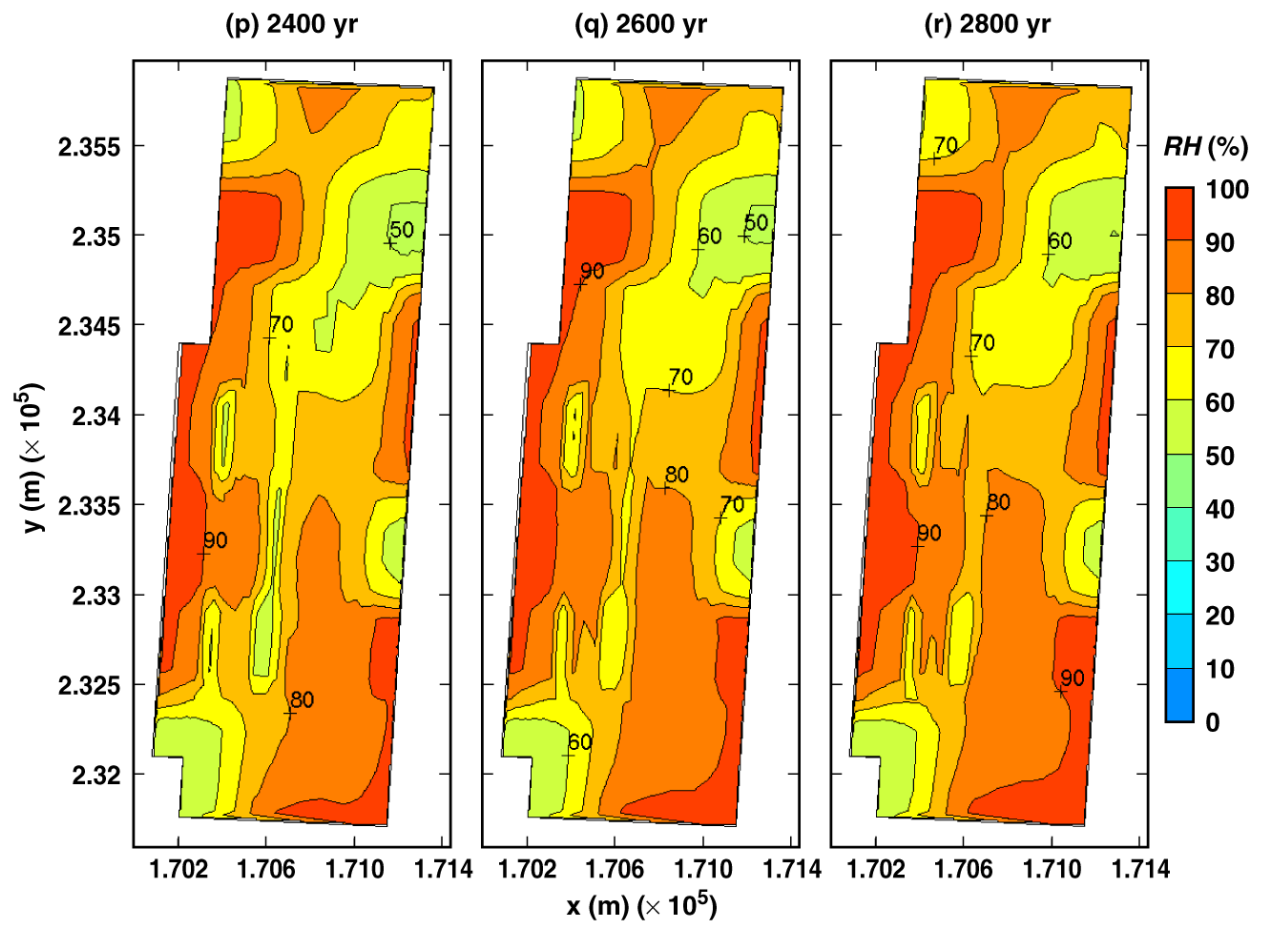
TB_AMR_lower_RH_wp_pwr2_246-286

Figure 6-18. Relative humidity on the surface of a 21-PWR WP for the low infiltration-flux case for the indicated times.



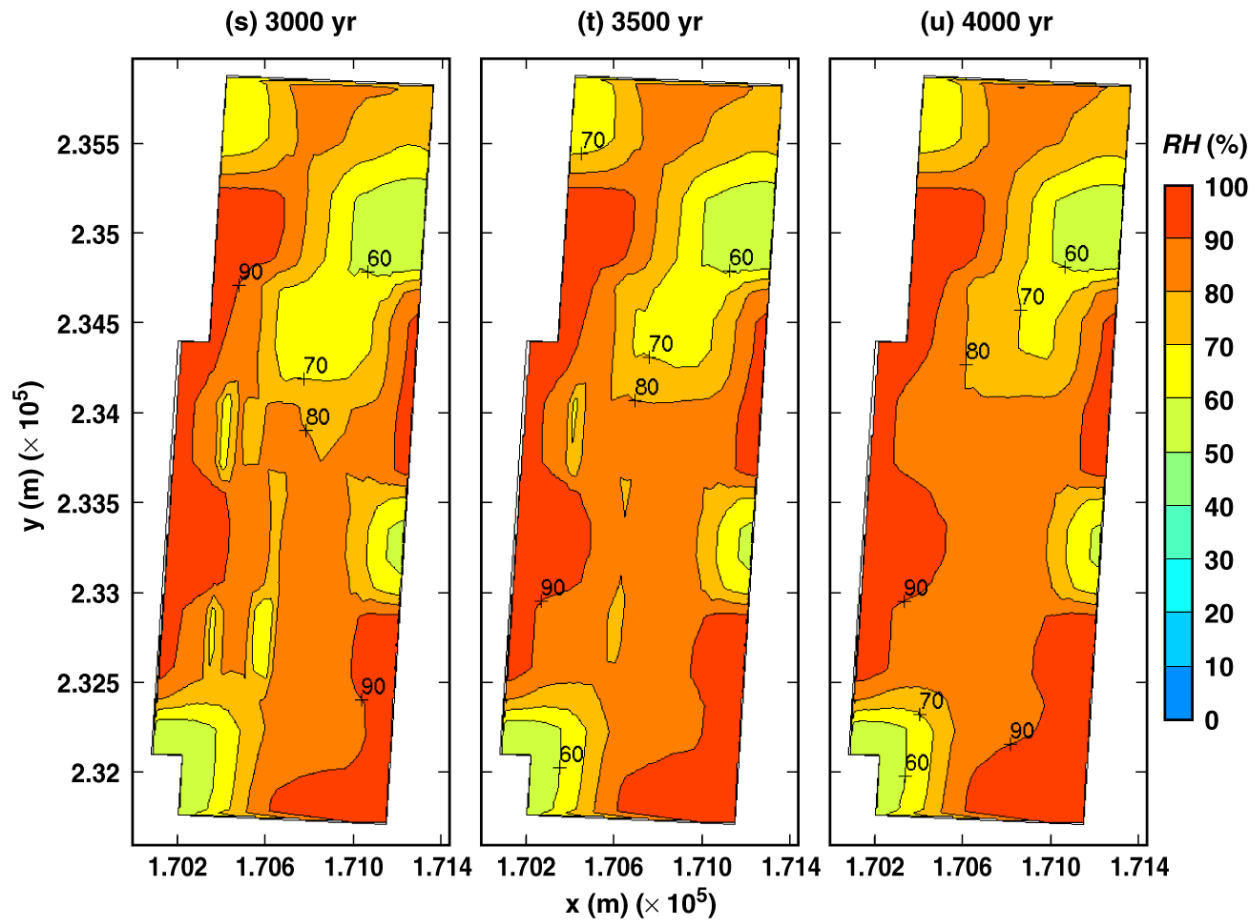
TB_AMR_lower_RH_wp_pwr2_305-335

Figure 6-18. Relative humidity on the surface of a 21-PWR WP for the low infiltration-flux case for the indicated times.



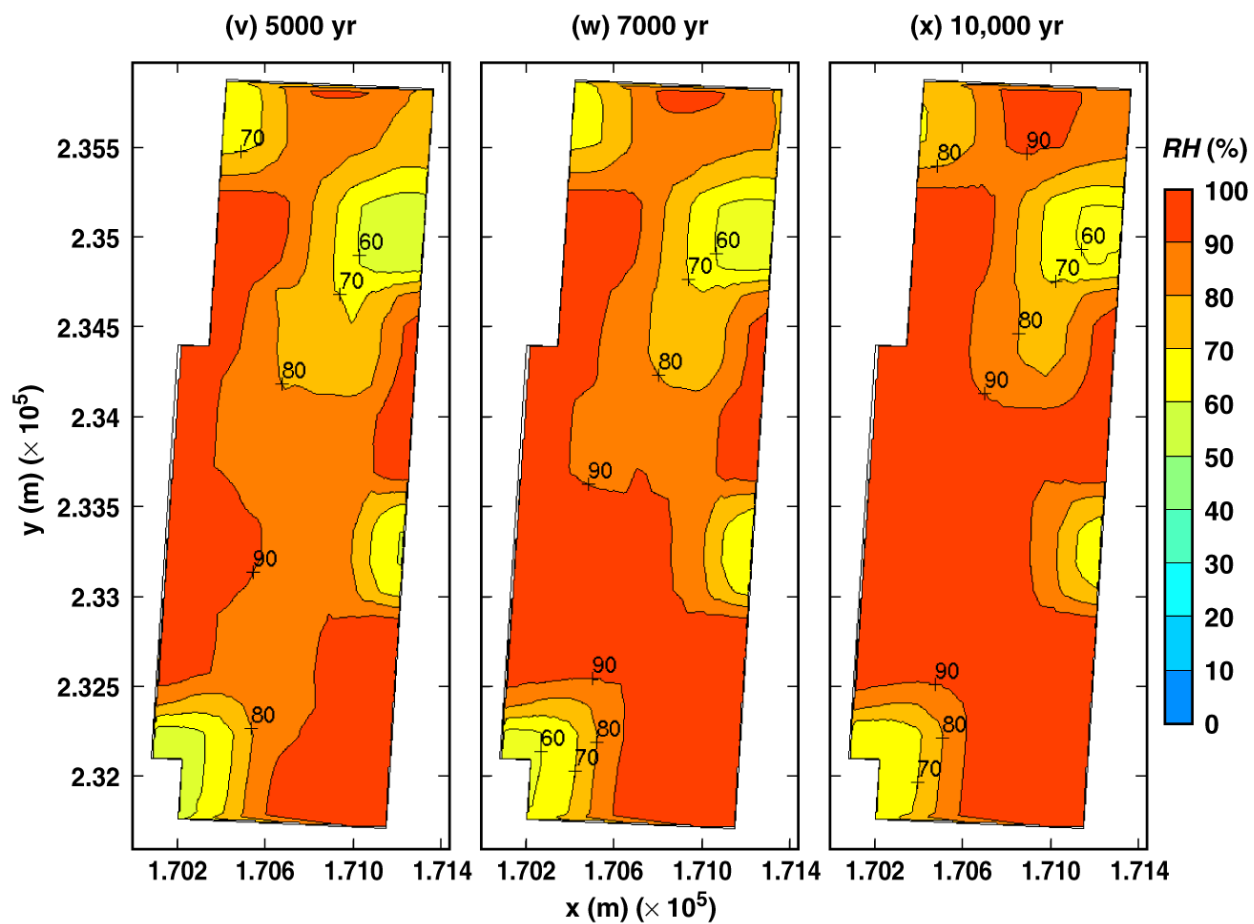
TB_AMR_lower_RH_wp_pwr2_343-351

Figure 6-18. Relative humidity on the surface of a 21-PWR WP for the low infiltration-flux case for the indicated times.



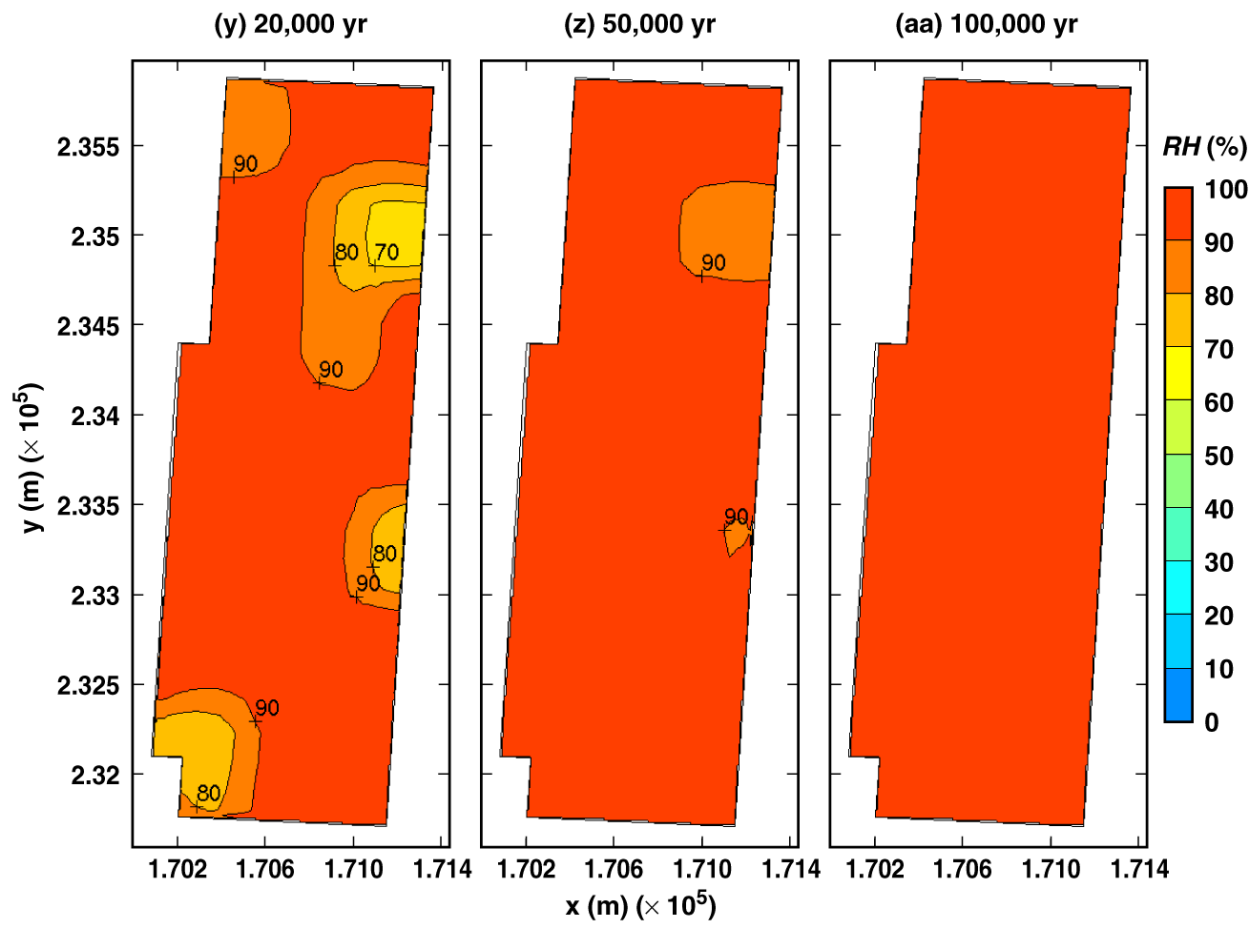
TB_AMR_lower_RH_wp_pwr2_355-372

Figure 6-18. Relative humidity on the surface of a 21-PWR WP for the low infiltration-flux case for the indicated times.



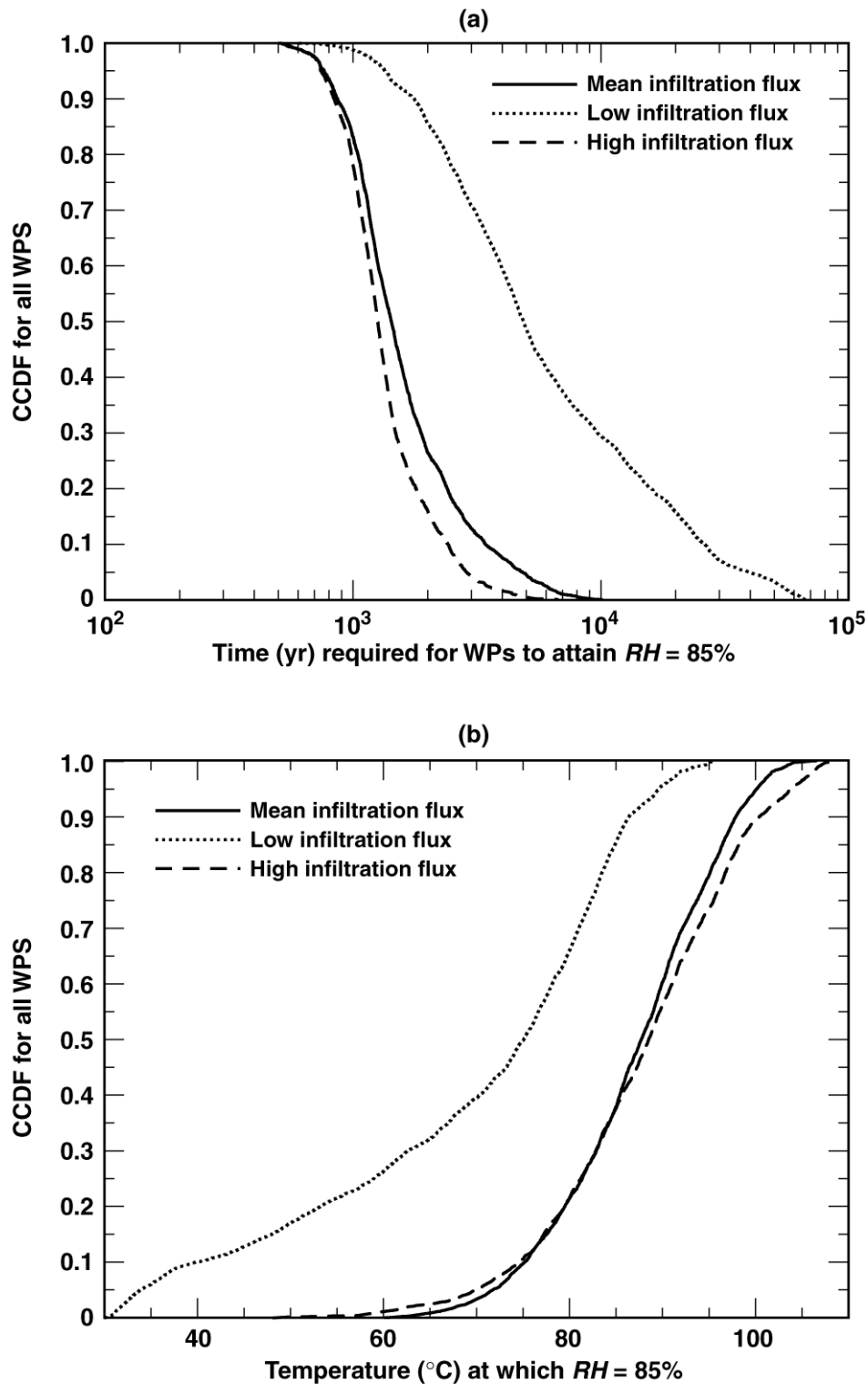
TB_AMR_lower_RH_wp_pwr2_390-402

Figure 6-18. Relative humidity on the surface of a 21-PWR WP for the low infiltration-flux case for the indicated times.



TB_AMR_lower_RH_wp_pwr2_411-434

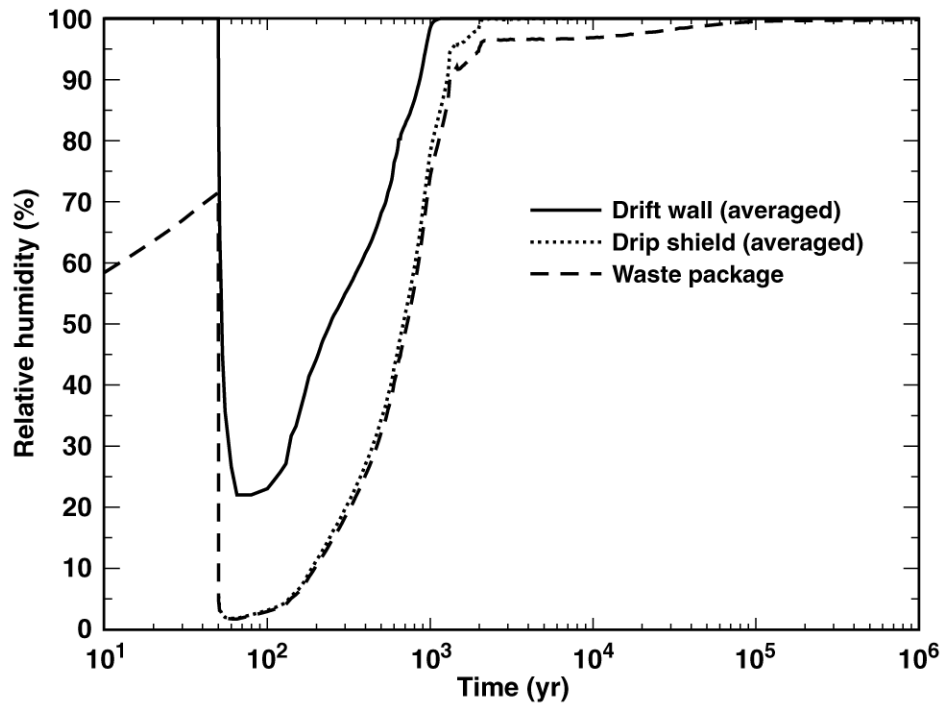
Figure 6-18. Relative humidity on the surface of a 21-PWR WP for the low infiltration-flux case for the indicated times.



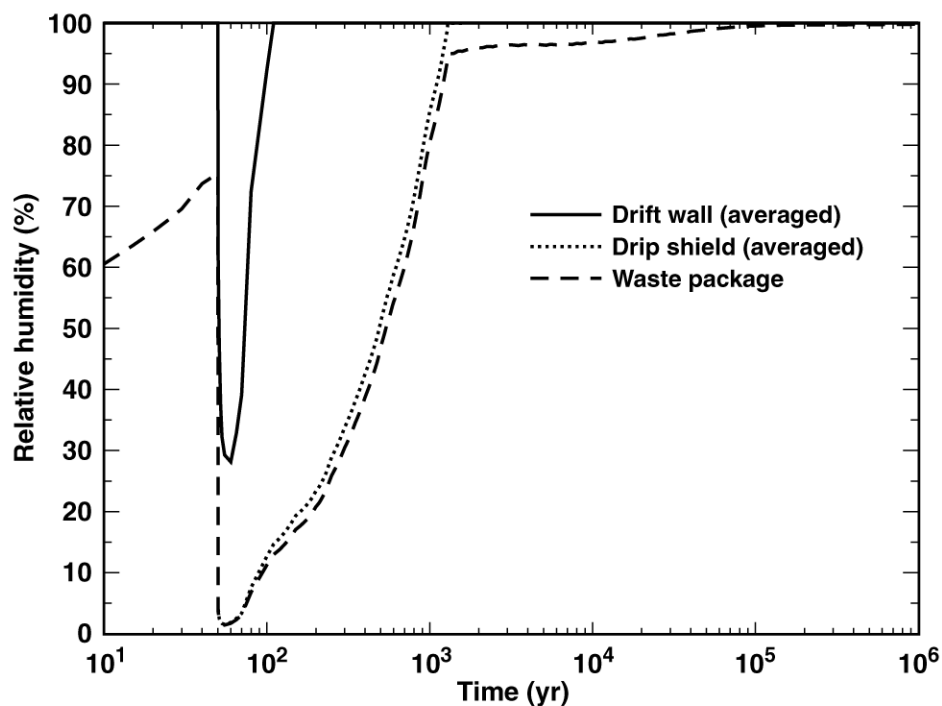
TB_AMR_CCDF_RH85_mlu

Figure 6-19. (a) The complementary cumulative distribution function (CCDF) for the time required to attain a relative humidity RH of 85% is plotted for the mean, high, and low infiltration-flux cases. CCDF of the WP temperature at which WPs reach an RH of 85% is plotted for the same cases.

(a) Center of Repository
Nevada State Coordinates: Easting = 170535.03 m, Northing = 233640.08 m



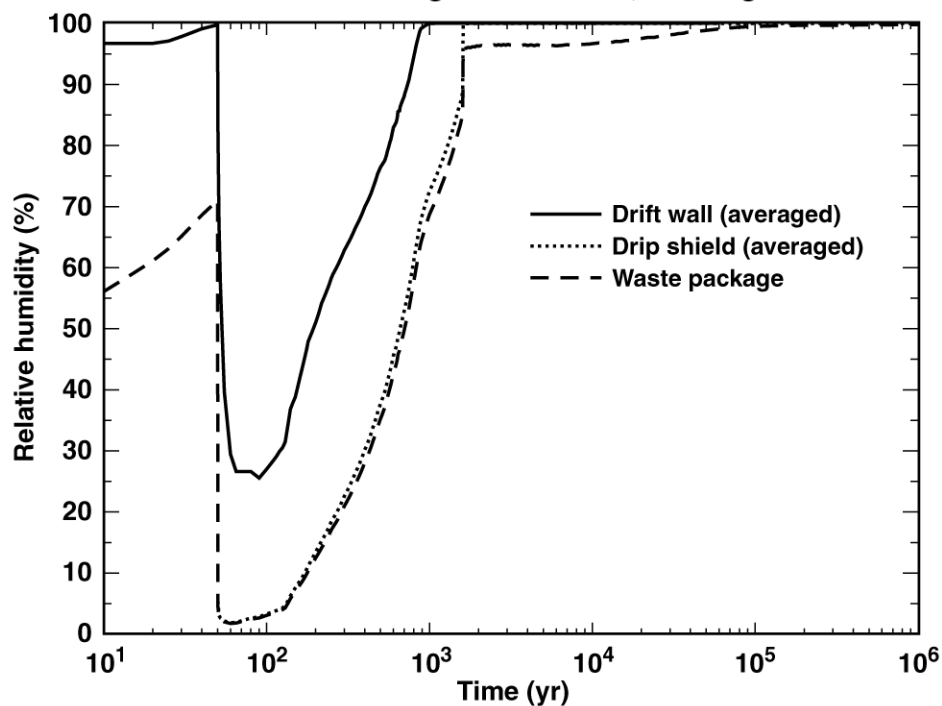
(b) Eastern Edge of Repository
Nevada State Coordinates: Easting = 171195.16 m, Northing = 233605.06 m



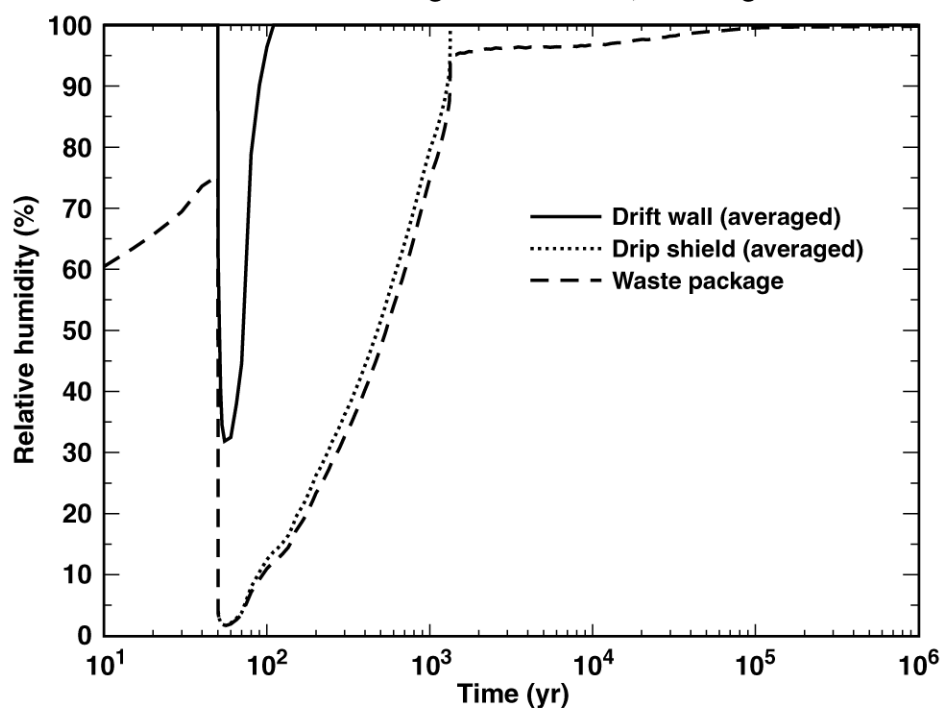
TB_AMR_RH_pwr2_13&24_mean

Figure 6-20. Relative humidity history on the surface of a 21-PWR WP for the mean infiltration-flux case at (a) the geographical center of the repository and (b) a location 27.5 m from the eastern edge of the repository. Note that the Nevada State coordinates are given.

(a) Center of Repository
Nevada State Coordinates: Easting = 170535.03 m, Northing = 233640.08 m



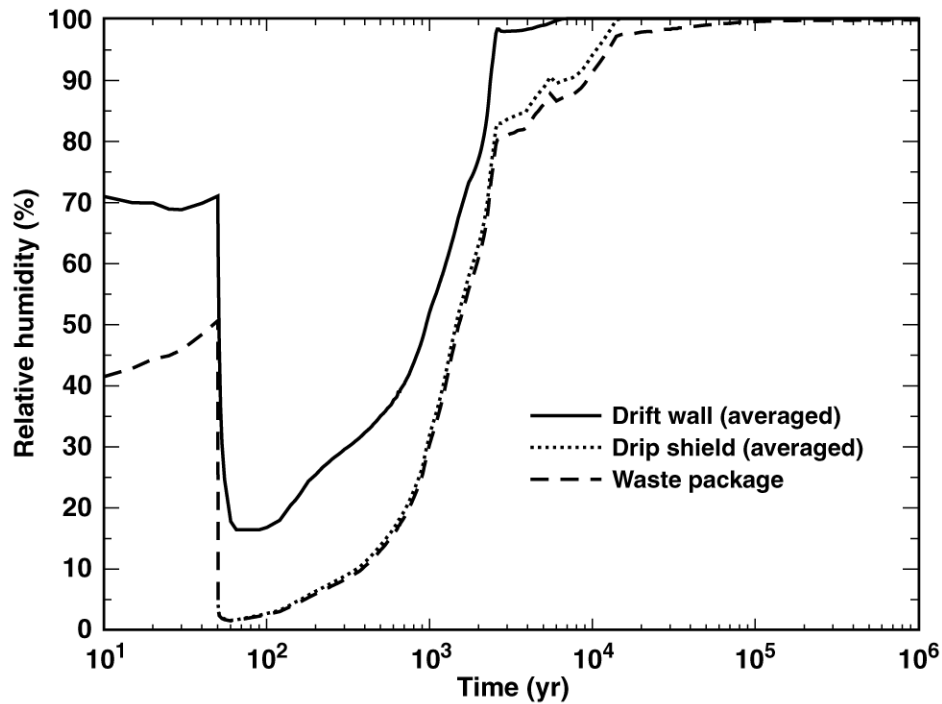
(b) Eastern Edge of Repository
Nevada State Coordinates: Easting = 171195.16 m, Northing = 233605.06 m



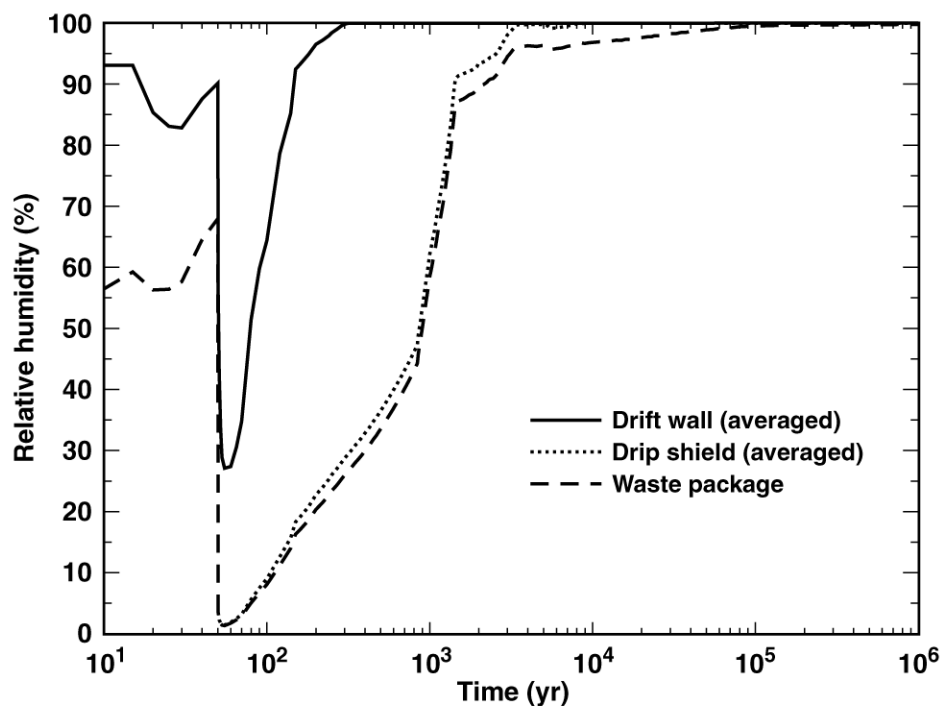
TB_AMR_RH_pwr2_13&24_17_upper

Figure 6-21. Relative humidity history on the surface of a 21-PWR WP for the high infiltration-flux case at (a) the geographical center of the repository and (b) a location 27.5 m from the eastern edge of the repository. Note that the Nevada State coordinates are given.

(a) Center of Repository
Nevada State Coordinates: Easting = 170535.03 m, Northing = 233640.08 m

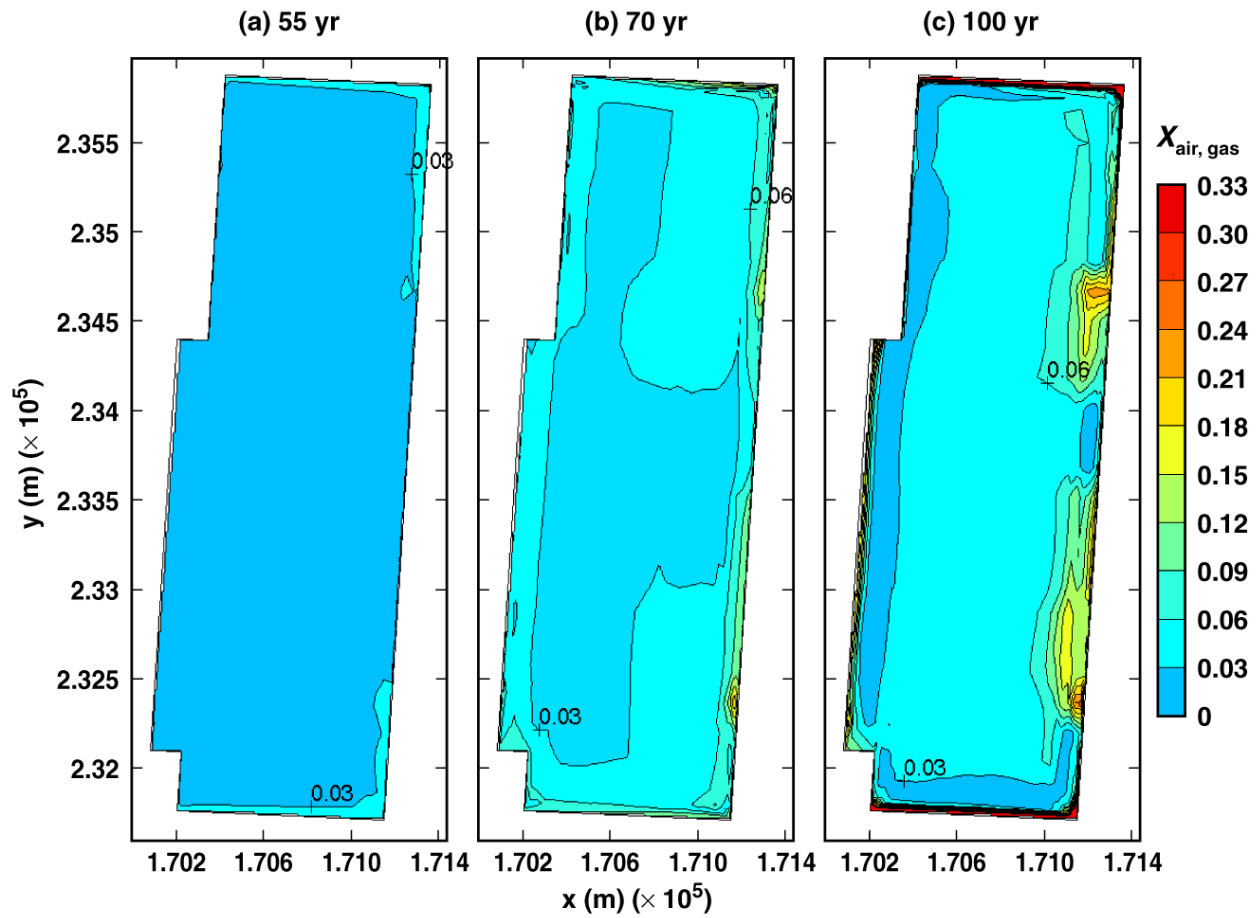


(b) Eastern Edge of Repository
Nevada State Coordinates: Easting = 171195.16 m, Northing = 233605.06 m



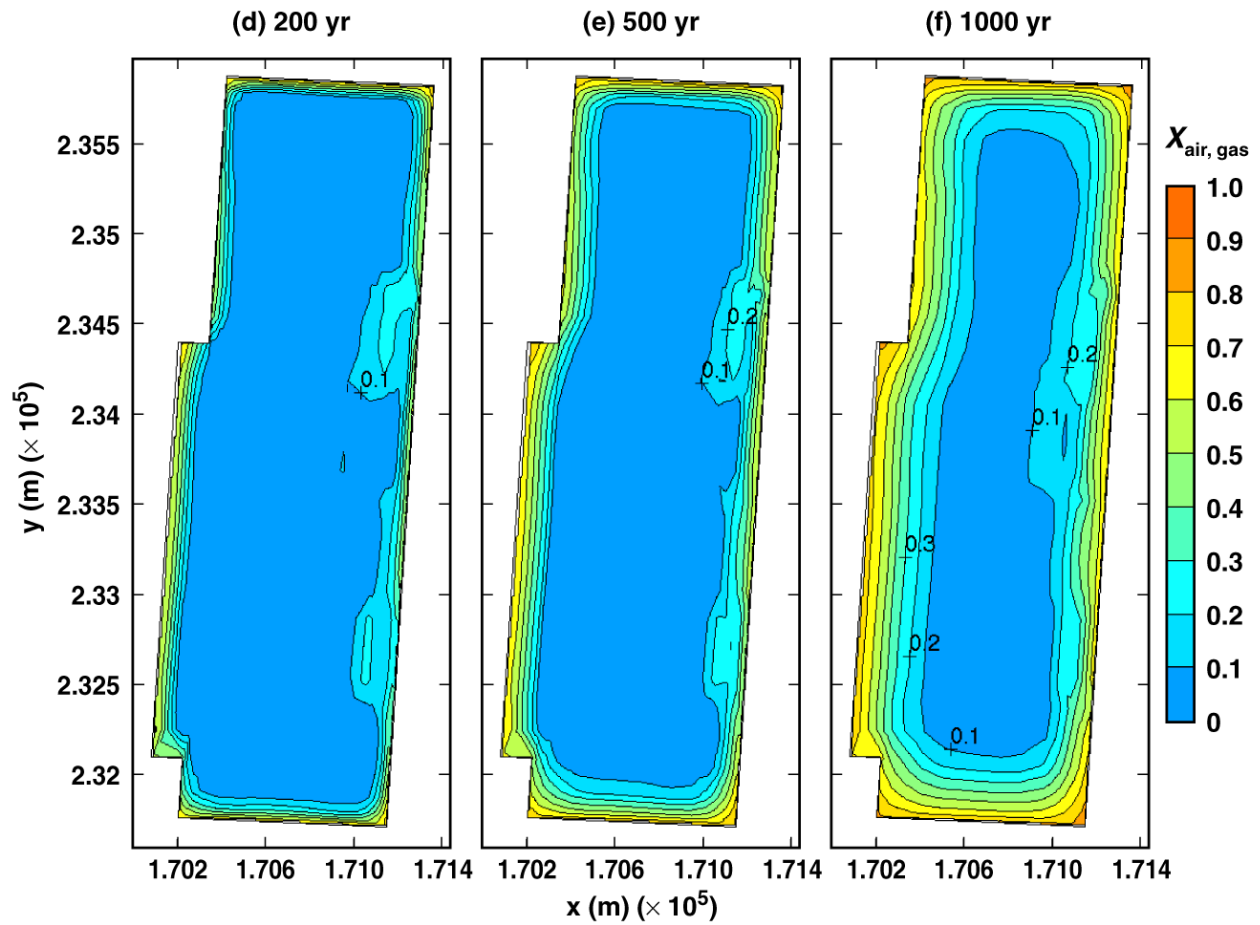
TB_AMR_RH_pwr2_13&24_17_lower

Figure 6-22. Relative humidity history on the surface of a 21-PWR WP for the low infiltration-flux case at (a) the geographical center of the repository and (b) a location 27.5 m from the eastern edge of the repository. Note that the Nevada State coordinates are given.



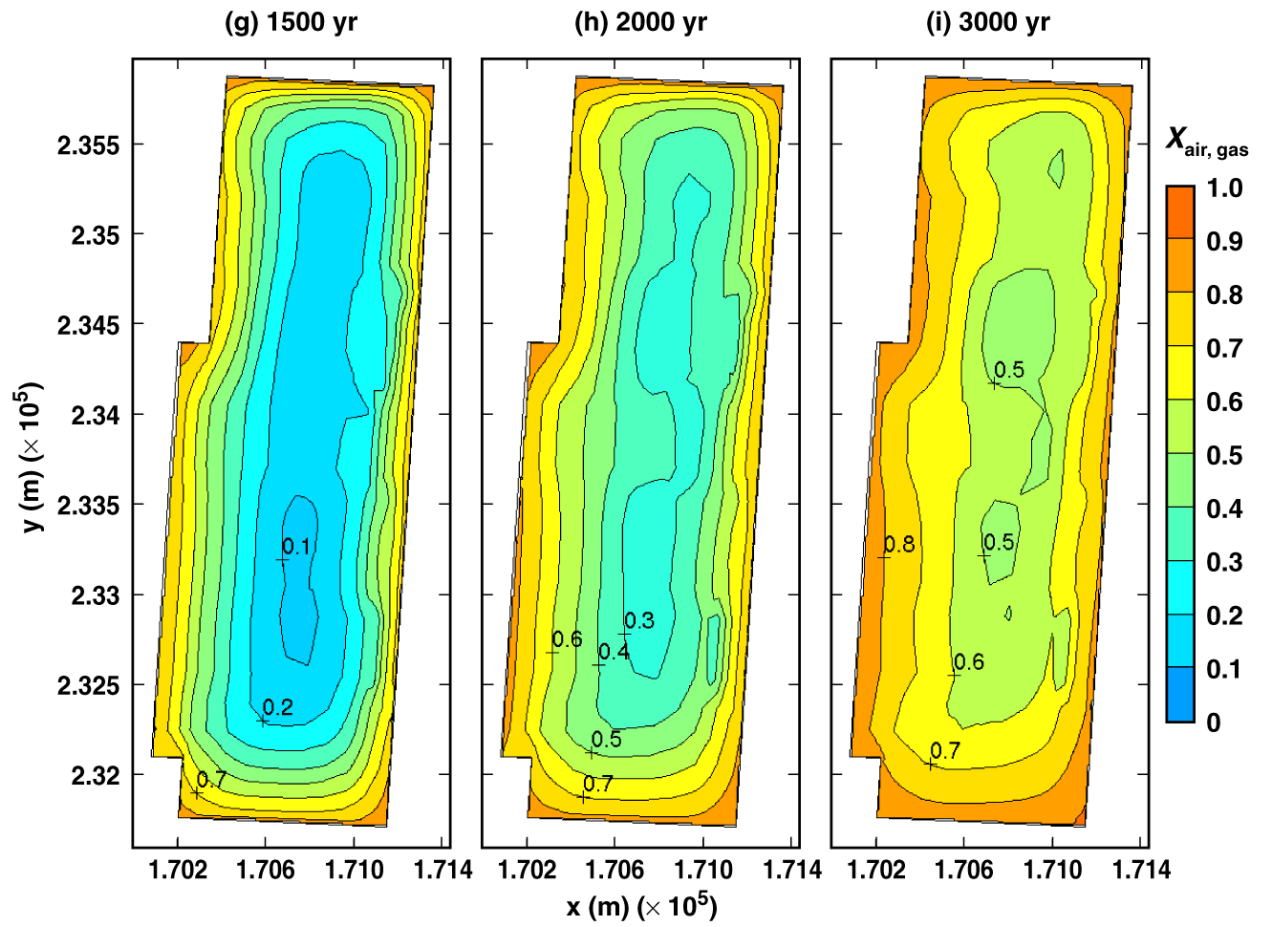
TB_AMR_mean_Xair_ds_pwr2_16-21

Figure 6-23. Gas-phase air-mass fraction averaged over the perimeter of the dripshield at the location of a 21-PWR WP for the mean infiltration-flux case for the indicated times.



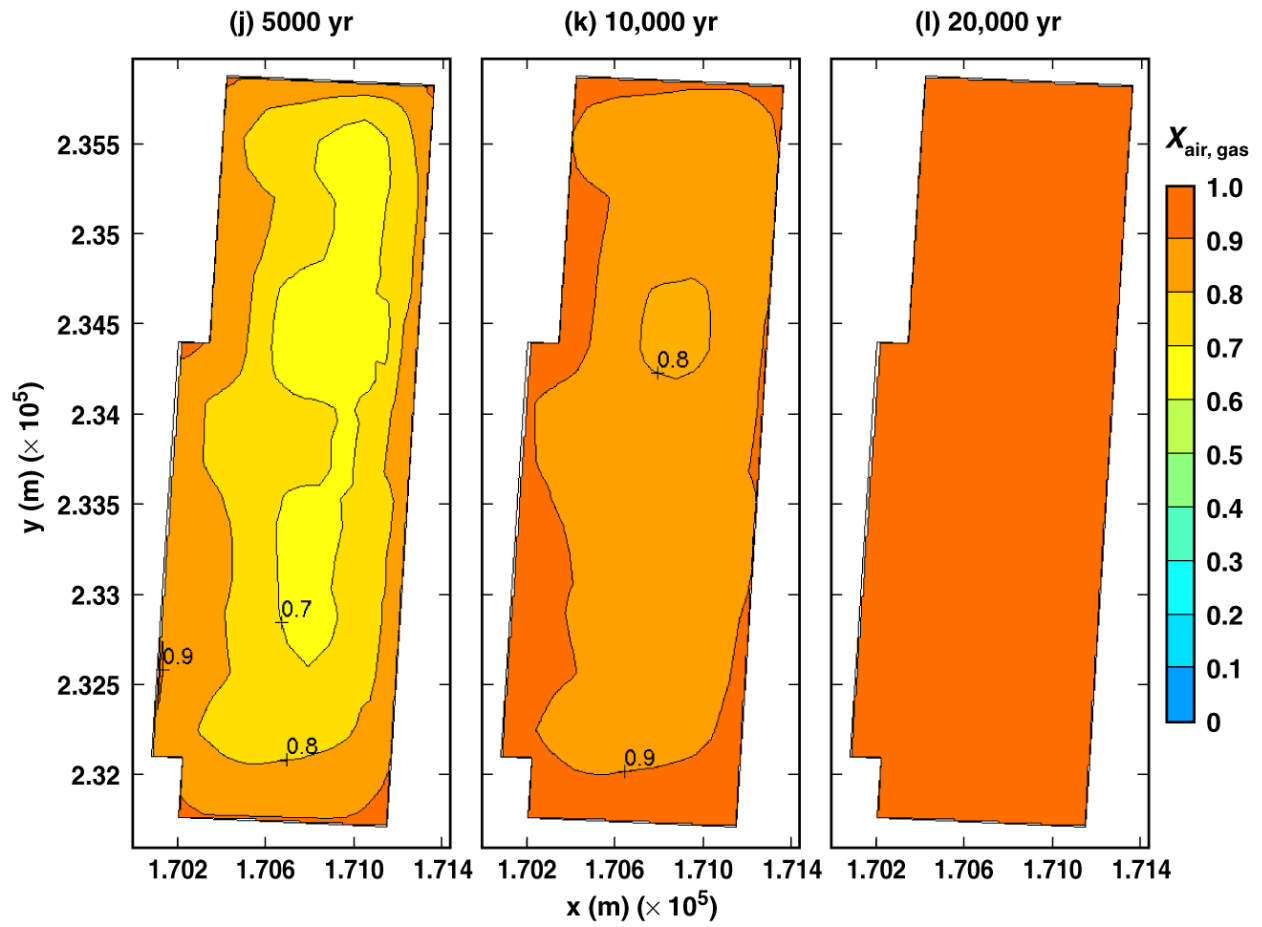
TB_AMR_mean_Xair_ds_pwr2_31-174

Figure 6-23. Gas-phase air-mass fraction averaged over the perimeter of the dripshield at the location of a 21-PWR WP for the mean infiltration-flux case for the indicated times.



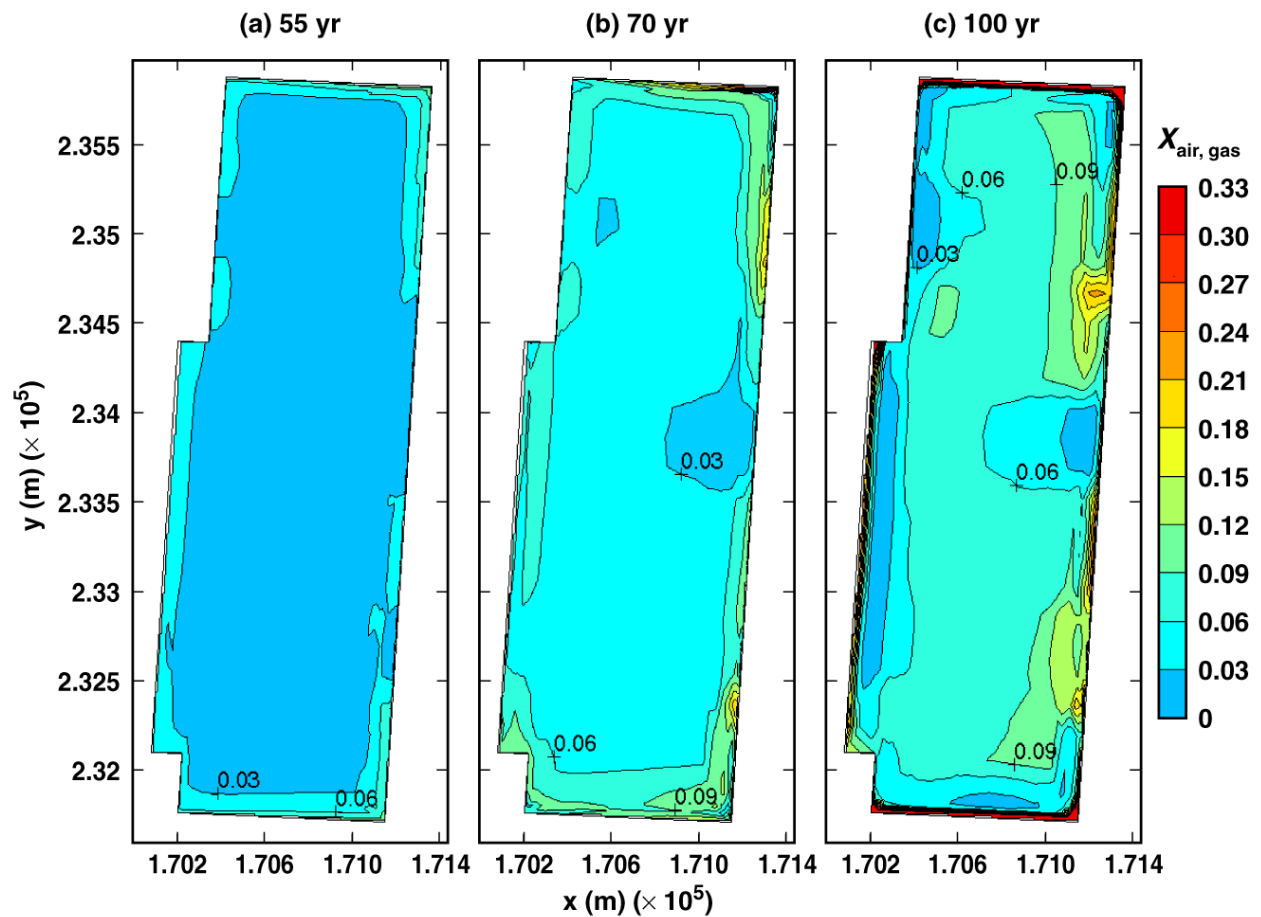
TB_AMR_mean_Xair_ds_pwr2_225-283

Figure 6-23. Gas-phase air-mass fraction averaged over the perimeter of the dripshield at the location of a 21-PWR WP for the mean infiltration-flux case for the indicated times.



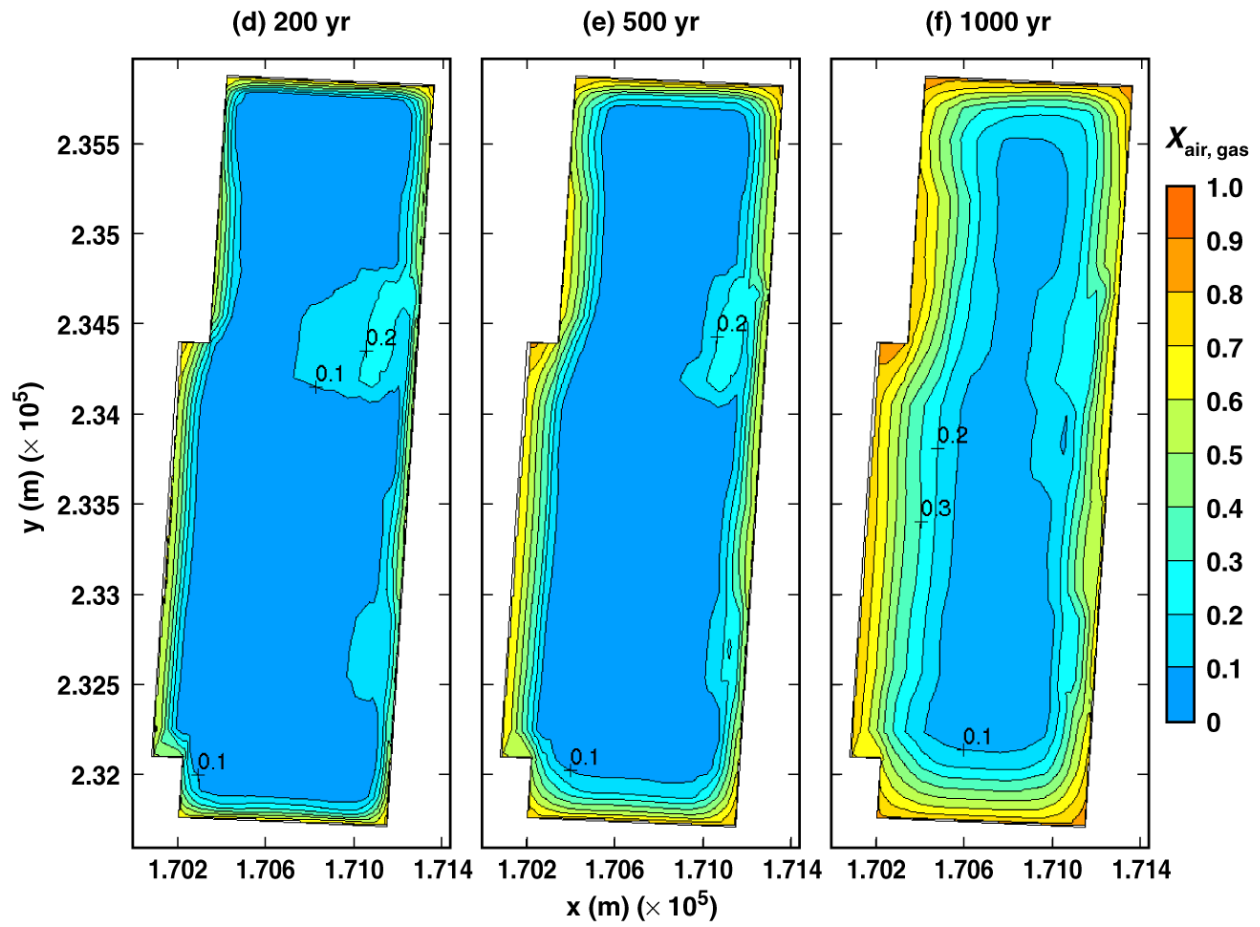
TB_AMR_mean_Xair_ds_pwr2_307-330

Figure 6-23. Gas-phase air-mass fraction averaged over the perimeter of the dripshield at the location of a 21-PWR WP for the mean infiltration-flux case for the indicated times.



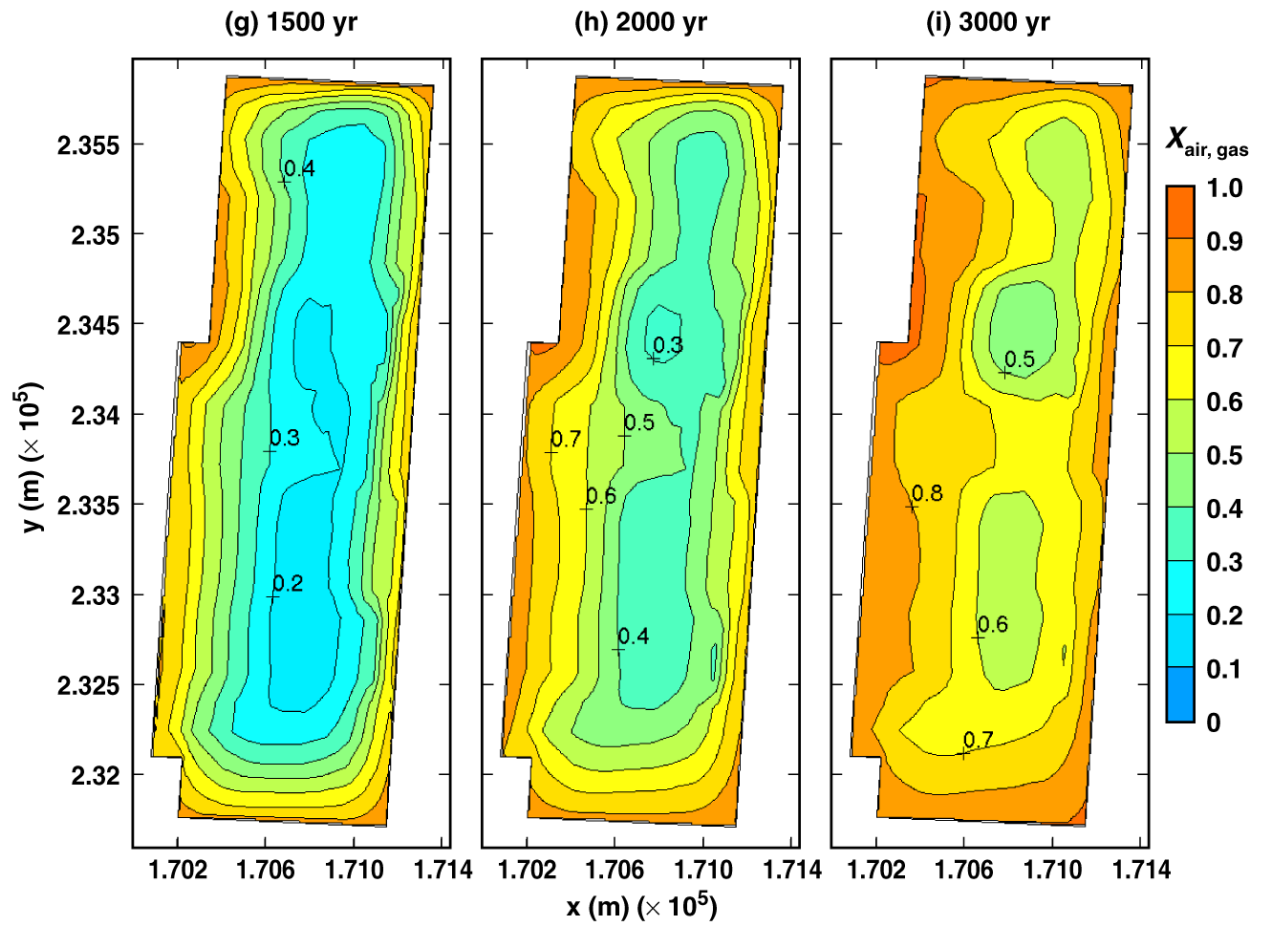
TB_AMR_upper_Xair_ds_pwr2_16-22

Figure 6-24. Gas-phase air-mass fraction averaged over the perimeter of the dripshield at the location of a 21-PWR WP for the high infiltration-flux case for the indicated times.



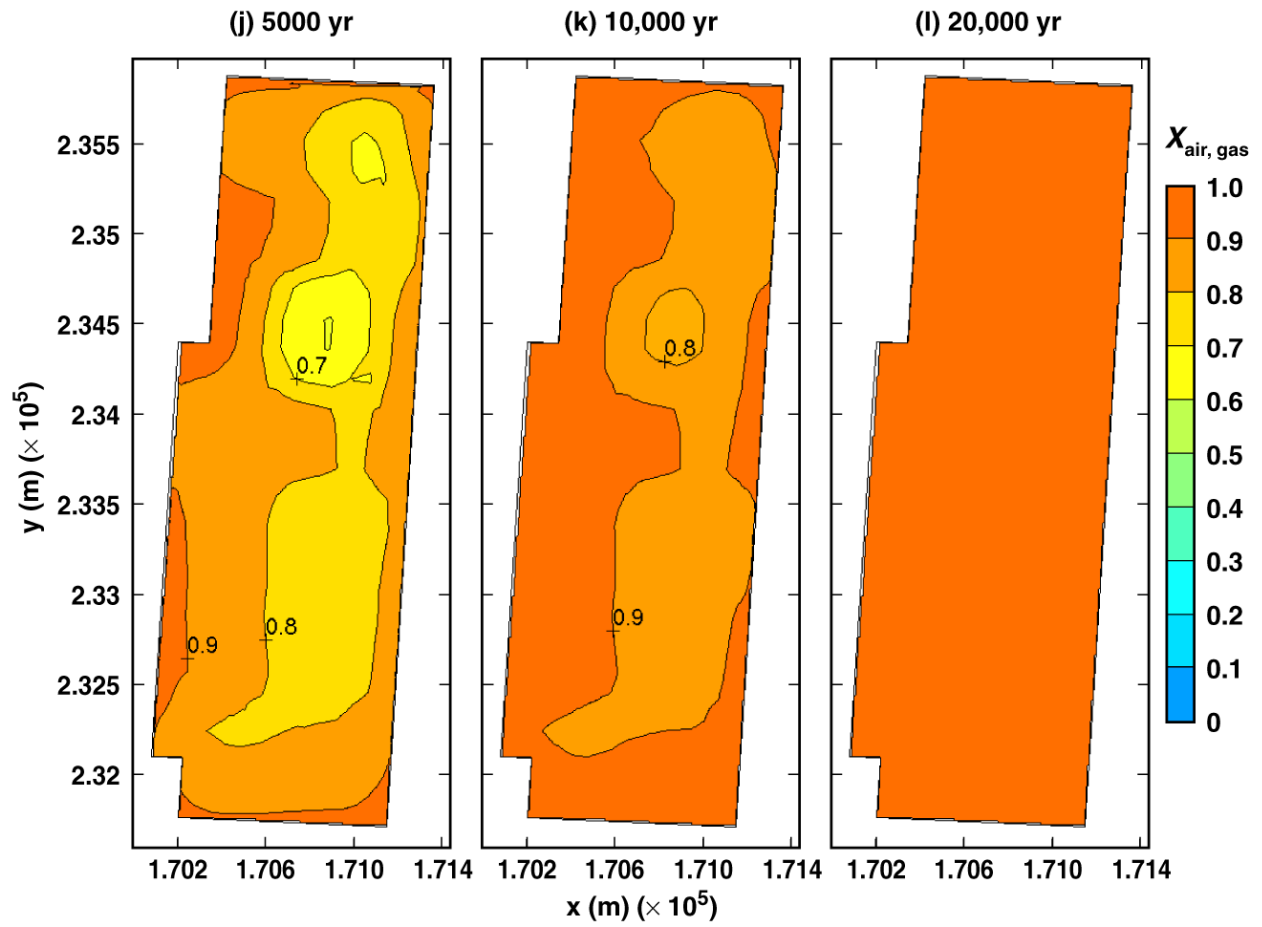
TB_AMR_upper_Xair_ds_pwr2_56-269

Figure 6-24. Gas-phase air-mass fraction averaged over the perimeter of the dripshield at the location of a 21-PWR WP for the high infiltration-flux case for the indicated times.



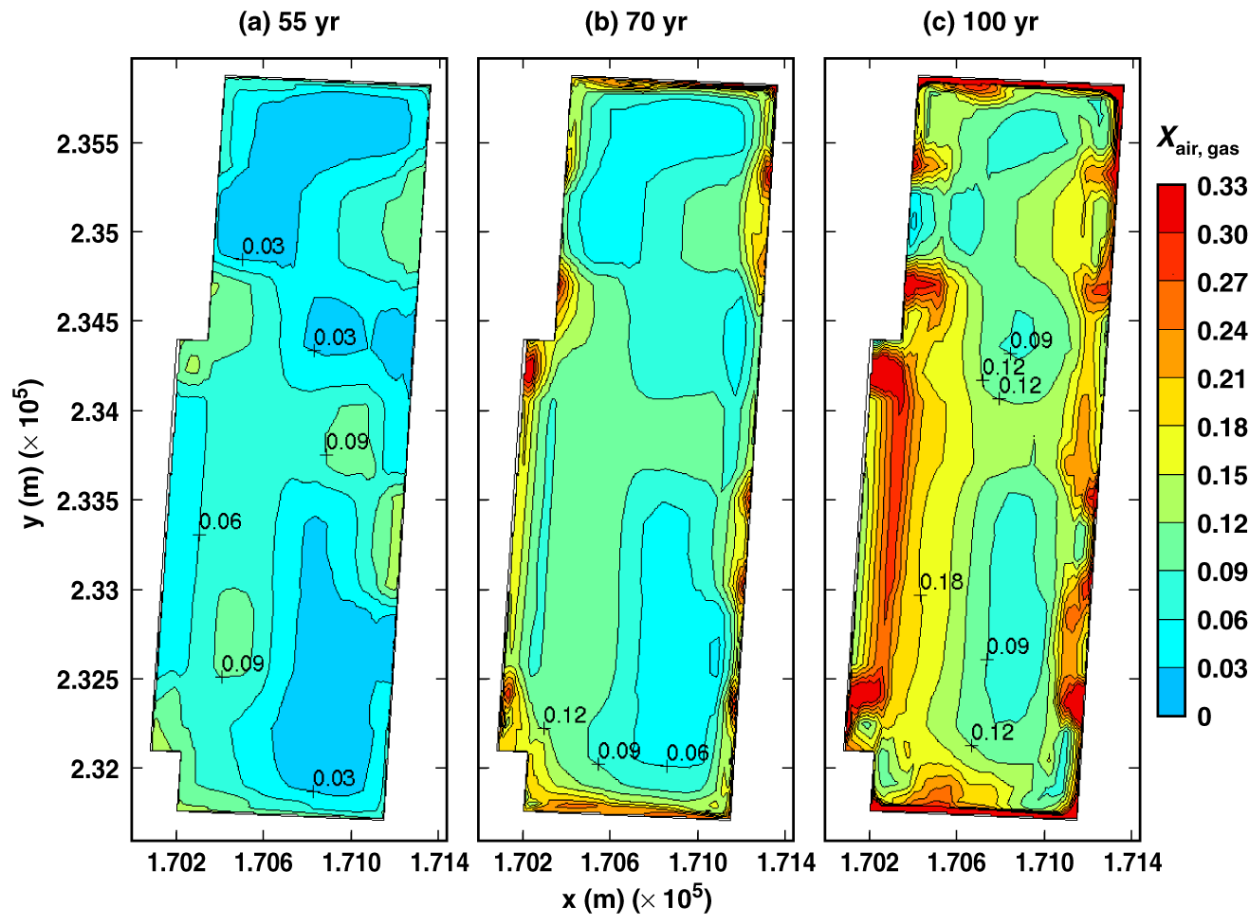
TB_AMR_upper_Xair_ds_pwr2_319-389

Figure 6-24. Gas-phase air-mass fraction averaged over the perimeter of the dripshield at the location of a 21-PWR WP for the high infiltration-flux case for the indicated times.



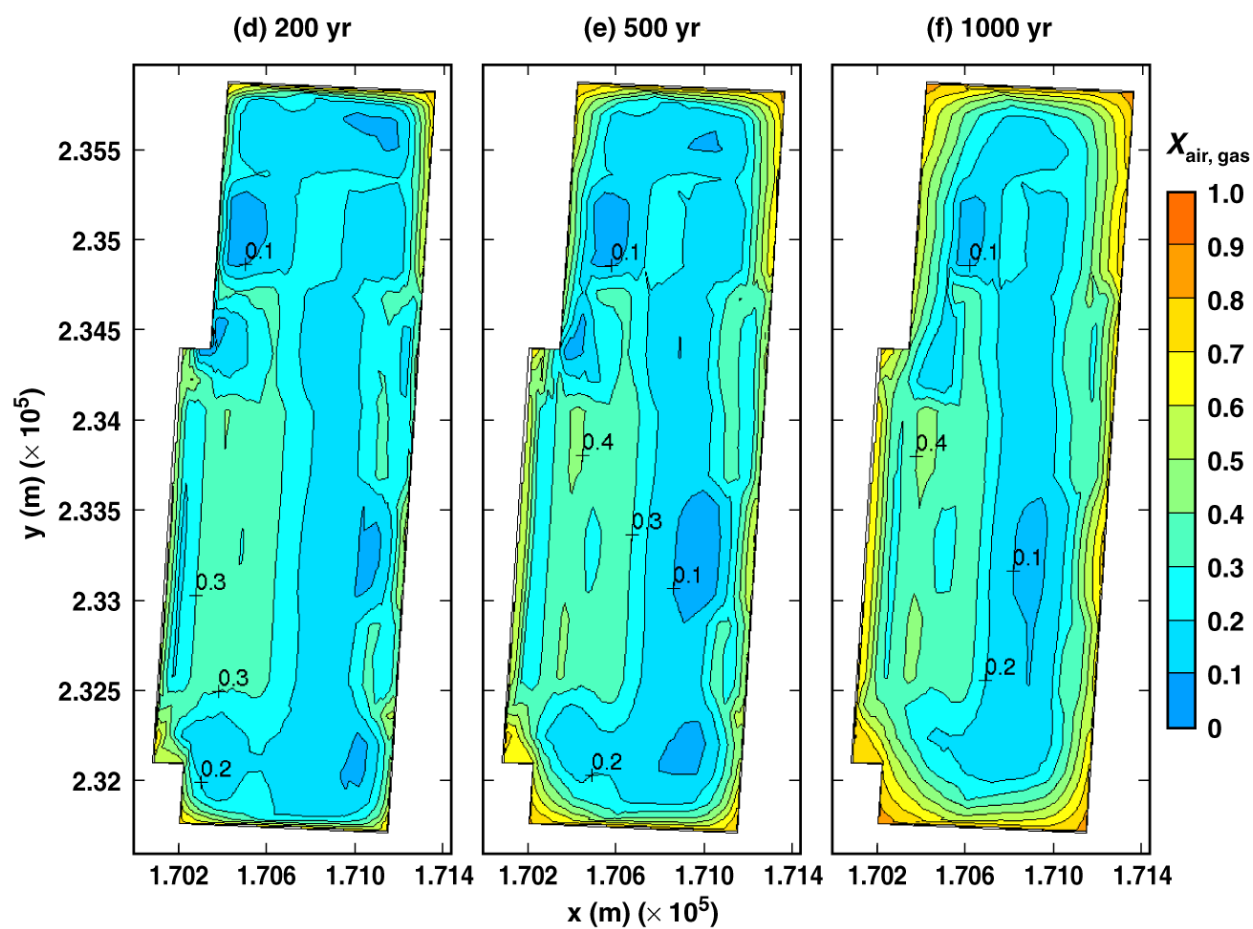
TB_AMR_upper_Xair_ds_pwr2_413-434

Figure 6-24. Gas-phase air-mass fraction averaged over the perimeter of the dripshield at the location of a 21-PWR WP for the high infiltration-flux case for the indicated times.



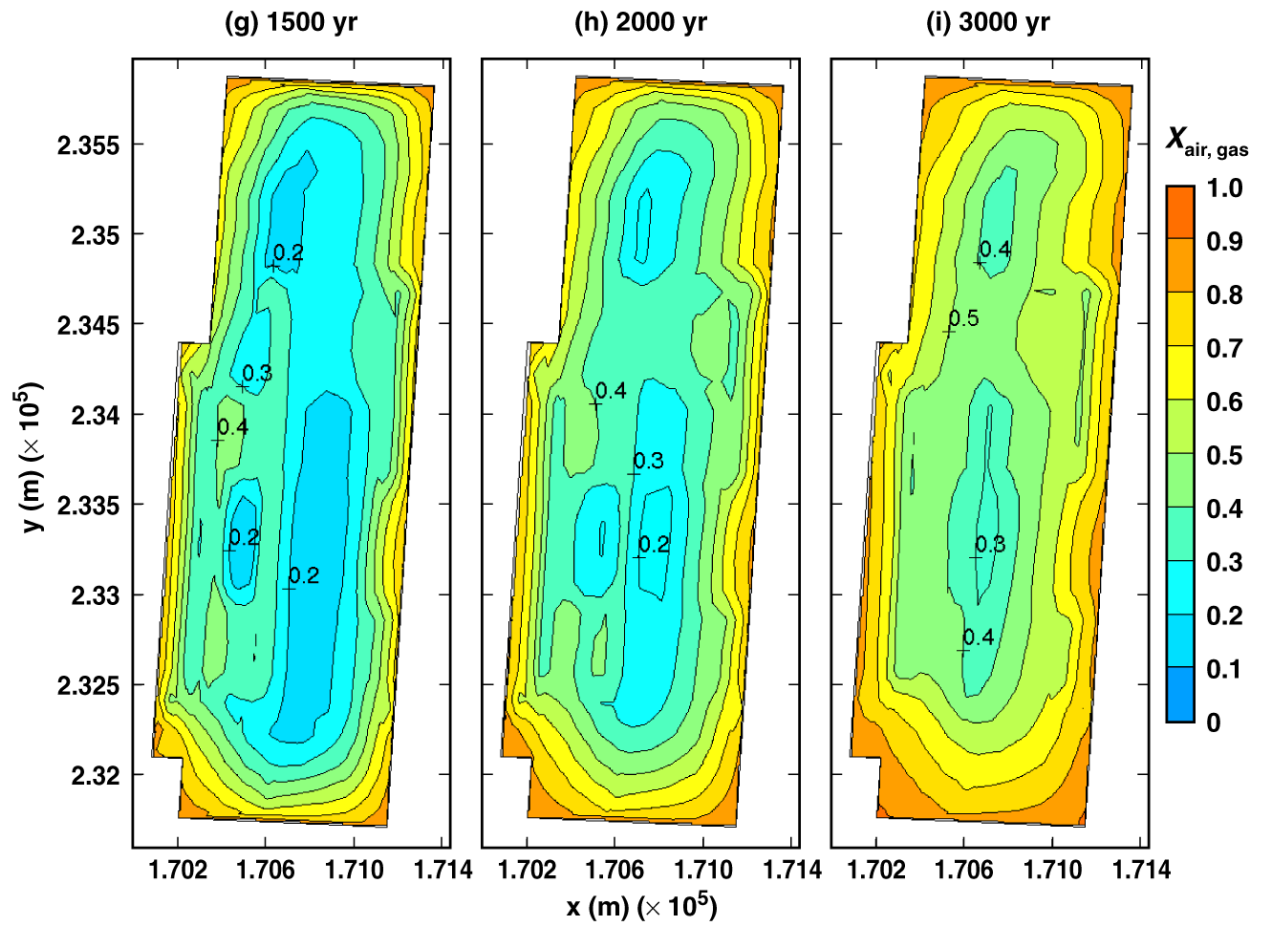
TB_AMR_lower_Xair_ds_pwr2_16-22

Figure 6-25. Gas-phase air-mass fraction averaged over the perimeter of the dripshield at the location of a 21-PWR WP for the low infiltration-flux case for the indicated times.



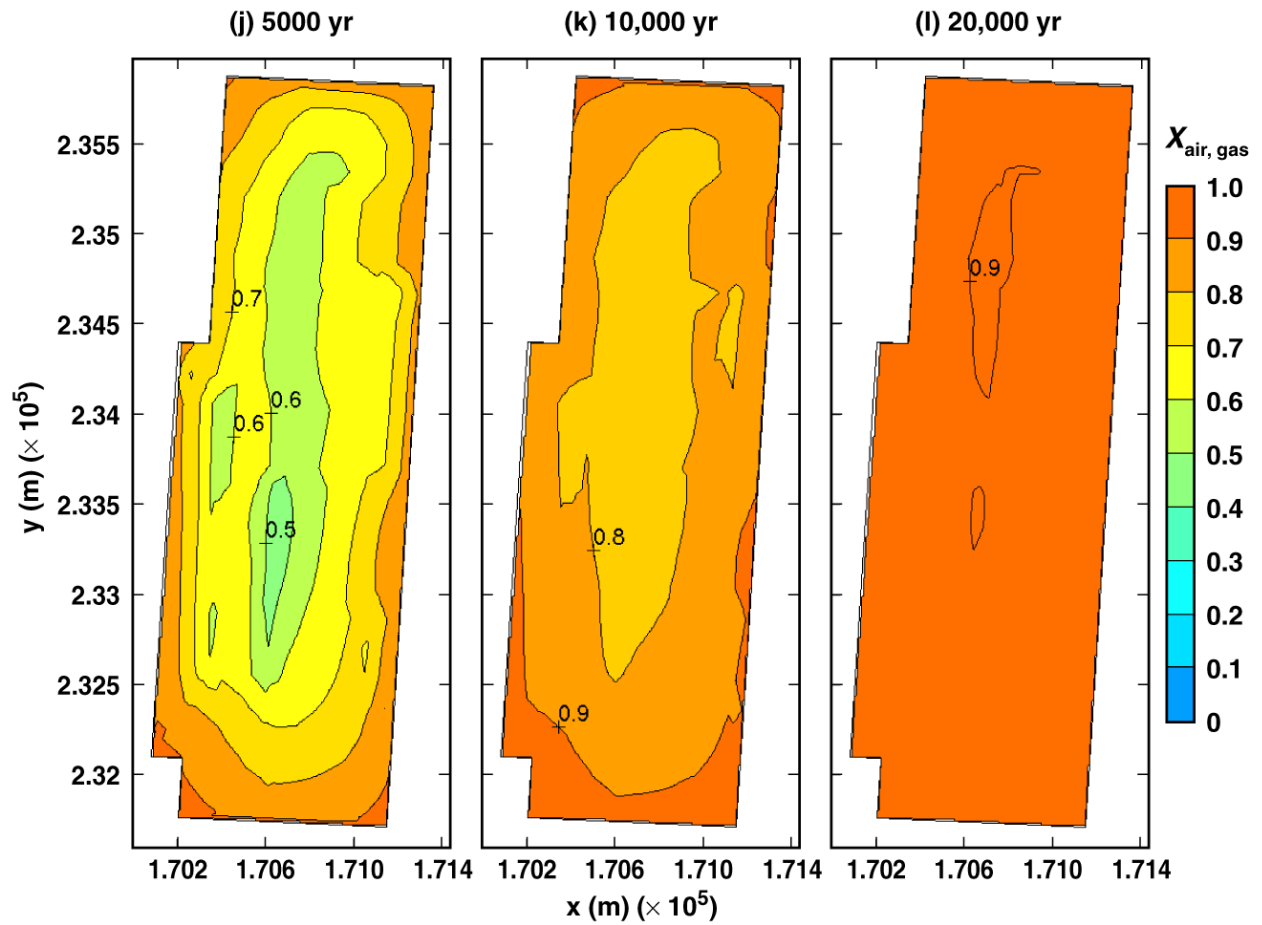
TB_AMR_lower_Xair_ds_pwr2_28-219

Figure 6-25. Gas-phase air-mass fraction averaged over the perimeter of the dripshield at the location of a 21-PWR WP for the low infiltration-flux case for the indicated times.



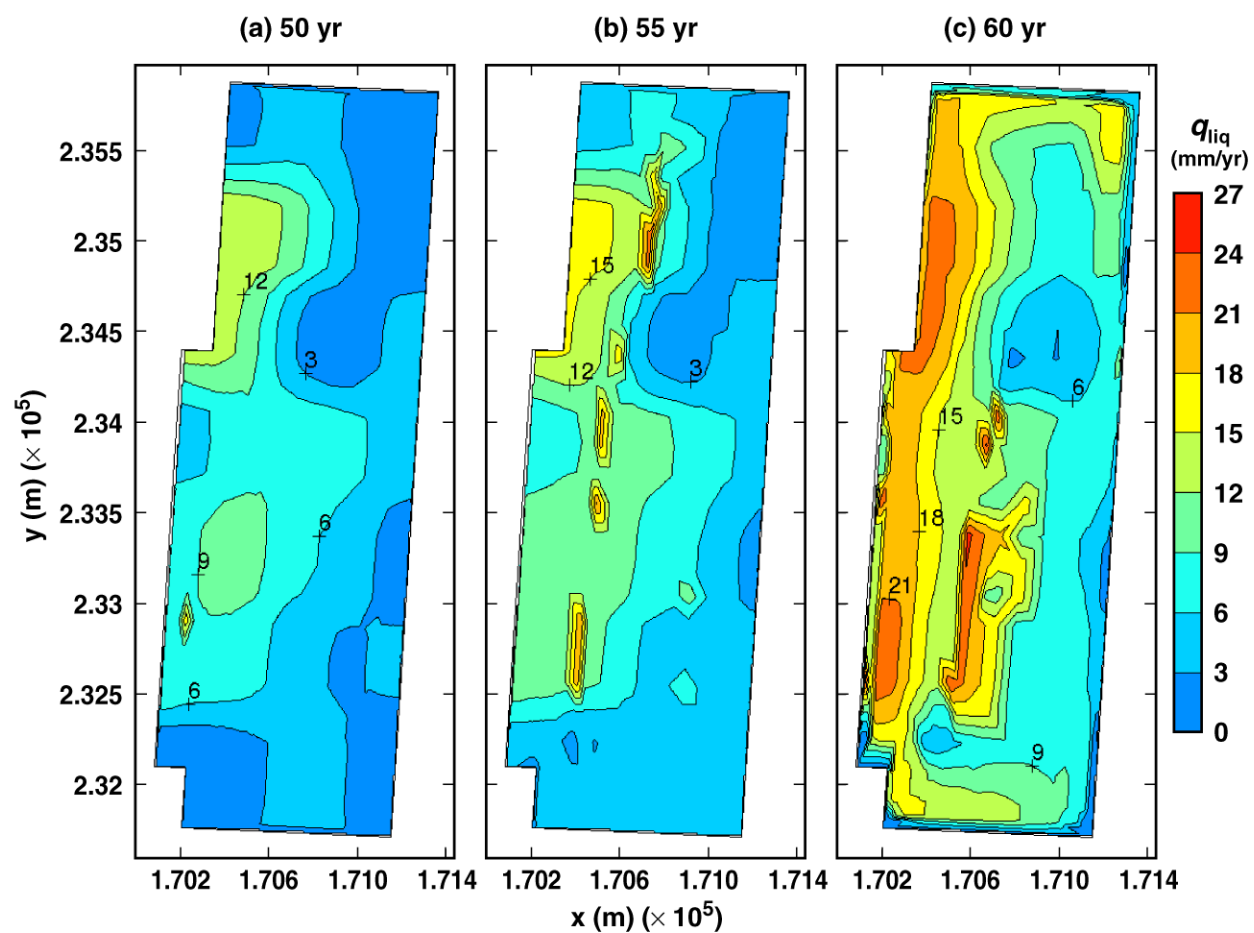
TB_AMR_lower_Xair_ds_pwr2_276-355

Figure 6-25. Gas-phase air-mass fraction averaged over the perimeter of the dripshield at the location of a 21-PWR WP for the low infiltration-flux case for the indicated times.



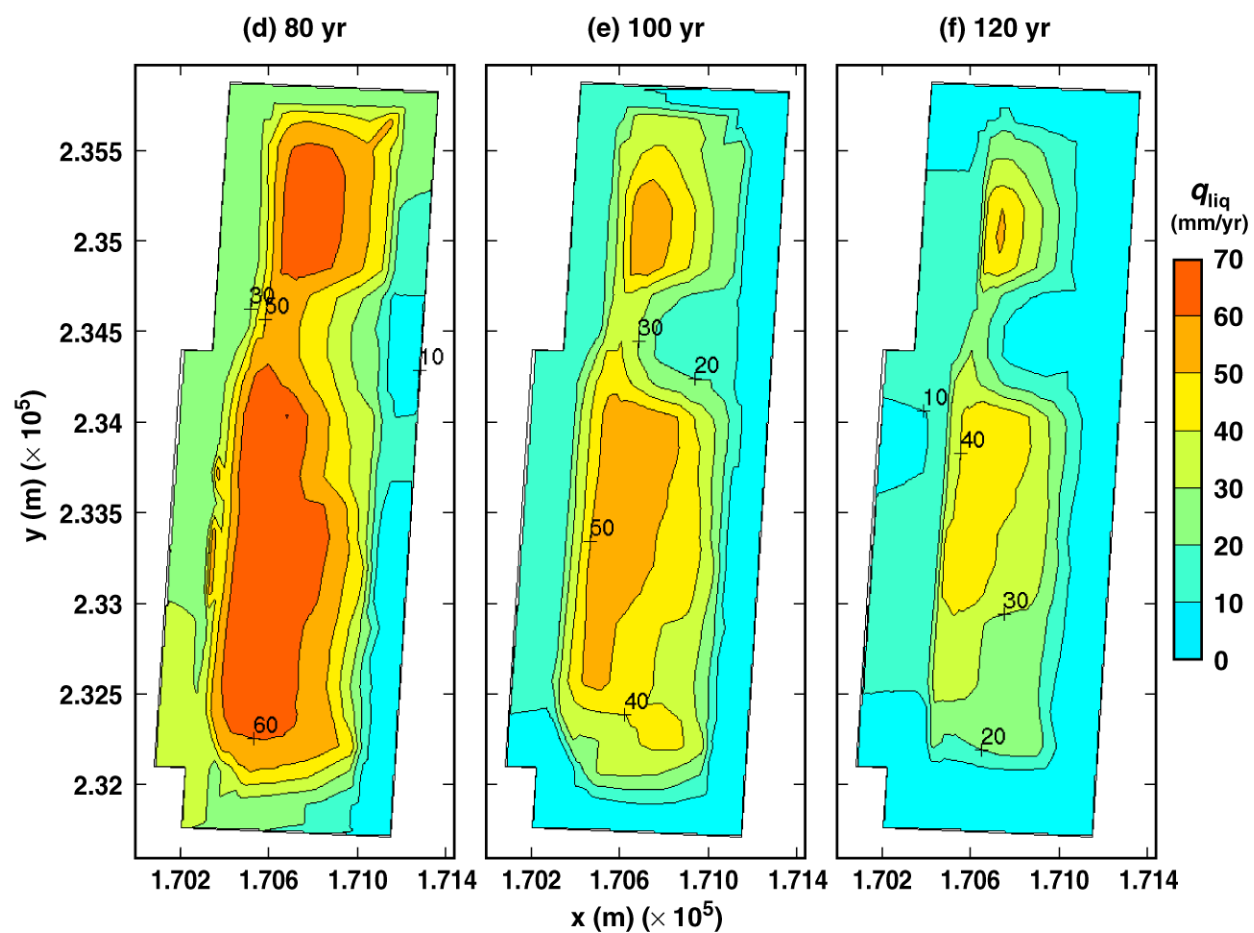
TB_AMR_lower_Xair_ds_pwr2_390-402

Figure 6-25. Gas-phase air-mass fraction averaged over the perimeter of the dripshield at the location of a 21-PWR WP for the low infiltration-flux case for the indicated times.



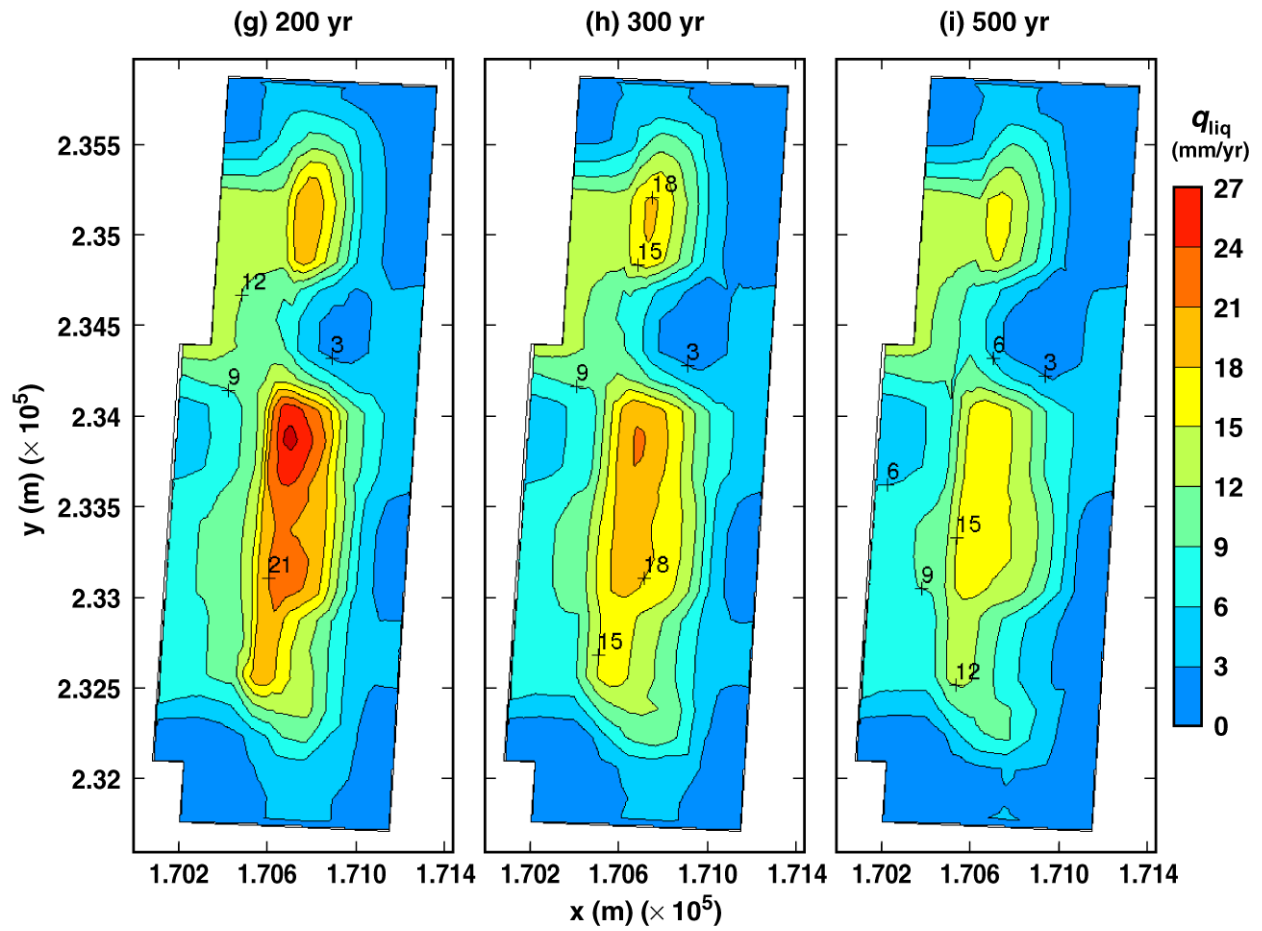
TB_AMR_mean_qliq_5m_pwr2_11-17

Figure 6-26. Liquid-phase flux 5 m above the crown of the drift for the mean infiltration-flux case for the indicated times.



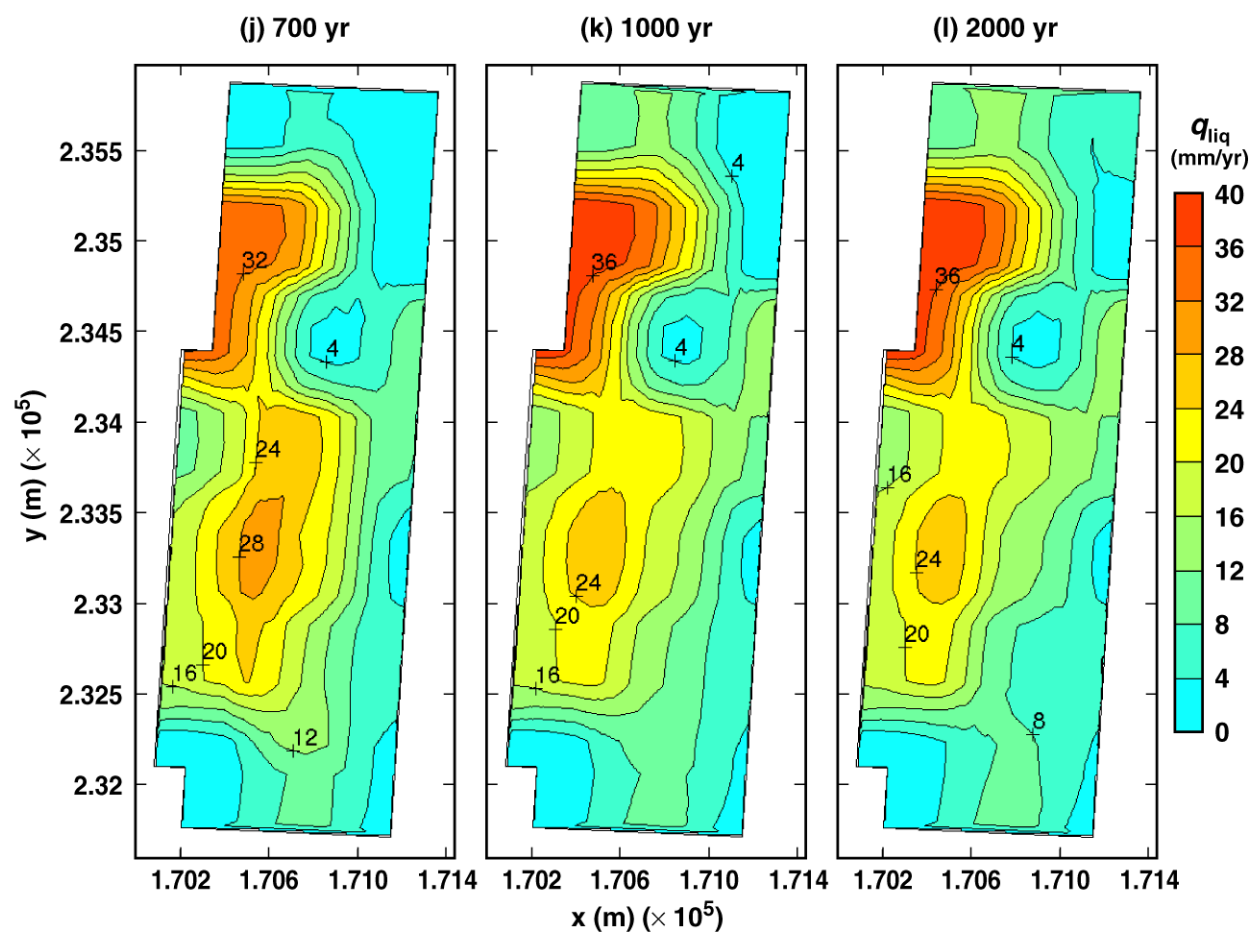
TB_AMR_mean_qliq_5m_pwr2_20-23

Figure 6-26. Liquid-phase flux 5 m above the crown of the drift for the mean infiltration-flux case for the indicated times.



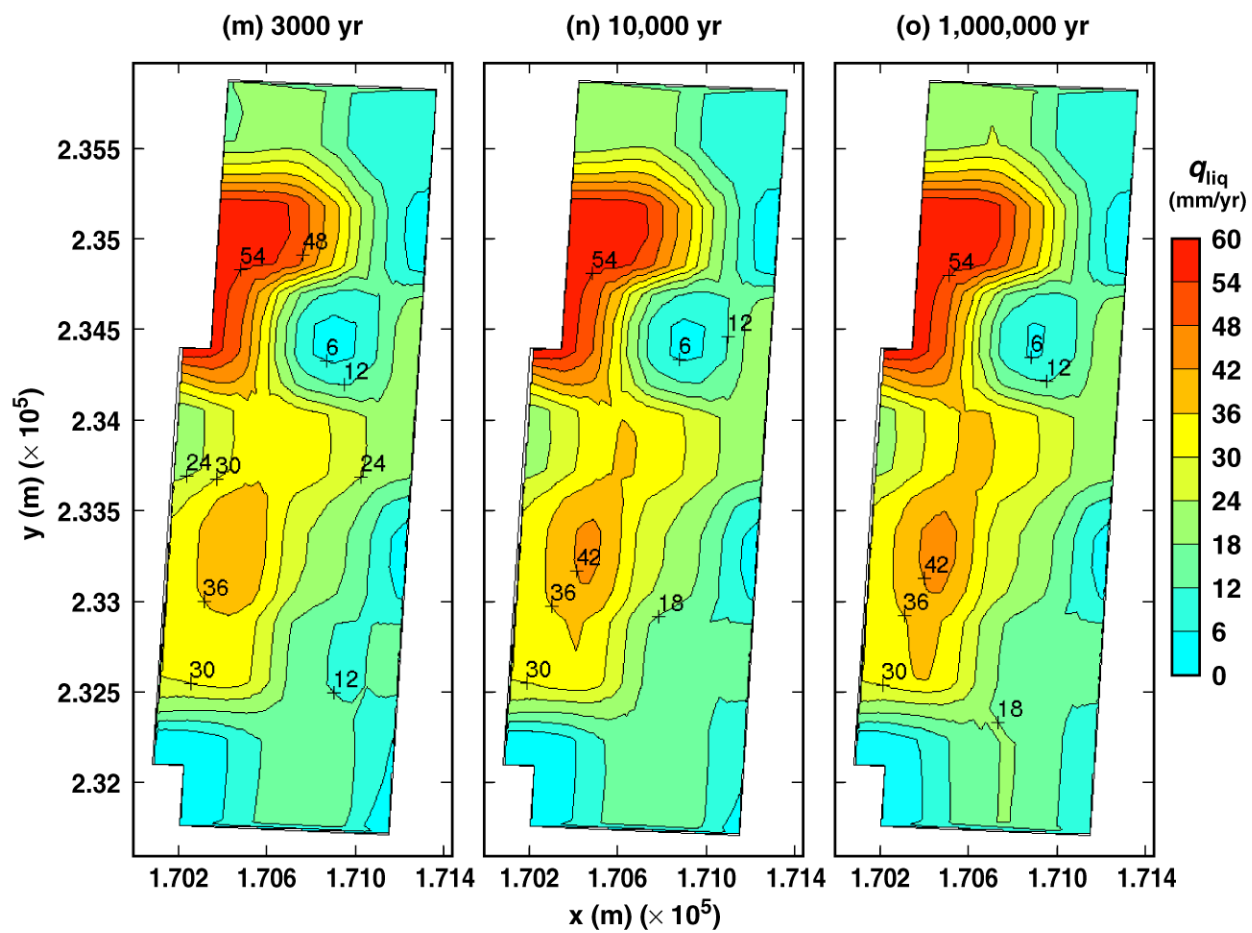
TB_AMR_mean_qliq_5m_pwr2_31-104

Figure 6-26. Liquid-phase flux 5 m above the crown of the drift for the mean infiltration-flux case for the indicated times.



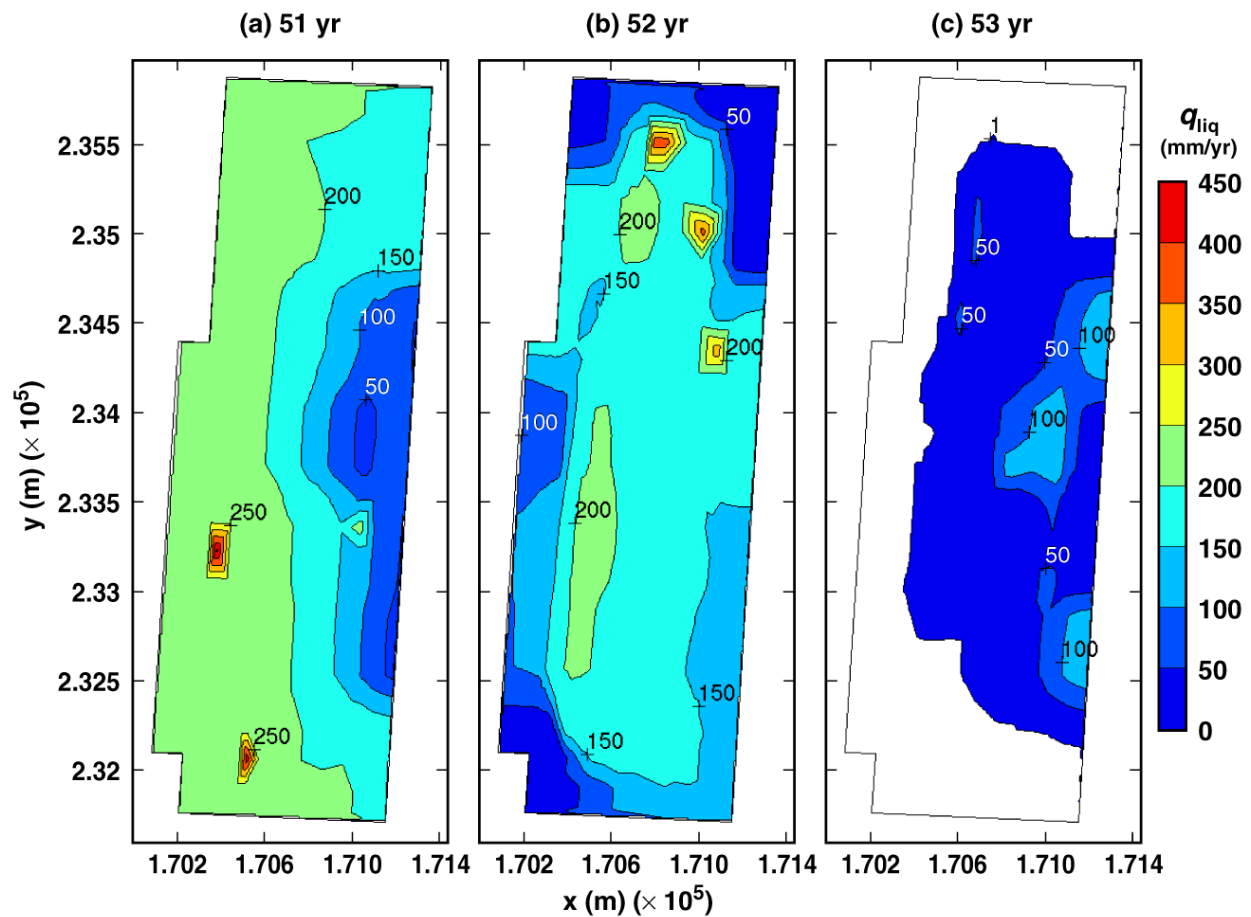
TB_AMR_mean_qliq_5m_pwr2_144-254

Figure 6-26. Liquid-phase flux 5 m above the crown of the drift for the mean infiltration-flux case for the indicated times.



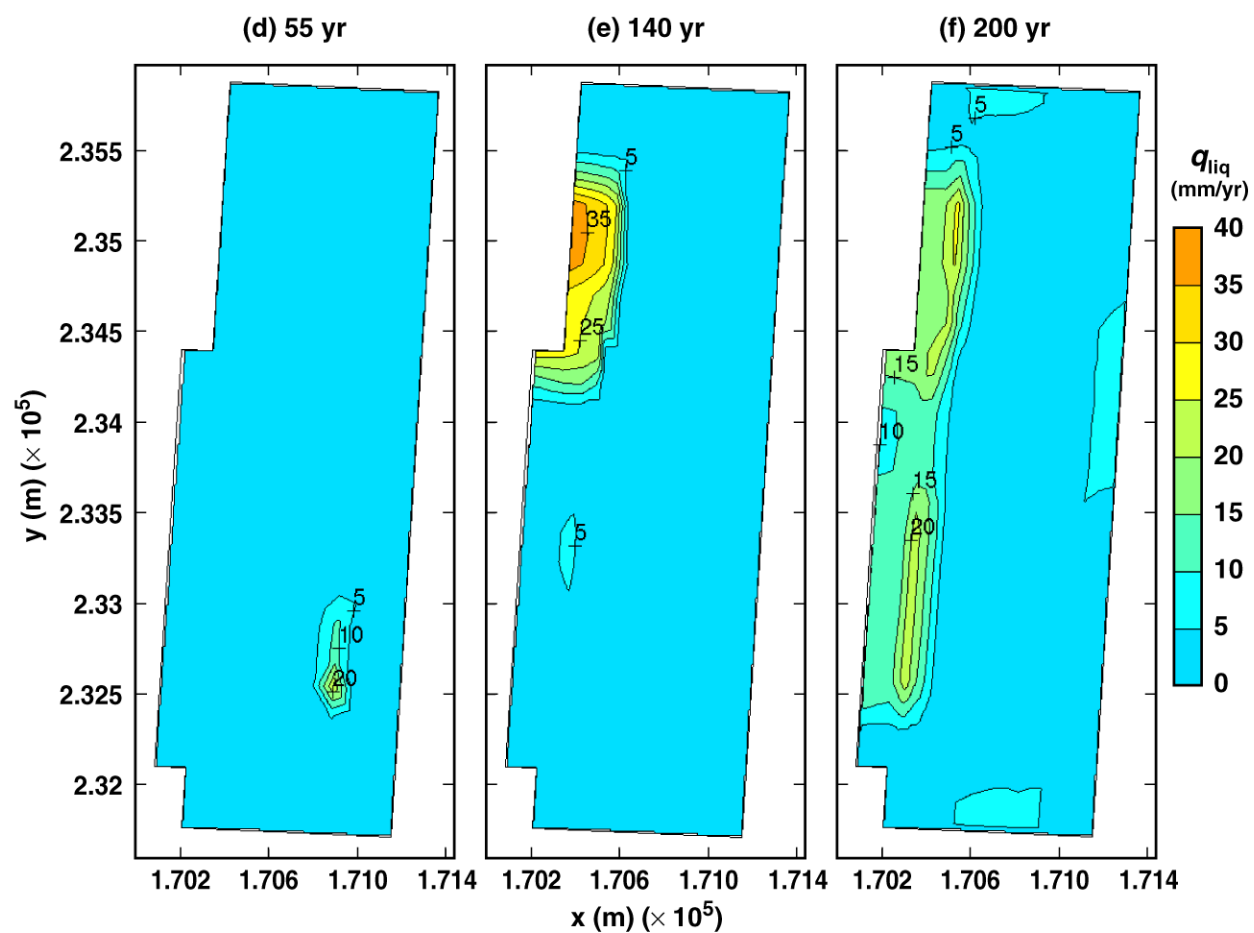
TB_AMR_mean_qliq_5m_pwr2_283-352

Figure 6-26. Liquid-phase flux 5 m above the crown of the drift for the mean infiltration-flux case for the indicated times.



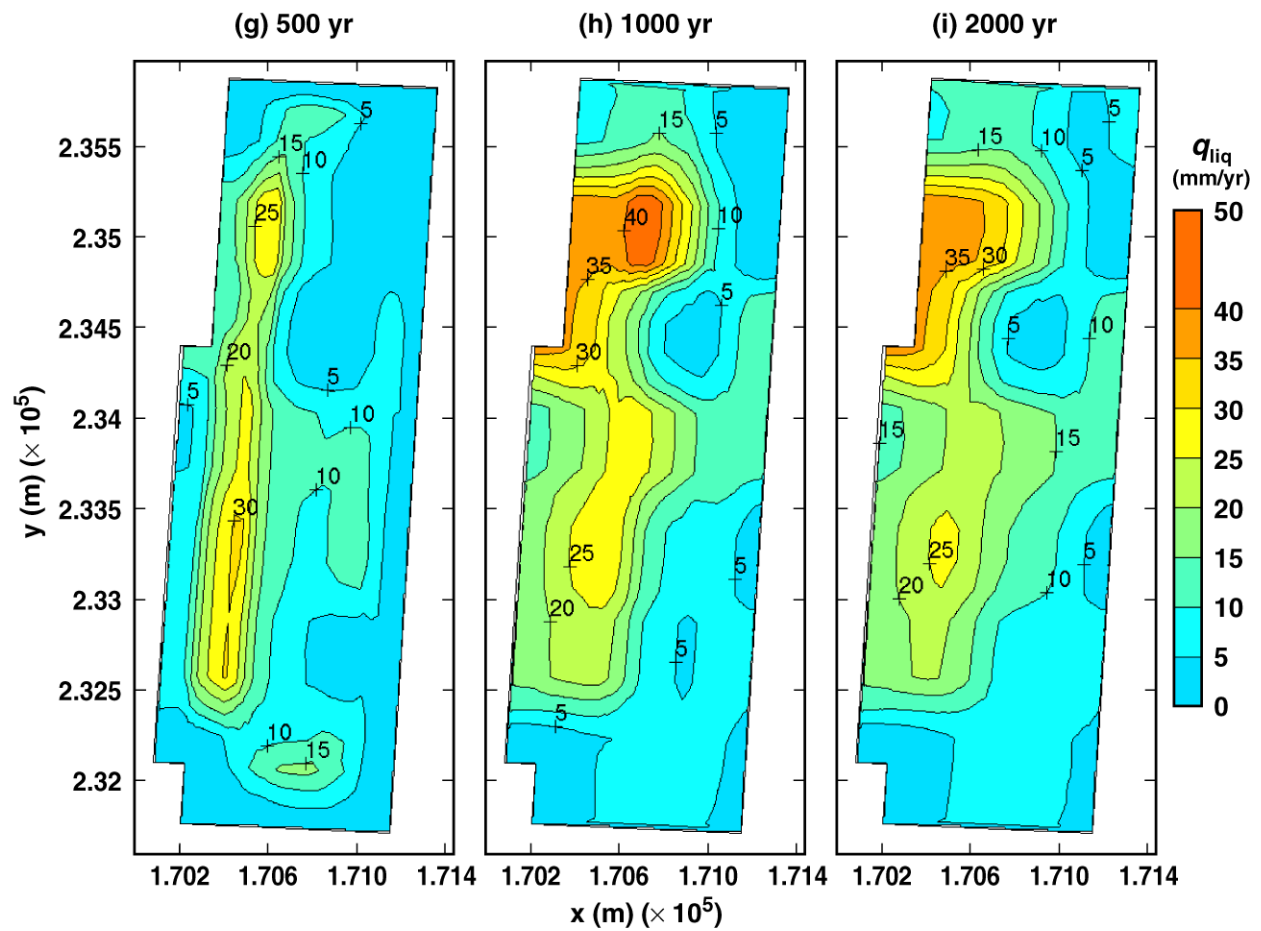
TB_AMR_mean_qliq_dw_pwr2_13-15

Figure 6-27. Liquid-phase flux 0.2 m above the crown of the drift for the mean infiltration-flux case for the indicated times.



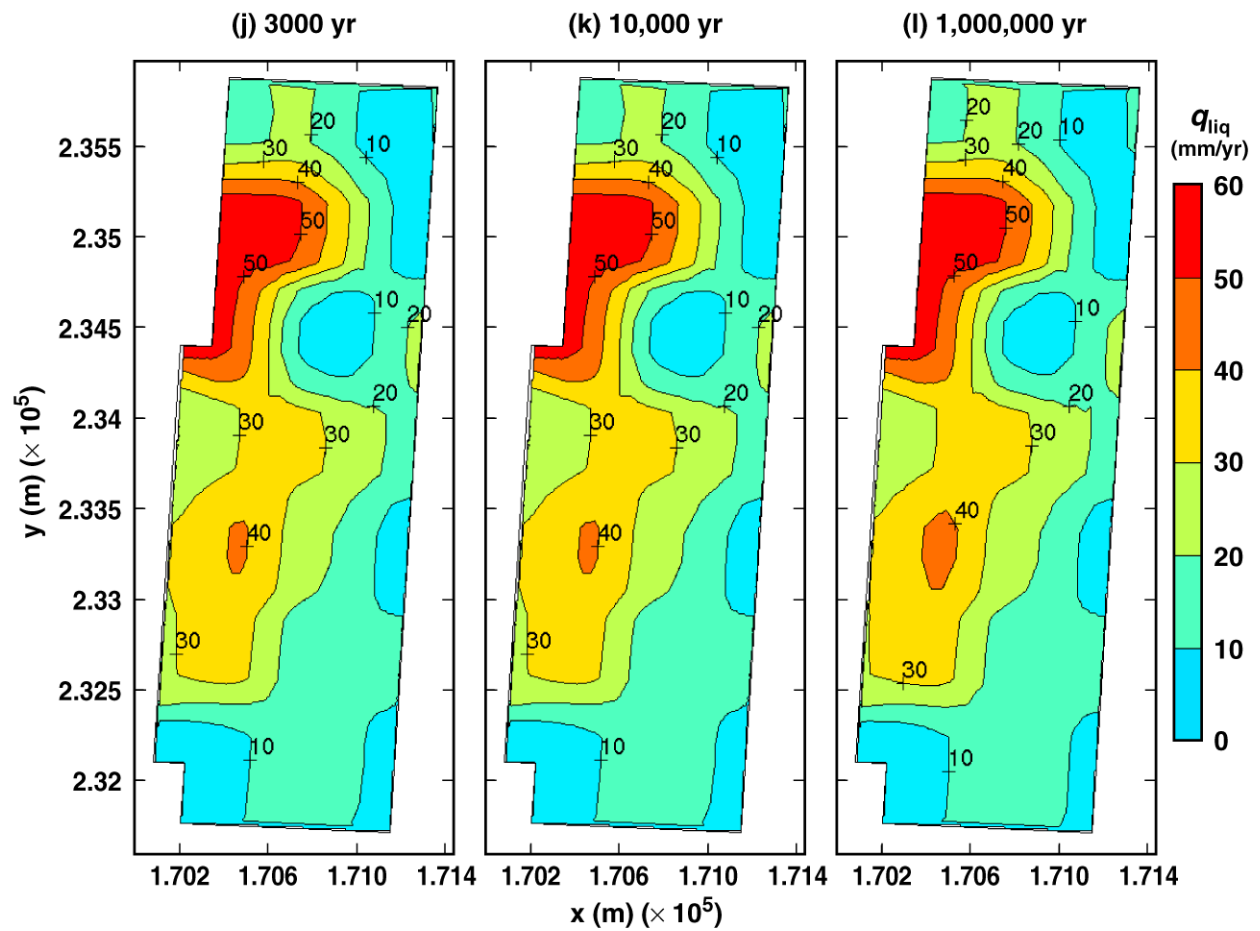
TB_AMR_mean_qliq_dw_pwr2_16-31

Figure 6-27. Liquid-phase flux 0.2 m above the crown of the drift for the mean infiltration-flux case for the indicated times.



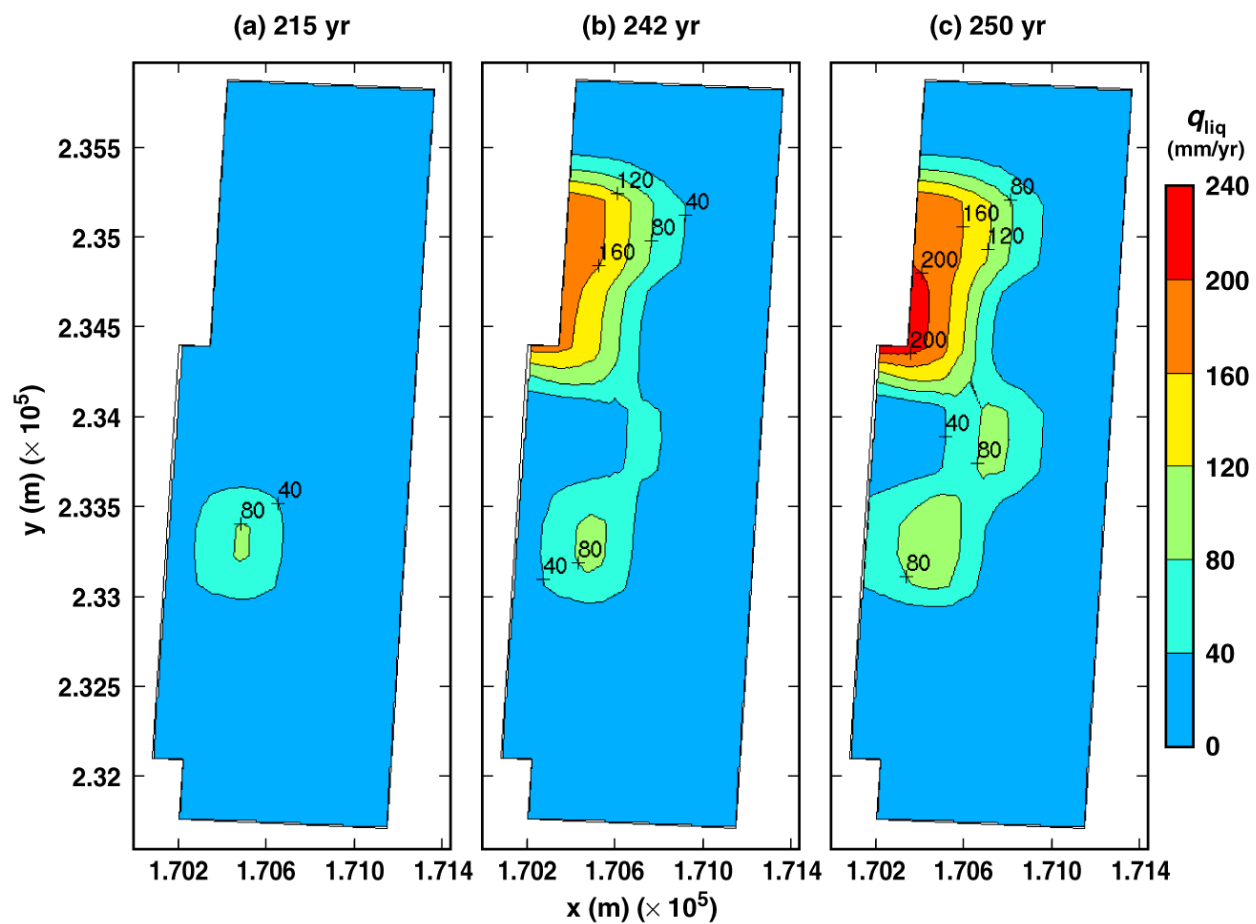
TB_AMR_mean_qliq_dw_pwr2_104-254

Figure 6-27. Liquid-phase flux 0.2 m above the crown of the drift for the mean infiltration-flux case for the indicated times.



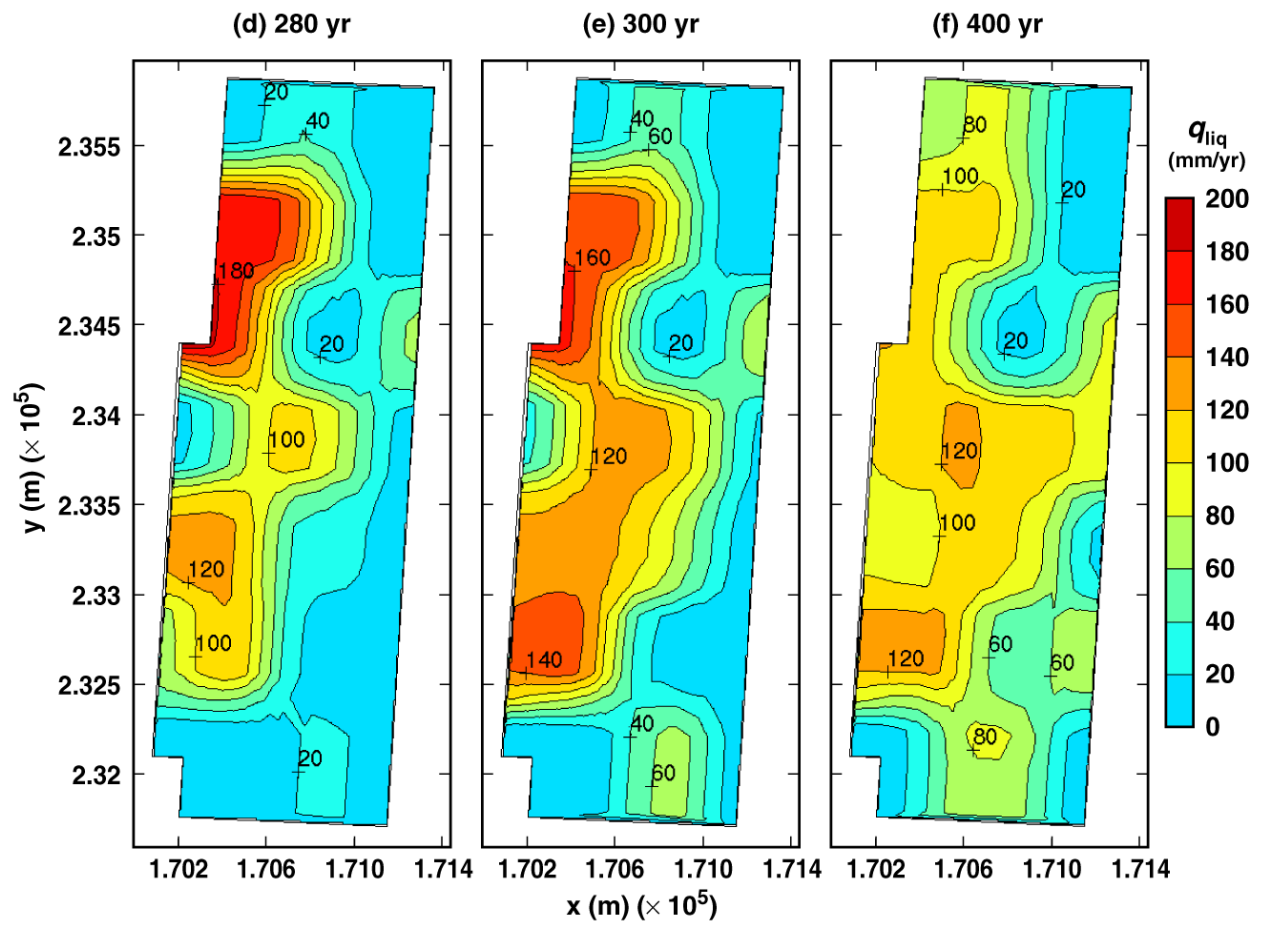
TB_AMR_mean_qliq_dw_pwr2_283-352

Figure 6-27. Liquid-phase flux 0.2 m above the crown of the drift for the mean infiltration-flux case for the indicated times.



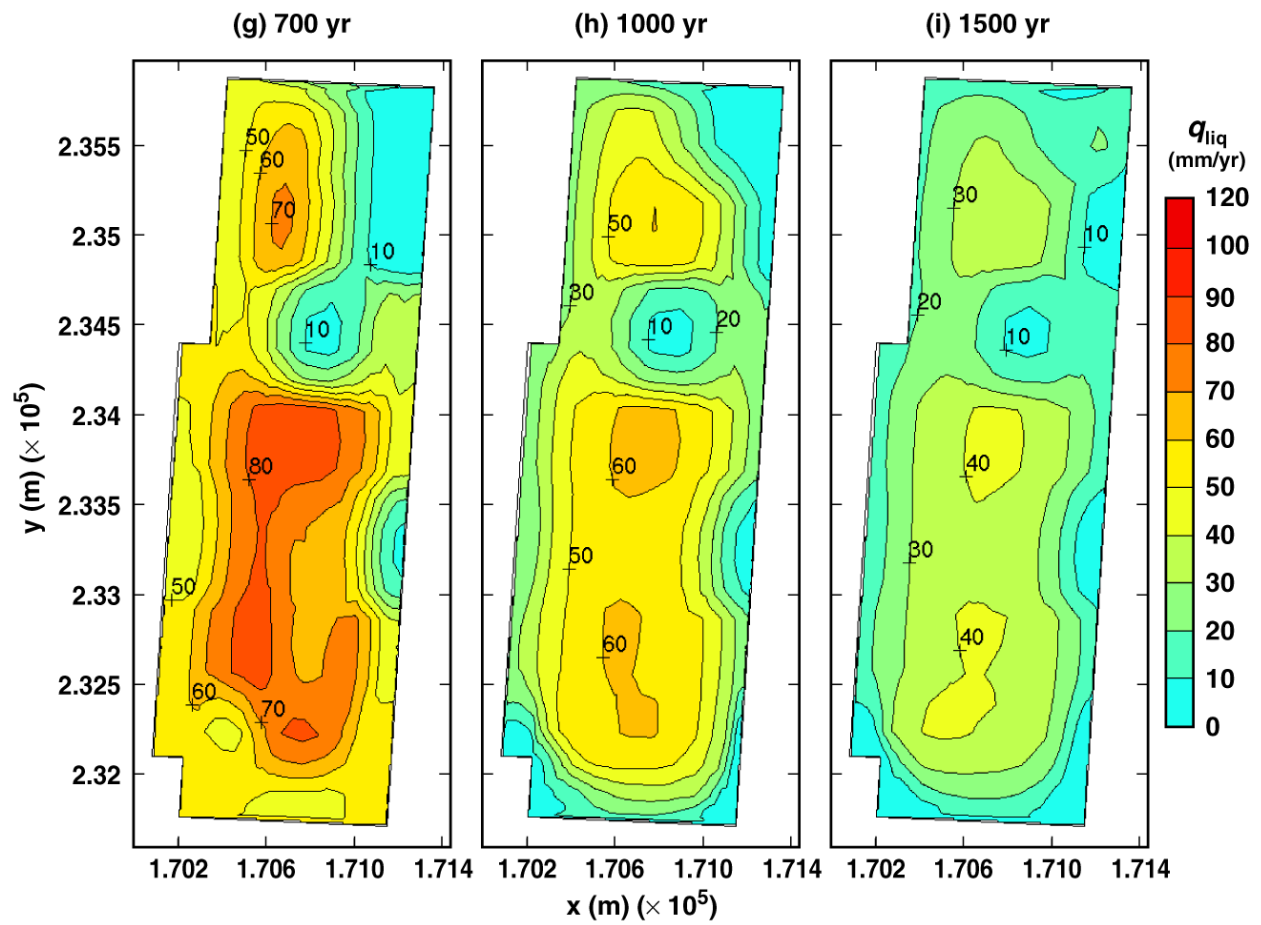
TB_AMR_mean_qliq_dsTop_avg_pwr2_34-49

Figure 6-28. Liquid-phase flux averaged over the upper surface of the dripshield for the mean infiltration-flux case for the indicated times.



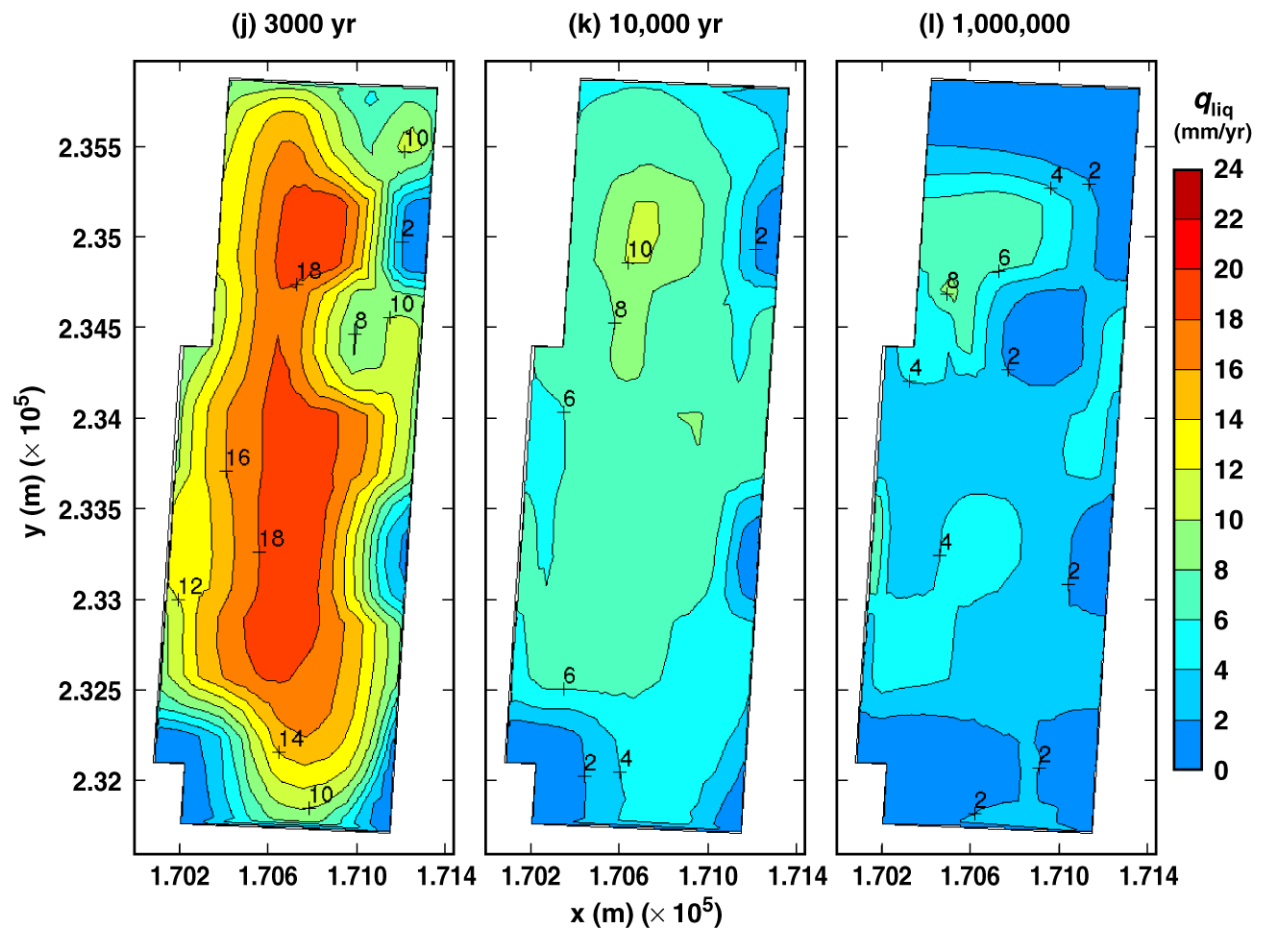
TB_AMR_mean_qliq_dsTop_avg_pwr2_60-84

Figure 6-28. Liquid-phase flux averaged over the upper surface of the dripshield for the mean infiltration-flux case for the indicated times.



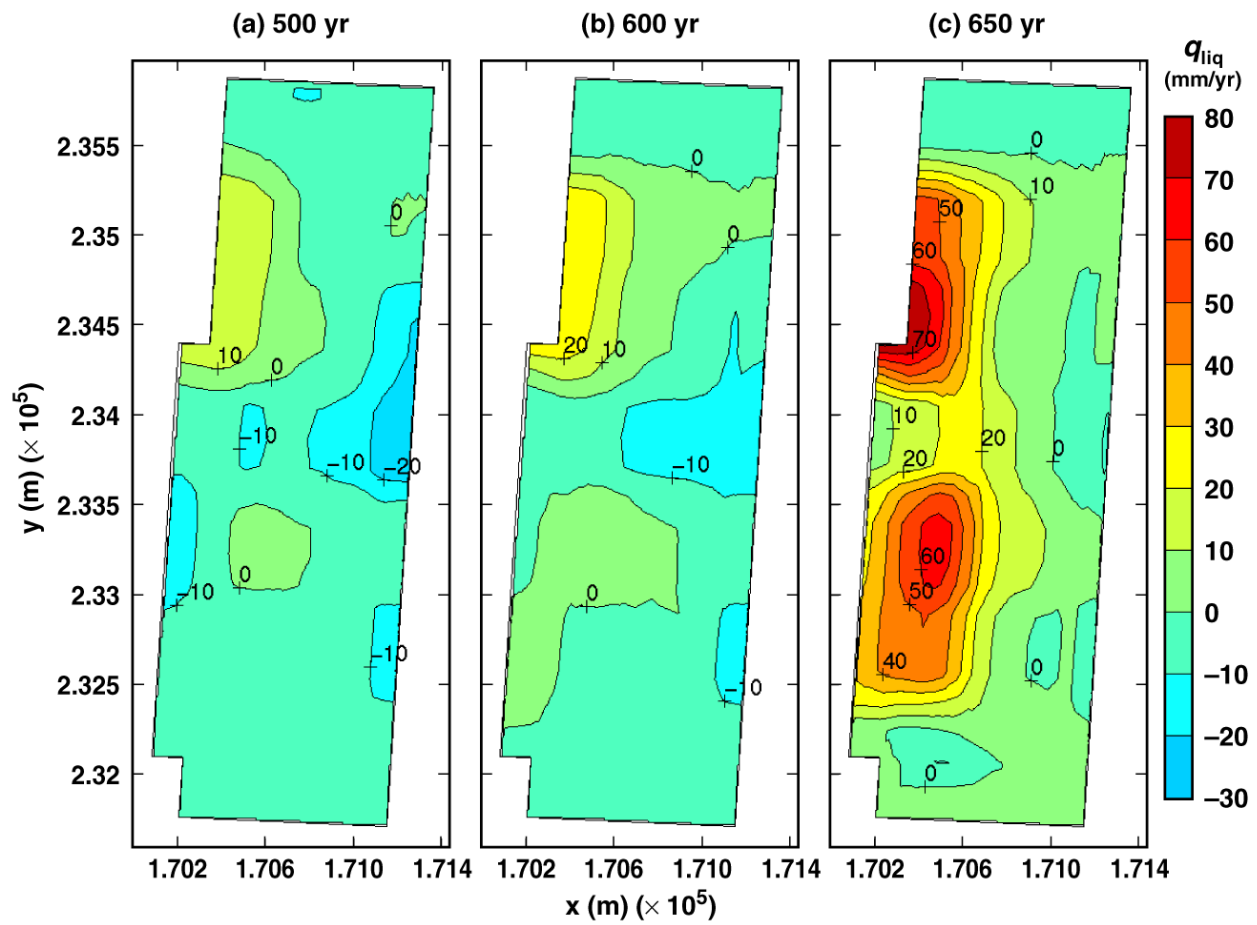
TB_AMR_mean_qliq_dsTop_avg_pwr2_144-225

Figure 6-28. Liquid-phase flux averaged over the upper surface of the dripshield for the mean infiltration-flux case for the indicated times.



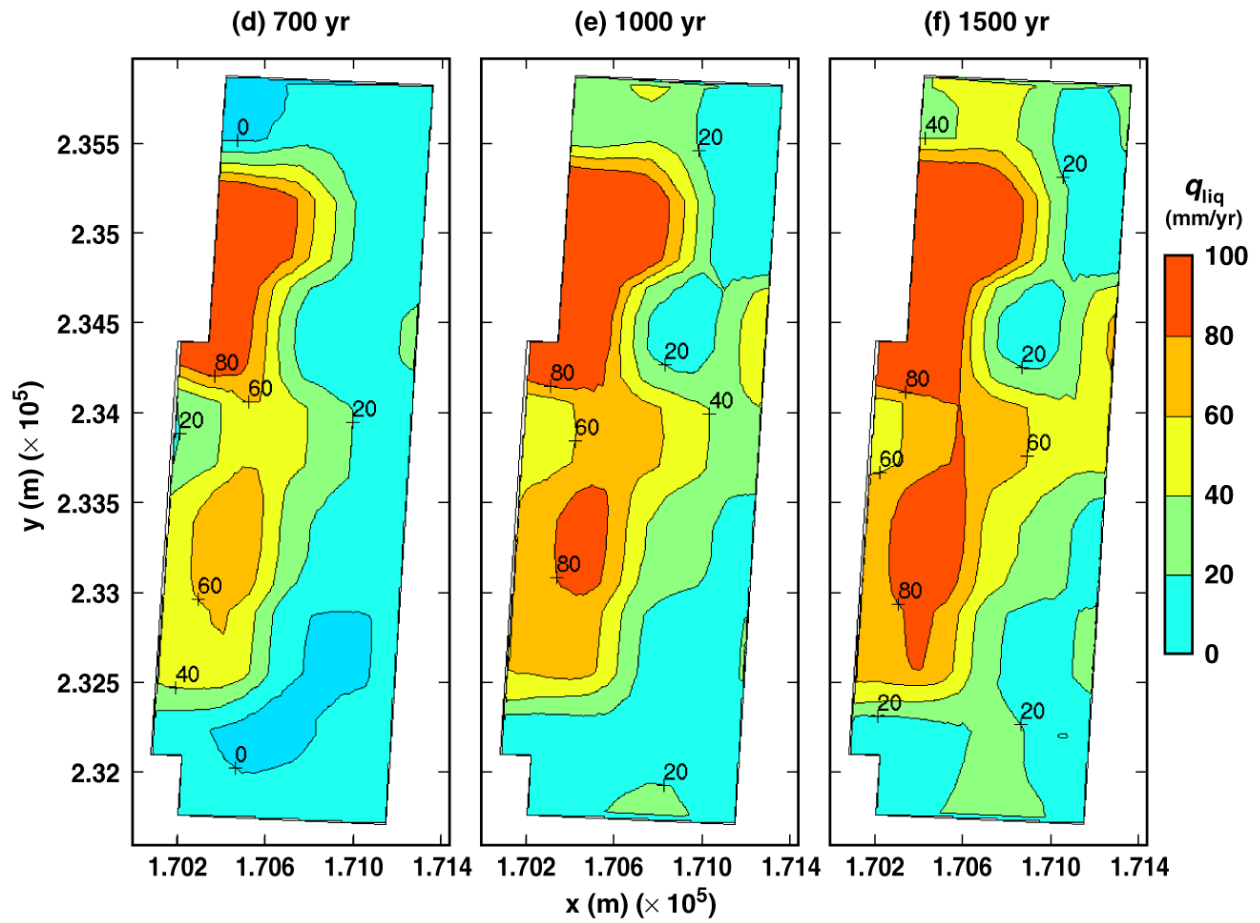
TB_AMR_mean_qliq_dsTop_avg_pwr2_283-352

Figure 6-28. Liquid-phase flux averaged over the upper surface of the dripshield for the mean infiltration-flux case for the indicated times.



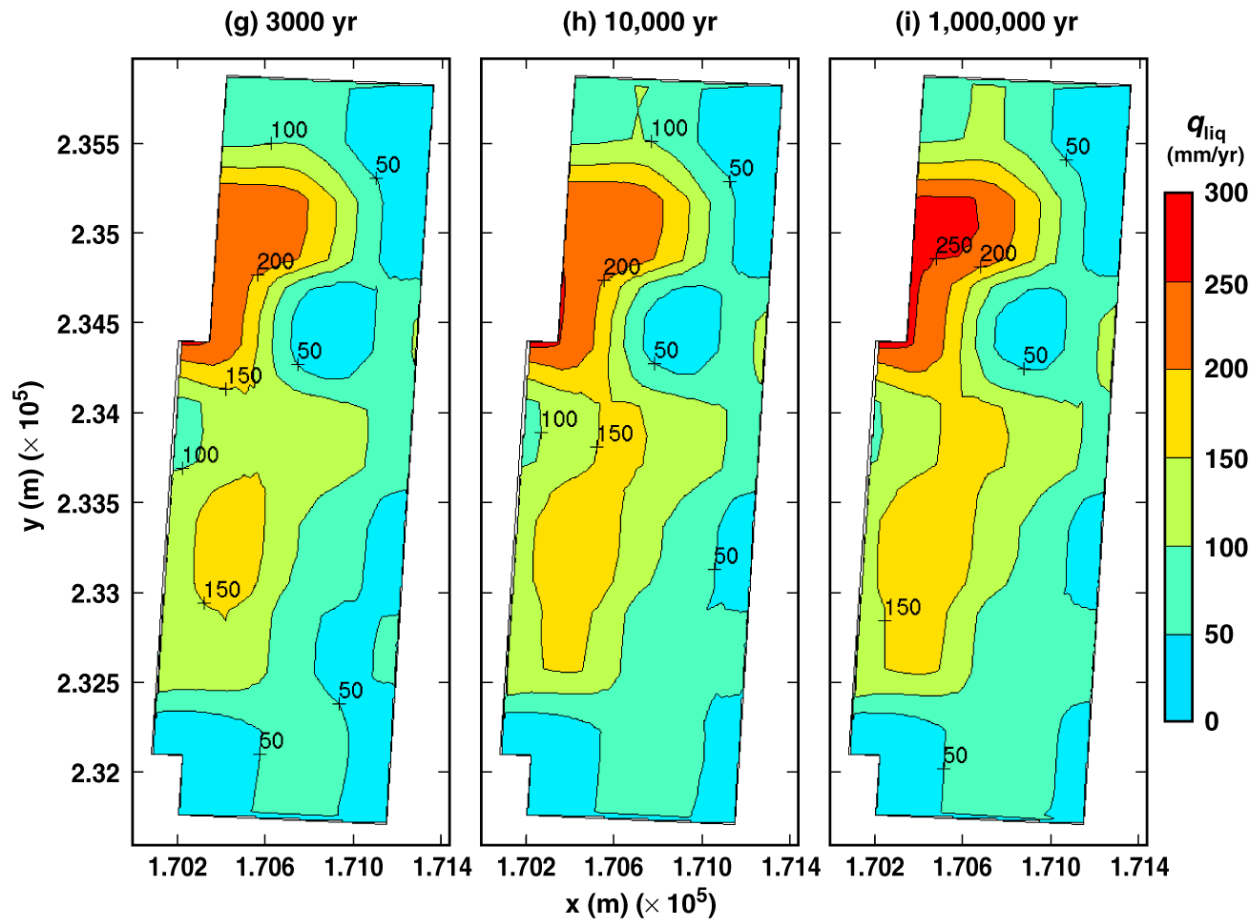
TB_AMR_mean_qliq_dsSide_pwr2_104-134

Figure 6-29. Liquid-phase flux adjacent to the lower side of the dripshield (i.e., adjacent to the base of the dripshield) for the mean infiltration-flux case for the indicated times.



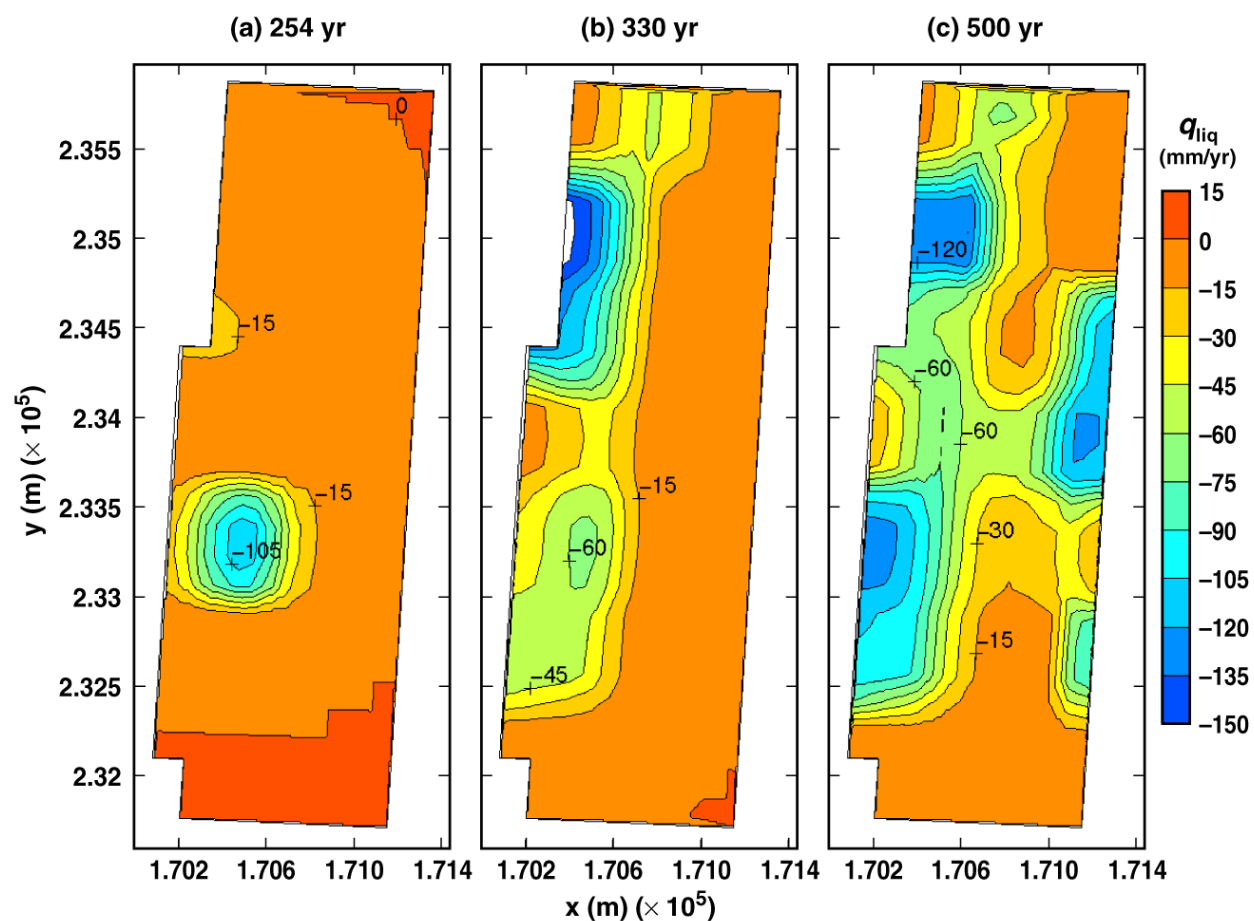
TB_AMR_mean_qliq_dsSide_pwr2_144-225

Figure 6-29. Liquid-phase flux adjacent to the lower side of the dripshield (i.e., adjacent to the base of the dripshield) for the mean infiltration-flux case for the indicated times.



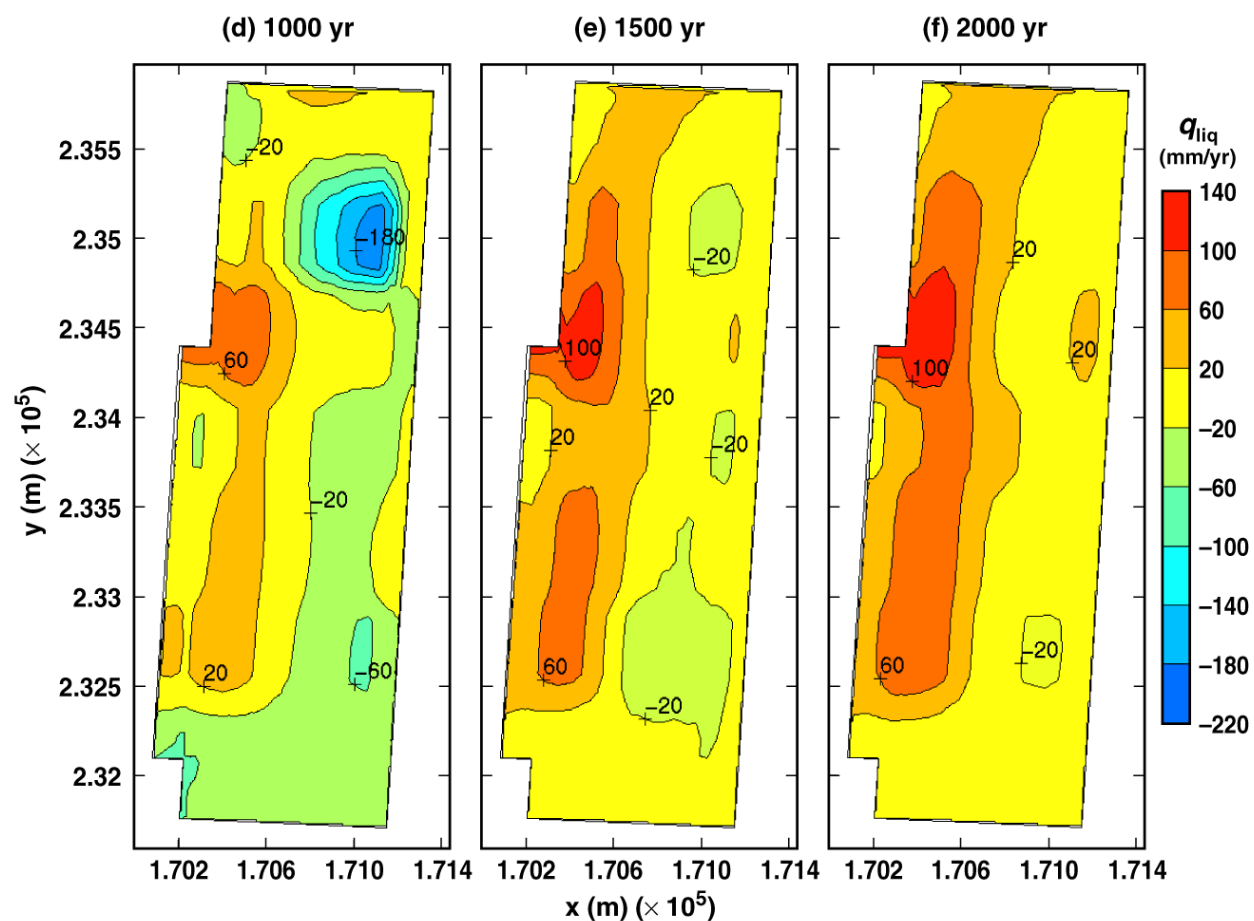
TB_AMR_mean_qliq_dsSide_pwr2_283-352

Figure 6-29. Liquid-phase flux adjacent to the lower side of the dripshield (i.e., adjacent to the base of the dripshield) for the mean infiltration-flux case for the indicated times.



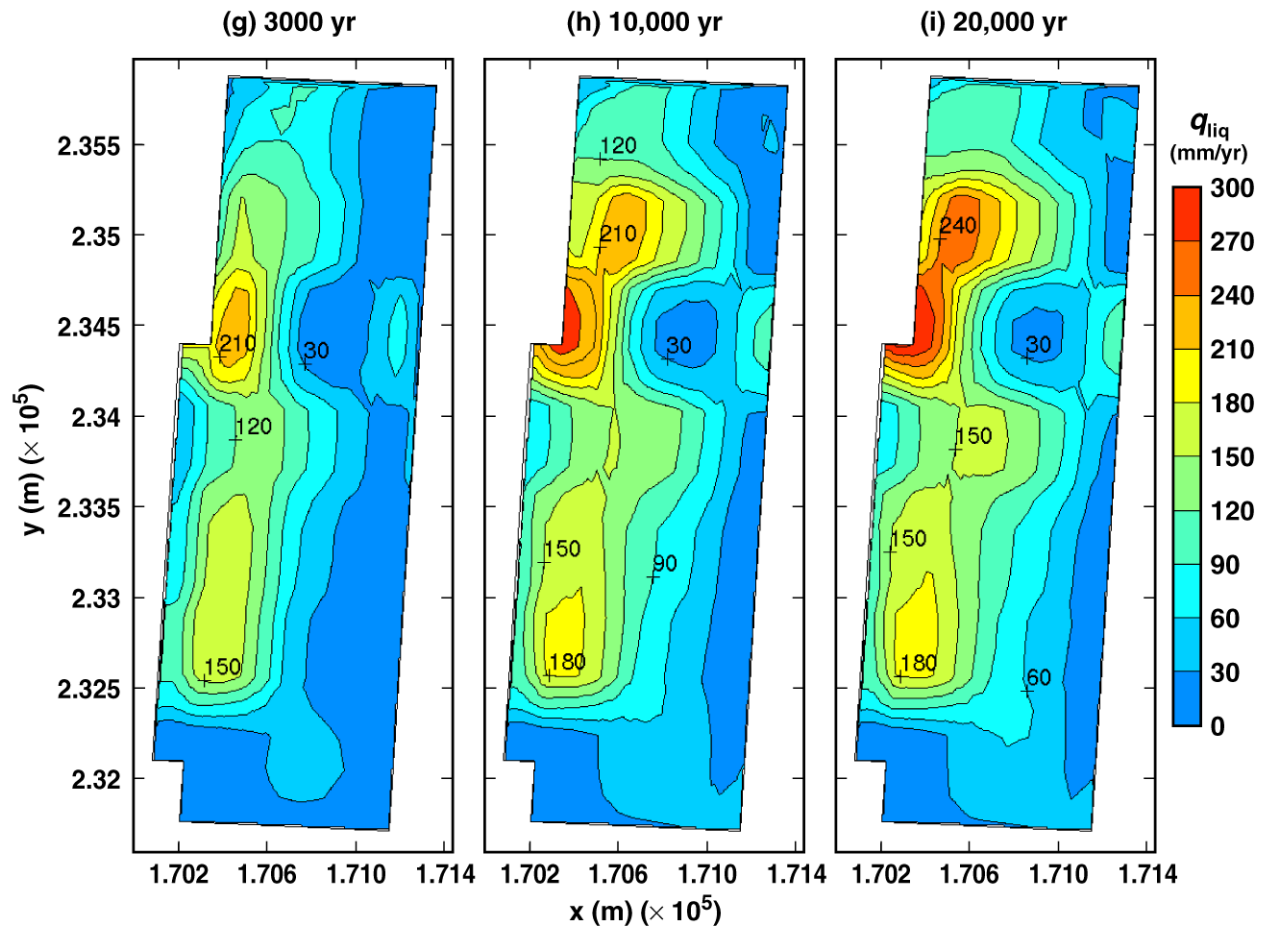
TB_AMR_mean_qliq_invert_pwr2_51-104

Figure 6-30. Liquid-phase flux averaged over the invert for the mean infiltration-flux case for the indicated times.



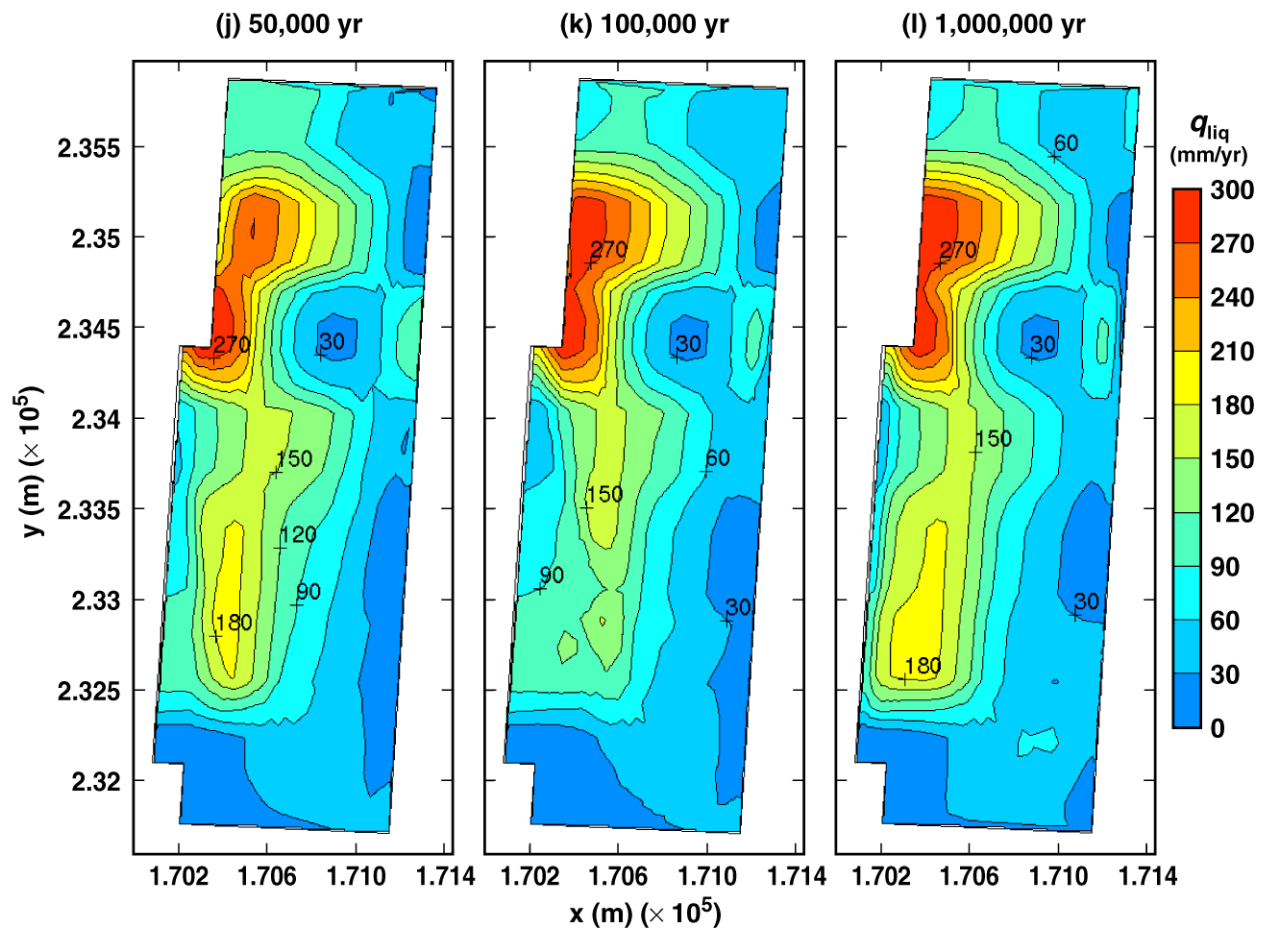
TB_AMR_mean_qliq_invert_pwr2_174-254

Figure 6-30. Liquid-phase flux averaged over the invert for the mean infiltration-flux case for the indicated times.



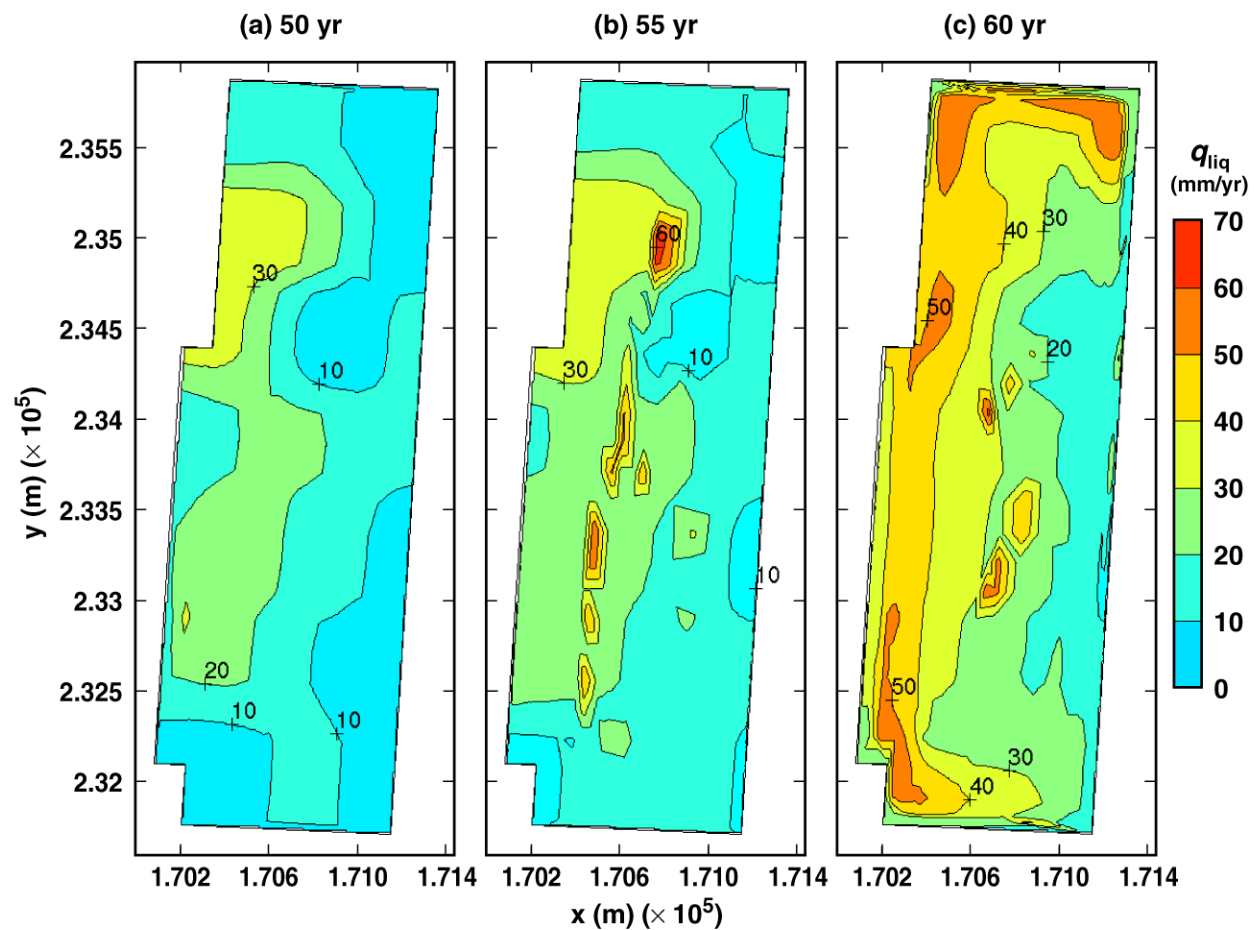
TB_AMR_mean_qliq_invert_pwr2_283-330

Figure 6-30. Liquid-phase flux averaged over the invert for the mean infiltration-flux case for the indicated times.



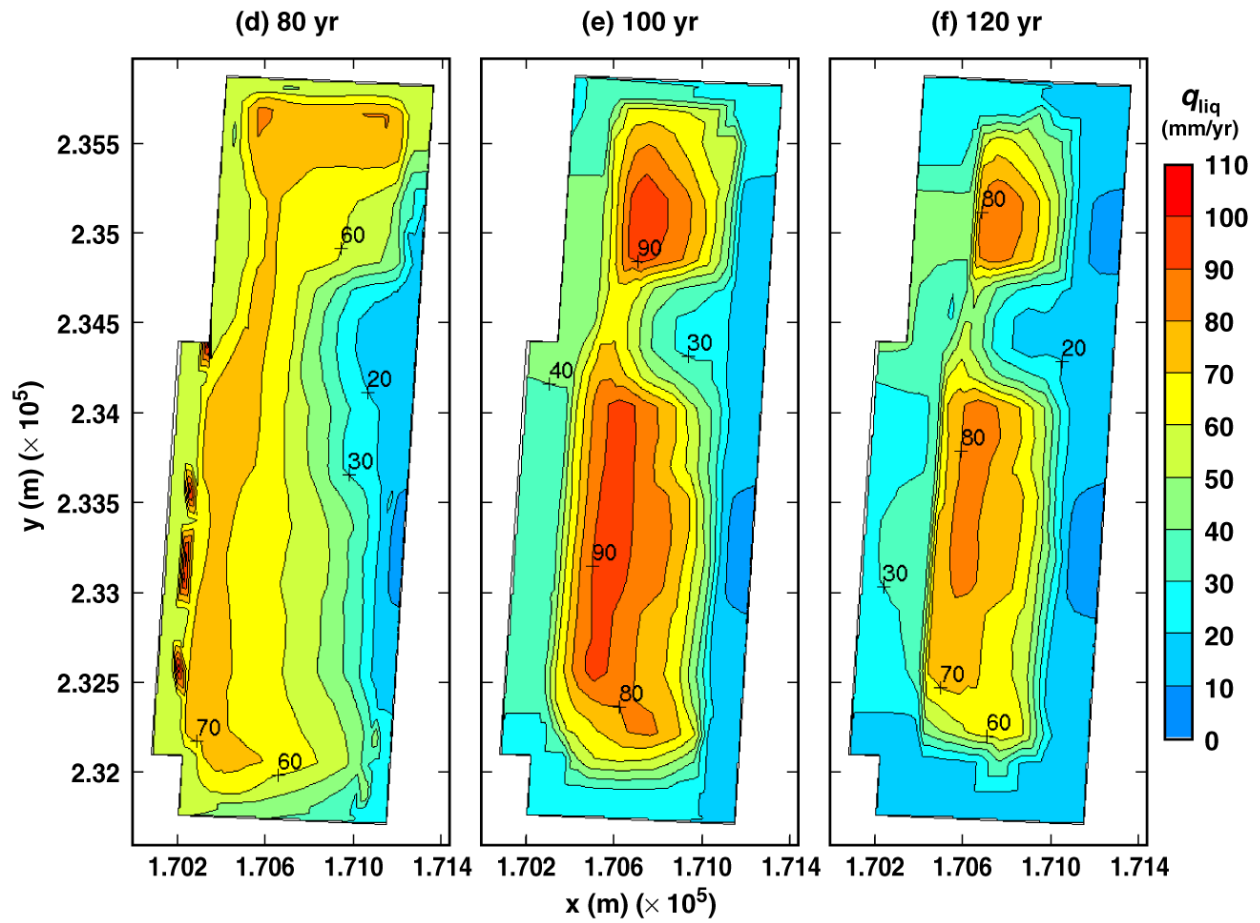
TB_AMR_mean_qliq_invert_pwr2_341-352

Figure 6-30. Liquid-phase flux averaged over the invert for the mean infiltration-flux case for the indicated times.



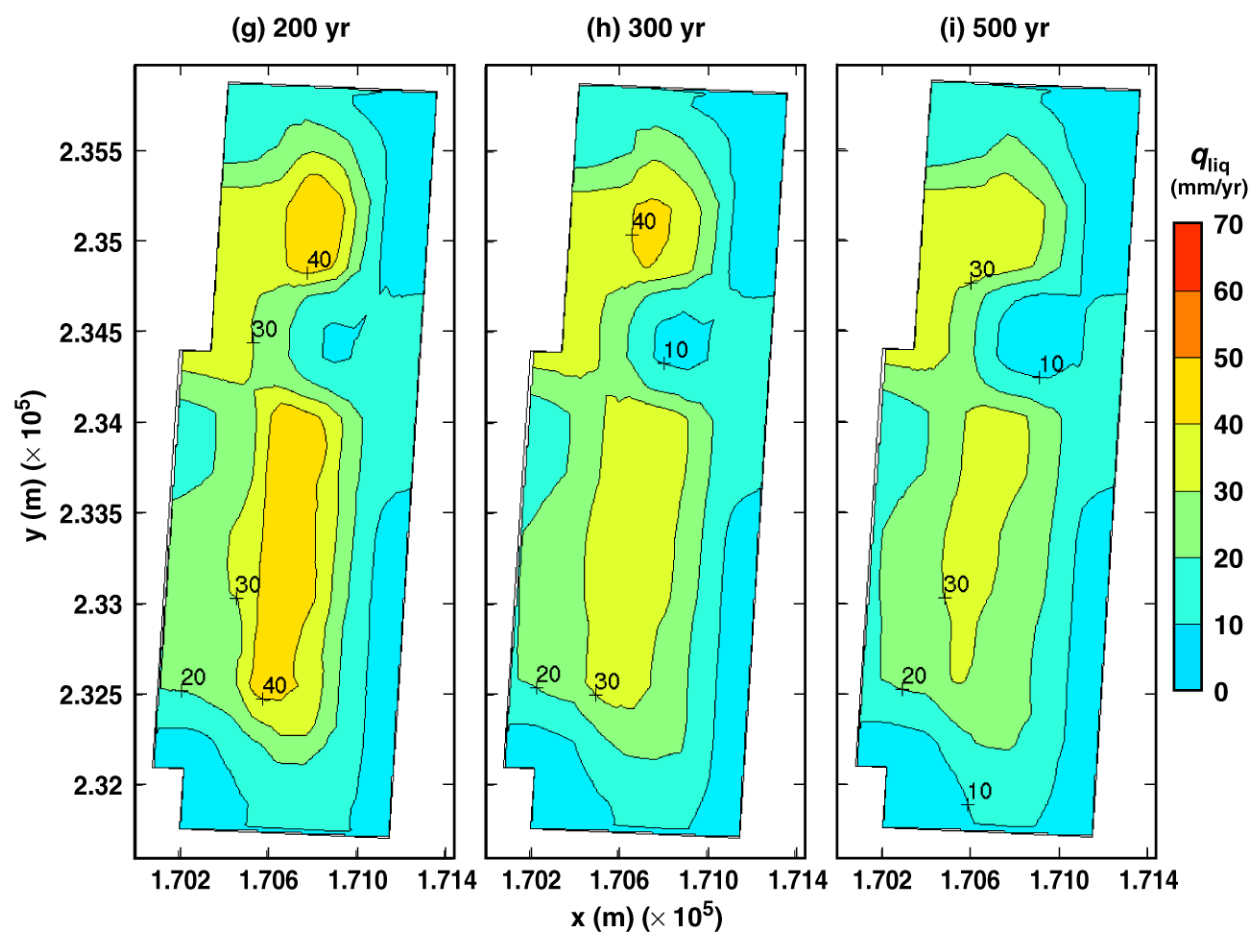
TB_AMR_upper_qliq_5m_pwr2_11-17

Figure 6-31. Liquid-phase flux 5 m above the crown of the drift for the high infiltration-flux case for the indicated times.



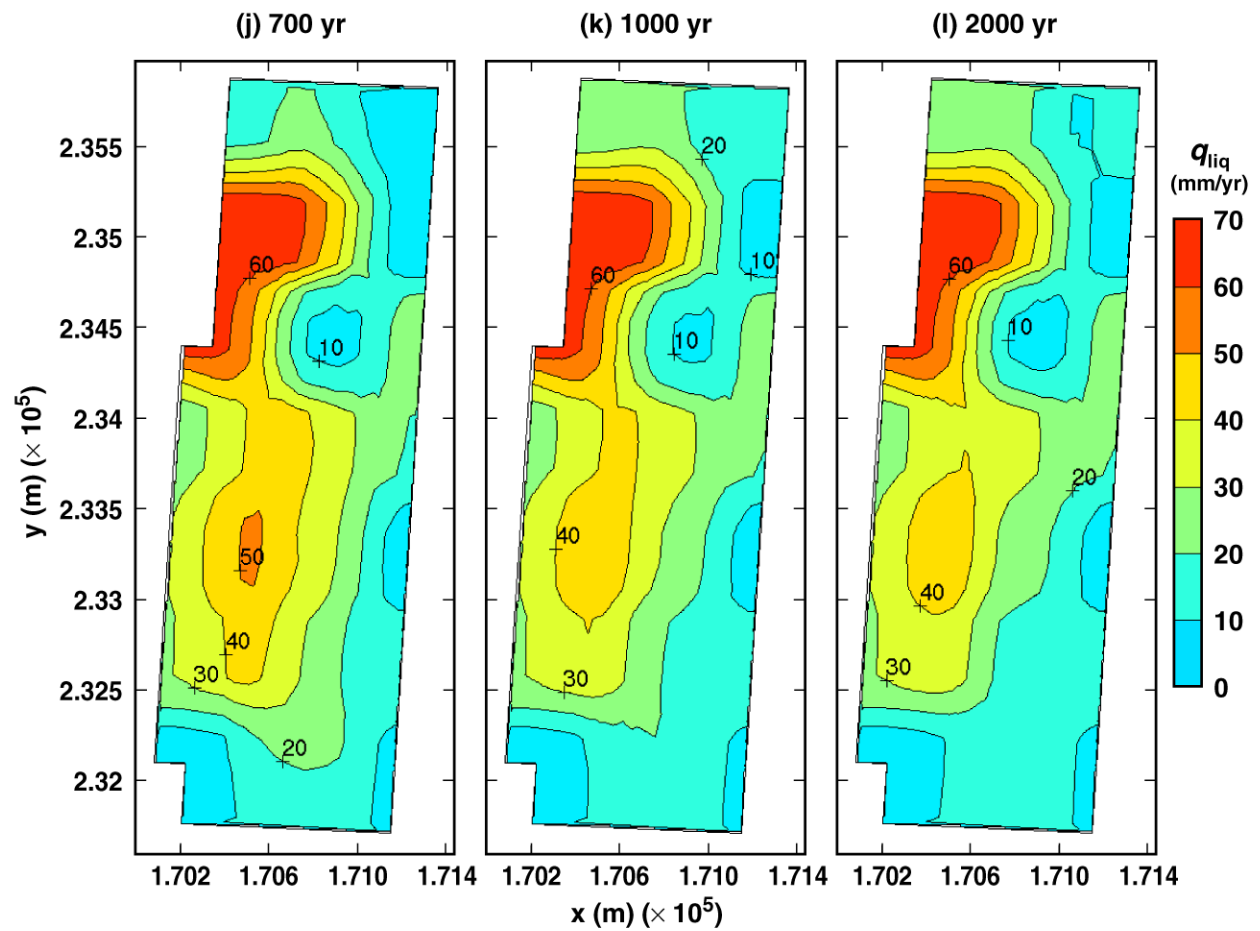
TB_AMR_upper_qliq_5m_pwr2_18-25

Figure 6-31. Liquid-phase flux 5 m above the crown of the drift for the high infiltration-flux case for the indicated times.



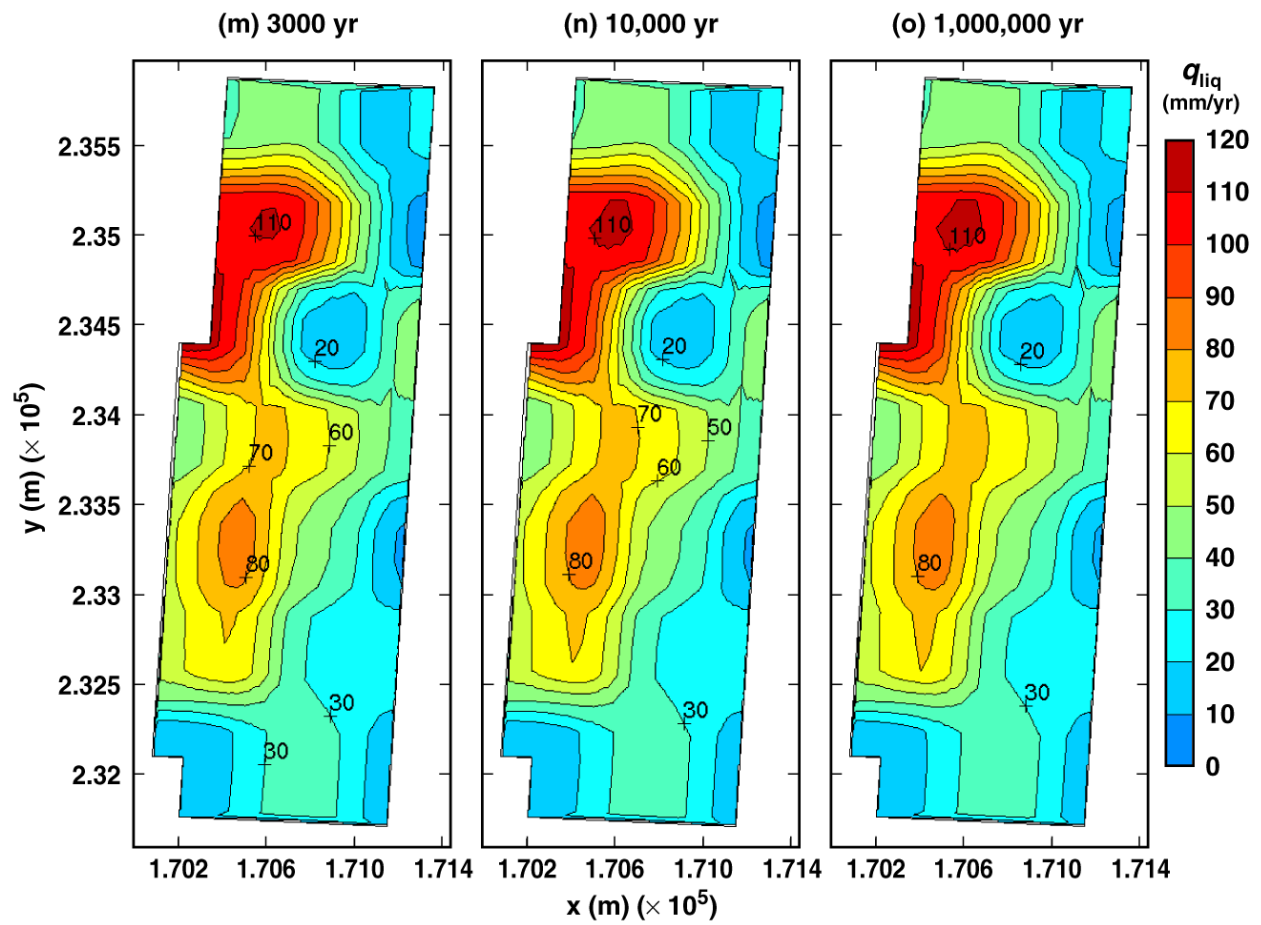
TB_AMR_upper_qliq_5m_pwr2_56-177

Figure 6-31. Liquid-phase flux 5 m above the crown of the drift for the high infiltration-flux case for the indicated times.



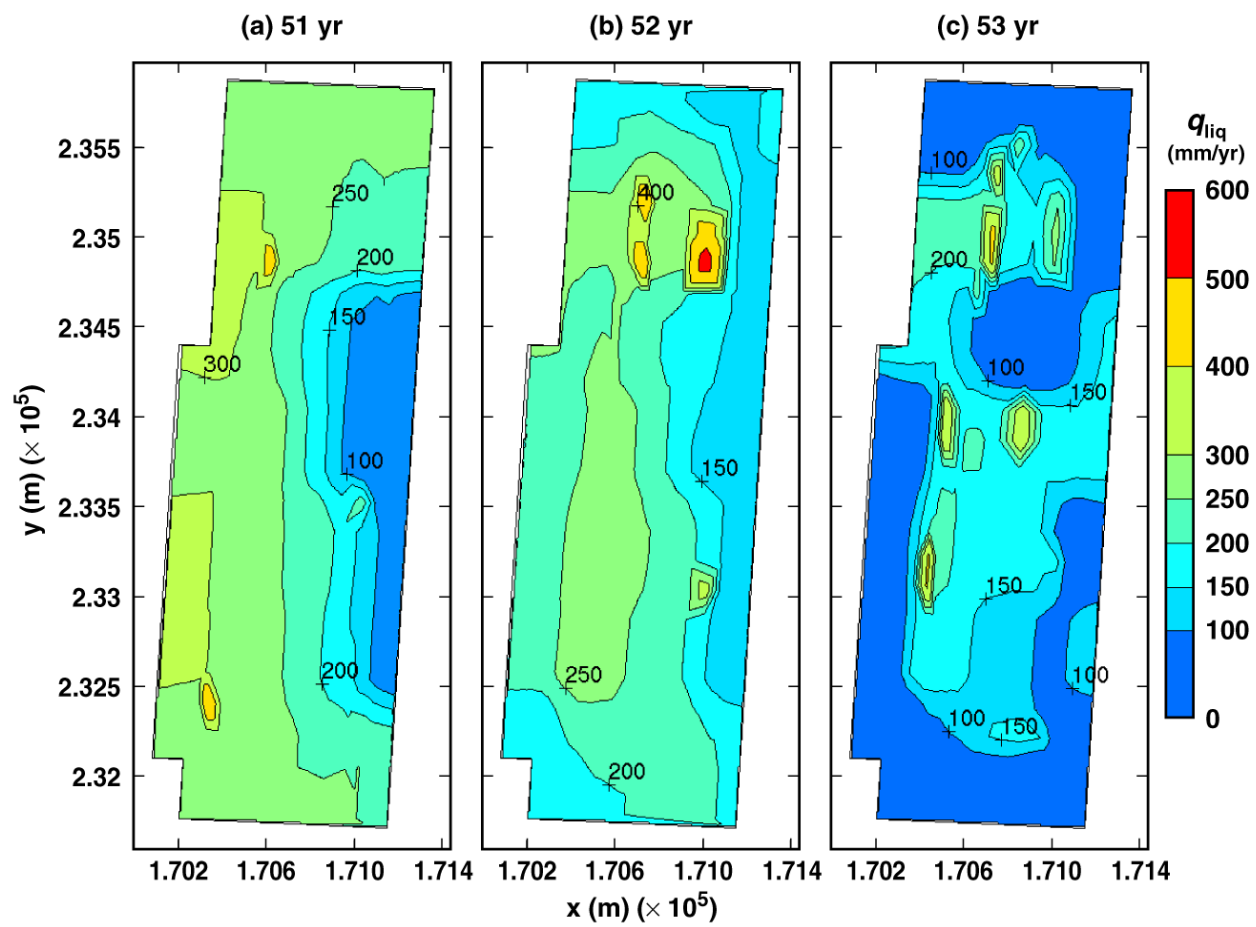
TB_AMR_upper_qliq_5m_pwr2_217-360

Figure 6-31. Liquid-phase flux 5 m above the crown of the drift for the high infiltration-flux case for the indicated times.



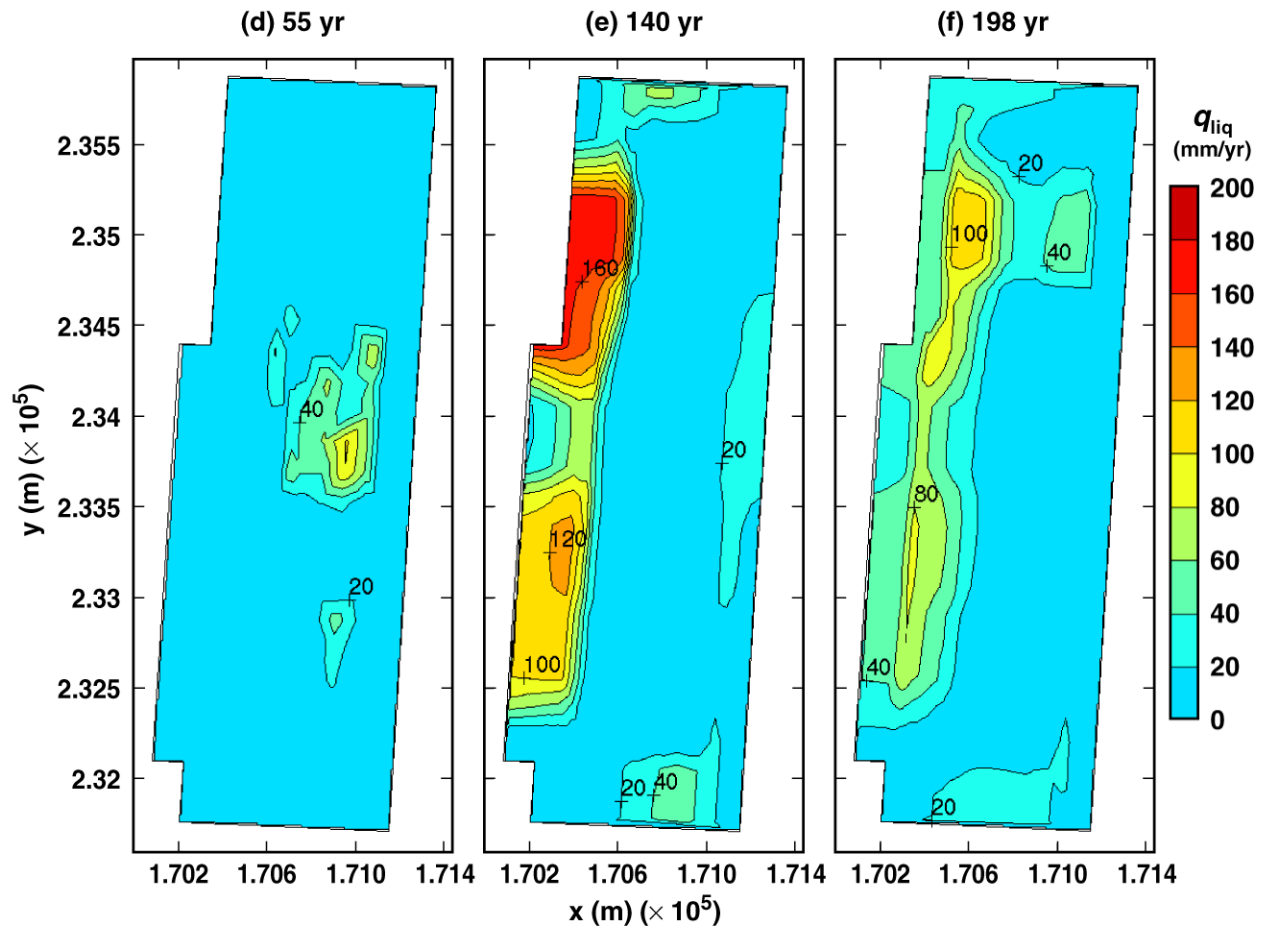
TB_AMR_upper_qliq_5m_pwr2_389-457

Figure 6-31. Liquid-phase flux 5 m above the crown of the drift for the high infiltration-flux case for the indicated times.



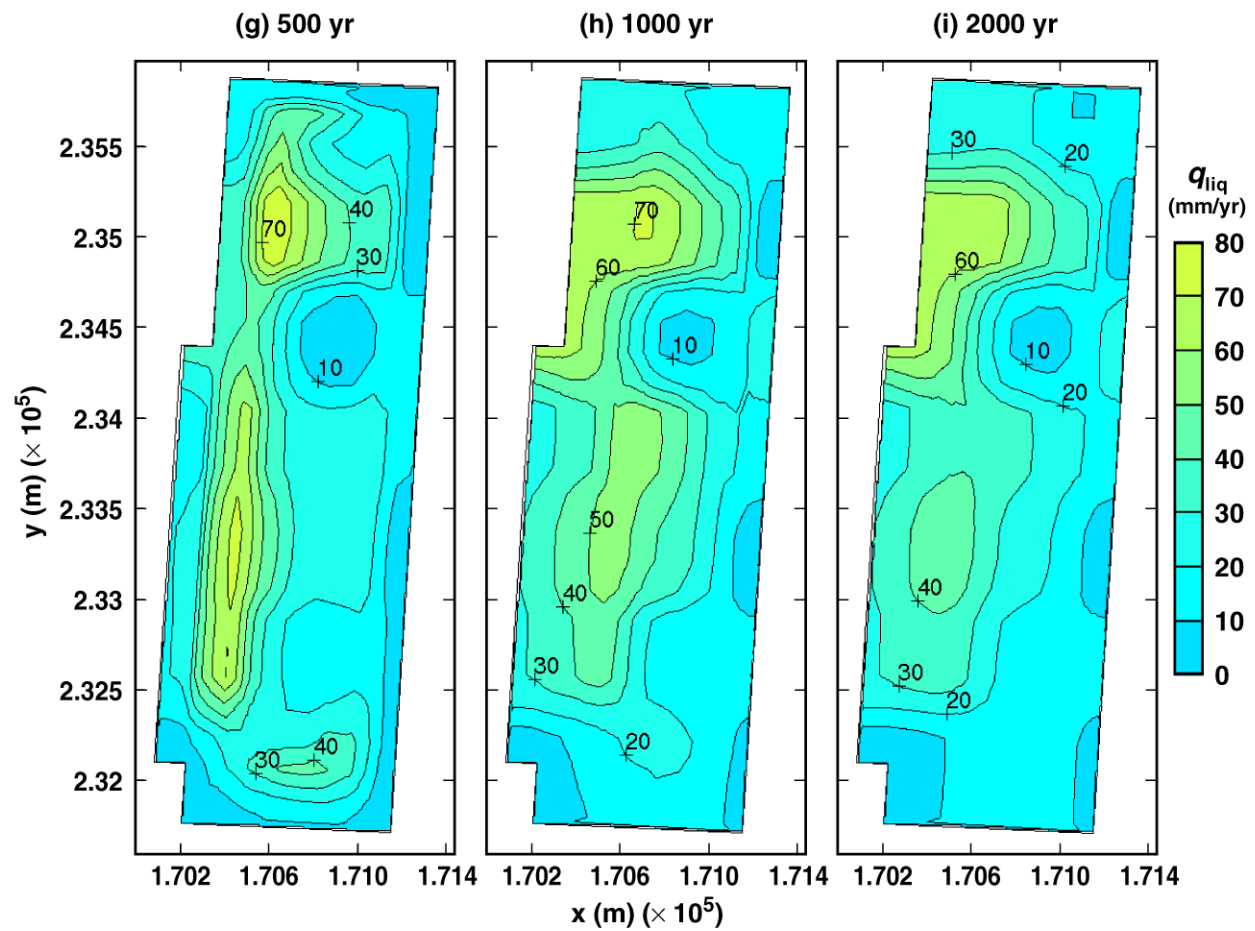
TB_AMR_upper_qliq_dw_pwr1_13-15

Figure 6-32. Liquid-phase flux 0.2 m above the crown of the drift for the high infiltration-flux case for the indicated times.



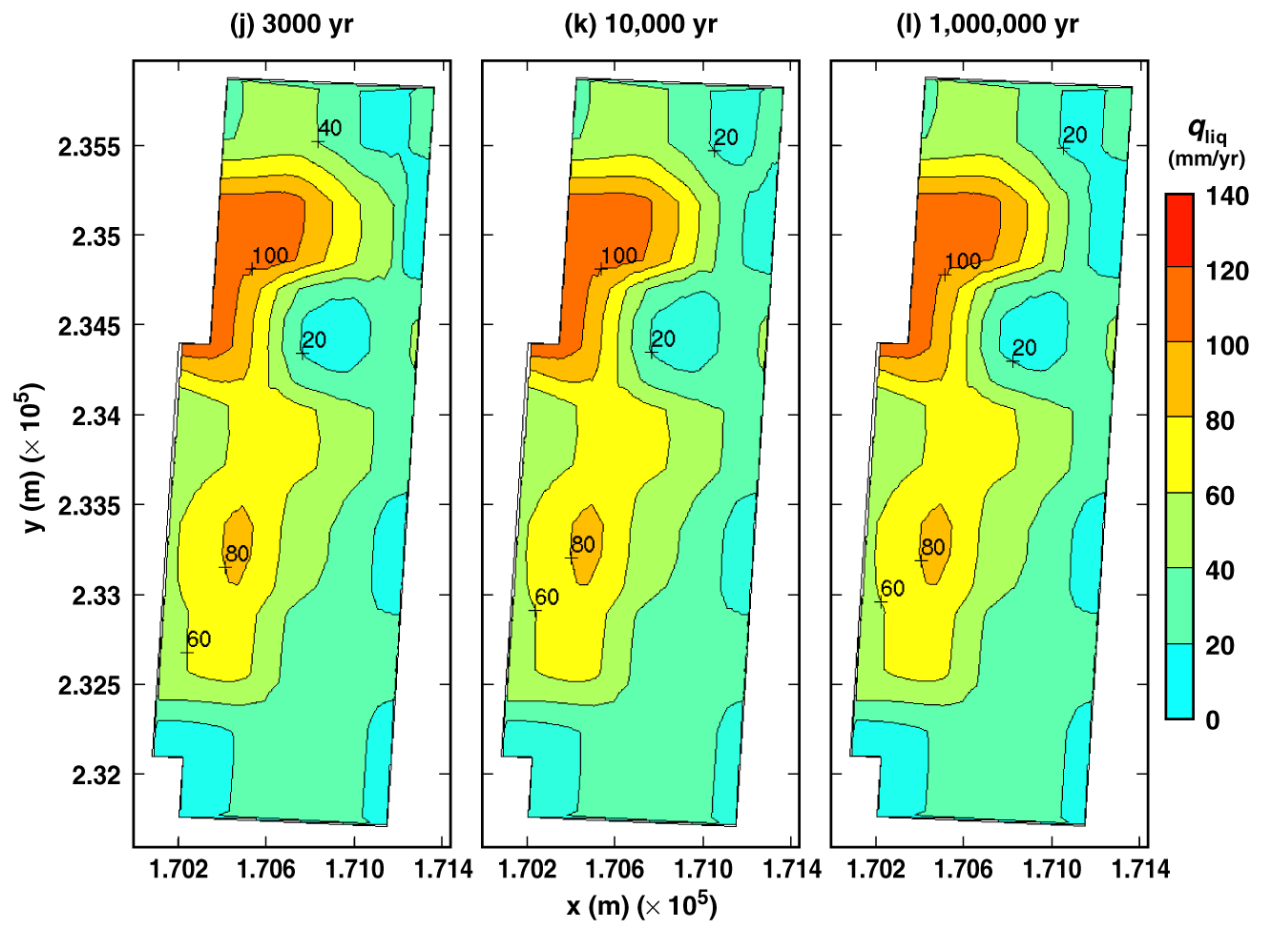
TB_AMR_upper_qliq_dw_pwr1_16-55

Figure 6-32. Liquid-phase flux 0.2 m above the crown of the drift for the high infiltration-flux case for the indicated times.



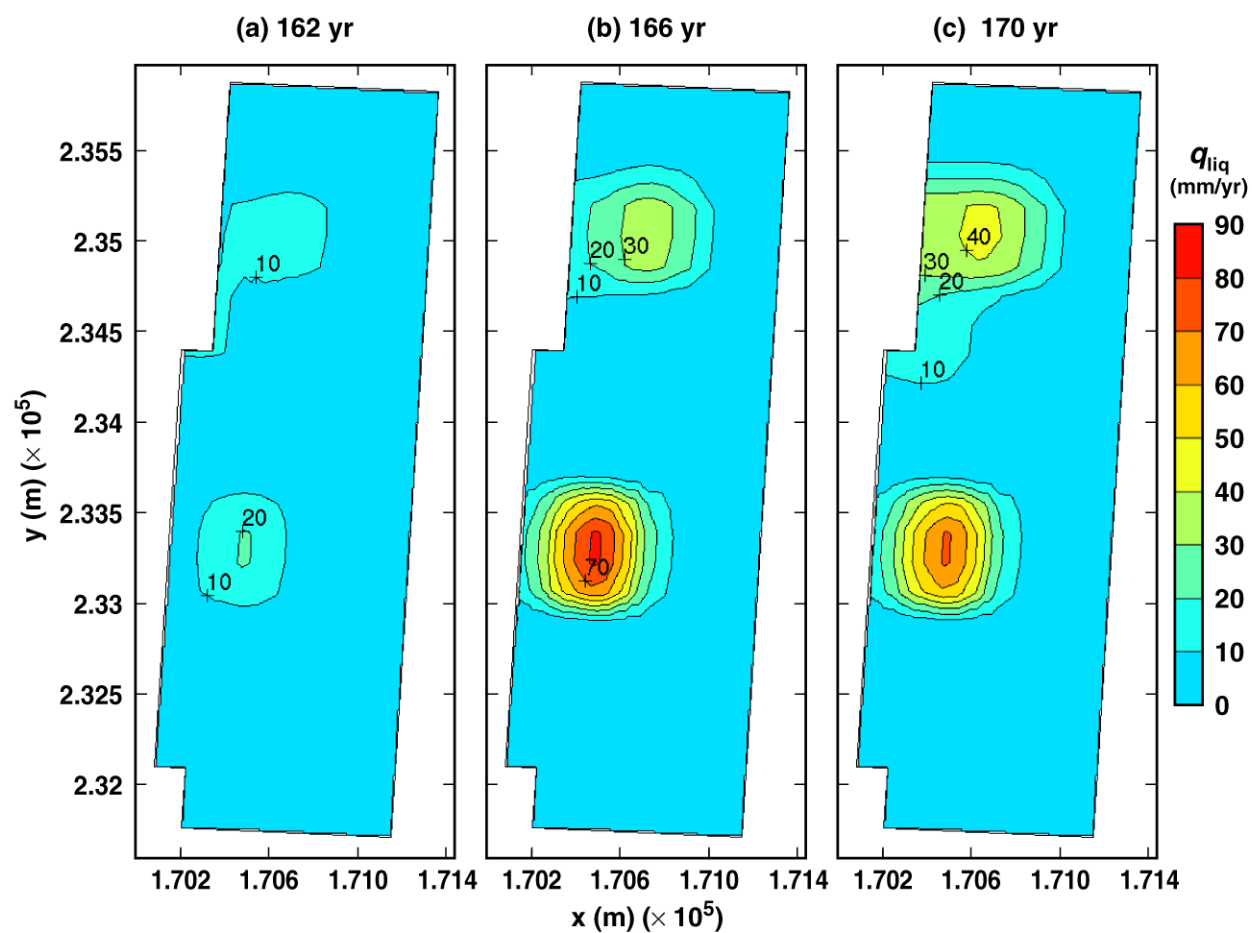
TB_AMR_upper_qliq_dw_pwr1_177-360

Figure 6-32. Liquid-phase flux 0.2 m above the crown of the drift for the high infiltration-flux case for the indicated times.



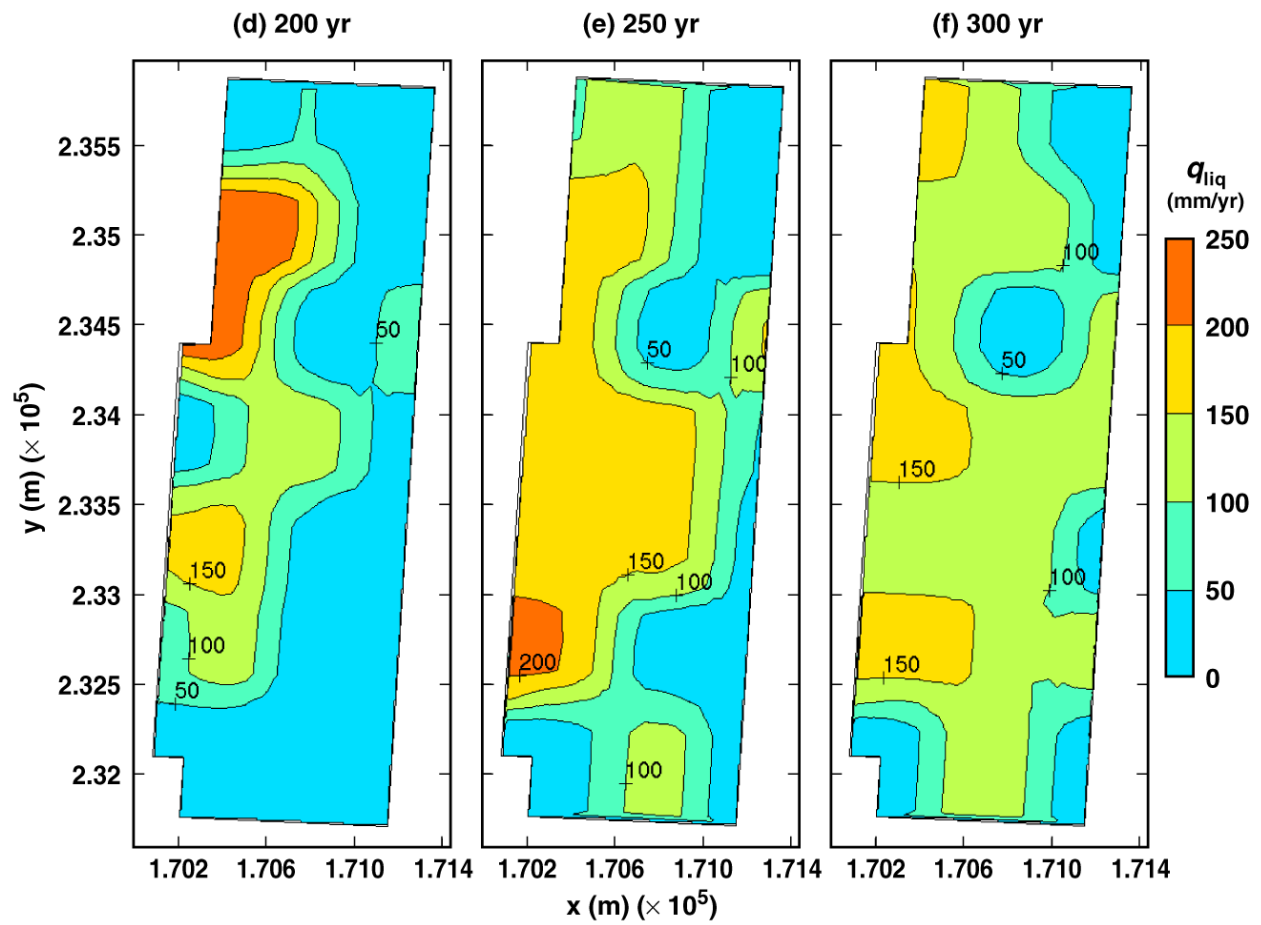
TB_AMR_upper_qliq_dw_pwr1_389-457

Figure 6-32. Liquid-phase flux 0.2 m above the crown of the drift for the high infiltration-flux case for the indicated times.



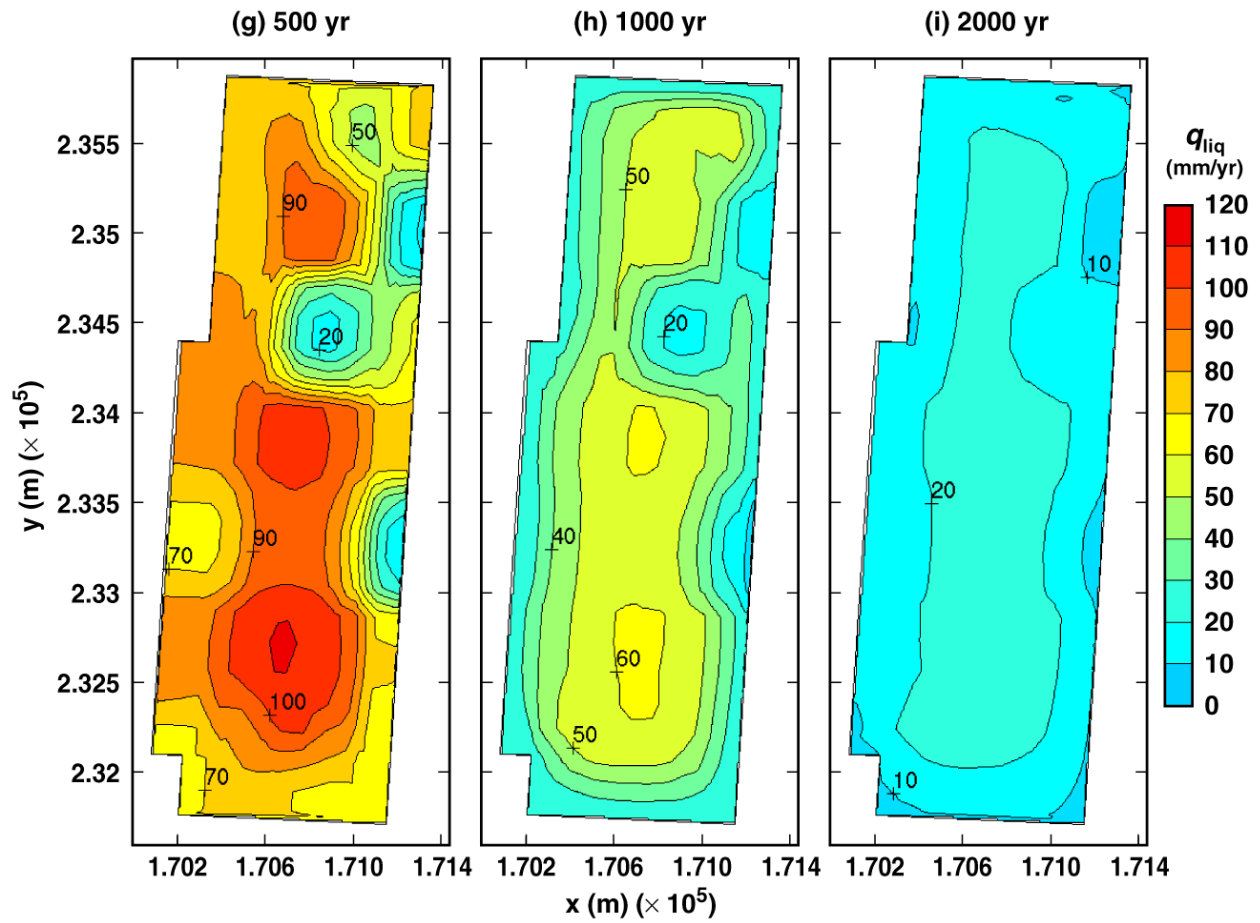
TB_AMR_upper_qliq_dsTop_avg_pwr2_34-39

Figure 6-33. Liquid-phase flux averaged over the upper surface of the dripshield for the high infiltration-flux case for the indicated times.



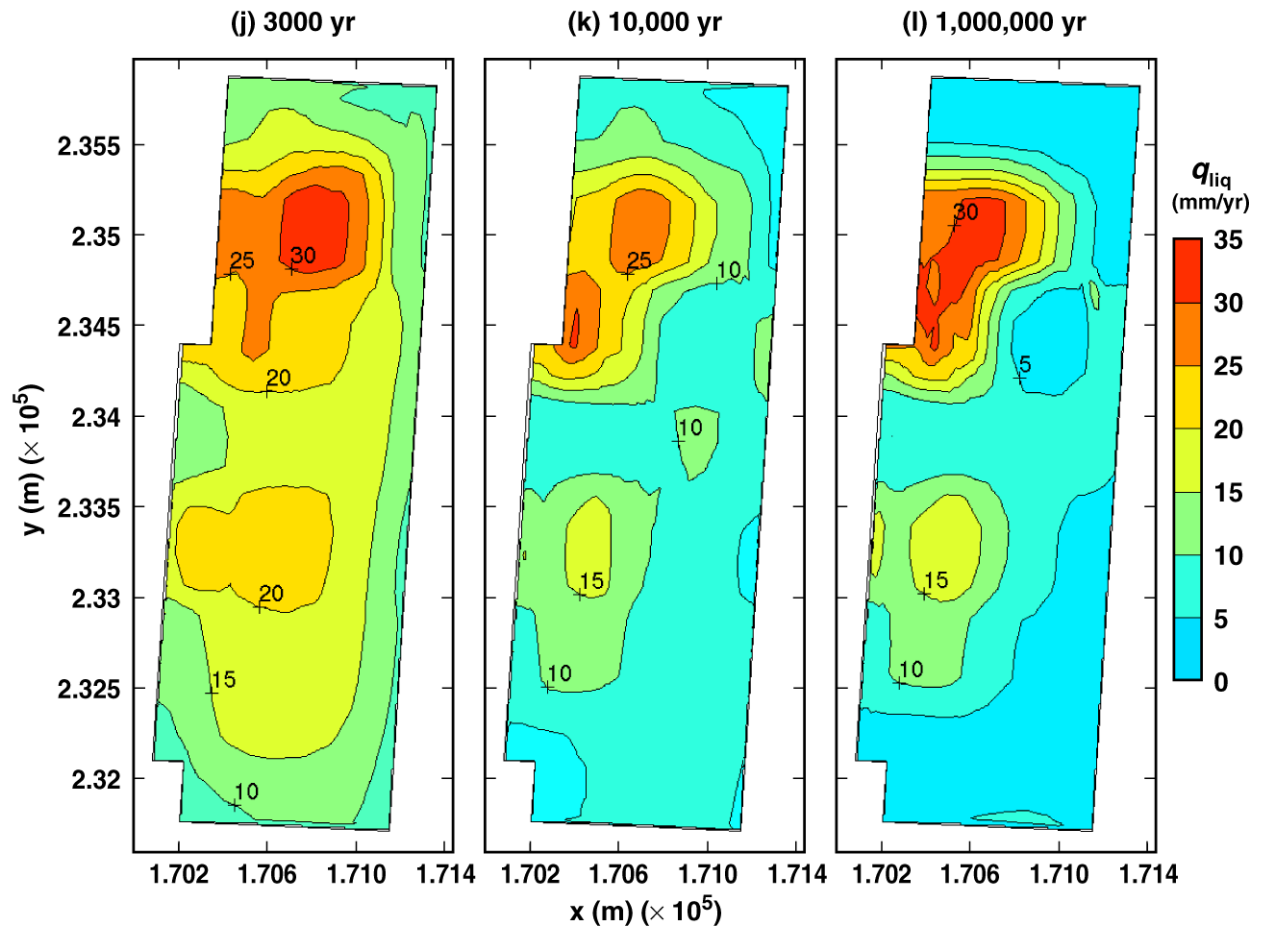
TB_AMR_upper_qliq_dsTop_avg_pwr2_56-107

Figure 6-33. Liquid-phase flux averaged over the upper surface of the dripshield for the high infiltration-flux case for the indicated times.



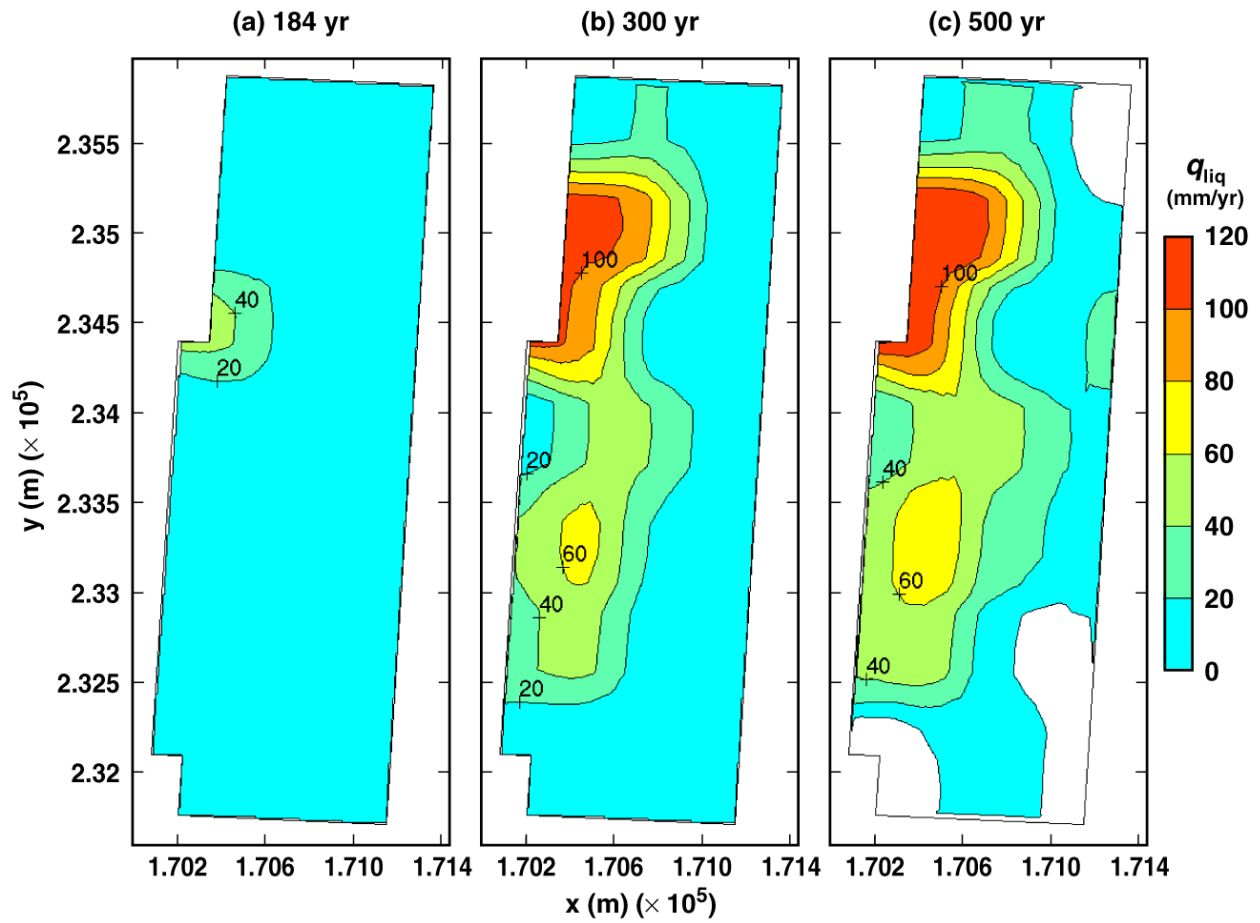
TB_AMR_upper_qliq_dsTop_avg_pwr2_177-360

Figure 6-33. Liquid-phase flux averaged over the upper surface of the dripshield for the high infiltration-flux case for the indicated times.



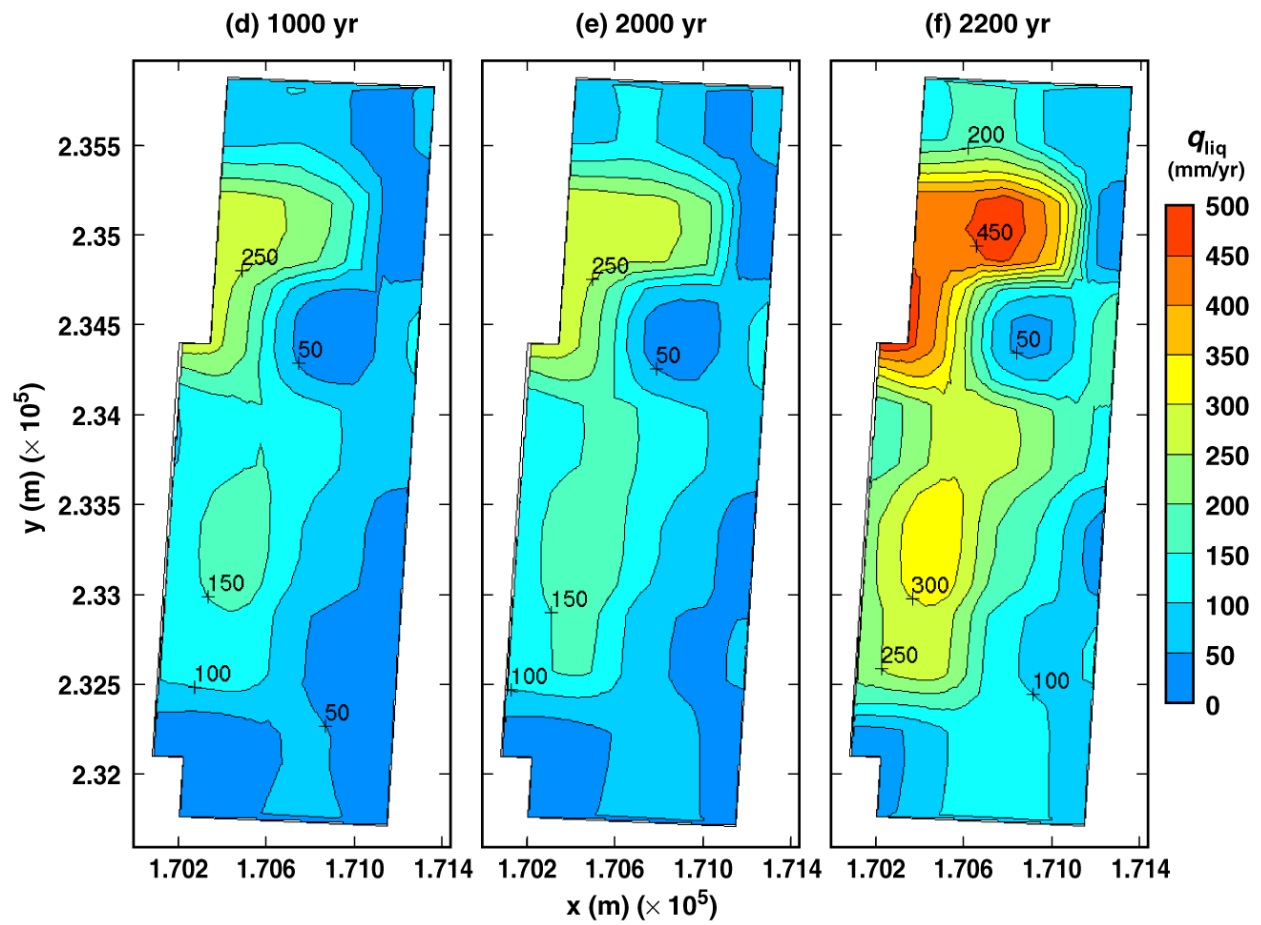
TB_AMR_upper_qliq_dsTop_avg_pwr2_389-457

Figure 6-33. Liquid-phase flux averaged over the upper surface of the dripshield for the high infiltration-flux case for the indicated times.



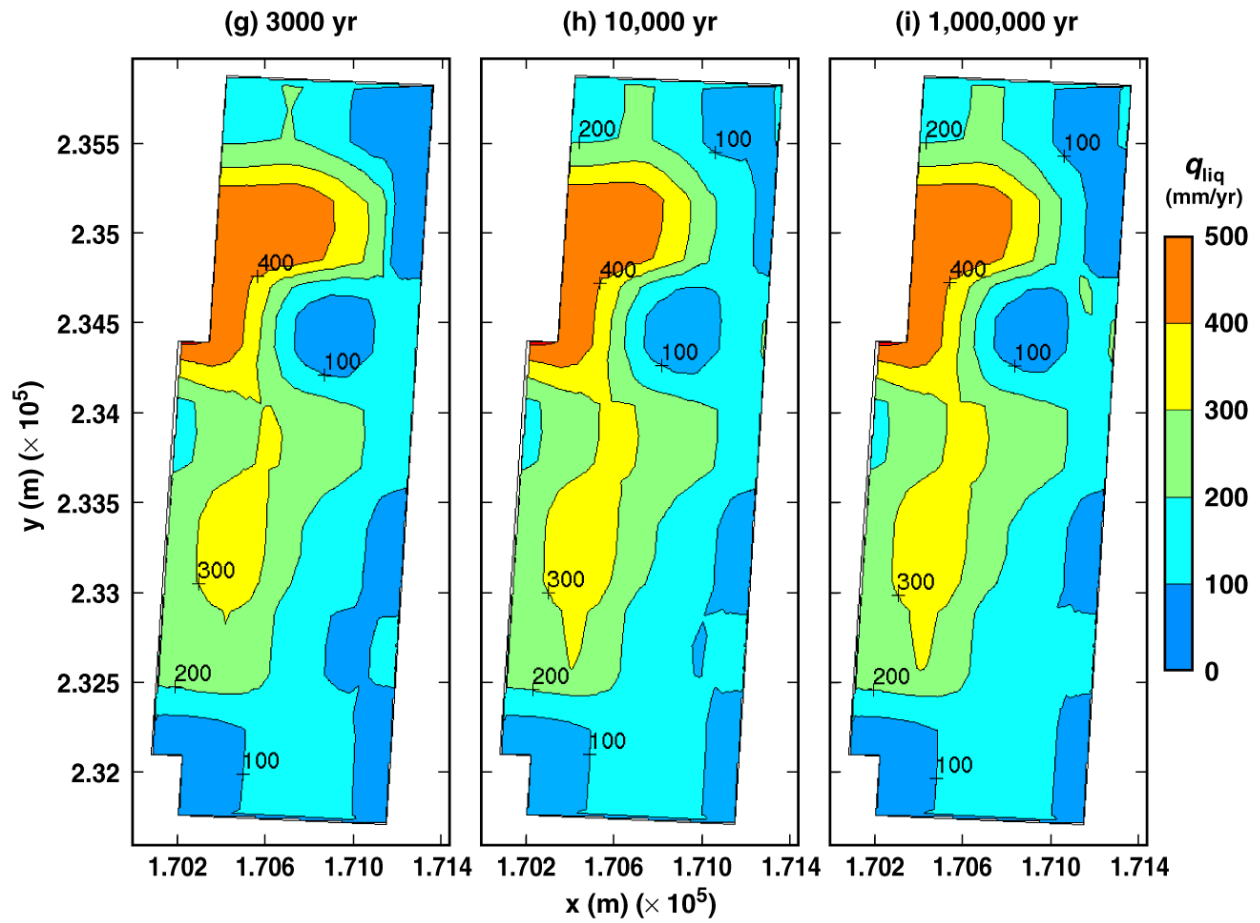
TB_AMR_upper_qliq_dsSide_pwr1_46-177

Figure 6-34. Liquid-phase flux adjacent to the lower side of the dripshield (i.e., adjacent to the base of the dripshield) for the high infiltration-flux case for the indicated times.



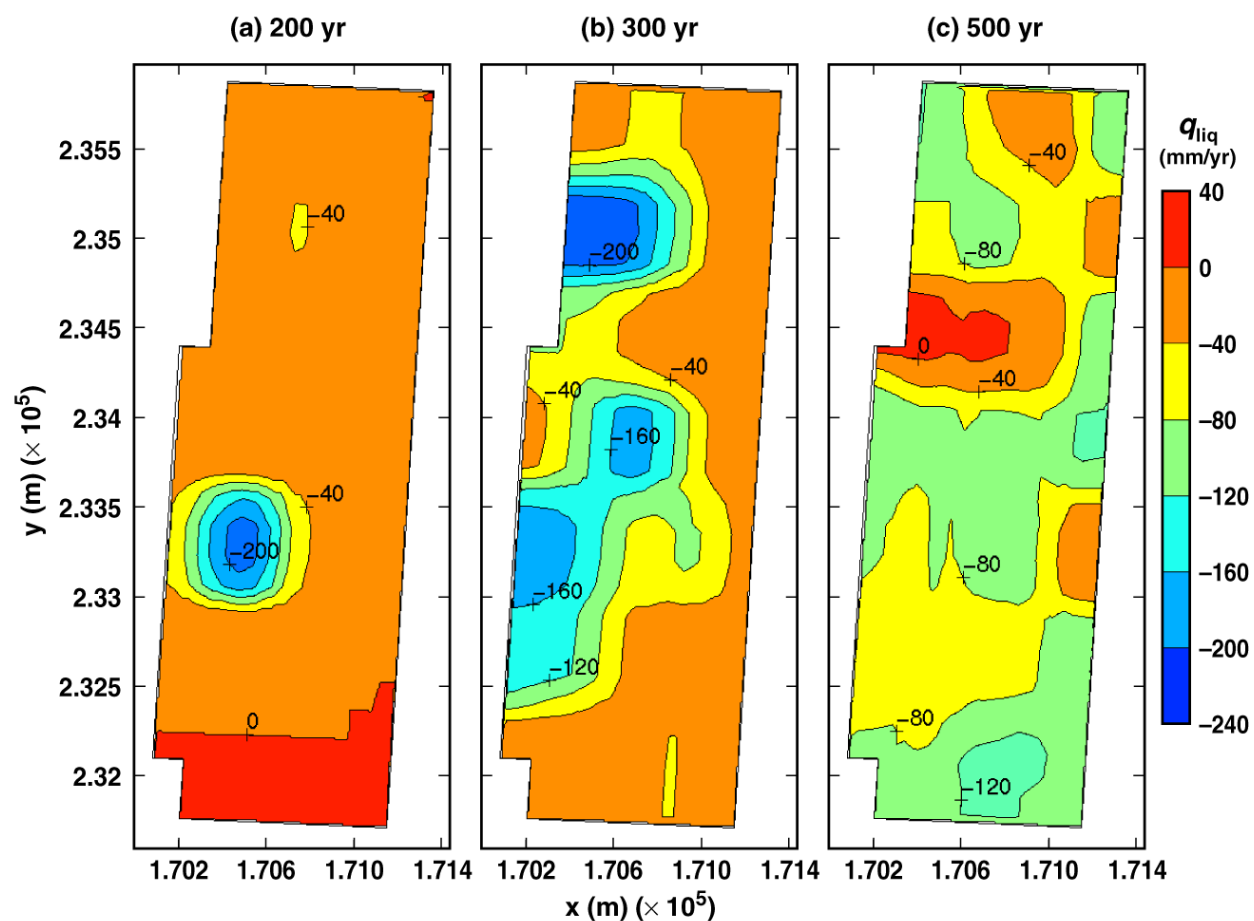
TB_AMR_upper_qliq_dsSide_pwr1_269-372

Figure 6-34. Liquid-phase flux adjacent to the lower side of the dripshield (i.e., adjacent to the base of the dripshield) for the high infiltration-flux case for the indicated times.



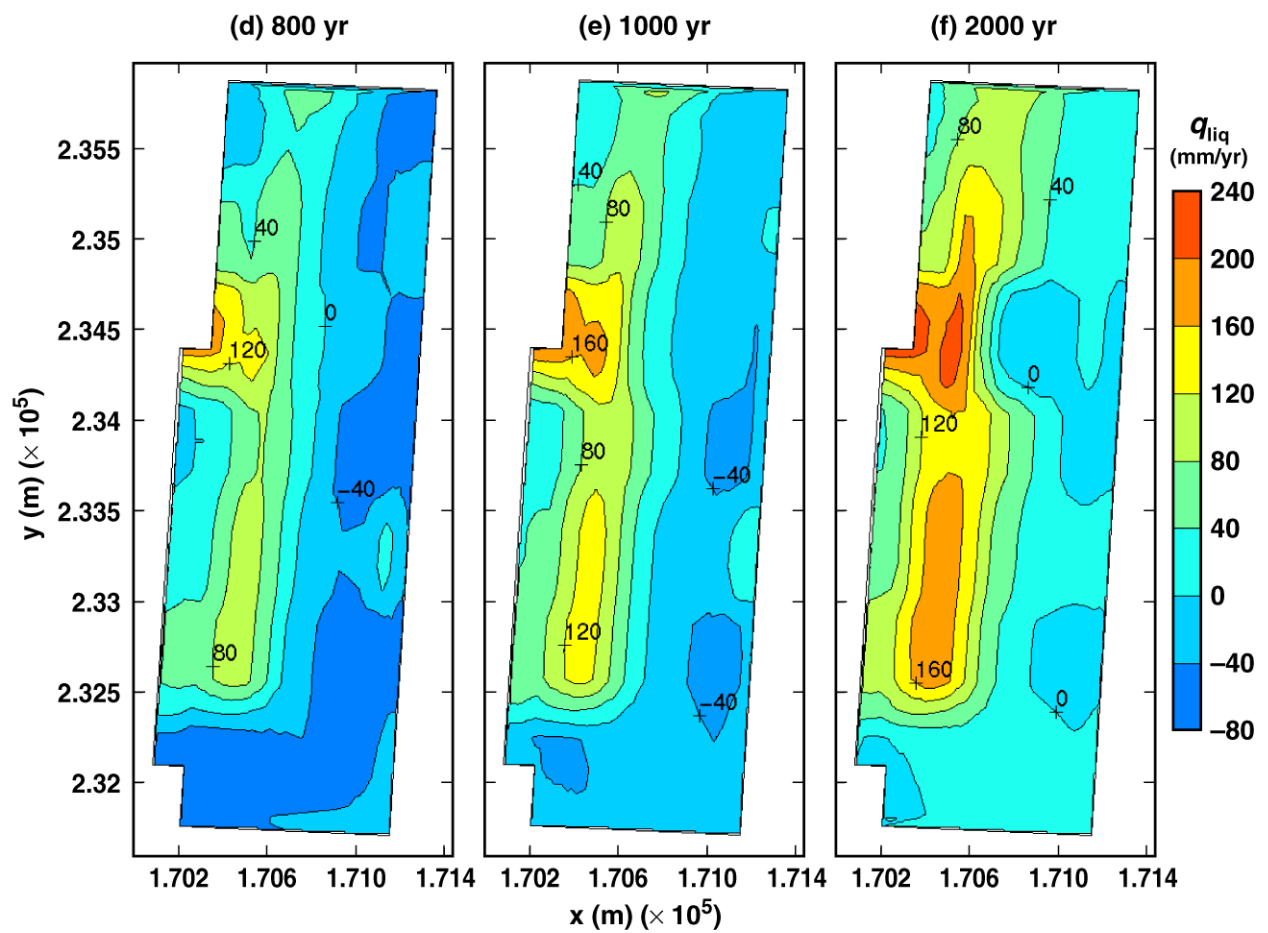
TB_AMR_upper_qliq_dsSide_pwr1_389-457

Figure 6-34. Liquid-phase flux adjacent to the lower side of the dripshield (i.e., adjacent to the base of the dripshield) for the high infiltration-flux case for the indicated times.



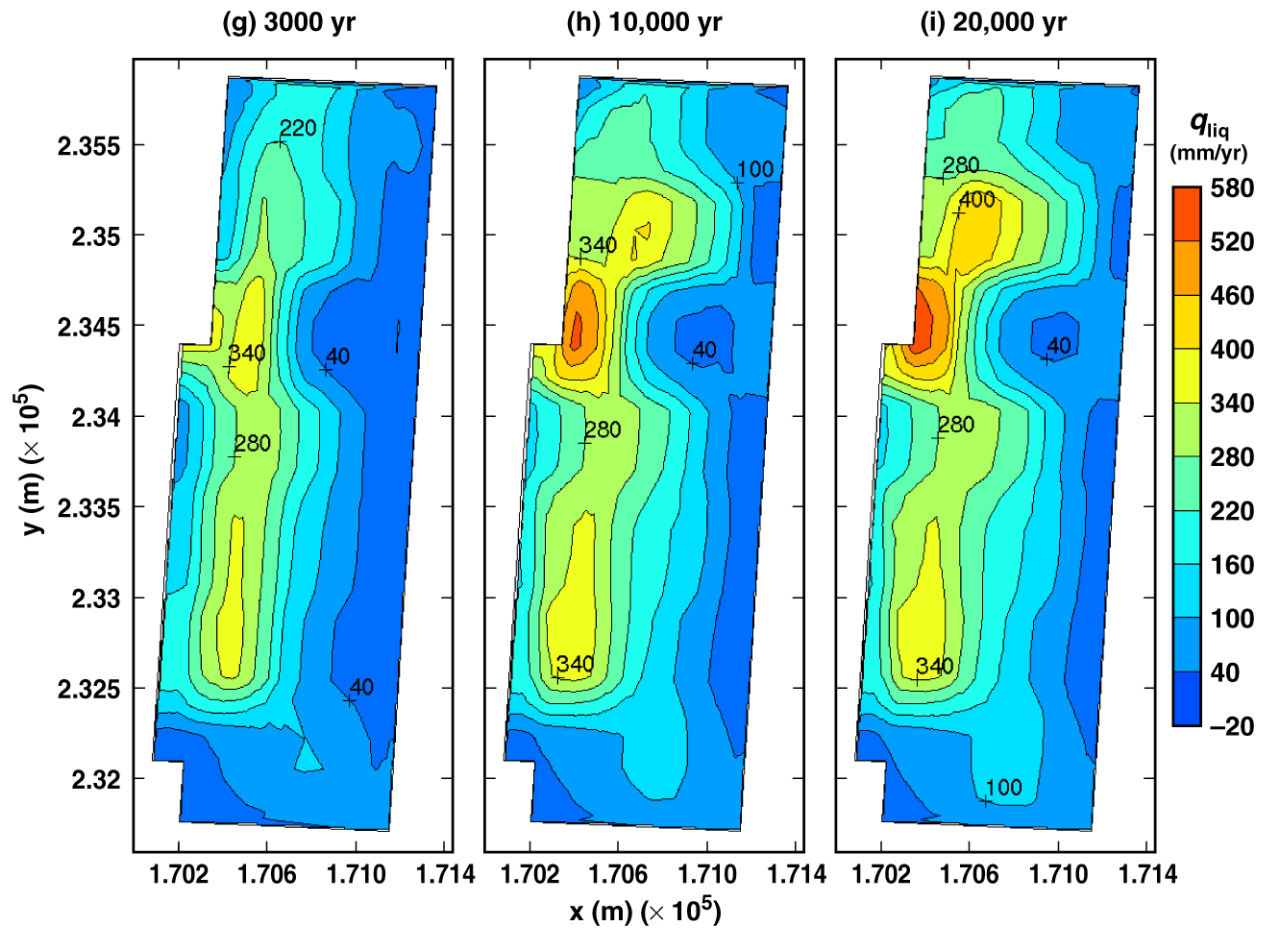
TB_AMR_upper_qliq_invert_pwr2_56-177

Figure 6-35. Liquid-phase flux averaged over the invert for the high infiltration-flux case for the indicated times.



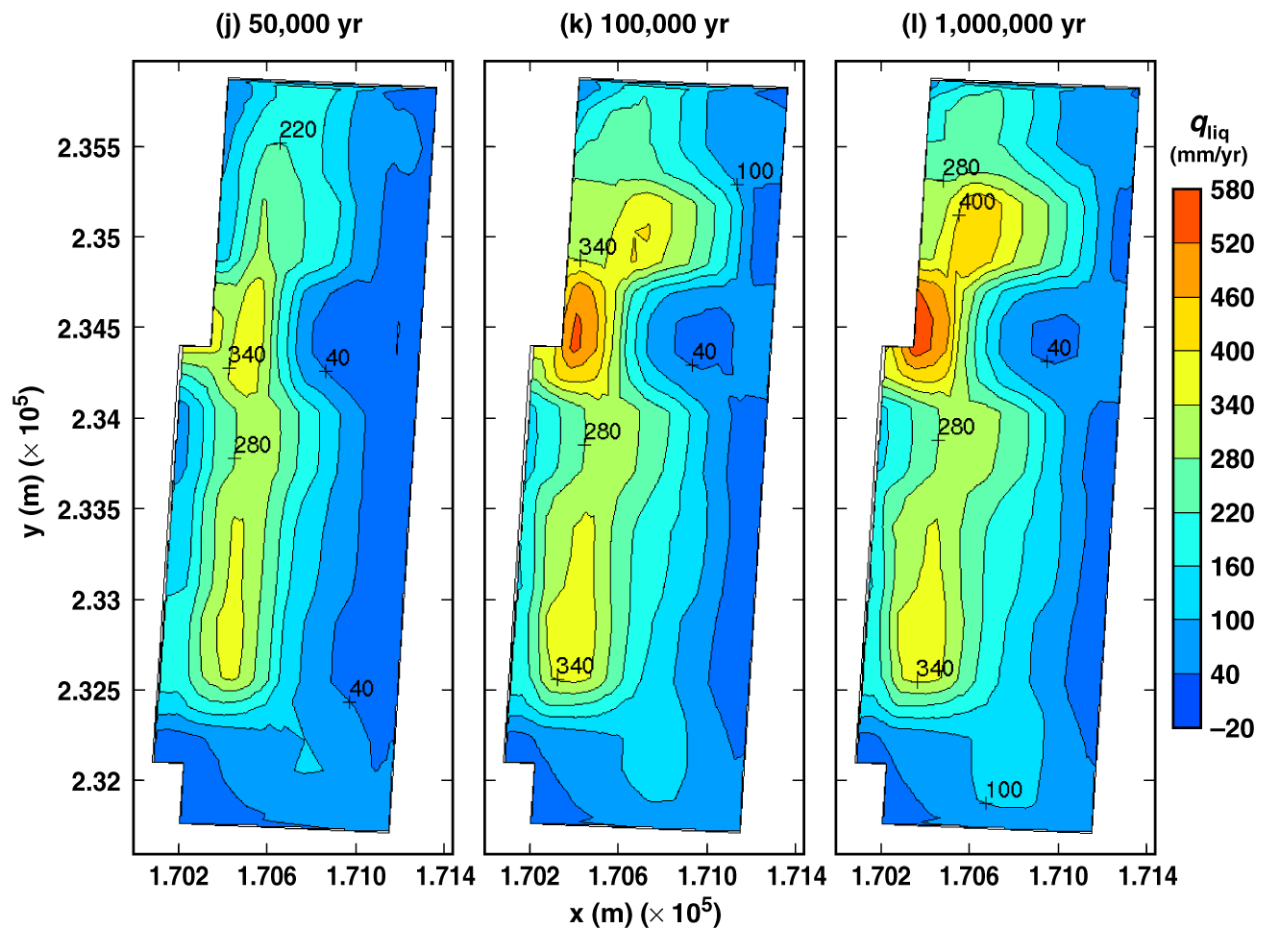
TB_AMR_upper_qliq_invert_pwr2_237-360

Figure 6-35. Liquid-phase flux averaged over the invert for the high infiltration-flux case for the indicated times.



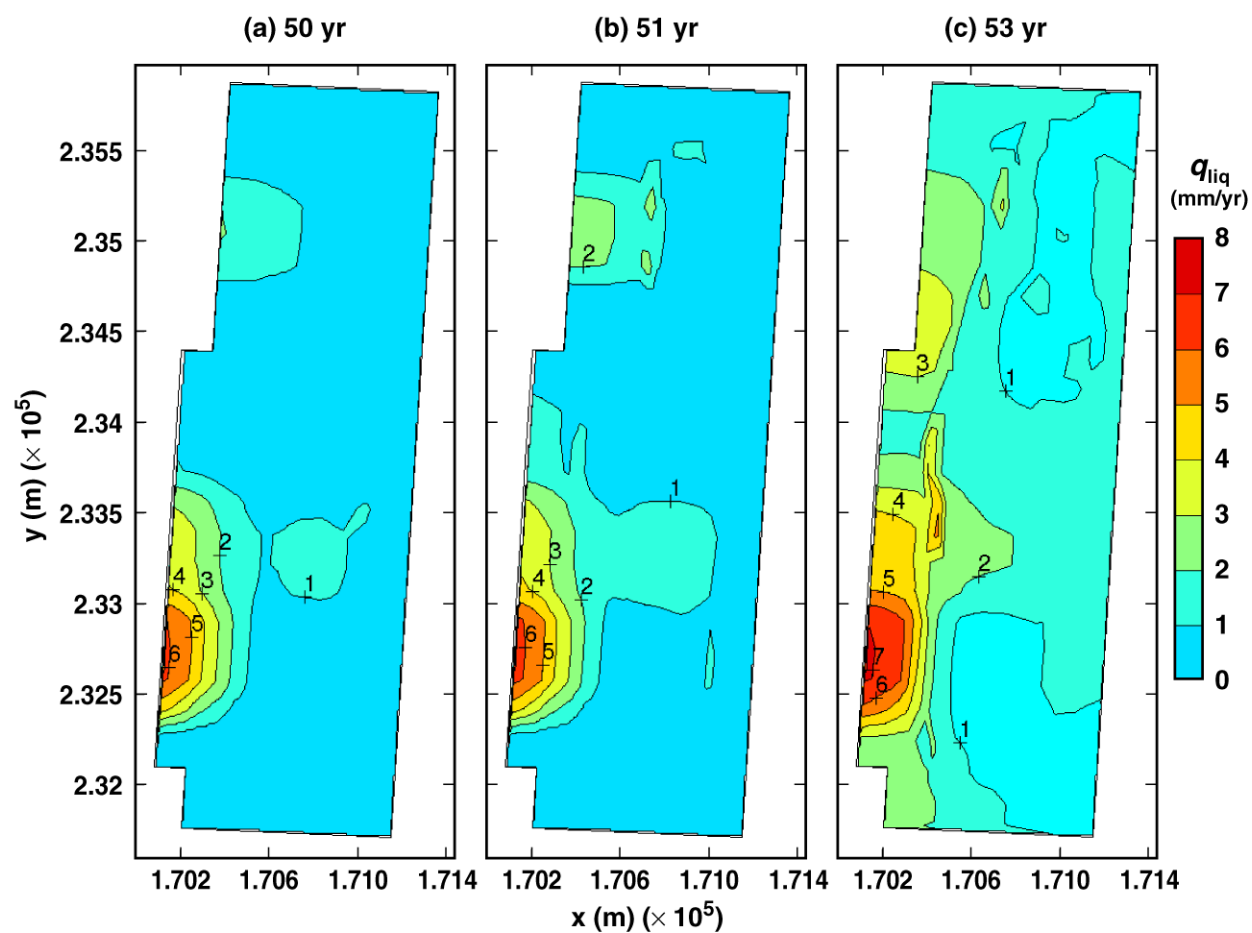
TB_AMR_upper_qliq_invert_pwr2_389-434

Figure 6-35. Liquid-phase flux averaged over the invert for the high infiltration-flux case for the indicated times.



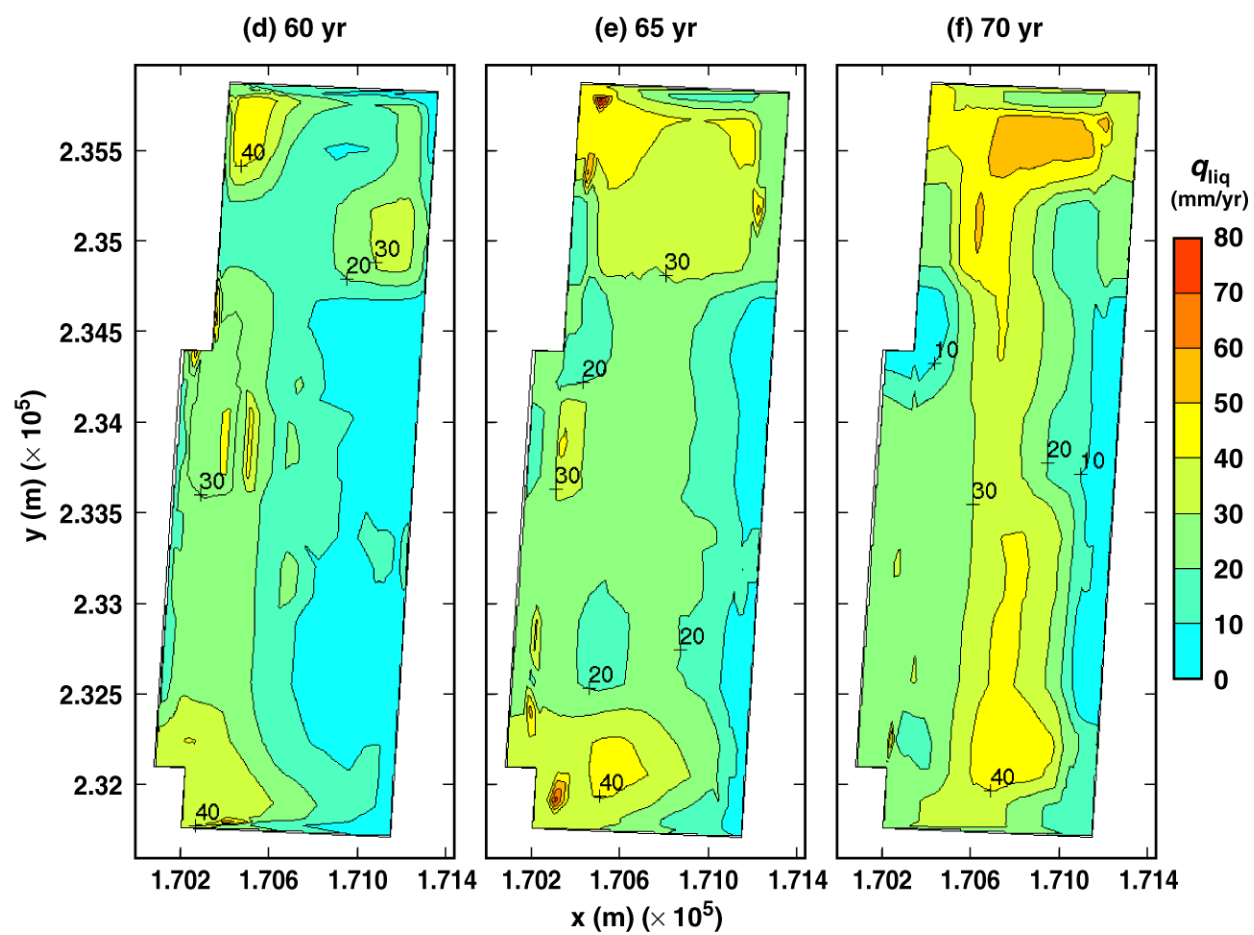
TB_AMR_upper_qliq_invert_pwr2_446-457

Figure 6-35. Liquid-phase flux averaged over the invert for the high infiltration-flux case for the indicated times.



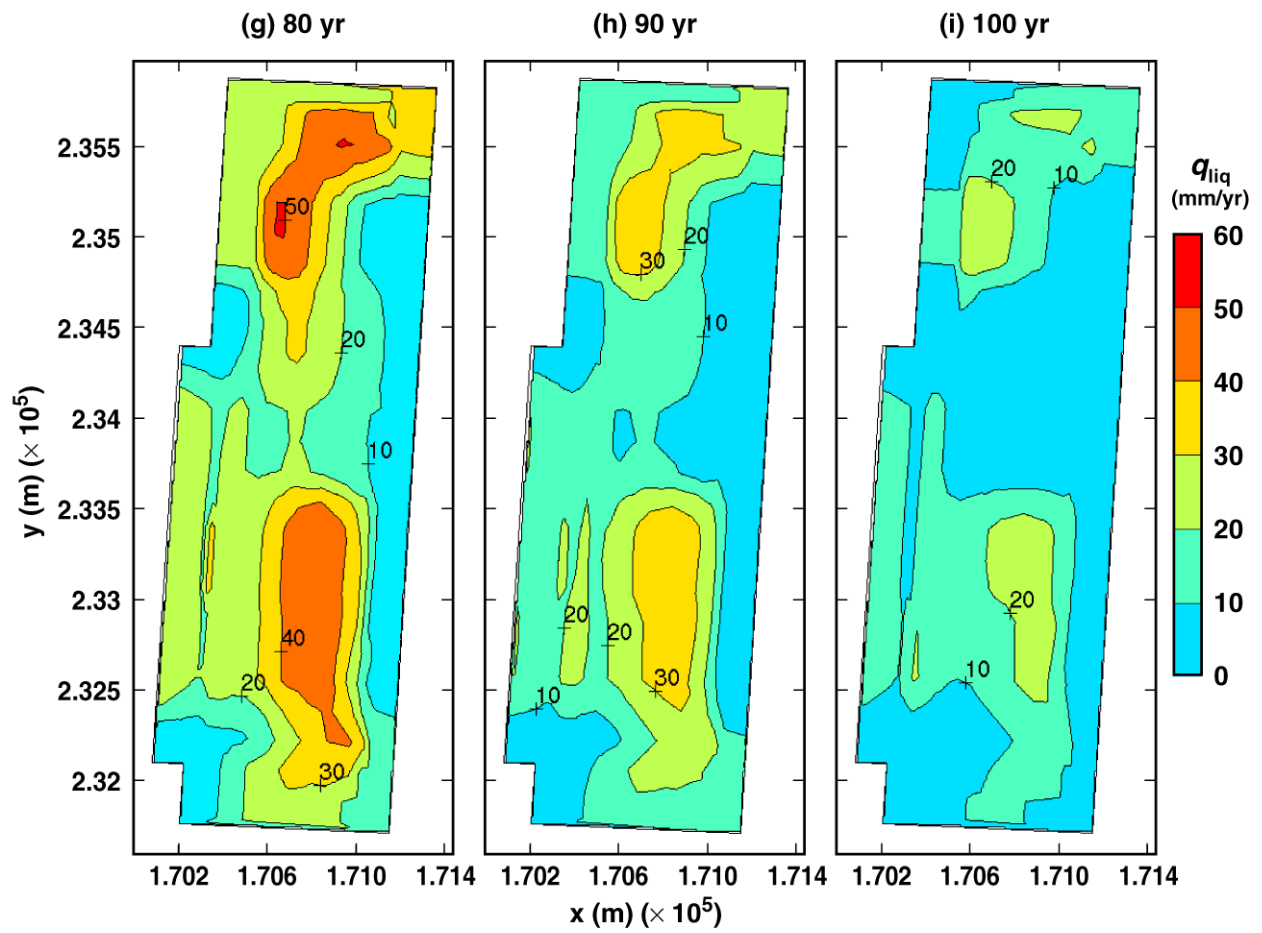
TB_AMR_lower_qliq_5m_pwr2_13-15

Figure 6-36. Liquid-phase flux 5 m above the crown of the drift for the low infiltration-flux case for the indicated times.



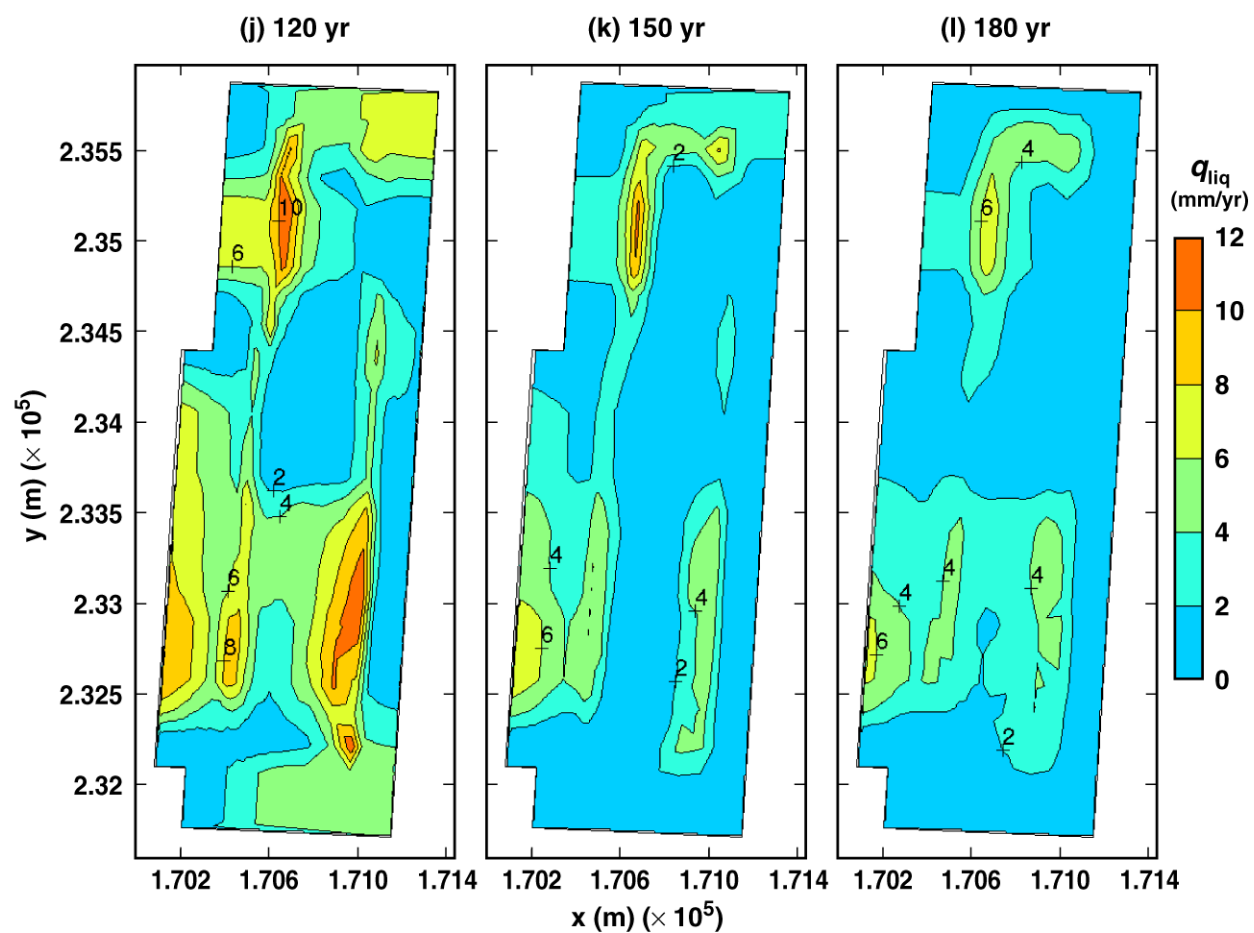
TB_AMR_lower_qliq_5m_pwr2_17-19

Figure 6-36. Liquid-phase flux 5 m above the crown of the drift for the low infiltration-flux case for the indicated times.



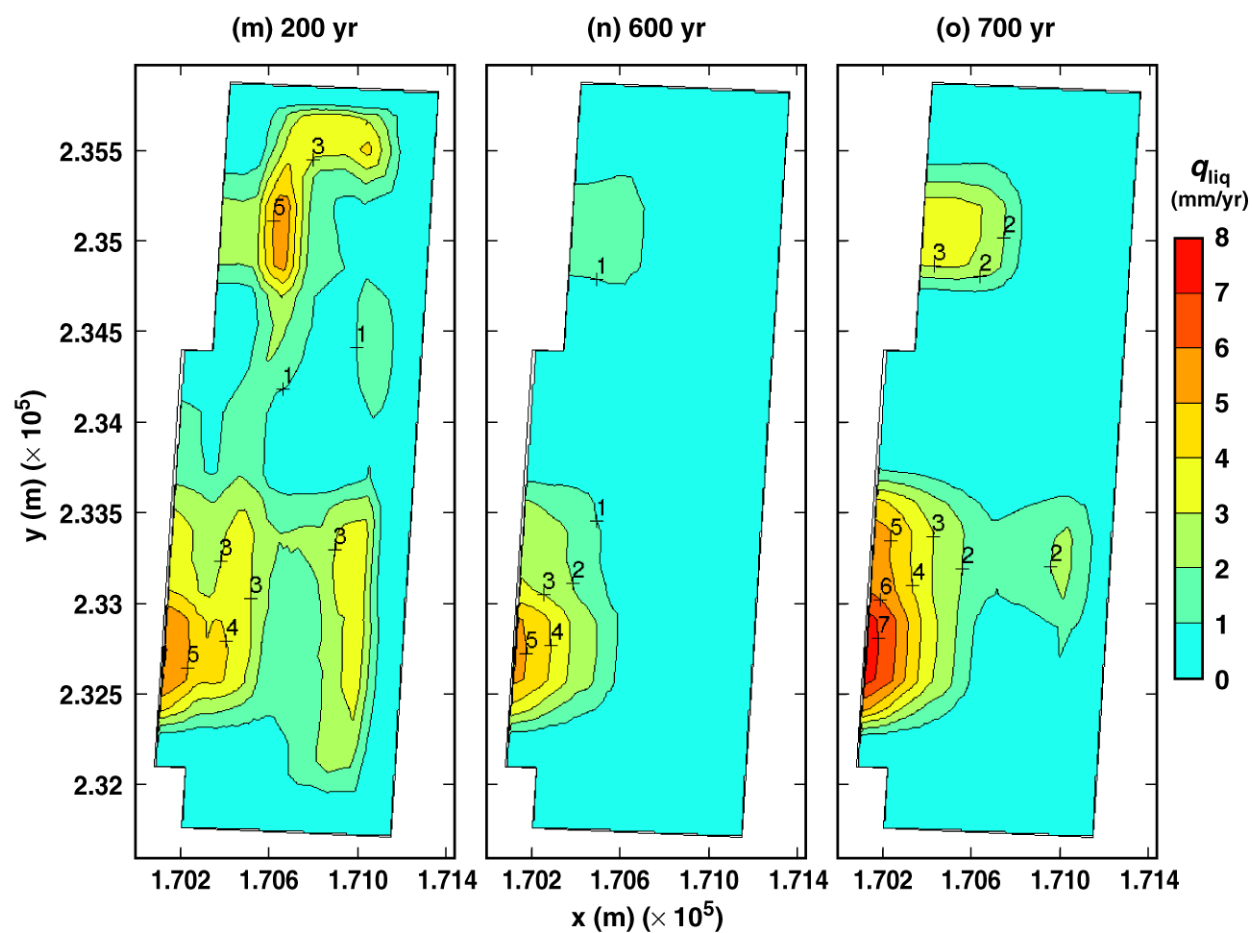
TB_AMR_lower_qliq_5m_pwr2_20-22

Figure 6-36. Liquid-phase flux 5 m above the crown of the drift for the low infiltration-flux case for the indicated times.



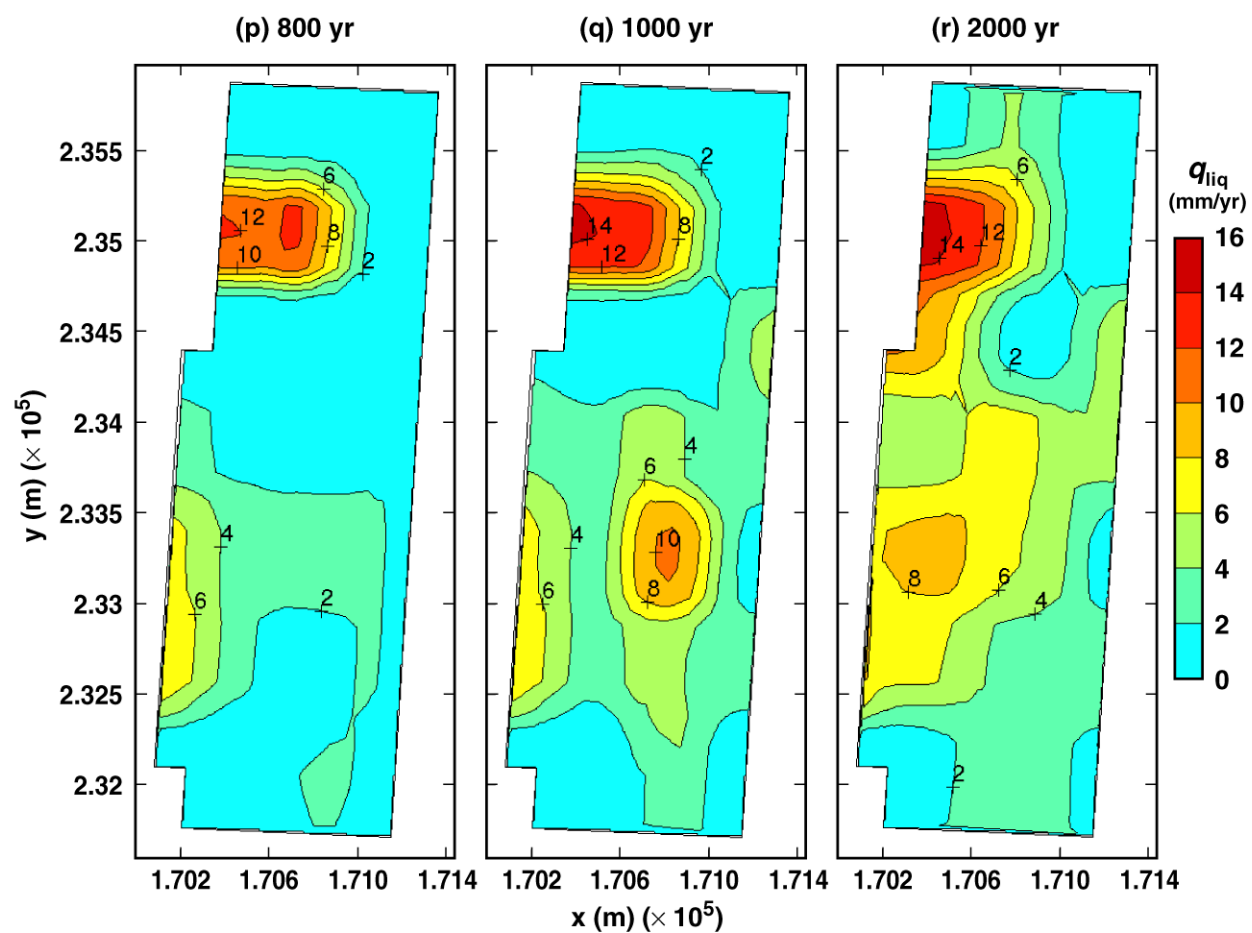
TB_AMR_lower_qliq_5m_pwr2_23-27

Figure 6-36. Liquid-phase flux 5 m above the crown of the drift for the low infiltration-flux case for the indicated times.



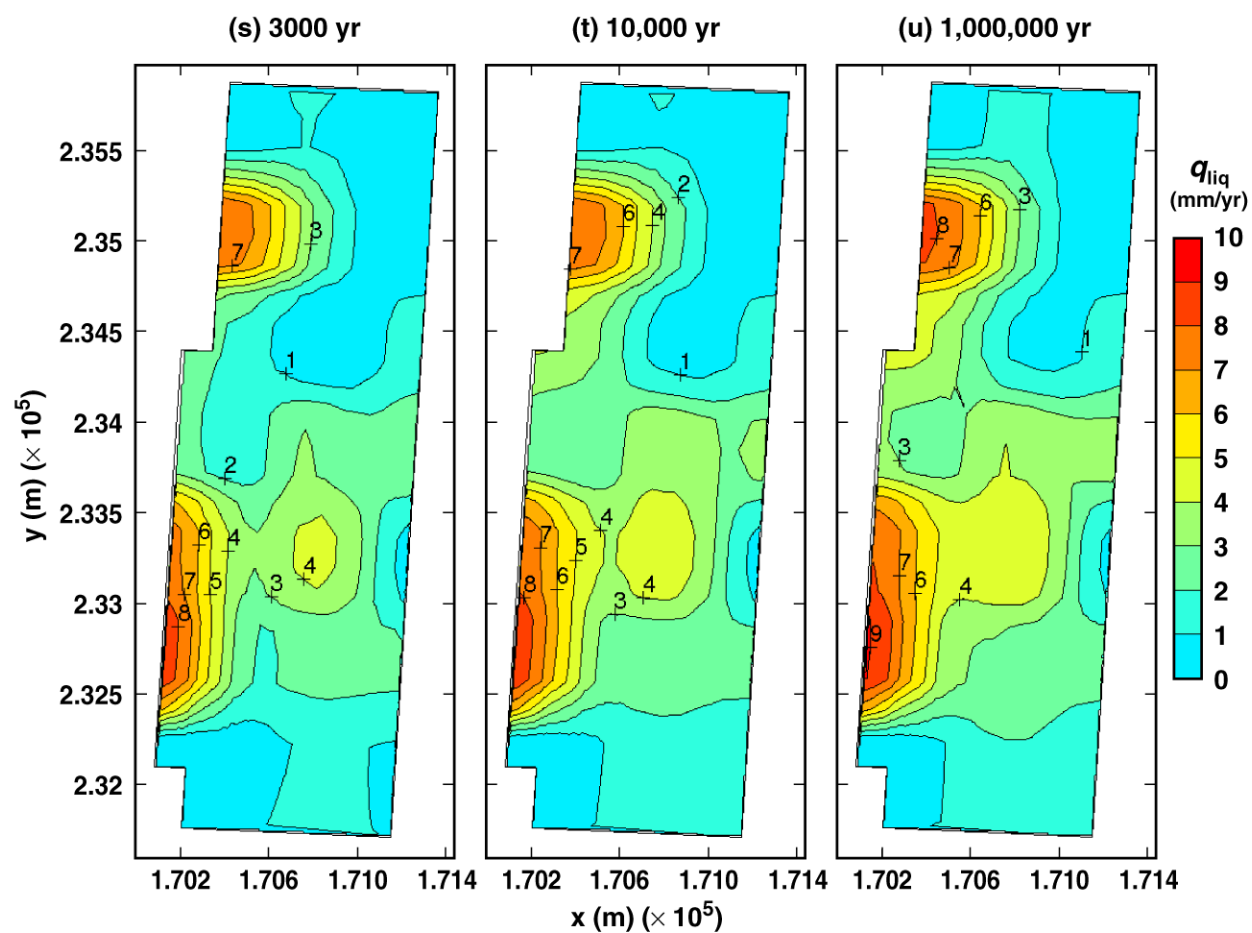
TB_AMR_lower_qliq_5m_pwr2_28-128

Figure 6-36. Liquid-phase flux 5 m above the crown of the drift for the low infiltration-flux case for the indicated times.



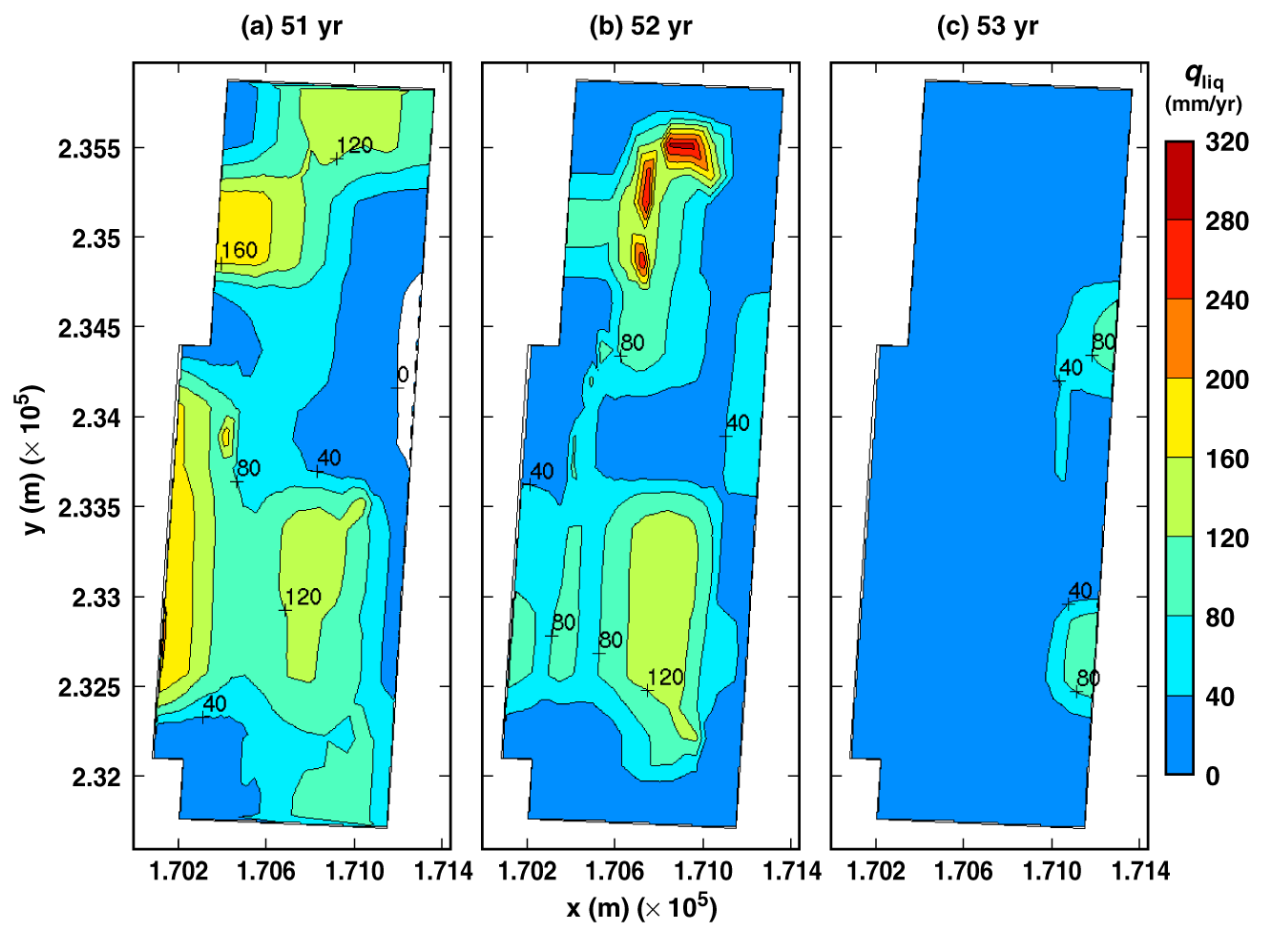
TB_AMR_lower_qliq_5m_pwr2_166-322

Figure 6-36. Liquid-phase flux 5 m above the crown of the drift for the low infiltration-flux case for the indicated times.



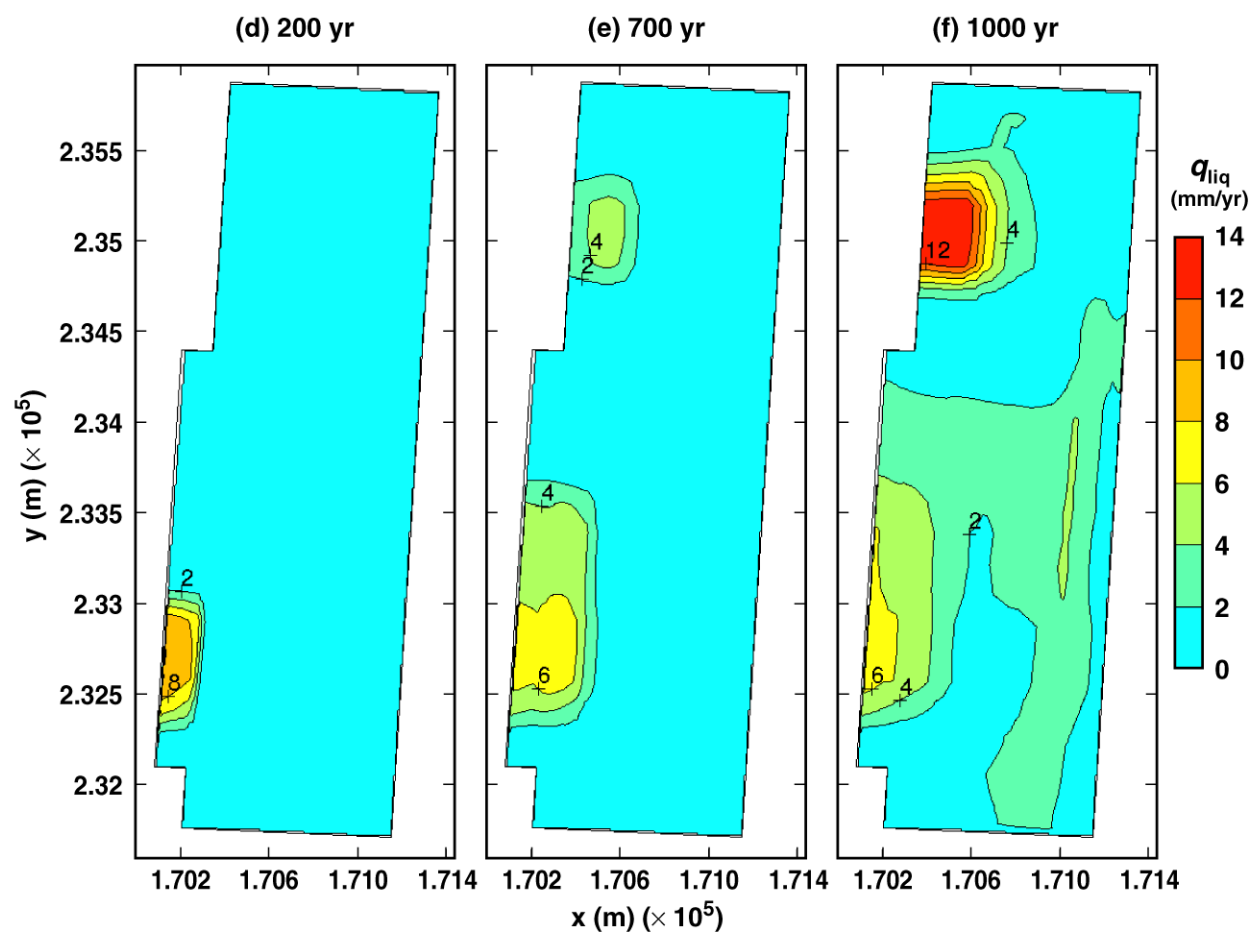
TB_AMR_lower_qliq_5m_pwr2_355-442

Figure 6-36. Liquid-phase flux 5 m above the crown of the drift for the low infiltration-flux case for the indicated times.



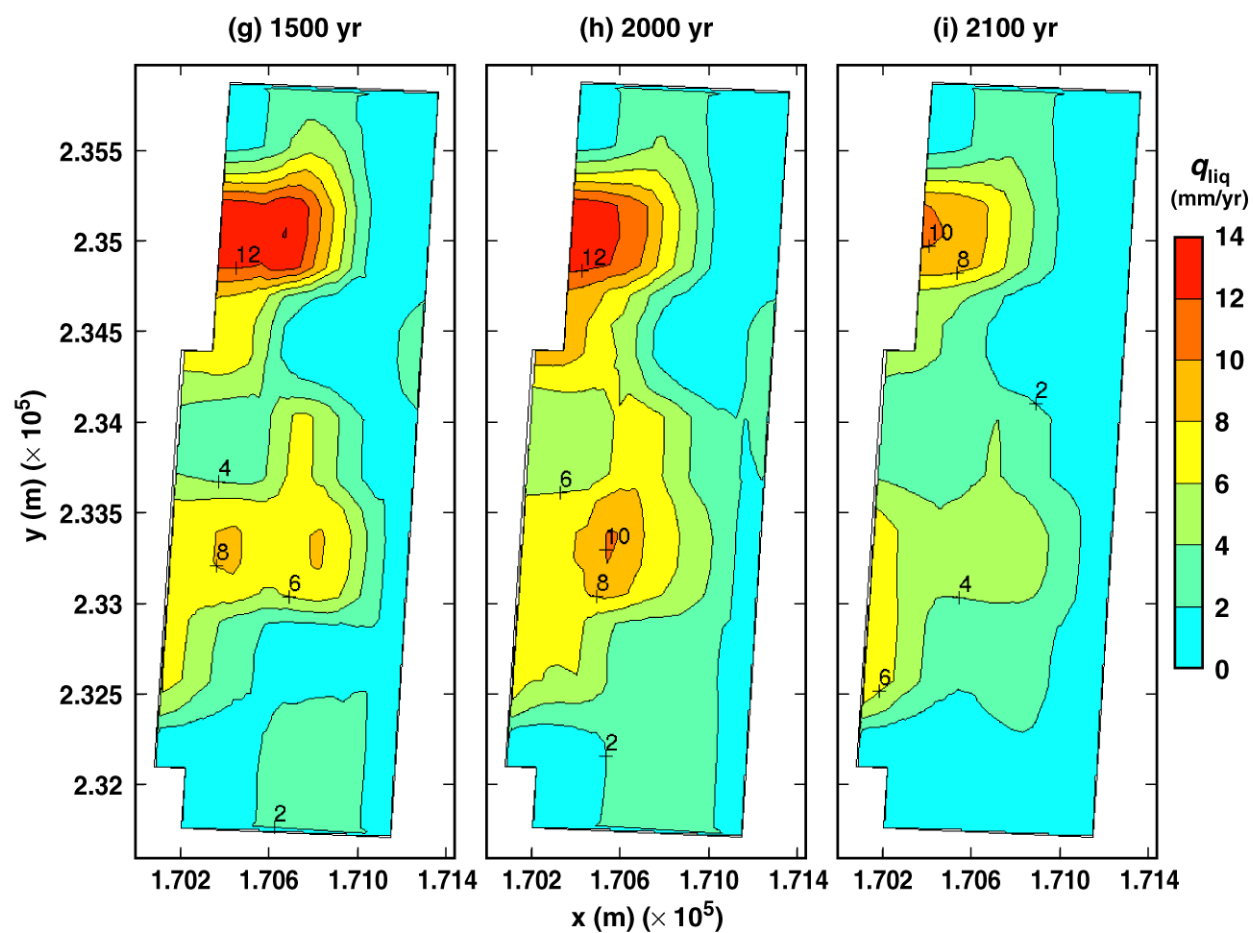
TB_AMR_lower_qliq_dw_pwr2_13-15

Figure 6-37. Liquid-phase flux 0.2 m above the crown of the drift for the low infiltration-flux case for the indicated times.



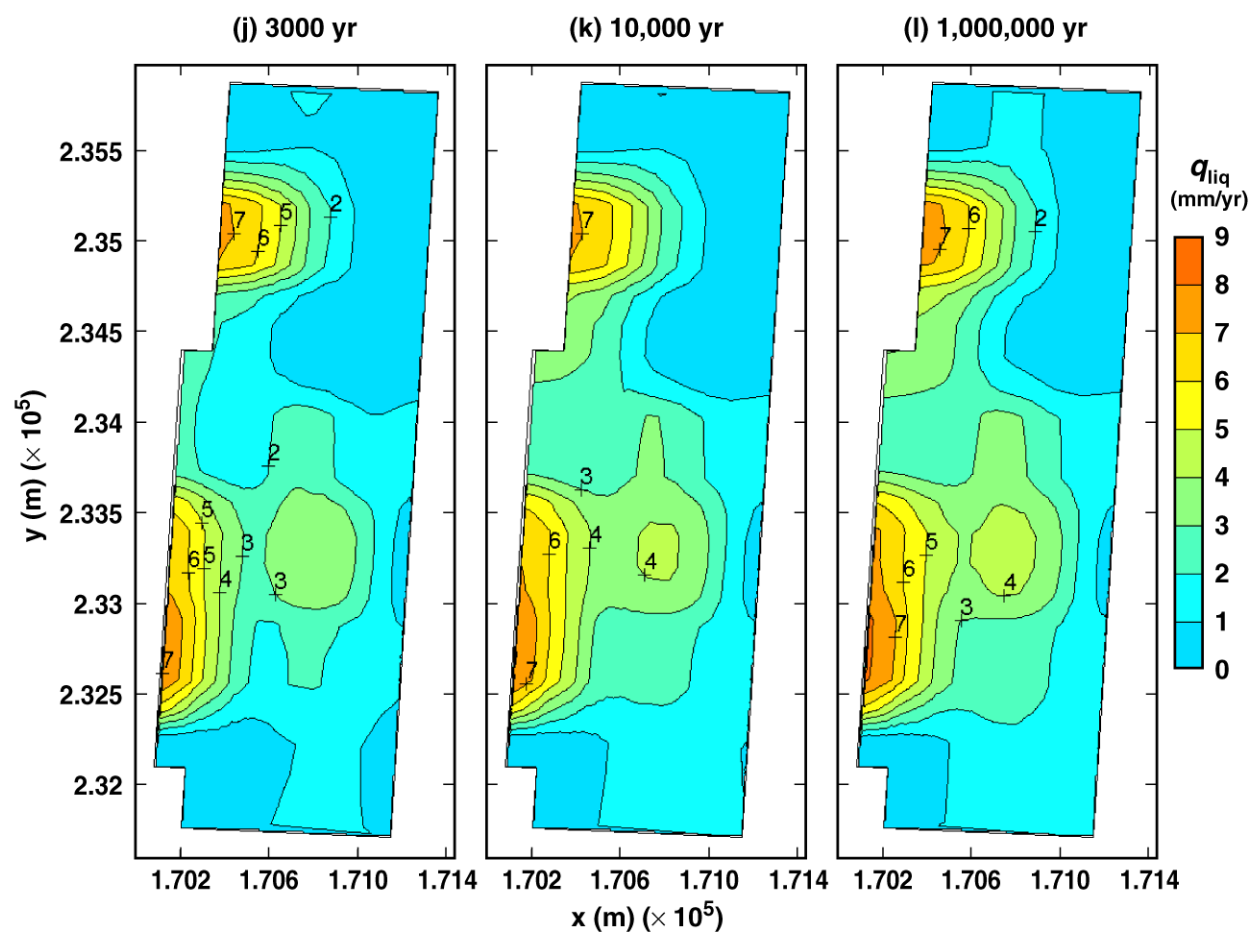
TB_AMR_lower_qliq_dw_pwr2_28-219

Figure 6-37. Liquid-phase flux 0.2 m above the crown of the drift for the low infiltration-flux case for the indicated times.



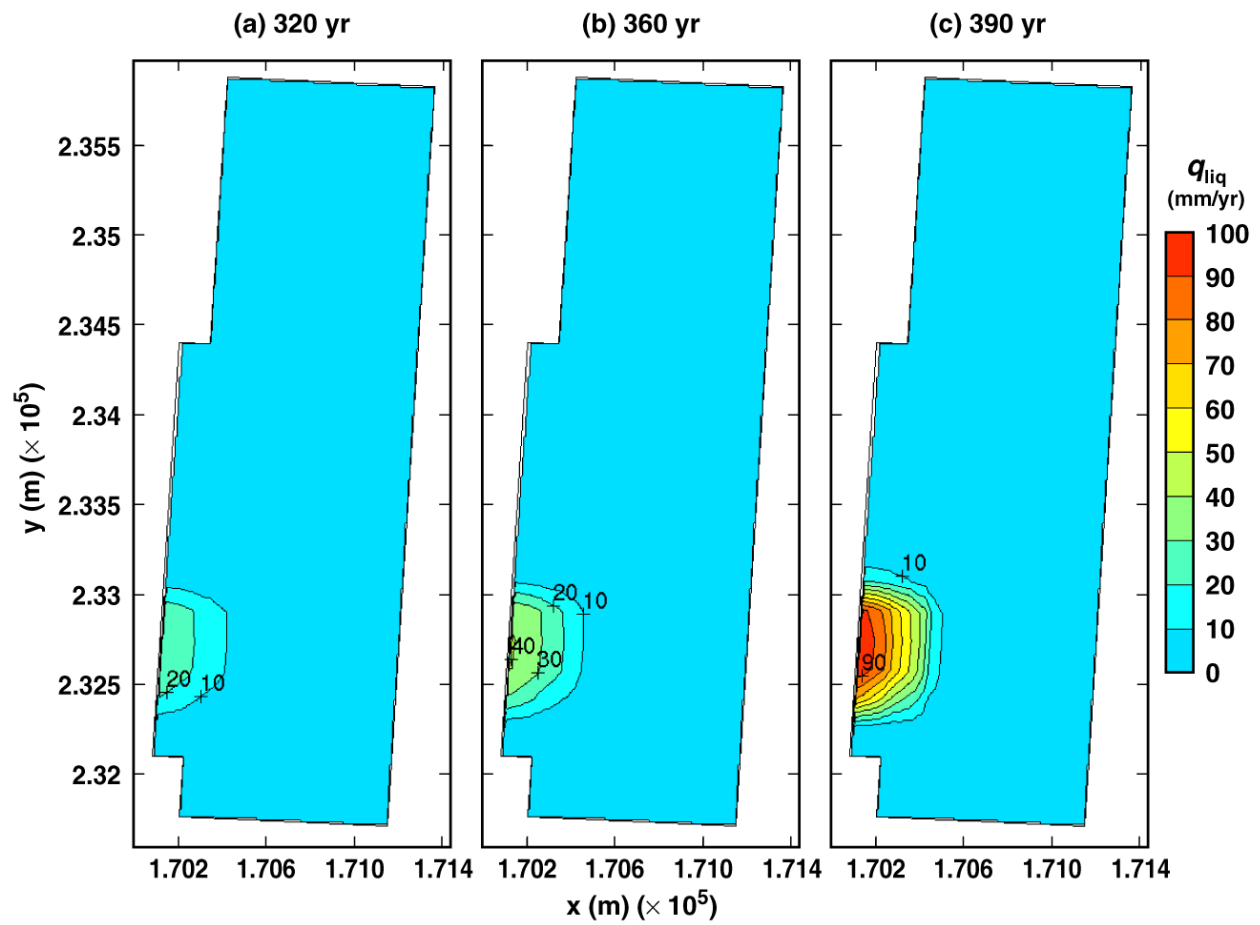
TB_AMR_lower_qliq_dw_pwr2_276-328

Figure 6-37. Liquid-phase flux 0.2 m above the crown of the drift for the low infiltration-flux case for the indicated times.



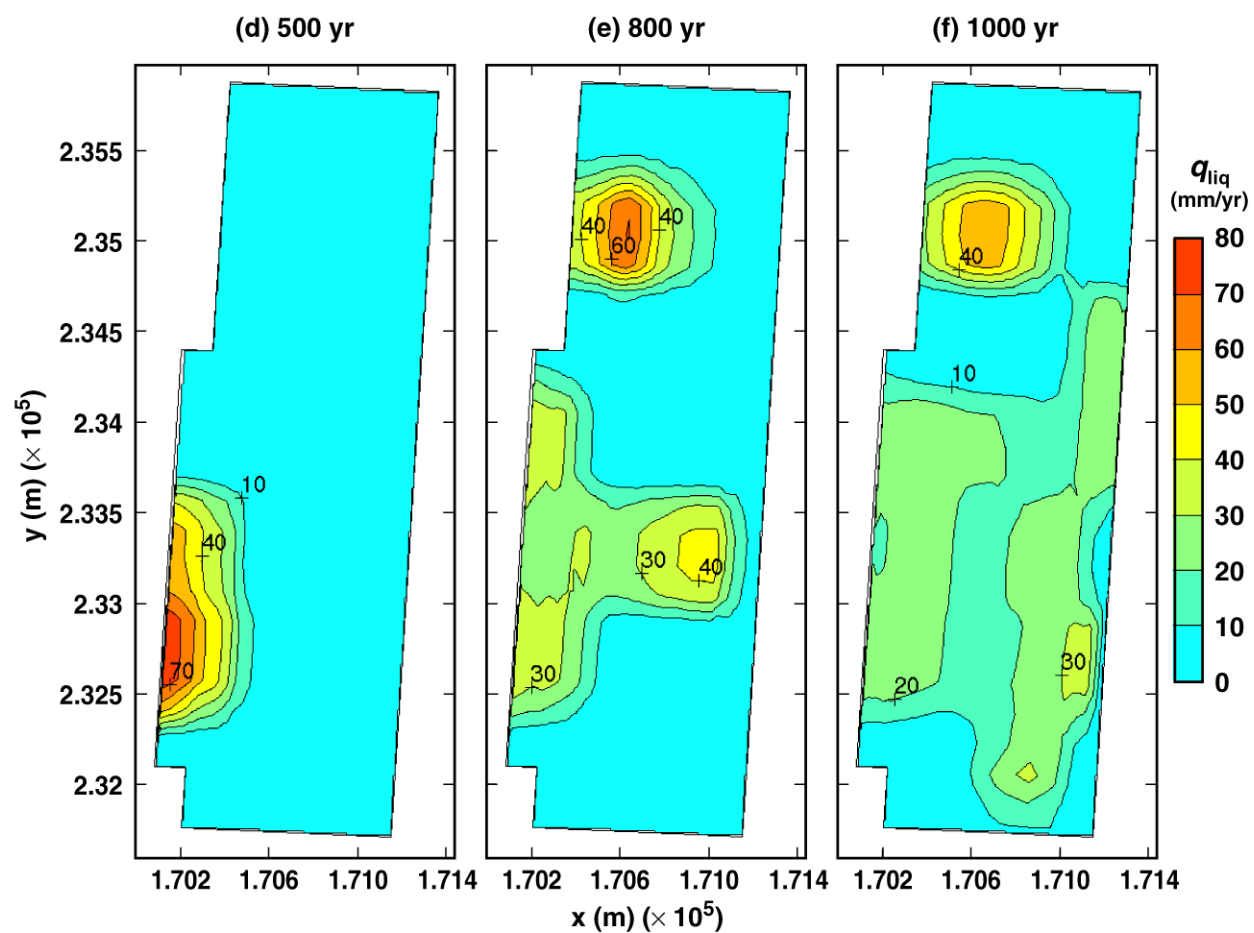
TB_AMR_lower_qliq_dw_pwr2_355-442

Figure 6-37. Liquid-phase flux 0.2 m above the crown of the drift for the low infiltration-flux case for the indicated times.



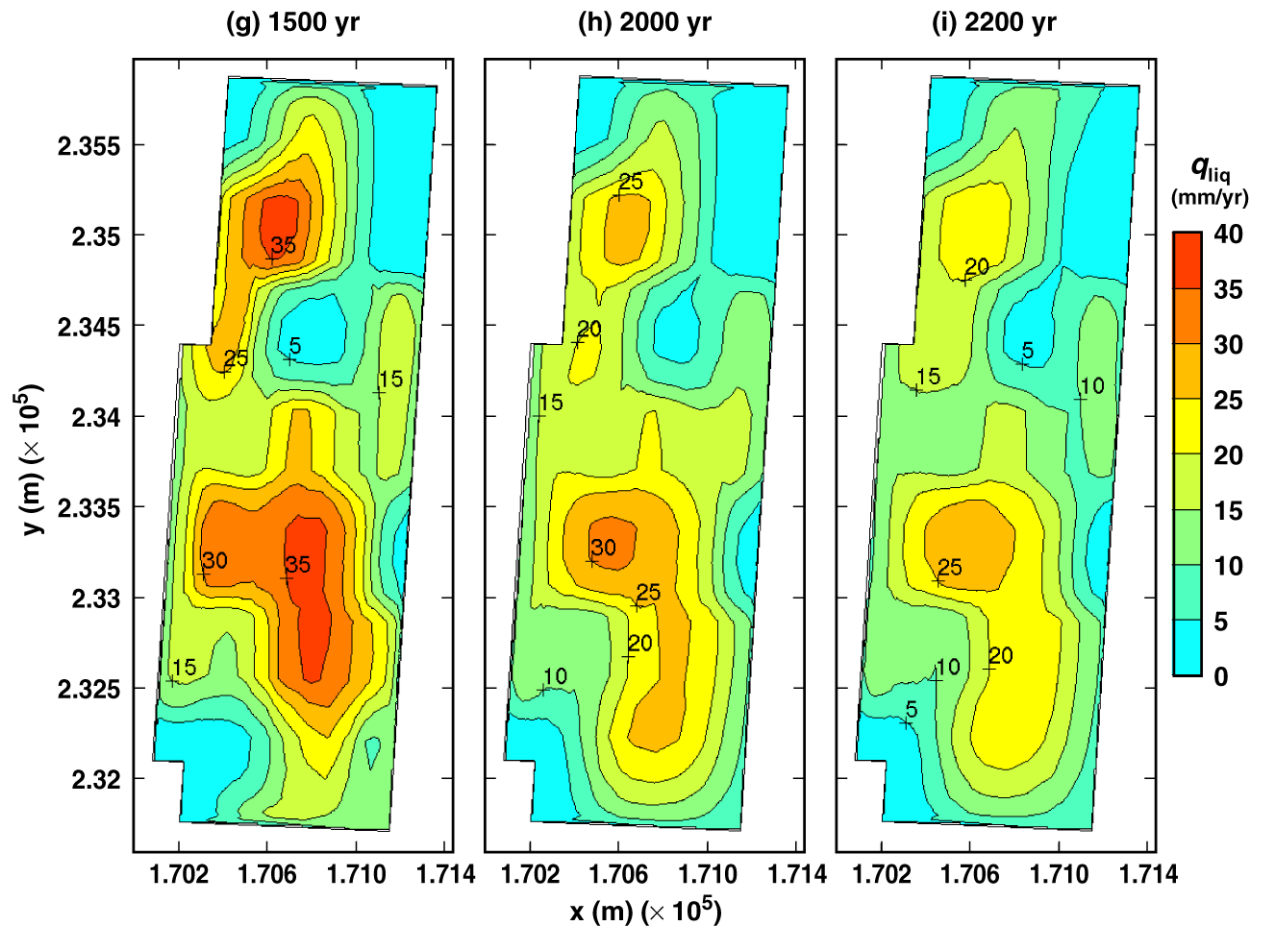
TB_AMR_lower_qliq_dsTop_avg_pwr2_38-55

Figure 6-38. Liquid-phase flux averaged over the upper surface of the dripshield for the low infiltration-flux case for the indicated times.



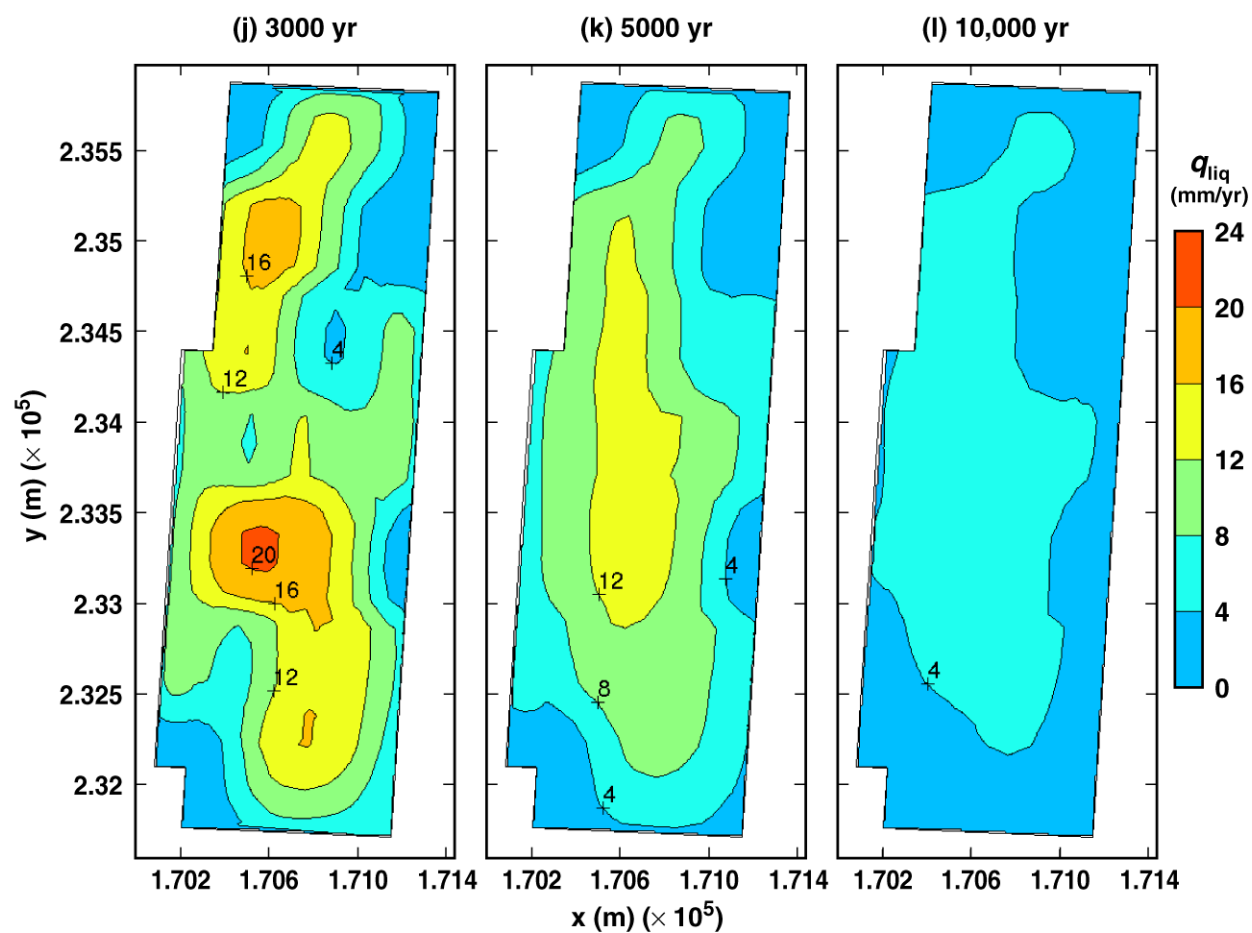
TB_AMR_lower_qliq_dsTop_avg_pwr2_77-219

Figure 6-38. Liquid-phase flux averaged over the upper surface of the dripshield for the low infiltration-flux case for the indicated times.



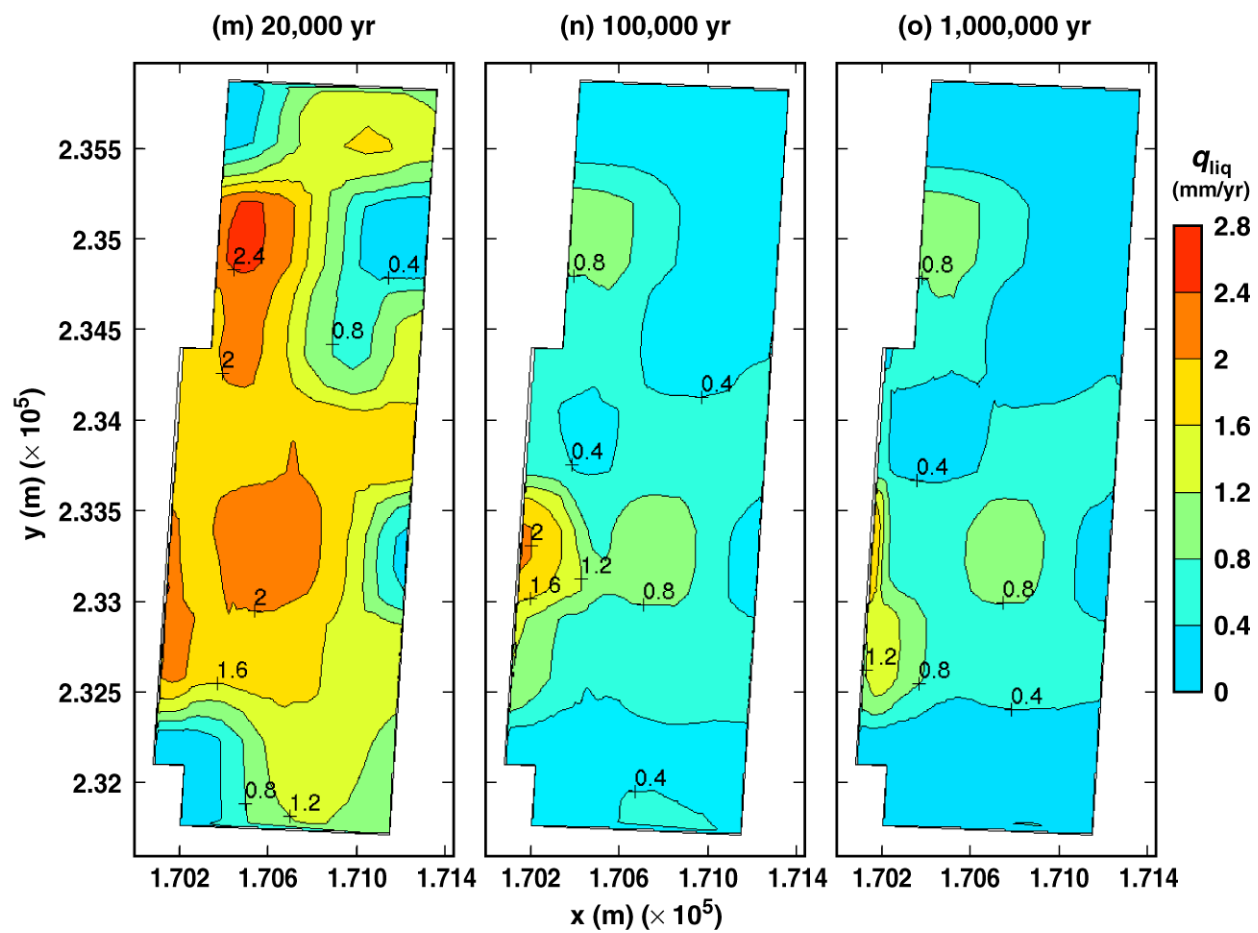
TB_AMR_lower_qliq_dsTop_avg_pwr2_276-335

Figure 6-38. Liquid-phase flux averaged over the upper surface of the dripshield for the low infiltration-flux case for the indicated times.



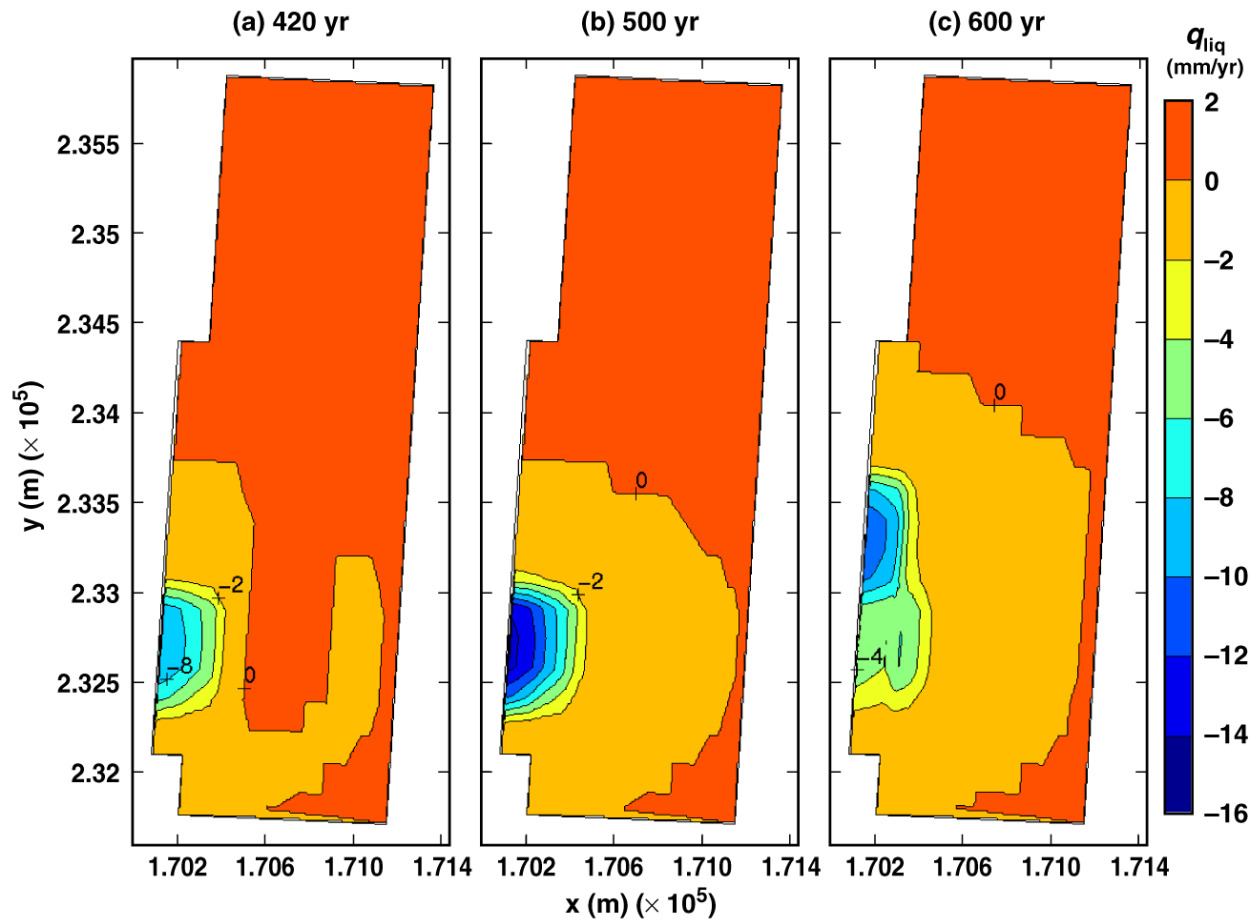
TB_AMR_lower_qliq_dsTop_avg_pwr2_355-402

Figure 6-38. Liquid-phase flux averaged over the upper surface of the dripshield for the low infiltration-flux case for the indicated times.



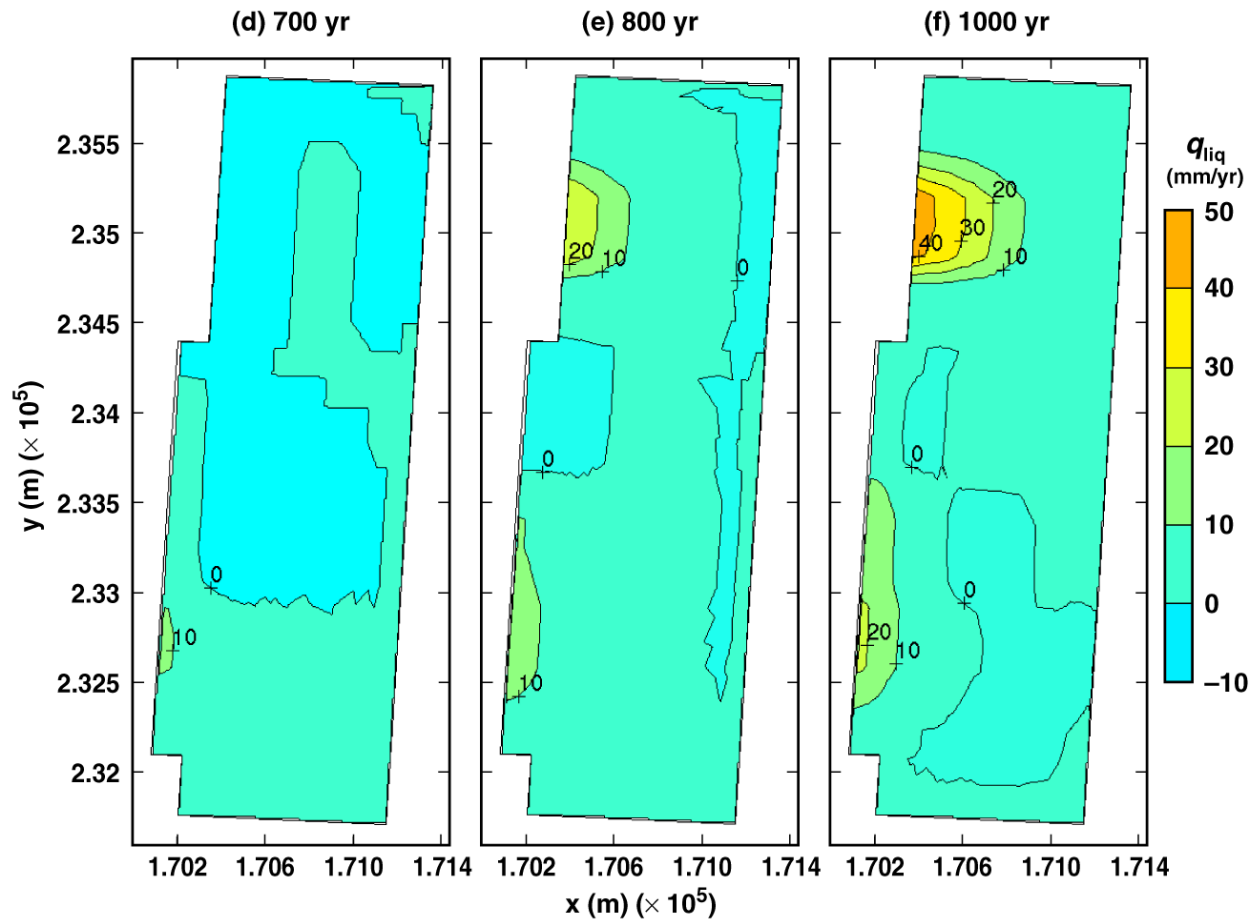
TB_AMR_lower_qliq_dsTop_avg_pwr2_411-442

Figure 6-38. Liquid-phase flux averaged over the upper surface of the dripshield for the low infiltration-flux case for the indicated times.



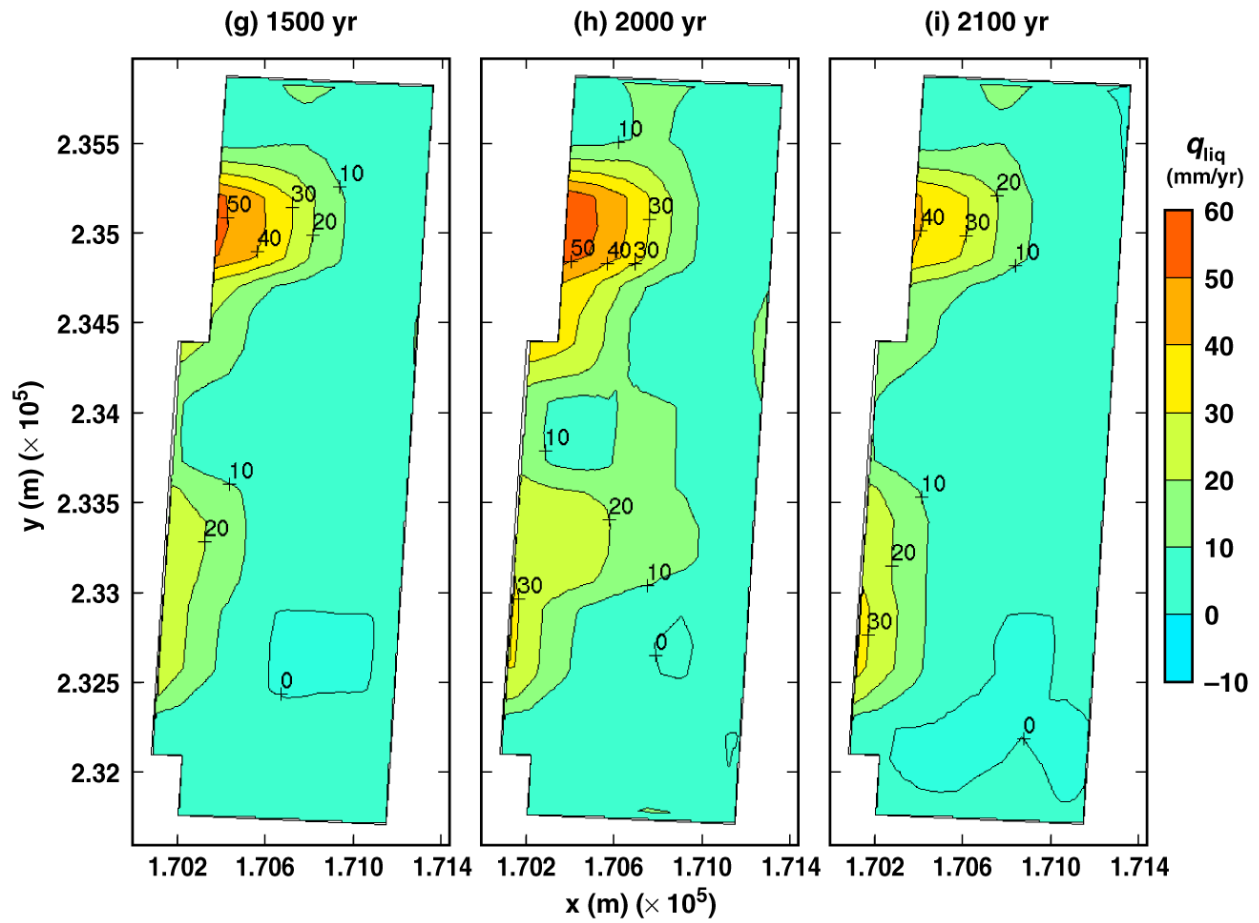
TB_AMR_lower_qliq_dsSide_pwr2_61-103

Figure 6-39. Liquid-phase flux adjacent to the lower side of the dripshield (i.e., adjacent to the base of the dripshield) for the low infiltration-flux case for the indicated times.



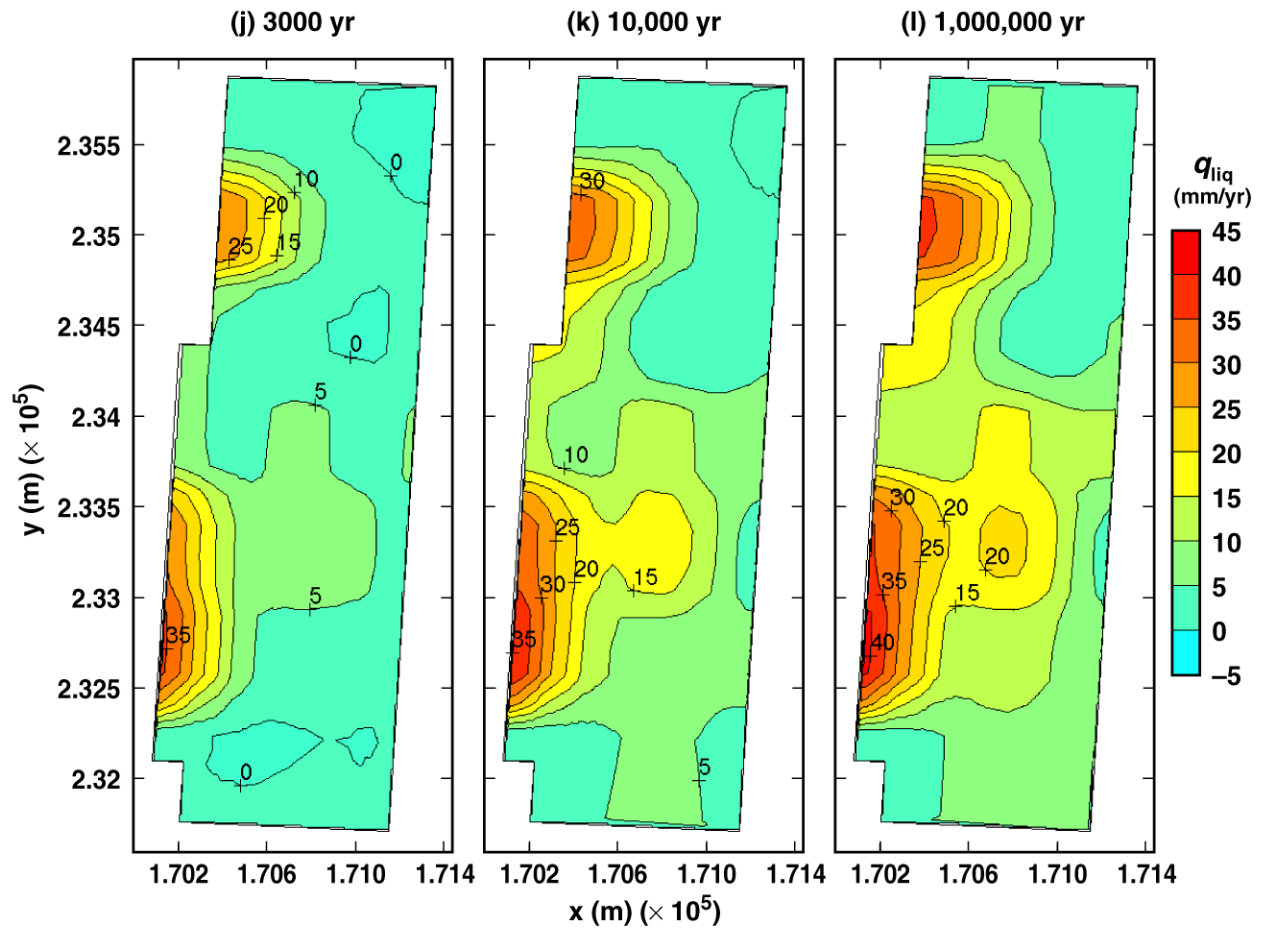
TB_AMR_lower_qliq_dsSide_pwr2_128-219

Figure 6-39. Liquid-phase flux adjacent to the lower side of the dripshield (i.e., adjacent to the base of the dripshield) for the low infiltration-flux case for the indicated times.



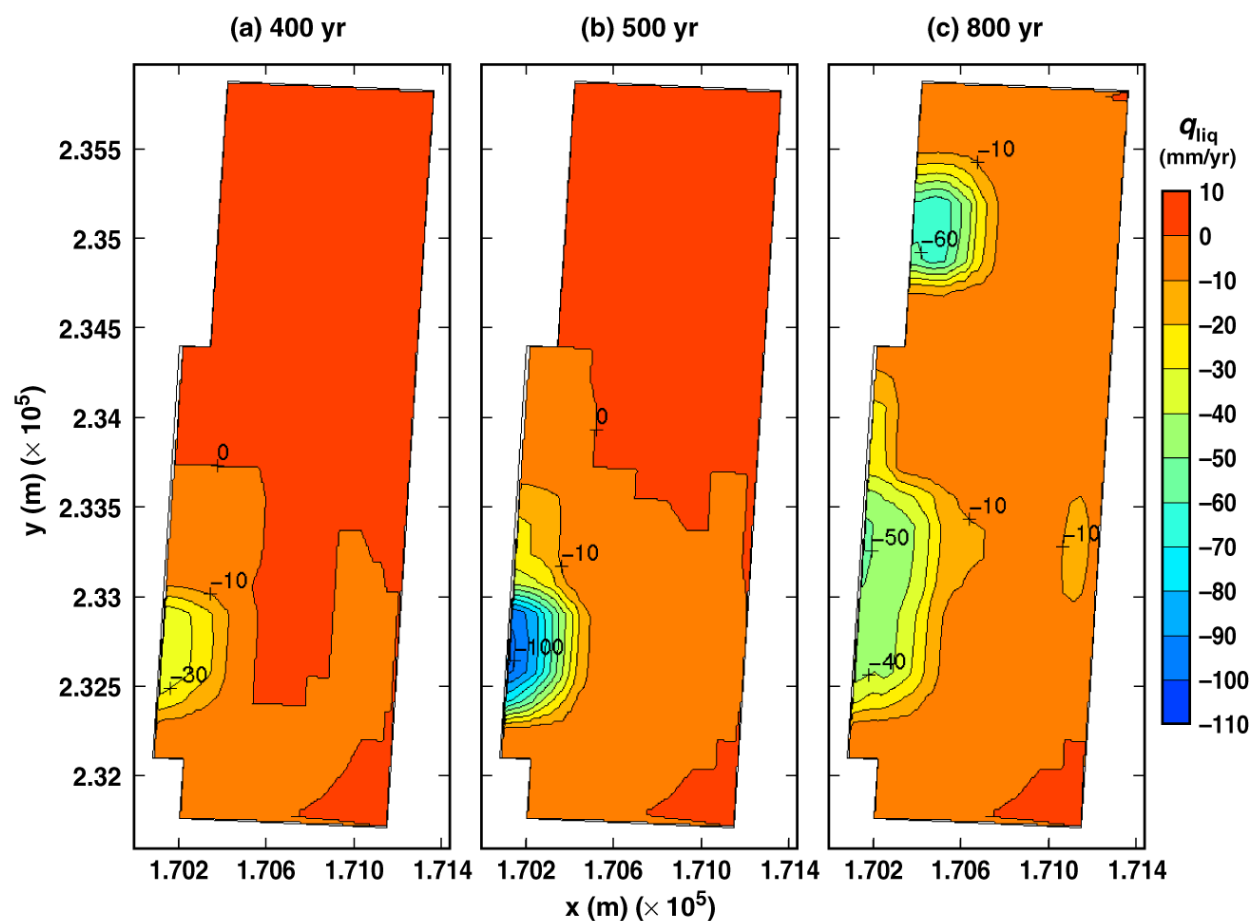
TB_AMR_lower_qliq_dsSide_pwr2_276-328

Figure 6-39. Liquid-phase flux adjacent to the lower side of the dripshield (i.e., adjacent to the base of the dripshield) for the low infiltration-flux case for the indicated times.



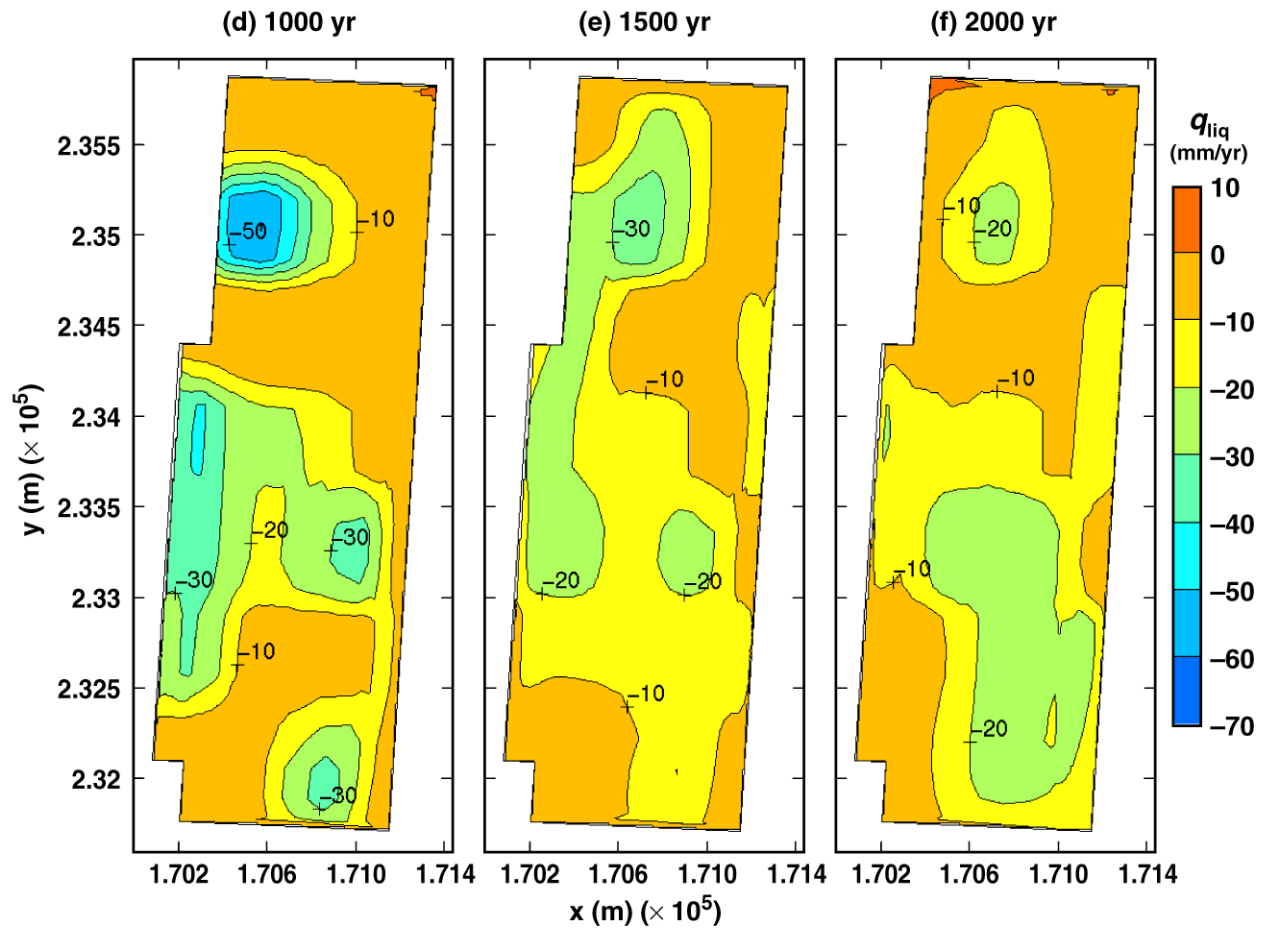
TB_AMR_lower_qliq_dsSide_pwr2_355-442

Figure 6-39. Liquid-phase flux adjacent to the lower side of the dripshield (i.e., adjacent to the base of the dripshield) for the low infiltration-flux case for the indicated times.



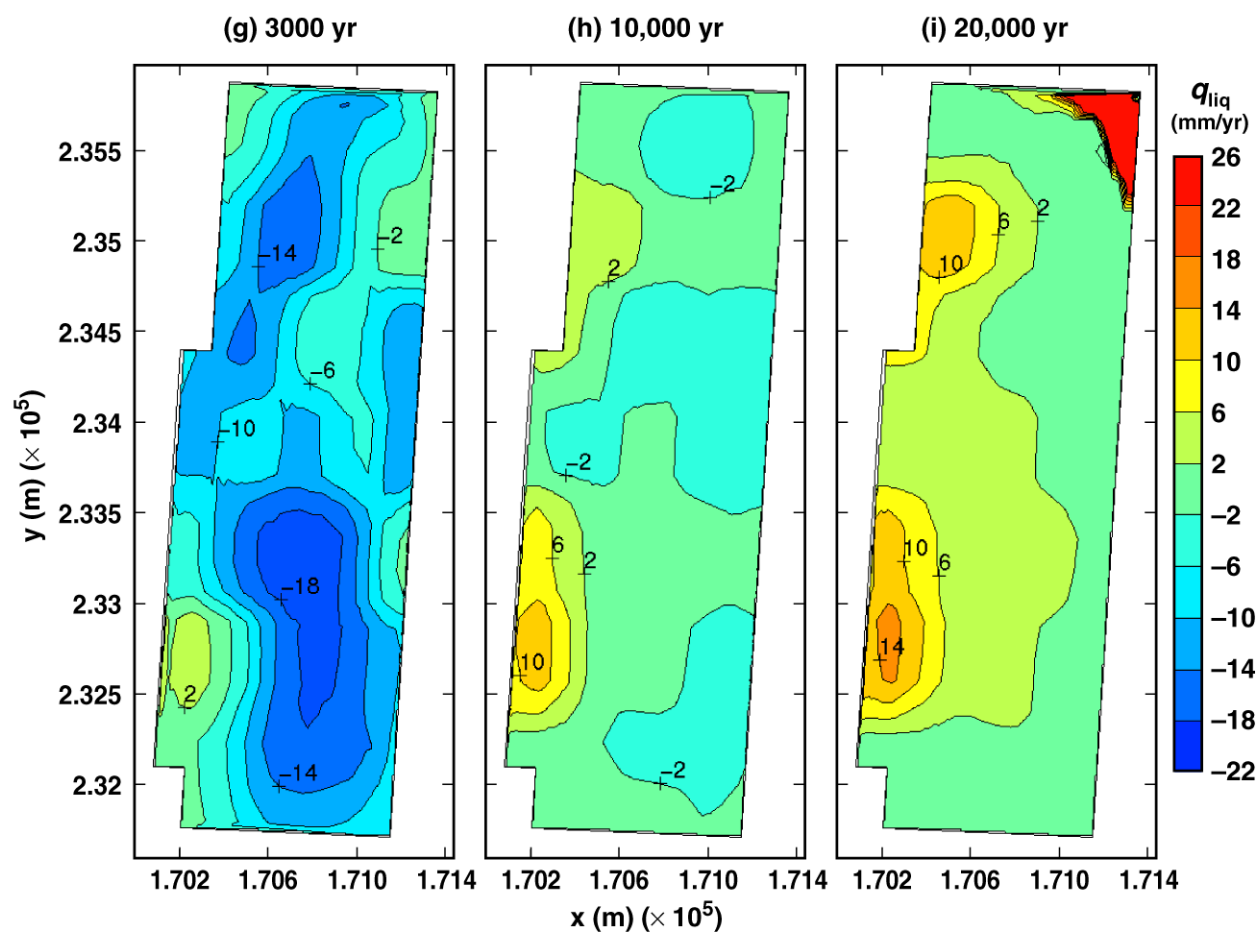
TB_AMR_lower_qliq_invert_pwr2_57-166

Figure 6-40. Liquid-phase flux averaged over the invert for the low infiltration-flux case for the indicated times.



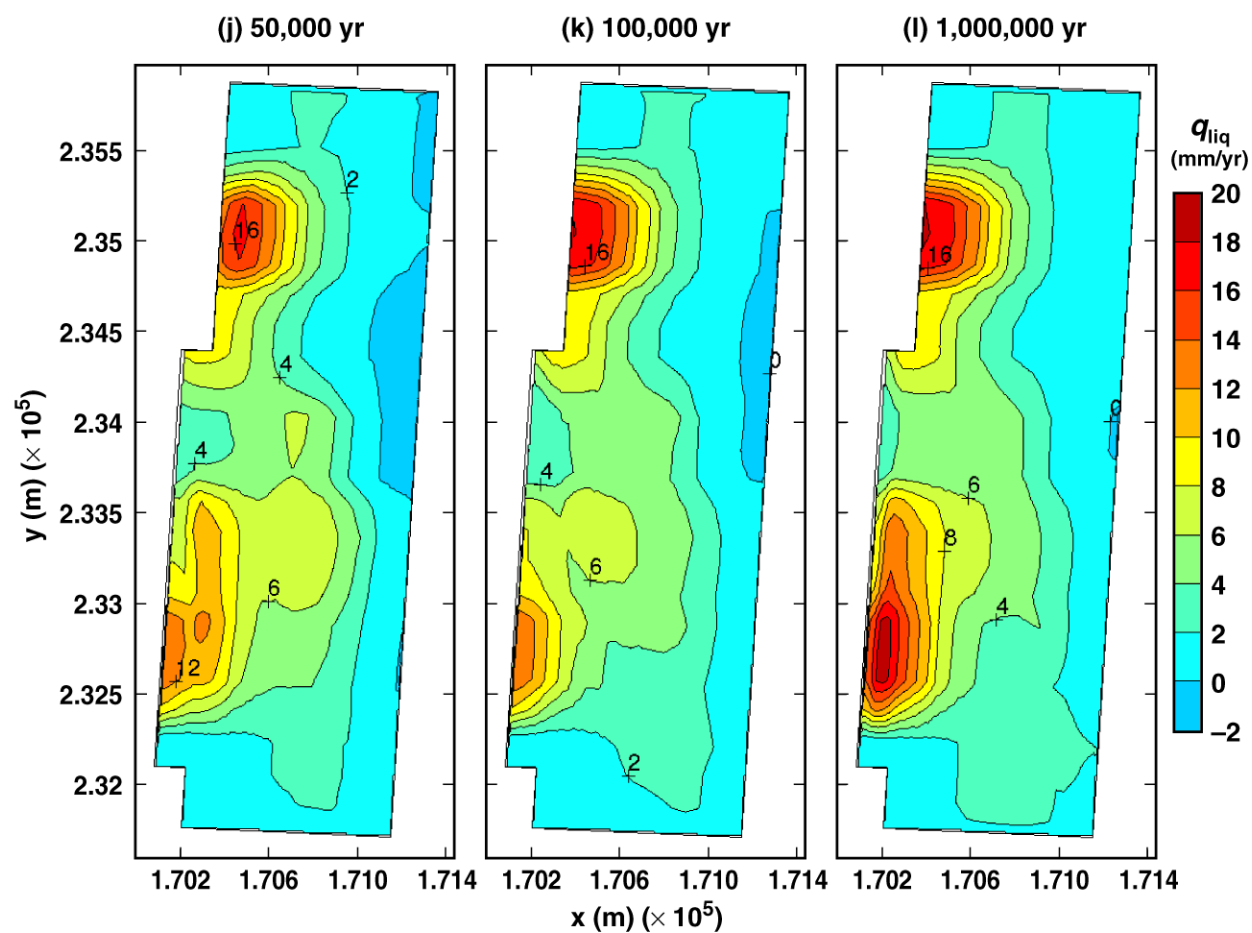
TB_AMR_lower_qliq_invert_pwr2_219-322

Figure 6-40. Liquid-phase flux averaged over the invert for the low infiltration-flux case for the indicated times.



TB_AMR_lower_qliq_invert_pwr2_355-411

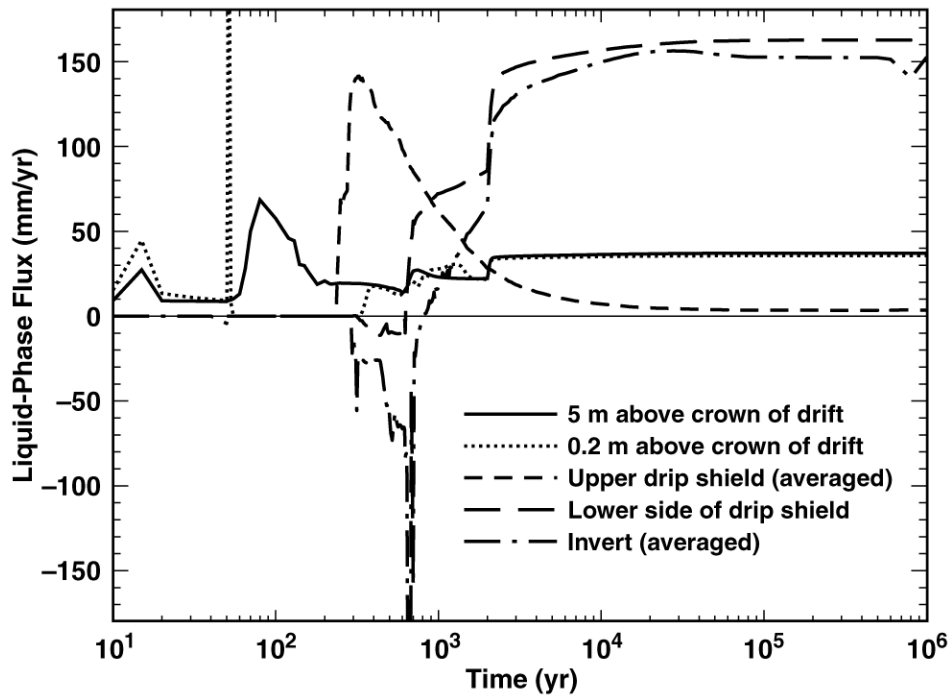
Figure 6-40. Liquid-phase flux averaged over the invert for the low infiltration-flux case for the indicated times.



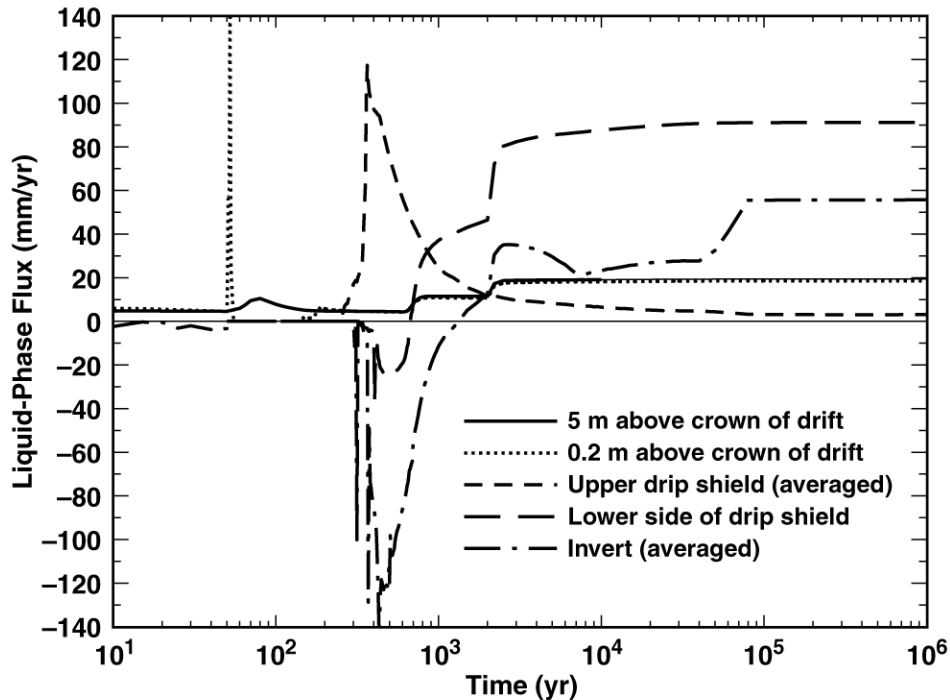
TB_AMR_lower_qliq_invert_pwr2_427-442

Figure 6-40. Liquid-phase flux averaged over the invert for the low infiltration-flux case for the indicated times.

(a) Center of Repository
Nevada State Coordinates: Easting = 170535.03 m, Northing = 233640.08 m

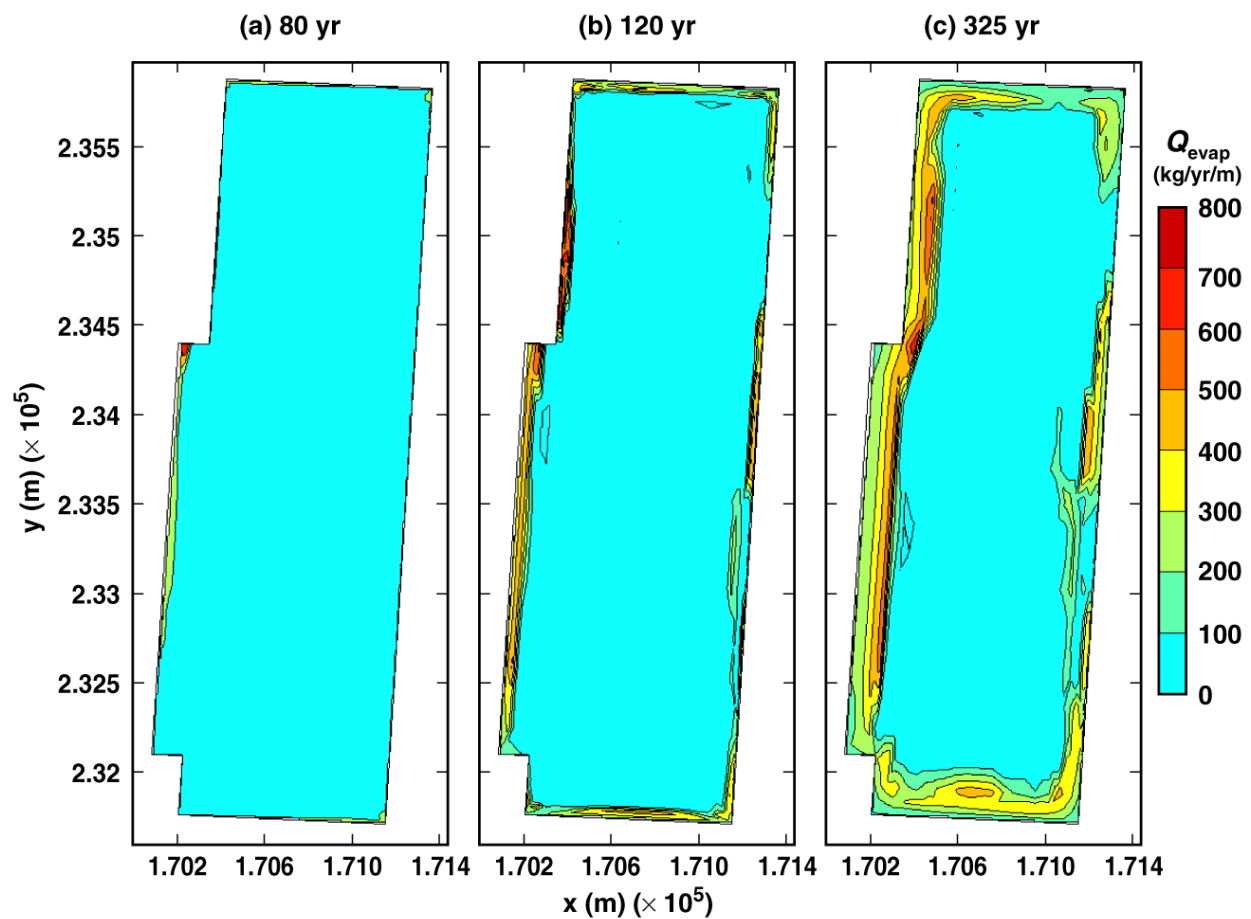


(b) Eastern Edge of Repository
Nevada State Coordinates: Easting = 171195.16 m, Northing = 233605.06 m



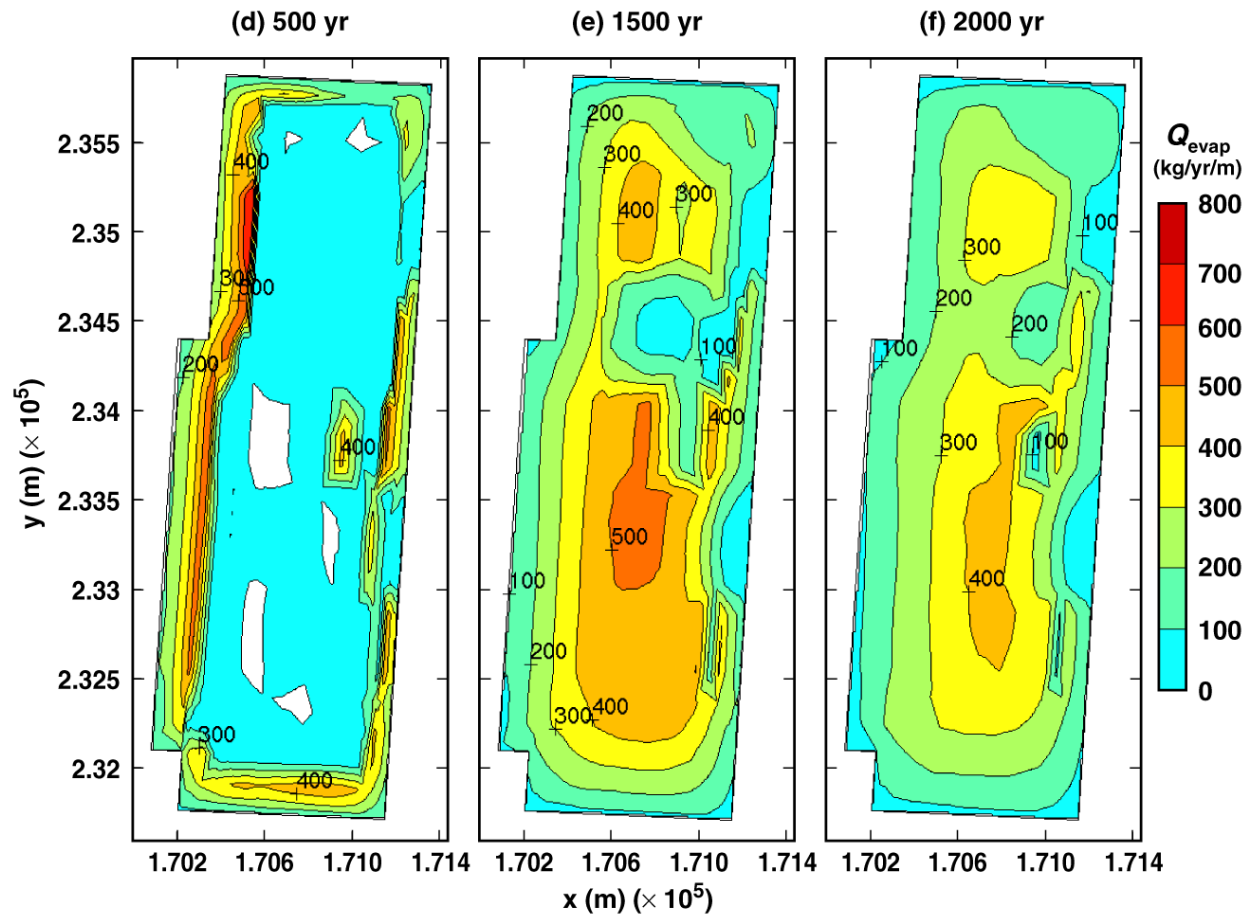
TB_AMR_qliq_hist_pwr2_13&24_17_mean

Figure 6-41. Liquid-phase flux history at indicated drift-scale locations for the mean infiltration-flux case at (a) the geographical center of the repository and (b) a location 27.5 m from the eastern edge of the repository. Note that the Nevada State coordinates are given.



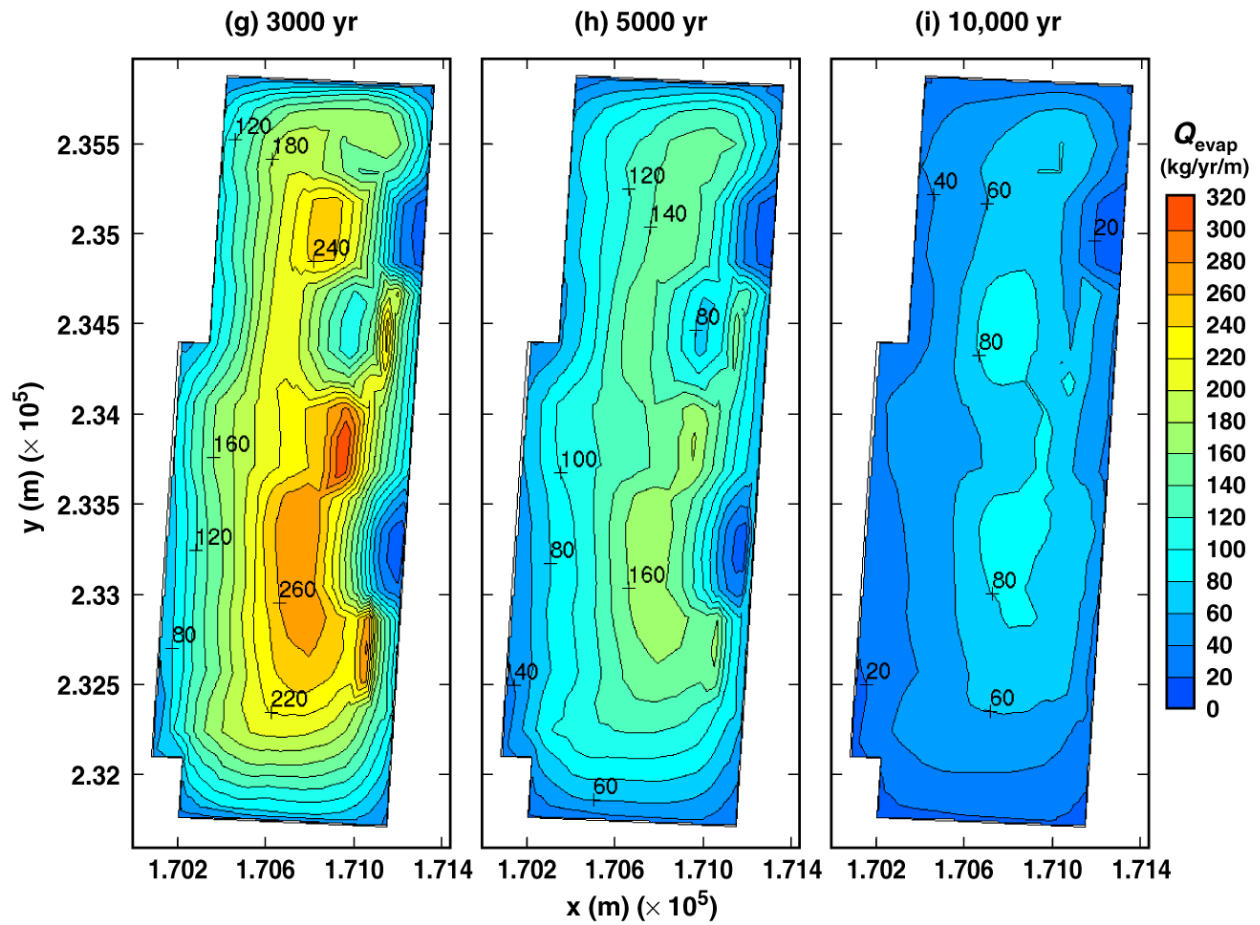
TB_AMR_Qevap_dsPerim_pwr2_20-69

Figure 6-42. Evaporation rate summed over the upper surface of the dripshield for the mean infiltration-flux case for the indicated times.



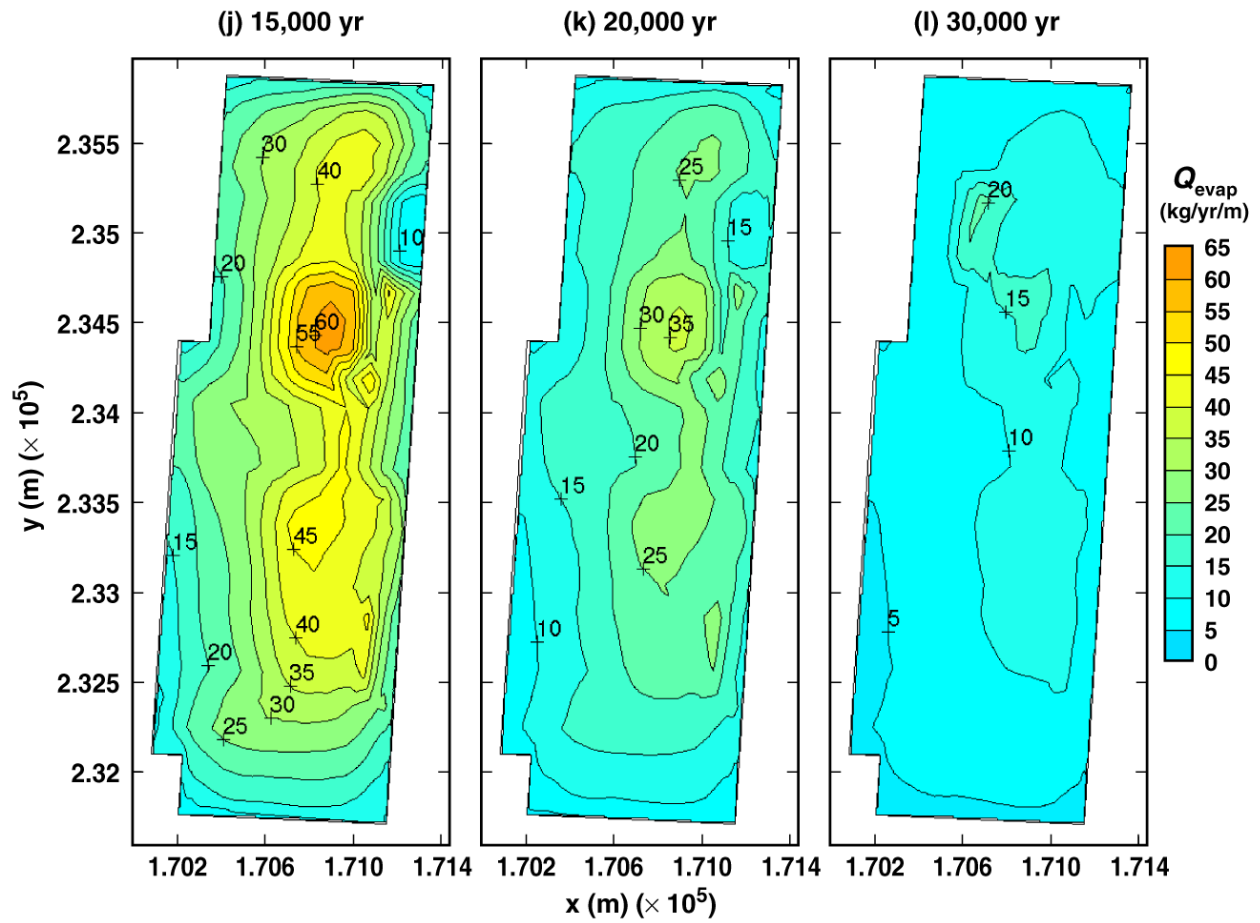
TB_AMR_Qevap_dsPerim_pwr2_104-254

Figure 6-42. Evaporation rate summed over the upper surface of the dripshield for the mean infiltration-flux case for the indicated times.



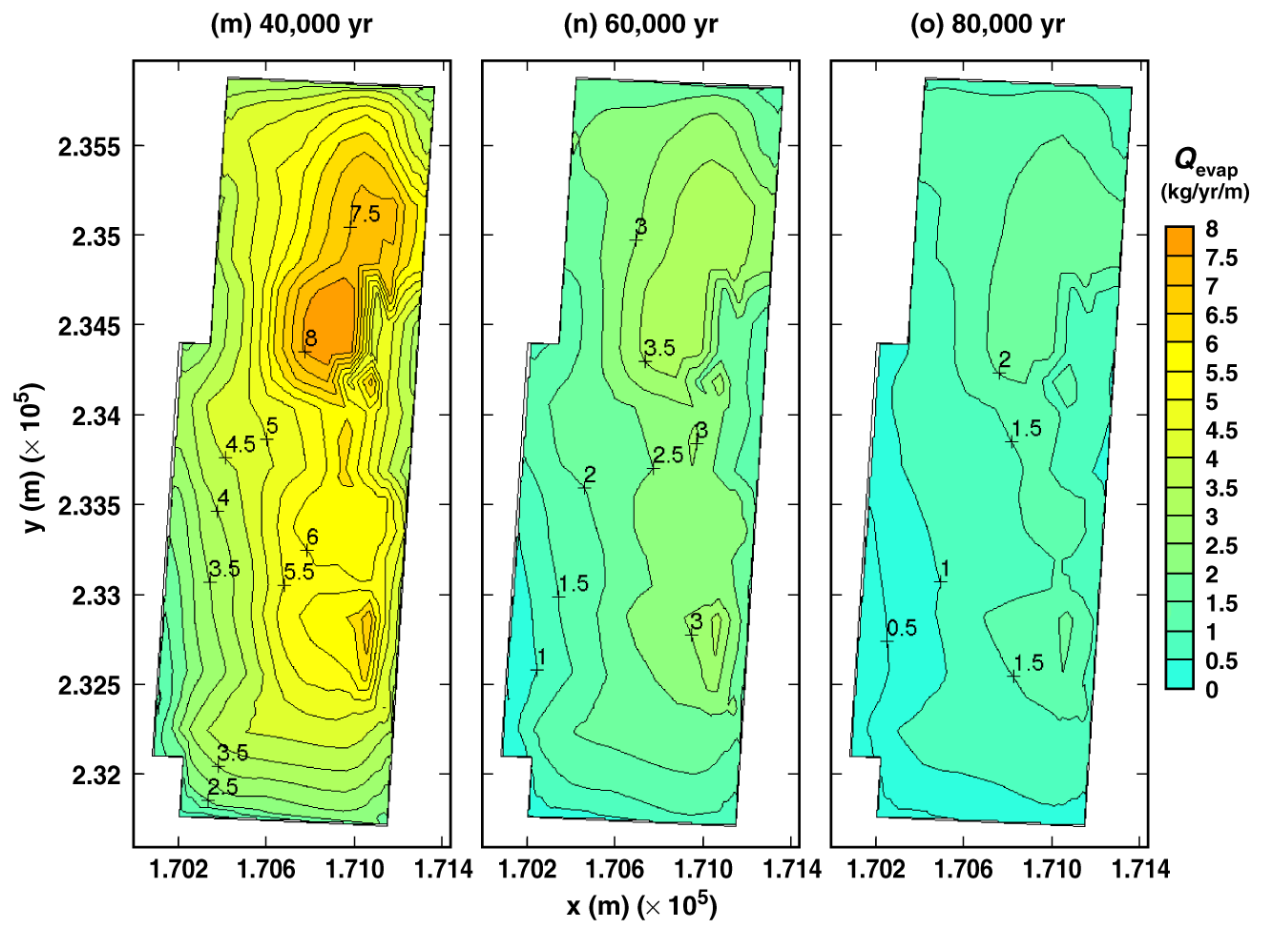
TB_AMR_Qevap_dsPerim_pwr2_283-319

Figure 6-42. Evaporation rate summed over the upper surface of the dripshield for the mean infiltration-flux case for the indicated times.



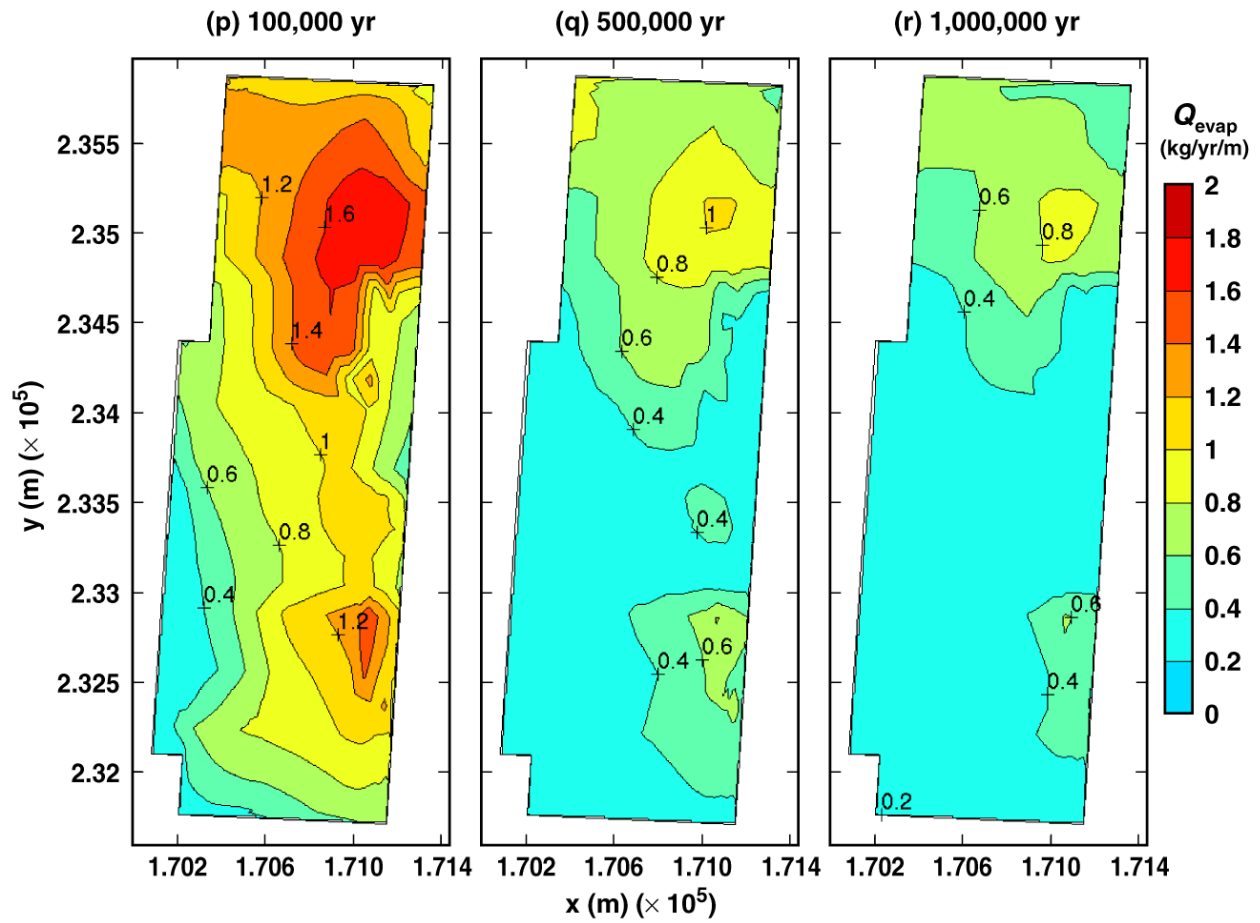
TB_AMR_Qevap_dsPerim_pwr2_326-335

Figure 6-42. Evaporation rate summed over the upper surface of the dripshield for the mean infiltration-flux case for the indicated times.



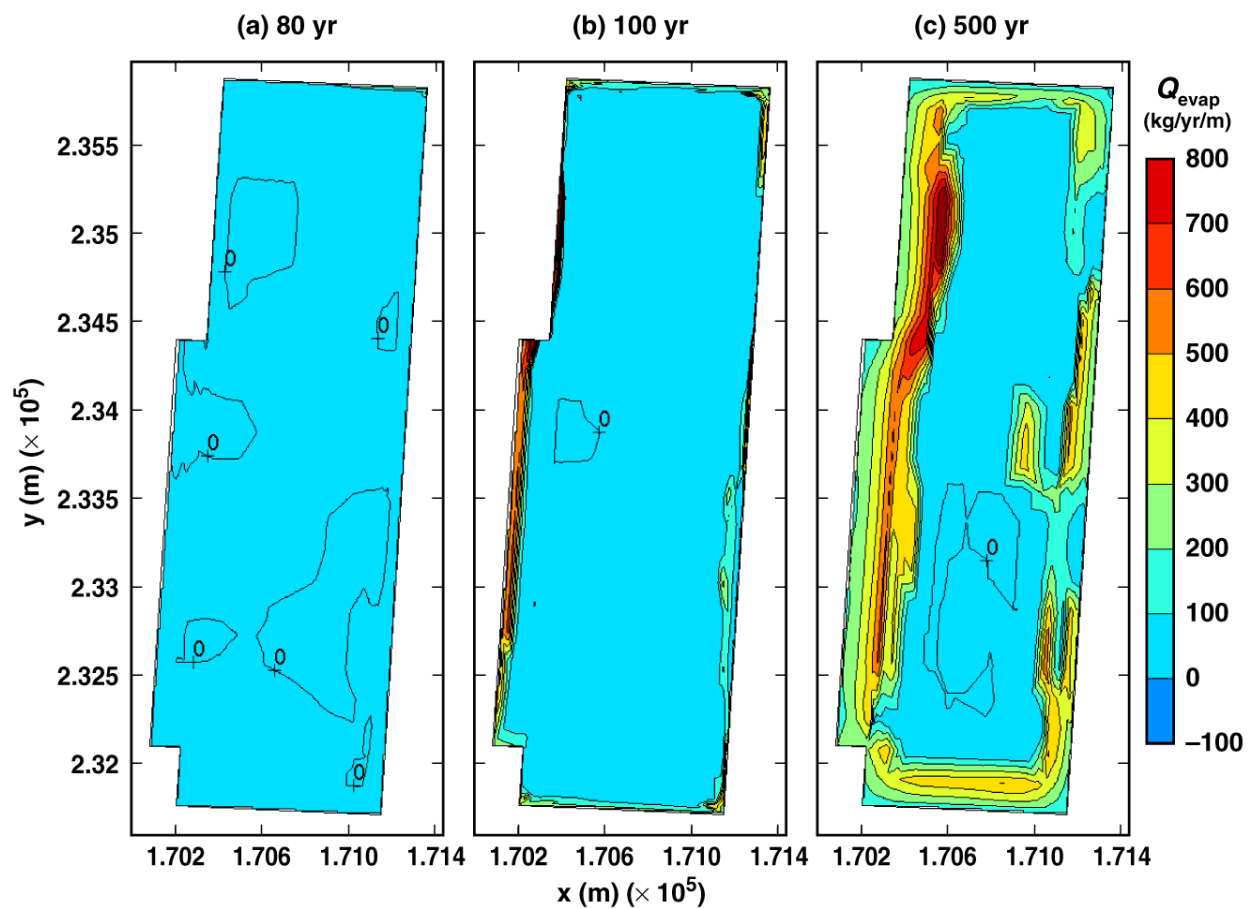
TB_AMR_Qevap_dsPerim_pwr2_340-343

Figure 6-42. Evaporation rate summed over the upper surface of the dripshield for the mean infiltration-flux case for the indicated times.



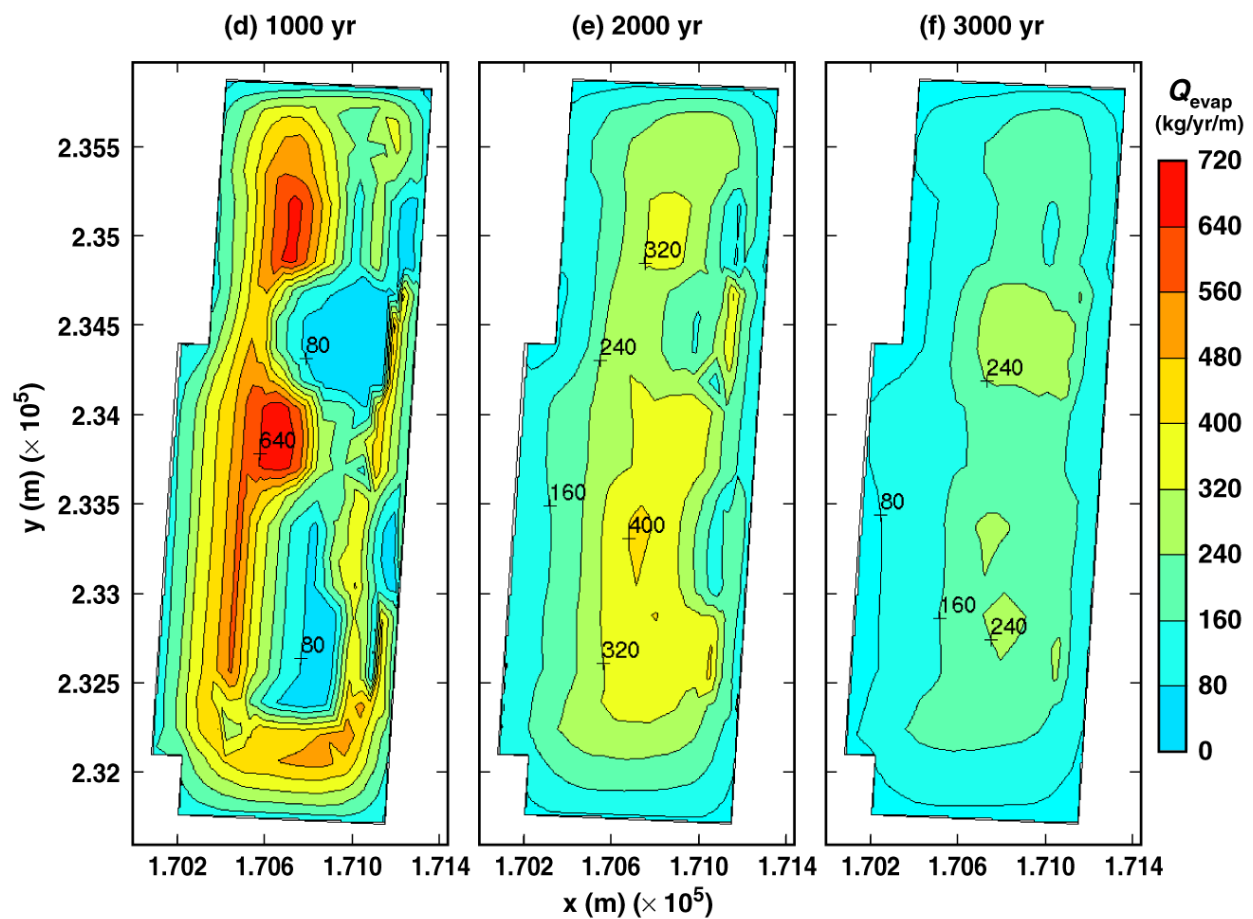
TB_AMR_Qevap_dsPerim_pwr2_344-352

Figure 6-42. Evaporation rate summed over the upper surface of the dripshield for the mean infiltration-flux case for the indicated times.



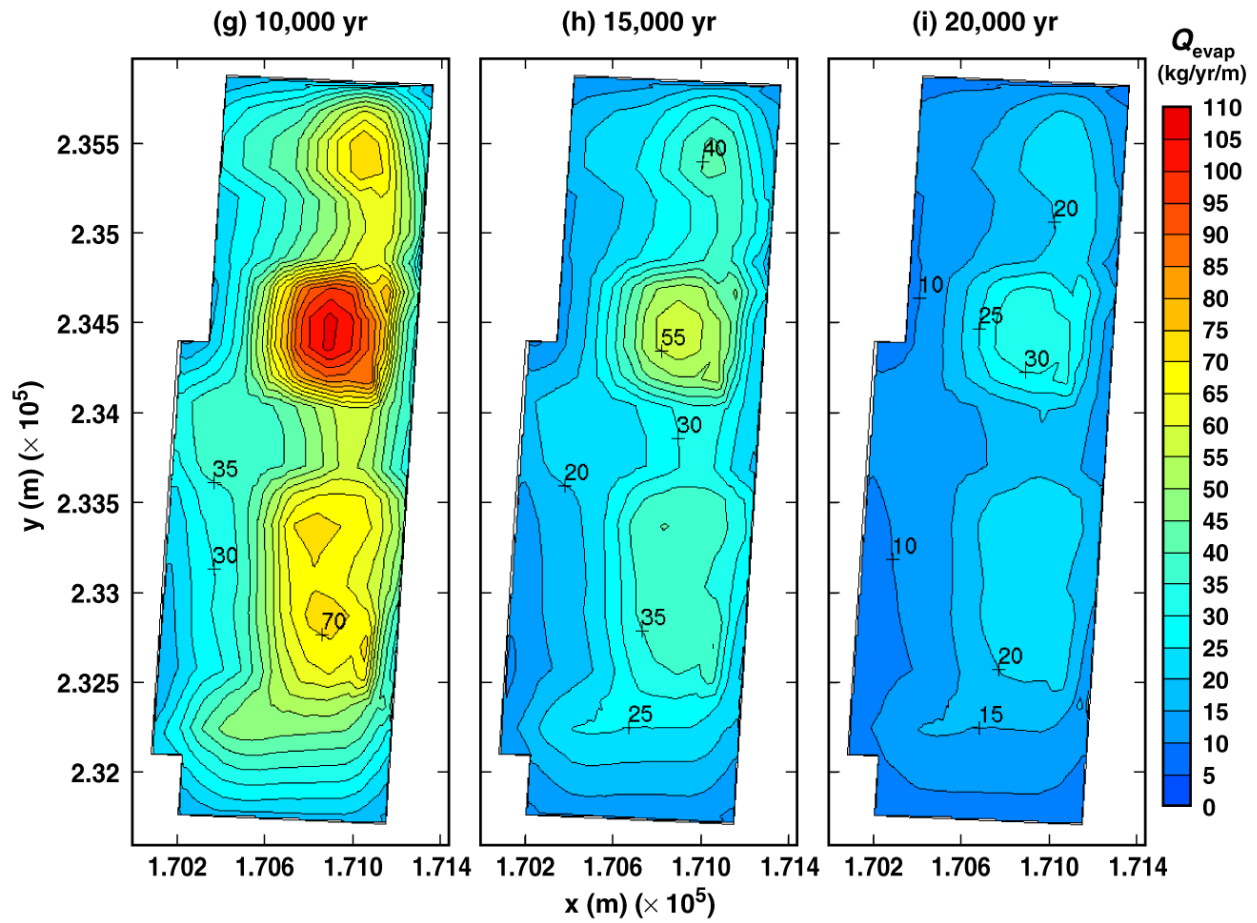
TB_AMR_upper_Qevap_dsPerim_pwr2_18-177

Figure 6-43. Evaporation rate summed over the upper surface of the dripshield for the high infiltration-flux case for the indicated times.



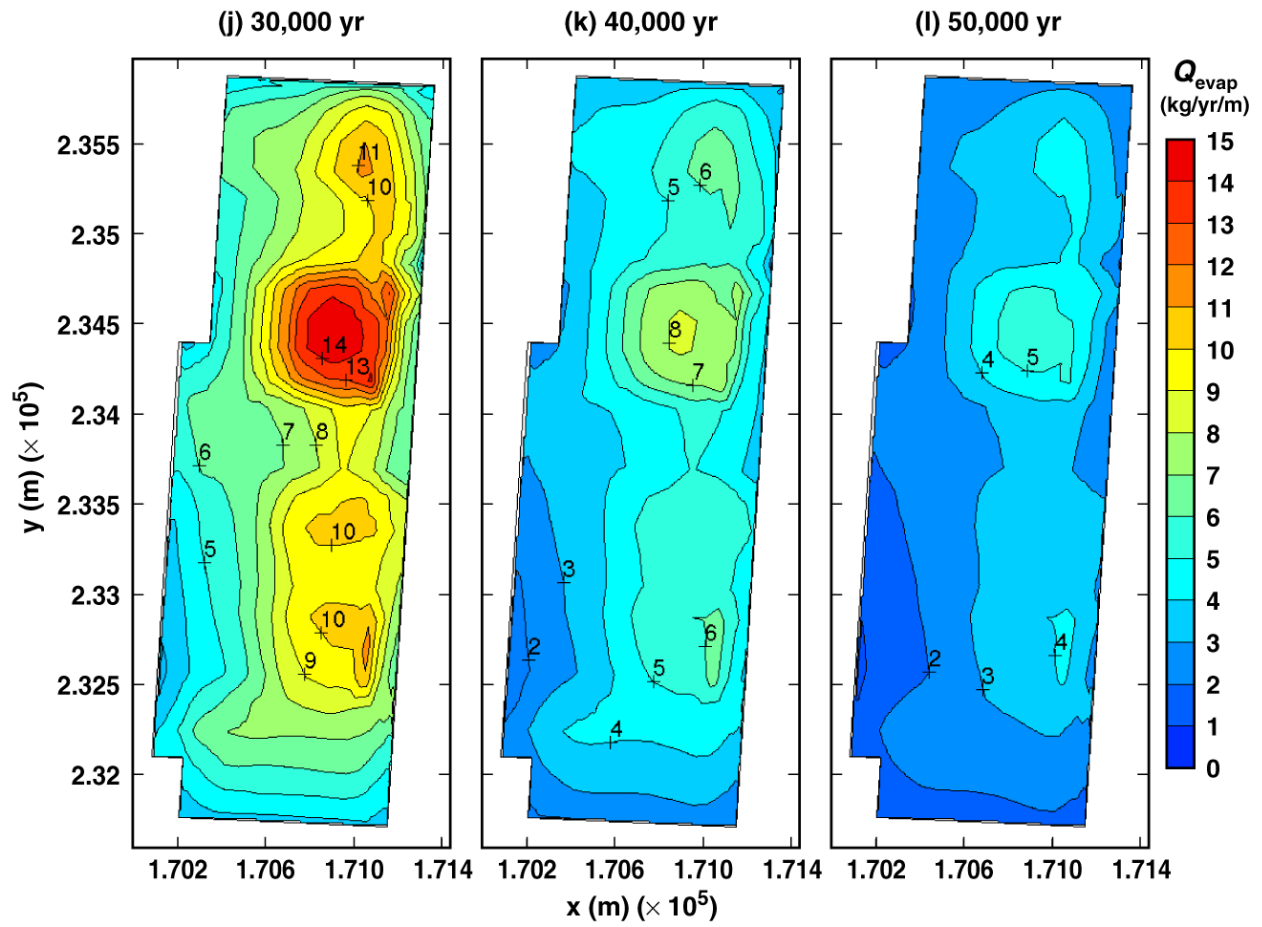
TB_AMR_upper_Qevap_dsPerim_pwr2_269-389

Figure 6-43. Evaporation rate summed over the upper surface of the dripshield for the high infiltration-flux case for the indicated times.



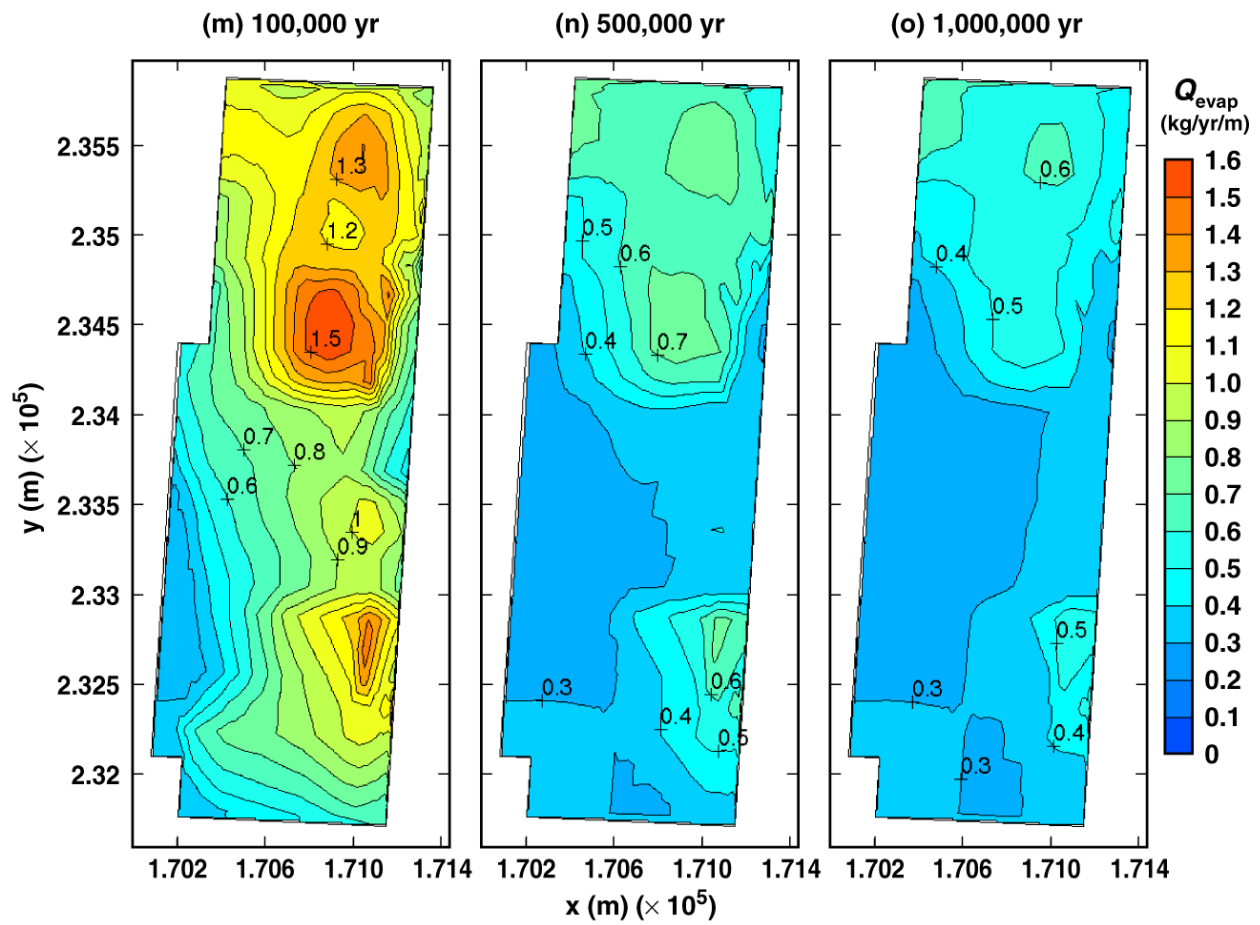
TB_AMR_upper_Qevap_dsPerim_pwr2_425-434

Figure 6-43. Evaporation rate summed over the upper surface of the dripshield for the high infiltration-flux case for the indicated times.



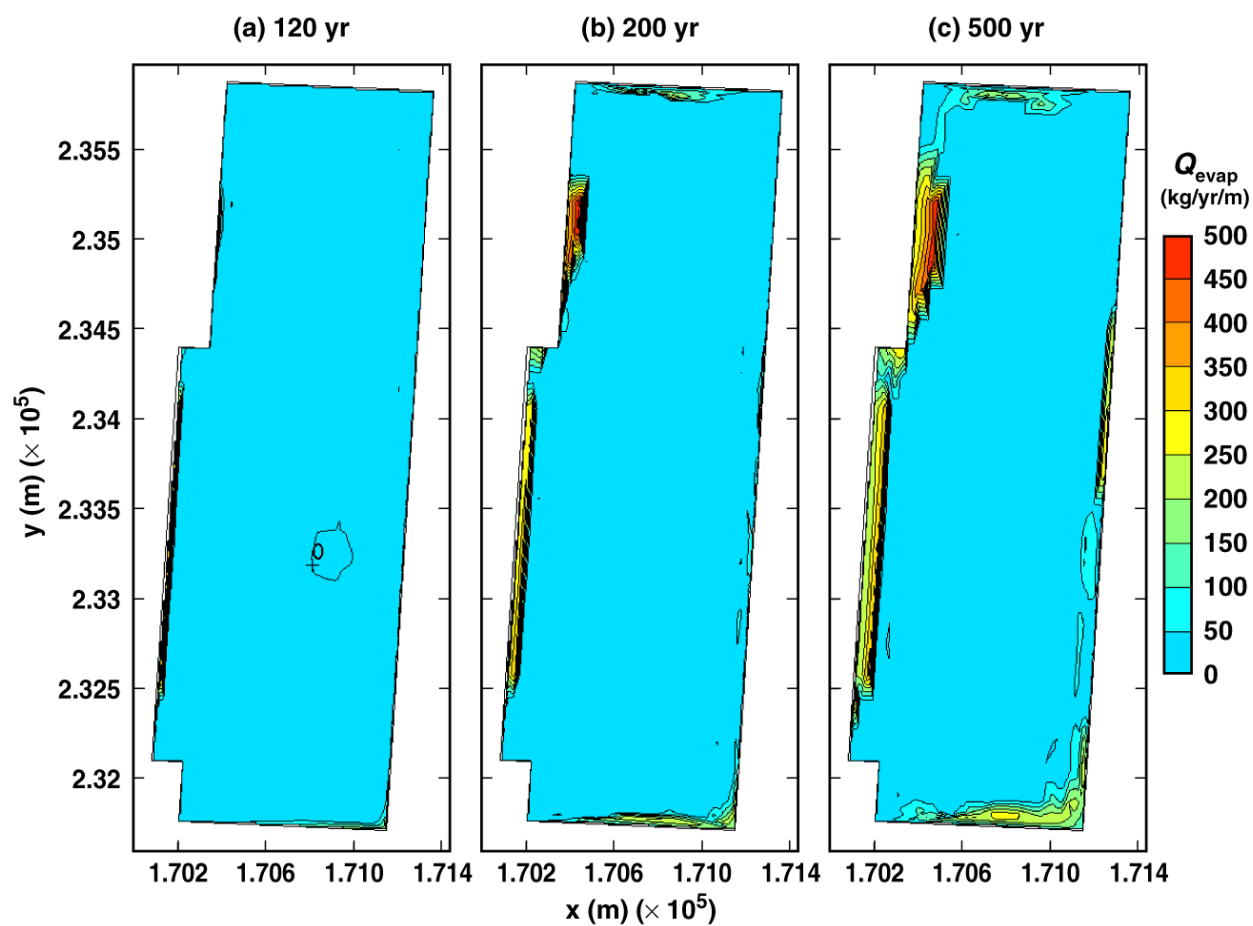
TB_AMR_upper_Qevap_dsPerim_pwr2_439-446

Figure 6-43. Evaporation rate summed over the upper surface of the dripshield for the high infiltration-flux case for the indicated times.



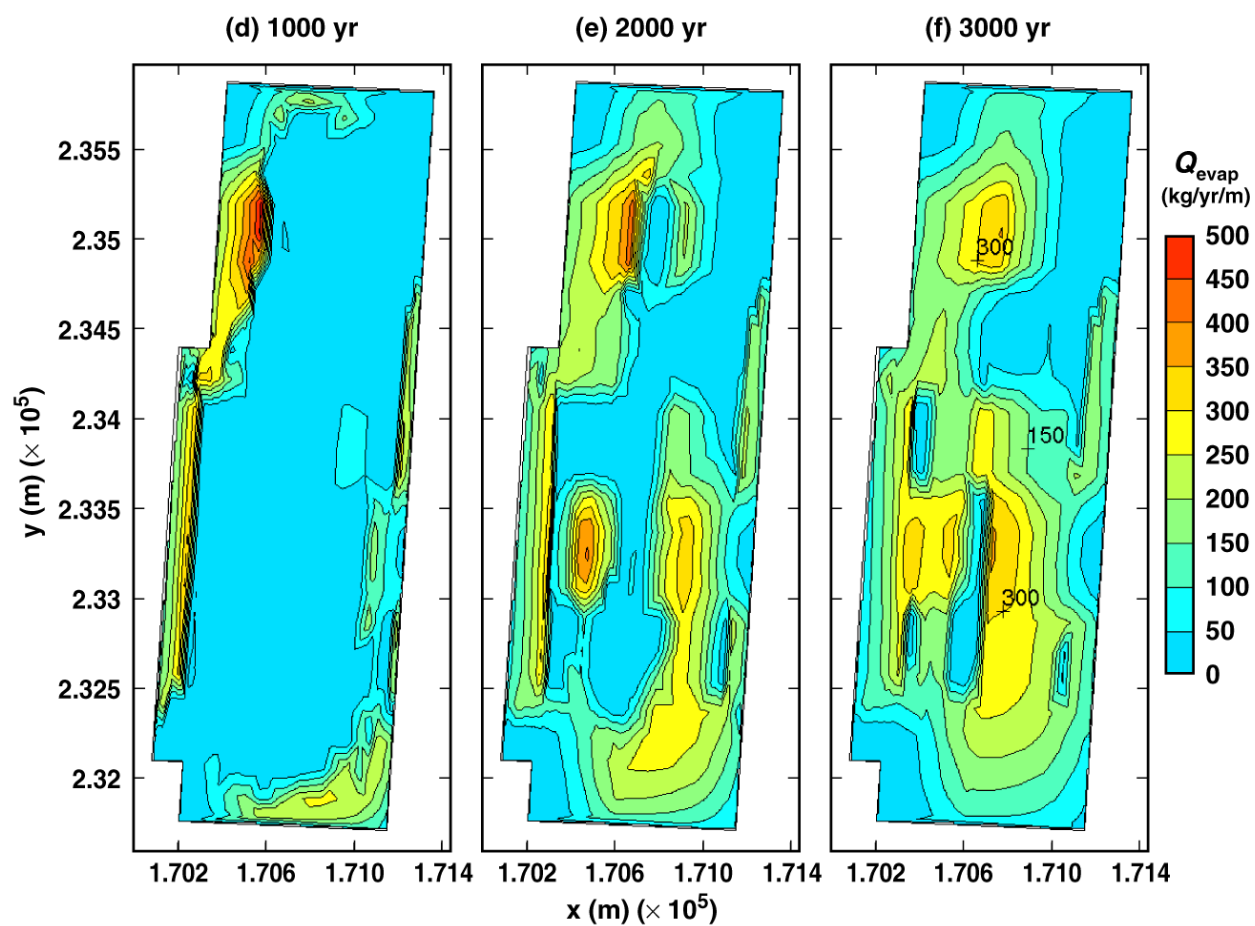
TB_AMR_upper_Qevap_dsPerim_pwr2_449-457

Figure 6-43. Evaporation rate summed over the upper surface of the dripshield for the high infiltration-flux case for the indicated times.



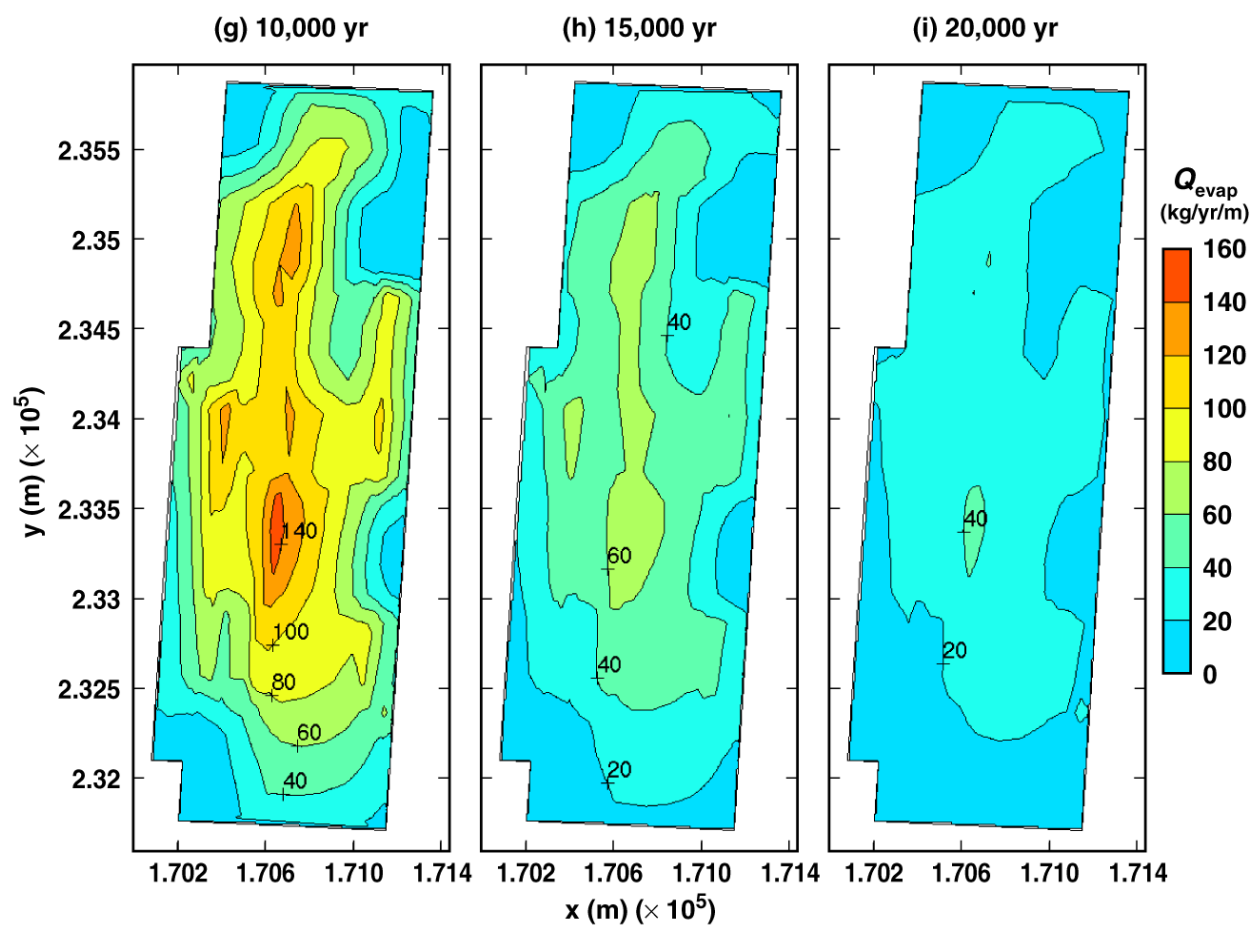
TB_AMR_lower_Qevap_dsPerim_pwr2_23-77

Figure 6-44. Evaporation rate summed over the upper surface of the dripshield for the low infiltration-flux case for the indicated times.



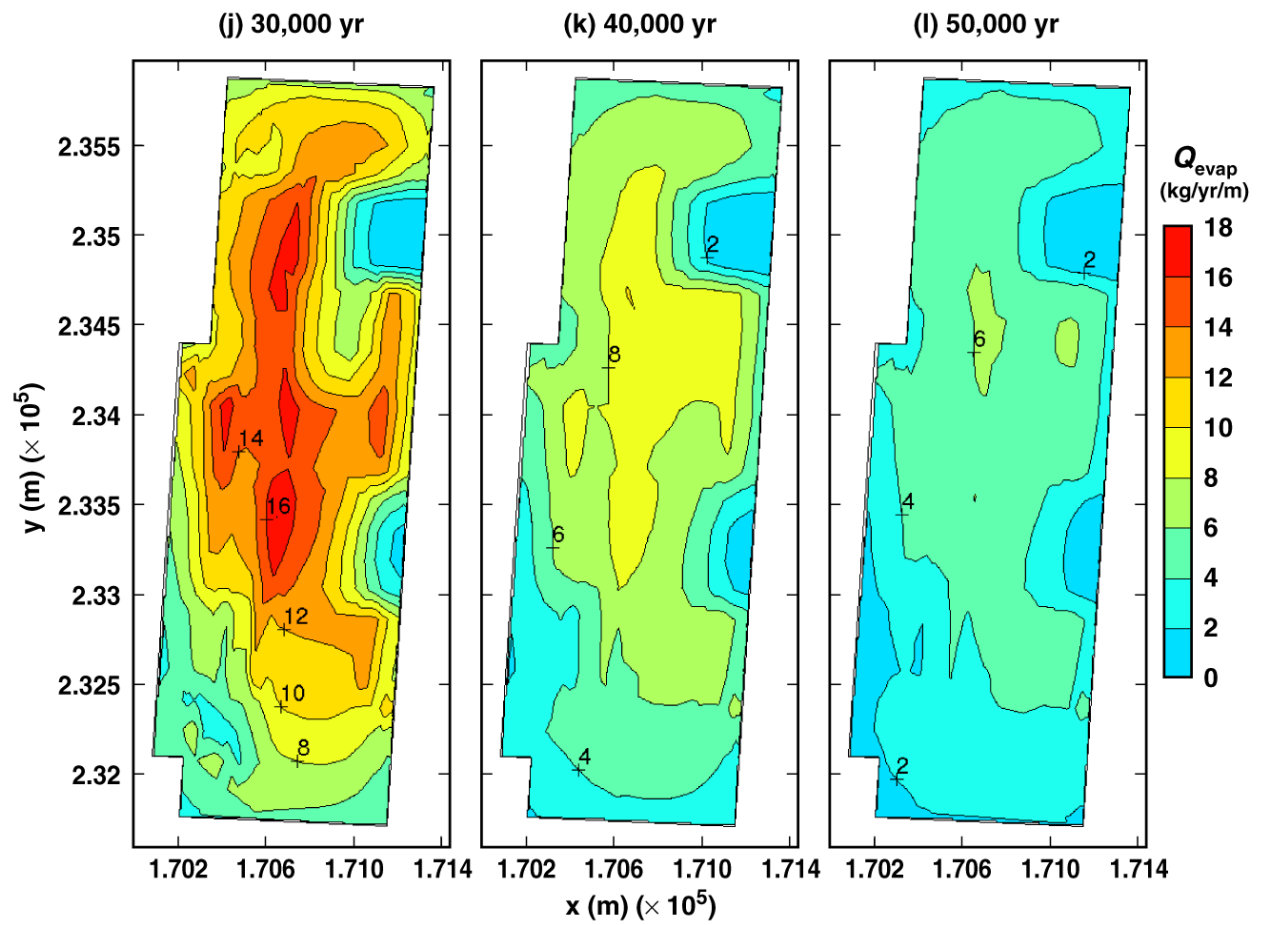
TB_AMR_lower_Qevap_dsPerim_pwr2_219-355

Figure 6-44. Evaporation rate summed over the upper surface of the dripshield for the low infiltration-flux case for the indicated times.



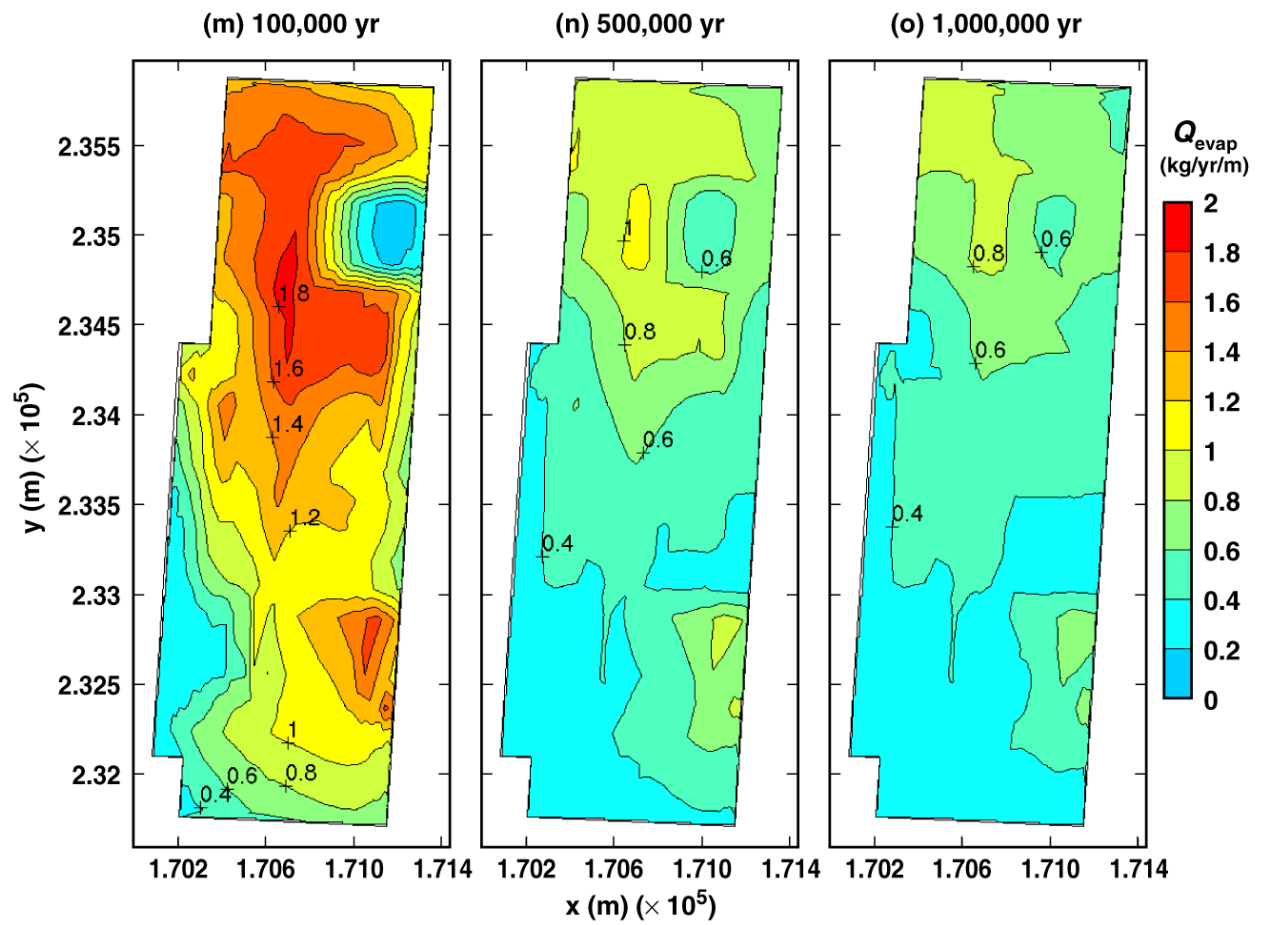
TB_AMR_lower_Qevap_dsPerim_pwr2_402-411

Figure 6-44. Evaporation rate summed over the upper surface of the dripshield for the low infiltration-flux case for the indicated times.



TB_AMR_lower_Qevap_dsPerim_pwr2_417-427

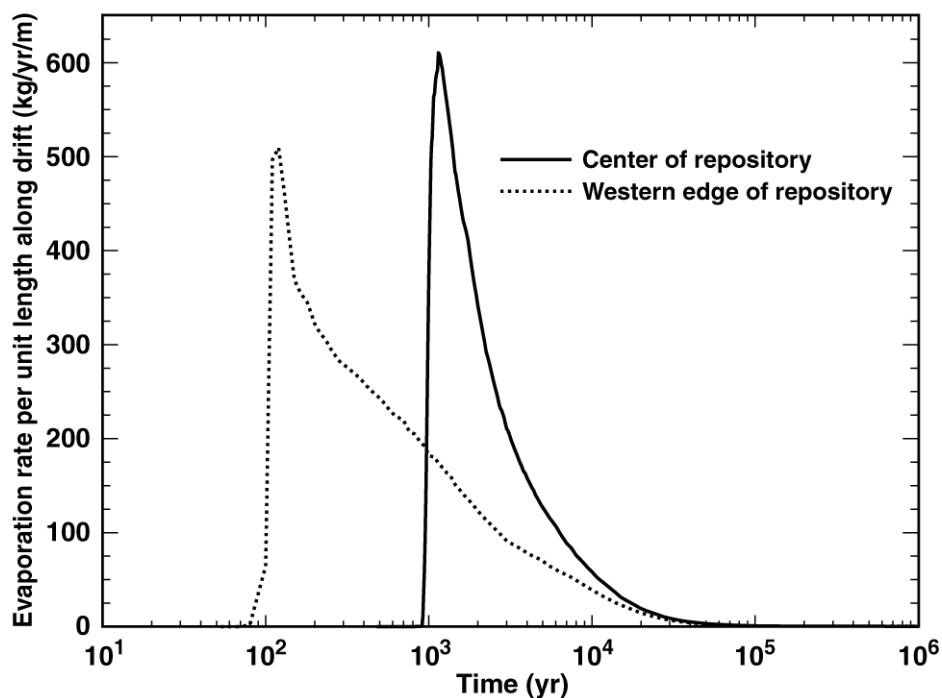
Figure 6-44. Evaporation rate summed over the upper surface of the dripshield for the low infiltration-flux case for the indicated times.



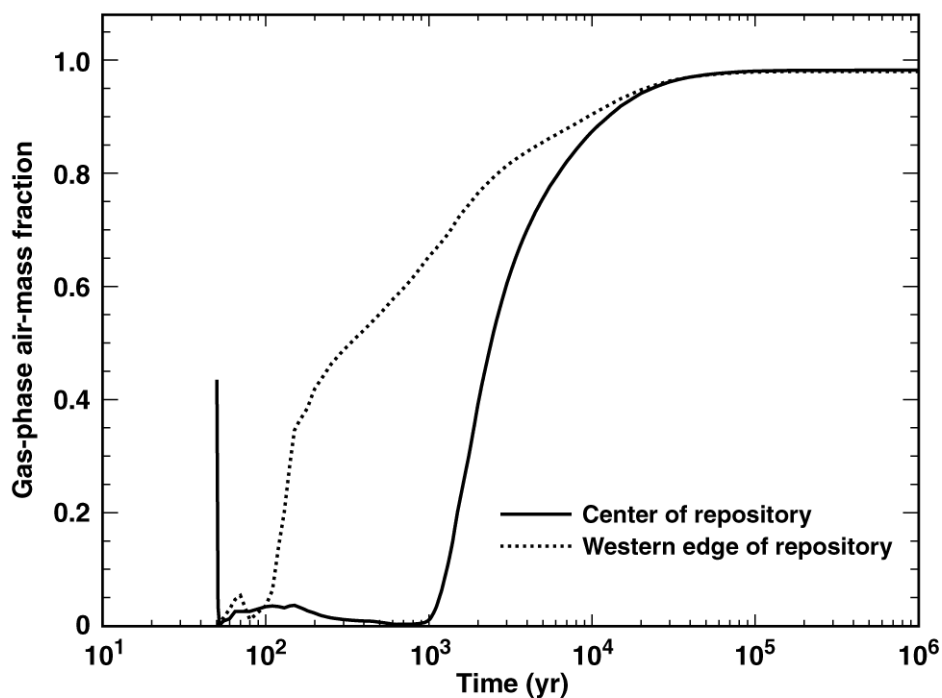
TB_AMR_lower_Qevap_dsPerim_pwr2_434-442

Figure 6-44. Evaporation rate summed over the upper surface of the dripshield for the low infiltration-flux case for the indicated times.

(a) Evaporation Rate on Drip Shield



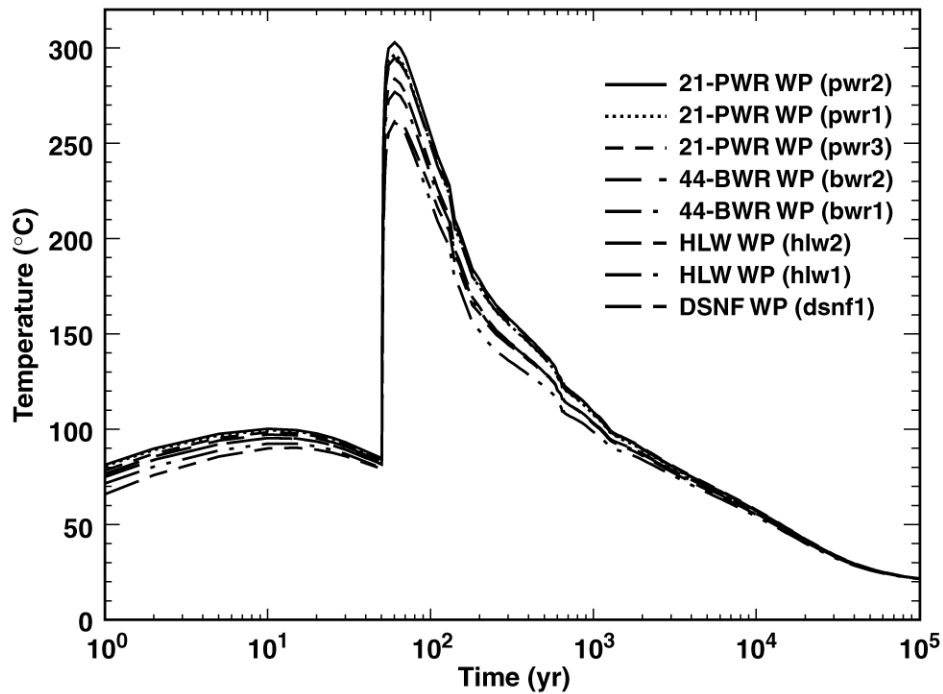
(b) Gas-Phase Air-Mass Fraction on Drip Shield



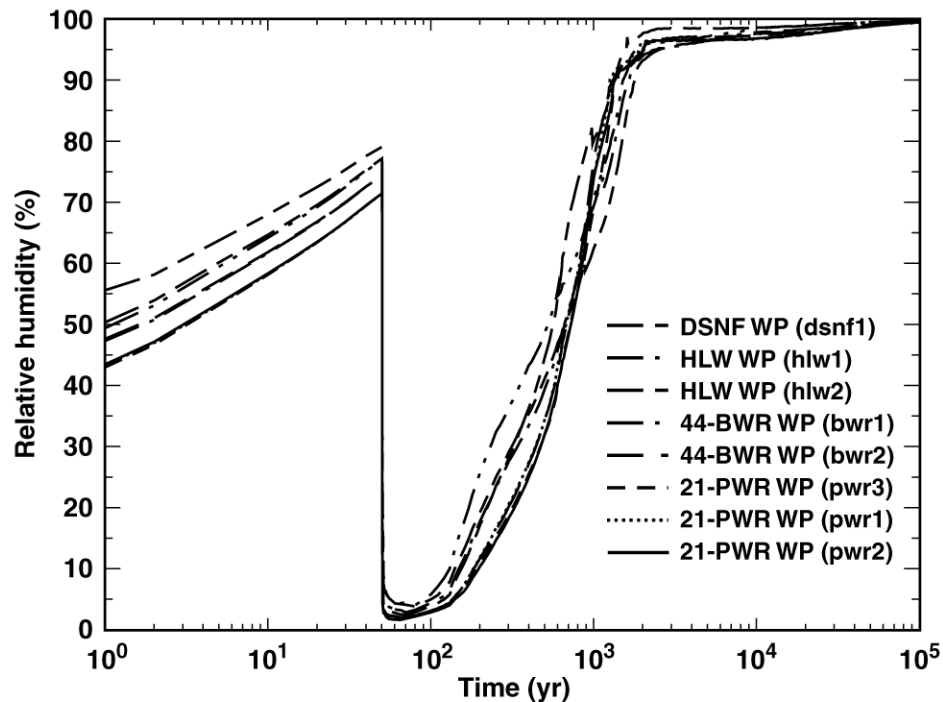
TB_AMR_Qevap&Xair_ds_hist_mean

Figure 6-45. Evaporation rate summed over the upper surface of the dripshield for the mean infiltration-flux case at (a) the geographical center of the repository and (b) a location 27.5 m from the eastern edge of the repository. Note that the Nevada State coordinates are given.

(a) Waste-Package Temperature
Nevada State Coordinates: Easting = 170535.03 m, Northing = 233640.08 m

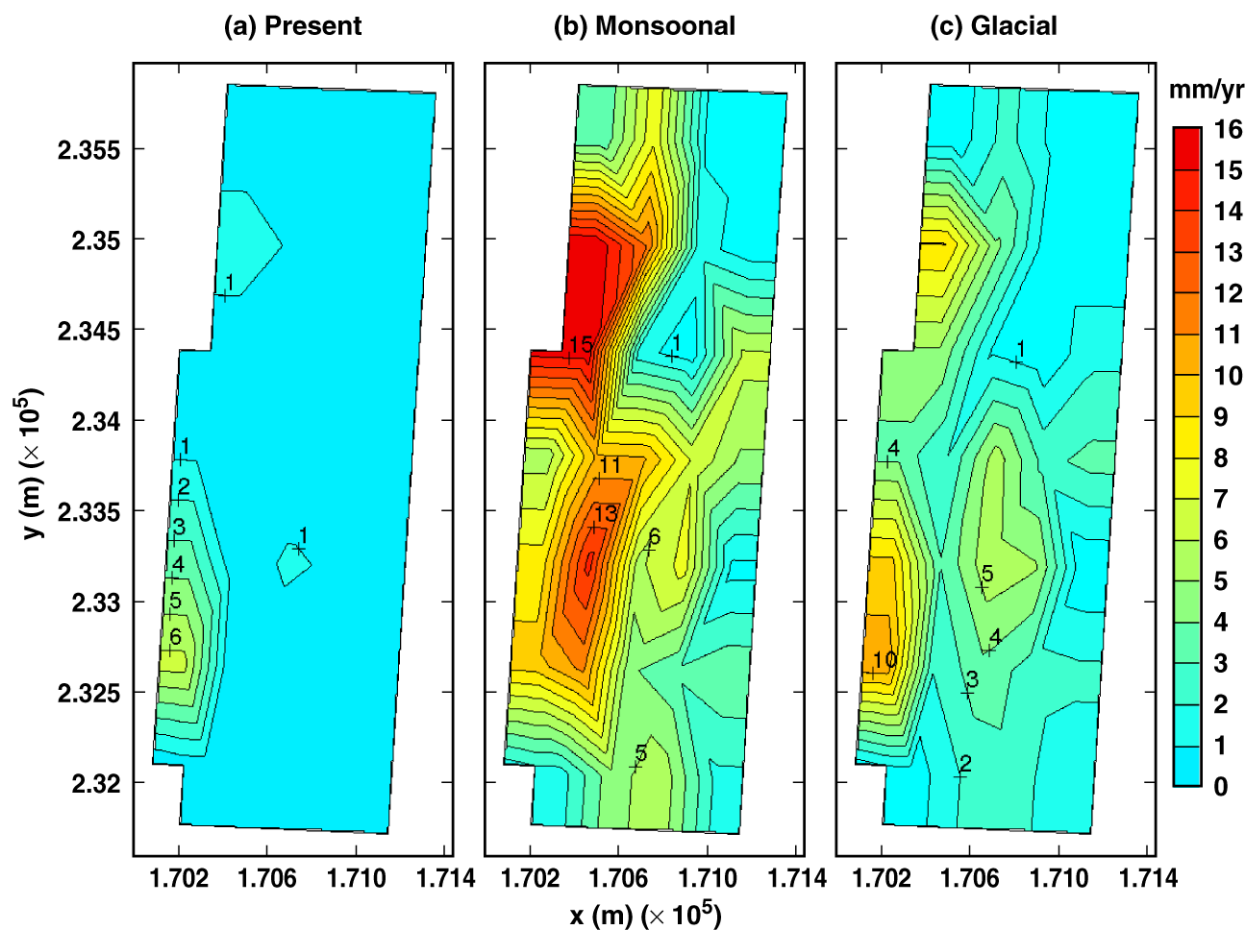


(b) Waste-Package Relative Humidity
Nevada State Coordinates: Easting = 170535.03 m, Northing = 233640.08 m



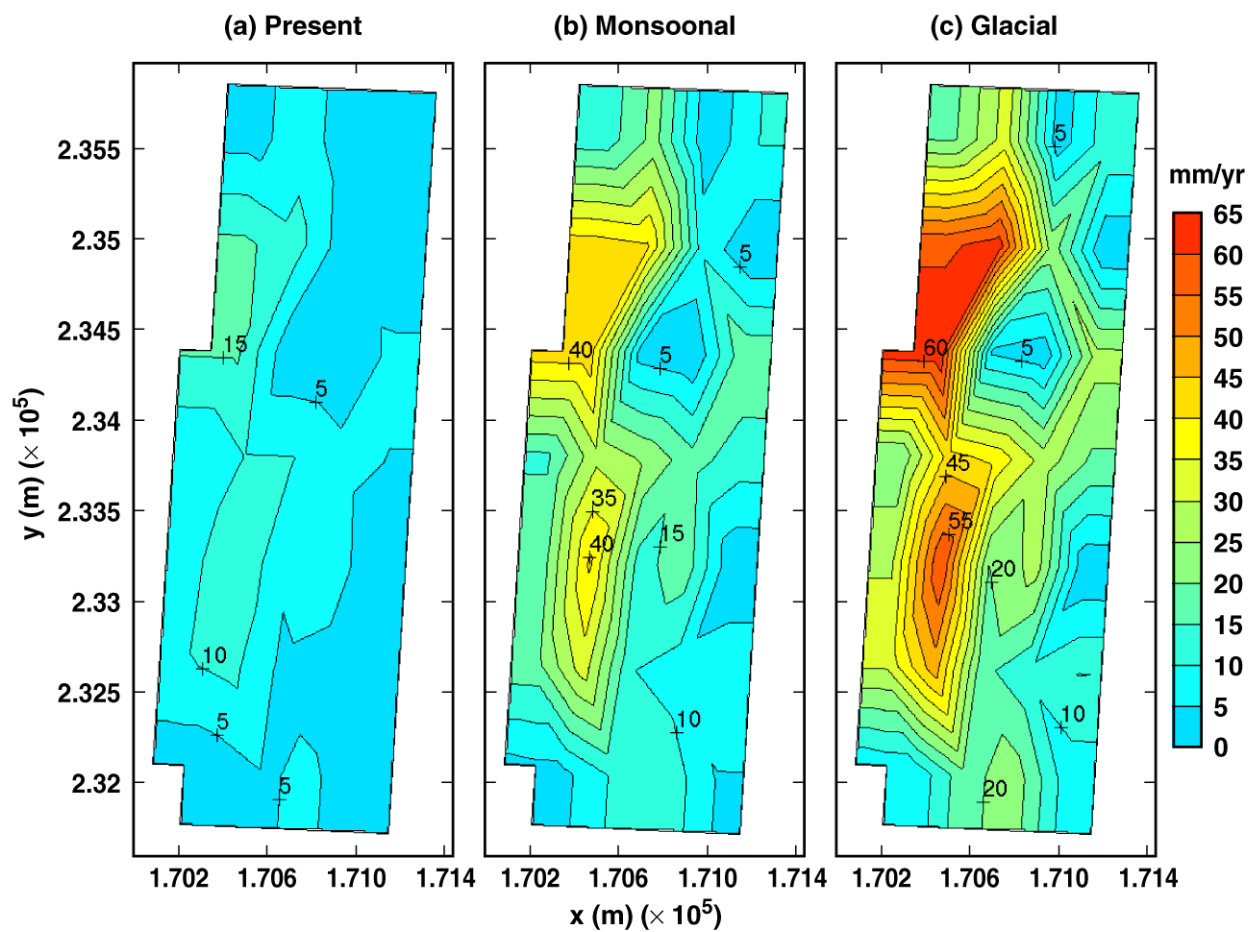
TB_AMR_T&RHwp_13-17_all

Figure 6-46. Temperature and relative humidity on the WP surface for the mean infiltration-flux case is plotted at the geographical center of the repository for the 4 different WP types and 8 different WP locations (along the drift) considered in the MSTHM (see Figure 4-1 for WP locations).



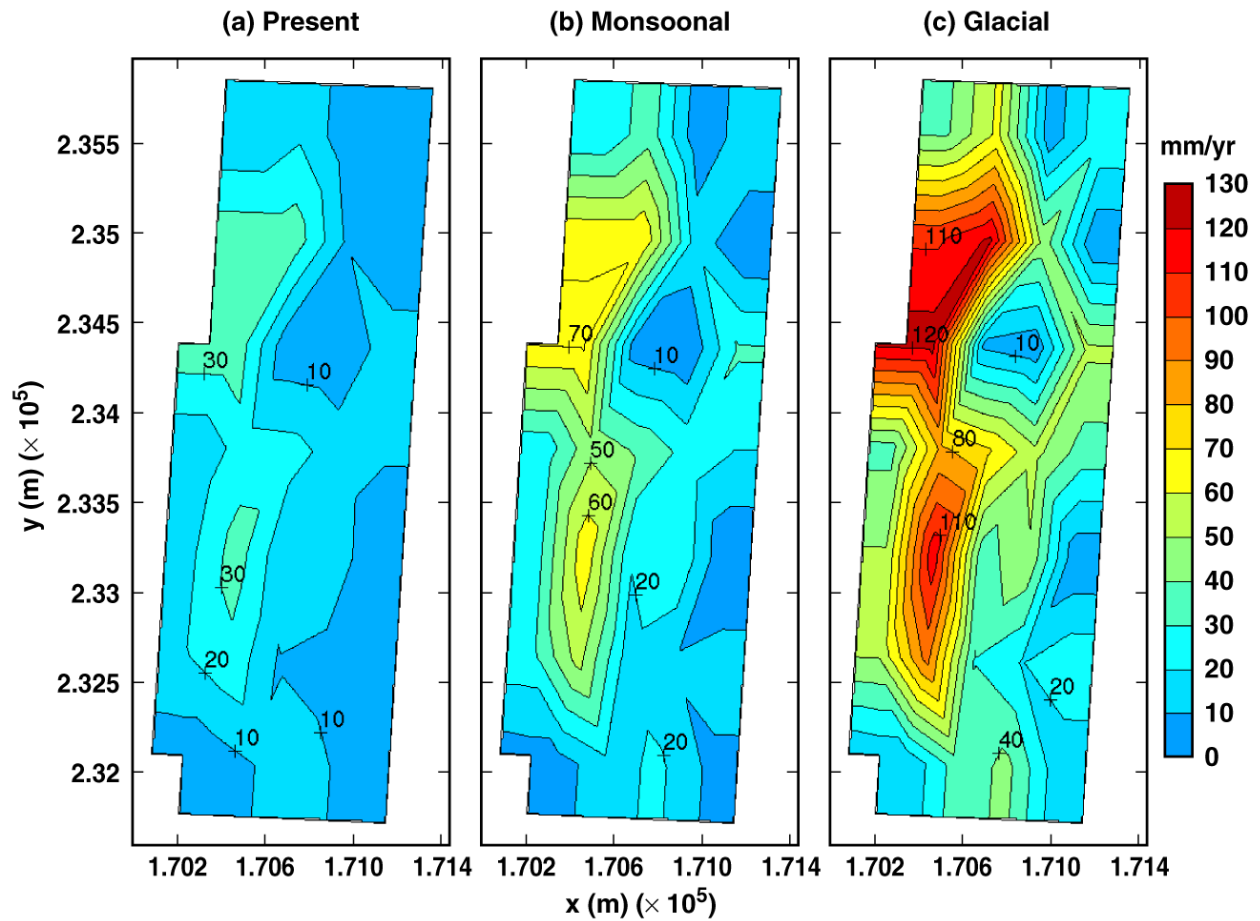
TB_AMR_infil_lower_p_m_g

Figure 6-47. The infiltration-flux distribution for the mean infiltration-flux case is plotted, including the present-day, monsoonal, and glacial climate periods.



TB_AMR_infil_medium_p_m_g

Figure 6-48. The infiltration-flux distribution for the high infiltration-flux case is plotted, including the present-day, monsoonal, and glacial climate periods.



TB_AMR_infil_upper_p_m_g

Figure 6-49. The infiltration-flux distribution for the low infiltration-flux case is plotted, including the present-day, monsoonal, and glacial climate periods.

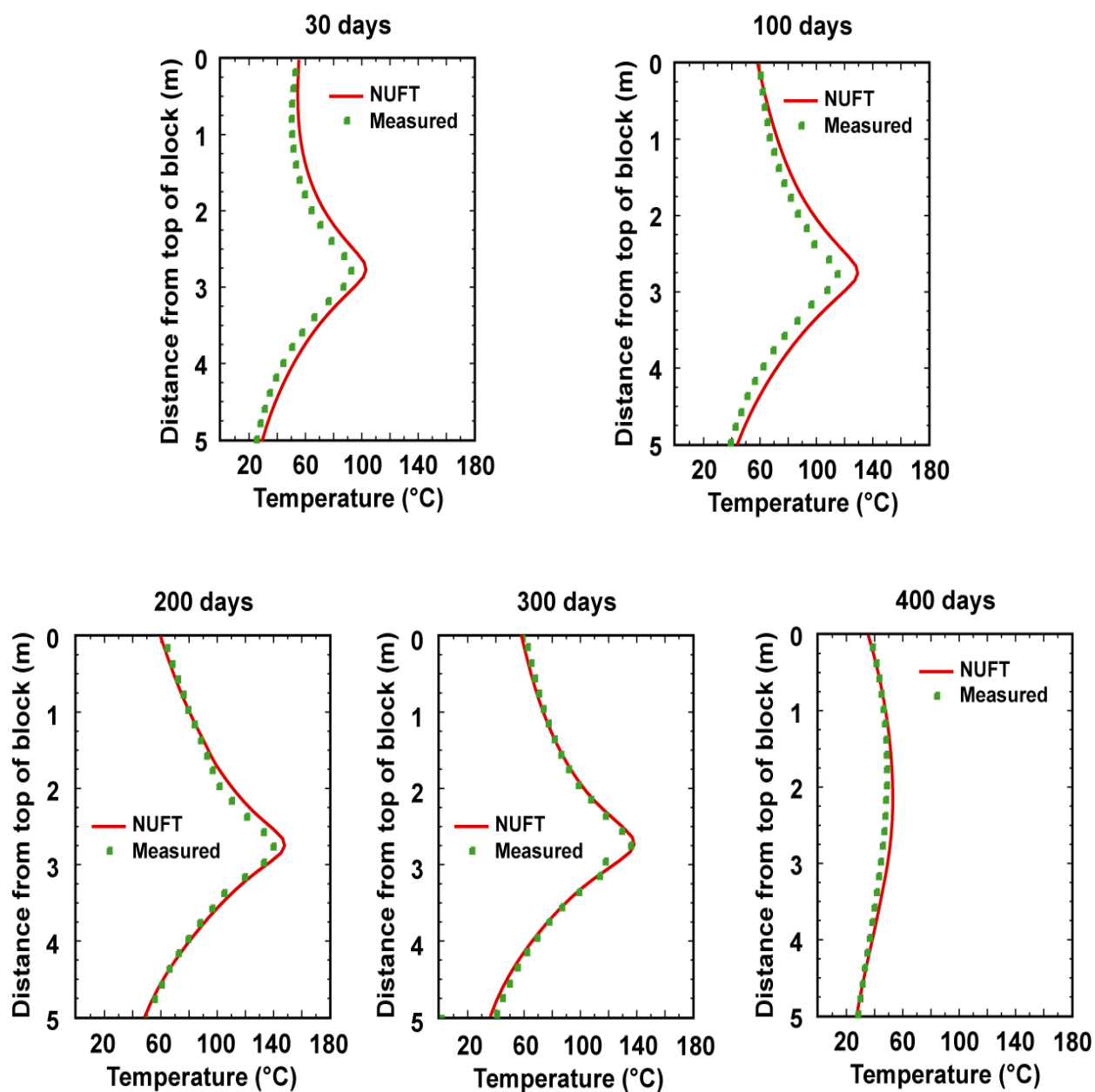


Figure 6-50. Comparison of the NUFT-simulated and measured temperatures along Borehole TT1 is given at six times from 30 to 400 days. The NUFT simulation used the drift-scale hydrologic property set that was used in the MSTHM calculations in this AMR.

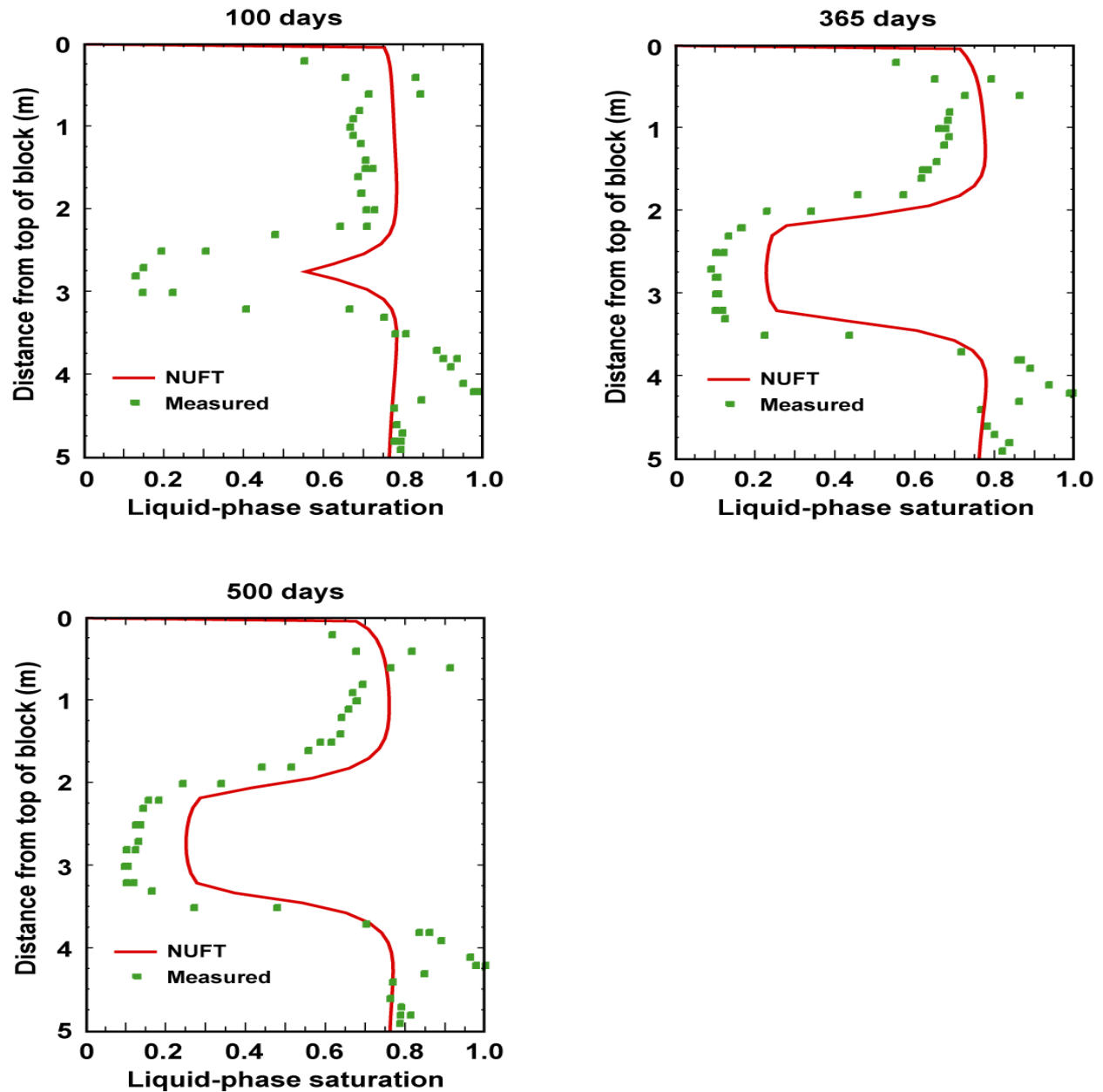


Figure 6-51. Comparison of the NUFT-simulated and measured liquid-phase saturation along Borehole TN3 is given at three times from 100 to 500 days. The NUFT simulation used the drift-scale hydrologic property set that was used in the MSTHM calculations in this AMR.

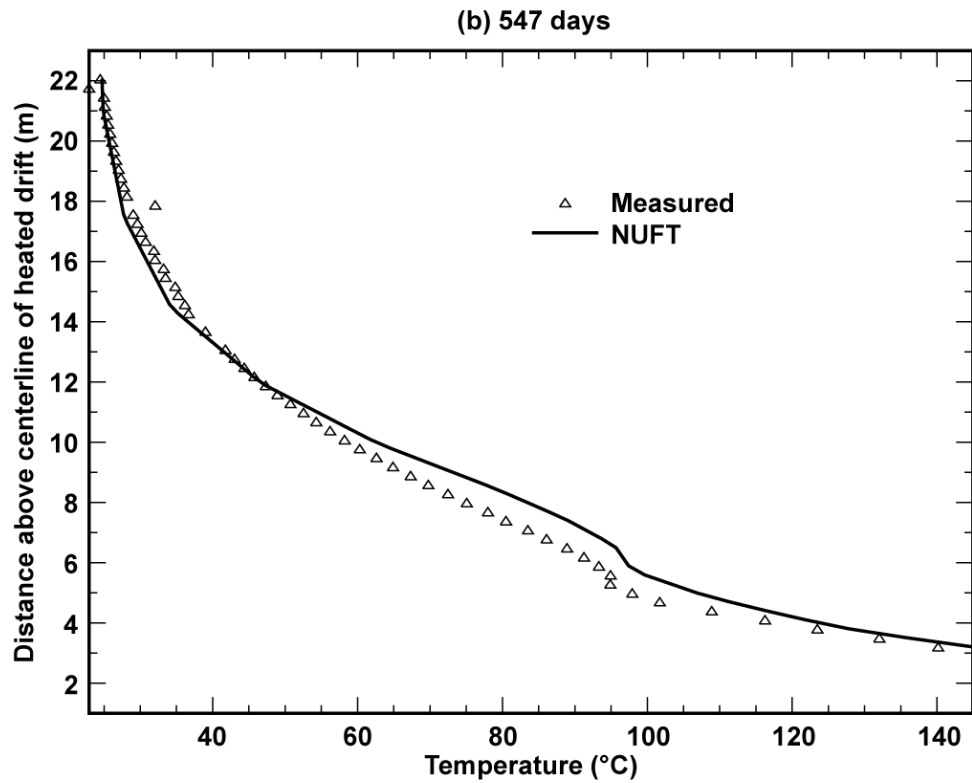
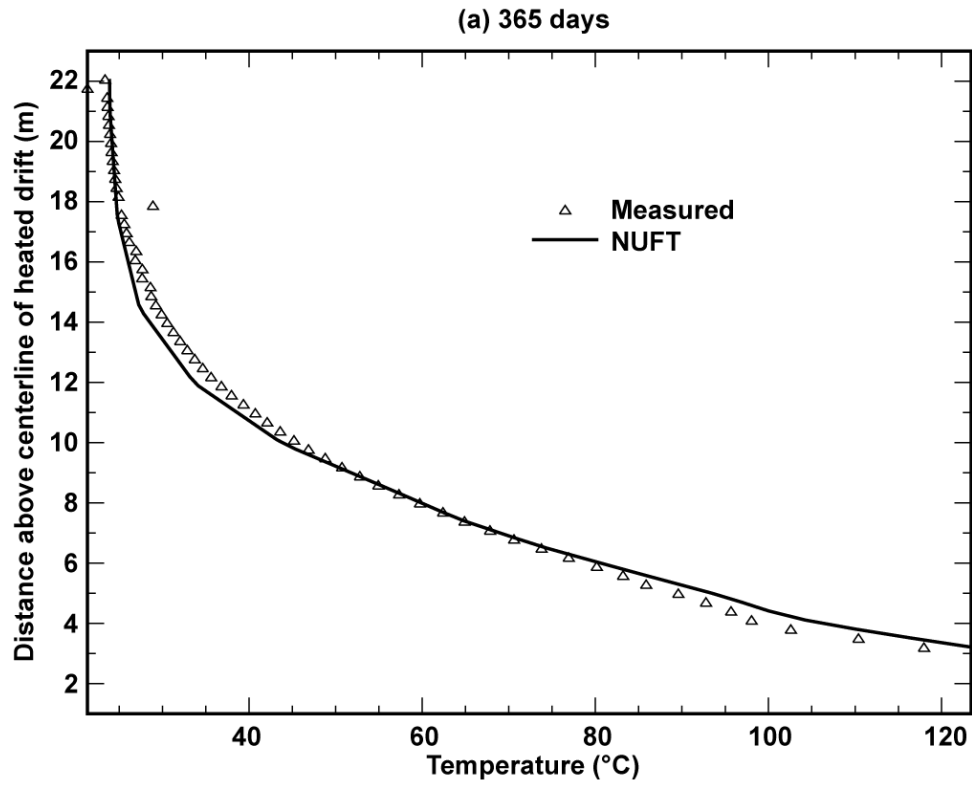


Figure 6-52. Comparison of the NUFT-simulated and measured temperatures along Borehole ESF-HD-137 is given at 365 and 547 days. The NUFT simulation used the drift-scale hydrologic property set that was used in the MSTHM calculations in this AMR.

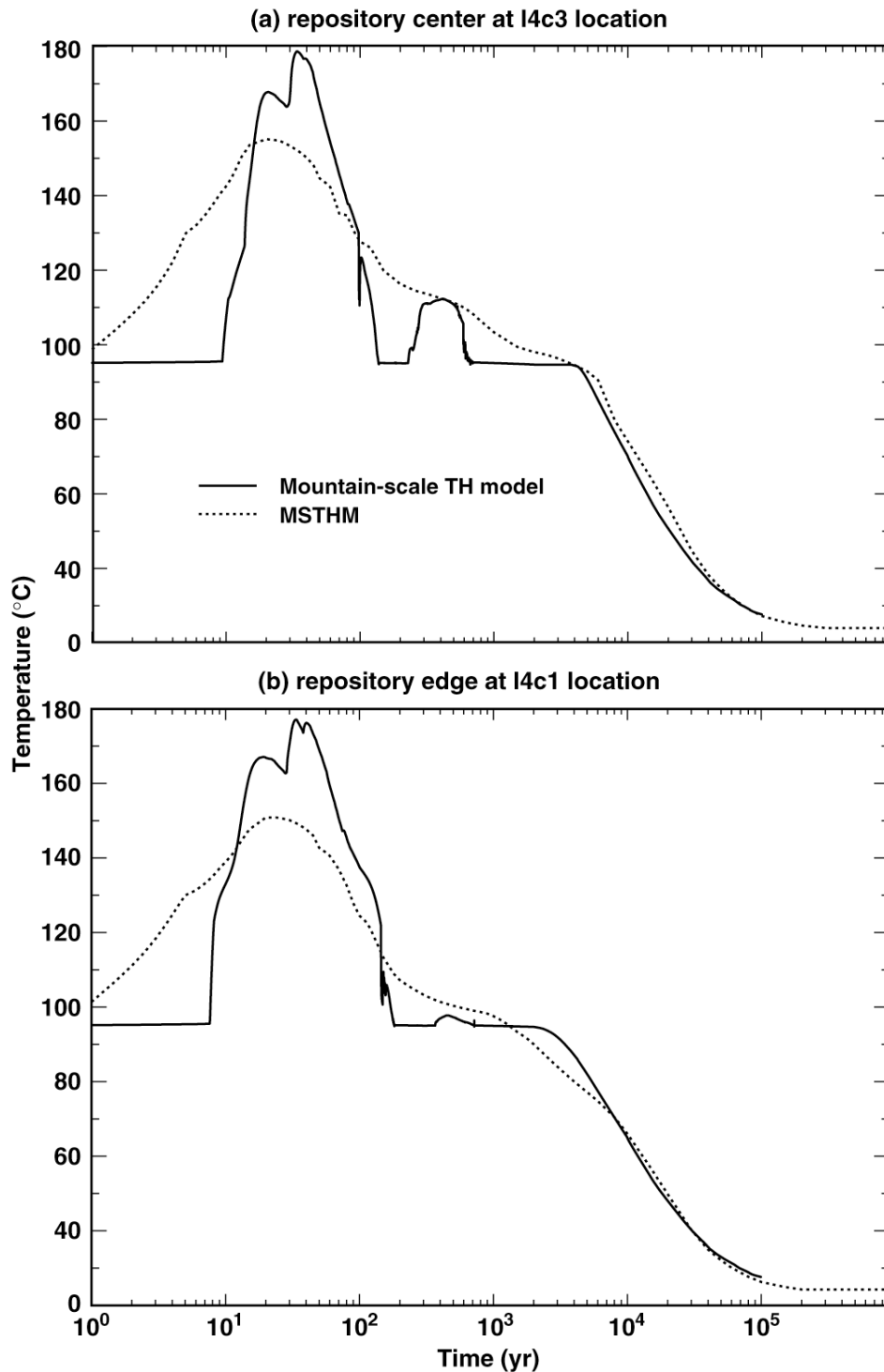


Figure 6-53. Comparison of predicted temperatures at (a) center of the repository (I4c3 location in Table 2-2 of Buscheck et al., 1998) and (b) 100 m from the edge of the repository (I4c1 location) for the 12/97 TSPA-VA base-case $1 \times 1 \alpha_{f, \text{mean}}$ parameter set, where the symbol I stands for the nominal infiltration-flux $q_{\text{inf}} = 7.8 \text{ mm/yr}$ for the present-day climate and the variable α_f is the van Genuchten "alpha" parameter for fractures. The MSTHM is used to predict drift-wall temperature adjacent to an "average" 21-PWR medium-heat CSNF WP. The east-west cross-sectional mountain-scale TH model is used to predict the drift temperature, which is averaged over the cross section of the drift, arising from a line-averaged heat-source representation of WP decay heat.

7. CONCLUSIONS

The purpose of the Multiscale Thermohydrologic Model (MSTHM) model was to describe the thermohydrologic evolution of the near-field environment (NFE) and EBS throughout the high-level nuclear waste repository at Yucca Mountain for a particular engineering design. TH information and data is provided throughout the entire repository area as a function of time in Figures 6-7 – 6-53 and data in CRWMS M&O 2000a of which appropriate developed data was submitted to the TDMS and was assigned the following DTN's: LL000113904242.089, LL000114004242.090, and LL000114104242.091.

The multiscale thermohydrologic model (MSTHM) calculates 38 TH variables in the NFE and EBS for 623 subdomains in the repository and for 8 different WPs as a function of time for about 352 calculational timesteps. The total of 38 TH arises from a combination of 10 thermodynamic variables (e.g., temperature T and relative humidity RH) and 13 drift-scale locations (e.g., WP and drip-shield surface) These TH variables are determined for three infiltration-flux scenarios, including the mean, high, and low infiltration-flux scenarios. For each calculational timestep, the MSTHM calculates $38 \times 623 \times 8$ TH data values, resulting in 189,392 data values. Multiplying by 352 calculational timesteps results in about 66 million TH data points for a complete time evolution of a given infiltration-flux scenario. These TH variables were requested by EBSO and PAO.

Temperature distributions in the NFE and EBS are influenced by a number of key factors:

- Repository-scale variability of percolation flux.
- Temporal variability of percolation flux (as influenced by climate change).
- Uncertainty in percolation flux (as addressed by the mean, high, and low infiltration-flux cases considered in this AMR).
- Repository-scale variability in hydrologic properties (e.g., those governing matrix imbibition diffusivity and capillary wicking in fractures).
- Edge-cooling effect (which increases with proximity to the edge of the repository).
- Dimensions and properties of the EBS components, such as the drip shield, engineered backfill and the invert.
- WP-to-WP variability in heat-generation rate.
- Repository-scale variability in overburden thickness.
- Repository-scale variability in thermal conductivity (with an emphasis on the host-rock units).

These factors, which are addressed in Section 6.11, influence (to varying degrees) the time-evolution of the key TH variables, such as liquid-phase flux, temperature, relative humidity, gas-phase air-mass fraction, and evaporation rate.

The software and most of the inputs used in this AMR are TBV; therefore, all conclusions are TBV. The impact of the uncertainty of some of the most important input variables (e.g., infiltration flux and thermal conductivity of the host-rock units) were addressed in previous sections of this AMR. The impact of uncertainty in all of the model inputs was not completely addressed because it was outside of the scope of work of this AMR. Changes to the inputs and/or software will require reproducing this model.

This document may be affected by technical product input information that requires confirmation. Any changes to the document that may occur as a result of completing the confirmation activities will be reflected in subsequent revisions. The status of the input information quality may be confirmed by review of the Document Input Reference System database.

During the pre-closure period, host-rock temperatures remain below the boiling point for the mean and high infiltration flux cases while boiling occurred in the host rock for the low flux case. During the pre-closure period peak WP temperatures of 100°C (for the mean flux case) and 110°C (for the low flux case) occur at 10 to 15 yr and at 20 to 25 yr peak drift-wall temperatures of 86°C (for the mean flux case) and of 96°C (for the low flux case) occur. Edge-cooling effects do not strongly affect pre-closure temperatures. After the initial heat-up stage, *RH* on WPs varies from 45 to 75% during the pre-closure period.

During the post-closure period, peak WP temperatures of 305°C (for the mean flux case) and 315°C (for the low flux case) occur at 60 yr. With regards to the influence of WP-to-WP variability in heat-generation rate, the difference in peak WP temperature between the hottest and coldest WP is 42°C.

During the post-closure period, peak temperatures on the lower drift wall of 195°C (for the mean flux case) and 205°C (for the low flux case) occur at 65 yr, upper drift wall peak temperatures of 125°C (for the mean flux case) and 134°C (for the low flux case) occur at 65 yr. The large (70°C) temperature difference between the upper and lower drift wall arises from the WP, drip-shield, and backfill configuration in the emplacement drift. Because the Overton-sand backfill is a very effective insulator ($K_{th} = 0.33 \text{ W/m-K}$) and because there is much more of this effective insulator above the WP and dripshield than below, much of the heat generation from WPs is focussed to the floor of the drift causing the large disparity in temperature between the lower and upper drift wall. To reduce this disparity, it would be necessary to balance the amount of insulation above and below the WP and drip shield.

During the very early post-closure period, the edge-cooling effect has a small effect on temperatures. By 100 yr, the influence of edge cooling is considerable, with WP temperatures varying by 120°C from the repository edge to the geographic center of the repository, with the outer 100 to 200 m of the repository are influenced by edge cooling at 100 yr. This large difference in temperature indicates a promising heat-management option for a repository with an

extended ventilation period (e.g., 100 yr). Because the influence of edge-cooling has penetrated significantly (100 to 200 m) in from the edge by 100 yr, it would be possible to emplace the hottest WPs in this edge region without incurring very high peak temperatures. The cooler WPs would be emplaced in the central repository region that does not experience edge-cooling effects. Thus, the center of the repository (which is an inherently hotter region) could receive a disproportionate share of cooler WPs, thereby reducing peak WP temperatures at the center of the repository. This heat-load balancing would also serve to reduce the variability in *RH* histories on WPs between the edge and center locations in the repository.

Liquid-phase flux in the host rock above the drift is influenced by dryout and the heat-pipe effect. Although one of the important objectives of the repository design analyzed in this report was to eliminate condensate buildup above the repository horizon, and thereby greatly reduce the magnitude of the heat-pipe effect, heat-pipe behavior above the dryout zone still enhances liquid-phase flux to well above ambient percolation fluxes. However, the duration of time that decay heat significantly enhances liquid-phase flux above the dryout zone is greatly reduced relative to the 80 MTU/acre repository analyzed in TSPA-VA. A noticeable increase in liquid-phase flux lasts for less than the duration of the present-day climate period (of 600 yr). Moreover, the magnitude of ambient percolation flux during the monsoonal-climate period ($600 < t < 2000$ yr) and during the glacial-climate period ($2000 \text{ yr} < t$) is comparable to (or even greater than) that generated by decay heat from WPs during the early pre-closure period.

Three key factors (including processes and conditions) influence the manner in which water seeps into and then flows through the drifts. The distribution of liquid flux in inside the drift has a dominant influence on other TH variables in the drift, such as relative humidity *RH*. These three factors are:

- **Capillary wicking in the Overton-sand backfill**, in conjunction with temperatures at the drift wall, influences the onset of seepage into the drift. During the early part of the pre-closure period the backfill is dry. As the temperature at the drift wall declines below the boiling point, water is able to wick (by capillary flow) from the fractures into the Overton-sand backfill. This wicking is facilitated by the van Genuchten α value for Overton sand being smaller than that of the fractures in the host-rock units. Had a coarser, well-sorted sand been used as backfill, with a value of α larger than that of the fractures in the host-rock units, then this wicking would not have taken place. Wicking by the Overton-sand backfill augments the influence of gravity-driven fracture flow; “capturing” flow in fractures over a region that is wider than the footprint of the drift.
- **Heat pipes**, which are the result of countercurrent water vapor and liquid water flow, strongly affect liquid-phase flux above the drip shield. Sometime after the onset of seepage, the magnitude of liquid-phase flux above the drip shield is much larger than the ambient percolation flux. Just as the magnitude of liquid-phase flux in the heat-pipe zone in the host-rock above the drift can greatly exceed the background percolation flux, the magnitude of liquid-phase flux in the heat-pipe zone in the backfill can greatly exceed the seepage flux entering the drift. The large temperature gradient in the backfill facilitates a large vapor flux away from the drip shield, while the high

capillarity of the Overton sand facilitates a large liquid-phase flux of water returning to the drip shield. This capillary-driven heat-pipe system in the backfill results in a large evaporative flux on the surface of the drip shield. Because the onset of seepage generally occurs when temperature on the drift wall drops below the boiling point, the onset of evaporation on the drip shield occurs earliest at the repository edge and then proceeds in towards the center of the repository.

- **Drip-shield, backfill, and invert geometry**, in conjunction with the hydrologic properties of the backfill and invert, strongly influence liquid-phase flux inside the drift. The liquid flow draining down the backfill along the side of the drip shield, encounters a restricted region for flow. If all of the water trying to shed around the drift were wicked into the drift, then this flux into the drift would be contributed by the percolation flux in a region that is at least 2.75 m wide (which corresponds to the half-width of the drift). Because the value of the van Genuchten α in the Overton sand backfill is smaller than in the fractures of the host rock, water draining down the side of the drip shield does not want to leave the backfill and enter the host rock; instead, all of it drains into the invert. If all of the percolation flux over a 2.75 m wide zone were focussed into the 0.69 m wide zone next to the drip shield, this would result in a “focussing” factor of four, which is comparable to the ratio which is observed between the liquid-phase flux next to the lower side of the drip shield and the host-rock percolation flux.

Relative humidity inside the drift is very dependent on whether water has seeped into the drift; the magnitude of the seepage is also important. An important EBS performance measure is how long *RH* on the WPs is low. *RH* reduction on WPs results from the following:

- **Relative humidity reduction at the drift wall** (and in the host rock) decreases strongly with proximity to the edge of the repository. Significant reduction in drift-wall *RH* persists for 100 to 1000 yr (depending on proximity to the edge) for the mean and high infiltration-flux cases and for about 200 to 2000 yr for the low flux case.
- **Relative humidity reduction on the drip shield** is relatively insensitive to proximity to the edge of the repository. Eventually, *RH* on the drip shield equilibrates with that in the host rock, thereby becoming nearly 100%. For the mean and high flux cases this takes about 1000 to 2000 yr to occur and for the low flux case this takes about 3000 to 6000 yr to occur. The end of the period of *RH* reduction on the drip shield corresponds to the time that seepage in the backfill has reached a steady-state condition.
- **Relative humidity reduction on the WP** persists long after *RH* reduction on the drip shield has ceased. The persistence of *RH* reduction between the drip shield and WP arises because of the temperature difference between the WP and drip shield. Because the interval between the WP and drip shield is an open cavity, thermal radiation controls this temperature difference. The use of an insulator (such as granular backfill) in the gap between the WP and drip shield would result in a much larger temperature

difference, which would result in a much larger reduction in *RH* between the drip shield and WP.

The maximum lateral extent of boiling (away from the drift wall) is a good indication of spatial extent of rock dryout (and *RH* reduction) around the emplacement drifts. The lateral extent of boiling is considerably greater for the low infiltration-flux case than for the mean or high flux cases. For the median WP location, the maximum lateral extent of boiling is 8.4 m, 9.1 m, and 10.5 m for the high, mean, and low flux cases, respectively. The hottest (and driest) WP location in the low flux case has a maximum lateral extent of boiling of 18 m; therefore, because the drifts are 81 m apart (Figure 4-1), a maximum of 44.4% of the repository horizon is driven to the boiling point. The hottest (and driest) WP location in both the mean and high flux cases have a maximum lateral extent of boiling of 9.7 m; therefore, a maximum of 24% of the repository horizon is driven to the boiling point. For the range of infiltration flux considered in this AMR, the maximum percentage of the repository horizon that can be driven to the boiling point lies between 24% and 44.4%.

There is much greater difference in dryout behavior (as evidenced by the maximum lateral extent of boiling and as evidenced by *RH* reduction) between the mean and low infiltration-flux cases than between the mean and high flux cases. Therefore, if one considers defining a percolation-flux threshold wherein rock dryout becomes significantly limited by percolation, then this percolation-flux threshold would appear to be close to that arising from the mean infiltration-flux case. Increasing percolation fluxes above those of the mean infiltration-flux case has a diminishing effect on decreasing the extent of boiling (and rock dryout).

7.1 UNCERTAINTIES OF THE AMBIENT AND THERMALLY PERTURBED SYSTEM

There are two primary categories of uncertainties: those associated with the EBS and those associated with the natural system. The natural-system uncertainties of primary interest concern the rock properties values in repository host rock and the infiltration flux. The key rock properties of concern are those hydrologic properties governing capillarity (i.e., matrix imbibition and capillary wicking in fractures) and thermal conductivity. In addition to parameter uncertainty, there are uncertainties in the ability to understand and predict unsaturated flow processes in fractured rock under ambient conditions and to coupled thermal-hydrologic-chemical and thermal-hydrologic-mechanical behavior. The EBS uncertainties of primary interest concern the hydrologic and thermal properties of the backfill and invert and WP-to-WP variability in heat-generation rate. An uncertainty that involves both the natural system and EBS concerns the distribution of seepage flux along the drifts. A discussion of the major uncertainties and how they are addressed in this AMR follows:

- Infiltration-flux uncertainty affects the local percolation flux, which affects the duration of dryout in the near-field host rock surrounding the drifts as well as rewetting the backfill and invert to ambient (humid) conditions. Dryout duration increases with decreasing percolation flux. This uncertainty is addressed by including the mean, high, and low infiltration-flux cases in this AMR. These three cases are judged to adequately span the range of uncertainty

of the infiltration flux. The low infiltration-flux cases had a considerably longer dryout duration than either the mean of high infiltration-flux cases.

- Matrix-imbibition diffusivity and capillary wicking in fractures uncertainty affects the duration of dryout in the near-field host rock surrounding the emplacement drifts. The rewetting of the host rock is also strongly affected by the magnitude of the local percolation flux, which depends on the ambient infiltration flux. Dryout duration increases with decreasing local percolation flux and with decreasing capillarity of the matrix and fractures in the host rock. This AMR considered a wide range of infiltration flux, which, in effect, is equivalent to considering a wide range of matrix-imbibition diffusivity and a wide range of capillarity of fractures in the host rock.
- Host-rock thermal-conductivity uncertainty affects the peak temperatures on the drift wall, dripshield, and WPs. It also has a minor influence on the duration of dryout of the near-field host rock surrounding the drifts. This uncertainty was addressed in Section 6.11.1.4.
- Backfill capillarity uncertainty affects the magnitude of the capillary wicking of water into the emplacement drifts. Coarse granular materials have low capillarity that result in low (or minimal) wicking of water into the drift, whereas fine granular materials have high capillarity that result in a high wicking flux into the drift, resulting in rapid wetting of the backfill to ambient (humid) conditions. The Overton sand backfill analyzed in this AMR results in very strong capillary wicking of water into the drift. After boiling ceases at the drift wall, the strong capillarity of the Overton sand causes wicking to wet the backfill relatively quickly to ambient (humid) conditions; therefore, it appears to be unlikely that this wetting behavior could occur significantly more quickly than predicted in this AMR. On the other hand, if the capillarity were found to be weaker than represented in this AMR, it is possible that the wetting could proceed significantly more slowly than predicted in this AMR.

Seepage-flux-distribution uncertainty can potentially affect how long it takes to wet the backfill and invert. Because of the high capillarity of the Overton sand backfill, water is wicked relatively quickly into the drift immediately after the drift-wall temperature has fallen below the nominal boiling point. Consequently, water enters the drift (by wicking) whether or not water would have seeped in the drift as a result of gravity drainage. The certainty with which water wicks into the drift (by capillarity) obviates the uncertainty of whether it would have seeped into the drift (by gravity drainage). Moreover, the large wicking capacity of the Overton sand also serves to attenuate (along the axis of the drift) any differences in local liquid-phase flux into the drift. Therefore, for the EBS design analyzed in this AMR (with Overton sand backfill), the uncertainty of seepage-flux distribution is negligible.

8. INPUTS AND REFERENCES

8.1 DOCUMENTS CITED

Bolz, R. E. and Tuve, G. L. 1973. *CRC Handbook of Tables for Applied Engineering Science*. 2nd Edition. Boca Raton, Florida: CRC Press. TIC: 246862.

Buscheck, T.A.; Gansemer, J.; Delorenzo, T. H.; Nitao, J. J.; and Shaffer, R. J. 1998. *Multiscale Thermohydrologic Model Sensitivity Analysis*. UCRL-ID-131489. Livermore, California: Lawrence Livermore National Laboratory. ACC: MOL.19980901.0245.

Buscheck, T.A. and Nitao, J. J. 1994. *The Impact of Buoyant, Gas-Phase Flow and Heterogeneity on Thermo-Hydrological Behavior at Yucca Mountain*. (UCRL-JC-115351) Livermore, California: Lawrence Livermore National Laboratory. ACC: NNA.19940524.0012.

CRWMS M&O (Civilian Radioactive Waste Management System Management and Operating Contractor) 1999a. Not Used.

CRWMS M&O 1999b. *Engineered Barrier System Performance Modeling (WP# 12012383MX)*. Activity Evaluation, July 12, 1999. Las Vegas, Nevada: CRWMS M&O. ACC: MOL.19990719.0317.

CRWMS M&O 1999c. *Classification of the MGR Ex-Container System*. ANL-XCS-SE-000001 REV 00. Las Vegas, Nevada: CRWMS M&O. ACC: MOL.19990928.0221.

CRWMS M&O 1999d. *Enhanced Design Alternative (EDA) II Repository Estimated Waste Package Types and Quantities*. Input Transmittal EBS-SR-99325.T. Las Vegas, Nevada: CRWMS M&O. ACC: MOL.19991103.0236.

CRWMS M&O 2000a. *Electronic Files for Revision 00 of the Multiscale Thermohydrologic Model*. ANL-EBS-MD-000049. Las Vegas, Nevada: CRWMS M&O. Submit to RPC URN-0255.

CRWMS M&O 2000b. *Thermal Tests Thermal-Hydrological Analysis/Model Report*. ANL-NBS-TH-000001 REV 00. Las Vegas, Nevada: CRWMS M&O. Submit to RPC URN-0212.

CRWMS M&O 2000c. *Development Plan for Multiscale Thermohydrologic Model*. TDP-EBS-MD-000024 REV 02. Las Vegas, Nevada: CRWMS M&O. Submit to RPC URN-0256.

DOE (U.S. Department of Energy) 2000. *Quality Assurance Requirements and Description*. DOE/RW-0333P, Rev. 9. Washington, D.C.: U. S. Department of Energy, Office of Civilian Radioactive Waste Management. ACC: MOL.19991028.0012.

Hardin, E.L. 1998. *Near-Field/Altered-Zone Models Report*. UCRL-ID-129179. Livermore, California: Lawrence Livermore National Laboratory. ACC: MOL.19980630.0560.

Hartman, H.L., ed. 1992. *SME Mining Engineering Handbook. 2nd Edition. Volume 2*. Littleton, Colorado: Society for Mining, Metallurgy, and Exploration. TIC: 206894.

Haukwa, C.; Wu, Y.S.; Hinds, J.J.; Zhang, W.; Ritcey, A.C.; Pan, L.H.; Simmons, A.M.; and Bodvarsson, G.S. 1998. *Results of Sensitivity Studies of Thermo-Hydrologic Behavior Conducted on Hydrologic Parameter Sets*. Milestone SP3CK5M4. Berkeley, California: Lawrence Berkeley National Laboratory. ACC: MOL.19980918.0001.

Incropera, F. P. and DeWitt, D. P. 1985. *Fundamentals of Heat and Mass Transfer*. New York, New York: John Wiley & Sons. TIC: 208420.

Incropera, F. P. and DeWitt, D. P. 1996. *Fundamentals of Heat and Mass Transfer. 4th Edition*. New York, New York: John Wiley & Sons. TIC: 243950.

Isaaks, E. H. and Srivastava, R. M. 1989. *Applied Geostatistics*. New York, New York: Oxford University Press. TIC: 200301.

Keenan, J.H.; Keyes, F.G.; Hill, P.G.; and Moore, J.G. 1969. *Steam Tables, Thermodynamic Properties of Water Including Vapor, Liquid, and Solid Phases*. New York, New York: John Wiley & Sons. TIC: 246766.

Kitanidis, P. K. 1997. *Introduction to Geostatistics: Applications in Hydrogeology*. New York, New York: Cambridge University Press. TIC: 236758.

Lide, D.R., ed. 1995. *CRC Handbook of Chemistry and Physics. 76th Edition*. Boca Raton, Florida: CRC Press. TIC: 216194.

Meyer, C. A.; McClintock, R. B.; Silvestri, G. J.; and Spencer, R. C., Jr. 1967. *1967 ASME Steam Tables, Thermodynamic and Transport Properties of Steam. 2nd Ed.* pages 13, 14, 17, 22. New York, New York: American Society of Mechanical Engineers. TIC: 246889.

Stroupe, E. P. 2000. "Approach to Implementing the Site Recommendation Design Baseline." Interoffice Correspondence from E. P. Stroupe (CRWMS M&O) to Dr. D. R. Wilkins, January 26, 2000, LV.RSO.EPS.1/00-004, with attachment. Las Vegas, Nevada: CRWMS M&O. ACC: MOL.20000214.0480.

Wilder, D.G., ed. 1996. *Near-Field and Altered-Zone Environment Report. Volume II*. UCRL-LR-124998. Livermore, California: Lawrence Livermore National Laboratory. ACC: MOL.19961212.0121; MOL.19961212.0122.

YMP (Yucca Mountain Project) 1998. *Q-List*. YMP/90-55Q, Rev. 5. Las Vegas, Nevada: Yucca Mountain Site Characterization Office. ACC: MOL.19980513.0132.

8.2 PROCEDURES CITED

AP-2.13Q, Rev 0, ICN 1. *Technical Product Development Plan*. Washington, D.C.: DOE OCRWM. ACC: MOL.19991115.0230.

AP-3.4Q, Rev 1, ICN 1. *Level 3 Change Control*. Washington, D.C.: DOE OCRWM. ACC: MOL.19991117.0140.

AP-3.10Q, Rev 2. *Analyses and Models*. Washington, D.C.: DOE OCRWM. ACC: .MOL.20000217.0246.

AP-3.14Q, Rev 0. *Transmittal of Input*. Washington, D.C.: DOE OCRWM. ACC: MOL.19990701.0621.

AP-3.15Q, Rev 1, ICN 1. *Managing Technical Product Inputs*. Washington, D.C.: DOE OCRWM. ACC: MOL. 20000218.0069.

AP-SI.1Q, REV 2, ICN 4. *Software Management*. Washington, D.C.: DOE OCRWM. ACC: MOL. 20000223.0508.

AP-SIII.3Q, Rev 0, ICN 2. *Submittal and Incorporation of Data to the Technical Data Management System*. Washington, D.C.: DOE OCRWM. ACC: MOL.19991214.0632.

QAP-2-0, Rev 5. *Conduct of Activities*. Las Vegas, Nevada: CRWMS M&O. ACC: MOL.19980826.0209.

QAP-2-3, Rev 10. *Classification of Permanent Items*. Las Vegas, Nevada: CRWMS M&O. ACC: MOL.19990316.0006.

8.3 SOURCE DATA

LB990861233129.001. Drift Scale Calibrated 1-D Property Set, FY99. Submittal Date: 08/06/1999.

LB990861233129.002. Drift Scale Calibrated 1-D Property Set, FY99. Submittal Date: 08/06/1999.

LB990861233129.003. Drift Scale Calibrated 1-D Property Set, FY99. Submittal Date: 08/06/1999.

LB991091233129.006. Thermal Properties and Tortuosity Factor for the UZ Model Layers for AMR U0090, "Analysis of Hydrologic Properties Data". Submittal Date: 10/15/1999.

LB99EBS1233129.001. Natural Environment Data for Engineered Barrier System (EBS) Basecase. Submittal Date: 11/29/99.

LB99EBS1233129.003. Natural Environment Data for Engineered Barrier System (EBS) Basecase. Submittal Date: 11/29/99.

LB99EBS1233129.004. Natural Environment Data for Engineered Barrier System (EBS) Basecase. Submittal Date: 11/29/99.

LL000113904242.089. TSPA-SR Lower Calculations. Submittal Date: 1/28/2000

LL000114004242.090. TSPA-SR Mean Calculations. Submittal Date: 1/28/2000

LL000114104242.091. TSPA-SR Upper Calculations. Submittal Date: 1/28/2000

LL970803004244.036. Data on Temperature of the Large Block Test (LBT). Submittal Date: 08/08/1997.

LL971204304244.047. Neutron Logging Activities at the Large Block Test (LBT). Submittal Date: 12/08/1997.

LL980919304244.075. Neutron Logging Activities at the Large Block Test (LBT). Submittal Date: 09/30/1998

MO9911MWDEBSWD.000. EBS Water Drainage Model. Submittal Date: 11/29/1999.

SNT05071897001.004. Total System Performance Assessment-Viability Assessment (TSPA-VA) Heat Loading Data. Submittal Date: 03/26/1998.

SN9907T0872799.002. Effective Thermal Conductivity for Drift-Scale Models Used in TSPA-SR (Total System Performance Assessment-Site Recommendation). Submittal Date: 07/27/1999.

SN9912T0872799.005. Effective Thermal Conductivity for the Extended Preclosure Period in the Drift-Scale Models Used in TSPA-SR (Total System Performance Assessment-Site Recommendation). Submittal Date: 12/16/1999.

SN9908T0872799.004. Tabulated In-drift Geometric and Thermal Properties Used in Drift-scale Models for TSPA-SR (Total System Performance Assessment-Site Recommendation). Submittal Date: 08/30/1999.

8.4 SOFTWARE SOURCES

Lawrence Livermore National Laboratory. 1999. *Software Code: NUFT V3.0s*. V3.0s. 10088-3.0s-00.

Lawrence Livermore National Laboratory. 2000. *Software Routine: CONVERTCOORDS V1.1*. V1.1. 10209-1.1-00.

Lawrence Livermore National Laboratory. 2000. *Software Routine: YMESH V1.53*. V1.53. 10172-1.53-00.

Lawrence Livermore National Laboratory. 2000. *Software Routine: RADPRO V3.22*. V3.22. Sun Ultra10. 10204-3.22-00.

Lawrence Livermore National Laboratory. 2000. *Software Routine: XTOOL V10.1*. V10.1. Sun Ultra10. 10208-10.1-00.

Lawrence Livermore National Laboratory. 1999. *Software Code: MSTHAC V6.2*. V6.2. Sun Ultra10. 10290-6.2-00.

9. ATTACHMENTS

	No. of Pages
Attachment I: QUALIFICATION OF MakeColumns.....	2
Attachment II: QUALIFICATION OF Define_EBS_fineGrid	6
Attachment III: QUALIFICATION OF ReadUnits	2
Attachment IV: QUALIFICATION OF AddLayers AND addlay	2
Attachment V: QUALIFICATION OF Heat_DDT AND heat_SMT.....	3
Attachment VI: QUALIFICATION OF Xairtab	3
Attachment VII: QUALIFICATION OF Infiltab	2
Attachment VIII QUALIFICATION OF Rock_sun	2
Attachment IX: QUALIFICATION OF SMT_surf_bc AND SMT_bot_bc	4
Attachment X: QUALIFICATION OF Bound	2
Attachment XI: QUALIFICATION OF COREY ROUTINES.....	3
Attachment XII: QUALIFICATION OF HeatgenAge	2
Attachment XIII: QUALIFICATION OF Chim_Surf_TP AND Chim_wt_TP	2
Attachment XIV: QUALIFICATION OF ColumnInfiltration.....	3
Attachment XV: QUALIFICATION OF Cover	3
Attachment XVI: QUALIFICATION OF Rme6.....	3
Attachment XVII: NORMALIZED INFILTRATION RATES.....	4
Attachment XVIII: INPUT AND OUTPUT FILES FOR RADPRO, XTOOL, MSTHAC, YMASH AND CONVERTCOORDS.....	1
Attachment XIX: QUALIFICATION OF SplitEXT.....	7
Attachment XX: DEVELOPMENT OF LINEAR EXTRAPOLATION FORMULA.....	2

ATTACHMENT I

QUALIFICATION OF MakeColumns

ROUTINE IDENTIFICATION

MakeColumns v1.0. This routine was compiled using C++ vSC4.2. The source code consists of two files: makeColumns.c and myFunctions.h (CRWMS M&O 2000a). Myfunctions.h is used to check input data format and memory allocation.

The input files are column_template and column.data. There are 31 output files, named <column>.dat, where column corresponds to the 31 chimney locations.

ROUTINE PURPOSE AND VALIDATION

The purpose of the routine is to create a family of YMESH input files for a family of chimneys at specified locations. The specific input files required by makeColumns are column_template and column.data. Column_template is almost a valid YMESH input file to generate a chimney mesh but lacks the section defining the starting location of the mesh. The purpose of MakeColumns is to add the missing information to the column_template for each chimney location. To verify that the routine is working correctly, the template file is compared to the output file, and the lines added are checked against the chimney locations (located in column.data) Column.data is a list of chimney locations (northings and eastings) and names, preceded by a few lines of header information.

To document that this routine in fact performed as expected, it was run first with the column_template and column.data files. The run produced a family of files licj.dat, where the names licj.dat were those associated with the chimney locations listed in column.data. When the UNIX routine diff was used to compare column_template with l7c4.dat, the only difference found was the following:

(diffinout, CRWMS M&O 2000a) Output from the diff function.

```
0a1,3
> rootMesh
> imbed mesh1 a 170338.0 232049.4 column_maxz
> end
```

indicating that the routine had created l7c4.dat by adding the three lines following the ">" to the top of column_template. To demonstrate that the routine used the correct coordinates for the starting point, the first few lines of column.data are reprinted below:

```
1  ## 1st data line: NV x/y coordinates of SW repository corner
2  ## 2nd data line: NV x/y coordinates of SE repository corner
3  170066.05    231769.42
4  171149.71    231711.85
5
6  170337.96    232049.39    l7c4
7  170574.34    232036.83    l7c3
(CRWMS M&O 2000a, column.data)
```

MakeColumns wrote the correct coordinates in each mesh definition file. Therefore, makeColumns provides the correct results over the range of input parameters in the input files column_template and column.data (CRWMS M&O 2000a).

ATTACHMENT II

QUALIFICATION OF Define_EBS_fineGrid

ROUTINE IDENTIFICATION

Define_EBS_fineGrid v1.3. This routine was compiled using C++ vSC4.2. The source code consists of three files: define_EBS_fineGrid.c, myFunctions.h, and changename.h (CRWMS M&O 2000a). MyFunctions.h is used to check input data format and memory allocation. Changename.h assigns the output filenames.

The 31 input files are <column>.nft. The corresponding output files are: <column>.nft.msh.dkm0.m, <column>.nft.msh.dkm0.f, <column>.nft.msh.dkm.m, <column>.nft.msh.dkm.f, <column>.nft.msh.dkm0, <column>.nft.msh.dkm.f and <column>.nft.msh.dkm.m. These files are located in CRWMS M&O 2000a.

ROUTINE PURPOSE AND VALIDATION

The purpose of this routine is to create NUFT mesh input for pre- and post-closure runs of the engineered barrier system (EBS) problem to be solved with the implicit dual permeability model (DKM, with a matrix and fracture mesh). Define_EBS_fineGrid takes as input a genmsh type file created by YMESH (<column>.nft). It then creates from it two sets of matrix and fracture mesh definition files (<column>.nft.msh.dkm0.m and <column>.nft.msh.dkm0.f, and <name>.nft.msh.dkm.m and <column>.nft.msh.dkm.f) and one other (<column>.nft.msh.dkm0.) It inserts into these output files an atmosphere layer, "atm," and a water table layer, "wt." It inserts the additional EBS layers, "hstrk", "dr", "bf", "wp", and "in" into the files <column>.nft.msh.dkm.f and <column>.nft.msh.dkm.m, which are NUFT input files (input using include). The EBS materials are placed in zones surrounding the first zone whose grid height, dz, is .303 meters, *replacing* the rock layers shown occupying the same zones in the dz section above.

In order to confirm that this routine performed its task as expected, a genmsh file was created by modifying l3c1.nft, leaving the information for the materials to be overwritten with EBS materials, plus all material layers above and one below the engineered system. The resulting file, called **testjl.nft**, is listed here:

```
1      (genmsh
2      (down 0. 0. 1.0)
3      (coord rect)
4      (dx 1.000)
5      (dy 1.000)
6      (dz
7          15.908 15.498 15.498 30.000 30.000 ;; 1- 5:tcw11 tcw12 tcw12 tcw12 tcw12
8          4.805 5.918 6.211 5.068 10.254 ;; 6- 10:tcw13 ptn21 ptn22 ptn23 ptn24
9          22.939 12.041 1.992 22.354 30.000 ;; 11- 15:ptn25 ptn26 tsw31 tsw32 tsw32
10         15.308 15.308 20.000 15.000 10.000 ;; 16- 20:tsw33 tsw33 tsw33 tsw33 tsw33
11         6.000 4.000 3.000 3.000 2.400 ;; 21- 25:tsw33 tsw33 tsw34 tsw34 tsw34
12         2.000 1.000 1.000 0.500 0.300 ;; 26- 30:tsw34 tsw34 tsw34 tsw34 tsw34
13         0.200 0.200 0.200 0.200 0.200 ;; 31- 35:tsw34 tsw34 tsw34 tsw34 tsw34
14         0.200 0.200 0.200 0.274 0.200 ;; 36- 40:tsw34 tsw34 tsw34 tsw34 tsw34
15         0.200 0.254 0.237 0.382 0.647 ;; 41- 45:tsw34 tsw34 tsw34 tsw34 tsw34
16         0.786 0.514 0.303 0.303 0.800 ;; 46- 50:tsw34 tsw34 tsw34 tsw34 tsw34
17         1.000 1.500 2.000 2.000 2.500 ;; 51- 55:tsw34 tsw34 tsw34 tsw34 tsw34
18         3.000 4.000 6.000 10.000 15.000 ;; 56- 60:tsw34 tsw34 tsw35 tsw35 tsw35
19     )
20     (mat
21         (tcw11 tcw11 1 nx 1 ny 1 1)
22         (tcw12 tcw12 1 nx 1 ny 2 5)
```



```

23      (tcw13      tcw13      1 nx 1 ny 6 6)
24      (ptn21      ptn21      1 nx 1 ny 7 7)
25      (ptn22      ptn22      1 nx 1 ny 8 8)
26      (ptn23      ptn23      1 nx 1 ny 9 9)
27      (ptn24      ptn24      1 nx 1 ny 10 10)
28      (ptn25      ptn25      1 nx 1 ny 11 11)
29      (ptn26      ptn26      1 nx 1 ny 12 12)
30      (tsw31      tsw31      1 nx 1 ny 13 13)
31      (tsw32      tsw32      1 nx 1 ny 14 15)
32      (tsw33      tsw33      1 nx 1 ny 16 22)
33      (tsw34      tsw34      1 nx 1 ny 23 57)
34      (tsw35      tsw35      1 nx 1 ny 58 60)
35      )
36      )
(CRWMS M&O 2000a, testjl.nft)

```

Running define_EBS_fineGrid on this input produced the following output files: testjl.nft.msh.dkm0, testjl.nft.msh.dkm0.m, testjl.nft.msh.dkm0.f, testjl.nft.msh.dkm.m, and testjl.nft.msh.dkm.f. These are printed on the following pages for visual inspection.

testjl.nft.msh.dkm0:

```

1      (dz
2      1e-30      15.9      15.5      15.5      30 ;; 1- 5: atm tcw11 tcw12 tcw12 tcw12
3      30      4.8      5.92      6.21      5.07 ;; 6- 10:tcw12 tcw13 ptn21 ptn22 ptn23
4      10.3      22.9      12      1.99      22.4 ;; 11- 15:ptn24 ptn25 ptn26 tsw31 tsw32
5      30      15.3      15.3      20      15 ;; 16- 20:tsw32 tsw33 tsw33 tsw33 tsw33
6      10      6      4      3      3 ;; 21- 25:tsw33 tsw33 tsw33 tsw34 tsw34
7      2.4      2      1      1      0.5 ;; 26- 30:tsw34 tsw34 tsw34 tsw34 tsw34
8      0.3      0.2      0.2      0.2      0.2 ;; 31- 35:tsw34 tsw34 tsw34 tsw34 tsw34
9      0.2      0.2      0.2      0.2      0.274 ;; 36- 40:tsw34 tsw34 tsw34 tsw34 tsw34
10     0.2      0.2      0.254      0.237      0.382 ;; 41- 45:tsw34 tsw34 tsw34 tsw34 tsw34
11     0.647      0.786      0.514      0.303      0.303 ;; 46- 50:tsw34 tsw34 tsw34 tsw34 tsw34
12     0.8      1      1.5      2      2 ;; 51- 55:tsw34 tsw34 tsw34 tsw34 tsw34
13     2.5      3      4      6      10 ;; 56- 60:tsw34 tsw34 tsw34 tsw35 tsw35
14     15      1e-30 ;; 61- 62:tsw35 wt
15     )
16     (mat
17     (atm      atm      1 nx 1 ny 1 1)
18     (tcw11      tcw11      1 nx 1 ny 2 2)
19     (tcw12      tcw12      1 nx 1 ny 3 6)
20     (tcw13      tcw13      1 nx 1 ny 7 7)
21     (ptn21      ptn21      1 nx 1 ny 8 8)
22     (ptn22      ptn22      1 nx 1 ny 9 9)
23     (ptn23      ptn23      1 nx 1 ny 10 10)
24     (ptn24      ptn24      1 nx 1 ny 11 11)
25     (ptn25      ptn25      1 nx 1 ny 12 12)
26     (ptn26      ptn26      1 nx 1 ny 13 13)
27     (tsw31      tsw31      1 nx 1 ny 14 14)
28     (tsw32      tsw32      1 nx 1 ny 15 16)
29     (tsw33      tsw33      1 nx 1 ny 17 23)
30     (tsw34      tsw34      1 nx 1 ny 24 58)
31     (tsw35      tsw35      1 nx 1 ny 59 61)
32     (wt      tsw35      1 nx 1 ny 62 62)
33     )
(CRWMS M&O 2000a, testjl.nft.msh.dkm0)

```

testjl.nft.msh.dkm0.m:

```

1      (dz
2      1e-30      15.9      15.5      15.5      30 ;; 1- 5: atm tcw11 tcw12 tcw12 tcw12
3      30      4.8      5.92      6.21      5.07 ;; 6- 10:tcw12 tcw13 ptn21 ptn22 ptn23
4      10.3      22.9      12      1.99      22.4 ;; 11- 15:ptn24 ptn25 ptn26 tsw31 tsw32
5      30      15.3      15.3      20      15 ;; 16- 20:tsw32 tsw33 tsw33 tsw33 tsw33
6      10      6      4      3      3 ;; 21- 25:tsw33 tsw33 tsw33 tsw34 tsw34
7      2.4      2      1      1      0.5 ;; 26- 30:tsw34 tsw34 tsw34 tsw34 tsw34
8      0.3      0.2      0.2      0.2      0.2 ;; 31- 35:tsw34 tsw34 tsw34 tsw34 tsw34

```

```

9      0.2      0.2      0.2      0.2      0.274 ;; 36- 40:tsw34 tsw34 tsw34 tsw34 tsw34
10     0.2      0.2      0.254      0.237      0.382 ;; 41- 45:tsw34 tsw34 tsw34 tsw34 tsw34
11     0.647      0.786      0.514      0.303      0.303 ;; 46- 50:tsw34 tsw34 tsw34 tsw34 tsw34
12     0.8      1      1.5      2      2 ;; 51- 55:tsw34 tsw34 tsw34 tsw34 tsw34
13     2.5      3      4      6      10 ;; 56- 60:tsw34 tsw34 tsw34 tsw35 tsw35
14     15      1e-30 ;; 61- 62:tsw35 wt
15   )
16   (mat
17     (atm      atm      1 nx 1 ny 1 1)
18     (tcw11      m-tcw11      1 nx 1 ny 2 2)
19     (tcw12      m-tcw12      1 nx 1 ny 3 6)
20     (tcw13      m-tcw13      1 nx 1 ny 7 7)
21     (ptn21      m-ptn21      1 nx 1 ny 8 8)
22     (ptn22      m-ptn22      1 nx 1 ny 9 9)
23     (ptn23      m-ptn23      1 nx 1 ny 10 10)
24     (ptn24      m-ptn24      1 nx 1 ny 11 11)
25     (ptn25      m-ptn25      1 nx 1 ny 12 12)
26     (ptn26      m-ptn26      1 nx 1 ny 13 13)
27     (tsw31      m-tsw31      1 nx 1 ny 14 14)
28     (tsw32      m-tsw32      1 nx 1 ny 15 16)
29     (tsw33      m-tsw33      1 nx 1 ny 17 23)
30     (tsw34      m-tsw34      1 nx 1 ny 24 58)
31     (tsw35      m-tsw35      1 nx 1 ny 59 61)
32   ) (wt      m-tsw35      1 nx 1 ny 62 62)
33 )
(CRWMS M&O 2000a, testjl.nft.msh.dkm0.m)

```

testjl.nft.msh.dkm0.f:

```

1      (dz
2      1e-30      15.9      15.5      15.5      30 ;; 1- 5: atm tcw11 tcw12 tcw12 tcw12
3      30      4.8      5.92      6.21      5.07 ;; 6- 10:tcw12 tcw13 ptn21 ptn22 ptn23
4      10.3      22.9      12      1.99      22.4 ;; 11- 15:ptn24 ptn25 ptn26 tsw31 tsw32
5      30      15.3      15.3      20      15 ;; 16- 20:tsw32 tsw33 tsw33 tsw33 tsw33
6      10      6      4      3      3 ;; 21- 25:tsw33 tsw33 tsw33 tsw34 tsw34
7      2.4      2      1      1      0.5 ;; 26- 30:tsw34 tsw34 tsw34 tsw34 tsw34
8      0.3      0.2      0.2      0.2      0.2 ;; 31- 35:tsw34 tsw34 tsw34 tsw34 tsw34
9      0.2      0.2      0.2      0.2      0.274 ;; 36- 40:tsw34 tsw34 tsw34 tsw34 tsw34
10     0.2      0.2      0.254      0.237      0.382 ;; 41- 45:tsw34 tsw34 tsw34 tsw34 tsw34
11     0.647      0.786      0.514      0.303      0.303 ;; 46- 50:tsw34 tsw34 tsw34 tsw34 tsw34
12     0.8      1      1.5      2      2 ;; 51- 55:tsw34 tsw34 tsw34 tsw34 tsw34
13     2.5      3      4      6      10 ;; 56- 60:tsw34 tsw34 tsw34 tsw35 tsw35
14     15      1e-30 ;; 61- 62:tsw35 wt
15   )
16   (mat
17     (atm      atm      1 nx 1 ny 1 1)
18     (tcw11      f-tcw11      1 nx 1 ny 2 2)
19     (tcw12      f-tcw12      1 nx 1 ny 3 6)
20     (tcw13      f-tcw13      1 nx 1 ny 7 7)
21     (ptn21      f-ptn21      1 nx 1 ny 8 8)
22     (ptn22      f-ptn22      1 nx 1 ny 9 9)
23     (ptn23      f-ptn23      1 nx 1 ny 10 10)
24     (ptn24      f-ptn24      1 nx 1 ny 11 11)
25     (ptn25      f-ptn25      1 nx 1 ny 12 12)
26     (ptn26      f-ptn26      1 nx 1 ny 13 13)
27     (tsw31      f-tsw31      1 nx 1 ny 14 14)
28     (tsw32      f-tsw32      1 nx 1 ny 15 16)
29     (tsw33      f-tsw33      1 nx 1 ny 17 23)
30     (tsw34      f-tsw34      1 nx 1 ny 24 58)
31     (tsw35      f-tsw35      1 nx 1 ny 59 61)
32   ) (wt      f-tsw35      1 nx 1 ny 62 62)
33 )
(CRWMS M&O 2000a, testjl.nft.msh.dkm0.f)

```

testjl.nft.msh.dkm.m:

```

1      (dz
2      1e-30      15.908      15.498      15.498      30.000 ;; 1- 5: atm tcw11 tcw12 tcw12 tcw12

```

```

3      30.000   4.805   5.918   6.211   5.068 ;; 6- 10:tcw12 tcw13 ptn21 ptn22 ptn23
4      10.254  22.939  12.041   1.992  22.354 ;; 11- 15:ptn24 ptn25 ptn26 tsw31 tsw32
5      30.000  15.308  15.308  20.000  15.000 ;; 16- 20:tsw32 tsw33 tsw33 tsw33 tsw33
6      10.000   6.000   4.000   3.000   3.000 ;; 21- 25:tsw33 tsw33 tsw33 tsw34 tsw34
7      2.400   2.000   1.000   1.000   0.500 ;; 26- 30:tsw34 tsw34 tsw34 tsw34 tsw34
8      0.300   0.200   0.200   0.200   0.200 ;; 31- 35:tsw34 tsw34 tsw34 tsw34 tsw34
9      0.200   0.200   0.200   0.200   0.274 ;; 36- 40:tsw34 tsw34 tsw34 tsw34 tsw34
10     0.200   0.200   0.254   0.237   0.382 ;; 41- 45:tsw34 tsw34 tsw34 tsw34 tsw34
11     0.647   0.786   0.514   0.303   0.303 ;; 46- 50:tsw34 tsw34 tsw34 tsw34 tsw34
12     0.800   1.000   1.500   2.000   2.000 ;; 51- 55:tsw34 tsw34 tsw34 tsw34 tsw34
13     2.500   3.000   4.000   6.000  10.000 ;; 56- 60:tsw34 tsw34 tsw34 tsw35 tsw35
14     15.000  1e-30                ;; 61- 62:tsw35      wt
15 )
16 (mat
17   (atm      atm      1 nx      1 ny      1 1)
18   (tcw11    m-tcw11   1 nx      1 ny      2 2)
19   (tcw12    m-tcw12   1 nx      1 ny      3 6)
20   (tcw13    m-tcw13   1 nx      1 ny      7 7)
21   (ptn21    m-ptn21   1 nx      1 ny      8 8)
22   (ptn22    m-ptn22   1 nx      1 ny      9 9)
23   (ptn23    m-ptn23   1 nx      1 ny     10 10)
24   (ptn24    m-ptn24   1 nx      1 ny     11 11)
25   (ptn25    m-ptn25   1 nx      1 ny     12 12)
26   (ptn26    m-ptn26   1 nx      1 ny     13 13)
27   (tsw31    m-tsw31   1 nx      1 ny     14 14)
28   (tsw32    m-tsw32   1 nx      1 ny     15 16)
29   (tsw33    m-tsw33   1 nx      1 ny     17 23)
30   (tsw34    m-tsw34   1 nx      1 ny     24 58)
31   (tsw35    m-tsw35   1 nx      1 ny     59 61)
32   (wt      m-tsw35   1 nx      1 ny     62 62)
33   ;; artificial backfill
34   (hstrk    m-tsw34   1 nx      1 ny     26 53)
35   (dr      m-dr-up    1      1 1 ny     33 33)
36   (dr      m-dr-up    1      3 1 ny     34 34)
37   (dr      m-dr-up    1      4 1 ny     35 36)
38   (dr      m-dr-up    1      5 1 ny     37 38)
39   (dr      m-dr-up    1      6 1 ny     39 40)
40   ;; bfill
41   (bf      m-bfill    1      1 1 ny     36 36)
42   (bf      m-bfill    1      2 1 ny     37 37)
43   (bf      m-bfill    1      3 1 ny     38 38)
44   (bf      m-bfill    1      4 1 ny     39 39)
45   (bf      m-bfill    1      5 1 ny     40 40)
46   (bf      m-bfill    1      6 1 ny     41 41)
47   (bf      m-bfill    1      7 1 ny     42 46)
48   (bf      m-bfill    1      6 1 ny     47 47)
49   (bf      m-bfill    1      5 1 ny     48 48)
50   ;; dripshield
51   (wp      lsnf       1      1 1 ny     44 44)      ;; Use WP instead of wp
52   (wp      lsnf       1      2 1 ny     45 45)
53   (wp      lsnf       1      3 1 ny     46 48)
54   ;; invert
55   (in      m-invert    1      4 1 ny     49 49)
56   (in      m-invert    1      2 1 ny     50 50) ;; bottom of invert
57 )
(CRWMS M&O 2000a, testjl.nft.msh.dkm.m)

```

testjl.nft.msh.dkm.f:

```

1      (dz
2      1e-30  15.908  15.498  15.498  30.000 ;; 1- 5: atm tcw11 tcw12 tcw12 tcw12
3      30.000   4.805   5.918   6.211   5.068 ;; 6- 10:tcw12 tcw13 ptn21 ptn22 ptn23
4      10.254  22.939  12.041   1.992  22.354 ;; 11- 15:ptn24 ptn25 ptn26 tsw31 tsw32
5      30.000  15.308  15.308  20.000  15.000 ;; 16- 20:tsw32 tsw33 tsw33 tsw33 tsw33
6      10.000   6.000   4.000   3.000   3.000 ;; 21- 25:tsw33 tsw33 tsw33 tsw34 tsw34
7      2.400   2.000   1.000   1.000   0.500 ;; 26- 30:tsw34 tsw34 tsw34 tsw34 tsw34
8      0.300   0.200   0.200   0.200   0.200 ;; 31- 35:tsw34 tsw34 tsw34 tsw34 tsw34
9      0.200   0.200   0.200   0.200   0.274 ;; 36- 40:tsw34 tsw34 tsw34 tsw34 tsw34
10     0.200   0.200   0.254   0.237   0.382 ;; 41- 45:tsw34 tsw34 tsw34 tsw34 tsw34
11     0.647   0.786   0.514   0.303   0.303 ;; 46- 50:tsw34 tsw34 tsw34 tsw34 tsw34

```

```

12      0.800  1.000  1.500  2.000  2.000 ;; 51- 55:tsw34 tsw34 tsw34 tsw34 tsw34
13      2.500  3.000  4.000  6.000 10.000 ;; 56- 60:tsw34 tsw34 tsw34 tsw35 tsw35
14      15.000 1e-30                ;; 61- 62:tsw35      wt
15  )
16  (mat
17    (atm      atm      1 nx 1 ny 1 1)
18    (tcw11    f-tcw11  1 nx 1 ny 2 2)
19    (tcw12    f-tcw12  1 nx 1 ny 3 6)
20    (tcw13    f-tcw13  1 nx 1 ny 7 7)
21    (ptn21    f-ptn21  1 nx 1 ny 8 8)
22    (ptn22    f-ptn22  1 nx 1 ny 9 9)
23    (ptn23    f-ptn23  1 nx 1 ny 10 10)
24    (ptn24    f-ptn24  1 nx 1 ny 11 11)
25    (ptn25    f-ptn25  1 nx 1 ny 12 12)
26    (ptn26    f-ptn26  1 nx 1 ny 13 13)
27    (tsw31    f-tsw31  1 nx 1 ny 14 14)
28    (tsw32    f-tsw32  1 nx 1 ny 15 16)
29    (tsw33    f-tsw33  1 nx 1 ny 17 23)
30    (tsw34    f-tsw34  1 nx 1 ny 24 58)
31    (tsw35    f-tsw35  1 nx 1 ny 59 61)
32    (wt      f-tsw35  1 nx 1 ny 62 62)
33    ;; artificial backfill
34    (hstrk    f-tsw34  1 nx 1 ny 26 53)
35    (dr      f-dr-up  1 1 1 ny 33 33)
36    (dr      f-dr-up  1 3 1 ny 34 34)
37    (dr      f-dr-up  1 4 1 ny 35 36)
38    (dr      f-dr-up  1 5 1 ny 37 38)
39    (dr      f-dr-up  1 6 1 ny 39 40)
40    ;; bfill
41    (bf      f-bfill  1 1 1 ny 36 36)
42    (bf      f-bfill  1 2 1 ny 37 37)
43    (bf      f-bfill  1 3 1 ny 38 38)
44    (bf      f-bfill  1 4 1 ny 39 39)
45    (bf      f-bfill  1 5 1 ny 40 40)
46    (bf      f-bfill  1 6 1 ny 41 41)
47    (bf      f-bfill  1 7 1 ny 42 46)
48    (bf      f-bfill  1 6 1 ny 47 47)
49    (bf      f-bfill  1 5 1 ny 48 48)
50    ;; dripshield
51    (wp      lsnf      1 1 1 ny 44 44) ;; Use WP instead of wp
52    (wp      lsnf      1 2 1 ny 45 45)
53    (wp      lsnf      1 3 1 ny 46 48)
54    ;; invert
55    (in      f-invert  1 4 1 ny 49 49)
56    (in      f-invert  1 2 1 ny 50 50) ;; bottom of invert
57  )
(CRWMS M&O 2000a, testjl.nft.msh.dkm.f)

```

The file testjl.nft.msh.dkm0 is identical to testjl.nft, with the following exceptions: lines 1-5 of testjl.nft are omitted, a top layer called atm is added, and a bottom layer called wt is added. The files testjl.nft.msh.dkm0.m and testjl.nft.msh.dkm0.f are the same as testjl.nft.msh.dkm0, except that the prefixes m- and f- respectively have been added to the beginning of each material name, except atm and wt (see lines 18-32 of each file).

The first 32 lines of the files testjl.nft.msh.dkm.m and testjl.nft.msh.dkm.f are the same as those in testjl.nft.msh.dkm0.m and testjl.nft.msh.dkm0.f, except that the precision is extended to three decimal places. This is the same precision that is present in the input file. The dkm files differ from the previous dkm0 files in having additional EBS material layers replace the material tsw34 between zones 33 and 50. The area above the backfill is meshed in lines 33-39. The backfill material is meshed in lines 40-49. The dripshield is meshed in lines 50-53, and the invert is meshed in lines 54-57. The resulting in-drift geometry represents the inputs from Sections 4.1.1.4 – 4.1.1.15.

This form is suitable for insertion in a NUFT input file for modeling the EBS with the dual permeability model. So define_EBS_fineGrid was confirmed as performing its task in a correct manner.

Therefore, define_EBS_fineGrid provides the correct results over the range of input parameters in the 31 input files <column>.nft (CRWMS M&O 2000a).

ATTACHMENT III QUALIFICATION OF ReadUnits

ROUTINE IDENTIFICATION

ReadUnits v1.0. This routine was compiled using C++ vSC4.2. The source code consists of the file readUnits.c and a data file called “units” containing the official list of Yucca Mountain rock layers.

The 32 input files are units and <column>.col (CRWMS M&O 2000a). The 31 output files are <column>.col.units (CRWMS M&O 2000a).

ROUTINE PURPOSE AND VALIDATION

The purpose of readUnits is to compute and print the total thickness of *all* rock layers for a chimney column. Input to the routine is the <column>.col files and a file called “units”, consisting of the complete list of Yucca Mountain rock layers by name. There is one output file for each <column>.col input file. The name of the output files are <column>.col.units. The output from this routine becomes a comment section in the nuft input files, and is used in Table 6.1.

To document that readUnits performs in the expected manner, dummy input files, “units” and “breakfast.col”, containing a wide range of values, were created by hand and fed into the routine. These files are shown below:

Units (CRWMS M&O 2000a):

```
ham
eggs
toast
choco
juice
```

breakfast.col (CRWMS M&O 2000a):

```
COLUMN INFORMATION (x,y = 100.5, 20000000.333)
b#1:1:7      ham Length: 50.000      z-distance: 29100.821
b#1:1:6      ham Length: 50.000      z-distance: 29050.821
b#1:1:5      ham Length: 50.000      z-distance: 29000.821
b#1:1:4      eggs Length: 8000.000    z-distance: 24925.821
b#1:1:3      toast Length: 1000.000   z-distance: 20425.821
b#1:1:2      toast Length: 1000.000   z-distance: 19425.821
b#1:1:1      toast Length: 1000.000   z-distance: 18425.821
b#1:1:-1     toast Length: 1000.000   z-distance: 17425.821
b#1:1:-2     choco Length: 2000.000   z-distance: 15925.821
b#1:1:-3     juice Length: 3000.000   z-distance: 13425.821
b#1:1:-4     juice Length: 4000.000   z-distance: 9925.821
b#1:1:-5     juice Length: 5000.000   z-distance: 5425.821
```

The resulting output file, breakfast.col.units (CRWMS M&O 2000a), is shown below:

```
;; breakfast.col.units
```

```

;; COLUMN INFORMATION (x,y = 100.5, 20000000.333)
;; unit thickness (m)
;;
;; ham      150.000
;; eggs     8000.000
;; toast    4000.000
;; choco    2000.000
;; juice    12000.000

;; repository elevation (m):          17925.821
;; host rock:                        toast

;; meters of host rock (toast) above repository:      3000.000
;; meters of host rock (toast) below repository:      1000.000

;; overburden thickness (m):          11199.999
;; distance from repository plane to top of chn (m):  1000.000
;; distance from repository plane to top of water table (m): 15000.000

```

Only mental calculation was required to determine that the lengths of all elements of the same material had been summed correctly by the routine to yield the material thicknesses printed in the output file. The repository location, where the z-coordinate of the element changes from 1 to -1, could be seen by visual inspection of the input file to be in material toast. The “repository elevation,” was half way between the elevations (z-distances) of the elements on either side, $(17425.821 + 18425.821) / 2 = 17925.821$. The thickness of toast above the repository, the elements with z coordinates 1, 2, and 3, was $1000 + 1000 + 1000 = 3000$ meters. The thickness of toast below the repository was just the 1000 meters. The overburden thickness, the distance from the top of the first element (b#1:1:7) to the bottom of the element with z coordinate of 1 (b#1:1:1) was $29125.821 - 17925.821 = 11200$ meters. The “top of chn,” the top of the material whose name began with “ch,” was separated from the repository plane by 1000 meters of toast. The repository was separated from the water table (the bottom of the last element) by 1000 meters of toast, 2000 meters of choco, and 12000 meters of juice, a total of 15000 meters. Since readUnits computed the values expected from this data set, it was confirmed as performing correctly.

Therefore, readUnits provides the correct results over the range of input parameters in the input files <column>.nft (CRWMS M&O 2000a).

ATTACHMENT IV QUALIFICATION OF AddLayers AND addlay

ROUTINE IDENTIFICATION

AddLayers v1.0 and addlay v1.0. This routine was compiled using C++ vSC4.2. The source code for addLayers consists of the files addLayers.c and changename.h. The source code for addlay is addlay.c. Changename.h assigns the output filenames.

The input files are l4c3.nft and l4c3.03v.nft. The output files are l4c3.nft.msh.dat and l4c3.03v.nft.msh.dat. The 31 input files for addlay are <column>.nft; the corresponding output files are <column>.nft.msh.dkm0. These files are located in CRWMS M&O 2000a

ROUTINE PURPOSE AND VALIDATION

The purpose of this routine is to modify a genmsh (mesh definition) file for a chimney from YMESH by adding two material layers to the mesh: an atmospheric “atm” layer at depth 0 and a water table “wt” layer at the bottom layer.

In order to confirm that this routine performed its simple task as expected, a very simple genmsh file was created by taking l5c3.nft and leaving only the information for the first five materials. The resulting file, called testj2.nft, is listed here:

```
(genmsh
  (down 0. 0. 1.0)
  (coord rect)
  (dx 1.000)
  (dy 1.000)
  (dz
    17.607 30.000 5.039 2.900 1.992 ;; 1- 5:tcw12 tcw12
tcw13 ptn21 ptn22
  )
  (mat
    (tcw12 tcw12 1 nx 1 ny 1 2)
    (tcw13 tcw13 1 nx 1 ny 3 3)
    (ptn21 ptn21 1 nx 1 ny 4 4)
    (ptn22 ptn22 1 nx 1 ny 5 5)
  )
)
```

After addLayers was run on it, the output, in file testj2.nft.add, was:

```
(genmsh
  (down 0. 0. 1.0)
  (coord rect)
  (dx 1.000)
  (dy 1.000)
  (dz
    1.0e-30 17.607 30.000 5.039 2.900 ;; 1 - 5: atm
tcw12 tcw12 tcw13 ptn21
    1.992 1.0e-30 ;; 6 - 7: ptn22 wt
  )
  (mat
    (atm atm 1 nx 1 ny 1 1)
    (tcw12 tcw12 1 nx 1 ny 2 3)
  )
)
```



```

(tcw13      tcw13 1      nx      1      ny      4      4)
(ptn21      ptn21 1      nx      1      ny      5      5)
(ptn22      ptn22 1      nx      1      ny      6      6)
(wt      wt      1      nx      1      ny      7      7)
)
)

```

Clearly the atm and wt layers have been added in the right places and the zones have been renumbered correctly. Nothing else was changed. So addLayers appears to be performing appropriately.

After addlay was run on testj2.nft, the output, in file testj2.nft.msh.dkm0 was:

```

(dz
1.0e-30      17.607      30.000      5.039      2.900 ;; 1 - 5: atm
tcw12 tcw12 tcw13 ptn21
1.992      1.0e-30      ;; 6 - 7: ptn22 wt
)
(mat
(atm atm 1 nx 1 ny 1 1)
(tcw12 tcw12 1 nx 1 ny 2 3)
(tcw13 tcw13 1 nx 1 ny 4 4)
(ptn21 ptn21 1 nx 1 ny 5 5)
(ptn22 ptn22 1 nx 1 ny 6 6)
(wt ptn22 1 nx 1 ny 7 7)
)

```

Addlay had removed the first five lines of the original file, intentionally. Also, it has added an atm layer and a wt layer in the expected places, except that in the “mat” section the wt is followed by the previous material, ptn22, instead of another wt.

Therefore, addlay provides the correct results over the range of input parameters in the input files l4c3.nft and l4c3.03v.nft (CRWMS M&O 2000a).

ATTACHMENT V

QUALIFICATION OF Heat_DDT AND heat_SMT

ROUTINE IDENTIFICATION

Heat_DDT v1.0 and heat_SMT v1.0. These Matlab macros run under Matlab v5.3.0.10183 (R11). The source code consists of heat_DDT.m and heat_SMT.m (CRWMS M&O 2000a).

The input and output files for heat_DDT are Dwpermeter and DDT-heat-01, respectively. The input and output files for heat_SMT are heatTSPA00.dat and SMT-heat-00 respectively (CRWMS M&O 2000a).

ROUTINE PURPOSE AND VALIDATION

The purpose of heat_DDT and heat_SMT is to write in NUFT heat generation input data extracted from data files originally received as an Excel spreadsheets. The input file for heat_DDT is DWpermeter, derived from 2-DWpermeter.txt by removing the title and column heading information at the top. The input file for heat_SMT is heatTSPA00.dat, derived from heatTSPA-SR-99184.txt by removing the title and column heading information at the top.

To demonstrate that heat_DDT was performing in the expected manner, it was necessary to show that data from the input file was being correctly transferred to the output file. This was accomplished by a combination of visual inspection and machine pattern search. First, the ancestor of DWpermeter, 2-DWpermeter.txt (CRWMS M&O 2000a), is listed below:

Time (years)	21-PWR Absorber Plates W/assy	44-BWR Absorber Plates W/assy	5-DHLW W/assy	4-DSNF W/assy	Averaged Heat Transfer W/meter	Average HT for 60% removal Efficiency W/meter
0.01	539.7	162.15	811.623125	198.25	1540.413	616.165
0.02	539.52	162.1	807.243694	197.043832	1538.978	615.591
0.03	539.35	162.04	805.118415	197.018252	1538.078	615.231
0.04	539.18	161.99	802.92873	196.992675	1537.19	614.876
0.05	539	161.94	800.803451	196.967101	1536.297	614.519
0.06	538.83	161.88	798.7427	196.941529	1535.411	614.164
0.07	538.66	161.83	796.617421	196.915959	1534.536	613.814
0.08	538.48	161.77	794.55667	196.890392	1533.632	613.453

The next step was to print the first few lines of the output file, DDT-heat-01 (CRWMS M&O 2000a).

```
(compflux
  (comp energy)
  (name hlwl)
  (range "hlwl*")
  (allocate-by-volume)
  (allocate-by-element ("hlwl*" 1.250000))
  (table
    0y 8.11623125e+02
    0.01y 8.11623125e+02
```

```

0.02y 8.07243694e+02
0.03y 8.05118415e+02
0.04y 8.02928730e+02
0.05y 8.00803451e+02
0.06y 7.98742700e+02
0.07y 7.96617421e+02
0.08y 7.9455667e+02

```

By inspection, it could be seen that the table in the output file consisted of times from column 1 and values from column 4 in the input file above. Therefore, this data was being transferred to NUFT. Using the UNIX search routine, grep, to search on the pattern “compflux” a total of eight similar tables were found. Visual inspection of these sections showed that the table in each section consisted of time values from column 1 and data values from another column of the input file, with some duplication. It appeared that the data from each column of the input file was being transferred faithfully to the tables in the output file. Therefore heat_DDT was demonstrated to correctly convey heat generation information to the NUFT input file.

To demonstrate that heat_SMT was conveying correct heat information to the NUFT input file, a similar approach was taken. The ancestor of heatTSPA00.dat, heatTSPA-SR-99184.txt (CRWMS M&O 2000a), is listed below:

Time-dependent Heat Generation Rates per Fuel Assembly (W)							Tot Repos. Watts
Time (years)	21-PWR Absorber	Plates	21-PWR Control Rods	12-PWR Long	44-BWR Absorber Plates	24-BWR Thick Absorber Plates	
		89,845	1,827	1,887	127,106	134	CSNF only
0.01		539.7	112.9	795.02	162.15	20.46	70808797.08
0.02		539.52	112.88	794.78	162.1	20.46	70785780.26
0.03		539.35	112.86	794.54	162.04	20.46	70762390.83
0.04		539.18	112.84	794.3	161.99	20.45	70740271.12
0.05		539	112.81	794.06	161.94	20.45	70717236.03

The beginning of the output file, SMT-heat-01 (CRWMS M&O 2000a), follows:

```

(compflux
  (comp energy)
  (name lsnf)
  (range "wp*")
  (allocate-by-volume)
  (allocate-by-element ("wp*" 1.0))
  (table
    0y 7.08087971e+07
    0.01y 7.08087971e+07
    0.02y 7.07857803e+07
    0.03y 7.07623908e+07
    0.04y 7.07402711e+07
    0.05y 7.07172360e+07

```

By visual inspection, the above table was seen to consist of “times” from column 1 and “total repository watts” values from column 7 of the input file.

Therefore, it was determined that data from the input file was being fully transferred to the output file, and heat_SMT was confirmed as behaving correctly over the range of input parameters in the input file heatTSPA00.dat.

ATTACHMENT VI QUALIFICATION OF Xairtab

ROUTINE IDENTIFICATION

Xairtab v1.8. This routine was compiled using C++ vSC4.2. The source code consists of the files xairtab.c, psat.c and psat.h (CRWMS M&O 2000a). Psat.h and psat.c contain the formulas used by Xairtab, and is used to check input data format and memory allocation.

ROUTINE PURPOSE AND VALIDATION

The purpose of Xairtab is to determine the air mass fraction and liquid enthalpy for points with given pressure and temperature. The input file is chimney_surface_TP and the output files are X.air (contains predicted air mass fractions) and Enthalpy.dat (contains predicted enthalpy values).

The validation of Xairtab is completed by verifying the output values with hand calculations for three of the input points.

The input to Xairtab is chimney_surface_TP, and the first few lines of that file are:

Chim	East, m	North, m	Surf Pres, Pa	Surf Tmp, C
17c4	170337.95	232049.39	0.84765539E+05	16.139
17c3	170574.34	232036.83	0.85048141E+05	16.422
17c2	170810.73	232024.27	0.85359688E+05	16.734

Xairtab calculates enthalpy and air mass fraction for each point as a function of temperature and pressure. The output from Xairtab contains 6 informational (header) lines, seven rows of air mass fraction data, another header, and 7 rows of saturated liquid enthalpy data. The data in lines 7-13 and 15-21 are in a matrix format corresponding to the rows and columns of the repository plan view grid (see Figure 5-2). As an example, data corresponding to 12c3 is the 3rd number in the second line of data (line 8 for air mass fraction and line 16 for saturated liquid enthalpy in the file jlenth). The output values for 17c2, 17c3, and 17c4 are the 2nd, 3rd, and 4th numbers (respectively) in lines 13 and 21 of jlenth.

9.85794485e-01	<u>9.86027539e-01</u>	<u>9.86244857e-01</u>	<u>9.86443222e-01</u>	0.0
				(CRWMS M&O 2000a, jlenth)
7.16445999e+01	<u>7.02654572e+01</u>	<u>6.89581833e+01</u>	<u>6.77724075e+01</u>	0.0
				(CRWMS M&O 2000a, jlenth)

The enthalpy values are interpolated in Table VI-1.

Table VI-1. Interpolated Enthalpy Values

(A) Column ID	(B) Temperature (°Celsius)	(C) Interpolated Enthalpy (J/gram)	(D) Predicted Enthalpy (J/g)
17c2	16.734	70.265	7.02654572e+01
17c3	16.422	68.9498	6.89581833e+01
17c4	16.139	67.772	6.77724075e+01

Source:

(A)-Identifier for location that corresponds to column (B) in the chimney_surface_TP (see p VI-1).

(B) Temperature at given location. Originates from chimney_surface_TP which is partially shown on p. VI-1.

(C) Enthalpy at the temperature in column (B) is found using linear interpolation from the values at 16 and 17 °C of 67.19 J/gram and 71.38 J/gram respectively (Section 4.1.6.1).

The underlined values correspond to the three numbers computed above. The xairtab enthalpy values agree with the values computed by hand to two significant figures, so the xairtab enthalpy calculation was considered to be correct.

The air mass fractions at the three points are verified using a formula for air mass fraction as a function of temperature. The results are given in table VI-2.

$$p = P_{c1} \cdot \left[\exp \cdot \left[\frac{1}{\theta} \cdot \frac{\sum_1^5 k_v (1-\theta)^v}{1 + k_6 (1-\theta) + k_7 (1-\theta)^2} - \frac{1-\theta}{k_8 (1-\theta)^2 + k_9} \right] \right] \quad (\text{Equation VI-1})$$

where:

β_K -Reduced saturation pressure. $=p/p_{c1}$. Here p/p_{c1} is substituted for β_K in Equation 1 to solve directly for saturation pressure.

$$p_{c1} = 22120000 \text{ J/m}^3.$$

p = Saturation pressure

θ -reduced (dimensionless) temperature. $= (t+273.15)/ 647.3$

t = temperature in degrees celsius.

$$K_1 = -7.691234564$$

$$K_2 = -2.608023696 \cdot 10^1$$

$$K_3 = -1.681706546 \cdot 10^2$$

$$K_4 = 6.423285504 \cdot 10^1$$

$$K_5 = -1.189464225 \cdot 10^2$$

$$K_6 = 4.167117320$$

$$K_7 = 2.097506760 \cdot 10^1$$

$$K_8 = 10^9$$

$$K_9 = 6$$

(Source: Meyer et al 1968, p. 14, 17, and 22)

Table VI-2. Saturation Pressures

(A) Column ID	(B) Temperature (°Celsius)	(C) Calculated vapor pressure (Pa)
l7c2	16.734	1905.27855
l7c3	16.422	1869.04899
l7c4	16.139	1836.18693

(A)-Identifier for location that corresponds to column (B) in the chimney_surface_TP (see p VI-1).

(B) Temperature at given location. Originates from chimney_surface_TP which is partially shown on p. VI-1.

(C) Saturation pressure found using Equation VI-1.

The total pressures at the locations in Table VI-2 are also known. Humid air is composed of dry air and water. The volume of air and water per unit volume of air is determined by the relative vapor and dry air pressure (dry air pressure is 1-vapor pressure). Given the molecular weight of water and dry air, the mass content of each per unit volume of humid air can be found. The air mass fraction is defined as the ratio of air mass to total mass, and is found in Table VI-3.

Table VI-3. Air Mass Fraction

(A) Column ID	(B) Total Pressure (Pa)	(C) Vapor Pressure (Pa)	(D) Vapor Mass (kg/m ³)	(E) Air Mass (kg/m ³)	(F) Air Mass Fraction (Calculated)	(G) Air Mass Fraction (xairtab)
l7c2	85359.688	1905.278552	0.40177061	28.3527029	0.986027544	.986027539
l7c3	85048.141	1869.048993	0.39557457	28.3626854	0.986244836	.986244857
l7c4	84765.539	1836.18693	0.38991511	28.3718034	0.986443261	.986443222

(A)-Identifier for location that corresponds to column (B) in the chimney_surface_TP (see p VI-1).

(B) Pressure at given location. Originates from chimney_surface_TP which is partially shown on p. VI-1.

(C) Vapor pressure from Table VI-2.

(D) = $18 * [(C) / (B)]$, where 18 is the molecular weight of water.

(E) = $29 * [(1-C) / (B)]$, where 29 is the average molecular weight of air (20% Oxygen, 80% Nitrogen).

(F) = $(E) / [(D) + (E)]$

(G) Output from xairtab (CRWMS M&O 2000a, X.air. See pg. VI-1).

The corresponding air mass fractions calculated in Table VI-3 compare to five significant figures, validating the air mass fraction portion of xairtab.

There are two outputs from xairtab, Enthalpy.dat and X.air. The content of these output files has been verified with hand calculations thus validating xairtab. Therefore, xairtab provides the correct results over the range of input parameters in the input file chimney_surface_TP (CRWMS M&O 2000a).

ATTACHMENT VII QUALIFICATION OF Infiltab

ROUTINE IDENTIFICATION

Infiltab v1.0. This Matlab macro runs under Matlab v5.3.0.10183 (R11). The source code is infiltab.m.

The input and output files for infiltab are infiltration.tex and <infil>.dat, respectively. The exact names of the 9 output files represented here by <infil> are listed in Table 3-5. All files are from CRWMS M&O 2000a.

ROUTINE PURPOSE AND VALIDATION

The purpose of infiltab is to split the infiltration flux data file, "infiltration.tex," into the nine component infiltration flux data files categorized by rate (upper, lower, or median) and climate (glacial, monsoon, or present day).

In order to demonstrate that infiltab was correctly extracting data for each rate-climate category from the input file, infiltration.tex, it was necessary to find the data for one category within the input file and then to compare it to the data printed into the output file for that category. The infiltration data for each category was known to be located in a designated column of the input file. In particular, the last column was known to contain data for the *upper* rate and *glacial* climate category. It was learned by inspection that the data in infiltration.tex began with that for chimney 17c5, the *last* chimney. So, for the demonstration of correctness for infiltab, the last column of infiltration.tex (written last line to first, starting with 17c5 as the first line) was compared to upper_g.dat. The two files are printed below:

infiltration.tex (with lines reversed in order):

9101	0.05	0.57	0.27	0.57	10.00	13.52	5.77	19.39	<u>26.78</u>
9102	0.21	0.88	0.55	0.88	0.94	2.13	2.00	1.01	<u>3.71</u>
9103	0.23	7.81	2.40	7.81	21.85	32.44	18.53	35.89	<u>62.48</u>
9104	0.00	3.02	0.25	3.02	11.58	19.06	10.69	20.12	<u>37.87</u>
9105	0.00	0.00	0.00	0.00	0.00	0.00	0.00	0.00	<u>0.00</u>
9201	0.00	0.41	0.13	0.41	0.25	0.73	0.97	0.10	<u>1.34</u>
9202	0.00	1.42	0.08	1.42	9.15	23.40	9.19	16.87	<u>46.73</u>
9203	0.68	12.01	4.17	12.01	40.75	63.17	36.36	69.45	<u>122.18</u>
9204	1.97	16.00	9.05	16.00	42.28	58.63	36.37	68.57	<u>108.20</u>
9205	0.00	0.00	0.00	0.00	0.00	0.00	0.00	0.00	<u>0.00</u>
9301	0.15	6.33	1.79	6.33	18.87	27.01	15.51	31.40	<u>52.22</u>
9302	0.01	0.48	0.23	0.48	0.49	1.27	1.18	0.50	<u>2.31</u>
9303	0.11	1.30	0.90	1.30	2.64	4.19	2.97	3.97	<u>7.49</u>
9304	0.00	15.88	4.94	15.88	43.99	65.03	37.94	72.10	<u>125.12</u>
9305	0.00	0.00	0.00	0.00	0.00	0.00	0.00	0.00	<u>0.00</u>
9401	0.18	4.79	3.31	4.79	12.09	18.88	10.98	19.40	<u>34.45</u>
9402	0.00	6.91	2.69	6.91	16.90	27.92	15.90	26.90	<u>53.15</u>
9403	0.05	10.14	5.52	10.14	24.09	38.66	23.59	38.05	<u>71.79</u>
9404	0.00	10.13	1.99	10.13	28.88	42.00	24.29	47.61	<u>82.01</u>
9405	0.84	5.45	3.58	5.45	14.47	20.21	12.30	23.50	<u>36.85</u>
9501	0.00	0.66	0.12	0.66	0.44	0.82	1.84	0.22	<u>1.51</u>

9502	0.81	7.40	5.08	7.40	17.71	27.10	16.54	28.03	<u>49.10</u>
9503	1.23	5.68	5.73	5.68	13.12	19.95	12.17	20.57	<u>34.15</u>
9504	0.00	14.41	3.04	14.41	40.97	60.24	34.85	67.52	<u>117.44</u>
9505	3.48	8.43	9.13	8.43	17.26	29.87	17.44	26.13	<u>50.59</u>
9601	0.08	3.88	2.28	3.88	9.43	15.08	9.00	14.99	<u>27.88</u>
9602	0.60	3.15	2.57	3.15	7.16	10.99	6.98	11.19	<u>19.39</u>
9603	0.16	4.18	3.70	4.18	10.30	16.57	9.57	16.43	<u>29.44</u>
9604	0.00	11.30	2.08	11.30	32.65	47.87	27.45	53.99	<u>93.67</u>
9605	6.42	9.41	10.79	9.41	17.75	30.73	18.59	26.12	<u>50.66</u>
9701	0.05	1.70	1.20	1.70	4.59	7.01	5.41	7.48	<u>12.83</u>
9702	0.10	5.55	2.44	5.55	13.73	22.42	12.63	21.90	<u>42.40</u>
9703	0.01	4.68	2.13	4.68	10.71	18.42	10.66	16.75	<u>34.71</u>
9704	0.00	1.49	0.39	1.49	3.25	5.21	3.61	5.01	<u>10.03</u>
9705	0.00	0.00	0.00	0.00	0.00	0.00	0.00	0.00	<u>0.00</u>

upper_g.dat:

```

2.6780000e+01 3.7100000e+00 6.2480000e+01 3.7870000e+01 0.0000000e+00
1.3400000e+00 4.6730000e+01 1.2218000e+02 1.0820000e+02 0.0000000e+00
5.2220000e+01 2.3100000e+00 7.4900000e+00 1.2512000e+02 0.0000000e+00
3.4450000e+01 5.3150000e+01 7.1790000e+01 8.2010000e+01 3.6850000e+01
1.5100000e+00 4.9100000e+01 3.4150000e+01 1.1744000e+02 5.0590000e+01
2.7880000e+01 1.9390000e+01 2.9440000e+01 9.3670000e+01 5.0660000e+01
1.2830000e+01 4.2400000e+01 3.4710000e+01 1.0030000e+01 0.0000000e+00
8.4875761e-07 1.1758367e-07 1.9802231e-06 1.2002409e-06 0.0000000e+00
4.2469574e-08 1.4810472e-06 3.8723377e-06 3.4292596e-06 0.0000000e+00
1.6550456e-06 7.3212475e-08 2.3738590e-07 3.9655172e-06 0.0000000e+00
1.0918484e-06 1.6845208e-06 2.2752916e-06 2.5992013e-06 1.1679133e-06
4.7857505e-08 1.5561613e-06 1.0823403e-06 3.7221095e-06 1.6033849e-06
8.8362069e-07 6.1454108e-07 9.3306288e-07 2.9687500e-06 1.6056034e-06
4.0663032e-07 1.3438134e-06 1.1000887e-06 3.1788793e-07 0.0000000e+00

```

By inspection it was noted that the first seven rows of upper_g.dat corresponded to the contents of the last (underscored) column of infiltration.tex, so it was confirmed that infiltrab was extracting the upper-glacial data to the upper-glacial output file all 35 chimneys for which data was provided. The rows after row 7 of the upper_g.dat were supposed to contain the same information converted to units required by NUFT. Hand calculation of a few values confirmed that they were equal to the earlier values divided by 3.1552e7, the ratio between millimeters/year and kilograms/second.

Therefore, infiltrab provides the correct results over the range of input parameters in the input file infiltration.tex. (CRWMS M&O 2000a).

ATTACHMENT VIII QUALIFICATION OF Rock_sun

ROUTINE IDENTIFICATION

Rock_sun v1.0. This Matlab macro runs under Matlab v5.3.0.10183 (R11). The source is rock_sun.m.

The input files for the routine are 1d-driftscale_<case>_flow.prn and 1d-driftscale_<case>_th.prn (case is basecase2, lowinf, and upperinf). The source DTN's for these files are given in Figure 3-7. The output files are dkm-afc-1Dds-mc-<infil>-00, where <infil> is li, mi, and ui. The output files are in CRWMS M&O 2000a.

ROUTINE PURPOSE AND VALIDATION

The purpose of rock_sun is to extract material property data from a pair of tables and rewrite it in NUFT material property input format. The input file pairs consist of a flow data and a thermal data file.

In order to demonstrate that rock_sun is correctly conveying material property information from the input files to the output file, it was necessary to extract information for just one sample material from one pair of input files to the corresponding output file. The file pair 1d_driftscale_lowinf_flow.prn and 1d_driftscale_lowinf_th.prn was chosen for input and the material ptn22 was chosen as the material to follow. Then, using the Unix pattern search routine, grep, lines containing data for material ptn22 were extracted from the input files and are printed below:

1d_driftscale_lowinf_flow.prn:

```
ptn22 3.27E-12 0.439 1.51E-5 0.390 0.16 1.00 1.00E-11 1.2E-2 9.39E-4 0.651
0.01 1.00 0.01 0.46 1.41
```

1d_driftscale_lowinf_th.prn:

```
ptn22 2340 1080 0.35 0.50 0.7
```

The following lines related to material ptn22 were extracted from the output files by hand:

```
(m-ptn22
  (cont-len-fac 3.623e-01) (cont-area-fac 1.410e+00)
  (exfac-adv (liquid 1.000e+00) (gas 1.000e+00))
  (solid-density 2.312e+03) (porosity 4.390e-01)
  (Kd (water 0.0) (air 0.0))
  (KdFactor (water 0.0) (air 0.0))
  (Cp 1.080e+03)
  (tcond tcondLin (solid 3.458e-01) (liquid 4.940e-01) (gas 3.458e-01))
  (K0 3.270e-12) (K1 3.270e-12) (K2 3.270e-12)
  (tort (gas 7.000e-01) (liquid 0.000e+00))
  (kr (liquid krlVanGen (Sr 1.600e-01) (m 3.900e-01) (Smax 1.0))
    (gas krgModCorey (Srl 1.600e-01) (m 3.900e-01) (Slmax 1.0)))
```

```

    (pc (liquid pcVanGen (Sr 1.600e-01) (m 3.900e-01) (alpha 1.510e-05) (Smax
1.0)))
    (krMC (liquid krMCintrinsic) (gas krMCintrinsic))
) ;;End of the material

(f-ptn22
  (cont-len-fac 1.304e-02) (cont-area-fac 1.000e+00)
  (exfac-adv (liquid 1.000e+00) (gas 1.000e+00))
  (solid-density 2.808e+01) (porosity 1.200e-02)
  (Kd (water 0.0) (air 0.0))
  (KdFactor (water 0.0) (air 0.0))
  (Cp 1.080e+03)
  (tcond tcondLin (solid 4.200e-03) (liquid 6.000e-03) (gas 4.200e-03))
  (K0 1.000e-11) (K1 1.000e-11) (K2 1.000e-11)
  (tort (gas 7.000e-01) (liquid 0.000e+00))
  (kr (liquid krlVanGen (Sr 1.000e-02) (m 6.510e-01) (Smax 1.0) (gamma
1.000e-02))
    (gas krgModCorey (Srl 1.000e-02) (m 6.510e-01) (Slmax 1.0)))
  (pc (liquid pcVanGen (Sr 1.000e-02) (m 6.510e-01) (alpha 9.390e-04) (Smax
1.0) (gamma 1.000e-02)))
  (krMC (liquid krMCactiveFrac (gamma 1.000e-02) (Sr 1.000e-02))
    (gas krMCactiveFrac (gamma 1.000e-02) (Sr 0.0)))
) ;;End of the material

```

By visual inspection it can be seen that the quantities Cp (heat capacity), gas tortuosity, matrix and fracture porosity, matrix and fracture permeability, and the three matrix and fracture van Genuchten coefficients for material ptn22 were transferred without change into the output files. The fracture values for thermal conductivity was multiplied by the fracture porosity, .012 (Table 4-3). The matrix values for this parameter were multiplied by 1-.012. So matrix and fracture values for thermal conductivity *add up* to the values shown in the input files. The same is true for the solid densities, which come from the rock grain data (Table 4-4). (There is only one rock of which matrix and fracture are considered fractional parts.) The active fracture terms were transferred without change to fracture gammas.

Visual inspection confirmed that the data from the input file for material ptn22 had found its way into the correct places in the output file. Rock_sun correctly transferred information from the input files to the output file.

Therefore, rock_sun provides the correct results over the range of input parameters in the input file l4c3.nft and l4c3.03v.nft (CRWMS M&O 2000a).

ATTACHMENT IX QUALIFICATION OF SMT_surf_bc AND SMT_bot_bc

ROUTINE IDENTIFICATION

SMT_surf_bc v1.1 and SMT_bot_bc v1.1. This routine was compiled using f77 vSC4.2. The source code files are, respectively, SMT_surf_bc.f and SMT_bot_bc.f.

The input files for SMT_surf_bc are surf_TP.out and tspa00-mesh00. The output file is SMT_surf_bc.out. The input files for SMT_bot_bc are tspa00-mesh00, T_bottom.dat, and column.data. The output file for this routine is SMT_bsmtbc.out.

These files are all located in CRWMS M&O 2000a.

ROUTINE PURPOSE AND VALIDATION

The purpose of SMT_surf_bc is to determine surface temperature boundary conditions for an entire SMTmesh using a scheme of weighting temperatures by inverse distance squared (Section 5.1.3). It takes as input the files surf_TP.out and tspa00-mesh00. The purpose of SMT_bot_bc is to determine bottom temperature boundary conditions for an entire SMT mesh also using a scheme of weighting temperatures by inverse distance squared. It takes as input the files column.data, T_bottom.dat and tspa00-mesh00.

In order to demonstrate that SMT_surf_bc performed its task correctly, it was necessary to compute a few boundary temperatures manually and compare them with those obtained by SMT_surf_bc. To do this, shortened versions of the two input files were created. The first 5 lines of surf_TP.out were extracted into a file called "topsurftp," and a five line file in the format of tspa00-mesh00, called "hatmo," was created manually. These short files are shown below:

topsurftp:

TPa 1	0.8283920E+05	14.2700	169398.594	236623.641
TPa 2	0.8725702E+05	18.6200	172705.438	230904.031
TPa 3	0.8555627E+05	17.0000	168909.656	233244.625
TPa 4	0.8530762E+05	16.8900	171465.906	237975.359
TPa 5	0.8597495E+05	17.5300	172320.453	237217.734

hatmo:

% atm@r#1:1:1	atm	0.000	165000.000	230000.000	0.000
% atm@r#1:1:2	atm	0.000	168000.000	231000.000	0.000
% atm@r#1:1:3	atm	0.000	169000.000	232000.000	0.000
% atm@r#1:1:4	atm	0.000	170000.000	233000.000	0.000
% atm@r#1:1:5	atm	0.000	175000.000	236000.000	0.000
\$end					

The inverse distance squared equation (presented below, Equation IX-1) is applied once for each of the five reference locations in the file hatmo above:

Equation IX-1:

$$V = \frac{\sum_{i=1}^n \left[\frac{V_i}{\left[\sqrt{(X_i - X_0)^2 + (Y_i - Y_0)^2} \right]^2} \right]}{\sum_{i=1}^n \left[\frac{1}{\left[\sqrt{(X_i - X_0)^2 + (Y_i - Y_0)^2} \right]^2} \right]}$$

where:

V	-Temperature at reference location
V ₁	Temperature from 1 st line in topsurftp (p. IX-1). = 14.27 °C
V ₂	Temperature from 2 nd line in topsurftp (p. IX-1). = 18.62 °C
V ₃	Temperature from 3 rd line in topsurftp (p. IX-1). = 17 °C
V ₄	Temperature from 4 th line in topsurftp (p. IX-1). = 16.89 °C
V ₅	Temperature from 5 th line in topsurftp (p. IX-1). = 17.53 °C
X ₁	Easting from 1 st line in topsurftp (p. IX-1). = 236623.641
X ₂	Easting from 2 nd line in topsurftp (p. IX-1). = 230904.031
X ₃	Easting from 3 rd line in topsurftp (p. IX-1). = 233244.625
X ₄	Easting from 4 th line in topsurftp (p. IX-1). = 237975.359
X ₅	Easting from 5 th line in topsurftp (p. IX-1). = 237217.734
Y ₁	Northing from 1 st line in topsurftp (p. IX-1). = 169398.594
Y ₂	Northing from 2 nd line in topsurftp (p. IX-1). = 172705.438
Y ₃	Northing from 3 rd line in topsurftp (p. IX-1). = 168909.656
Y ₄	Northing from 4 th line in topsurftp (p. IX-1). = 171465.906
Y ₅	Northing from 5 th line in topsurftp (p. IX-1). = 172320.453
n	=5

(Source: Isaaks and Srivastava 1989, p. 258)

The equation is applied five times resulting in:

For X₀=16500, and X₀=230000, V=16.86355269
For X₀=16800, and X₀=231000, V=16.99739973
For X₀=16900, and X₀=232000, V=16.99126247
For X₀=17000, and X₀=233000, V=16.95652811
For X₀=17500, and X₀=236000, V=17.07773881

Next, a version of SMT_surf_bc, called SMT_surf_jl, was created which would read only the first five lines of surf_TP.out and the file hatmo, instead of tspa00-mesh00. The output from SMT_surf_jl is compared to the interpolated temperatures in Table IX-1.

Table IX-1. Comparison of Interpolated Temperature with Results

Interpolated Temperature	Temperature from SMT_surf_jl.out
16.86355269	16.864
16.99739973	16.997
16.99126247	16.991
16.95652811	16.957
17.07773881	17.078

Because the SMT_surf_jl temperature values agreed with the manually interpolated results to five significant figures, the accuracy of SMT_surf_bc is demonstrated. It is concluded that SMT_surf_bc is validated.

SMT_bot_bc is validated in a similar manner. A modified version of SMT_bot_bc, called SMT_bot_jl, was created and run on reduced sets of input data and the compared with manually calculated results. To create the reduced input sets, the *last* five lines of column.data in *reversed order* and the first five lines of T_bottom.dat were extracted into files “botcd” and “toptbot” respectively, and a mesh00-tspa00 type file, “bsmnt,” was created manually. (In file bsmnt are lines with material atm and bsmnt. Only the bsmnt lines are processed, but the atm lines between them are required by SMT_bot_bc.) These three input files are shown below:

botcd:

171234.27	235534.78	11c1
170997.88	235547.34	11c2
170761.50	235559.90	11c3
170525.11	235572.45	11c4
171203.08	234947.60	12c1

toptbot:

```
4.6579969e+01
4.7254456e+01
4.6677340e+01
4.7112262e+01
4.9763102e+01
```

bsmnt:

% atm@r#1:1:1	atm	0.000	165000.000	230000.000	0.000
% bsm@r#1:1:1	bsmnt	0.000	165000.000	230000.000	0.000
% atm@r#1:1:1	atm	0.000	165000.000	230000.000	0.000
% bsm@r#1:1:2	bsmnt	0.000	168000.000	231000.000	0.000
% atm@r#1:1:1	atm	0.000	168000.000	231000.000	0.000
% bsm@r#1:1:3	bsmnt	0.000	169000.000	232000.000	0.000
% atm@r#1:1:1	atm	0.000	169000.000	232000.000	0.000
% bsm@r#1:1:4	bsmnt	0.000	170000.000	233000.000	0.000
% atm@r#1:1:1	atm	0.000	170000.000	233000.000	0.000
% bsm@r#1:1:5	bsmnt	0.000	175000.000	236000.000	0.000
% atm@r#1:1:1	atm	0.000	175000.000	236000.000	0.000

\$end

The inverse distance squared equations (Equation IX-1) is again applied for each of the reference locations in the file bsmnt above:

Equation IX-1:

$$V = \frac{\sum_{i=1}^n \left[\frac{V_i}{\left[\sqrt{(X_i - X_0)^2 + (Y_i - Y_0)^2} \right]^2} \right]}{\sum_{i=1}^n \left[\frac{1}{\left[\sqrt{(X_i - X_0)^2 + (Y_i - Y_0)^2} \right]^2} \right]}$$

where:

V	-Temperature at reference location
V ₁	Temperature from 1 st line in toptbot (p. IX-3). = 4.6579969e+01 °C
V ₂	Temperature from 2 nd line in toptbot (p. IX-3). = 4.7254456e+01 °C
V ₃	Temperature from 3 rd line in toptbot (p. IX-3). = 4.6677340e+01 °C
V ₄	Temperature from 4 th line in toptbot (p. IX-3). = 4.7112262e+01 °C
V ₅	Temperature from 5 th line in toptbot (p. IX-3). = 4.9763102e+01 °C
X ₁	Easting from 1 st line in botcd (p. IX-3). = 235534.78
X ₂	Easting from 2 nd line in botcd (p. IX-3). = 235547.34
X ₃	Easting from 3 rd line in botcd (p. IX-3). = 235559.90
X ₄	Easting from 4 th line in botcd (p. IX-3). = 235572.45
X ₅	Easting from 5 th line in botcd (p. IX-3). = 234947.60
Y ₁	Northing from 1 st line in botcd (p. IX-3). = 171234.27
Y ₂	Northing from 2 nd line in botcd (p. IX-3). = 170997.88
Y ₃	Northing from 3 rd line in botcd (p. IX-3). = 170761.50
Y ₄	Northing from 4 th line in botcd (p. IX-3). = 170525.11
Y ₅	Northing from 5 th line in botcd (p. IX-3). = 171203.08
n	=5

The equation is applied five times resulting in:

For X ₀ =16500, and X ₀ =230000, V=47.49872
For X ₀ =16800, and X ₀ =231000, V=47.53671
For X ₀ =16900, and X ₀ =232000, V=47.56805
For X ₀ =17000, and X ₀ =233000, V=47.65188
For X ₀ =17500, and X ₀ =236000, V=47.50749

Next, a version of SMT_bot_bc, called SMT_bot_jl, was created which would read only the first five lines of T_bottom.dat and the file bsmnt, instead of tspa00-mesh00. The output from SMT_bot_jl is compared to the interpolated temperatures in Table IX-2.

Table IX-2. Comparison of Interpolated Temperature with Results.

Interpolated Temperature	Temperature from SMT_bot_jl.out
47.49872	47.499
47.53671	47.537
47.56805	47.568
47.65188	47.652
47.50749	47.507

It can be seen by visual inspection that the SMT_bot_jl values agreed with the interpolated values to five significant digits, demonstrating the accuracy of SMT_bot_jl. Therefore SMT_bot_bc is considered validated.

ATTACHMENT X QUALIFICATION OF Bound

ROUTINE IDENTIFICATION

Bound v1.0. This Matlab macro runs under Matlab v5.3.0.10183 (R11). The source is bound.m.

The input files for this routine are temperature_W, temperature_S, <column>.nft.msh.dkm0, <column>.col.units, and tcond_wet.dat and the output file is T_bottom.dat. These files can be found in CRWMS M&O 2000a.

ROUTINE PURPOSE AND VALIDATION

The purpose of bound is to compute the temperature at 1000 meters below the water table.

This routine calculates the temperature 1000m below the water table by making 2 key assumptions (5.3.1 and 5.3.2). The first is that there is no heat loss in the horizontal direction. The second is that the heat flux from the surface to the water table is constant. Given conservation of energy, a fixed heat flux, temperature at the water table, temperature at the ground surface, and thermal conductivity of the materials between the ground surface and the water table, the heat flux from the surface to the water table is found. By assuming this heat flux continues downward 1000m, and given thermal conductivity values of the water table, the temperature 1000m below the water table is found. This temperature becomes a fixed boundary condition.

Bound is validated through a test case. The test case is a five layer stratigraphic column represented in 4 files.

1. llc1.col.dat- contains material thicknesses.
2. tcond_alpha.dat- contains material thermal conductivities
3. tempS- contains the surface temperature, and
4. tempW- contains the water table temperature

llc1.col.dat:

alpha	5.000
beta	10.000
gamma	20.000
delta	40.000
eps	30.000
zeta	20.000

(CRWMS M&O 2000A)

tcond_alpha.dat:

alpha	.5
beta	.75
gamma	1.00
delta	1.50
eps	2.00
zeta	2.50

(CRWMS M&O 2000A)

tempS:

1.5000000e+01

(CRWMS M&O 2000A)

tempW:

The test case is run using a modified source code called bound2 which outputs the testcase results in the file T_bottom2.dat. These results are then compared to the results from the manually calculated value found using Equation XX-5 (from Attachment XX):

$$T_b = T_w + \frac{B \cdot (T_w - T_s)}{\lambda_w} \cdot \sum_{i=1}^n \frac{Z_i}{\lambda_i}$$

where:

- T_b -Temperature at distance B below the top of the water table.
- T_w -Temperature at top of the water table, = 32.5 °C (CRWMS M&O 2000a, tempW)
- T_s -Temperature at the ground surface, = 15 °C (CRWMS M&O 2000a, tempS)
- B -Distance the water table is extended downward, =1000m (Section 6.2).
- λ₁ -Thermal conductivity of alpha, = 0.5 (CRWMS M&O 2000a, tcond_alpha.dat).
- λ₂ -Thermal conductivity of beta, = 0.75 (CRWMS M&O 2000a, tcond_alpha.dat).
- λ₃ -Thermal conductivity of gamma, = 1.0 (CRWMS M&O 2000a, tcond_alpha.dat).
- λ₄ -Thermal conductivity of delta, = 1.5 (CRWMS M&O 2000a, tcond_alpha.dat).
- λ₅ -Thermal conductivity of eps, = 2.0 (CRWMS M&O 2000a, tcond_alpha.dat).
- λ₆ -Thermal conductivity of zeta, = 2.5 (CRWMS M&O 2000a, tcond_alpha.dat).
- λ_w -Thermal conductivity of the water table, = 2.5 (CRWMS M&O 2000a, tcond_alpha.dat).
- Z₁ -Thickness of the alpha, = 5 (CRWMS M&O 2000a, 11c1.col.dat).
- Z₂ -Thickness of the beta, = 10 (CRWMS M&O 2000a, 11c1.col.dat).
- Z₃ -Thickness of the gamma, = 20 (CRWMS M&O 2000a, 11c1.col.dat).
- Z₄ -Thickness of the delta, = 40 (CRWMS M&O 2000a, 11c1.col.dat).
- Z₅ -Thickness of the eps, = 30 (CRWMS M&O 2000a, 11c1.col.dat).
- Z₆ -Thickness of the zeta, = 20 (CRWMS M&O 2000a, 11c1.col.dat).
- n =6

The equation is applied resulting in:

$$T_b = 157.94803 \text{ }^{\circ}\text{C}$$

The corresponding output file from bound2, a modified version of bound which computes the temperature for only one chimney, 11c1, was the following:

1.5794803e+02

The result from bound2 agrees with the result from Equation XX-5, calculated above.

Therefore, bound provides the correct results over the range of input parameters in the input files temperature_W, temperature_S, <column>.nft.msh.dkm0, <column>.col.units, and tcond_wet.dat (CRWMS M&O 2000a).

ATTACHMENT XI

QUALIFICATION OF COREY ROUTINES

ROUTINE IDENTIFICATION

LDTH-i-li-corey, LDTH-i-mi-corey, LDTH-i-ui-corey, LDTH-01-li-corey, LDTH-01-mi-corey, LDTH-01-ui-corey, LDTH-01v-li-corey, LDTH-01v-mi-corey, LDTH-01v-ui-corey, SDT-01i, SDT-01, SDT-01v. All of these routines are v1.0. These scripts were developed using the c-shell version SunOS 5.6.

The input and output file names for these scripts are outlined in Table 3-5.

ROUTINE PURPOSE AND VALIDATION

The purpose of these scripts is to build NUFT input files from component files. For the specific input and output files associated with each script see Table 3-5.

To demonstrate that these scripts behave in the expected manner, the script LDTH-01-mi-corey was executed and one of the resulting output files, l6c3-LDTH50--01.in, was inspected visually to determine if the correct values for infiltration flux had been inserted. Since LDTH-01-mi-corey is supposed to select median level fluxes (as opposed to lower or upper, as indicated by the -mi- in the name) the median infiltration flux files for current, monsoon, and glacial climates were printed out. These are shown below:

Median_p.dat:

5.7000000e-01	8.8000000e-01	7.8100000e+00	3.0200000e+00	0.0000000e+00
4.1000000e-01	1.4200000e+00	1.2010000e+01	1.6000000e+01	0.0000000e+00
6.3300000e+00	4.8000000e-01	1.3000000e+00	1.5880000e+01	0.0000000e+00
4.7900000e+00	6.9100000e+00	1.0140000e+01	1.0130000e+01	5.4500000e+00
6.6000000e-01	7.4000000e+00	5.6800000e+00	1.4410000e+01	8.4300000e+00
3.8800000e+00	3.1500000e+00	4.1800000e+00	1.1300000e+01	9.4100000e+00
1.7000000e+00	5.5500000e+00	4.6800000e+00	1.4900000e+00	0.0000000e+00
1.8065416e-08	2.7890467e-08	2.4752789e-07	9.5715010e-08	0.0000000e+00
1.2994422e-08	4.5005071e-08	3.8064148e-07	5.0709939e-07	0.0000000e+00
2.0062120e-07	1.5212982e-08	4.1201826e-08	5.0329615e-07	0.0000000e+00
1.5181288e-07	2.1900355e-07	3.2137424e-07	3.2105730e-07	1.7273073e-07
2.0917850e-08	2.3453347e-07	1.8002028e-07	4.5670639e-07	2.6717799e-07
1.2297160e-07	9.9835193e-08	<u>1.3247972e-07</u>	3.5813895e-07	2.9823783e-07
5.3879310e-08	1.7590010e-07	1.4832657e-07	4.7223631e-08	0.0000000e+00

Median_m.dat:

1.0000000e+01	9.4000000e-01	2.1850000e+01	1.1580000e+01	0.0000000e+00
2.5000000e-01	9.1500000e+00	4.0750000e+01	4.2280000e+01	0.0000000e+00
1.8870000e+01	4.9000000e-01	2.6400000e+00	4.3990000e+01	0.0000000e+00
1.2090000e+01	1.6900000e+01	2.4090000e+01	2.8880000e+01	1.4470000e+01
4.4000000e-01	1.7710000e+01	1.3120000e+01	4.0970000e+01	1.7260000e+01
9.4300000e+00	7.1600000e+00	1.0300000e+01	3.2650000e+01	1.7750000e+01
4.5900000e+00	1.3730000e+01	1.0710000e+01	3.2500000e+00	0.0000000e+00
3.1693712e-07	2.9792089e-08	6.9250761e-07	3.6701318e-07	0.0000000e+00
7.9234280e-09	2.8999746e-07	1.2915188e-06	1.3400101e-06	0.0000000e+00
5.9806034e-07	1.5529919e-08	8.3671400e-08	1.3942064e-06	0.0000000e+00
3.8317698e-07	5.3562373e-07	7.6350152e-07	9.1531440e-07	4.5860801e-07
1.3945233e-08	5.6129564e-07	4.1582150e-07	1.2984914e-06	5.4703347e-07

2.9887170e-07	2.2692698e-07	<u>3.2644523e-07</u>	1.0347997e-06	5.6256339e-07
1.4547414e-07	4.3515467e-07	<u>3.3943966e-07</u>	1.0300456e-07	0.0000000e+00

Median_g.dat:

1.3520000e+01	2.1300000e+00	3.2440000e+01	1.9060000e+01	0.0000000e+00
7.3000000e-01	2.3400000e+01	6.3170000e+01	5.8630000e+01	0.0000000e+00
2.7010000e+01	1.2700000e+00	4.1900000e+00	6.5030000e+01	0.0000000e+00
1.8880000e+01	2.7920000e+01	3.8660000e+01	4.2000000e+01	2.0210000e+01
8.2000000e-01	2.7100000e+01	1.9950000e+01	6.0240000e+01	2.9870000e+01
1.5080000e+01	1.0990000e+01	1.6570000e+01	4.7870000e+01	3.0730000e+01
7.0100000e+00	2.2420000e+01	1.8420000e+01	5.2100000e+00	0.0000000e+00
4.2849899e-07	6.7507606e-08	1.0281440e-06	6.0408215e-07	0.0000000e+00
2.3136410e-08	7.4163286e-07	2.0020918e-06	1.8582023e-06	0.0000000e+00
8.5604716e-07	4.0251014e-08	1.3279665e-07	2.0610421e-06	0.0000000e+00
5.9837728e-07	8.8488844e-07	1.2252789e-06	1.3311359e-06	6.4052992e-07
2.5988844e-08	8.5889959e-07	6.3228955e-07	1.9092292e-06	9.4669118e-07
4.7794118e-07	3.4831389e-07	<u>5.2516481e-07</u>	1.5171780e-06	9.7394777e-07
2.2217292e-07	7.1057302e-07	<u>5.8379817e-07</u>	1.6512424e-07	0.0000000e+00

Each infiltration table above has two sets of 7 rows of 5 values each. The 7 rows correspond to the 7 values of l and the 5 items correspond to the 5 values of c. The first set of rows is unscaled data. The second set is scaled to NUFT units. In each table above, the NUFT-scaled infiltration value for the column l6c3 is underlined. Next, the lines of NUFT input related to infiltration flux were printed out as shown below:

l6c3-LDTH50--01.in (CRWMS M&O 2000a)

```
;; Implicit DKM with active fracture concept (AFC)
;; NBS material properties from 1D drift-scale mean infiltration flux
property set assembled by Ken Lee
;; AML = 50 MTU/acre; half drift spacing = 48.6 m
;; l6c3.col.units
...
(srctab
  (compflux
    (comp water)
    (name infil)
    (range "*.f*:::2")
    (mult-by-area z)
    (allocate-by-element ("*"1.0))
    (table 0.0 1.3247972e-07 600.00y 1.3247972e-07 ;; 4.1800000e+00
mm/yr
      600.001y 3.2644523e-07 2000.00y 3.2644523e-07 ;; 1.0300000e+01
mm/yr
      2000.001y 5.2516481e-07 1.0e30 5.2516481e-07) ;; 1.6570000e+01
mm/yr
    (enthalpy 0.0 6.94E+04 1E+30 6.94E+04 )
  )

  (include "/auto/ymp/data26/TSPA00/heatgen/LDTH-SDT-0.3Qheat-50y_vent-00")
) ;; end srctab
```

It was noted that the values on the first line of the “table” matched the underscored value from Median_p.dat, the values on the second line matched the underscored value from Median_m.dat,

and the values on the third line matched the underscored value from Median_g.dat. Therefore it was concluded that infiltration fluxes were being correctly gathered and inserted in the NUFT input file by the script, and that the script was behaving in the expected manner. The remaining scripts contain the same operation and logic commands but differ in the input and output filenames designated in each script (see Table 3-5). All NUFT input files created using the routines identified in the Attachment have been checked with visual inspection based on the same process described above. All assembly scripts listed in this attachment are considered validated.

ATTACHMENT XII QUALIFICATION OF HeatgenAge

ROUTINE IDENTIFICATION

HeatgenAge v1.2 This routine was compiled using C++ vSC4.2. The source consists of two functions: heatgenAge.c and myFunctions.h. Myfunctions.h is used to check input data format and memory allocation.

The input files for this routine are DDT-heat-01, line-load-heat, and SMT-heat-00. The corresponding output files are given in Table 3-5. All files are located in CRWMS M&O 2000a.

ROUTINE PURPOSE AND VALIDATION

The purpose of heatgenAge is to modify NUFT heat generation input data in two ways: to age the fuel by a given number of years and to ventilate the system for a number of years. The input to heatgenAge is any file in NUFT heat generation table input format.

In order to document that heatgenAge performs in the expected manner, a simple heat generation file, called "simple," was created by hand. Next, heatgenAge was executed on the file 'simple' to do four years of aging, resulting in output file "simple_age." Finally, heatgenAge was executed on simple again but to do six years of ventilation with 80% heat retention, resulting in output file "simple_vent." The input file and output files are shown below:

simple:

```
(table
  0.y 1000.
  2.y 500.
  4.y 200.
  6.y 100.
  8.y 50.
  10.y 25.
  12.y 12.
  14.y 6.
)
```

simple_age:

```
;;heatgen file based on simple
;;fuel aged 4 years
(table
  0.000y 200.000
  2.000y 100.000
  4.000y 50.000
  6.000y 25.000
  8.000y 12.000
  10.000y 6.000
  14.000y 6.000
)
```

simple_vent:

```

;;heatgen file based on simple
;;fuel aged -vent years
;;drifts ventilated for 6 years
;;ventilation results in a fraction of .80 available for heating
(table
  0.000y 800.000
  2.000y 400.000
  4.000y 160.000
  6.000y 80.000
  6.001y 99.975
  8.000y 50.000
  10.000y 25.000
  12.000y 12.000
  14.000y 6.000
)

```

By inspection of the files `simple` and `simple_age`, it was seen that the data had aged, that is, year four had been made zero, all previous time data had been dropped, and all later times had been reduced by four years. Additionally, a final entry with time four years beyond the last and heat value the same as the last was appended to the end of the table. An entry just after the end of the ventilation is added to capture the temperature spike (at time 6.001y). Therefore, `heatgenAge` was confirmed as aging the fuel properly.

By inspection of the files, `simple` and `simple_vent`, it was seen that the system had been ventilated for the first six years so that the heat values were only 80% of the original. After the six years, no ventilation was done, and the heat values were unchanged from file `simple`. Therefore, `heatgenAge` was confirmed as ventilating the system correctly.

In summary `heatgenAge` was demonstrated to perform in the expected manner with regard to fuel aging and ventilation. Therefore, `heatgenAge` provides the correct results over the range of input parameters in the input files `DDT-heat-01`, `line-load-heat`, and `SMT-heat-00`, (CRWMS M&O 2000a).

ATTACHMENT XIII QUALIFICATION OF Chim_Surf_TP AND Chim_wt_TP

ROUTINE IDENTIFICATION

Chim_Surf_TP v1.0 and Chim_wt_TP v1.0. This routine was compiled using f77 v SC4.2. The source codes are chim_surf_TP.f and chim_wt_TP.f (CRWMS M&O 2000a).

The input files for these routines are tspa99_primary_mesh and bcs_99.dat (source DTN's are given in Figure 3-5), and column.data (CRWMS M&O 2000a). The output file from Chim_Surf_TP is outpt. The output file from Chim_wt_TP is outpt_wt (output files are located in CRWMS M&O 2000a).

ROUTINE PURPOSE AND VALIDATION

The purpose of this routine is to calculate the temperature and pressure at a given location using the inverse distance cubed method. The specific input files used for this calculation are: tspa99_primary_mesh, bcs_99.dat, and column.data (CRWMS M&O 2000a).

Documentation of the accuracy of this routine is in the form of a test case. The test case is the interpolation of temperature at an arbitrary location (170000N, 230000E) given five temperatures at various locations. Due to the reduction in file size and format minor changes were made to chim_surf_TP in order to execute the test case. The modified source code (CRWMS M&O 2000a, chim_surf_bc_tst.f) is used to execute the test case for chim_surf_TP and chim_wt_TP. The input file for the test case is chim_test and the output file is chim_out. The corresponding hand calculation for benchmarking the test case follows.

Substituting the distance between points equation into the inverse distance cubed equation (Section 5.1.3) yields:

$$T = \frac{\sum_{i=1}^n \frac{T_i}{\left((X - X_i)^2 + (Y - Y_i)^2\right)^{\frac{3}{2}}}}{\sum_{i=1}^n \frac{1}{\left((X - X_i)^2 + (Y - Y_i)^2\right)^{\frac{3}{2}}}}$$

Eq. XIII-1

where:

T	-Interpolated temperature
X	-Reference Easting, =170000.
Y	-Reference Northing, =230000
T ₁	-Temperature at point 1, =14.27
T ₂	-Temperature at point 2, =18.62
T ₃	-Temperature at point 3, =17.00
T ₄	-Temperature at point 4, =16.89
T ₅	-Temperature at point 5, =17.53
X ₁	-Easting at point 1, 236623.643

X_2 -Easting at point 2, = 230904.031
 X_3 -Easting at point 3, = 233244.625
 X_4 -Easting at point 4, = 237975.359
 X_5 -Easting at point 5, = 237217.733
 Y_1 -Northing at point 1, = 169398.601
 Y_2 -Northing at point 2, = 172705.438
 Y_3 -Northing at point 3, = 168909.656
 Y_4 -Northing at point 4, = 171465.906
 Y_5 -Northing at point 5, = 172320.452
 n -Number of points in data set, =5

Note: Northings and Eastings were randomly selected from tspa99_primary_mesh (CRWMS M&O 2000a).

The reference Northings and Eastings were arbitrarily selected, but would normally be contained in column.data.

Temperatures were randomly selected from bcs_99.dat (CRWMS M&O 2000a).

Source: Isaaks and Srivasta 1989, p258

The hand calculation results based on Equation XIII-1 indicate that $T = 17.8140$ for the test case.

The test case was run using the routine and the predicted temperature is 17.8140°C (CRWMS M&O 2000a-chim_out) as identical to the hand calculations result.

The same interpolation is done for temperature and pressure in both routines, and therefore it is reasonable to consider the pressure to be validated as well. The routines, Chim_Surf_TP v1.0 and Chim_wt_TP v1.0, are essentially identical but read in different segments of data in bcs_99.dat for surface and water table respectively. This test case therefore documents the accuracy of both Chim-Surft TP v1.0 and Chim_wt_TP v1.0 for predicting temperature and pressure at given points over the range of input parameter in the input files used (tspa99_primary_mesh, bcs_99.dat, and column.data).

ATTACHMENT XIV QUALIFICATION OF ColumnInfiltration

ROUTINE IDENTIFICATION

ColumnInfiltration v1.1. This routine was compiled using C++ vSC4.2. The source code for this routine is columnInfiltration.c (CRWMS M&O 2000a).

The input files used for this calculation are: Glaciall.NV, Glacialm.NV, Glacialu.NV, Monsoonl.NV, Monsoonm.NV, Monsoonu.NV, Yml.NV, Ymm.NV, Ymu.NV, and column.data (CRWMS M&O 2000a). The output file is infiltration.tex (CRWMS M&O 2000a).

ROUTINE PURPOSE AND VALIDATION

The purpose of this routine is to calculate the infiltration at a given location using Gaussian interpolation method (Assumption 5.1.2).

The Gaussian weighting function is:

$$I = \sum_{i=1}^n I_i \cdot W_i \quad (\text{Eq XIV-1})$$

where

$$W = e^{-\left[\left(\frac{D}{\text{Scale}}\right)^2\right]} \quad (\text{Eq XIV-2})$$

where:

- I -Interpolated infiltration
- I_i -Value at point i, D meters away
- D -Plan distance between points.
- n -Number of points in data set
- W -Calculated weight assigned to each value ($W=W_i$)
- Scale -Effective radius of influence (Scale = 50ft)

Source: (Isaaks and Srivastava 1989, p. 208) and (Kitanidis 1997, p. 54)

Documentation of the accuracy of this routine is in the form of a test case. The test case involves the interpolation of the infiltration rate at an arbitrary reference location (242000N, 168000E) given infiltration rates at five various points. The input files for the test case are mason.NV and columninfiltration_tst.dat (CRWMS M&O 2000a). The output file from this test case is columninfiltration_tst.out (CRWMS M&O 2000a). The hand calculation that verifies the accuracy of the test case follows:

Combining Equations 3 and 4 from Section 4.1.6.4, and replacing distance with the distance between two points formula:

$$I = \sum_{i=1}^n I_i \cdot e^{-\left[\left(\frac{\sqrt{(X-X_i)^2 + (Y-Y_i)^2}}{\text{Scale}} \right)^2 \right]}$$

$$I = \sum_{i=1}^n I_i \cdot e^{-\left(\frac{(X-X_i)^2 + (Y-Y_i)^2}{\text{Scale}^2} \right)}$$

where:

- I -Interpolated infiltration
- X -Reference Easting, =168000.
- Y -Reference Northing, =242000
- I₁ -Infiltration at point 1, =1.94718
- I₂ -Infiltration at point 2, =1.23309
- I₃ -Infiltration at point 3, =0
- I₄ -Infiltration at point 4, =0.45
- I₅ -Infiltration at point 5, =0.54
- X₁ -Easting at point 1, = 242645.935
- X₂ -Easting at point 2, = 242645.830
- X₃ -Easting at point 3, = 242645.725
- X₄ -Easting at point 4, = 242645.621
- X₅ -Easting at point 5, = 242645.516
- Y₁ -Northing at point 1, = 168192.021
- Y₂ -Northing at point 2, = 168222.029
- Y₃ -Northing at point 3, = 168252.037
- Y₄ -Northing at point 4, = 168282.045
- Y₅ -Northing at point 5, = 168312.053
- n -Number of points in data set

Scale -Effective radius of influence (Scale = 50ft)

* Note: Northings, Eastings, and infiltration rates were selected randomly from Glaciall.NV (CRWMS M&O 2000a).

I = 1.941933.

The test case was run and the predicted infiltration rate is 1.941933 (CRWMS M&O 2000a-columninfiltration_tst.out). The verification of the results to 7 significant figures demonstrates the accuracy of this routine and for predicting infiltration rates at given points, and that the

routine gives the expected results. Therefore, ColumnInfiltration is qualified over the range of input parameters in the input file column.data and the 9 input files *.NV (CRWMS M&O 2000a).

ROUTINE IDENTIFICATION

Cover v1.1. This routine was developed using Matlab v5.3.0.10183 (R11). The source code is cover.m (CRWMS M&O 2000a).

The input and the output files for this routine are dft1.dat and shape1.dat respectively (CRWMS M&O 2000a).

ROUTINE PURPOSE AND VALIDATION

The purpose of this routine is to develop a block model of the repository from information contained in dft1.dat (CRWMS M&O 2000a), which is listed in Table XV-2. The output of this routine contains the edges of the block model in the file shape1.dat (CRWMS M&O 2000a), which is listed in Table XV-1. The resulting repository block model is intended to have a similar area to the original layout. The block model is used to develop infiltration rates over the repository footprint.

Range of validation: this routine is limited to developing a block model from information in the file shape1.dat (CRWMS M&O 2000a). Validation is achieved by verifying that the objective of the code (i.e., similar footprint area) was achieved. The area outlined in dft1.dat (CRWMS M&O 2000a) is calculated and compared to the area contained in the block model (shape1.dat).

Table XV-1. Area of Repository Block Model

Easting	Northing	Equation IV-1
171368.06	235822.06	4303909
170422.51	235872.29	-121804376
170343.91	234392.62	-125402076
170205.80	234399.95	-195258392
170083.53	232098.24	-196365687
170221.63	232090.90	-28610852
170204.16	231762.08	-32257943
171149.71	231711.85	347432200
171368.06	235822.06	352179357
Total area:		<u>4216139</u>

The exact area of a solid by coordinates is found by the following equation:

$$Area = \frac{1}{2} \cdot [x_1(y_2 - y_{(n)}) + x_2(y_3 - y_1) + \dots + x_{(n)}(y_1 - y_{(n-1)})] \quad (\text{Eq. XV-1})$$

where:

Area -area enclosed by coordinates
 x -x coordinate
 y -y coordinate

n -last point of figure
Source: (Hartman 1992, p. A-37)

The routine is verified by finding the area of the repository using equation XV-1. The routine predicted an area of 4,216,139 ft² (see Table XV-1), and the actual area is 4,310,041 ft² (see Table XV-2). This is an error of less than three percent. This documents the accuracy of the output of this routine. Therefore, cover provides the correct results over the range of input parameters in the input file dft1.dat (CRWMS M&O 2000a).

Table XV-2. Actual Area of Repository in Ft²

East Boundary		West Boundary		from Equation IV-1	
Northing	Easting	Northing	Easting	East pts	West pts
235997.80	170544.61	235732.05	171362.51	19825810.91	26327279.22
235964.55	170515.90	235690.53	171359.24	-8505333.09	10680821.43
235898.04	170458.47	235607.39	171353.01	-12019879	14298551.92
235823.52	170425.70	235523.64	171348.62	-13295761	14349590.18
235742.01	170414.44	235439.90	171344.23	-14059191.3	14348365.82
235658.52	170409.28	235356.16	171339.84	-14227470.8	14347998.2
235575.03	170404.11	235272.42	171335.46	-14227039.1	14348488.1
235491.54	170398.95	235188.67	171331.07	-14226608.3	14348120.46
235408.05	170393.78	235104.93	171326.68	-14226176.7	14346896.18
235324.56	170388.62	235021.19	171322.29	-14225745.9	14346528.56
235241.07	170383.45	234937.45	171317.90	-14238944.9	14347017.54
235157.42	170378.77	234853.70	171313.51	-14259851.2	14346649.89
235073.68	170374.38	234769.96	171309.12	-14267150.6	14345425.71
234989.94	170369.99	234686.22	171304.73	-14267634.8	14345058.09
234906.19	170365.60	234602.48	171300.35	-14267267.2	14345547.81
234822.45	170361.21	234518.73	171295.96	-14266047.7	14345180.17
234738.71	170356.83	234434.99	171291.57	-14265680.9	14343956.07
234654.97	170352.44	234351.25	171287.18	-14266165.1	14343588.45
234571.22	170348.05	234267.51	171282.79	-14120149.9	14344077.25
234489.19	170338.41	234183.76	171278.40	-13495060.5	14343709.61
234412.77	170311.48	234100.02	171274.01	-12918977.3	14342485.6
234337.48	170281.06	234016.28	171269.62	-12819609.6	14342117.98
234262.20	170250.64	233932.54	171265.24	-12817319.4	14342607.52
234186.91	170220.23	233848.79	171260.85	-12985250.2	14342239.88
234109.63	170195.95	233765.05	171256.46	-13568021.1	14341015.96
234027.47	170186.69	233681.31	171252.07	-13998706.2	14340648.34
233945.12	170178.03	233597.57	171247.68	-14015011.7	14341136.96
233862.76	170169.37	233513.82	171243.29	-14014298.5	14340769.32
233780.41	170160.72	233430.08	171238.90	-14013586.1	14339545.49
233698.05	170152.06	233346.34	171234.51	-14013723.7	14339177.87
233615.69	170143.41	233262.60	171230.13	-14012160.5	14339667.24
233533.34	170134.75	233178.85	171225.74	-14011447.3	14339299.6
233450.98	170126.10	233095.11	171221.35	-14010735	14338075.85
233368.63	170117.44	233011.37	171216.96	-14010021.8	14337708.23
233286.27	170108.78	232927.63	171212.57	-14010159.1	14338196.67
233203.91	170100.13	232843.88	171208.18	-14008596.2	14337829.03
233121.56	170091.47	232760.14	171203.79	-14007883	14336605.37
233039.20	170082.82	232676.40	171199.40	-14007170.6	14336237.76
232956.85	170074.16	232592.66	171195.02	-14006457.4	14335870.97
232874.49	170065.50	232508.92	171190.63	-14006594.6	14336359.31
232792.13	170056.85	232425.17	171186.24	-14317086.2	14335991.67
232706.11	170059.48	232341.43	171181.85	-14949078.6	14334768.12
232616.32	170073.70	232257.69	171177.46	-15270917.5	14334400.5
232526.53	170087.93	232173.95	171173.07	-15272195.2	14334888.75
232436.74	170102.15	232090.20	171168.68	-15273472	14334521.11
232346.95	170116.37	232006.46	171164.29	-15274748.9	14333297.64
232257.16	170130.59	231922.72	171159.91	-15276025.7	14332930.86
232167.37	170144.81	231838.98	171155.52	-15277302.5	14333419.02
232077.58	170159.03	231755.23	171151.13	-15277728.5	14333051.38
231987.80	170173.25	231671.49	171146.74	-15279005.3	14331828.01
231898.01	170187.47	231587.75	171142.35	-11461275.2	10748595.29
231853.11	170194.58	231545.88	171140.16	-29965308.7	-22706876.4
		SUM:		-709051221	713361262
					4310041

ATTACHMENT XVI QUALIFICATION OF Rme6

ROUTINE IDENTIFICATION

Rme6 v1.1. This routine was compiled using C++ vSC4.2. The source code for this routine is rme6.c (CRWMS M&O 2000a).

The input files are tspa99_primary_mesh, UZ99_3.grd, and l4c3.dat (CRWMS 2000a). The output file name is LSL99-YMESH (CRWMS 2000a).

ROUTINE PURPOSE AND VALIDATION

The purpose of this routine is to reformat and combine the files tspa99_primary_mesh and UZ99_3.grd into a single file, LBL99-YMESH which YMESH V1.53 reads as “world view” data.

To demonstrate that rme6 performed in the correct manner, it was necessary to inspect a few lines from sections of the two input files and the output file to see that key information had been transferred correctly. The first several lines of the element and connectivity sections of tspa99_primary_mesh were extracted to files “elem10” and “conn10” and read into Microsoft Excel 97 in order to enhance their readability for this document. The first several lines of the UZ99_3.grd were extracted into a file “vert9,” manually joined in groups of three consecutive ones (as the data will be joined later), and read into Excel in order to make them comprehensible in this document. The resulting three Excel generated tables of input data are shown below.

tspa99_primary_mesh:

ELEME

1Aa 1	tcw11	2.332E+05	169398.601	236623.643	1626.0963
12a 1	tcw12	3.244E+06	169398.601	236623.643	1606.4657
1Ba 1	tcw12	3.244E+06	169398.601	236623.643	1569.837
21a 1	ptn21	6.724E+05	169398.601	236623.643	1547.7263
22a 1	ptn22	1.502E+06	169398.601	236623.643	1535.4527
23a 1	ptn23	1.238E+06	169398.601	236623.643	1519.984
24a 1	ptn24	2.919E+06	169398.601	236623.643	1496.5161
25a 1	ptn25	2.684E+06	169398.601	236623.643	1464.887
2Ca 1	ptn25	2.684E+06	169398.601	236623.643	1434.5821

CONNE

22a 1	21a 1	3	8.4773E+00	3.7963E+00	8.8566E+04	-1E+00	1.69E+05	2.37E+05	1.54E+03
21a 1	1Ba 1	3	3.7963E+00	1.8314E+01	8.8566E+04	-1E+00	1.69E+05	2.37E+05	1.55E+03
1Ba 1	12a 1	3	1.8314E+01	1.8314E+01	8.8566E+04	-1E+00	1.69E+05	2.37E+05	1.59E+03
12a 1	1Aa 1	3	1.8314E+01	1.3163E+00	8.8566E+04	-1E+00	1.69E+05	2.37E+05	1.62E+03
23a 1	22a 1	3	6.9915E+00	8.4773E+00	8.8566E+04	-1E+00	1.69E+05	2.37E+05	1.53E+03
24a 1	23a 1	3	1.6477E+01	6.9915E+00	8.8566E+04	-1E+00	1.69E+05	2.37E+05	1.51E+03
25a 1	24a 1	3	1.5152E+01	1.6477E+01	8.8566E+04	-1E+00	1.69E+05	2.37E+05	1.48E+03
2Ca 1	25a 1	3	1.5152E+01	1.5152E+01	8.8566E+04	-1E+00	1.69E+05	2.37E+05	1.45E+03

26a 1	2Ca 1	3	6.0487E+00	1.5152E+01	8.8566E+04	-1E+00	1.69E+05	2.37E+05	1.42E+03
-------	-------	---	------------	------------	------------	--------	----------	----------	----------

UZ99_g.grd:

169251.917	236795.473	169201.033	236473.209	0	a 1	B-1
169201.033	236473.209	169428.63	236411.341	0	a 1	b14
169428.63	236411.341	169501.175	236823.139	0	a 1	b 2
169501.175	236823.139	169251.917	236795.473	0	a 1	a31
172943.786	230984.566	172730.132	231087.475	0	a 2	b33
172730.132	231087.475	172487.977	231043.026	0	a 2	a94
172487.977	231043.026	172606.485	230777.016	0	a 2	b30
172606.485	230777.016	172683.106	230740.154	0	a 2	b99
172683.106	230740.154	172829.738	230784.794	0	a 2	c 0

The first several lines of each section of output file LBL99-YMESH are shown below as written.

LBL99-YMESH:

\$elc

% 1Aa_1	tcw11	2.332000e+05	1.693986e+05	2.366236e+05	1.626096e+03
% 12a_1	tcw12	3.244000e+06	1.693986e+05	2.366236e+05	1.606466e+03
% 1Ba_1	tcw12	3.244000e+06	1.693986e+05	2.366236e+05	1.569837e+03
% 21a_1	ptn21	6.724000e+05	1.693986e+05	2.366236e+05	1.547726e+03
% 22a_1	ptn22	1.502000e+06	1.693986e+05	2.366236e+05	1.535453e+03
% 23a_1	ptn23	1.238000e+06	1.693986e+05	2.366236e+05	1.519984e+03
% 24a_1	ptn24	2.919000e+06	1.693986e+05	2.366236e+05	1.496516e+03
% 25a_1	ptn25	2.684000e+06	1.693986e+05	2.366236e+05	1.464887e+03
% 2Ca_1	ptn25	2.684000e+06	1.693986e+05	2.366236e+05	1.434582e+03

\$con

% 22a_1	21a_1	3	8.477300e+00	3.796300e+00	8.856600e+04	-1.000000e+00
% 21a_1	1Ba_1	3	3.796300e+00	1.831400e+01	8.856600e+04	-1.000000e+00
% 1Ba_1	12a_1	3	1.831400e+01	1.831400e+01	8.856600e+04	-1.000000e+00
% 12a_1	1Aa_1	3	1.831400e+01	1.316300e+00	8.856600e+04	-1.000000e+00
% 23a_1	22a_1	3	6.991500e+00	8.477300e+00	8.856600e+04	-1.000000e+00
% 24a_1	23a_1	3	1.647700e+01	6.991500e+00	8.856600e+04	-1.000000e+00
% 25a_1	24a_1	3	1.515200e+01	1.647700e+01	8.856600e+04	-1.000000e+00
% 2Ca_1	25a_1	3	1.515200e+01	1.515200e+01	8.856600e+04	-1.000000e+00
% 26a_1	2Ca_1	3	6.048700e+00	1.515200e+01	8.856600e+04	-1.000000e+00

\$vertices

169251.92	236795.47	169201.03	236473.21	0.00	3601	1*
169201.03	236473.21	169428.63	236411.34	0.00	3601	3714
169428.63	236411.34	169501.17	236823.14	0.00	3601	3702
169501.17	236823.14	169251.92	236795.47	0.00	3601	3631
172943.79	230984.57	172730.13	231087.48	0.00	3602	3733
172730.13	231087.48	172487.98	231043.03	0.00	3602	3694
172487.98	231043.03	172606.48	230777.02	0.00	3602	3730
172606.48	230777.02	172683.11	230740.15	0.00	3602	3799
172683.11	230740.15	172829.74	230784.79	0.00	3602	3800

By visual inspection it was clear that all the information from the ELEME section of tspa99_primary_mesh was entered unchanged into the \$elc section of LBL99-YMESH except the blank character in the middle of element names, like “22a 1,” had been replaced by an underscore. Also, by inspection, it was clear that the first seven fields of information from the CONNE section of tspa99_primary_mesh had been transferred to the \$con section of LBL99-YMESH without major change except for the blank-to-underscore change in element names. The last 3 columns of CONNE information were eliminated because they were not needed in the output file. Finally, by inspection it was observed that the (x,y) edge vertex coordinates and succeeding zero value from UZ99_3.grid were not modified in transfer to the \$vertices section of LBL99-YMESH, but the names of the two columns separated by the edge, such as “a 1” and “B-1” in the first row of \$vertices, had been *converted to integers* as required by YMESH. YMESH was able to read LBL99-YMESH as input and to draw an image of the mesh which was in agreement with other pictures of Yucca Mountain coring meshes. Therefore, it was concluded that rme6 was performing the task of converting data in the expected manner to a correct YMESH world view format.

ATTACHMENT XVII NORMALIZED INFILTRATION RATES

In this attachment the x,y locations of the 31 blocks in the repository block model are justified. This information is then used to normalize the infiltration rates at the 31 points (Table XVII-1)

The repository block model developed in Attachment XV, shape1.dat (see Figure XVII-1), is divided into 31 sections. The block model is composed of a rectangle with a smaller rectangle attached to the southern half of the west boundary of the repository. The 31 sections of the block model are derived by divided the block model into 4 columns with seven rows, plus one additional column (3 rows) in the extension on the southwest side of the repository (Table XVII-1 and Figure XVII-1). The location of the 31 elements (Table XVII-1) is easily checked with coordinate geometry. One example is given:

The Northern row of elements are L1c1-L1c4, as shown in the example below. To check their spacing, find the distance between the points and then verify that the slope of the line segments between points is similar. The similar distances and slopes between points verifies that the first row of points represent block elements of similar size. Calculations presented in Table XVI-1 verify that the repository block elements are similarly sized. The information in Table XVI-1 is in the file column.data (CRWMS M&O 2000a).

ID	Easting (ft)	Northing (ft)	Points	Distance (ft)	Slope (radians)
l1c1	171234.3	235534.8	c1-c2	236.7	-0.053
l1c2	170997.9	235547.3	c2-c3	236.7	-0.053
l1c3	170761.5	235559.9	c3-c4	236.7	-0.053
l1c4	170525.1	235572.4			

(Portion of Table XVII-1)

Note: Slope is the quotient of ΔY and ΔX .

The average infiltration rate in the modeled repository is different than the average infiltration rate in the actual repository. To offset this difference, the infiltration rates at the 31 locations are normalized (Table XVII-2). The normalized infiltration rate is the product of the estimated infiltration rate and a normalization factor. The normalization factor is the quotient of the average normalized infiltration and the actual infiltration. The average normalized infiltration is the average of the estimated infiltration at the 31 block element locations (CRWMS M&O 2000a, *.out). The average actual infiltration is included in the output from ColumnInfiltration (CRWMS M&O 2000a, *_convert.out).

(NORTHINGS)

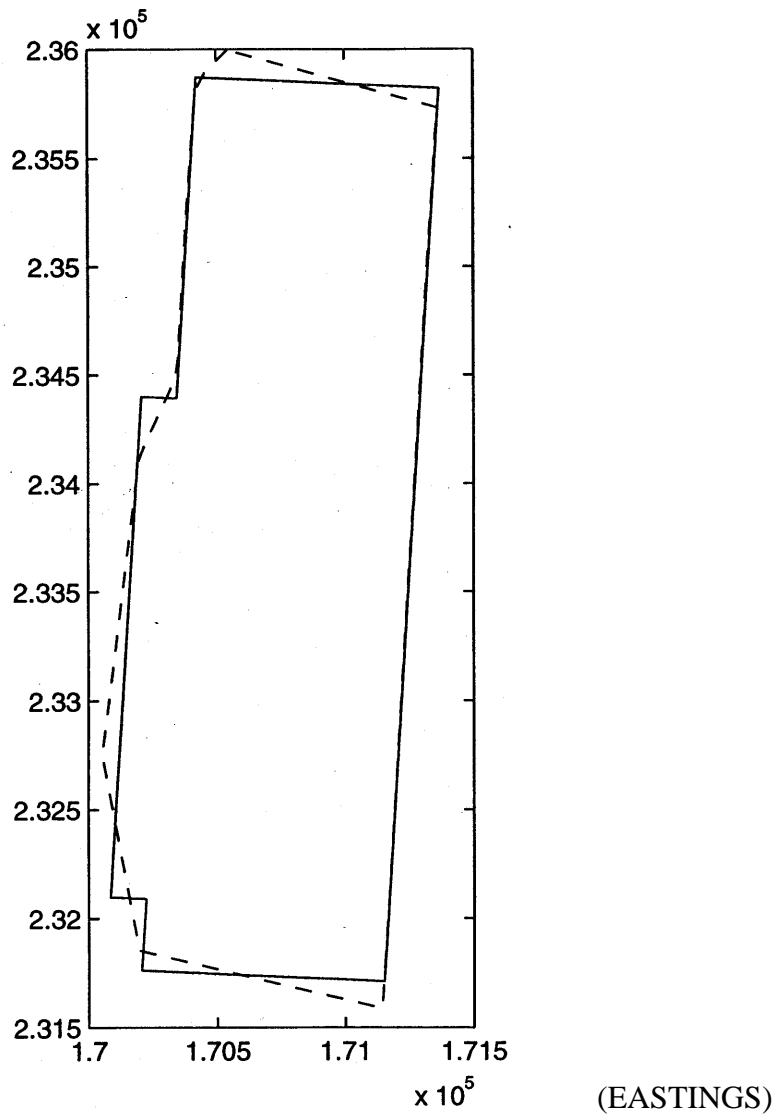


Figure XVII-1. Repository and Repository Block Model

Note: The dotted line is from the drift endpoints in the file dft1.dat (CRWMS M&O 2000a) and the solid line is from the file shape1.dat (CRWMS M&O 2000a) from Attachment XV.

Table XVII-1. Repository Block Model Element Locations

Block ID	Easting ft	Northing ft	Points	Distance	Slope
				(ft)	(radians)
I7c4	170338	232049.4	c4-c3	236.6	-0.053
I7c3	170574.3	232036.8	c3-c2	236.7	-0.053
I7c2	170810.7	232024.3	c2-c1	236.7	-0.053
I7c1	171047.1	232011.7			
I6c5	170221.2	232644.4	c5-c4	217.0	-0.053
I6c4	170437.9	232632.9	c4-c3	217.1	-0.053
I6c3	170654.7	232621.4	c3-c2	217.0	-0.053
I6c2	170871.4	232609.9	c2-c1	217.0	-0.053
I6c1	171088.1	232598.4			
I5c5	170252.4	233231.6	c5-c4	217.0	-0.053
I5c4	170469.1	233220.1	c4-c3	217.1	-0.053
I5c3	170685.9	233208.6	c3-c2	217.0	-0.053
I5c2	170902.6	233197.1	c2-c1	217.0	-0.054
I5c1	171119.3	233185.5			
I4c5	170283.6	233818.8	c5-c4	217.0	-0.053
I4c4	170500.3	233807.3	c4-c3	217.1	-0.054
I4c3	170717.1	233795.7	c3-c2	217.0	-0.053
I4c2	170933.8	233784.2	c2-c1	217.0	-0.053
I4c1	171150.5	233772.7			
I3c4	170462.7	234398.1	c4-c3	236.7	-0.053
I3c3	170699.1	234385.5	c3-c2	236.7	-0.053
I3c2	170935.5	234373	c2-c1	236.7	-0.053
I3c1	171171.9	234360.4			
I2c4	170493.9	234985.3	c4-c3	236.7	-0.053
I2c3	170730.3	234972.7	c3-c2	236.7	-0.053
I2c2	170966.7	234960.1	c2-c1	236.7	-0.053
I2c1	171203.1	234947.6			
I1c4	170525.1	235572.4	c4-c3	236.7	-0.053
I1c3	170761.5	235559.9	c3-c2	236.7	-0.053
I1c2	170997.9	235547.3	c2-c1	236.7	-0.053
I1c1	171234.3	235534.8			

Table XVII-2. Interpolated and Normalized Infiltration Rates

	INTERPOLATED									NORMALIZED								
	Glacial			Mons oon			YM			Glacial			Mons oon			YM		
	Low	Mean	Hi	Low	Mean	Hi	Low	Mean	Hi	Low	Mean	Hi	Low	Mean	Hi	Low	Mean	Hi
l7c4	0.278	3.684	7.090	1.025	2.256	3.487	0.000	1.025	2.559	0.392	5.211	10.031	1.493	3.252	5.014	0.000	1.493	3.608
l7c3	1.511	13.020	24.530	3.212	7.432	11.651	0.006	3.212	7.559	2.131	18.418	34.705	4.677	10.710	16.751	0.010	4.677	10.657
l7c2	1.731	15.849	29.967	3.814	9.524	15.235	0.057	3.814	8.961	2.442	22.420	42.398	5.554	13.726	21.904	0.101	5.554	12.632
l7c1	0.848	4.958	9.067	1.168	3.184	5.200	0.030	1.168	3.839	1.196	7.013	12.829	1.700	4.588	7.476	0.053	1.700	5.413
l6c5	7.645	21.725	35.804	6.462	12.314	18.165	3.594	6.462	13.185	10.785	30.732	50.657	9.410	17.746	26.117	6.423	9.410	18.588
l6c4	1.476	33.842	66.208	7.761	22.656	37.551	0.000	7.761	19.471	2.082	47.872	93.674	11.302	32.651	53.989	0.000	11.302	27.449
l6c3	2.623	11.716	20.810	2.870	7.149	11.427	0.088	2.870	6.790	3.700	16.574	29.442	4.180	10.303	16.429	0.158	4.180	9.572
l6c2	1.824	7.766	13.708	2.161	4.970	7.780	0.333	2.161	4.950	2.573	10.986	19.395	3.147	7.163	11.186	0.596	3.147	6.978
l6c1	1.617	10.660	19.702	2.663	6.545	10.426	0.043	2.663	6.385	2.281	15.079	27.875	3.879	9.432	14.990	0.076	3.879	9.001
l5c5	6.474	21.117	35.760	5.787	11.980	18.172	1.947	5.787	12.368	9.134	29.872	50.594	8.428	17.265	26.127	3.479	8.428	17.436
l5c4	2.157	42.583	83.009	9.896	28.430	46.963	0.000	9.896	24.717	3.043	60.237	117.443	14.412	40.972	67.522	0.000	14.412	34.845
l5c3	4.065	14.103	24.140	3.900	9.104	14.308	0.690	3.900	8.635	5.735	19.949	34.154	5.680	13.120	20.571	1.233	5.680	12.173
l5c2	3.604	19.155	34.706	5.078	12.287	19.495	0.451	5.078	11.730	5.085	27.097	49.103	7.395	17.707	28.029	0.807	7.395	16.537
l5c1	0.084	0.577	1.071	0.455	0.303	0.150	0.000	0.455	1.302	0.118	0.816	1.515	0.663	0.436	0.216	0.000	0.663	1.835
l4c5	2.536	14.289	26.043	3.742	10.042	16.342	0.471	3.742	8.728	3.577	20.214	36.847	5.449	14.472	23.496	0.842	5.449	12.305
l4c4	1.412	29.690	57.967	6.957	20.036	33.115	0.000	6.957	17.227	1.992	41.998	82.014	10.132	28.876	47.611	0.000	10.132	24.286
l4c3	3.915	27.330	50.745	6.966	16.716	26.467	0.029	6.966	16.737	5.523	38.660	71.795	10.144	24.091	38.053	0.052	10.144	23.595
l4c2	1.910	19.740	37.570	4.744	11.727	18.710	0.001	4.744	11.278	2.694	27.923	53.155	6.909	16.900	26.900	0.003	6.909	15.899
l4c1	2.349	13.348	24.346	3.292	8.391	13.491	0.098	3.292	7.791	3.314	18.881	34.446	4.794	12.093	19.396	0.176	4.794	10.983
l3c4	3.505	45.970	88.435	10.902	30.526	50.151	0.000	10.902	26.916	4.944	65.028	125.120	15.877	43.993	72.104	0.000	15.877	37.945
l3c3	0.636	2.965	5.293	0.895	1.830	2.765	0.059	0.895	2.106	0.897	4.194	7.489	1.304	2.637	3.975	0.105	1.304	2.969
l3c2	0.163	0.899	1.634	0.333	0.341	0.350	0.006	0.333	0.836	0.230	1.271	2.312	0.485	0.492	0.503	0.012	0.485	1.179
l3c1	1.269	19.091	36.912	4.350	13.093	21.837	0.085	4.350	11.005	1.791	27.005	52.224	6.335	18.869	31.395	0.151	6.335	15.514
l2c4	6.417	41.445	76.473	10.985	29.341	47.696	1.105	10.985	25.800	9.052	58.627	108.195	15.998	42.285	68.574	1.974	15.998	36.372
l2c3	2.955	44.655	86.354	8.247	28.275	48.303	0.380	8.247	25.791	4.169	63.168	122.176	12.011	40.749	69.448	0.680	12.011	36.359
l2c2	0.054	16.541	33.029	0.973	6.352	11.731	0.000	0.973	6.517	0.076	23.399	46.730	1.416	9.154	16.866	0.001	1.416	9.188
l2c1	0.092	0.518	0.944	0.278	0.174	0.069	0.000	0.278	0.692	0.130	0.733	1.336	0.406	0.250	0.099	0.000	0.406	0.975
l1c4	0.174	13.472	26.770	2.071	8.032	13.993	0.001	2.071	7.583	0.245	19.057	37.875	3.015	11.575	20.119	0.002	3.015	10.690
l1c3	1.702	22.932	44.162	5.363	15.164	24.965	0.130	5.363	13.144	2.400	32.439	62.482	7.809	21.854	35.894	0.232	7.809	18.530
l1c2	0.390	1.506	2.622	0.602	0.652	0.703	0.119	0.602	1.419	0.550	2.130	3.709	0.877	0.940	1.010	0.212	0.877	2.001
l1c1	0.189	9.560	18.931	0.394	6.941	13.489	0.027	0.394	4.094	0.266	13.523	26.784	0.574	10.004	19.393	0.047	0.574	5.772
Avg Int.	2.116	17.571	33.026	4.108	11.154	18.200	0.315	4.108	10.326	2.985	24.856	46.726	5.982	16.074	26.166	0.562	5.982	14.558
Actual	2.985	24.856	46.726	5.982	16.074	26.166	0.562	5.982	14.558	2.985	24.856	46.726	5.982	16.074	26.166	0.562	5.982	14.558

(Normalized value)=(Interpolated value * Actual avg/Avg of interpolated values). All values are in mm/yr.

Avg. Int. = Average of Interpolated values, or the average of each column.

Actual = actual average of infiltration values that occur within the repository footprint. This value is included in the *_convert.out files (CRWMS M&O 2000a).

ATTACHMENT XVIII INPUT AND OUTPUT FILES FOR RADPRO, XTOOL, MSTHAC, YMESH AND CONVERTCOORDS

The input files for RADPRO v3.22 are DDT60-03v.radin, l4c3-DDT60-03v.radin, DDT60-03pbf.radin, l4c3-DDT60-03pbf.in and l4c3-DDT60-03bff.in and the output files are DDT60-03v.radout, DDT60-03pbf.radout and DDT60-03.radout (CRWMS M&O 2000a).

The input files for XTOOL v10.1 are the NUFT output files listed on Table 3-6 through Table 3-9 (CRWMS M&O 2000a). There are not output files since XTOOL is a graphical presentation routine.

The input files for MSTHAC v6.0 are the results from the NUFT output files listed on Table 3-6 through Table 3-9 and the outfiles are TSPA_SR_mean.ext, TSPA_SR_lower.ext and TSPA_SR_upper.ext (CRWMS M&O 2000a).

The input file for YMESH v1.53 is LBL99-YMESH and the output file is column.dat (CRWMS M&O 2000a).

The input files for CONVERTCOORDS v1.1 are ym*.dat, monsoon*.dat and glacial*.dat and the output files are ym*.NV, monsoon*.NV and glacial*.NV (CRWMS M&O 2000a).

ATTACHMENT XIX QUALIFICATION OF SplitEXT

ROUTINE IDENTIFICATION

SplitEXT v1.0. This routine was compiled using C++ vSC4.2. The source consists of the files splitEXT.c and myFunctions.h (CRWMS M&O 2000a). MyFunctions.h is used to check input data format and memory allocation.

The 3 input files are TSPA_SR_<infil>.ext, TSPA_SR_<infil>_T_pillar_Xdist.ext (CRWMS 2000a). The 111 output files are TSPA_SR_<infil>_<variable>.ext (CRWMS 2000a).

ROUTINE PURPOSE AND VALIDATION

XTOOL is the graphical post-processor for NUFT. Files to be read by XTOOL have a special format and names ending in “.ext.” MSTHAC, a data extraction tool, writes .ext files. The purpose of splitEXT is to split a MSTHAC .ext output file containing output for many variables and several waste packages into separate .ext files containing the output for just *one* of the variables and *all* of the waste packages.

In order to check that splitEXT performs in the expected manner, a sample MSTHAC type .ext file, bb.ext, was created. This file contained data for two variables, bread and butter, and three waste packages, wp1, wp2, and wp3. A listing follows:

bb.ext:

```
1          1
2  splitEXT example
3          10
4  internal
5  NUFT version cvs-9-23-98b (SUN/SOLARIS)
6  0
7  VARIABLE
8  $gdef
9  $type rectangular
10 $nx 2
11 $ny 2
12 $nz 1
13 $order xyz
14 $dx
15 1.000000
16 1.000000
17 $dy
18 1.000000
19 1.000000
20 $dz
21 1.000000
22 $end_internal_grid
23 $OperatingSystem SunOS s139.es.llnl.gov 5.5.1 Generic_103640-03 sun4u sparc
24 SUNW,Ultra-2
```

```

25 $C-Compiler cc: WorkShop Compilers 4.2 30 Oct 1996 C 4.2
26 $FortranCompiler f77: WorkShop Compilers 4.2 30 Oct 1996 FORTRAN 77 4.2
27 $RunID 0000
28 $RunDate Thu Dec 2 01:39:27 1999
29 6
30 bread_wp1
31 bread_wp2
32 bread_wp3
33 butter_wp1
34 butter_wp2
35 butter_wp3
36 0
37 4
38 h@m.i.r#1:1:1
39 h@m.i.r#2:1:1
40 h@m.i.r#1:2:1
41 h@m.i.r#2:2:1
42 0
43 THIST
44 EVAR bread_wp1
45 T *
46 E *
47
48 THIST
49 EVAR bread_wp2
50 T *
51 E *
52
53 THIST
54 EVAR bread_wp3
55 T *
56 E *
57
58 THIST
59 EVAR butter_wp1
60 T *
61 E *
62
63 THIST
64 EVAR butter_wp2
65 T *
66 E *
67
68 THIST
69 EVAR butter_wp3
70 T *
71 E *
72
73
74 0.0000000000000000e+00
75 1
76 4
77 1.000000e+01
78 2.000000e+01
79 3.000000e+01
80 4.000000e+01
81 0.0000000000000000e+00

```



```

82          2
83          4
84 0.100000e+02
85 1.100000e+02
86 4.100000e+02
87 9.100000e+02
88 0.000000000000000e+00
89          3
90          4
91 3.100000e+03
92 3.200000e+03
93 3.300000e+03
94 3.500000e+03
95 0.000000000000000e+00
96          4
97          4
98 4.640000e+04
99 4.270000e+04
100 4.080000e+04
101 4.010000e+04
102 0.000000000000000e+00
103          5
104          4
105 5.000000e+05
106 5.160000e+05
107 5.090000e+05
108 5.040000e+05
109 0.000000000000000e+00
110          6
111          4
112 2.000000e+06
113 4.000000e+06
114 8.000000e+06
115 1.600000e+07

```

bb_bread.ext:

```

1          1
2 splitEXT example
3          10
4 internal
5 NUFT version cvs-9-23-98b (SUN/SOLARIS)
6 0
7 VARIABLE
8 $gdef
9 $type rectangular
10 $nx 2
11 $ny 2
12 $nz 1
13 $order xyz
14 $dx
15 1.000000
16 1.000000
17 $dy
18 1.000000

```

```

19 1.000000
20 $dz
21 1.000000
22 $end_internal_grid
23 $OperatingSystem SunOS s139.es.llnl.gov 5.5.1 Generic_103640-03 sun4u sparc
24 SUNW,Ultra-2
25 $C-Compiler cc: WorkShop Compilers 4.2 30 Oct 1996 C 4.2
26 $FortranCompiler f77: WorkShop Compilers 4.2 30 Oct 1996 FORTRAN 77 4.2
27 $RunID 0000
28 $RunDate Thu Dec 2 01:39:27 1999
29 3
30 bread_wp1
31 bread_wp2
32 bread_wp3
33 0
34 4
35 h@m.i.r#1:1:1
36 h@m.i.r#2:1:1
37 h@m.i.r#1:2:1
38 h@m.i.r#2:2:1
39 0
40 THIST
41 EVAR bread_wp1
42 T *
43 E *
44
45 THIST
46 EVAR bread_wp2
47 T *
48 E *
49
50 THIST
51 EVAR bread_wp3
52 T *
53 E *
54
55 0.000000
56 1
57 4
58 10.000000
59 20.000000
60 30.000000
61 40.000000
62 0.000000
63 2
64 4
65 10.000000
66 110.000000
67 410.000000
68 910.000000
69 0.000000
70 3
71 4
72 3100.000000
73 3200.000000
74 3300.000000
75 3500.000000

```

bb_butter.ext:

```
1          1
2  splitEXT example
3          10
4  internal
5  NUFT version cvs-9-23-98b (SUN/SOLARIS)
6  0
7  VARIABLE
8  $gdef
9  $type rectangular
10 $nx 2
11 $ny 2
12 $nz 1
13 $order xyz
14 $dx
15 1.000000
16 1.000000
17 $dy
18 1.000000
19 1.000000
20 $dz
21 1.000000
22 $end_internal_grid
23 $OperatingSystem SunOS s139.es.llnl.gov 5.5.1 Generic_103640-03 sun4u sparc
24 SUNW,Ultra-2
25 $C-Compiler cc: WorkShop Compilers 4.2 30 Oct 1996 C 4.2
26 $FortranCompiler f77: WorkShop Compilers 4.2 30 Oct 1996 FORTRAN 77 4.2
27 $RunID 0000
28 $RunDate Thu Dec 2 01:39:27 1999
29 3
30 butter_wp1
31 butter_wp2
32 butter_wp3
33 0
34 4
35 h@m.i.r#1:1:1
36 h@m.i.r#2:1:1
37 h@m.i.r#1:2:1
38 h@m.i.r#2:2:1
39 0
40 THIST
41 EVAR butter_wp1
42 T *
43 E *
44
45 THIST
46 EVAR butter_wp2
47 T *
48 E *
49
50 THIST
51 EVAR butter_wp3
52 T *
53 E *
```

```

54
55 0.000000
56 1
57 4
58 46400.000000
59 42700.000000
60 40800.000000
61 40100.000000
62 0.000000
63 2
64 4
65 500000.000000
66 516000.000000
67 509000.000000
68 504000.000000
69 0.000000
70 3
71 4
72 2000000.000000
73 4000000.000000
74 8000000.000000
75 16000000.000000

```

The file bb.ext was input to splitEXT and produced the output files bb_bread.ext and bb_butter.ext (CRWMS M&O 2000a, also listed above).

The splitEXT output files contain the relevant data from the master input file bb.ext. This is verified through visual inspection. SplitEXT splits input files with multiple variables into multiple files, each containing a portion of the original file. The file bb.ext is split into the files bb_bread.ext and bb_butter.ext. This is verified in Table XIX-1 by showing the source in bb.ext for every line in the output files.

Table XIX-1. splitEXT Validation.

bb.ext	bb_bread.ext	bb_butter.ext
1-28	1-28	1-28
29	=bb.ext line 29 /2	=bb.ext line 29 /2
30-32	30-32	
33-35		30-32
36-42	33-39	33-39
43-57	40-54	
58-72		40-54
73		55
74-95	54-75	
96-115		56-75

Lines 56, 63, and 70 contain the numbers 1, 2, and 3 (respectively). The corresponding lines in bb.ext contain the numbers 4, 5, and 6 (respectively). These lines represent the variable number in the file. In bb.ext the variable butter_wp3 is variable 6 (bb.ext lines 35 and 110). In the file bb_butter.ext, the variable butter_wp3 is the 3rd variable (see lines 32 and 70).

Based on the visual comparison in table XIX-1, splitEXT operates as expected and provides accurate results over the range of input parameters in the input files (CRWMS M&O 2000a, all *.ext files).

ATTACHMENT XX DEVELOPMENT OF LINEAR EXTRAPOLATION FORMULA

An equation for extrapolating for the temperature 1000m below the water table is developed.

Beginning with the conduction equation (Source: Incropera and Dewitt 1985, pg. 5):

$$q = \lambda \cdot \frac{\Delta T}{Z} \quad \text{Eq. XX-1a}$$

For multiple layers of material, with constant heat flux:

$$\lambda_o = \frac{\sum Z_i}{\sum \frac{Z_i}{\lambda_i}} \quad \text{Eq. XX-1b}$$

Solving for the heat flux between the ground surface and water table:

$$q = \lambda_o \cdot \frac{T_w - T_s}{\sum Z_i} \quad \text{Eq. XX-2}$$

Solving for the heat flux across the water table:

$$q = \lambda_w \cdot \frac{T_b - T_w}{B} \quad \text{Eq. XX-3}$$

Combining Equations XX-2 and XX-3:

$$\lambda_w \cdot \frac{T_b - T_w}{B} = \lambda_o \cdot \frac{T_w - T_s}{\sum Z_i}$$

Solving for T_b :

$$T_b = T_w + B \cdot \frac{\lambda_o}{\lambda_w} \cdot \left(\frac{T_w - T_s}{\sum Z_i} \right) \quad \text{Eq. XX-4}$$

where:

- q -heat transfer per unit time per unit area. Constant (Assumption 5.3.2)
- λ -Thermal conductivity of material
- ΔT -Thermal gradient
- Z -Distance in direction of heat transfer
- Z_i -Thickness of the i^{th} material in a stack of layered materials.
- T_s -Temperature at top of multi layered material
- T_w -Temperature at bottom of multi layered material
- B -Distance the water table is extended downward
- T_b -Temperature at distance B below the top of the water table.
- λ_i -Thermal conductivity of the i^{th} material
- λ_o -Average thermal conductivity of a layered material
- Z_i -Thickness of the i^{th} material

* Heat transfer is in a linear direction because there is no lateral heat transfer (Assumption 5.3.1).
Substituting and rearranging:

$$T_b = T_w + B \cdot \frac{\left(\frac{\sum Z_i}{\sum \frac{Z_i}{\lambda_i}} \right)}{\lambda_w} \cdot \left(\frac{T_w - T_s}{\sum dZ_i} \right)$$

$$T_b = T_w + \frac{B \cdot (T_w - T_s)}{\lambda_w} \cdot \sum \frac{Z_i}{\lambda_i} \quad \text{Eq. XX-5}$$

where:

- T_b -Temperature at distance B below the top of the water table.
- T_w -Temperature at bottom of multi layered material
- T_s -Temperature at top of multi layered material
- B -Distance the water table is extended downward
- λ_i -Thermal conductivity of the ith material
- λ_w -Average thermal conductivity of a layered material.
- Z_i -Thickness of the ith material in a stack of layered materials.